TWENTYFIFTH EUROPEAN ROTORCRAFT FORUM

Paper n° C11

HIGH RESOLUTION AERODYNAMIC ANALYSIS OF FULL HELICOPTER CONFIGURATIONS

SPYROS G. VOUTSINAS, DIMITRIS G. TRIANTOS
NATIONAL TECHNICAL UNIVERSITY OF ATHENS, GREECE

SEPTEMBER 14-16, 1999
ROME, ITALY

ASSOCIAZIONE INDUSTRIE PER L'AEROSPAZIO, I SISTEMI E LA DIFESSA
ASSOCIAZIONE ITALIANA DI AERONAUTICA ED ASTRONAUTICA

High Resolution Aerodynamic Analysis of Full Helicopter Configurations

Spyros G. Voutsinas, Dimitris G. Triantos
National Technical University of Athens, Fluids Section,
PO Box 64070, 15710 Zografou, Athens, Greece
tel.: (+)301-7721096, fax: (+)301-7721057, e-mail: aiolos@fluid.mech.ntua.gr

Abstract

A general framework for cost effective unsteady flow predictions of high resolution around full helicopter configurations is formulated. Starting point is the Helmholtz decomposition of the velocity field in which the vortical part is associated mainly to the wake whereas the potential (irrotational part) is associated to the flow induced by the presence of moving solid boundaries. Reduction of computational cost to a minimum, is accomplished by combining vortex blob approximation of the wakes with boundary integral representations of the potential part. High resolution is achieved by introducing particle-mesh techniques in the wake and sub-grid evaluation of the boundary integral terms. In the present paper the basic part of the methodology is described and numerical results are presented for the limiting case of incompressible and inviscid fluids. Viscous as well as compressibility effects can be introduced by domain decomposition techniques, which are most suitable for taking into account such localised and close to the boundaries flow particularities. These issues are also discussed and some preliminary results are presented.

1 INTRODUCTION

The flow problems associated to helicopters and tilt rotor aircrafts constitute a separate category in CFD, because of the dominant role of several independently moving bodies and of strong vortex-to-solid interactions. To complete the picture, one should add the flexibility of the blades, the controls as well as noise which has always been an issue of major concern. This constitutes the complete aeromechanical problem. From an analysis point of view, the ultimate goal is the definition of the suitable theoretical framework within which aerodynamics, aeroelasticity and aeracoustics can be treated in combined form. This perspective has been pointed out by Morino [1] who proposes as general framework the Poincare decomposition. Alternatively one could use the Helmholtz decomposition [2]. The difference of these two theorems is in the rotational part of the flow which in the Helmhotz decomposition is expressed as volume convolution of the vorticity instead of getting it indirectly as in the Poincare theorem [1]. This is a fundamental difference, which forces all of the subsequent analysis. At NTUA the Helmholtz decomposition has been chosen for its direct link to Vortex Methods (VMs) which to our experience can provide powerful computational tools.

The most important issue when considering the complete aeromechanical problem for multi-component aircraft configurations is the computational cost. It is true that current research developments concentrate mostly on grid based CFD methods such as the finite volume and finite element methods. Besides being popular, CFD methods contain in principle all the physics and so their only drawback is the cost. It is expected that computer hardware will be able to overcome the present barriers and that in future, simulations of high resolution will be possible. Meanwhile, fast engineering tools are needed and most probably they will be always used for everyday calculations even if CFD concludes its developments soon and successfully.

Key point towards cost effective modelling is the proper use of the domain decomposition concept. To this end the flow-field is decomposed into the *near-field* in which the regions close and around the solid boundaries are contained, and the *far-field* which contains the wakes of the different components. The near-field will include any weak shock waves, the boundary layer regions as well as the part of the wakes in contact with the solid boundaries. The rationale for such a decomposition is twofold:

a) Regarding numerics, there are basically two possibilities: either use a grid based field method or a grid-free Lagrangian vortex method. Field methods are most suitable in handling boundary conditions, flow non-linearities such as shock waves and boundary layers, as well as turbulence closure. Because of the finite extent of the grid, specific inflow conditions are required. They can be set either by extending the grid over a large region and then set undisturbed conditions or by matching with a far-field solution. Extension of the grid is possible only at the expense of high numerical diffusion of free vorticity leading to suppression of the wake induced effects. This leaves matching as the only reasonable choice. On the other hand vortex methods are most suitable in solving vortex convection problems in particular because of their having minimum numerical diffusion. This is due to their inherent ability to concentrate the numerical points only in regions of significant vorticity. However vortex methods have major difficulties in handling viscous boundary conditions and therefore they are inappropriate for the near-field. All of the above, makes the combination of a field method for the near-field with a vortex method in the far-field quite attractive.

b) The limiting case of incompressible (or subsonic)

and inviscid flows has always played an important role in aerodynamics. From an engineering point of view, such an approximation besides giving a first estimate of loads and of the flow in general, for certain flight conditions, can be even a reasonable compromise. In the past, a lot of work was done on panel methods, recently renamed to Boundary Element Methods (BEMs). Extensions to compressible flows were also realised based on the full-potential equations [3, 4]. Finally, always within the same general context, there exists work on also including viscous effects based on viscous-inviscid strong interaction theory [5, 6, 7]. Common theoretical background for all these works, is the theory of boundary integral equations. The most attractive feature of this theory is that it produces grid-free numerical models which are for this reason, computationally efficient. There is an extensive literature on all aspects of boundary integral methods which is not possible to review here. There is however one important aspect which is usually overlooked. Boundary integral theory constitutes the suitable theoretical tool for defining correct matching procedure between field and vortex methods [8, 9]. There are few works in this connection, all dealing with 2D flows [8, 10]. We are not aware of any work on 3D flows. Possibly this is because all previous work concerned $\psi-\omega$ field methods which are not extendible to 3D. Also worth noticing is the lack of work on turbulent flows even for 2D flows. This is probably because almost all the work on turbulence closure has been developed for $\vec{u}-p$ and not $\psi-\omega$ formulations. In the present paper boundary integral methods are used in defining coupling conditions of $\vec{u}-p$ field methods with vortex methods.

Based on the above remarks, research work at NTUA was directed towards the development of a concise prediction tool for multi-component configurations with several options for the near-field analysis all sharing the same far-field analysis formulated by grid-free vortex methods. The code was named GENUVP (=GENeral Unsteady Vortex Particle code) because of its relation to vortex particle or vortex blob approximations. In its current state, the basic version of GENUVP, performs unsteady calculations on multi-component configurations containing one or more rotors [11, 12]. The model also includes rigid body controls and beam like elastic deformations of all blades [13, 14]. Acoustic pressure predictions are performed a posteriori using the aerodynamic results and the Ffowcs-Williams Hawkings equation [15]. The basic version uses boundary element methods (BEM) for approximating the near-field,. There are also two more versions still in the process of development. The first uses a home-made Euler finite volume solver (FLUX3D) [16] whereas the second uses an also home-made incompressible Navier Stokes solver equipped with the Spalart Almaras turbulence model (NS3D) [17]. So far they have been successfully tested the first in the case of the flow over a wing and the second in the case of the flow over a wind turbine blade with massive separation extending from the hub up-to about half of its span. The present paper focuses on the basic version of GENUVP. However indicative results from the other two versions are also presented.

2 MATHEMATICAL FORMULATION

2.1 Helmholtz decomposition

Consider the unsteady flow of an incompressible and inviscid fluid around a multi-component configuration consisted of N_B bodies. The bodies are allowed to move independently, a necessary feature for helicopter configurations. Let $\vec{u}(\vec{x};t),\vec{x}\in D,t\geq 0$ denote the velocity of the fluid where D is the flow field. Then according to Helmholtz decomposition theorem, $\vec{u}$ can be split in two parts: an irrotational and a rotational one. Usually the presence of solid boundaries is included in the irrotational part $\vec{u}_{solid}$ whereas the wakes are, as expected, included in the rotational part $\vec{u}_{wake}$. So,

$$\vec{u}(\vec{x};t)=\vec{u}_{ext}(\vec{x};t)+\vec{u}_{solid}(\vec{x};t)+\vec{u}_{wake}(\vec{x};t) \tag{1}$$

where $\vec{u}_{ext}$ denotes a given external field possibly varying in space and time. Green's theorem provides the means to express $\vec{u}_{solid}$ through surface singularity distributions suggesting the use of BEM's in approximating this term. As for $\vec{u}_{wake}$, Biot-Savart law gives,

$$\vec{u}_{wake}(\vec{x}_o;t)=\int_{D_\omega(t)}\frac{\vec{\omega}(\vec{x};t)\times(\vec{x}_o-\vec{x})}{4\pi\left|\vec{x}_o-\vec{x}\right|^3}dD \tag{2}$$

where $D_\omega(t)$ denotes the support of vorticity. From (2), the use of VMs in approximating $\vec{u}_{wake}$ is straightforward. So decomposition (1) implies as suitable numerical model the combination of BEMs with VMs. The two parts in (1) must be linked to each other through appropriate conditions which will feed $\vec{u}_{wake}$ with vorticity continuously in time. The exact form of these conditions is discussed in section 2.4.

2.2 Boundary Integral Methods and the approximation of $\vec{u}_{solid}$

Boundary Integral Methods are based on Green's theorem and are used in describing the kinematics of fluid flows. Consider a flow field D extended to infinity and bounded by a closed surface S containing all solid boundaries together with their wakes. In potential theory, wakes are introduced as vortex sheets, i.e. moving surfaces across which the velocity exhibits a tangential discontinuity whereas pressure remains continuous. In this context the scalar potential ϕ associated to a velocity field $\vec{u}$, admits the following representation:

$$(3) \qquad \phi(\vec{x}_o) = -\int_S \sigma(\vec{x})\frac{1}{4\pi r}dS - \int_S \mu(\vec{x})\frac{\partial}{\partial \nu}\frac{1}{4\pi r}dS$$

where $r = |\vec{x}_o - \vec{x}|$, $\vec{\nu}$ denotes the unit normal to S with direction towards D and σ, μ denote surface distributions of the jumps of $\partial\phi/\partial\nu$ (sources) and $-\phi$ (dipoles) respectively. Differentiating (3) [18],

$$(4) \qquad \vec{u}(\vec{x}_o) = \int_S \sigma(\vec{x})\frac{\vec{r}}{4\pi r^3}dS + \int_S \vec{\gamma}(\vec{x}) \times \frac{\vec{r}}{4\pi r^3}dS$$

where $\vec{\gamma}$ denotes the surface vorticity defined as $\vec{\gamma} = \nabla\mu \times \vec{\nu}$. Since there is only the non-entry boundary condition to satisfy for determining the two unknowns σ, μ, an artificial interior problem is specified which extends ϕ within S. Depending on the character of the interior problem chosen, the different formulations can be classified either as *indirect* or as *direct*.

Indirect formulations were first introduced by Hess [19, 18]. In all of the different existing variants, non-lifting bodies are represented by sources, thin lifting surfaces by dipoles and thick wings by a combination of the two. In the last case, μ is given specific functional form leaving free only the values of the circulation distribution which is determined by proper use of the Kutta condition along the edge of the wing. For lifting bodies active boundary is also the wake which is introduced as a surface carrying dipoles.

Direct formulations were first introduced by Morino [20] who assumed the volume within S to be stagnant. So,

$$(5) \qquad \phi(\vec{x}_o) = -\int_S \frac{\partial\phi}{\partial\nu}(\vec{x})\frac{1}{4\pi r}dS + \int_S \phi_S(\vec{x})\frac{\partial}{\partial\nu}\frac{1}{4\pi r}dS$$

In (5) $\partial\phi/\partial\nu$ is given directly by the non-entry boundary condition whereas ϕ_S is determined as solution of the integral equation obtained from (5) for $\vec{x}_o \in S$. Worth noticing is that Morino's direct potential formulation is the same for lifting and non-lifting bodies. The difference will come from the wake which imposes the existence of a discontinuity for ϕ_S along a line on the surface of any lifting body. For a blade or a wing this line can coincide with the trailing edge and the discontinuity is identical to the circulation distribution also determined by the Kutta condition.

Similarly, the direct counterpart of (4) for the velocity has the form:

$$(6) \qquad \vec{u}(\vec{x}_o) = \int_S \vec{\nu}(\vec{x}).\vec{u}(\vec{x})\frac{\vec{r}}{4\pi r^3}dS + \int_S (\vec{\nu}(\vec{x}) \times \vec{u}(\vec{x})) \times \frac{\vec{r}}{4\pi r^3}dS$$

in which $\vec{\nu}.\vec{u}$ is known from the boundary condition leaving as unknown the tangential to S velocity $\vec{\nu} \times \vec{u}$. For $\vec{x}_o \in S$, the vector product of (6) with $\vec{\nu}(\vec{x}_o)$ gives two integral equations one for each of the two unknown components of $\vec{\nu} \times \vec{u}$. The doubling of the size of the problem is certainly a drawback in using the direct velocity formulation. However the direct calculation of the surface velocity renders this formulation most suitable for coupling BEMs with either integral viscous boundary layer models or with field methods. For lifting bodies, again the wake is introduced as dipole surface, which in the direct velocity formulation is transformed into surface vorticity. More on the wake of lifting bodies and the conditions that quantify the singularity distributions on it will be discussed in subsequent sections.

Regarding the numerics of BEM's there are basically two approximation philosophies: either use dense paneling with piecewize constant singularity distributions [18,19], or introduce high order schemes [21, 22, 23]. Low order schemes are easy to implement but lead to high cost which in fact led some groups to develop high order methods. Besides being more complicated in coding them, they do not match easily with vortex methods, which have zero order accuracy. Also high order panel methods have order mismatch with standard finite volume methods, which use piecewize constant approximations in space. Finally, for lifting bodies special writing of the Kutta condition is needed [24]. For these reasons we decided to proceed with zero order BEM's without disregarding their high cost when paneling gets dense. Fortunately, it is possible to reduce significantly the cost by applying sub-grid techniques.

As pointed out early by Hess [19], exact integral evaluations are necessary only when the distance between control point and the panel center is small. In fact when the distance of the evaluation point from the panel gets bigger than 4 times the maximum diagonal of the panel, the integral evaluation can be reduced to a point calculation. Reversing this result, one can expect that the error will be also small if distant panels are grouped into larger ones over which the integrals are evaluated [25]. A strategy to such a grouping has been implemented by introducing a sequence of paneling at different levels of refinement (Fig.1). Calculations start at the lowest level (coarse paneling). Depending on the distance between the panel center and the evaluation point, the calculations will either proceed with the integral evaluation over the large panel or pass to the next and more refined level of paneling. Consider a panel of surface S, which contains n panels of the highest level in which the unknown singularity X is defined. Let I_1 denote the value of the integral evaluated over S for unitary singularity strength. Then the collective contribution of the n panels is approximated by:

$$(7) \qquad I = \sum_{i=1}^{n} I_1 \frac{S_i}{S} X_i$$

where S_i denotes the surface area of the i-th high level panel. Depending on the number of unknowns the final system is either solved directly or iteratively in which

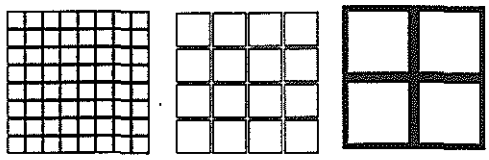

(a) The three levels of paneling

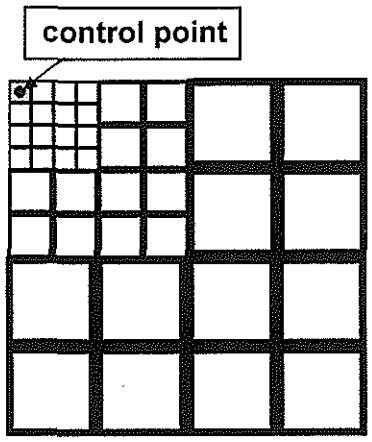

(b) The activation of the different levels

Figure 1 The sub-grid scheme for the evaluation of the boundary integrals

case the matrix need not be stored. Thus panelings of the order of several thousands can be used even on ordinary Workstations.

2.3 Vortex Blob Approximations and the management of the wake

Vortex methods were first introduced by Rosenhead back in 1930 [26]. Until early 70's, vortex like methods were applied in aeronautics as part of panel methods to approximate the wake of lifting bodies usually as a set of vortex filaments. Almost simultaneously Basu and Hancock [27] were the first to introduce point vortices in order to predict the unsteady flow around a moving airfoil, whereas Rehbach [28] was the first to formulate a 3D point vortex method for predicting unsteady separated flows over delta wings. At the same period Chorin [29] published his pioneering work on how vortex methods can be applied to simulate the unsteady viscous flow around a cylinder. An excellent review of 3D vortex methods was written by Leonard [30]. In 1982 Beale and Majda publish the first complete work on the mathematical theory of vortex methods [31]. Since then a lot of papers have been published on vortex methods and their applications to all sorts of areas in fluid mechanics which is impossible to review [32]. So the presentation will be restricted to the type of method we implemented in GENUVP.

Vortex methods are defined as one-point quadrature numerical schemes in approximating the volume integral in (2). To this end $D_\omega(t)$ is decomposed into volume elements $D_{\omega,j}(t), j \in J(t)$ to each of which a point vortex is defined so that the zero and first moments of $\vec{\omega}$ are conserved:

Let $\vec{\Omega}_j(t)$ and $\vec{Z}_j(t)$ denote the intensity and the position of the j-th vortex. Then,

$$(8) \qquad \vec{\Omega}_j(t) = \int_{D_{\omega,j}} \vec{\omega}(\vec{x};t)dD,$$

$$\vec{\Omega}_j(t) \times \vec{Z}_j(t) = \int_{D_{\omega,j}} \vec{\omega}(\vec{x};t) \times \vec{x} dD$$

so that,

$$(9) \qquad \vec{\omega}(\vec{x};t) = \sum_{j \in J(t)} \vec{\Omega}_j(t)\delta(\vec{x} - \vec{Z}_j(t)),$$

$$\vec{u}_{wake}(\vec{x}_o;t) = \sum_{j \in J(t)} \frac{\vec{\Omega}_j(t) \times (\vec{x}_o - \vec{Z}_j(t))}{4\pi \left|\vec{x}_o - \vec{Z}_j(t)\right|^3}$$

Because the velocity given by (9b) is highly singular, instead of the Dirac function $\delta(.)$ in (9a), a smooth approximation is used known as cut-off or regularizing function which can be viewed as localized vorticity distribution function. That is why such vortices are called vortex blobs. Following, Beale and Majda [33], (9b) is written as:

$$(10) \qquad \vec{u}_{wake}(\vec{x}_o;t) = \sum_{j \in J(t)} \frac{\vec{\Omega}_j(t) \times \vec{R}_j}{4\pi R_j^3} f_\varepsilon(R_j)$$

where $\vec{R}_j = \vec{x}_o - \vec{Z}_j$, ε denotes the cut-off length and $f_\varepsilon(R_j) = 1 - \exp(R_j/\varepsilon)^3$. Usually ε is associated to the numerical scales determined by the time step and the grid size of the paneling.

Convection of free vorticity is carried out in Lagnrangian description as defined by the corresponding material equations:

$$(11) \qquad \frac{d\vec{Z}_j}{dt} = \vec{u}(\vec{Z}_j;t), \frac{d\vec{\Omega}_j}{dt} = \left(\vec{\Omega}_j \nabla\right)\vec{u}(\vec{Z}_j;t) = \vec{D} \cdot \vec{\Omega}_j$$

where $\vec{D}$ denotes the deformation tensor. For compressible (barotropic) fluids, (11b) should be modified to include density variations, by substituting $\vec{\Omega}$ by $\vec{\Omega}/\rho$. In this case to each blob, besides the intensity and the position, also the local density is associated. The density is determined by solving the continuity equation, again in Lagrangian form.

Conventional vortex methods involve direct evaluation of the velocity and the deformation at every blob position based on Biot Savart law. This means that for N vortex blobs a complete time step requires N^2 point-to-point calculations. In engineering applications N will increase continuously in time and so the computational cost will grow exponentially leading at large times to prohibitive levels. One way of having reasonable cost, is the use of *Particle-Mesh (PM)* techniques [34] which will reduce the cost to *N.logN* operations. The concept is simple: For a large number of blobs, $\vec{u}$ and $\vec{D}$ are evaluated at the nodes of a cartesian grid containing $D_\omega(t)$. Then local inter polation is used to determine $\vec{u}$ and $\vec{D}$ at the exact positions of the blobs. To this end, the vector potential

$\vec{A}$ of $\vec{u}_{wake}$ is introduced: $\nabla \times \vec{u}_{wake} = \vec{A}$ and the corresponding Poisson equation:

$$(12) \qquad \nabla^2 \vec{A} = -\vec{\omega}, \quad in\ D_\omega$$

is solved by means of a Fourier type method implemented by Daube [35]. This choice has been made in order to keep the cost to a minimum. More specifically at every time step the PM calculation procedure involves the following steps:

The projection step.
Vorticity is evaluated over a cartesian mesh that includes all vortex blobs, by projecting the intensity of the vortex blobs located within a cell of the mesh to the vertices of the cell:

$$(13) \qquad \vec{\omega}_{i,j,k} = \frac{1}{\delta D} \sum_n \vec{\Omega}_n \zeta(\vec{x}_{i,j,k} - \vec{Z}_n)$$

where $\vec{\omega}_{i,j,k}$ is the nodal vorticity and $\vec{x}_{i,j,k}$ is the position of node (i,j,k), δD is the volume of the grid cell, and $\zeta(.)$ is the projection function. The projection function has the form:

$$(14) \qquad \zeta(\vec{x}) = w(x) \cdot w(y) \cdot w(z)$$

with $w(.)$ being defined by one of the following functions,

$$w(x) = \begin{cases} 1 & -h/2 \le x \le h/2 \\ 0 & elsewhere \end{cases}$$

NGP (nerest grid point) scheme of zero order

$$w(x) = \begin{cases} 1 - \dfrac{|x|}{h} & -h/2 \le x \le h/2 \\ 0 & elsewhere \end{cases}$$

CIC (cloud in cell) scheme of first order

$$w(x) = \begin{cases} \frac{1}{2}(x^2 + 3hx + 2h^2 + c)/2h^2, & -3h/2 \le x \le -h/2 \\ 1 - (x^2 + c)/h^2, & -h/2 \le x \le h/2 \\ \frac{1}{2}(x^2 - 3hx + 2h^2 + c)/2h^2, & h/2 \le x \le 3h/2 \\ 0, & elsewhere \end{cases}$$

TSC (triangular shape cloud) scheme of second order

where h is the grid step and c is a free parameter. A fair compromise is the CIC scheme.

The solution step.
Equation (12) is discretized with standard central differences leading to three heptadiagonal linear systems,

$$(16) \qquad \frac{\vec{A}_{i+1,j,k} - 2\vec{A}_{i,j,k} + \vec{A}_{i-1,j,k}}{\Delta x^2} + \frac{\vec{A}_{i,j+1,k} - 2\vec{A}_{i,j,k} + \vec{A}_{i,j-1,k}}{\Delta y^2} + \frac{\vec{A}_{i,j,k+1} - 2\vec{A}_{i,j,k} + \vec{A}_{i,j,k-1}}{\Delta z^2} = -\vec{\omega}_{i,j,k}$$

The values of $\vec{A}$ at the boundary nodes of the grid, are provided by point-to-point Biot-Savart calculations:

$$(17) \qquad \vec{A}_{i,j,k} = \sum_n \frac{\vec{\Omega}_n}{4\pi \left| \vec{Z}_n - \vec{x}_{i,j,k} \right|}$$

To solve (16) first a two-dimensional Fourier transform is performed resulting tri-diagonal linear systems. Then the Thomas algorithm is applied. Finally a reverse two-dimensional Fourier transform follows, which provides the nodal values of $\vec{A}$. Once the nodal values of the vector potential are obtained, standard central differences are used to evaluate the velocity $\nabla \times \vec{A}$ and the deformation vector $\vec{d} = (\vec{\omega}\nabla)\vec{u}$ at the nodes of the grid.

The interpolation step.
The velocity and the deformation of vorticity of each vortex blob are calculated by means of the same procedure used for interpolating the nodal values of vorticity as follows:

$$(18) \qquad \vec{u}_n = \sum \vec{u}_{i,j,k} \zeta(\vec{Z}_n - \vec{x}_{i,j,k})$$

$$\frac{d\vec{\Omega}_n}{dt} = \vec{d}_n = \sum \vec{d}_{i,j,k} \zeta(\vec{Z}_n - \vec{x}_{i,j,k})$$

where $\vec{u}_n$ and $\vec{d}_n$ denote the velocity and rate of deformation of the nth vortex blob, whereas $\vec{u}_{i,j,k}$ and $\vec{d}_{i,j,k}$ denote the velocity and rate of deformation at grid node i,j,k. Summation in (18) runs over the neighbouring nodes according to the interpolation scheme.

Accuracy in PM methods is restricted by the cell size. In order to improve the error estimate of PM schemes, Anderson [36] proposed the introduction of local corrections. Because of the 1/r character of the Green function associated to (12), the PM approximation at a point $\vec{x}_o$, will be correct as far as concerns distant blobs. For those blobs contained in a *correction area* defined around $\vec{x}_o$, a correction $\Delta\vec{u}$ is added to $\vec{u}_o$ as calculated by (18a). $\Delta\vec{u}$ is defined as the velocity directly induced by the blobs contained in the correction area minus their contribution already included in the PM calculation of $\vec{u}_o$. The second term is estimated by subtracting their contribution to $\vec{A}$ at the neighbouring nodes to $\vec{x}_o$ before (18) is applied. Experience showed that even corrected PM schemes are not sufficiently accurate and therefore they should not be applied to areas of major importance. In GENUVP a mixed scheme has been followed which excludes from the PM calculations areas close to the solid boundaries. In these areas the Biot Savart law is used. For example in the case of helicopters, the PM region starts downstream the tail rotor and extends to infinity.

2.4 The near-to-far field coupling conditions

For an inviscid flow, vorticity can be released into the free flow along specific surface lines such as the

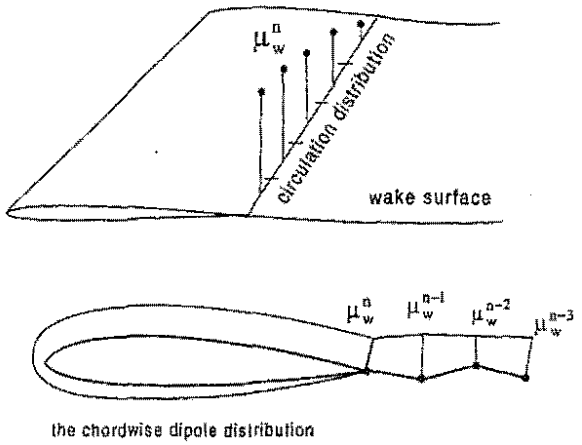

Figure 2 The dipole distribution on the wind and along the wake

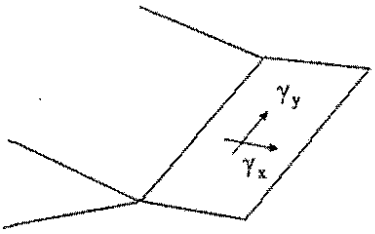

Figure 3 The wake element in the velocity direct formulation

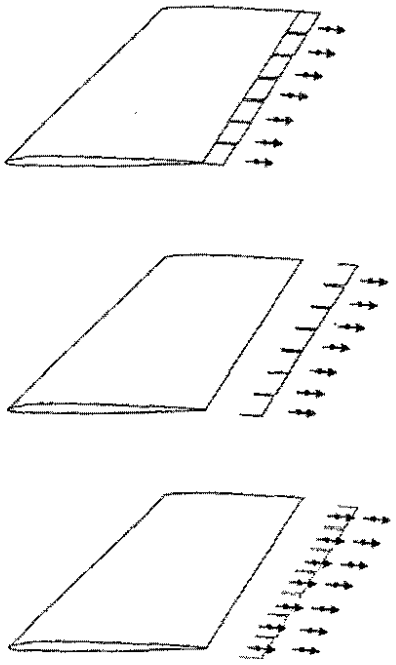

Figure 4 The generation of vortex blobs

trailing edge and the tip of any lifting body as well as a a prescribed separation line. This process produces the wake. In most panel approximations, wakes are introduced as vortex sheets, which retain their surface character. Depending on the formulation, the extra unknowns will be either the dipole intensity or the surface vorticity over the wake surface. In the first case, the dipole intensity at the points of emission is determined by the zero pressure jump condition. Kelvin's theorem then fixes this value for all subsequent time, provided that the wake evolves in a Lagnangian way following the mean flow (See Fig. 2 where superscript n denotes the time step). In the second case there are two unknowns (Fig.3). Again the zero pressure jump is used but now together with the divergence free condition of the surface vorticity. So the surface vorticity of the part of the wake produced during the current time step is determined. In GENUVP, only the strip of wake generated during the current time step retains its "surface" character (Fig. 4). Subsequently, surface vorticity is treated in particle form through integration. From every panel of the near wake, one or more vortex blobs are generated depending on the desirable length scale. For consistency reasons with the general invariance constraints, the integration should conserve the zero and first moments of vorticity as in (8) except that instead of $\vec{\omega}$, the surface vorticity $\vec{\gamma}$ is introduced. This also holds when the wake is represented by dipoles. In this case it is important to include in the integration also the line vortex elements which appear along the boundaries of the wake panels (Fig. 5).

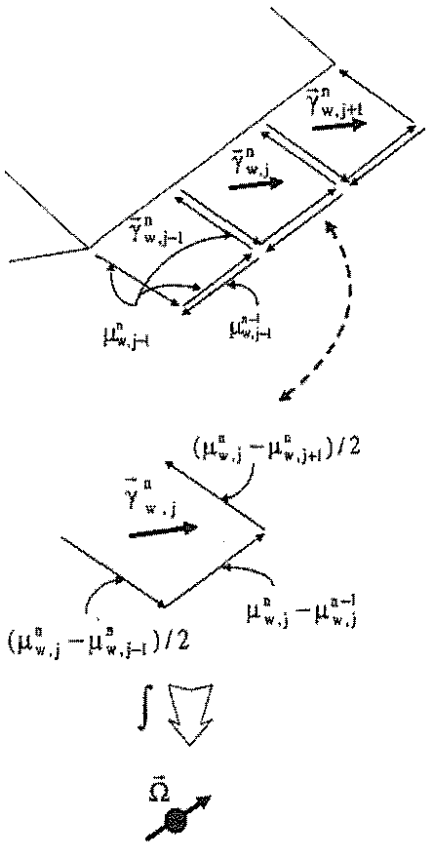

Figure 5 The integration scheme for generating vortex blobs

In a number of applications, it is important to also include separation. A reasonable large-scale approximation is possible by assuming that the principle consequence of separation is the formation of

a pronounced shear layer. For an inviscid approximation, this layer will reduce to a second vortex sheet carrying the corresponding vorticity in condensed form. Provided that the location of separation is known, it is possible to determine the vorticity fed into this second sheet by imposing a zero pressure jump condition. The double wake concept was first introduced for simulating the flow over a delta thin-wing [37]. For thick airfoils Vezza and Galbraith [38] formulated a method of this type based on vorticity representations whereas in [39] the source-dipole method of Basu and Hancock was extended to unsteady separated flows. Also in [39] a 3D thin wing model was formulated for rotating blades in which vorticity is also released from the leading edge at a rate determined by coupling the whole calculation with a section-by-section application of the ONERA stall model. In all these works the location of separation is input externally. In [40] a fully predictive method is proposed for unsteady flows around airfoils, in which separation is predicted by means of a strong viscous-inviscid interaction scheme similar to the one Drela formulated for steady flows [7].

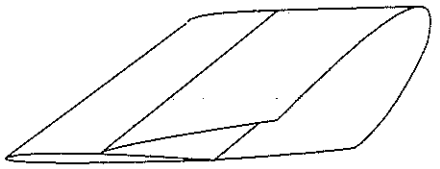

a) The double-wake model in "vortex sheet" form

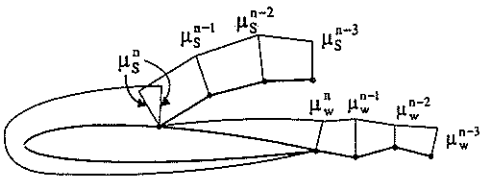

b) The dipole distribution on the wing and the two vortex sheets

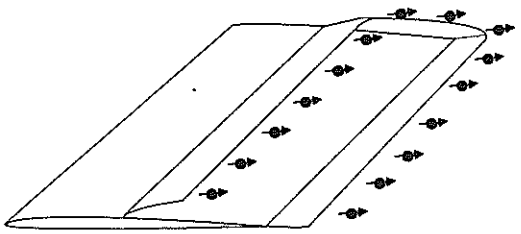

c) The double wake model in hybrid form (sheet model of the near wake and blob model in the far wake)

Figure 6 The double-wake scheme in the case of a source-dipole indirect formulation

Figure 6 shows schematically the double wake model in the case of an indirect source-dipole formulation. The bound dipole distribution is given a two-branch form defined by two parameters μ_w, μ_s. Both branches are linear with respect to the surface length. The two wakes will start from the trailing edge and the separation point respectively. Continuity for the dipole distribution is imposed at both emission points. According to Kelvin's theorem, the values of μ_w, μ_s are fixed to their initial values at all subsequent times. So the dipole distribution over the two wakes is fully defined by the history of the values of μ_w, μ_s. In order to determine the extra unknown μ_s, just downstream of separation, the velocity normal to the separation line is set to zero. Similarly a double wake can be also defined for the direct velocity formulation in which case the div free condition for the surface vorticity should be applied also at the separation point.

2.5 Extension to aeroelastic analysis

Aeroelastic coupling requires in addition to the structural model, two interfaces. The first will communicate to the aerodynamic part of the calculation the deformations in order to deform the geometry of the bodies as well as the deformation velocities which will be added into the non-entry boundary conditions as external velocity. The second will feed back to the structural model the aerodynamic loads plus their derivatives with respect to the deformation velocities which will determine the aerodynamic damping of the system. In rotor applications, a simple but powerful structural model which is easy to implement, is the beam approximation. Rigid body motions such as rotation, pitch, teeter as well as any other control at the hub, can be directly included. The model implemented in GENUVP was first developed for wind turbine blades [13, 14]. In considers flap and lead-lag bending, torsion and radial tension. The calculation process concerns time domain calculations during which at every step the aerodynamic and structural calculations are performed sequentially.

2.6 Extension to viscous flows

The main issue in coupling field with vortex methods is the correct formulation of the coupling conditions. Let S denote the solid boundary and D the flow-field, which is decomposed into the near field D_{in} and the far-field D_o separated by a closed surface S_o (Fig 7). In D_{in} a grid based Navier Stokes solver is used. On S the non-slip boundary condition is applied whereas on S_o, the velocity is assumed known. In order to determine the velocity on S_o, one can use either a purely vortex model or a *boundary projection technique.*

For the purely vortex model, (1) is applied over the entire flowfield with $\vec{u}_{solid}$ denoting the body velocity and $\vec{u}_{wake}$ denoting the velocity induced by the entire vorticity field. This part is calculated by the particle-mesh technique. Of course the vorticity used in this calculation, will be that of the previous time step and so the scheme will be explicit. Upon conclusion of every time step vorticity is convected in the form of blobs. Those found outside D_{in} are retained as vortex blobs belonging to the far field.

In the boundary projection scheme, (1) is applied in D_o by adding to (6) the extra volume term for the vorticity contained only in the far-field. As explained earlier, expression (6), when applied on S_o, provides for a given normal velocity distribution

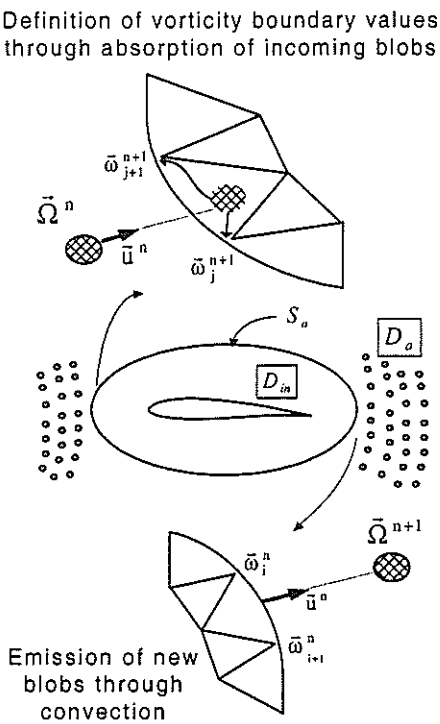

Figure 7 The coupling of a grid-based method with a vortex blob representation of the far field.

$u_n = \vec{u} \cdot \vec{\nu}$, the two tangential components u_1, u_2 of $\vec{u}$ on S_o. This means that the only unknown is u_n. Using the definition of $\vec{\omega}$, u_n can be expressed in terms of u_1, u_2 and $\vec{\omega}$. A surface Poisson equation is derived which is integrated over S_o. So the only unknowns left, are the surface values of $\vec{\omega}$. They can be determined by integrating (11b) in a Lagrangian sense as in [10]:

$$(19) \qquad \vec{\omega}(\vec{x};t+\delta t) = \vec{\omega}(\vec{x} - \vec{u}(\vec{x};t);t) + \delta t \cdot (\vec{\omega}(\vec{x} - \vec{u}(\vec{x};t);t)\nabla)\vec{u}(\vec{x} - \vec{u}(\vec{x};t);t) + v.t.$$

where *v.t.* stands for the viscous terms. At the end of every step vorticity is convected. During this process, vortex particles from the far field can cross S_o on their way into the near field. In this case they are distributed over the boundary nodes. Also vorticity from the near field can cross S_o on its way into the wake. In this case the amount of vorticity which is leaving the near field, is transformed into vortex blobs (Fig 7).

2.7 Extension to compressible flows

For compressible flows, a volume convolution term for the velocity divergence should be added to (1). For aerodynamic calculations and flows with weak shocks only, this term will be important in the inner region only, provided of course that D_{in} is sufficiently large. In this case the analysis presented in the previous section can be followed with some modifications. In the purely vortex model, the velocity divergence term should be added in the convection velocity calculations of the vorticity whereas the projection model will remain the same since in D_o compressibility effects are assumed negligible.

3 RESULTS & DISCUSSION

Figure 8 shows an early stage of the computations on a full helicopter configuration using the basic version of GENUVP. All components are included. Wakes are produced by, the main and tail rotor blades, the end-plates and the stabilisers.

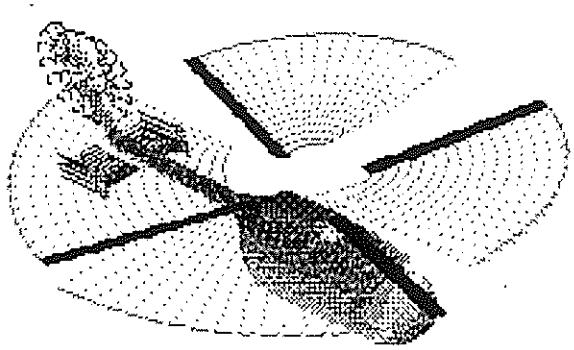

Figure 8 Simulation of full helicopter configuration.

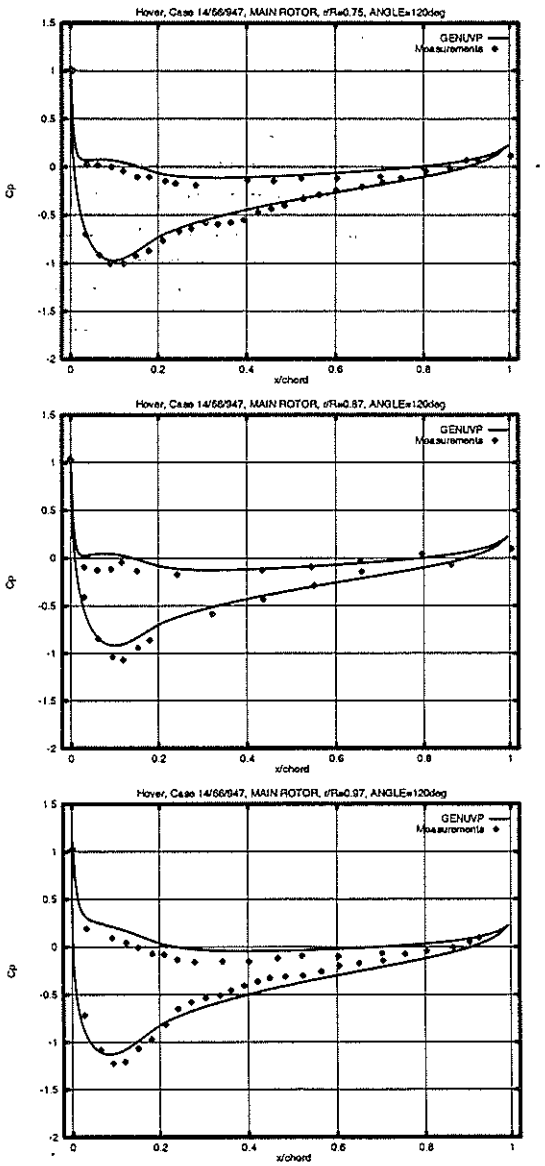

Figure 9 Pressure distributions at 0.75, 0.87 and 0.95 of the BO105 main rotor in low speed hover

Figures 9 and 10 give comparisons of predicted pressure distributions against measurements obtained on the BO105 main rotor blade in the DNW wind tunnel [41]. A three level surface grid of about 10000 panels was used with 90 time steps per revolution. Convergence to a periodic solution was attained after 7 full revolutions. A run of this type for the complete configuration would last 5 days on a single processor Workstation. The first case corresponds to a hover flight situation whereas the second to a descent at 6°, both at Ma=0.645. Results are presented at 0.75, 0.87 and 0.97 radial stations. In the hover case one azimuth position is given, whereas in the descent case results are shown at azimuth positions 330° and 30° (advancing side) and at 240° (retrieving side). The agreement with measurements is reasonable. There are however differences especially at the 30° azimuth position of the descent case which indicate that the time step as well as the density of the vortex blobs during BVI, need further refinement.

The next test concerns the HART experiment [42]. In Figure 11 the calculated vortex trajectories

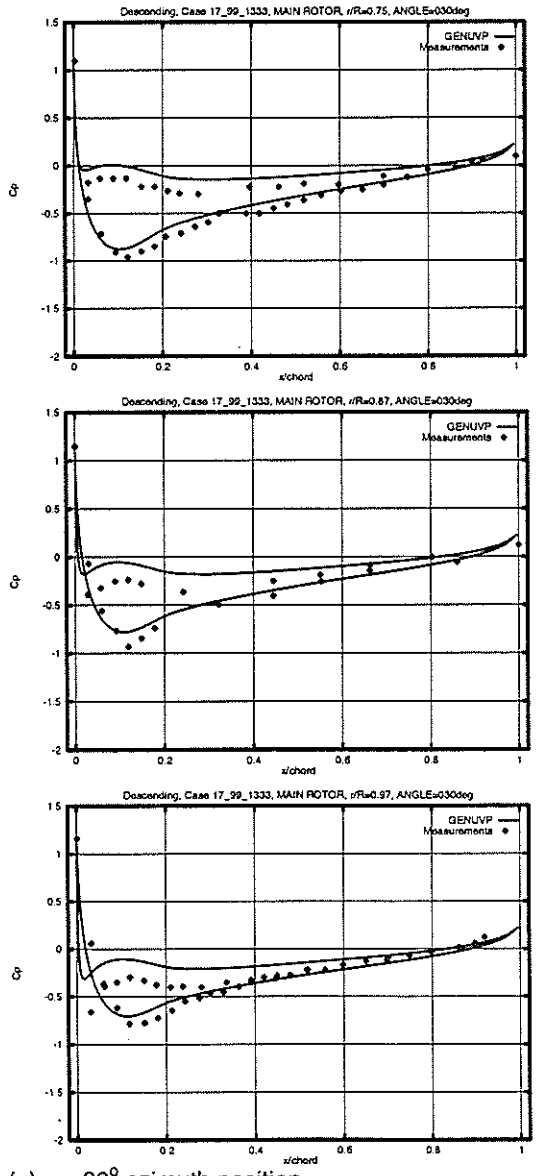

(a) 30° azimuth position

are compared to measurements. Although the agreement is quite satisfactory, it is noted that for a complete validation, comparisons should include also velocities. This is a task under way within the future main-tail rotor interaction tests for the BO105 planned to take place in the DNW.

In Figure 12 compressible results are presented for the case of the ONERA M6 wing in steady flow (Ma =0.8395, α=3.06^0). In the inner region FLUX3D was used over a grid of 280x40x27 extending to 5

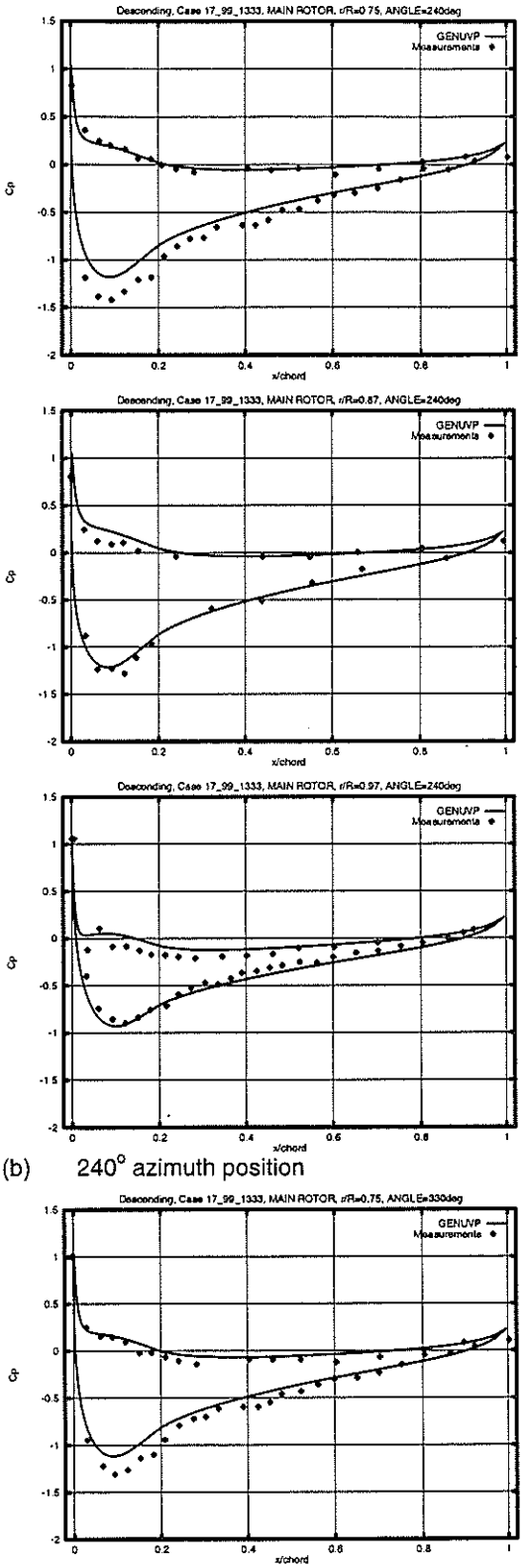

(b) 240° azimuth position

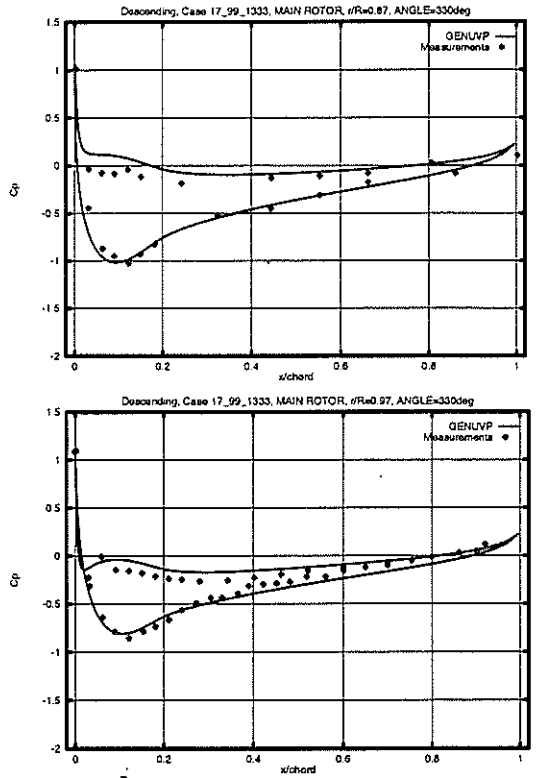

(c) 330° azimuth position

Figure 10 Pressure distributions at 0.75, 0.87 and 0.97 of the BO105 main rotor blade at low speed descent

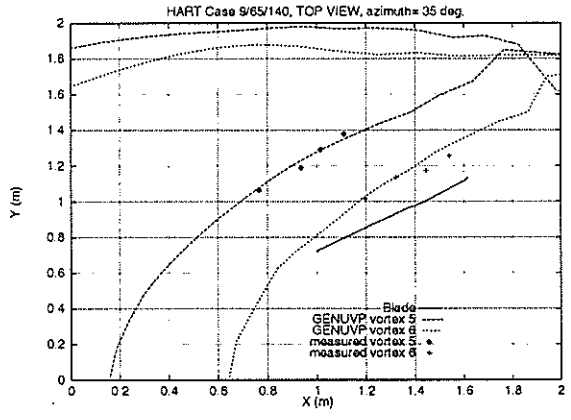

Figure 11 Vortex trajectories from the HART experiment

chords around the wing. In these calculations only the vortex type of coupling was tested. The comparison is quite favourable at least for FLUX3D. As regards the testing of the coupling there is need for a detailled parametric study and therefore the results from this point of view should be regarded as preliminary.

Finally in Figure 13, results from again a steady calculation are presented, this time in the case of an incomopressible turbulent flow. The test refers to the case of wind turbine measured by NREL in the USA [43] for which the assumption of incompressibility is certainly valid. The interesting feature in this test is that at mean wind speed of 13m/s, the flow exhibits massive separation over a large extent of the blade. In the inner

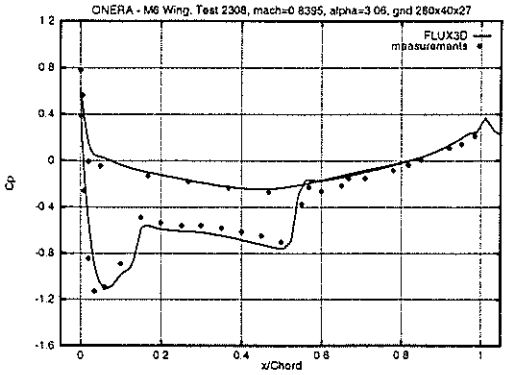

(a) Section 2, y/b=0.44

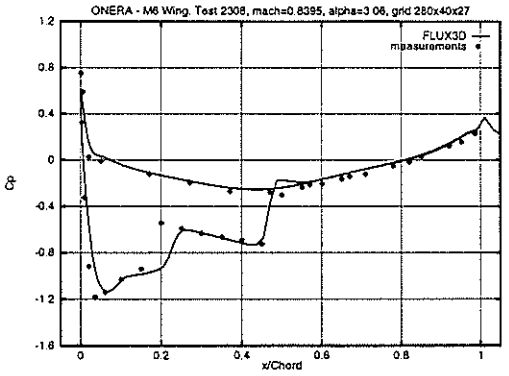

(b) Section 3, y/b=0.65

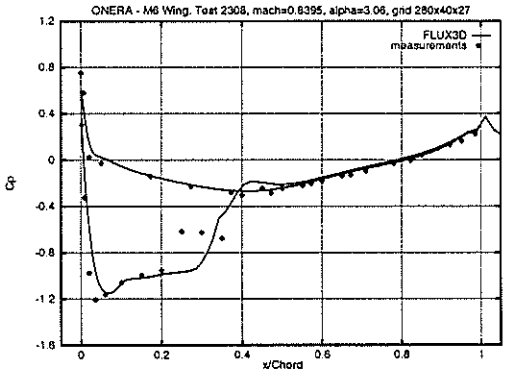

(c) Section 4 y/b=0.8

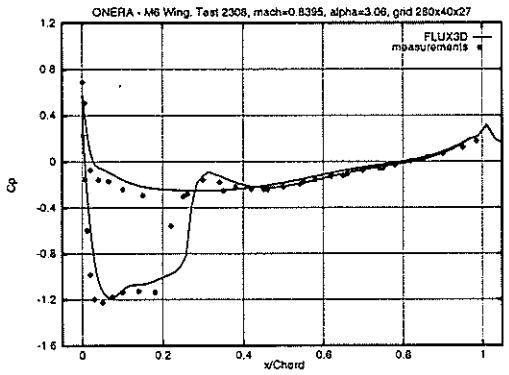

(d) Section 6, y/b=0.90

Figure12 Steady calculations around the ONERA M6 Wing

part covering the region around the blade, NS3D was used. The grid in NS3D is curvilinear and the

arrangement staggered. Also for the pressure, NS3D is based on the SIMPLE algorithm, whereas for turbulence closure the Spalart-Almaras model is used. The coupling with an outer vortex type solution, which again was based on the vortex type model, permits to confine the grid near the blade (again of the order of 5 chord lengths) and yet include the wake induced effects, which to a large extent regulate the flow. For full convergence and for a grid of about 10^6 points, the run lasts about 2 days on a single processor of a modern workstation. This is a quite encouraging result since full CFD calculations with multi-block techniques extending the grid both upstream and downstream of the rotor, as reported by NREL, need 10^7 points and

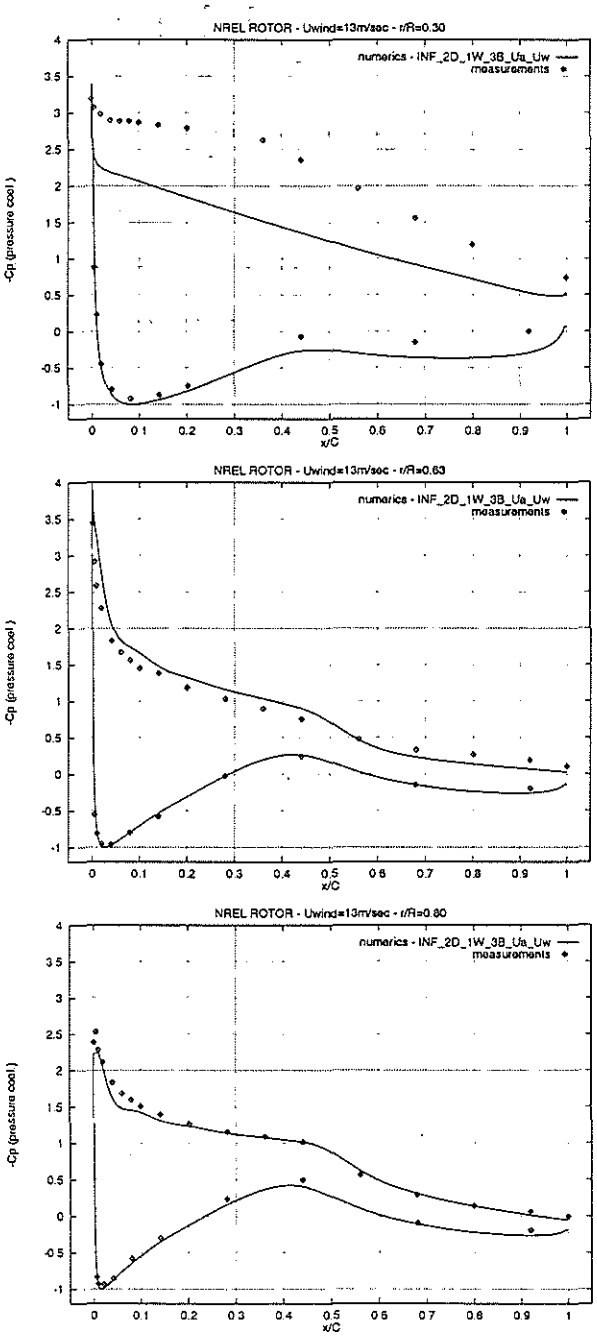

Figure 13 Pressure coefficient distribution for the case of a wind turbine operating at 13m/s wind inflow.

several days on high performance computers. As regards the quality of results they are quite satisfactory. There are however differences in the hub region. They could be due to the absence of the hub in the numerical simulations and the artificial boundary condition applied over the first inboard station.

4 CONCLUSIONS

In the present paper Helmholtz decomposition was used in formulating cost effective numerical schemes of high resolution for unsteady flow simulations around multi-component configurations.

First the case of incompressible and inviscid flows was considered, for which Boundary Element and Vortex methods were coupled. High resolution under reasonable cost was accomplished by introducing: (a) Particle-Mesh techniques in the wake, and (b) Sub-grid quadrature for calculating the boundary integrals. Due to its grid-free character, the method is suitable to also include aeroelastic and linear acoustic couplings.

Next, extensions to compressible and/or viscous flows were considered within the context of domain decomposition methods. In this connection two ways for coupling standard CFD methods in the near field with vortex methods in the far field have been proposed, based velocity integral relations of boundary element type.

A series of typical validation tests was presented and predictions were compared to measured data. The overall quality of the predictions is supportive of the promising features of the whole methodology.

AKNOWLEDGEMENTS

The work presented herein, has been funded jointly by the Commission of the European Union under: the HELIFLOW (BE-95-1311) BRITE/EURAM III project, the VISCEL (JOR3-CT98-0208) and COMTER_ID (JOR3-CT95-0033) JOULE III projects, by the Greek, General Secretariat of Research and Technology under contract EPET#573 and by the Research Committee of the National Technical University of Athens under contracts 66/23 and 66/56.

The authors would like to thank all participants to the HELINOISE and HART projects for providing the measured and technical data used in validating the methods presented herein. From a scientific point of view, the authors thank Prof. L. Morino for all the invaluable discussions and remarks. To a large extent this work has been inspired by his pioneering work.

REFERENCES

1. L. Morino (1991) "Helmholtz and Poincare potential-vorticity decompositions for the analysis of unsteady compressible viscous flows", in *Boundary Element Methods in Non-linear Fluid Dynamics 6*, Ed. P.K. Banerjee, L.Morino, Elsevier New York.
2. S.M. Richardson, A.R.H. Cornish (1977) "Solution of three dimensional incompressible flow problems", J. Fluid Mech. Vol 82, 309-319
3. O. A. Kandil, E.C. Yates (1986) "Transonic vortex flows past Delta wings: Integral equation approach",

AIAA J., Vol 24, pp.1729-1736.
4. D. Wehr, L. Zerle, S. Wagner (1996) "Coupling Euler and potential methods for the calculation of helicopter rotors in unsteady forward flight", 22"d European Rotorcraft Forum, Brighton UK.
5. LeBalleur, 1981; "Strong Matching Method for Computing Transonic Viscous Flows including Wakes and Separations. Lifting Airfoils", Rec. Aerospatiale no. 1981-3
6. R.C. Lock. and B.R. Williams (1987) "Viscous-Inviscid Interactions in External Aerodynamics", Prog. Aerospace Sci, vol. 24, pp 51-171
7. M. Drela (1989) "XFOIL: An Analysis and Design System for Low Reynolds Number Airfoils" Conference on Low Reynolds Number Aerodynamics, University Notre Dame.
8. J.C. Nedelec, C. Johnson (1973) " On the coupling of integral and finite element methods", Math. Computation, Vol 35, 1963-1979
9. L. Quadrapelle and M. Napolitano (1984) "A method for solving the factorized vorticity-stream function equations by finite elements", Int. J. Num. Meth. Fluids, Vol 4, pp. 109-125.
10. LJ..Guermond, S. Huberson and W.Z. Shen (1993) "Simulation of 2D external viscous flows by means of domain decomposition", J.Comp. Physics
11. S.G. Voutsinas, M.A. Belessis,. and K.G. Rados (1995) "Investigation of Yawed Operation of Wind Turbines by means of a Vortex Particle Method", *AGARD-CP-552 Proc. Aerodynamics and Aeroacoustics of Rotorcraft*, Berlin, paper 11
12. S.G. Voutsinas (1990) " A GENeralized Unsteady Vortex Particle method for solving the unsteady flow around multi-component configua5rations", NTUA Report.
13. V.A. Riziotis and S.G. Voutsinas (1997) "GAST: A General Aerodynamic and Structural Prediction Tool for Wind Turbines", Proc. EWEC'97, Dublin.
14. S.G. Voutsinas, V.A. Riziotis and D. Mourikis (1996) "Aeroelastic analysis of full wind turbine configurations including controls", NTUA Report
15. S.G. Voutsinas, D.G. Triantos (1999) "Aeracoustics of full helicopter configurations using vortex particle flow approximations", Proc. CEAS Forum on Aeracoustics of Rotors and Propellers, 9-11 June 1999, Rome, Italy.
16. S.G. Voutsinas, D.G. Triantos (1999) "A coupled finite volume – vortex method for simulating unsteady compressible flows equations", NTUA Report
17. Y. Perivolaris, V.A. Riziotis, G. Tzabiras and S.G. Voutsinas (1990) "Viscous and aeroelastic effects on wind turbines", NTUA Report
18. J. L. Hess (1972) "Calculation of potential flow about arbitrary three-dimensional lifting bodies", McDonnell Douglas Rep., MDC J5679-01
19. J.L. Hess and A.M.O. Smith (1968) "Calculation of Non-Lifting potential flow about artitrary three-dimensional bodies", McDonell Douglas Rep. No ES 40622
20. L. Morino (1974) "A general theory of unsteady compressible potential aerodynamics", NASA CR-2464.
21. A. Roberts and K. Rundle (1972) "Computation of incompressible flow around bodies and thick wings using the spline-mode system", BAC(CAD) Report Aero Ma 19.
22. F.T. Johnson, E.N. Tinoco, P. Lu and M.A. Epton (1980) "Three-dimensional flow over wings with leading-edge vortex separation" AIAA J., Vol.18
23. M. Gennaretti, G. Calcagno, A. Zamboni and L. Morino (1998) "A high order boundary element formulation for potential incompressible aerodynamics", The Aeronautical Journal, pp.211-219.
24. L. Fornasier (1984) "A source equality Kutta condition for panel methods" AIAA J. Vol 22, 1167-1169
25. J.C. Vassberg (1997) "A fast surface panel method capable of solving million-element problems", AIAA paper 97-0168
26. L. Rosenhead (1931) "The formation of vortices from a surface of discontinuity", Proc. Royal Soc. Ser.A, 134
27. B.C. Basu and G.J. Hancock (1978) "The Unsteady Motion of a Two-Dimensional Airfoil in Incompressible, Inviscid Flow", J. Fluid Mech., 87
28. C. Rehbach (1973) "Calcul d'ecoulements autour d'ailes sans epaisseur avec nappes tourbillonnaires evolutives", Recherche Aerospatiale, No 2, 53-61.
29. A. J. Chorin (1973) "Numerical study of slightly viscous flow", J. Fluid Mech. Vol. 57.
30. A. Leonard (1985) "Computing three-dimensional incompressible flows with vortex filaments", Ann. Rev. Fluid Mech., Vol 17, 523-559
31. J. T. Beale, A. Majda (1982) : "Vortex Methods", Mathematics of Computation, Vol. 39.
32. Y. Gagnon, G-H Cottet, D.G. Drischel, A.F. Ghoniem and E. Meiburg (Ed) (1996) "Vorte flows and related numerical methods II", http://www.emath.fr/Maths/Proc.
33. J. T. Beale, A. Majda (1985) "Higher order accurate vortex methods with explicit velocity kernels", J. Computational Physics, Vol. 58.
34. R. W. Hockney, J. W. Eastwood (1981) "Computer simulation using particles", McGraw-Hill.
35. O. Daube (1995) "A Fast Poisson solver based on a Fourier Method", personal communication.
36. C. Anderson (1986) "A method of local corrections for computing the velocity due to a distribution of vortex blobs", J. Comp.Physics, Vol 62, 111-123
37. D.Levin, J.Katz (1981) "Vortex-lattice method for the calculation of the nonsteady separated flow over Delta wings", J. Aircraft, Vol. 18
38. M. Vezza and R.A. Galbraith,R.A. (1985) "An inviscid model of unsteady aerofoil flow with fixed upper surface separation", *J. for Numerical Methods in Fluids*, Vol. 5, pp. 577-592
39. S.G. Voutsinas and V.A. Riziotis (1996) "Vortex Particle Modeling of Stall on Rotors. Application to Wind Turbines", Proceedings of the Fluids Engineering Division Summer Meeting, ASME, San Diego, FED Vol 238, 25-32
40. S. G. Voutsinas, V. A. Riziotis (1999) "A viscous-inviscid interaction model for dynamic stall simulations on airfoils" AIAA paper 990038.
41. W. R. Splettstoesser, B. Junker, K. J. Schultz, W. Wagner, W. Weitemeyer, A. Protopsaltis, D. Fertis (1993) "The HELINOISE Aeroacoustic Rotor Test in The DNW -Test Documentation and Representative Results-", DLR Mitteilung 93-09.
42. W. R. Splettstoesser, R. Kube, U.Seelhorst, W. Wagner, A. Boutier, F. Micheli, E. Mercker, K. Pengal (1995) "Higher harmonic control aeracoustic rotor test (HART). Test documentation and representative results", DLR IB 129-95/28.
43. J.G. Schepers et al (Ed) (1997) "Final Report of IEA Annex XIV: Field Rotor Aerodynamics", ECN Report ECN-C-97-027

TWENTYFIFTH EUROPEAN ROTORCRAFT FORUM

Paper n° C12

APPLICATION OF COMPUTATIONAL FLUID DYNAMICS TO THE DESIGN OF THE BA 609

BY

J. C. NARRAMORE, D. A. PLATZ, A. G. BRAND

BELL HELICOPTER TEXTRON INC., FORT WORTH, TEXAS, USA

SEPTEMBER 14–16, 1999
ROME
ITALY

ASSOCIAZIONE INDUSTRIE PER L'AEROSPAZIO, I SISTEMI E LA DIFESA
ASSOCIAZIONE ITALIANA DI AERONAUTICA ED ASTRONAUTICA

APPLICATION OF COMPUTATIONAL FLUID DYNAMICS TO THE DESIGN OF THE BA 609

J. C. Narramore
D. A. Platz
A. G. Brand
Bell Helicopter Textron, Inc.
Fort Worth, Texas, U.S.A

1. ABSTRACT

Cost and weight considerations factor heavily into the design of the BA 609 civil tiltrotor. Therefore, aerodynamic design solutions must be developed in a timely manner within stringent constraints. Computational, empirical, and wind tunnel testing tools are being used to produce optimal aerodynamic solutions that satisfy these constraints. Because of the detailed results that are available from computational fluid dynamics (CFD) methods, these tools are being used to produce new aerodynamic design solutions that address complex flow issues. This paper describes some of the successes obtained by using computational fluid dynamic methods during the design of the BA 609 Civil Tiltrotor.

2. INTRODUCTION

To predict aerodynamic characteristics and air-loads, Bell Helicopter has pursued several approaches including wind tunnel testing, empirical methods, analytical methods, and computational fluid dynamics (CFD) methods. The goal of constantly improving the design process has led to the development of many new techniques and upgrades in aerodynamic design methodology. The advent of computational methods for aerodynamic design and analysis for rotorcraft vehicles provides new opportunities to improve the design approach. As these methods are developed, computational results are continually compared to wind tunnel test data to validate the accuracy of the computations (Ref. 1).

Developments in high-speed computers have also had an impact on the time required to perform aerodynamic design and the types of problems that may be solved. As computers have become more capable, solutions with increasing detail have been produced. In addition, improved modeling of the physics of the flow and of the configuration geometry is also made possible. Interactive graphic workstations have allowed a new approach to the design of aerodynamic components and the development of computational grids for complex shapes. Supercomputers have generated solutions to problems that heretofore would have taken too long to be of practical use in the design process.

The development of CFD methodology at Bell Helicopter Textron, Inc. was initiated in the early 1970's with two-dimensional (2–D) airfoil analysis and design methods. This included both incompressible and transonic full-potential methods. In the early 1980's, three-dimensional (3–D) potential flow solutions became the standard for distributing external airloads on rotorcraft. In 1987, evaluations of transonic full-potential codes for rotor blades were conducted. Navier-Stokes methods were being used for some practical rotorcraft component problems in 1991. By 1995, full rotorcraft configurations were being analyzed using Navier-Stokes codes. This growth in capability has paralleled advances in computer hardware and the development of tools that improve the productivity for CFD methods. As a result of this growth in capability, state-of-the-art methods were in place to aid in the design of the BA 609.

3. CFD TOOLS

Several aerodynamic computational tools have been used during the design of the BA 609. These tools are used for grid generation, Navier-Stokes analysis, surface manipulation, and inverse airfoil design.

3.1 Grid Generation

Surface grids are generated from point distributions extracted from a CATIA surface definition. For the 3-D aircraft models, surface grids for the individual components are generated with proper overlap at the intersections using the GRIDGEN (Ref. 2) code. A body conforming volume grid for each surface component is produced using a hyperbolic grid generator code, HYPGEN (Ref. 3). This code generates highly clustered and smoothly varying grids by solving a hyperbolic differential equation. A graphical user interface simplifies input and execution and a check for negative cell volumes is conducted while executing. The PEGSUS (Ref. 4) code is used to develop the hole cutting and connectivity stencils for the component grids.

3.2 Navier-Stokes Code

The primary CFD analysis tool being used at Bell Helicopter is the OVERFLOW code (Ref. 5) developed by Pieter Buning at NASA. OVERFLOW is a Navier-Stokes code with various boundary conditions and turbulence models available. A primary advantage of this code is its ability to solve problems using overset grids. This feature allows complex geometries to be modeled to any desired level of accuracy. For the cases used in the BA 609 studies, OVERFLOW was run using the Spalart-Allmaras turbulence model (fully turbulent), central-differencing of the spatial terms, and the three-factor diagonal implicit scheme.

3.3 Post Processing

FOMOCO (Ref. 6) is used to calculate the forces and moments from the OVERFLOW solution. Since OVERFLOW uses overset grids, the overlapped regions of the surface grids must be eliminated and connectivity established between adjacent grids before the surface pressures are integrated. The FOMOCO code performs these operations. Visualization tools are used to interpret the computational results. These include the FAST code (Ref. 7), which reads OVERFLOW-generated files and the Bell ADAM post processor that visualizes surface pressures, integrates forces, and distributes airloads to NASTRAN models.

3.4 Inverse Design Tools

Inverse tools currently being used include conformal mapping methods for single element airfoils and predictor/corrector techniques for multi-element and transonic airfoil design (Ref. 1). Inverse airfoil design methods are advantageous over trial-and-error perturbation methods since the pressure distribution, which determines the boundary layer development and the lift (moment) of the section, is specified *a priori*. Thus, the performance is specified and the coordinates that will produce that performance are determined. If geometric constraints are critical, inverse design methods can be used to determine the best aerodynamic configuration with the given constraints. Since inverse conformal methods are extremely fast (Ref. 1), these design methods are nearly instantaneous on a modern graphic workstation. As soon as a selected design parameter is adjusted, the result appears on the screen. The ability to work interactively on a graphic workstation greatly improves productivity for airfoil design.

4. APPLICATION OF CFD

During the design of the BA 609, CFD methods were used to develop performance enhancing surface contours. CFD was also used as a tool to generate airload distributions for structural design. The CFD methods were used to develop new inboard rotor and empennage airfoils, to improve the wing-to-fuselage fairing, to reduce the size and lower the drag of the tail cone, to determine inlet and exhaust locations, and to provide airload distributions for the structural design of landing gear doors, wing fairings, spinners, nacelles, over-wing fairings, conversion actuator fairings, wing skins, tail surfaces, and fuselage.

4.1 Development of New Inboard Rotor Airfoils

To minimize costs and risks, the V-22 rotor airfoils were also used on the BA 609 rotor. However, since the flex beam motions inside the blade cuff do not scale directly and reduced steady pitch link loads were desired, the inboard blade airfoils required redesign. The goal was to reduce the pitching moment in the inboard region by 60% while maintaining the V-22 lift characteristics and minimizing the drag. The approach taken was to use very fast inverse conformal mapping techniques to generate airfoils with desired moment characteristics that satisfy the clearance constraints. The trailing edge was then blunted by fitting a straight line to the airfoil surface aft of 98% chord. The resulting airfoil was analyzed using potential flow with boundary layer methods to determine if the performance of the new section was acceptable. Finally, OVERFLOW Navier-Stokes analysis of the new design shapes and the baseline V-22 airfoils was conducted to make the final section selection.

Fig. 1 illustrates the user interface for an inverse conformal mapping solution that was generated. The upper left window depicts the input pressure distribution and the lower left window shows the resulting airfoil and clearance constraint. The panel on the right shows the input parameters that define the specified pressure distribution. Since this method is a conformal mapping, the trailing edge thickness of the airfoil is zero. Input velocity parameters were adjusted to provide a thick trailing edge when a linear fit to the trailing edge is computed at 98% chord. Using the inverse methods, a family of airfoils with different trailing edge thicknesses was created, all satisfying the clearance constraint. After defining the geometry, a Navier-Stokes trade study was conducted to determine the trailing edge thickness required to satisfy the maximum lift design requirement. Fig. 2 shows a typical grid distribution about a candidate inboard region airfoil. Results indicate that as the trailing edge thickness is increased, the maximum lift capability is increased; however, the drag level also increases. The trailing edge thickness for the final airfoil was chosen to maintain the maximum lift capability of the corresponding V-22 airfoil section. In Fig. 3, the resulting BA 609 28% thick airfoil is compared to the V-22 28% airfoil. Fig. 4 shows that the BA 609 airfoil lift curve slope is steeper than the V-22 airfoil, and that the maximum lift coefficient is matched by the final BA 609 airfoil shape. In Fig. 5, the drag curve of the BA 609 airfoil is compared to the V-22 airfoil. The figure indicates that minimum drag is equivalent and the low drag region is much wider for the BA 609 section. The pitching moment of the two airfoils is compared in Fig. 6. Results show that the pitching moment at zero lift coefficient was reduced by 66% with the BA 609 cuff airfoil.

As a result of this procedure, new inboard BA 609 airfoils were developed that provide improvements in performance compared to using scaled V-22 airfoils. In addition, because of the reduction in pitching moment, the pitch link loads were also reduced.

4.2 Wing-to-fuselage Fairing Design

With a three-dimensional CFD solution, we can examine the flow in detail at any location on the aircraft. In

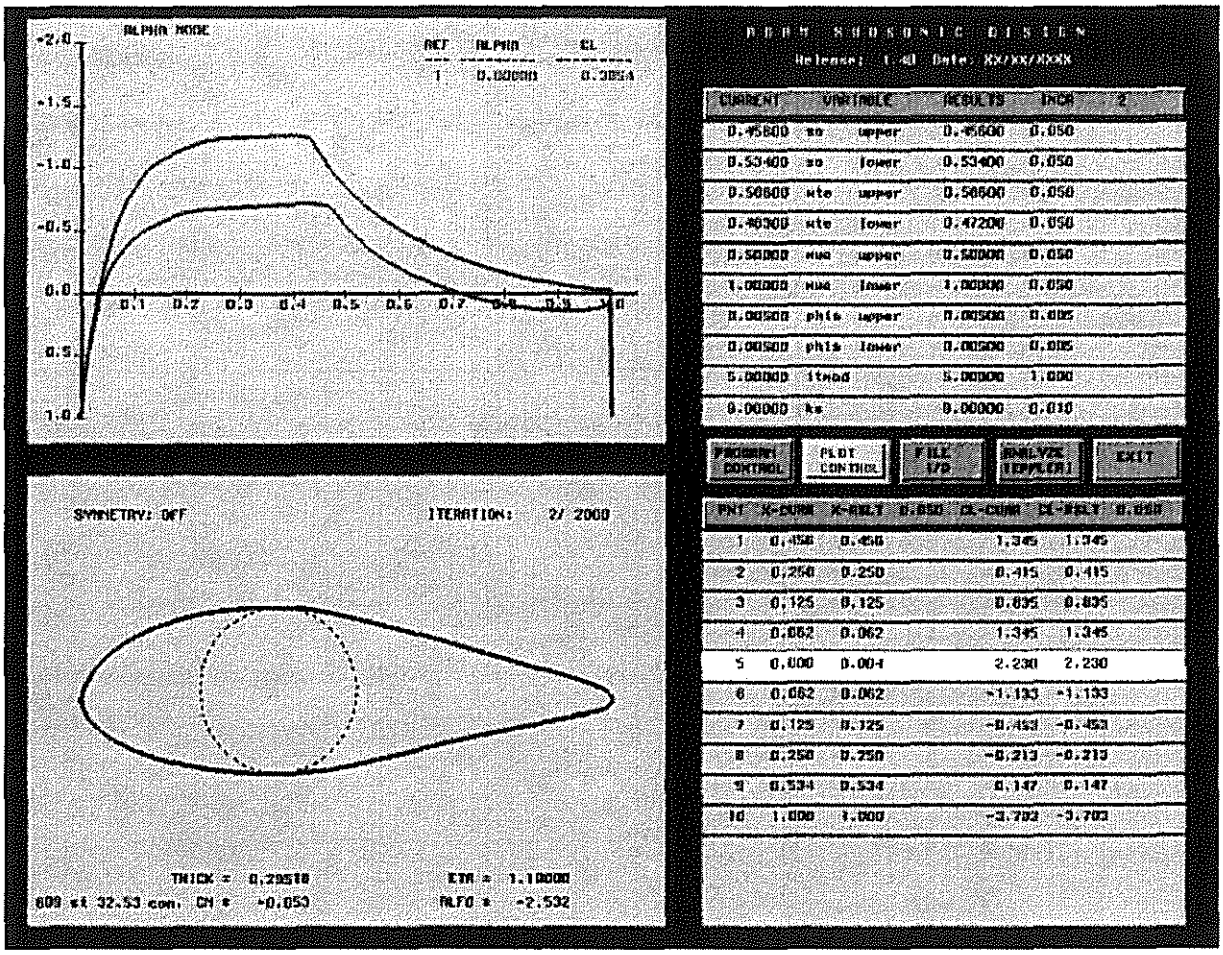

Fig. 1. User graphical interface for subsonic inverse airfoil design method.

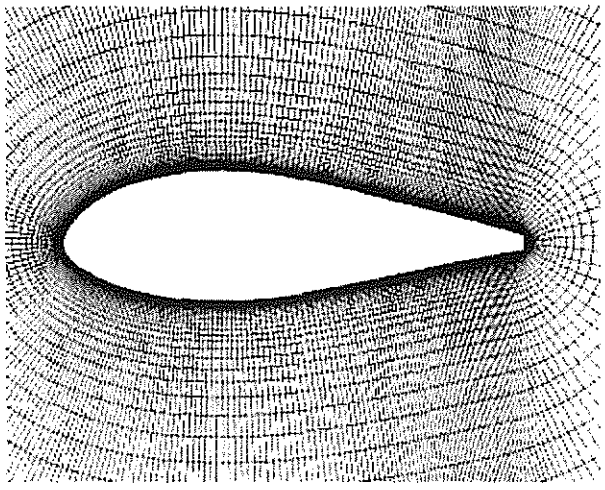

Fig. 2. Typical grid for Navier-Stokes analysis is 301 × 101 × 3 nodes.

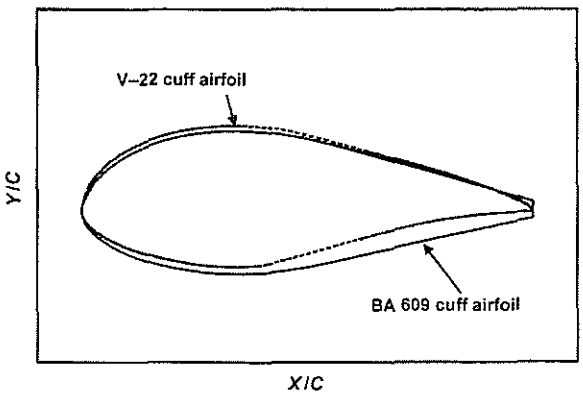

Fig. 3. The BA 609 cuff airfoil has less camber and more trailing edge thickness.

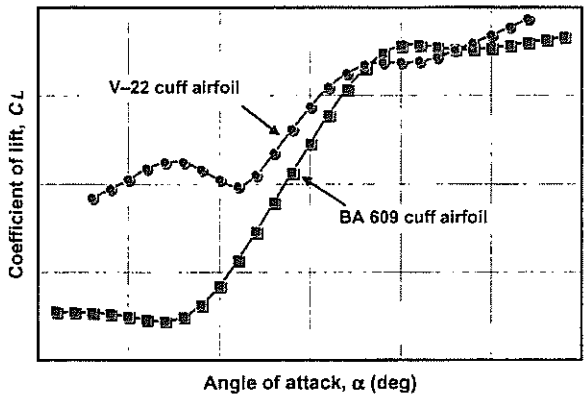

Fig. 4. The BA 609 cuff airfoil improves the lift coefficient versus angle of attack.

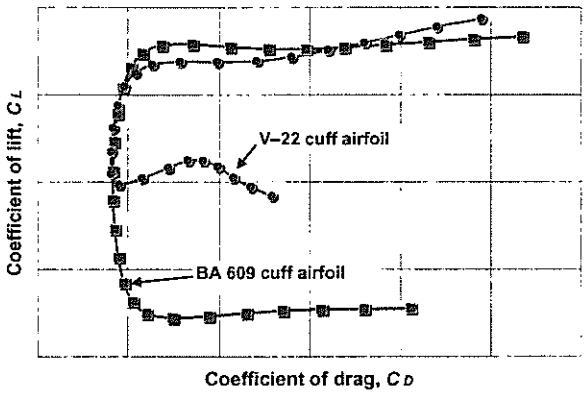

Fig. 5. The BA 609 cuff airfoil drag curve is much wider than for the V–22 cuff airfoil.

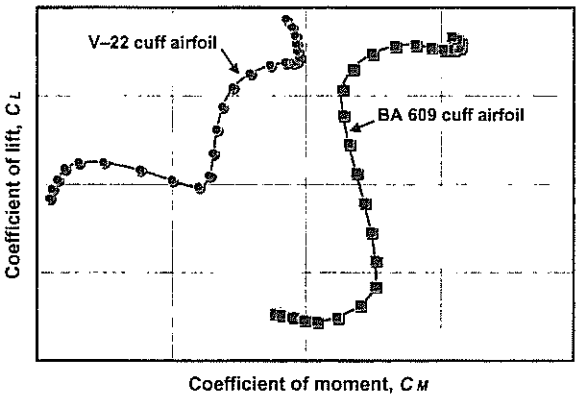

Fig. 6. The BA 609 cuff airfoil pitching moment is reduced by 66%.

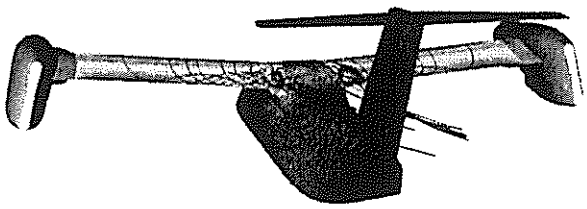

Fig. 7. Computed flow about the baseline BA 609 at wind tunnel conditions.

this capacity, CFD technology provides an unmatched diagnostic capability for rotorcraft design. In the BA 609, CFD was used to determine the cause of an aerodynamic issue found in a wind tunnel test and a CFD-based design solution was implemented to correct that issue.

Preliminary BA 609 tests, conducted at the Texas A&M University 7- × 10-ft (2- × 3-m) wind tunnel, found that the vertical tail effectiveness was reduced at high angles of attack. This situation could lead to decreased directional stability of the aircraft and was undesirable.

To investigate this situation, the BA 609 was modeled using computational fluid dynamic methods while the wind tunnel test was still in progress. A three-dimensional model had been generated to represent the baseline configuration. The OVERFLOW code generated results for angles of attack where the reduced tail effectiveness was observed in the wind tunnel test. These runs were performed on a Cray supercomputer at NASA Ames Research Center. A typical solution for this three-dimensional model of the BA 609 required approximately 15 hours of CPU time on a Cray C90. Fig. 7 shows the computed flow for the baseline BA 609 model at the wind tunnel model conditions. The solution indicated a flow separation in the area where the wing joins the body at this high angle of attack. The separated flow creates a large region of turbulence, which moves aft along the fuselage and impinges on the vertical tail. Based on evaluations of these computational results, a modification to the wing/fuselage fairing was pursued to improve the effectiveness of the vertical tail at high angles of attack.

A project was initiated to develop a new wing/fuselage fairing using the computational methods to generate results. The objective of this computational design effort was to eliminate the computed flow separation at the wing-to-fuselage junction. New fairing shapes were created by adjusting the surface grids at the wing/fuselage intersection and regenerating the volume grid and holes for these grids. Two iterations were required to produce a configuration that produced substantially improved computed flow. These geometry iterations and the generation of computational results for the new designs required a total of three weeks for completion. Fig. 8 shows a comparison of the computed results for the modified fairing and the original baseline design. It shows that the new fairing significantly reduces the flow separation at the wing-to-fuselage junction. Based on these results it was felt that the BA 609 configuration could be improved with the CFD-developed fairing.

The surface coordinates of the new design were transferred to CATIA and stereolithography was used to

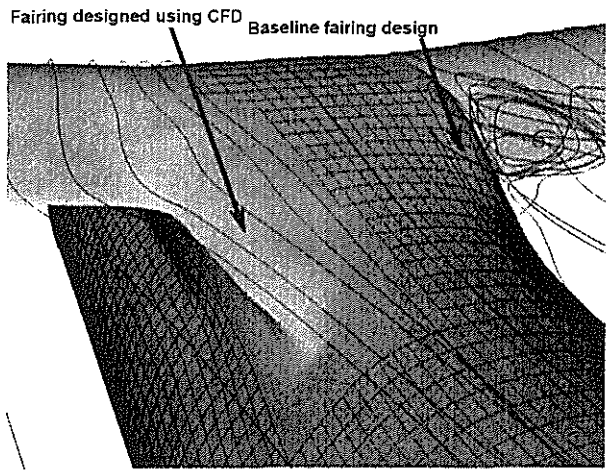

Fig. 8. The new BA 609 at wing/fuselage fairing significantly reduces flow separation.

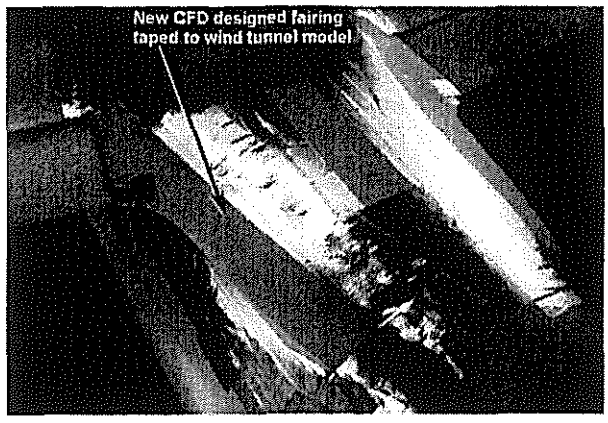

Fig. 9. Wind tunnel testing of the new fairing design produced improved performance.

generate a part for the wind tunnel model shown in Fig. 9. That part was sent to the wind tunnel in time to be incorporated into the model while the test was still in progress.

Wind tunnel testing with the new fairing showed a 16% improvement in the directional stability and a 0.18 ft^2 (0.0167 m^2) reduction in the drag. Since no parts had to be fabricated for the computational analysis, CFD was able to provide a low-cost alternative to conventional trial and error wind tunnel testing methods and provided significant insight into the cause of reduced vertical tail effectiveness.

4.3 Midwing Exhaust Pressures

In order to cool equipment in the midwing area, inlets and exhausts for cooling flow are necessary. Initial evaluations of the size and placement of the inlet and exhaust were based on a panel method solution (Ref. 8). When final sizing and placement studies were conducted, the OVERFLOW code was used to provide additional midwing fairing pressure information. At low angles of attack, the panel method and Navier-Stokes solutions were equivalent, as is shown in Fig. 10. In this figure, the pressures aft of the wing on the BA 609 from the panel code and OVERFLOW are given. The pressure coefficients shown in the left of the figure are at the station shown by the plane in the right of the figure. As can be seen, at an angle of attack of zero degrees, the panel method solution is very similar to the Navier-Stokes solution. This indicates that the flow is smooth and that there is no flow separation on the fuselage at this cruise condition. However, at very high angles of attack, the boundary layer thickens and the pressures from the panel method produce results that are different from the Navier-Stokes results (Fig. 11). The recovery of pressure aft of the wing is not as positive for the Navier-Stokes solution as the panel method would indicate. Because the Navier-Stokes code models the thickening of the boundary layer and flow separation, it was used for the placement and sizing determination of the midwing fairings for the BA 609. Using the Navier-Stokes results ensures that adequate cooling flow is obtained at all flight conditions.

4.4 Distribution of Airloads

Computational fluid dynamic results are also being used to calculate airload distributions on the BA 609. During the design of external components, surface pressures are needed to establish the airload contribution to the total load. Critical load conditions are established for each external component by considering combinations of maximum local flow velocity, extremes in local flow direction, and Mach number as determined by the design flight envelope and maneuvering requirements. CFD analysis is run at the selected critical flight conditions to produce a detailed distribution of pressures on the surface of the model. The Navier-Stokes grid model that was used for these runs is represented in Fig. 7. Therefore, the approach was efficient in that only new cases were run for the airload distributions on the existing grid model.

For the external structural components, the CFD pressure results for each case are mapped onto a NASTRAN model using a method developed at Bell. Fig. 12 shows a NASTRAN surface geometry for the BA 609 nacelle. Pressures from an OVERFLOW run have been mapped onto this geometry. The surface pressures are depicted by colors in this figure. The dark regions depict suction pressures and the lighter regions depict positive pressures. As part of this process, input files are generated that represent the distributed pressure on the NASTRAN model. This deck is transferred to the structural loads groups to provide air load information for the design of the structure. For the BA 609, this allowed fast generation of critical air loads and incorporation of this CFD information into the structural design codes.

5. SUMMARY

Computational fluid dynamics is becoming an integral part of the aircraft design process. Navier-Stokes codes allow details to be modeled and new designs to be produced that improve the aerodynamic characteristics. In addition, methods have been developed that allow the CFD air load distributions to be mapped to the

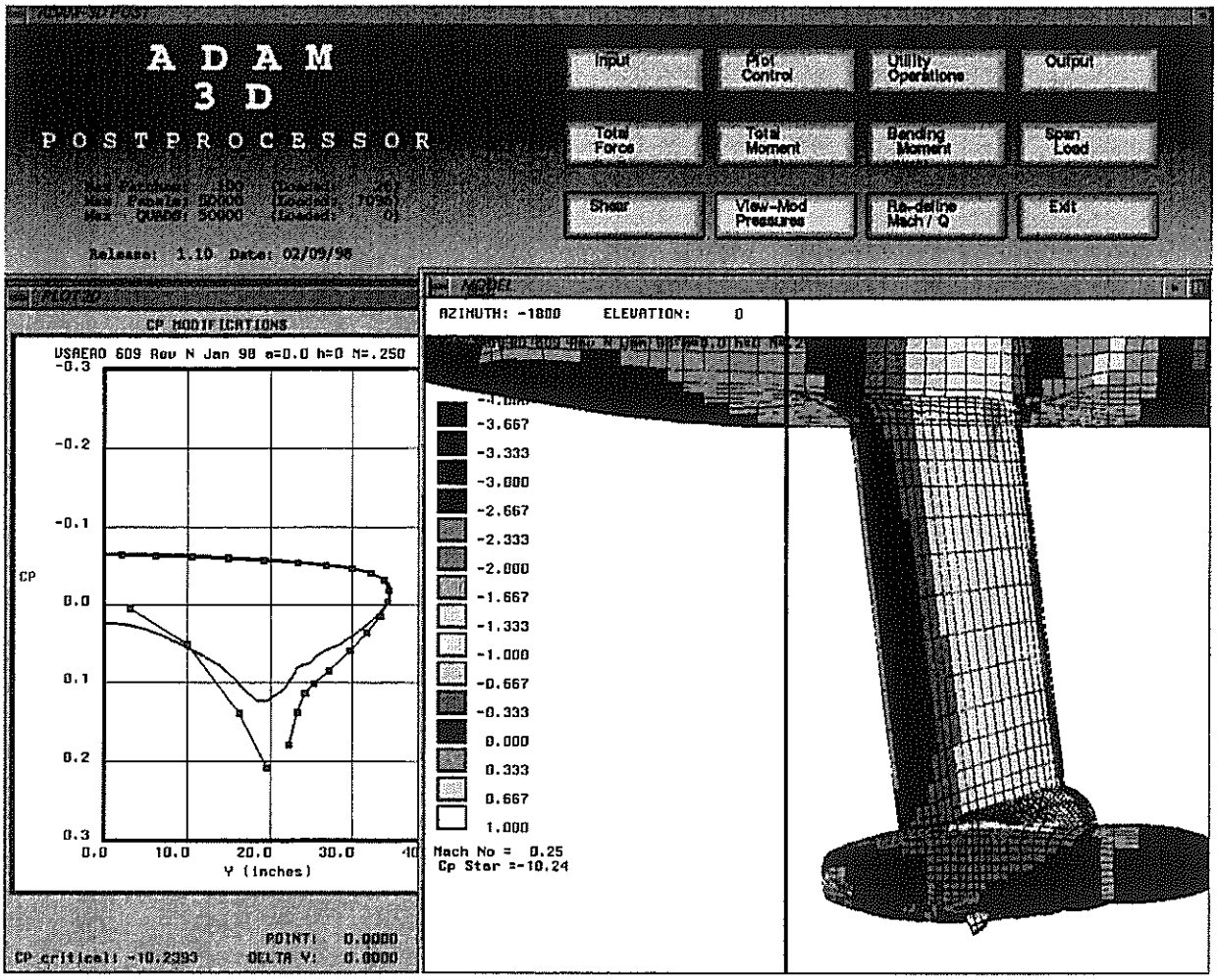

Fig. 10. Panel method and Navier-Stokes pressures are similar at low angles of attack.

NASTRAN structural design code. As a result of the application of CFD to the design of the BA 609, new design concepts are being developed that improve the performance, lower the operating cost, and provide the minimum weight solution.

6. ACKNOWLEDGEMENTS

The authors wish to express their appreciation to Ashok Agnohotri, Ross Menger, Bob Milliken, and Ted Trept for valuable discussions during the preparation of this paper, Don Axley for technical assistance, and Chuck Gatlin who finalized the graphics and layout.

7. REFERENCES

1. J. C. Narramore, "Computational Fluid Dynamics Development and Validation at Bell Helicopter," AGARD Conference Proceedings No. 552, "Aerodynamics and Aeroacoustics of Rotorcraft", Paper No. 15, August 1996.
2. J. P. Steinbrenner and J. R. Chawner, "The GRIDGEN Version 9 Multiple Block Grid Generation Software," MDA Engineering Report 94-01, August 12, 1994.
3. W. M. Chan, I. T. Chiu, and P. G. Buning, "User's Manual for the HYPGEN Hyperbolic Grid Generator and the HGUI Graphical User Interface," NASA TM-108791, October 1993.
4. N. E. Suhs and R. W. Tramel, "PEGSUS 4.0 User's Manual," AEDC-TR-91-8, AEDC/PA, Arnold Air Force Base, Tenn., 1991.
5. P. G. Buning, D. C. Jespersen, T. H. Pulliam, W. M. Chan, J. P. Slotnick, S. E. Krist, and K. J. Renze, "OVERFLOW User's Manual Version 1.7v," NASA Langley Research Center, Hampton, VA, 1997.
6. W. M. Chan and P. G. Buning, "User's Manual for FOMOCO Utilities - Force and Moment Computation Tools for Overset Grids," NASA TM-110408, July 1996.
7. Val Watson, "Software for Visualization of Fluid Dynamics," presented at the Computational Fluid Dynamics Conference, NASA Ames Research Center, March 12-14, 1991.
8. B. Maskew, "VSAERO User's Manual," NASA CR 166-476, November 1982.

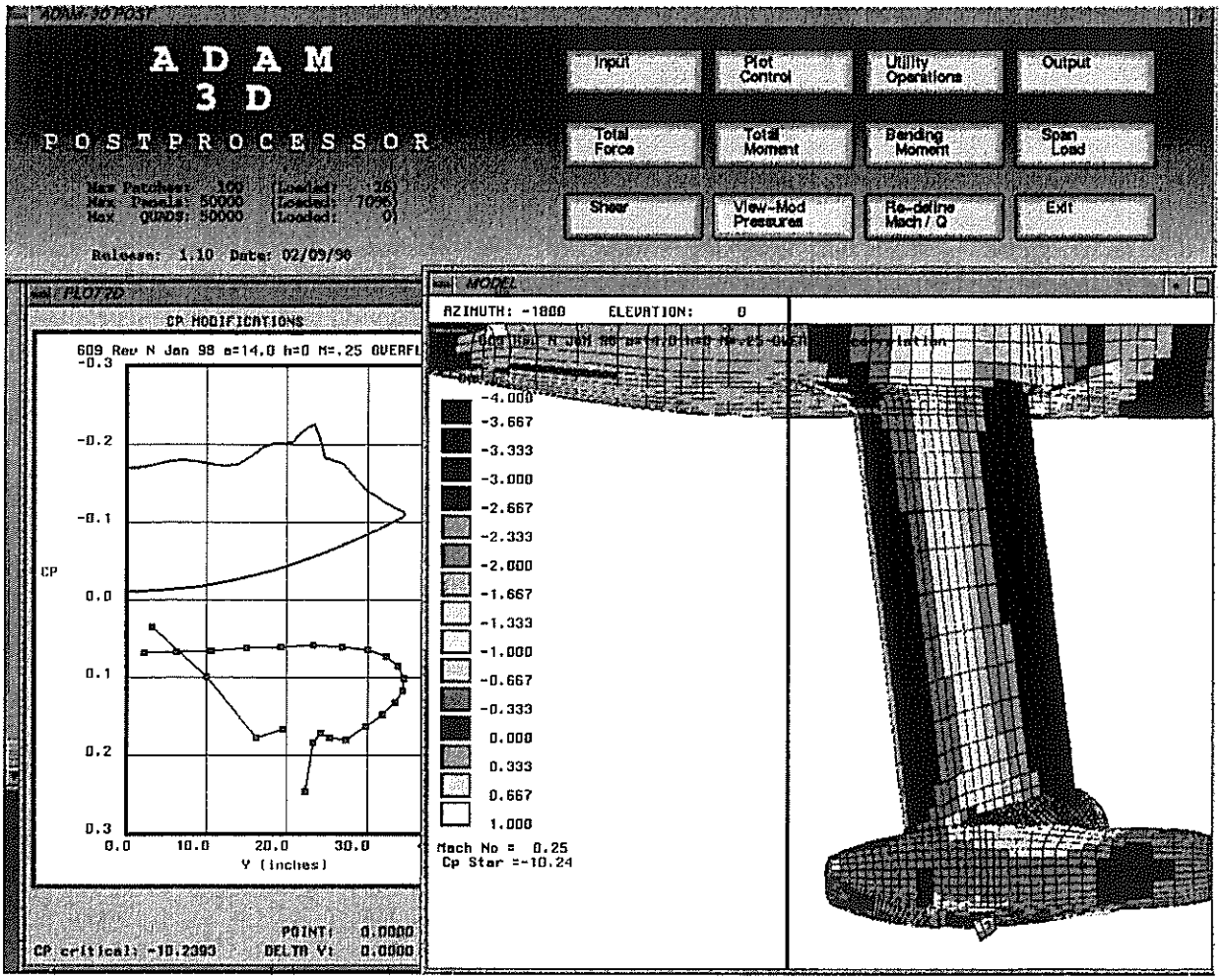

Fig. 11. At very high angles of attack, Navier-Stokes improves the pressure prediction.

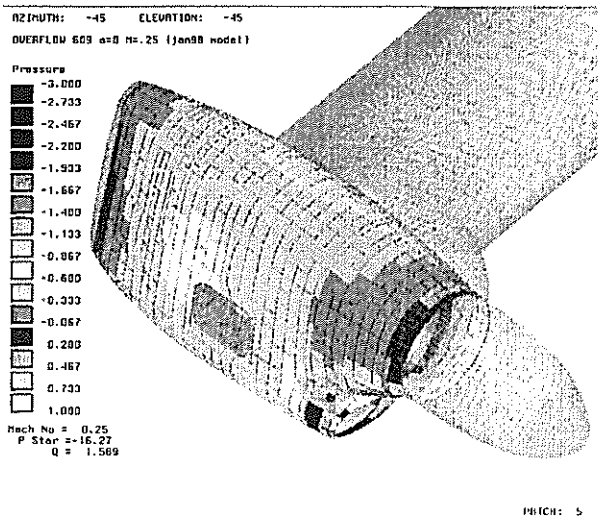

Fig. 12. CFD pressures were mapped onto the NASTRAN surface model.

TWENTY FIFTH EUROPEAN ROTORCRAFT FORUM

Paper no. C13

ACTIVE SUPPRESSION OF STALL ON HELICOPTER ROTORS

BY

KHANH NGUYEN
ARMY/NASA ROTORCRAFT DIVISION
NASA AMES RESEARCH CENTER, MOFFETT FIELD, CA

SEPTEMBER 14-16, 1999
ROME
ITALY

ASSOCIAZIONE INDUSTRIE PER L'AEROSPAZIO, I SYSTEMI E LA DIFESA
ASSOCIAZIONE ITALIANA DI AERONAUTICA ED ASTRONAUTICA

Active Suppression of Stall on Helicopter Rotors

Khanh Nguyen
Army/NASA Rotorcraft Division
NASA Ames Research Center, Moffett Field, CA

Abstract

This paper describes the numerical analysis of a stall suppression system for helicopter rotors. The analysis employs a finite element method and includes advanced dynamic stall and vortex wake models. The stall suppression system is based on a transfer function matrix approach and uses blade root actuation to suppress stall directly. The rotor model used in this investigation is the UH-60A rotor. At a severe stalled condition, the analysis predicts three distinct stall events spreading over the retreating side of the rotor disk. Open loop results show that 2P input can reduce stall only moderately, while the other input harmonics are less effective. The responses of the stall index, a measure of stall, to individual input harmonics are highly nonlinear. Such nonlinear stall behavior makes the closed-loop controller ineffective in suppressing stall and the combined effects of individual harmonics non-additive. Also, stall reduction does not guarantee gains in rotor performance.

1. Introduction

Active control has the potential to directly suppress rotor blade stall and thus can expand the helicopter flight envelope. Unlike fixed-wing aircraft, stall does not limit the low speed operation of helicopters. Stall on rotor blades limits the rotor structural envelope, in particular, the helicopter maximum speed and the rotor loading capabilities. At the stall boundary, the large blade pitching moment induced by stall can cause stall flutter and excessive loading, leading to fatigue of structural components. In addition, stall increases the rotor shaft torque, causes excessive vibration, and adversely affects the aircraft handling qualities. Successful control of stall can enhance the utility of rotorcraft.

Classical treatments of rotor stall indicate that stall typically occurs near the retreating blade tip. In forward flight, a blade encounters a time-varying dynamic pressure due to the combined effects of blade rotation and vehicle forward speed. Thus, the dynamic pressure is greater on the advancing side than the retreating side. To balance the roll moment on the rotor, the basic trim control provides low angle of attack on the advancing side and high angle of attack on the retreating side. As the rotor loading or the forward speed increases, stall is initiated due to the large angle of attack requirement on the retreating side.

Operating in an unsteady environment, the blade encounters the most severe type of stall known as dynamic stall. In forward flight, the blade experiences time-varying dynamic pressure and angle of attack arising from blade pitch inputs, elastic responses, and non-uniform rotor inflow. If supercritical flow develops under dynamic conditions, then dynamic stall is initiated by leading edge or shock-induced separation. Even with limited understanding about the development of supercritical flow in the rotor environment, flow visualization results of oscillating airfoil tests at low Mach number suggest that supercritical flow is associated with the bursting of the separation bubble as it encounters the large adverse pressure gradient near the blade leading edge [1]. Dynamic stall is characterized by the shedding of strong vortices from the leading edge region. The leading edge vortex produces a large pressure wave moving aft on the airfoil upper surface and creating abrupt changes in the flow field. The pressure wave also contributes to large lift and moment overshoots in excess of static values and prolongs flow separation, both causing significant nonlinear hysteresis in the airfoil behavior.

The other type of stall typically observed in two-dimensional wind tunnel tests involves trailing edge separation. The phenomenon of trailing edge separation is associated with either static or dynamic conditions. Separation starts from the airfoil trailing edge, and with increasing angle of attack, the separation point progresses towards the leading edge region. Trailing edge separation contributes to nonlinear behavior, such as hysteresis, in lift, drag and pitching moment due to the loss in circulation. In contrast to dynamic stall that is characterized by abrupt changes in airfoil behavior, trailing edge stall progresses at a moderate rate.

A recent investigation of blade pressure data from the UH-60A Airloads Program [2] has helped improve understanding about rotor stall behavior. Test results reveal that stall is not confined solely to the retreating side but rather spreads to the first quadrant of the rotor disk. Since stall is strongly coupled with the blade dynamics, especially the torsion mode, this coupling manifests in a stall cycle that begins in the fourth quadrant of the rotor disk and continues up to the first quadrant in two cycles (three stall peaks). The stall cycle has a frequency

closely matched with the blade torsion frequency. Flight test data also indicate that rotor stall exhibits behavior similar to that observed in airfoil oscillating tests where the shedding of the strong leading edge vortex dominates the flow pattern.

Passive control of blade stall typically employs the tailoring of blade twist and planform for efficient blade load distribution. Modern rotors often employ blade construction with multi-airfoil sections -- thick, high-lift sections inboard and thin, transonic sections for the tip region. These designs aim to provide efficient rotor disk loading and low drag and thus, are employed primarily for performance benefits; however, they also provide stall alleviation. The design of the BERP rotor [3] is one notable example of passive methods. The BERP blade has multiple airfoil sections and a prominent tip shape designed to operate efficiently in the transonic regime (low angle of attack advancing blade tip) and to generate high lift in subsonic flow condition (retreating blade tip).

In an effort to expand the helicopter flight envelope, this analytical study explores the use of high frequency blade pitch actuation to alleviate blade stall. The availability of high-frequency blade-mounted actuators has made active stall suppression realizable. Earlier investigations of active rotor control have focussed on swashplate actuation [4]. This scheme places a limit on the number of harmonics available for excitation at $N-1$, N, and $N+1$ per rev, where N is the number of blades per rotor. With the blade-mounted actuators, the excitation frequency is not limited by the swashplate constraint but by the bandwidth of the actuators. ZF Luftfahrttechnik GmbH of Germany built and flight-tested an individual-blade-control type actuator with excitation frequencies varying from two to twelve per rev on an MBB BO-105 helicopter [5]. More recently, the same company is building larger actuators to be retrofitted into a full-scale UH-60A rotor for wind tunnel testing at NASA Ames.

2. Previous Stall Suppression Works

In the fifties and early sixties, Stewart [6], Payne [7], and Arcidiacono [8], conducted separate analyses to investigate the potential of using higher harmonic control to delay the onset of retreating blade stall. These investigators discovered that higher harmonic control could be used in combination with the basic trim control to redistribute lift on the rotor. Such lift redistribution could be adjusted to relieve retreating blade stall while maintaining the rotor trim states. The resulting effect would be to raise the speed limitation of helicopters.

In 1961, Bell Helicopter Company conducted a flight test on an UH-1A helicopter equipped with a rotor head mechanism capable of generating two-per-rev blade pitch [9]. The test explored the potential of 2P blade pitch to improve rotor performance and cabin vibration. Test results showed no reduction in the rotor shaft torque with any combinations of amplitude and phase of the 2P input. A post-test analysis revealed that the drag reduction on the retreating side due to 2P control was offset by an increase in profile drag in the fore and aft portions of the rotor disk. Even though stall alleviation was not attempted in the test program, such conclusions confirmed the previous analytical predictions that 2P control could be used to redistribute the rotor loading.

In the early eighties, Kretz [10] wind tunnel tested a "stall barrier feedback" system on a six-foot diameter two-bladed rotor for stall suppression. The system relied on three pressure sensors mounted at 85 percent blade radial station to monitor stall. The pressure sensors provided feedback signals that activated the high frequency actuators to avoid stall. The feedback pressure signals were based on the threshold values adapted from airfoil test data. Test results yielded no concrete conclusions to substantiate the benefits of this stall suppression system.

3. Scope of Current Investigation

The objective of the current study is to analytically evaluate the effectiveness of an automatic stall suppression system for helicopters using higher harmonic blade root input. The effects of stall suppression on rotor performance are also investigated. Stall suppression is formulated as an optimization problem in which the stall behavior of a rotor is quantified and subsequently minimized using higher harmonic control (HHC). Thus, the system suppresses stall directly.

In this paper, the term higher harmonic control refers to blade pitch input with harmonic content greater than one per-rev. Since the focus of the paper is on the aerodynamic performance aspects of stall suppression, the effects of HHC on blade loads, control system loads, and vibratory hub loads, which can be significant, are not discussed.

The analysis used in this study will be described, followed by a description of the HHC system for stall suppression. The analysis is then used to model a stalled condition for the UH-60A rotor. An evaluation of the open and closed-loop stall suppression system is provided. Finally, specific findings from this study are presented.

4. Aeroelastic Analysis

The NASA Ames-version of the University of Maryland Advanced Rotorcraft Code (UMARC) [11] is adopted to investigate the potential of active control to suppress rotor stall. UMARC/A is a finite element code that includes advanced unsteady aerodynamics and vortex-wake modeling. The structural and aerodynamic modeling of UMARC/A makes

the code a suitable analysis for studying active control effects on rotor behavior.

The rotor blade is modeled as an elastic, isotropic Bernoulli-Euler beam undergoing small strain and moderate deflections. The blade degrees of freedom are flap bending, lead-lag bending, elastic twist, and axial deflections. The finite-element-method based on Hamilton's principle allows a discretization of the blade model into a number of beam elements, each with fifteen degrees of freedom.

The blade airloads are calculated using a nonlinear unsteady aerodynamic model proposed by Leishman and Beddoes [12]. This model consists of an attached compressible flow formulation along with a representation of the nonlinear effects due to trailing edge separation and dynamic stall. In the attached flow formulation, the normal force (or lift) and pitching moment includes both circulatory and impulsive (noncirculatory) components. Physically, the circulatory components model the shed wake effects, while the impulsive components originate from the pressure wave generated by the airfoil motion. For dynamic stall modeling, an artificial normal force c_N' is computed based on the attached flow lift and the dynamics of the pressure distribution, represented by a time-lag model. This quantity incorporates the effects of stall delay and is used as a criterion of stall onset.

The trailing edge separation model is based on Kirchhoff's formulation, which relates the separation location f to the airfoil force and moment behavior. The variation of the separation location with angle of attack is constructed from static airfoil data, then the results are curve-fitted. The value of the separation location is a measure of the degree of nonlinearity in the lift behavior. Information about the flow separation point also allows the reconstruction of the airfoil static behavior, a precursor to the modeling of the airfoil dynamic characteristics.

For dynamic stall, stall onset is based on the criterion that leading edge separation initiates only when the artificial normal force c_N' attains a critical value, c_{N1}, corresponding to a critical leading edge pressure. In this model, c_{N1} is the maximum lift coefficient from the airfoil tables and is a function of the Mach number. Once initiated, the excess lift due to dynamic stall is governed by the dynamics of the vortex lift, defined as the difference in lift between the attached (linear) and separated flow (nonlinear) regimes. The vortex motion over the airfoil upper surface induces a large change in the pitching moment. The vortex induced pitching moment is computed based on the vortex lift and the position of the center of pressure.

A prescribed wake model is used for the inflow calculation. The coupled blade response and trim control settings are solved for simulated wind tunnel conditions. For trim, the rotor shaft orientation is prescribed, and the blade collective and cyclic pitch inputs are automatically adjusted to desired values of thrust and hub moments or blade flapping schedules. A modal reduction technique is employed in the blade response solution to reduce the computational requirement. The modal equations are solved iteratively using a robust finite-element-in-time method in which the periodic boundary conditions are inherent in the formulation. The converged solution satisfies the governing equations for both rotor trim and blade response, which include higher harmonic control effects.

5. Higher Harmonic Control System

The controller algorithm, based on a transfer function matrix approach, is implemented in UMARC/A. Depending on the control objectives considered (to suppress stall or to reduce rotor shaft torque) each element of the transfer matrix represents the sensitivity of the controlled parameter (z) to each harmonic of the blade root actuation (u). In this investigation, the transfer matrix is computed using a finite-difference-method in which each harmonic of the control input (sine and cosine components) is perturbed individually. The control law is formulated as an optimization problem:

$$\min\ (qz_i^2 + u_i^T R u_i) \qquad (1)$$

subjected to

$$z_i = z_{i-1} + (1-r)T_i(u_i - u_{i-1}) \qquad (2)$$

In Eq. 1, the parameters q (a scalar) and R (a diagonal matrix) assign relative weightings to the controlled parameter z_i and each component of the input vector, respectively. Since the controller is based on a harmonic method, the controller cycle i is once-per-rotor revolution.

For stall suppression, z_i is the stall index computed at each controller cycle by:

$$z_i = \sum_{m}^{42} \sum_{n}^{120} F(r_m, \psi_n) \qquad (3)$$

where the double summation is over the 5040 computation points over the rotor disk (42 points in the radial direction X 120 azimuth steps), and the lift excess F is:

$$F(r,\psi) = \begin{cases} (c_N' - c_{N1})M^2 & \text{if } c_N' \geq c_{N1} \\ 0 & \text{otherwise} \end{cases} \qquad (4)$$

Note that F is defined over the entire rotor disk, with r being the blade radial station, ψ the azimuth angle, and M the local Mach number. With this definition, the stall index is a measure of the

severity of stall on the rotor disk in term of the excess lift over the stall area. The excess lift is the amount of artificial lift c_N' over the airfoil maximum lift c_{N1}, adapted from the dynamic stall model described earlier.

In Eq. 2, the control rate factor r, with value between 0 and 1, limits the control update rate, and i denotes the controller cycle. The transfer matrix updating is an option in which T_i is updated at each controller cycle, based on a secant method [13]. The T matrix updating, when used in combination with the control rate limit, helps improve the convergence of the controller when nonlinear effects dominate. This approach was successfully applied to another control problem – vibration suppression of rotors under stalled conditions – with significant nonlinearity in the model [4].

The vector u_i represents the control input that includes harmonics from 2 to 6 per rev:

$$u_i = [\theta_{2c} \quad \theta_{2s} \quad \ldots \quad \theta_{6c} \quad \theta_{6s}]^T \qquad (5)$$

In terms of the elements of u_i, the higher harmonic schedule for the *jth* blade is:

$$\theta^j_{HHC}(\psi) = \sum_{k=2}^{6} A_k \cos(k\psi^j - \phi_k) \qquad (6)$$

Besides stall suppression, a second controller is also investigated. This controller aims to improve the rotor performance using higher harmonic blade root pitch. For this system, the controlled parameter (Eq. 3) is simply the rotor shaft torque. Except for the change in the definition of z, this controller retains the same structure as that of the stall suppression controller. Note that this controller does not restrict the input harmonic to 2P as in other investigations (such as [14] or [15]) but includes a wide range of input harmonics (2P to 6P).

6. Rotor Model

This study uses the UH-60A as the rotor model. The rotor is fully-articulated with 20 deg swept tip blades. The blade is modeled with eight elastic beams along with a coincident flap-lag hinge for root boundary conditions. The pitch-link is modeled with a restraining spring. The blade sweep is not modeled explicitly, but the sweep effects are included using chordwise offsets of center of gravity and aerodynamic center. Table 1 lists the generic rotor parameters and the computed blade frequencies. The airfoil tables of the SC-1095 and the SC-1095R8 are adapted from those reported in Ref. 15.

In order to simplify the analysis, a wind tunnel trim simulation is used. The prescribed variables are the rotor shaft tilt, cyclic flappings, and rotor thrust (C_T/σ). The baseline flight condition corresponds to a C_T/σ of 0.13, advance ratio of 0.236, and 3 deg forward shaft tilt. The computed airloads are shown in Fig. 1. The lift distribution shown in Fig. 1(a) does not reveal any significant stall events. However, the drag distribution (Fig. 1(b)) suggests more than one stall event inboard of the blade midspan on the retreating side of the rotor disk. The lift excess $F(r,\psi)$, defined in Eq. 4 as a measure of stall, is shown in Fig. 1(c). This figure clearly shows that the inboard drag rises are associated with the three stall events starting near 180 deg azimuth and continuing into the first quadrant. With regards to the flight test data of Ref. 2 which shows that the three stall events occur near the blade tip, these computed results suggest that the analysis is probably deficient in the inflow modeling.

7. Open Loop Study

An open-loop study provides the sensitivity of the stall index to the amplitude and phase variation of single harmonic inputs. For each harmonic, the input phase is varied at constant amplitude, and then the amplitude at the optimum phase is varied. These results aim to provide insight into the input-output behavior of the system and help define the type of controller (linear versus nonlinear) to use. The effectiveness of the closed-loop system is also estimated based on open-loop data. Representative results are presented in this paper.

Figure 2 shows the variation of stall index to the 2P phase sweep in increment of 30 deg at 1 deg amplitude for the same flight condition (μ = 0.236, C_T/σ = 0.13) mentioned above. From Eq. 6, 210 deg phase (for minimum stall) indicates that the blade pitch is minimum at 15 and 195 deg azimuth. Since Fig. 1(c) indicates that the peak stall region occurs between 180 and 240 deg azimuth, this result suggests that stall is reduced by lowering the blade pitch at the peak stall region.

The effects of 2P amplitude variation in increment of 0.5 deg at 210 deg phase on the stall index are shown in Fig. 3. This result indicates that the stall index varies nonlinearly with the 2P amplitude. Increasing the 2P amplitude above 1 deg generates more stall. The 1 deg amplitude appears to be an optimum value for this phase angle.

For the 2P phase sweep at the same operating condition, the shaft torque variation exhibits a different trend than that of the stall index. Such results, shown in Fig. 4, indicate that the shaft torque is reduced at all phase angles of 2P input at 1 deg amplitude. While minimum stall occurs at 210 phase angle (Fig. 2), the minimum torque is at 60 deg. In fact, in the phase region where stall is minimum, the rotor shaft torque only achieves a moderate reduction compared to the minimum value at 60 deg phase.

Since the three stall events are spread over the retreating side of the rotor disk, the open loop re-

sults with the other harmonics (3P–6P) show rather complicated responses with HHC input. For example, the 3P results (Fig. 5) show two local minima for stall at 120 and at 270 deg phases. The first minimum phase input reduces the first stall event and increases the second event shown in Fig. 6(a), and vice versa for the second minimum phase input (Fig. 6(b)). Neither input phase causes significant stall reduction. The maximum stall case is shown in Fig. 6(c), in which the 30 deg phase input increases the first stall event significantly while reducing the second event by only a small amount. The 4P input can increase stall significantly while reducing stall only moderately with variation in phase at 0.7 deg of 4P amplitude. The 5P input is less effective than the 4P input, while the 6P input, like the 3P component, shows little potential to reduce stall. Results of the open loop study with individual blade pitch harmonics from 2P–6P suggest that 2P is the most effective type of input for stall reduction for this flight condition.

8. Closed Loop Study

For the closed loop study, the analysis employs trial open loop input to generate the transfer function and then operates automatically to minimize the stall index (Eq. (3)). The HHC amplitude (the RMS value of all harmonics) is constrained to be less than 3 deg. This study yields no satisfactory stall reduction. Different combinations of the number of input harmonics yield results that, at best, match the open loop 2P results shown above. A typical closed loop result using a controller with 2P and 4P input is shown in Fig. 7. This figure shows the stall index variation with the controller cycle. The controller reduces stall only by a small amount at the first cycle and then converges to a steady state value larger than the uncontrolled value. Using transfer matrix updating only causes a periodic shooting of the stall index above the steady-state value. Since 2P and 4P are the two best individual inputs for stall reduction, these results suggest that the combined effects of the different input are not additive for stall reduction. In particular, the combination of 2P and 4P input does not reduce the stall but rather generates more stall. The nonlinear behavior associated with active stall control for this rotor system would require a more robust, nonlinear controller.

The same controller performs quite satisfactorily when used to reduce the rotor shaft torque with 2P input. Again, the HHC amplitude is constrained to be less than 3 deg. The result is shown in Fig. 8. The controller using 2P input converges to a steady 7.2 percent reduction in shaft torque. The transfer matrix update algorithm causes a small deviation at the 5th controller cycle.

9. Concluding Remarks

Analytical study of stall suppression for a UH-60A rotor is conducted at a moderate forward speed ($\mu = 0.236$) and high thrust ($C_T/\sigma = 0.13$) condition. The UMARC/A analysis predicts three distinct stall events spreading over the retreating side of the rotor disk for this flight condition. The results of this investigation show that stall on the UH-60A rotor can be reduced only moderately with higher harmonic control at this stalled condition. Open loop results show that 2P input can reduce stall moderately, while the other input harmonics are less effective. The responses of the stall index, a measure of stall, to individual input harmonic are highly nonlinear. Such nonlinear behavior makes the closed-loop controller ineffective in suppressing stall and the combined effects of individual harmonics non-additive.

Furthermore, since stall is only one of the phenomena affecting rotor performance, stall reduction does not guarantee a gain in rotor performance (i.e., reduction in shaft torque at constant operating conditions). The blade pitch schedule that improves rotor performance would be different from the one that reduces stall.

For future plans, this study will include better inflow models to improve the stall prediction capabilities of the UMARC/A analysis. Also, the study will focus on the stall reduction potential of HHC at higher forward speeds. High speed flight conditions may exhibit different stall patterns that can be suppressed more effectively with active control than the flight condition considered in this paper.

References

1. McCroskey, W. J., Carr, L. W., and McAlister, K. W., "Dynamic Stall Experiments on Oscillating Airfoils," *AIAA Journal*, Vol. 14, No. 1, 1976, pp. 57-63.
2. Bousman, W. G., "A Qualitative Examination of Dynamics Stall from Flight Test Data," *Journal of the American Helicopter Society*, Vol. 43, No. 4, 1998, pp. 279-295.
3. Perry, F. J., "Aerodynamics of the World Speed Record," Proceedings of the American Helicopter Society 43rd Annual Forum, St. Louis MO, May 1987.
4. Nguyen, K. and Chopra, I., "Application of Higher Harmonic Control to Rotors Operating at High Speed and Thrust," Journal of the American Helicopter Society, Vol. 35, No. 3, 1990, 336-342.
5. Richter, P. and Eisbrecher, H. D., "Design and First Flight Tests of Individual Blade Control Actuators," Proceedings of the Sixteenth European Rotorcraft Forum, Glasgow, UK, Sep 1990.

6. Stewart, W., "Second Harmonic Control on the Helicopter Rotor," Aeronautical Research Council, RM-2997, London, Aug 1952.
7. Payne, P. R., "Higher Harmonic Rotor Control," *Aircraft Engineering*, Vol. 30, No. 354, 1958, pp. 222-226.
8. Arcidiacono, P. J., "Theoretical Performance of Helicopters Having Second and Higher Harmonic Feathering Control," *Journal of the American Helicopter Society*, Vol. 6, No. 2, 1961, pp. 8-19.
9. Drees, J. M. and Wernicke, R. K., "An Experimental Investigation of a Second Harmonic Feathering Device on the UH-1A Helicopter," United States Army Transportation Research Command, TR-62-109, Fort Eustis, VA, June 1963.
10. Kretz, M., "Active Expansion of Helicopter Flight Envelope," Proceedings of the Fifteenth European Rotorcraft Forum, Amsterdam, The Netherlands, Sep 1989, Paper No. 53.
11. Gunjit, S. B., Chopra, I., and Nguyen, K., "Development of UMARC (University of Maryland Advanced Rotorcraft Code)," Proceedings of the American Helicopter Society 46th Annual Forum, Washington, D.C., May 1990.
12. Leishman, J. G., and Beddoes, T. S., "A Semi-Empirical Model for Dynamic Stall," *Journal of the American Helicopter Society*, Vol. 34, No. 3, 1989, pp. 3-17.
13. Dennis, J. E., Jr. and Schnabel, R. B., *Numerical Method for Unconstrained Optimization and Nonlinear Equations*, Prentice Hall, New Jersey, 1983, pp. 168-193.
14. Jacklin, S., Nguyen, K., Blaas, A., Richter, P., "Full Scale Wind Tunnel Test of a Helicopter Individual Blade Control System," Proceedings of the American Helicopter Society 50th Annual Forum, Washington, D.C., May 1994.
15. Nguyen, K. and Chopra, I., "Effects of Higher Harmonic Control on Rotor Performance and Control Loads," *Journal of Aircraft*, Vol. 29, No. 3, 1992, pp. 336-342.
16. Shanley, J. P., "Validation of UH-60A CAMRAD/JA Input Model," SER-701716, Nov 1991.

Table 1 Blade and rotor properties

Number of blades	4
Blade radius, R	26.833 ft
Blade airfoils	
0.48R–0.84R	SC-1095R8
other stations	SC-1095
Flapping hinge offset	0.0468 R
Rotor solidity	
Thrust weighted, σ	0.08317
Blade pretwist	Nonlinear
equivalent linear rate	-15.67 deg
Computed blade frequencies, per rev	
(@ 258 rpm and 10 deg $\theta_{.75}$)	
Rigid lag	0.283
Rigid flap	1.039
First elastic flap	2.779
First torsion	4.011
First elastic lag	4.538
Second elastic flap	5.021

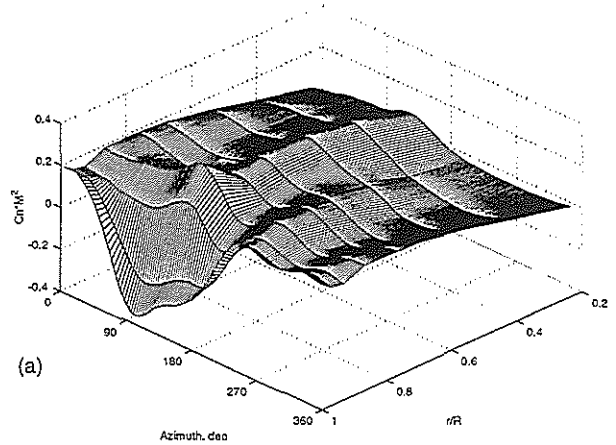

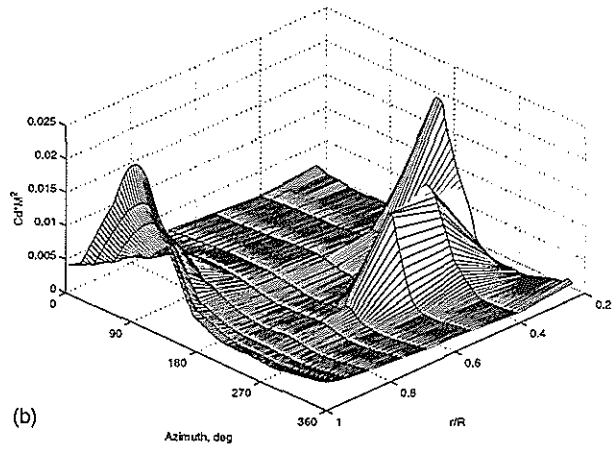

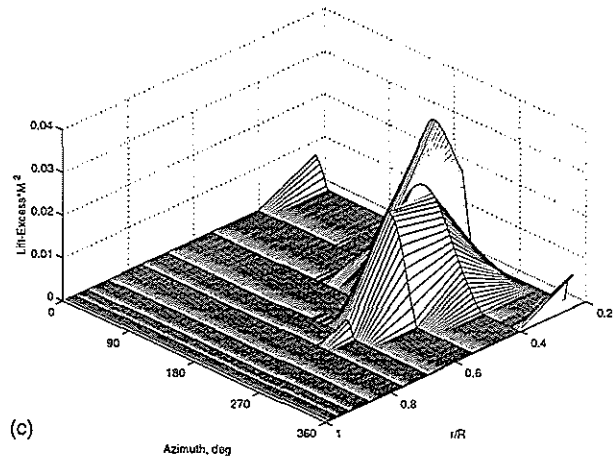

Fig. 1. Blade airloads over rotor disk: (a) normal force (or lift), b) drag, c) lift excess F(r,ψ) (μ = 0.236, $C_T/\sigma = 0.13$).

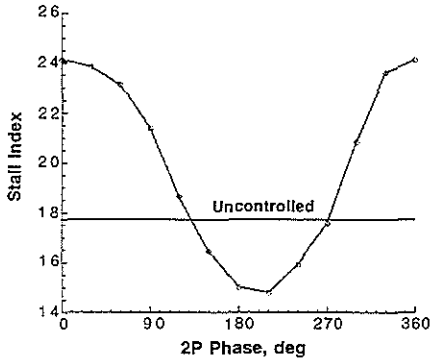

Fig. 2. Variation of stall index with 2P phase, 1 deg amplitude (μ = 0.236, $C_T/\sigma = 0.13$).

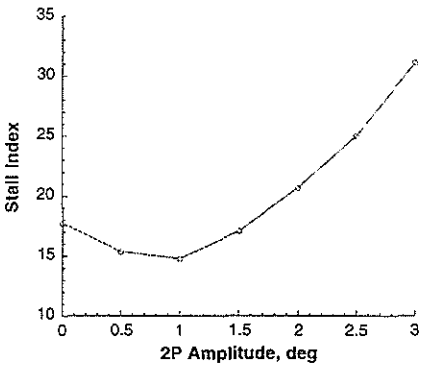

Fig. 3. Variation of stall index with 2P amplitude, 210 deg phase angle (μ = 0.236, $C_T/\sigma = 0.13$).

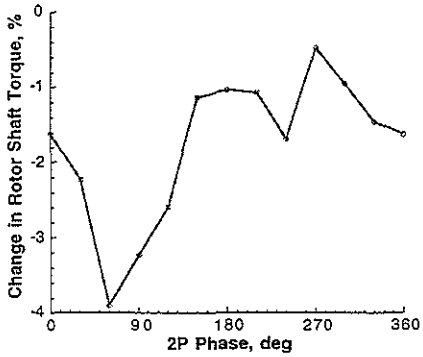

Fig. 4. Reduction in rotor shaft torque with 2P phase angle, 1 deg amplitude (μ = 0.236, $C_T/\sigma = 0.13$).

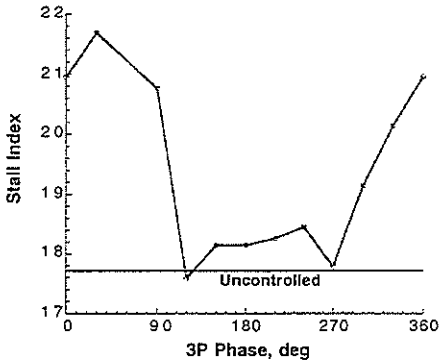

Fig. 5 Variation of stall index with 3P phase angle, 0.7 deg amplitude ($\mu = 0.236$, $C_T/\sigma = 0.13$).

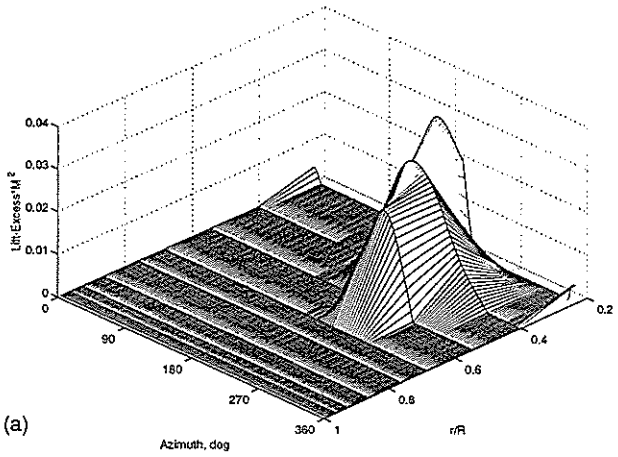

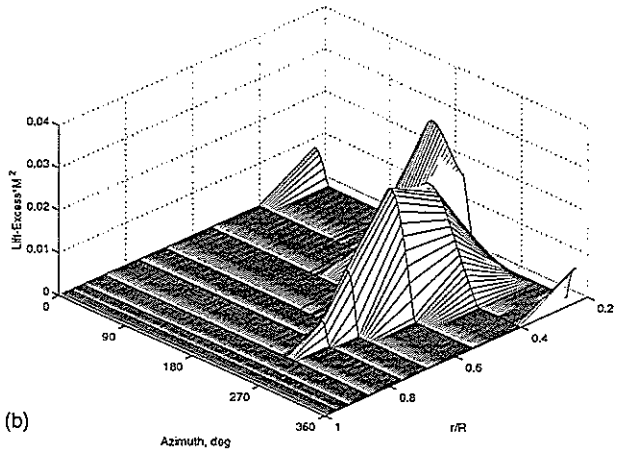

Fig. 6. Lift excess over rotor disk: (a) 120 deg 3P phase, (b) 270 deg 3P phase, (c) 30 deg 3P phase ($\mu = 0.236$, $C_T/\sigma = 0.13$).

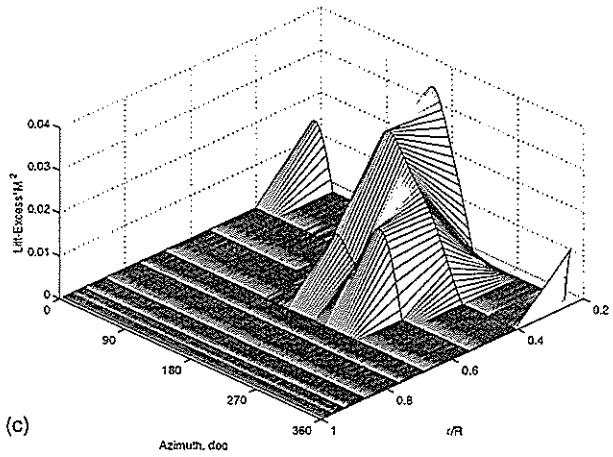

Fig. 6. Concluded.

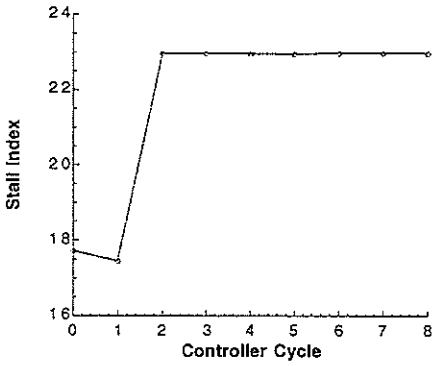

Fig. 7. Response of stall index to controller with 2P and 4P input ($\mu = 0.236$, $C_T/\sigma = 0.13$).

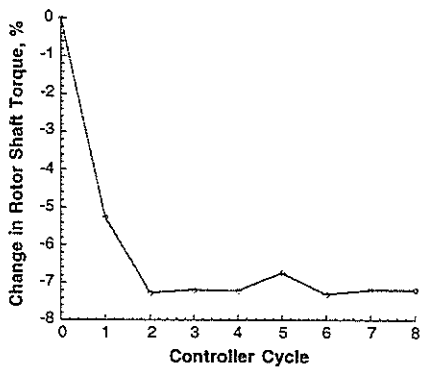

Fig. 8. Reduction in rotor shaft torque with 2P controller ($\mu = 0.236$, $C_T/\sigma = 0.13$).

TWENTY-FIFTH EUROPEAN ROTORCRAFT FORUM

Paper No. C14

Numerical Simulation of the BK117 / EC145 Fuselage Flow Field

by

Eberhard Schöll

EUROCOPTER DEUTSCHLAND GmbH, München, Germany

September 14-16, 1999

Rome

Italy

ASSOCIAZIONE INDUSTRIE PER L'AEROSPAZIO, I SISTEMI E LA DIFESA
ASSOCIAZIONE ITALIANA DI AERONAUTICA ED ASTRONAUTICA

Numerical Simulation of the BK117 / EC145 Fuselage Flow Field

Eberhard Schöll

EUROCOPTER DEUTSCHLAND GmbH, 81663 München, Germany

The need for increasing their competitiveness and reducing development times forces the helicopter industry to introduce improved aerodynamic tools for analyzing the flowfields around helicopter components. CFD methods have rapidly matured over the last few years and are now powerful enough to be integrated in the industrial design process. At EUROCOPTER DEUTSCHLAND, a commercial CFD software was installed and applied during the BK117 upgrade development program. An extensive validation by calculating the flowfield around the existing BK117 fuselage and comparing the results to wind tunnel test data was performed in order to prove the accuracy and reliability of the CFD method. The fuselage aerodynamics of the upgrade helicopter EC145 were investigated by simple wind tunnel tests measuring the aerodynamic coefficients and CFD calculations. The application of the CFD method supplemented the wind tunnel tests and provided surface pressure distributions as input for stress analysis of the fuselage structure. Furthermore, a first attempt was made to use CFD simulations for estimating the aerodynamic efficiencies of horizontal stabilizer and endplates and for simulating the influence of the rotor downwash by activating the actuator disk model of the CFD software.

Introduction

As time-to-market for the design and development of a new helicopter or an upgrade of an existing helicopter has to be decreased to be competitive in the world market, there is a pressing need for improved aerodynamic methodologies capable of analyzing the flowfield around helicopter components such as main rotor or fuselage and empenage in various flight conditions.

The unique ability of helicopters to hover or fly at very low speed in any directions and the unsteady operation of its rotating rotor blades generate numerous specific and complex aerodynamic problems which have permanently been challenging the engineer's skills since the pioneering flights. Up to recent times, theoretical and numerical methods were unable to satisfactorily cope with these problems and the empirical approach based on flight tests and wind tunnel tests was extensively used by the industry.

Flight tests are extremely expensive and time consuming while the solutions found are often palliatives rather than optimized configurations. The wind tunnel methodology can be more efficient for conventional problems such as fuselage drag reduction but many low speed interactional conditions have been found difficult to simulate with sufficient confidence.

Paper presented at the 25th European Rotorcraft Forum, Rome, Italy, September 14-16, 1999

CFD methods developed by the research community have rapidly matured over the last few years and are now available as powerful commercial products. Solutions with engineering accuracy for surface pressure can be obtained for realistic three-dimensional configurations such as those applicable to complete commercial aircraft. Therefore, the fixed-wing industry increasingly uses those CFD methods and has already incorporated them in its design methodology thus reducing the number of wind tunnel tests with a greater number of configurations being explored numerically.

In the rotorcraft industry, CFD applications have historically lagged behind fixed-wing applications by five to ten years due to much smaller market size, less personnel with CFD experience and higher complexity of rotorcraft aerodynamics. But the need for increasing the competitiveness has forced the helicopter industry to invest in introducing CFD methods into their design processes. Recently, first industrial CFD applications were published showing the efforts to improve the aerodynamic design of helicopter components. Hassan et al. [1] conducted Euler simulations for the isolated AH-64D™ Longbow Apache™ fuselage in order to investigate and solve tail buffeting problems in low speed descent flight. Serr and Cantillon [2] simulated air intake flowfields using a Navier-Stokes method with the goal to meet engine manufacturer requirements by design optimization. Performance prediction and flowfield analysis of a rotor in hover by

application of a coupled Euler/Boundary Layer method was presented by Beaumier et al. [3].

In 1997, a development program was started at EUROCOPTER DEUTSCHLAND (ECD) to upgrade the BK117-C1 helicopter currently in service to the new BK117-C2 helicopter with first deliveries in 2000. This upgrade includes the redesign of the fuselage in order to increase the cabin volume. Due to the restricted program time scale and the high costs of an extensive wind tunnel test campaign it was decided to perform only simple wind tunnel tests for evaluating the aerodynamic coefficients of the redesigned BK117-C2 fuselage and to supplement these tests by CFD calculations using a commercial CFD software. This paper deals with the first CFD applications at ECD during the fuselage design phase of the upgrade helicopter BK117-C2.

The BK117 upgrade development program has entered the flight testing phase with the first prototype taken off to its maiden flight in June 1999. Furthermore, it was decided to give the BK117-C2 upgrade helicopter its official name EC145, which is now used for the remainder of the paper.

Aerodynamic Design of the EC145

Based on the BK117 helicopter, which was developed from 1978 to 1982 in a cooperation between ECD (formerly Messerschmitt-Bölkow-Blohm (MBB)) and Kawasaki Heavy Industries (KHI), this cooperation was renewed to develop the EC145. The main technical features of the EC145 are

- a new fuselage shape with increased length and width for increased payload volume and improved accessibility,
- a completely new cockpit design based on the EC135 helicopter including advanced avionics,
- rotor blades with advanced planform and modern airfoils for increased performance, and
- new hydraulics and a new control system using flexballs for connecting pilot controls and hydraulic actuators.

The complete upper deck including engine, gearbox and dynamic system as well as tail boom, vertical fin and tail rotor were left unchanged.

The aerodynamic and aeroacoustic layout of the new rotor blades and first results of flight tests on a BK117 test helicopter were presented by Bebesel et al. [4]. Besides the improved performance, a low noise radiation could be confirmed for the new EC145 rotor blades.

The design of the EC145 fuselage shape required the investigation of the aerodynamic characteristics to provide information on fuselage airloads and flight stability for the upgrade helicopter. For the determination of the fuselage aerodynamic coefficients in the full incidence and sideslip angle range measurements using a 1:5 scaled model were performed in the EUROCOPTER wind tunnel at Marignane in July 1997 (Reymond et al. [5]). The increased cabin volume and the new cockpit shape changed the fuselage contribution to the aerodynamic stability of the EC145. To retain the same stability characteristics as for the BK117, the horizontal stabilizer and the endplates had to be adapted. Therefore, the CFD flow simulations of the EC145 fuselage should supplement the wind tunnel tests in order to provide

- an accurate prediction of the surface pressure distributions for the determination of airloads for stress analysis of local fuselage parts such as doors and windows, and
- an estimation of the horizontal stabilizer pitching and endplates yawing efficiencies for design changes of the empenage.

Choice of Numerical Method

The choice of the numerical method used for the CFD simulation of the EC145 fuselage was based on industrial and technical requirements:

- The CFD software should have an user-friendly graphical interface and a good documentation to reduce user training and speed-up the handling.
- Maintenance of the CFD software and user support should be guaranteed.
- The CFD software has to be parallized and capable of running efficiently on workstation clusters since this is the only hardware configuration affordable and available at EUROCOPTER.
- A flexible post-processing should allow for an extensive flowfield analysis and load integration.
- The complex fuselage and empenage geometry ask for a flexible and efficient grid generation strategy. This can only be fulfilled by using the unstructured grid approach.

- The freestream velocities encountered by the fuselage are below Ma = 0.3 and therefore the incompressible flow model is best suited for fuselage flow simulations.
- The CFD method should converge fast and accurately predict the surface pressure distribution.

During an European research project it was demonstrated that commercially available unstructured CFD methods are mature to fulfill the requirements listed above and that accurate predictions of fuselage surface pressure distributions can be obtained (Costes et al. [6]). After an assessment of some commercial CFD methods, the FLUENT/UNS software [7] was chosen and introduced in the aerodynamic department of ECD. FLUENT/UNS solves the incompressible Navier-Stokes equations for conservation of mass and momentum on unstructured grids with additional conservation equations for the turbulent kinetic energy and dissipation in order to model turbulent flows. Furthermore, the FLUENT/UNS software offers the possibility to introduce an actuator disk model into the computational domain which allows for consideration of the influence of main rotor downwash on the fuselage and empenage aerodynamics.

Since the simulations reported in this paper were the first of this type performed at ECD, no attempt has been made to adapt or optimize turbulence modeling. For all calculation reported herein the standard k-ε model with default parameters has been selected. Furthermore, the hardware resources available at ECD restricted the number of grid points. Hence, the obtained grid resolution was inadequate for accurately predicting viscous and turbulent effects and an accurate simulation of flow separation, skin friction, and drag forces was therefore not expected.

CFD Method Validation by BK117 Fuselage Flow Simulations

Before stepping into the aerodynamic simulation of the EC145 fuselage, the chosen CFD method FLUENT/UNS was validated by calculating the flowfield around the present BK117 fuselage. For this fuselage, wind tunnel measurements including surface pressure data are available, which were acquired during wind tunnel test campaigns in 1978 and 1981 by KHI (Nakano et al. [8], [9]). To support the introduction of FLUENT/UNS into ECD, the company FLUENT DEUTSCHLAND performed demonstrative flow calculations for the BK117 fuselage. The geometrical surface description of the BK117 fuselage was given to FLUENT DEUTSCHLAND as a CAD surface description. A geometry model suitable for CFD flow simulations was created by removing gaps and overlaps of the CAD surface and by closing the engine inlets and exhaust outlets. The final BK117 fuselage geometry is shown in Figure 1 together with the computational domain as defined by FLUENT DEUTSCHLAND.

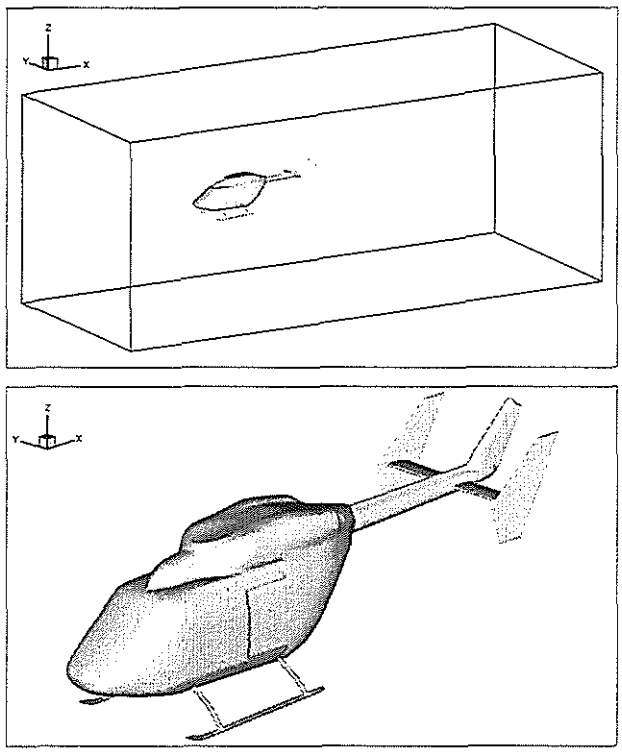

Figure 1: Computational domain and geometrical model for the BK117 fuselage flow simulation.

For generation of the surface grid depicted in Figure 2, the ANSA software was used which allows for a fast and efficient triangulation of the complex fuselage surface with a high degree of automatisation. The tetrahedrals of the volume grid were generated using TGRID, which is part of the FLUENT/UNS software package. The final grid consists of 86.000 surface triangles and 500.000 tetrahedral volume elements.

For method validation, three different flow conditions were selected. Zero incidence and zero sideslip angle $\alpha = 0°$, $\beta = 0°$ was considered as reference case. One high incidence angle case ($\alpha = -15°$, $\beta = 0°$) and one high sideslip angle case ($\alpha = 0°$, $\beta = 10°$) should verify the CFD method accuracy at the limits of operational flight range. Flow computations were converged up to a

residual drop of 3 to 4 orders of magnitude and the convergence of the pressure field was assured by monitoring the change in overall fuselage lift coefficient.

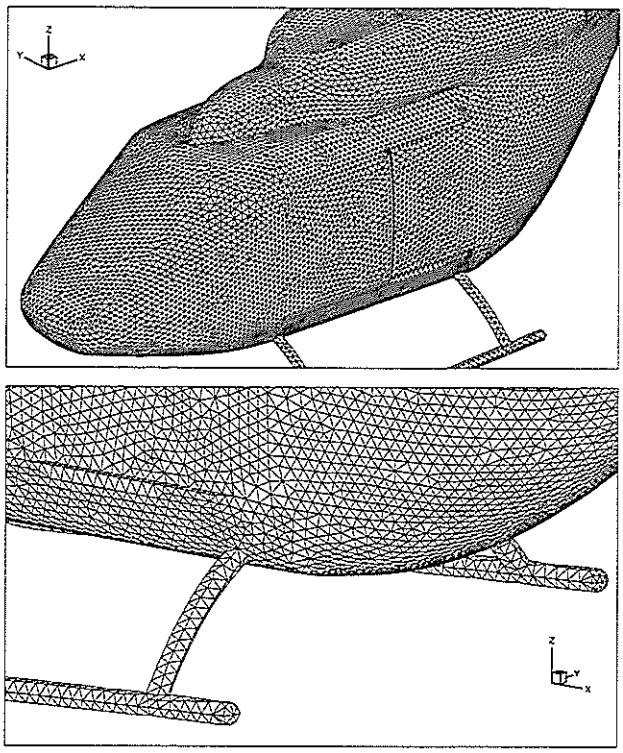

Figure 2: Details of the BK117 fuselage surface grid.

Figure 3 depicts a sketch of the cross sections for which the comparisons of calculated and measured surface pressure distributions are presented.

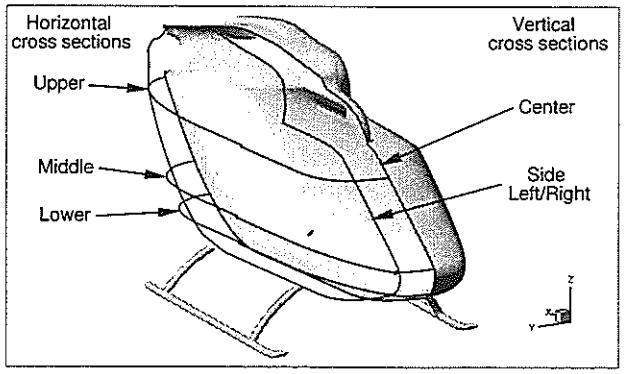

Figure 3: Analyzed cross sections for pressure coefficient distributions.

Reference Case: $\alpha = 0°$, $\beta = 0°$

The flow condition with zero incidence and zero sideslip angle was chosen as reference case for setting up, investigating and verifying the parameters defining convergence behavior and accuracy of FLUENT/UNS.

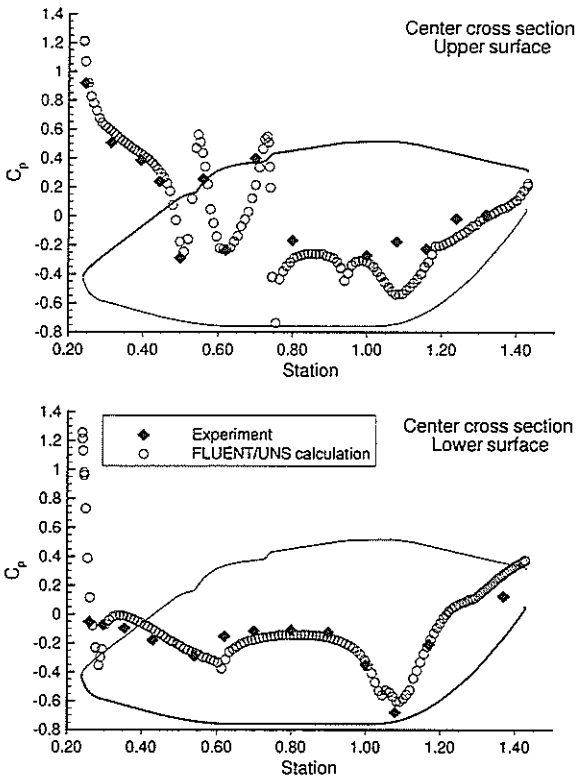

Figure 4: Pressure coefficient distributions at center cross section ($\alpha=0°$, $\beta=0°$).

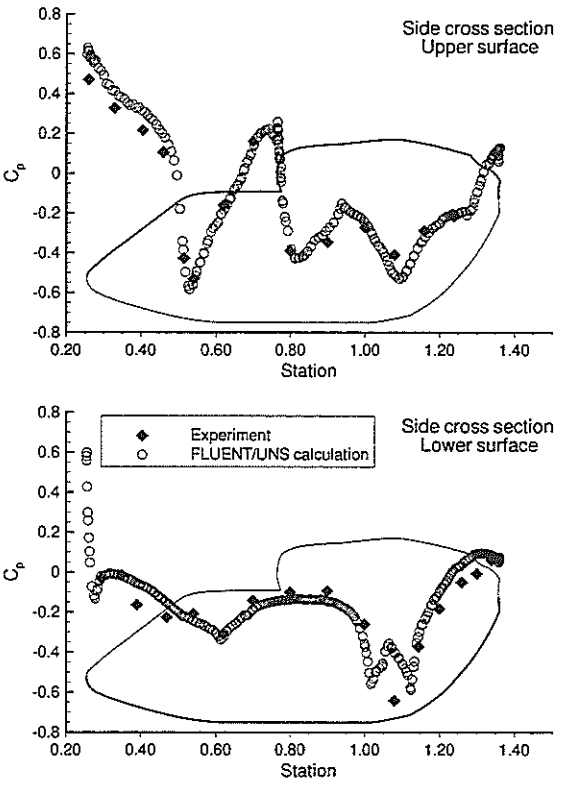

Figure 5: Pressure coefficient distributions at side cross section ($\alpha=0°$, $\beta=0°$).

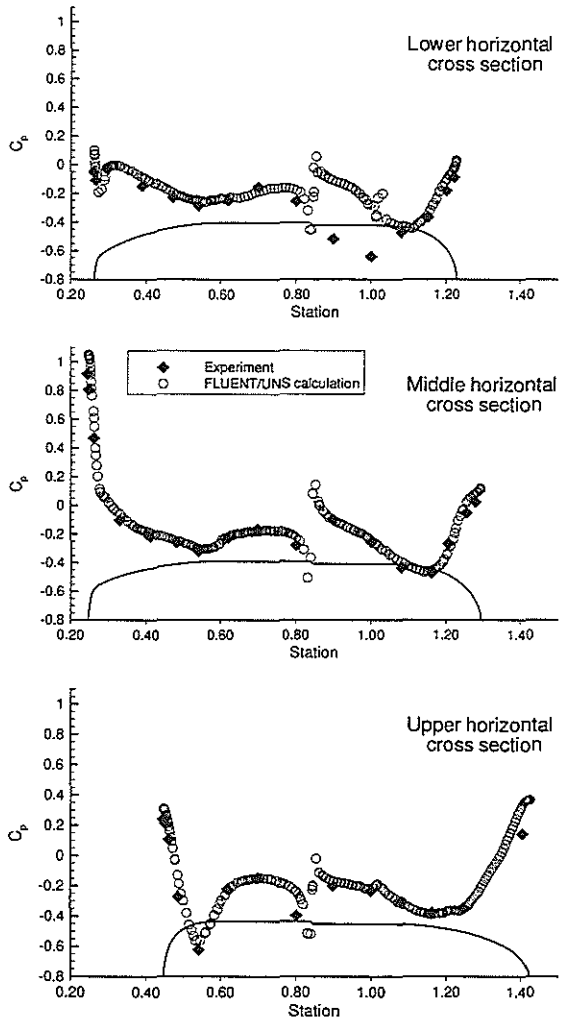

Figure 6: Pressure coefficient distributions at horizontal cross sections (α=0°, β=0°).

The comparison of calculated and measured pressure coefficient distributions in vertical and horizontal cross sections are presented in Figures 4, 5, and 6, respectively. The overall agreement between CFD simulation results and experimental data is very good.

A more detailed analysis reveals that the discrepancies found in the aftbody region on the lower surface (Figures 4, 5) are due to low grid resolution combined with an insufficient turbulence modeling. The pressure level on the aftbody (clamshell doors) is predicted too high and the suction peak in the high curvature region at the beginning of the aftbody is not correctly resolved.

In contrast to the CFD model, the wind tunnel model was equipped with a rotating rotor hub including blade stubs. Therefore, the calculated pressure distribution on the upper surface deviates from the measured values after station 1.0 (upper part of Figure 4).

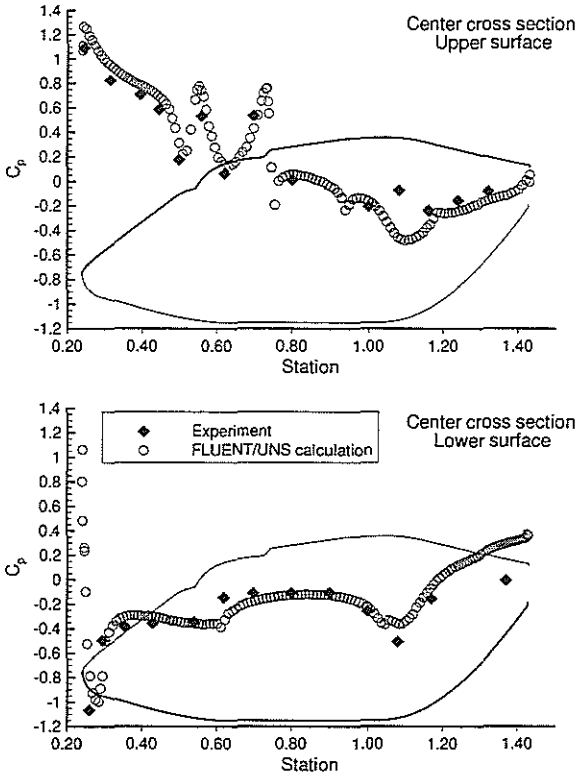

Figure 7: Pressure coefficient distributions at center cross section (α=-15°, β=0°).

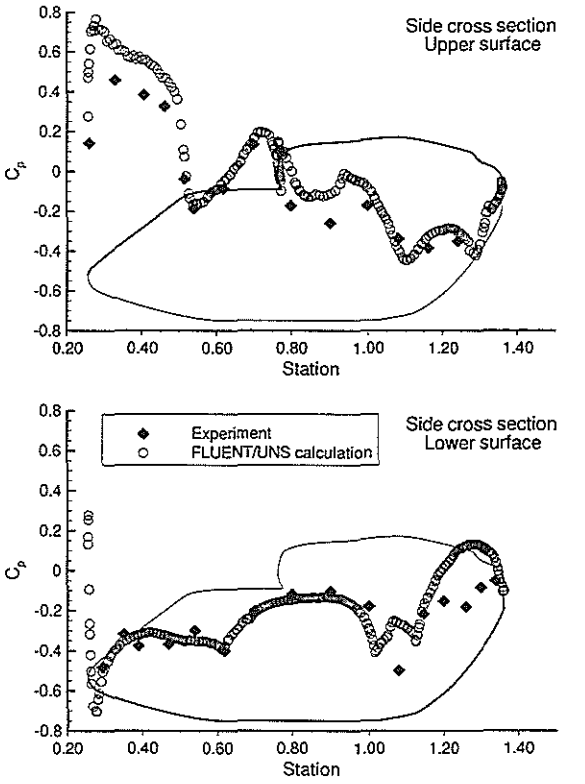

Figure 8: Pressure coefficient distributions at side cross section (α=-15°, β=0°).

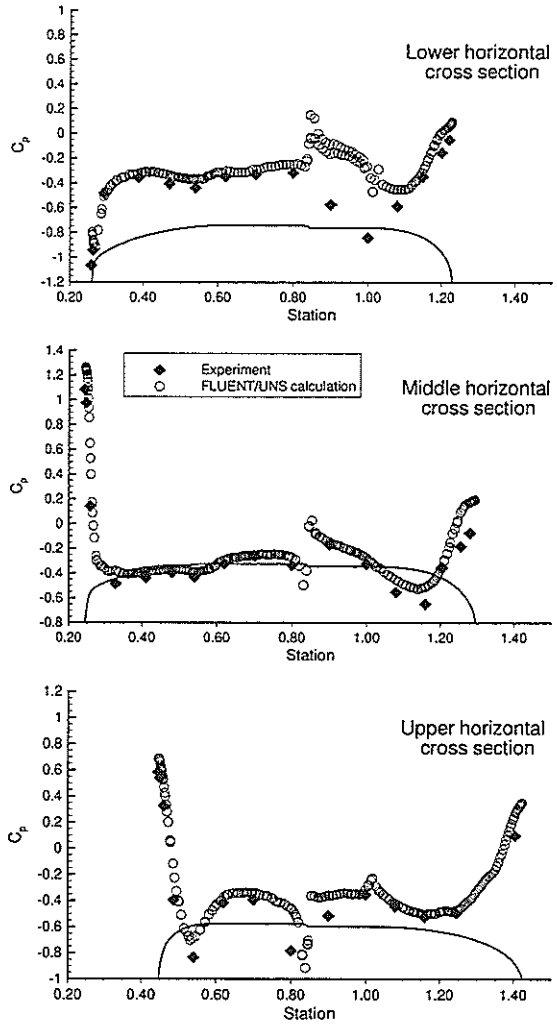

Figure 9: Pressure coefficient distributions at horizontal cross sections (α=-15°,β=0°).

The discrepancies found in the nose region for the side vertical cross section can be explained by inadequate grid resolution of the high geometrical curvature in horizontal direction. Due to the layout of the Figures, these differences can not be clearly identified in the pressure distributions of the horizontal cross sections (Figure 6).

Finally, the big differences at the lower horizontal cross section between stations 0.8 and 1.0 are attributed to a different geometrical representation of the sliding door attachment in the computational model and the wind tunnel model.

High Incidence Angle Case: α = -15°, β = 0°

Fuselage flow conditions with high incidence angles are usually encountered during climb or due to main rotor downwash in very low speed flight.

The calculated and measured pressure distributions for the vertical cross sections are shown in Figures 7 and 8, and for the three horizontal cross sections in Figure 9.

For the comparison of CFD simulation results and experimental data, the same conclusions as for the reference case can be drawn: a good overall agreement but increased differences in high curvature regions due to insufficient grid resolution and turbulence modeling. The high freestream incidence pronounces the discrepancies in the nose region at the side vertical cross sections and on the fuselage aftbody.

High Sideslip Angle Case: α = 0°, β = -10°

In contrast to fixed-wing fuselages, helicopter fuselages often operate under high sideslip angles occurring during sideward flight or low speed trimming with zero bank angle.

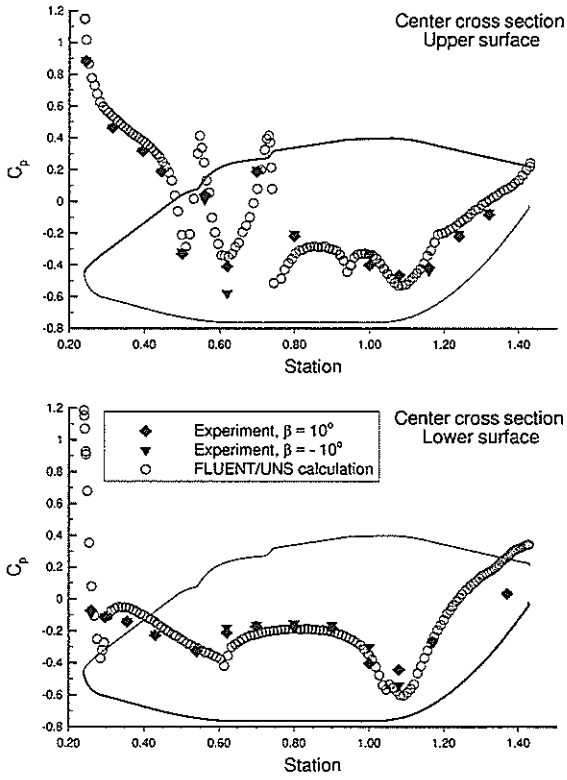

Figure 10: Pressure coefficient distributions at center cross section (α=0°, β=-10°).

Figures 10, 11, 12 and 13 show the pressure distributions for the cross sections defined in Figure 3. Since the fuselage shape is symmetrical up to the tail boom, the calculated pressure results in the center cross section are compared to experimental values for the wind tunnel cases with positive (α = 0°, β = 10°) and negative (α = 0°, β = -10°) sideslip angle. Furthermore, results for both right and left side cross sections are presented.

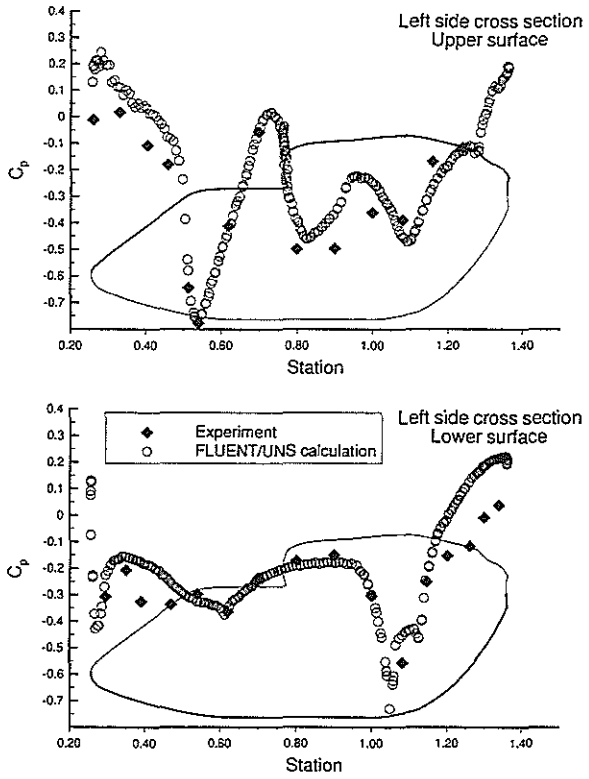

Figure 11: Pressure coefficient distributions at left side cross section (α=0°, β=-10°).

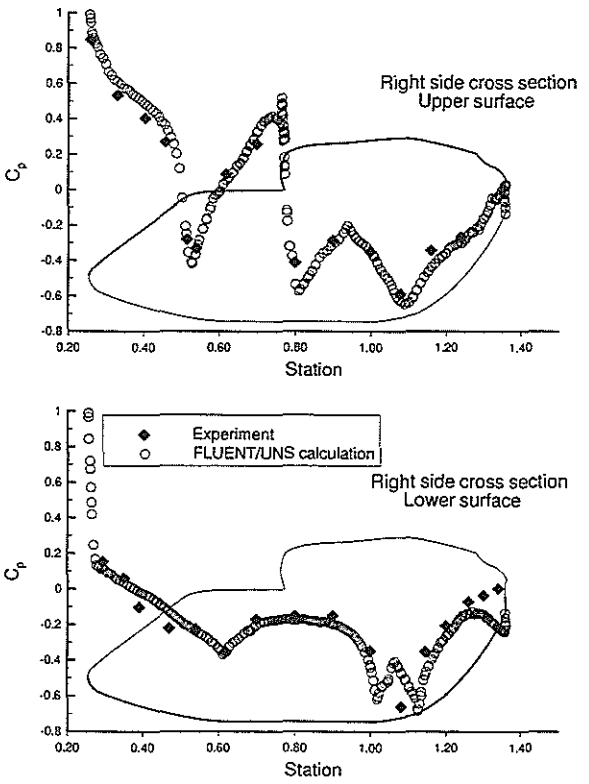

Figure 12: Pressure coefficient distributions at right cross section for α=0° and β=-10°.

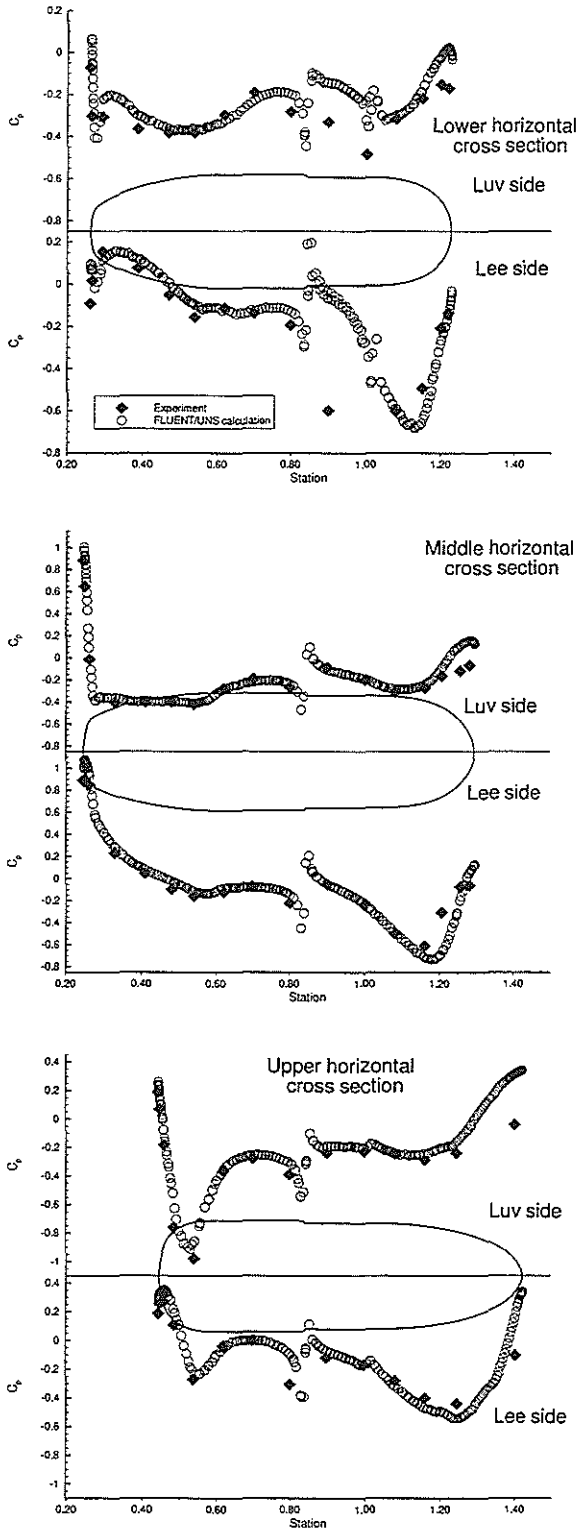

Figure 13: Pressure coefficient distributions at horizontal cross sections (α=0°,β=-10°).

As for the previous two validation test conditions, the overall agreement between measurements and calculation results is good. Problem areas with greater discrepancies are again high curvature regions at the cockpit and the aftbody. The comparison of pressure distributions

for the horizontal cross sections prove, that the CFD method is able to accurately simulate the flowfield on the luv side as well as on the lee side of the fuselage.

Prediction of Horizontal Stabilizer Efficiency

The CFD method validation was concluded with an assessment of the ability to predict the lift efficiency of the BK117 horizontal stabilizer and its contribution to the BK117 fuselage pitching moment. The pitching moment contribution of the horizontal stabilizer does not only influence the aircraft's stability and handling qualities, but also determines the pitching moment to be produced by the main rotor and thus the rotor shaft loading.

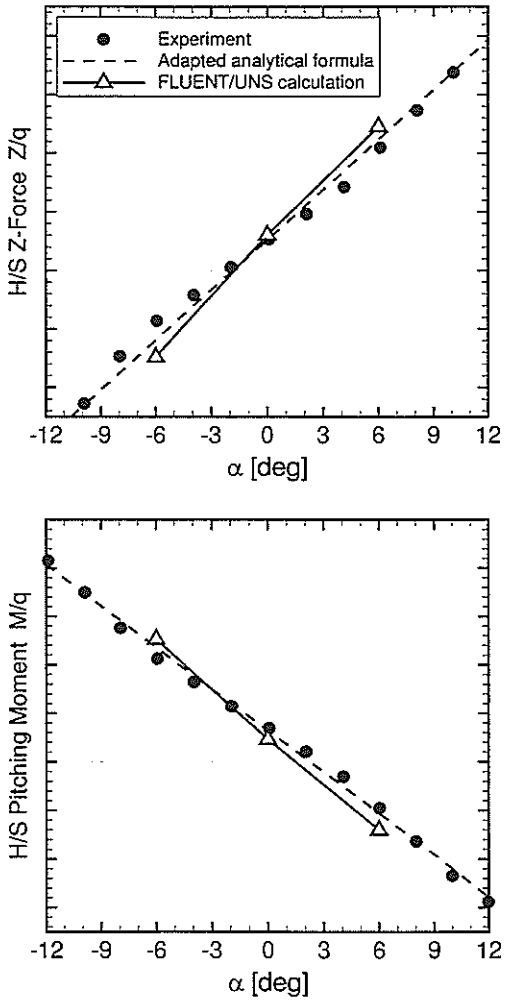

Figure 14: BK117 horizontal stabilizer Z-force and pitching moment contribution.

In Figure 14 the BK117 horizontal stabilizer (H/S) force in fuselage z-direction and the H/S pitching moment contribution predicted by the CFD calculations are compared to the results of the wind tunnel tests (Nakano et al. [8]). As ordinate the fuselage freestream incidence angle is used. The H/S force and pitching moment contribution were obtained by integrating the calculated pressure distribution on the horizontal stabilizer using the corresponding tool of the FLUENT/UNS software.

In contrast to the CFD model, the wind tunnel model was equipped with a fixed rotor hub and small blade stubs. Despite the missing hub wake influence in the CFD simulations, the agreement between calculated values and wind tunnel data is very good. The H/S pitch efficiency, which is determined by the slope of the pitching moment curve, is predicted to be slightly higher than obtained by experiment. Obviously, the CFD method is able to account correctly for the influence of the fuselage wake on the H/S aerodynamics.

For the pre-design of the EC145 horizontal stabilizer, simple analytical formulas for estimating the H/S lift curve slope and pitch stability contribution were used (Hoerner and Borst [10]). All wake and interference effects were taken into account by introducing efficiency factors which were adapted to the BK117 wind tunnel test data. The results obtained by these adapted analytical formulas are also shown in Figure 14.

EC145 Fuselage Flow Simulations

The geometrical definition of the EC145 fuselage shape was prepared as a CATIA model by the ECD pre-design department. In the aerodynamics department, this model was revised to remove all CAD surface gaps and overlaps and supplemented by closure surfaces for engine inlets and exhaust outlets. Furthermore, the main rotor disk plane was introduced in order to allow for activation of the FLUENT/UNS actuator disk model. The computational domain was increased compared to the BK117 simulation model to reduce as much as possible any farfield influence on the calculation results. Figure 15 presents the computational domain and the final geometry of the EC145 fuselage CFD model.

The surface grid generation was performed using PCUBE, a grid generation software developed by ICEM CFD which is included in the FLUENT/UNS software package. Although the graphical user interface of PCUBE greatly facilitates the set-up of the surface grid generation process, the computational time required and the low quality of the triangularisation at high

curvature regions deteriorates much the efficiency of the unstructured grid generation.

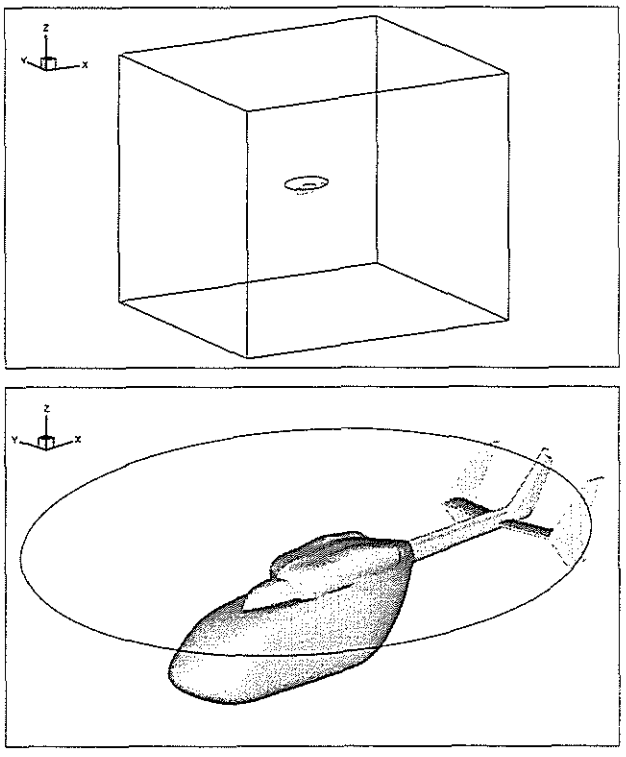

Figure 15: Computational domain and geometry model with main rotor actuator disk for EC145.

Since the goal of the EC145 fuselage flow simulations was not only to provide pressure distributions on the fuselage surface, but to assess the capability of estimating empenage aerodynamic loads by CFD methods, the surface grid was refined on the horizontal stabilizer (H/S) and the endplates (E/P) as shown in Figure 16.

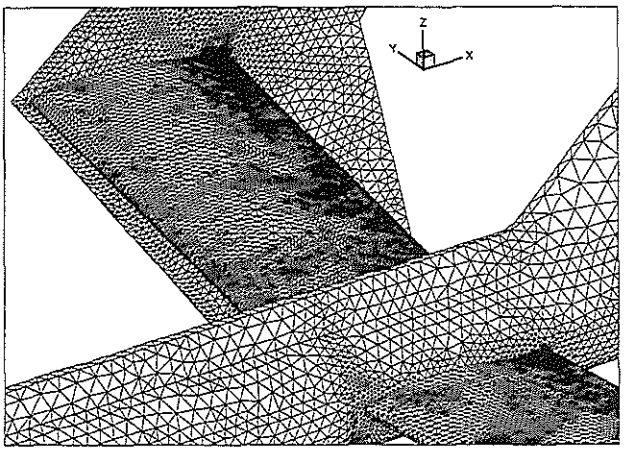

Figure 16: EC145 fuselage surface grid detail.

The finally obtained surface grid consists of 51.000 triangles and the volume grid produced automatically without any user input by TGRID contains 363.000 tetrahedral elements.

Flow calculations using the same parameter set-up as for the BK117 validation cases were run for various flight conditions covering the full incidence and sideslip angle range of a helicopter. All computations were converged up to a residual drop of about 3 orders of magnitude and the monitoring of the overall lift coefficient was used as an indicator of the level of pressure field convergence.

Prediction of Surface Pressure Distributions

For demonstration purposes, Figures 17 and 18 show calculated pressure distributions at the center vertical cross section and two horizontal cross sections for an incidence angle of α = -18° and a sideslip angle of β = 10°. This is a representative flight condition for a push-over maneuver which is one of the extreme cases for limit load estimation and stress analysis of the fuselage structure. The predicted pressure distributions are supposed to have the same inaccuracies in the high curvature regions cockpit and aftbody as found in the BK117 validation.

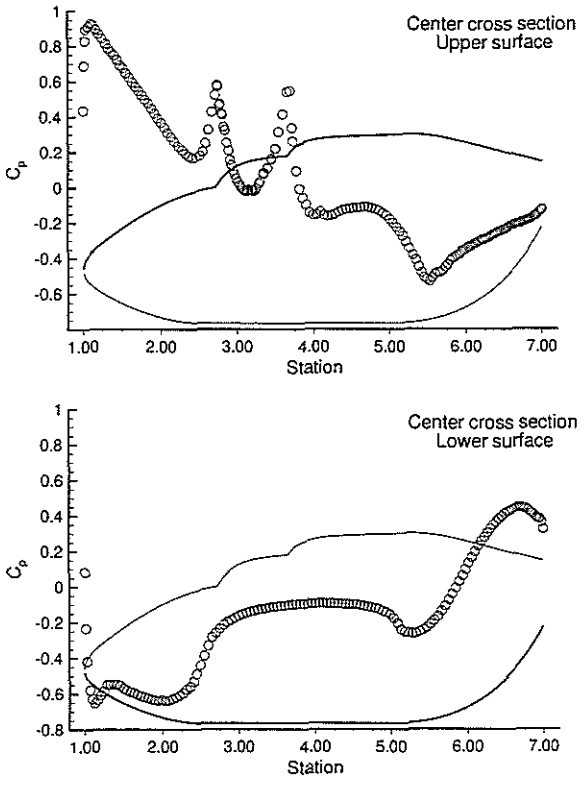

Figure 17: Pressure coefficient distributions at center cross section (α=-18°, β=10°).

All calculated surface pressure distributions were provided to the stress analysis department and used as air pressure load input for

- FEM simulations and stress analysis of the fuselage structure,
- FEM simulations and determination of the necessary thickness of the wind screen Plexiglas window, and
- stress analysis and structural design of side windows, sliding and clam shell doors.

Furthermore, a preliminary definition of the location of the static ports for altimeter and flight speed indicator could be made based on the calculated pressure distributions.

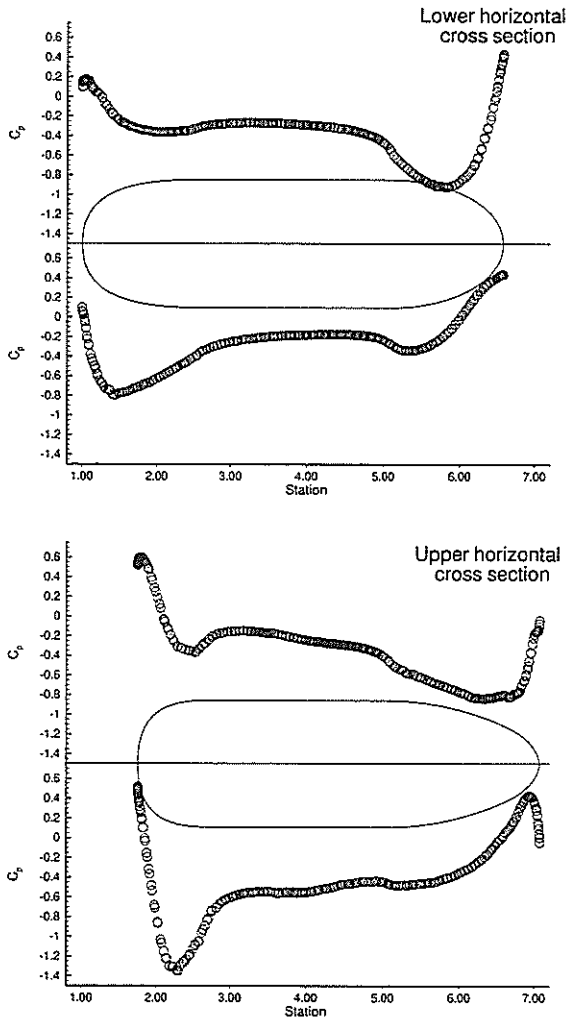

Figure 18: Pressure coefficient distributions at horizontal cross sections (α=-18°, β=10°).

Prediction of Empenage Efficiencies

Compared to the BK117, the new fuselage shape changes the aerodynamic stability of the EC145 helicopter. In order to retain or even improve the BK117 stability characteristics, the EC145 horizontal stabilizer (H/S) and endplates (E/P) have to be redesigned.

Using the simple analytical formulas adapted to the BK117 wind tunnel results, a first version of the EC145 empenage was defined and tested in the wind tunnel (see Reymond et al. [5]). Figure 19 shows the analytically predicted slopes of H/S lift force and pitching moment efficiency in very good agreement with the measured aerodynamic coefficients. In this and the following Figures, α and β denote the fuselage freestream incidence and sideslip angles.

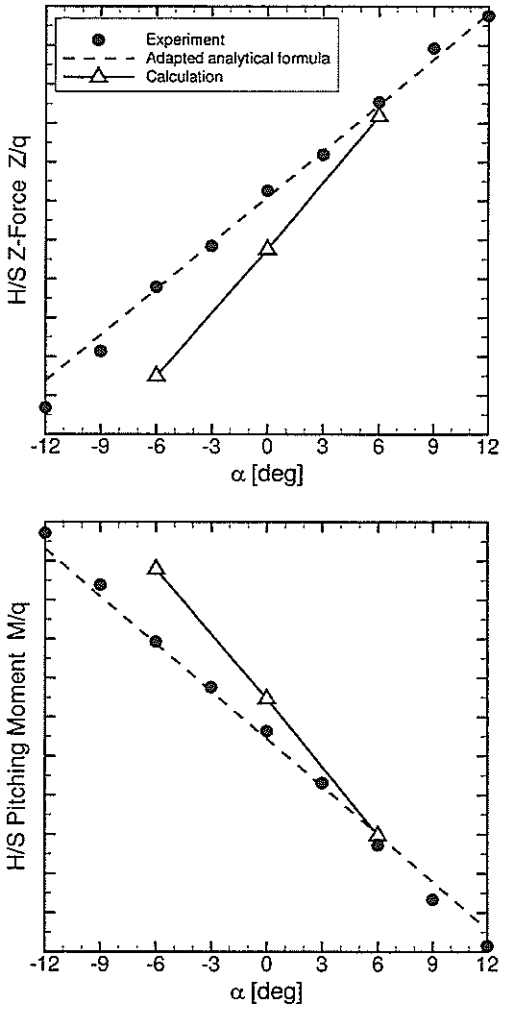

Figure 19: EC145 horizontal stabilizer Z-force and pitching moment contribution, old design.

For three incidence angles the H/S force and moment values were extracted from the CFD simulation results. The calculated coefficients for α = 6° are very close to the experimental data, but for α = 0° and α = -6° the gap between CFD

calculation and wind tunnel data increases. In the wind tunnel experiment, the model was equipped with a rotating hub and comparatively large blade stubs. Therefore, the difference between calculation and experiment may be explained by the missing rotor hub wake in the CFD computations, since for negative incidence angles this wake starts to interact with or even impinges on the H/S. If the EC145 results are compared to BK117 validation (Figure 14), the hub rotation and the increased size of the blade stubs seem to significantly influence the estimation of the H/S aerodynamics.

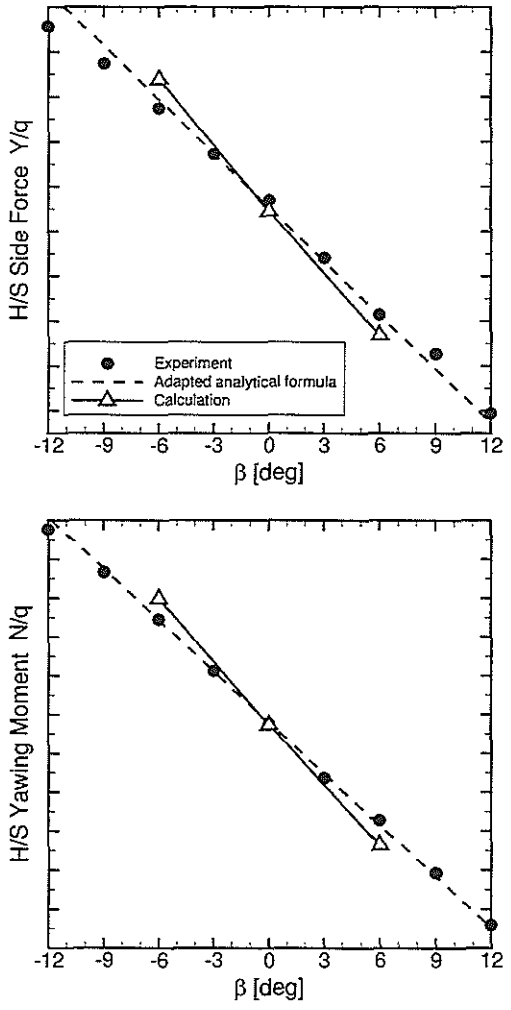

Figure 20: EC145 endplates side force and yawing moment contribution, old design.

Figure 20 presents the slopes of E/P side force and yawing moment as predicted by the adapted analytical formulas together with the aerodynamic coefficients measured in the wind tunnel and calculated by the CFD simulations. With the analytical formulas the slopes measured later-on in the wind tunnel tests were accurately predicted.

The agreement of the CFD results and the experimental data is very good and much better than for the H/S. This supports the explanation of the missing rotating hub wake causing the differences in calculated and measured H/S aerodynamic coefficients, since these wake effects are not experienced by the E/P. For zero sideslip angle ($\beta = 0°$), the experimental E/P force and moment coefficients were accurately simulated while the slopes are slightly overpredicted by the CFD method.

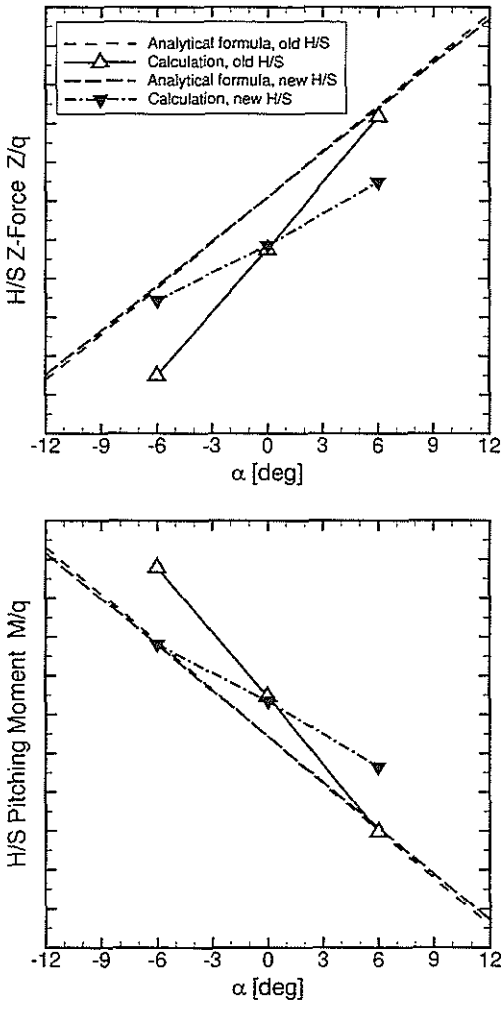

Figure 21: EC145 horizontal stabilizer Z-force and pitching moment contribution, new design.

Unfortunately, some design changes of the H/S and E/P were necessary due to structural and design constraints during the development phase of the EC145. By using the adapted analytical formulas, the geometry of the new empenage was designed to have equal aerodynamic efficiencies as the old one. The new H/S was increased in span and has a smaller chord. For the new E/P, the leading edge back sweep of the upper and lower

part was increased. The final H/S and E/P designs were introduced in the CFD geometry model, the computational grid was regenerated and flow calculations were performed in order to analyze more accurately the differences in aerodynamic efficiencies caused by the redesign.

Calculated lift force and pitching moment coefficients for the new H/S design are compared to the results for the old version in Figure 21. The aerodynamic efficiency, characterized by the force and moment slopes, is reduced significantly by the new H/S design. Currently, no explanation can be found for this unexpected behavior and a more detailed analysis will be performed to investigate the cause of this H/S efficiency deterioration.

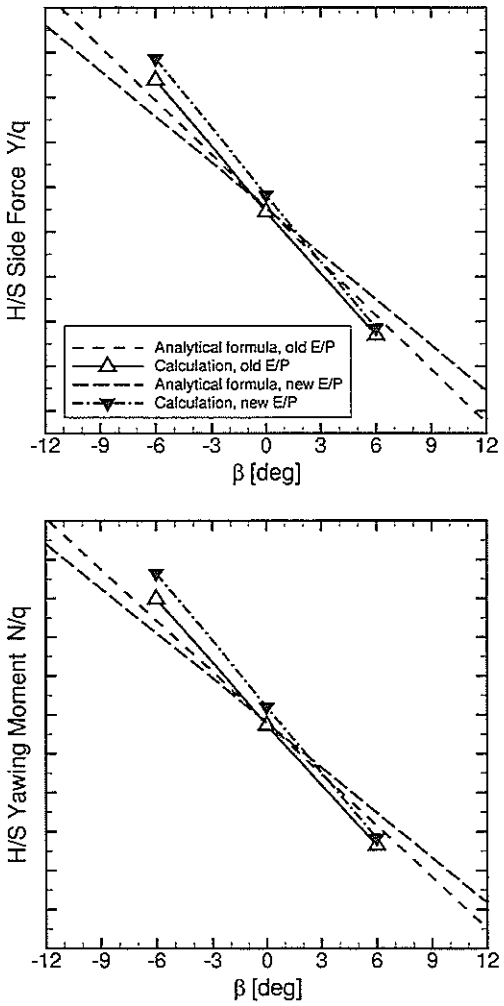

Figure 22: EC145 endplates side force and yawing moment contribution, new design.

Figure 22 shows the CFD prediction results for the aerodynamic characteristics of the old and new E/P versions. It is clearly demonstrated that the objective not to change the E/P efficiency by the redesign was reached, although the trend of efficiency reduction by the new design as indicated by the analytical formulas is reversed in the CFD results. Nevertheless, the differences in aerodynamic coefficients of both E/P designs are small and should not change the analysis concerning helicopter loads and handling qualities for the yaw axis.

Simulation of Main Rotor Downwash Influence

Finally, CFD simulations were performed to investigate the influence of main rotor downwash on the aerodynamic coefficients of the horizontal stabilizer. FLUENT/UNS provides an actuator disk model with the possibility to specify arbitrary pressure jump distributions across a predefined surface. In a first attempt to activate this model, a constant pressure jump distribution derived from the main rotor thrust was prescribed in the main rotor disk plane (see Figure 15). Although this approach does not account for the strong tip downwash velocities induced by the tip vortices of the main rotor blades, the averaged influence of the main rotor induced velocity field on the integrated aerodynamic H/S loads should be captured.

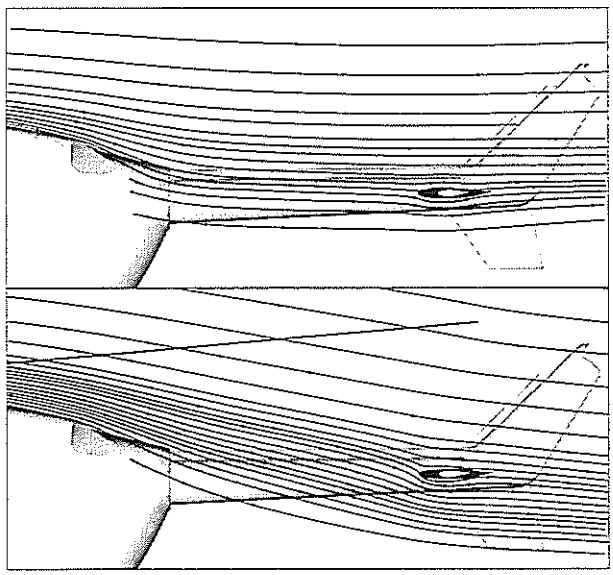

Figure 23: Streamlines in a vertical cross section plane for a CFD simulation of the EC145 fuselage with and without main rotor actuator disk model.

The effect of the main rotor actuator disk model is visualized by the streamlines drawn in Figure 23 for the flow case $\alpha = 0°$ and $\beta = 0°$. Due to the rotor-induced downwash velocity field the local H/S incidence angle is strongly changed.

The effect on the aerodynamic efficiency of the H/S is presented in Figure 24. As expected, the

change in local H/S incidence angle causes the H/S to produce much more downlift and thus a higher pitching moment contribution. Furthermore, the linear correlation between H/S force or moment coefficient and fuselage freestream incidence angle is no longer valid and non-linear effects are introduced by the rotor downwash.

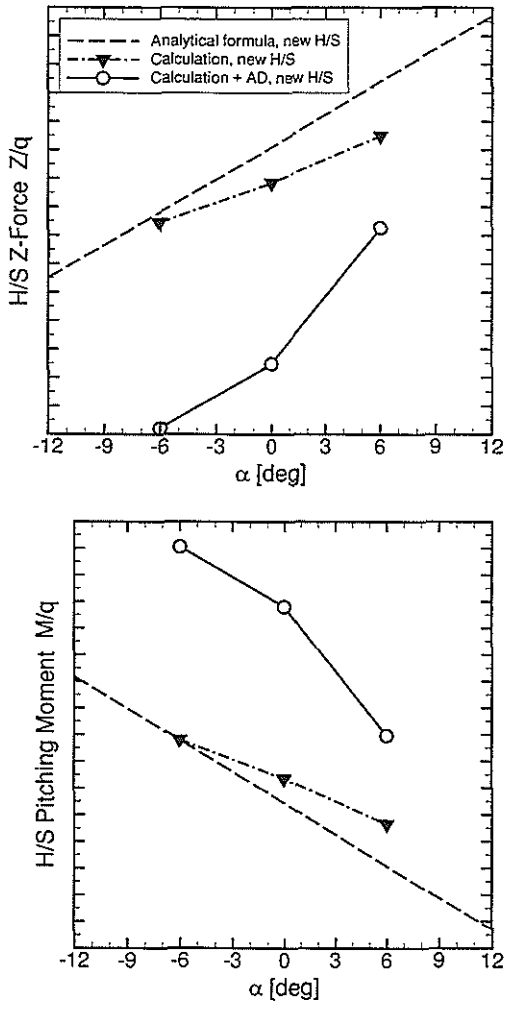

Figure 24: EC145 horizontal stabilizer Z-force and pitching moment contribution, influence of rotor downwash.

These results clearly demonstrate the importance of incorporating a model for the main rotor downwash velocity field into fuselage CFD simulations to be able to reliably predict horizontal stabilizer efficiencies for helicopters.

Conclusions

At EUROCOPTER DEUTSCHLAND the commercial CFD software FLUENT/UNS was introduced into the industrial design process and was used for the first time in the EC145 development program. The CFD method was extensively validated by simulating the BK117 fuselage flowfield. The accuracy of the predicted surface pressure was found to be good and the calculated empenage aerodynamic load coefficients show a satisfactory agreement with wind tunnel data. EC145 fuselage CFD simulations supplemented the wind tunnel test by providing surface pressure distributions, by estimating horizontal stabilizer and endplates efficiencies and by investigating the aerodynamic influence of empenage redesign and main rotor downwash.

The main conclusions regarding the technical results obtained using the commercial CFD method FLUENT/UNS are:

- a good and robust convergence of the numerical scheme.
- surface pressure distributions can be reliably predicted in the full incidence and sideslip angle range and were successfully utilized as input for stress analysis of fuselage structure.
- aerodynamic efficiencies of endplates can be calculated with sufficient engineering accuracy for design purposes.
- the prediction of horizontal stabilizer aerodynamic efficiencies depend strongly on the incorporation of all interaction effects such as those induced by rotating rotor hub wake and main rotor downwash.

Further work at ECD on fuselage CFD simulation will be devoted to

- a more detailed analysis and improved prediction of the interactional aerodynamics of horizontal stabilizers,
- a more refined main rotor actuator disk modeling employing realistic pressure jump distributions in the rotor disk plane, and
- incorporation of the tail rotor as actuator disk model in order to investigate the influence of tail rotor induced velocities on endplates.

For the prediction of fuselage drag and other flow features associated with viscous effects the pure unstructured approach seems to be not suitable due to the enormous number of grid elements required to resolve boundary layers. The current developments dealing with the hybrid approach employing prisms in the boundary layer looks promising and attempts will be made in the future towards first applications to helicopter fuselages.

Regarding the efficiency enhancement of the industrial design process by the introduction and application of a CFD method it can be concluded that

- the geometry modeling for CFD applications should be improved by taking into account the requirements of CFD in the construction of the CAD models,
- the unstructured approach strongly facilitate the grid generation task for the complex geometry of a helicopter fuselage,
- the performance of the PCUBE tool and the time required for surface grid generation is not acceptable and has to be improved (in fact it was reported that the current unstructured grid generator tool of ICEM CFD has an appreciable enhanced performance compared to PCUBE),
- the graphical user interface of FLUENT/UNS allows for an easy selection of all parameters and fast set-up of calculations even for an inexperienced user,
- for some analysis the post-processing tool of FLUENT/UNS turns out to be insufficient, but a lot of interfaces to common and powerful visualization and analysis tools (e.g. TECPLOT) overcome this drawback.

Although there are things to improve, the CFD capability enabled ECD to strongly accelerate the aerodynamic design process of the EC145 fuselage and a significant amount of time and cost for wind tunnel tests was saved.

In order to further enhance its aerodynamic prediction capabilities, EUROCOPTER in cooperation with the French and German research establishments ONERA and DLR started a long-term research project called CHANCE in July 1998. The main goal of this research partnership is the development, validation and industrialization of a CFD method capable to simulate the flow fields around isolated helicopter components (main rotor, fuselage, tail rotor) as well as around the complete helicopter.

Acknowledgements

The author would like to thank Dr. H. Rexroth and W. Seibert from FLUENT DEUTSCHLAND for preparing the BK117 fuselage geometry model, for generating the BK117 computational grid, and for performing demonstrative test calculations. Furthermore, W. Seibert's assistance during the first EC145 calculations is acknowledged.

REFERENCES

[1] HASSAN A.A., THOMPSON T., DUQUE E.P., MELTON J.
Resolution of Tail Buffet Phenomena for AH-64D Longbow Apache: A Case Study on the Application of a Modern CFD Analysis Tool for Improved Helicopter Aerodynamic Design
Proceedings of the 52nd Annual Forum of the American Helicopter Society, 1997.

[2] SERR CH., CANTILLON M.
Navier-Stokes Calculation: An Industrial Tool for Air Intake Optimization
Paper No. 93, Proceedings of the 22nd European Rotorcraft Forum, Brighton, UK, 1996.

[3] BEAUMIER P., CASTELLIN C., ARNAUD G.
Performance Prediction and Flowfield Analysis of Rotors in Hover Using a Coupled Euler/Boundary Layer Method
Paper No. AE12, Proceedings of the 24th European Rotorcraft Forum, Marseilles, France, 1998.

[4] BEBESEL M., POLZ G., SCHÖLL E.
Aerodynamic and Aeroacoustic Layout of the ATR (Advanced Technology Rotor)
Proceedings of the 55th Annual Forum of the American Helicopter Society, Montreal, Canada, 1999.

[5] REYMOND J., TONOLLI B., MISTRAL L.
BK117-C1/-C2 Wind Tunnel Tests
Internal Report E/IM.E No. 3388, Eurocopter, September 1997

[6] COSTES M., COLLERCANDY R., KROLL N., FRHR. VON GEYR H., RENZONI P., AMATO M., KOKKALIS A., ROCCHETTO A., SERR C., LARREY E., FILIPPONE A., WEHR D.
Navier-Stokes Calculations of Helicopter Fuselage Flowfield and Loads
Proceedings of the 54th Annual Forum of the American Helicopter Society, Washington, D.C., 1998.

[7] User's Guide for FLUENT/UNS and RAMPANT
Release 4.0, Vol. 1-3, Fluent Incorporated, April 1996.

[8] NAKANO M., IKEBE Y.
Wind Tunnel Test Result of BK117 Airframe – Test Series 3 –
Internal Report KKA-78-088, Kawasaki Heavy Industries, 1978.

[9] NAKANO M., IKEBE Y., MIYAJIMA K.
Pressure Distributions of BK117 Airframe – Wind Tunnel Test Report –
Internal Report KKA-81-211, Kawasaki Heavy Industries, 1981.

[10] HOERNER S.F., BORST H.V.
Fluid-Dynamic Lift
published by L.A. Hoerner, Hoerner Fluid Dynamics, Brick Town, N.J., 1975

TWENTYFIFTH EUROPEAN ROTORCRAFT FORUM

PAPER C-15

AERODYNAMIC PERTURBATIONS ON THE FRIGATE LA FAYETTE DECK EFFECTS ON THE HELICOPTER FLIGHT DYNAMICS

A.Taghizad*, Ch.Verbeke,A.Desopper***

*ONERA – Département Commande des Systèmes et Dynamique du Vol
BA 701 – Ecole de l'Air
13661 Salon – Air
FRANCE

**ONERA-IMFL – Département Aérodynamique Appliquée
5 Boulevard Paul Painlevé
59045 Lille cedex
FRANCE

SEPTEMBER 14-16, 1999
ROME –ITALY

ASSOCIAZIONE INDUSTRIE PER L'AEROSPAZIO, ISISTEMI E LA DIFESA
ASSOCIAZIONE ITALIANA DI AERONAUTICA ED ASTRONAUTICA

Aerodynamic Perturbations on the Frigate La Fayette Deck Effects on the Helicopter Flight Dynamics

A. Taghizad, Ch. Verbeke, A. Desopper
(ONERA)

ABSTRACT

A specific study has been carried out at ONERA since 1997 under the support of the French Ministry of Defence (SPAé) in order to develop an aerodynamic model of the frigate La Fayette landing area and to improve ship landing operations simulation realism.

Wind tunnel tests have been performed in ONERA-Lille on a 1/50th scaled model frigate to measure the 3D unsteady aerodynamic field around the landing deck with a hot films anemometer. Mean velocity and turbulence components have been measured for different wind conditions. During these tests the air-sea boundary layer was also simulated. Two test campaigns were performed one in 1997 and one in 1998.

The La Fayette aerodynamic wake model includes a mean wake model and a turbulence model for the velocity fluctuations. The turbulence model is based on the power spectral densities of velocity fluctuations measurements.

This model was connected to the Eurocopter Helicopter Overall Simulation Tool (HOST). Simulations of flights above the deck with this model demonstrated important effects of the ship air-wake on the helicopter flight dynamics.

1. Introduction

Flying a helicopter above or around a frigate deck, landing on it or taking off from it, are considered by pilots as highly risked operations. Indeed, not only the frigate moves, but also in the neighbourhood of the deck, the helicopter has to face with the changing aerodynamic wake of the ship superstructure. This unsteady flow provides high mean speed gradients to which aerodynamic turbulence (fluctuations) is added. These conditions have important effects on helicopter global performance, and behaviour.

Under SPAé funding, ONERA has performed wind tunnel tests on a 1/50th scaled La Fayette frigate model, and has developed an aerodynamic wake model of the ship landing area. This model was then used in order to study the effects on flight mechanics.

The work has been carried out between 1997 and 1998. The 97 activities were described in a previous paper [1].

The following topics are presented in this paper :

- Wind tunnel tests and data analysis,
- Air-wake model development in HOST (Helicopter Overall Simulation Tool),
- Demonstration of the effects on helicopter loads and flight dynamics,
- Real-time version of the air-wake model.

2. Wind tunnel tests and data analysis

2.1 Test equipment

Wind tunnel measurements were carried out in the ONERA-IMFL low speed wind tunnel (SH). This wind tunnel has a closed circuit and a test section of 2.4 m in diameter. The first 50 meters of the marine atmospheric boundary layer was also simulated. The measurements were performed on a 1/50th scaled La Fayette frigate model, configured with its Crotale Missiles (figure 1).

3D unsteady velocities were measured using crossed hot film anemometer. Two velocity components were simultaneously measured (u, v), and then (u, w) after a 90° rotation of the sensor. Thus, 2 redundant longitudinal velocity measurements (Uv, Uw) were provided. Speed measurements error is estimated as 2.6% of the infinite upstream wind.

The measurements were performed in a volume surrounding the landing deck. Figures 2 and 3 show the test volume and the selected test points positions inside ; 8 horizontal planes above the deck were considered.

Detailed data measurements were realised in 1997 with a 50 kt wind and three side-slip conditions (0°, 15° and 180°). Some tests at 25 kts and 0° of side-slip were also performed. All these measurements were done with a 0° bank angle on the ship. In order to study the effects of the ship bank angle on the air-wake a new campaign was organised in 1998 with a 50 knot wind at 15° of side-slip and 10° of frigate bank angle.

Figure 4 gives a summary of these test configurations.

2.2 Velocity decomposition

The three velocity components are decomposed into two parts : the mean value and the fluctuations around this mean value. For example, the longitudinal velocity is decomposed into:

$$U(x, y, z, t) = U_{mean}(x, y, z) + u(x, y, z, t)$$

U_{mean} : the longitudinal velocity mean value,
u : fluctuations around U_{mean}
x, y, z : space co-ordinates of the local point
t : time

The fluctuations (u, v and w) can be considered as turbulent terms.

In addition, measured velocities are normalised by the free stream velocity.

$$Um(x,y,z) = \frac{U_{mean}(x,y,z)}{V_{free\ stream}}$$

$$Du = \frac{u(x,y,z,t)}{V_{free\ stream}} = \frac{U(x,y,z,t)}{V_{free\ stream}} - Um(x,y,z)$$

The normalised velocity fluctuations are characterised by their Power Spectral Densities (PSD):

$$Du \Rightarrow pu : longitudinal\ turbulence\ PSD$$

$$Dv \Rightarrow pv : lateral\ turbulence\ PSD$$

$$Dw \Rightarrow pw : vertical\ turbulence\ PSD$$

This approach is similar to the one used in [2] and [3].

For the frequency, the results will be presented function of the scale 1 frigate (wind tunnel frequency / 50).

2.3 Ship air-wake mean velocity distribution

Wind speed and side-slip effects

Figures 5 and 6 give the mean velocity components (Um, Vm, Wm) evolution respectively along the vertical axis and the lateral axis (height 4.4 m above the deck), on the deck centre (point A), for a 50 kt wind speed without side-slip (ß = 0°) and for a zero degree ship bank angle.

These figures show a clear downward deviation of the flow (Wm<0), due to the hangar wall cliff-effect (h=6.60m). The longitudinal component of the mean air-wake decreases with the height above the deck. The maximum vertical velocity is reached on the centre line, while the longitudinal velocity decreases to a minimum in the same area. The lateral velocity component shows that the air-wake is deviated from both sides toward the centre.

Figure 7 is the 3D flow visualisation of measurements at 50 kts with 15° side-slip conditions. Arrows represent the mean velocity projections on visualisation planes, whereas coloured areas show turbulence levels. Light colours corresponds to the highest turbulence level. The effect of the lateral hangar wall can easily be seen.

Ship bank angle effect

The 1998 wind tunnel campaign was carried out to study the effect of the frigate bank angle (ϕ) on the ship air-wake. Figures 8, 9 and 10 present the mean velocity components evolution along the vertical axis on 3 different locations of the deck.

These plots show a visible longitudinal speed reduction below the hangar height but also high lateral speeds. This lateral speed decreases when moving towards the deck and even changes sign when moving to the right side of the deck.

Figures 11, 12 and 13 illustrate lateral and longitudinal sections of the air-wake. These figures show that 3D vortices exist. Figure 14 is a 3D illustration of the air-wake in term of velocity arrows and longitudinal speed levels.

Comparisons of the results with and without frigate roll angle show that this bank angle introduces major changes on the mean air-wake, with the apparition of 3D vortices above the landing deck.

2.4 Aerodynamic wake fluctuations

Wind speed and side-slip effects

Figure 15 gives an example of normalised velocity fluctuations on the deck centre (point A), at 2.4 m above it, for a 50 kt wind speed and 0° side-slip.

Figure 16 shows a 3D presentation of the vertical velocity (w) Power Spectral Density (PSD) evolution along the vertical, the lateral and the longitudinal axes on point A. We can notice high turbulence rates concentrated below the hangar wall height, above the deck.

Figure 17 presents a comparison of the 3 velocity components spectral densities on different test planes above the deck centre, at 50 knots of wind and side-slips of 0° and 15°. As general remarks for the 2 cases, it can be noticed that on planes below the hangar height (first 3 rows from the bottom), spectral densities show a maximum energy concentration approximately around 0.5 Hz. This maximum of energy decreases with the height. For the planes above the hangar height, PSDs start getting flat. Large differences can be seen on the power densities amplitudes between 0° and 15° side-slip configurations.

Ship bank angle effect

Figure 18 presents the velocity components power spectral densities along the vertical axis on the deck centre. It can be noticed again that the highest turbulence appear below the hangar height, mainly between the 3rd and the 5th test plane. Figure 19 is a 3D visualisation of the longitudinal turbulence levels.

Comparisons of results with and without frigate roll angle show that major changes occurs with the frigate bank angle. Both the maximum speed fluctuations areas the PSDs maximum amplitudes change when the frigate has a roll angle.

2.5 Synthesis

From all the wind tunnel measurements, the following conclusions can be done :

- A detailed database is available at 50 kts of frontal wind (ß=0°) and 0° ship bank angle ($\phi = 0°$).
- A detailed database is also available at 50 kts with 15° of side-slip and $\phi = 0°$. The mean flow and the speed fluctuations PSDs change considerably with the side-slip. However, interpolations between 15° and 0° of side-slip at 50 kts will be "tolerated", in order to extend the database to intermediate side-slips.
- A partial database has been generated at 25 kts, without side-slip and ship bank angle ($\phi = 0°$). PSDs results have shown the respect of Strouhal number similarity. The measurements show that except above the deck, the mean wind and the PSDs normalised components have similar evolutions. Above the deck, these components will have to be interpolated or extrapolated using the results at 25 and 50 kts in order to extend the database at other speeds.
- A detailed database is available at 50 kts with 15° side-slip and 10° ship bank angle. The ship angle introduction brings important changes on both mean wake and turbulence terms. However, despite these discrepancies, the air-wake parameters observation tend to show quit close evolutions of mean velocities and PSDs. Therefore, assuming quasi-static conditions, an interpolation of the results at 50 knots of wind speed and 15° side-slip in 0° and 10° bank angle configurations can be envisaged.
- A 50 kt rear wind database at $\phi = 0°$ has been also generated.

3. Air-wake model development in a flight dynamics code

3.1 Model realisation

The La Fayette air-wake model includes a mean wake model and a model of velocity fluctuations (turbulence).

a- Mean air-wake model

The test area above and around the ship deck is actually a grid according to the test points definition. At any point (H) of this area the 3 mean air-wake components are interpolated, using the mean air-wake measurements of neighbouring points.

The approach consists in locating for example the helicopter centre of gravity in the test area elementary parallelepiped (figure 20). The mean air-wake on this point is defined via its components in the frigate axes, using a linear combination of measured mean velocities on the elementary parallelepiped tops, in respect with their distance to the considered point.

In order to avoid any velocity discontinuity when going in/out of the test area, a transition region has been defined, where velocities are interpolated between the test area and the free stream. Figure 21 illustrates this method.

b- Velocity fluctuations model (turbulence)

Velocity fluctuations are generated using the 3 velocity components PSDs.

The approach consists in locating the helicopter centre of gravity in the test area elementary parallelepiped. Fluctuations PSDs on this point are defined using a linear combination of measured PSDs on the elementary parallelepiped tops, in respect with their distance to the considered point. Fluctuations are then processed using a signal generation method ensuring the similarity between PSDs of measurements and of the generated signal.

The method consists in:

a- Calculation of measured velocity fluctuations PSD.

b- Identification of a mathematical model (S) fitting the experimental PSD.

c- Velocity fluctuations computation from the identified PSD, using the following method [4]:

Example of u generation:

$$u(x,y,z,t) = 2\sum_{i=1}^{N}\sqrt{S(x,y,z,f_i)\cdot\Delta f}\cdot\cos\left[2\pi f_i t + \varphi_i(x,y,z)\right]$$

N: Number of samples in S

f_i: Temporal frequency for i^{th} sample

φ: Random phase between 0 and 2π with a uniform probability density

Figure 22 is an example of vertical turbulence generation on the deck centre (height = 2.4m) at 50 knots of wind speed.

The frigate air-wake model has been connected to the Eurocopter simulation code HOST (Helicopter Overall Simulation Tool) [5]. The connection was first done by assuming the helicopter as a mass point. A first model was developed with the test results obtained during the 1997 test campaign at $\phi = 0°$ [1].

3.2 Model improvements

For this task the objective was first to complete the previous ship air-wake model with the test campaign data on ship bank angle effect and to improve some aspects of the physical modelling.

Model validity domain extension

With the last wind tunnel tests data, the model validity domain can be extended to the configurations in which the ship has bank angles up to 10° starboard.

The new validity domain of the model becomes :

AT $\phi = 0°$:

$\beta = 0°$	→ AIR-WAKE CALCULATION AT ANY WIND CONDITION,
$\beta = 15°$	→ AIR-WAKE CALCULATION AT 50 KNOTS OF WIND,
β in]0°,15°[	→ AIR-WAKE CALCULATION AT 50 KNOTS OF WIND BY INTERPOLATION,
$\beta = 180°$	→ AIR-WAKE CALCULATION AT ANY WIND CONDITION,

AT $\phi = 10°$:

$\beta = 15°$	→ AIR-WAKE CALCULATION AT 50 KNOTS OF WIND,

AT ϕ in]0°,10°[:

$\beta = 15°$	→ AIR-WAKE CALCULATION AT 50 KNOTS OF WIND BY INTERPOLATION.

Model user domain extension

In order to improve operational simulations realism, one of the requirements was to realise an air-wake model able to take into account the complete ship motion (roll, vertical, swerve, pitch,..).

Because of the limited data base available, and the fact that the ship motion can lead to configurations where the air-wake model comes out of its validity domain, this requirement could be fulfilled only under very extensive and simplifying hypotheses. The task consisted in extending the validity domain by extrapolations on the parameters such as the side-slip (β) and the bank-angle (ϕ).

The main hypotheses are the followings :

- No ϕ effect on the air-wake for frontal winds (β = 0°),
- For V=50 kts, β=15° : interpolation/extrapolation on ϕ,
- For V=50 kts, 0<β<30°: interpolation/extrapolation on ϕ and β,
- For V=50kts, -30°<β<0: interpolation/extrapolation on ϕ and β, using symmetry to the longitudinal axis,
- For V=50 kts, $|\beta| > 30°$: only atmospheric boundary layer effect,
- For any other V, extension of the results at 25 and 50 knots,
- The remaining ship state parameters (vertical, swerve, pitch, ...) act only on the deck test area position, without any additional effect on the aerodynamics.

Separation of the effects of the wind velocity and of the ship velocity

Wind tunnel tests have been performed using an atmospheric boundary layer simulation facility. In such a case the relative blown wind to the ship is considered to be the atmospheric wind in the boundary layer.

But in reality, the relative wind is a combination of the atmospheric wind and of the ship speed :

$$V_{relative} = V_{air/ship} = V_{wind} - V_{ship}$$

In an extreme situation, when there is no wind and the ship is moving, the model as described above provides an air-wake submitted also to the atmospheric boundary layer effect, whereas no influence should exist.

The following approach was used to cancel this effect. Let's consider $\Delta u = U_{air\_wake} - U_{bound\_layer}$ as the isolated frigate effect.

$$\left(\frac{\Delta u_{tests}}{V_{wind\_tunnel}}\right) = \left(\frac{U_{air\_wake}}{V_{wind\_tunnel}}\right) - \left(\frac{U_{bound\_layer}}{V_{wind\_tunnel}}\right)$$

$\left(\frac{U_{bound\_layer}}{V_{wind\_tunnel}}\right)$ is independent of the wind intensity and is only a function of the altitude (f(Z)).

$\left(\frac{U_{air\_wake}}{V_{wind\_tunnel}}\right)$ is given by the test measurements.

So, in real conditions, when $V_{relative}$ is a combination of the wind and the ship speed,

$$\Delta u = \left(\frac{\Delta u_{tests}}{V_{wind\_tunnel}}\right) \cdot V_{relative} .$$

Then, the air-wake speed is calculated by $U = \Delta u + U_{bound\_layer}$

or

$$U = \left(\frac{\Delta u_{tests}}{V_{wind\_tunnel}}\right) \cdot V_{relative} + f(Z) \cdot V_{wind}$$

Multi-element air-wake model

In the first version of the air-wake model the 3 unsteady airspeed components are calculated on the helicopter Centre of Gravity (CoG) and applied to its different elements (main rotor, horizontal stabiliser, ...). The evolution considered here consists in determining the local airspeed of each element using its relative position to the CoG.

This improvement raises the question of speed perturbations phases in different spatial locations. Additional wind tunnel tests would have to be organised in order to consider this topic. The tests should contain simultaneous speed measurements on different deck points. The analysis of speed fluctuations phases from one point to another will provide some lights on the turbulence spatial propagation.

Despite the lack of simultaneous measurements data, this evolution have been implemented in the model, with the possibility of changing the phase between the

different points, or just taking into account the mean velocity field, which is independent of perturbations phase problem.

This version of the model is a major evolution but it needs a large computer memory capacity and higher calculation time.

Results of simulations with and without this improvement are presented in paragraph 4.

4. Demonstration of the effects on helicopter loads and flight dynamics

In order to demonstrate the frigate aerodynamic wake effects on helicopter flight dynamics, off time open loop simulations of flights above the deck were carried out with HOST.

4.1 Mass point model – ship in roll motion

Results of a Dauphin descending flight , obtained with the mass point version of the model, at a speed of 10 knots and -1° slope angle are presented on figures 23 and 24.

The frigate faces with a 50 knot wind at 15° side-slip. It has a sinusoidal roll motion of 5 seconds period and 5° amplitude ($\phi = -5 \sin \frac{2\pi t}{T}$, $T = 5s$).

The helicopter is trimmed with the local mean air-wake conditions at the starting point located on the longitudinal symmetry axis (y=0), 11.9 m above the deck (Z=9.5 m in the frigate axes) and 23 m behind its rear extremity (X=25 m in the frigate axes).

The simulation being realised in open loop, the helicopter controls keep their trim values. Figure 23 illustrates the local wind components (UF-FGW, VF-FGW, WF-FGW), the helicopter flight parameters (helicopter attitudes, ground speed components, ...) and trajectory coordinates. Figure 24 shows the aerodynamic loads on different helicopter elements (main rotor, fuselage and horizontal stabiliser). Blades flapping are also presented on this figure.

The plots show the unsteady airspeed effects on different flight parameters. Aerodynamic loads and moments are very sensitive to airspeed fluctuations, therefore these parameters are highly disturbed. Helicopter angular rates follow these variations with a first order dynamic. The effect on the vertical speed is similar. These primary parameters variations end up by changing helicopter attitudes and speed.

During this simulation the helicopter tends to come into the wind direction (15° left) by turning on the left side (-7° in roll and -10° in heading).

4.2 Multi-element model simulations, without ship motion

Simulations of hovering flights above the deck have been performed with the multi-element model and the flight parameters were compared with those generated with the mass point model.

The mutli-element model is based on the calculation of the local wind speeds for the fuselage, the main rotor and the horizontal stabiliser. Since the tail rotor and the fin are located close to the horizontal stabiliser, the airspeed calculated for this element was also applied to the 2 others.

Since no conclusion on turbulence spatial length was available, the speed fluctuations phases were considered to be the same at the different locations.

The hover flights were generated with a 50 knot wind at 13° side-slip. The helicopter was trimmed with the local mean airspeeds at the starting point located on the longitudinal symmetry axis (y=0) at 4.50 m above the deck and 2.5 m in front of its rear extremity (x=0 in frigate axes).

Figures 25 and 26 illustrate the local wind components and the helicopter flight parameters (attitudes, ground speed components, trajectory coordinates, loads, moments and blade flapping) for the multi-element model. Figures 27 and 28 are the same evolutions generated with the mass point model.

The 2 simulations show important changes on the helicopter dynamics and consequently on the trajectories. The main difference is seen on the helicopter initial reaction. With the mass point model the helicopter starts by pitching down and so going forward whereas, with the multi-element model it initiates first a pitch up which results in a deceleration and a rearward flight.

So, the introduction of actual airspeeds for the helicopter's main components has a non negligible effect on the reactions to the ship air-wake. However, it has to be emphasised that this study was performed with the assumption that the turbulence phase doesn't change with the spatial position. So, further investigations should be performed to study this effect.

5. Model for real-time simulation

In order to carry out piloted simulation tests in the real-time environment of Eurocopter simulator "SPHERE", the ship air-wake model was modified and partly simplified to reduce its calculation time.

In this purpose, the computer memory capacity use and calculation algorithms were optimally rearranged.

In addition, the 3 turbulence components power spectral densities are no longer calculated by

interpolations, but several characteristic PSDs were defined according to the area flown by the helicopter. So, the PSDs are calculated once and stocked in the memory.

Thus, with these modifications the turbulence generation procedure is much quicker.

First piloted simulation tests were carried out by Eurocopter. All the pilots emphasised the significant improvement of ship landing operations simulation realism provided by the ship air-wake model.

6. Conclusion

This paper presents an ONERA activity on helicopter ship landing operations simulation improvement.

The first phase of this activity started with wind tunnel tests in ONERA-IMFL, on a 1/50th model of the French frigate La Fayette. A detailed database was provided at 50 kts for 3 wind side-slip configurations (0°, 15°,180°). A partial database was also generated at 25 kts of wind with 0° side-slip. The effect of the frigate roll angle was also studied for a side-slip angle of 15° and a roll angle of 10°. The data analysis showed important aerodynamic effects due to the hangar cliff-effect and ship lateral wall effects.

These data were used in order to define and to develop a ship air-wake model of the La Fayette deck area. It includes a mean air-wake model and a model of velocity fluctuations (turbulence).

This model, connected to the Eurocopter HOST code (Helicopter Overall Simulation Tool) demonstrated important effects of the ship mean and turbulence aerodynamic wake on helicopter loads, moments and on its flight dynamics.

References

1. A. Taghizad, Ch. Verbeke, A. Desopper (ONERA) *Aerodynamic perturbations encountered by a helicopter landing on a ship – Effects on the helicopter flight dynamics.* AGARD symposium organised by Fluid Dynamics Panel, held in Amsterdam, The Netherlands, 5-8 October 1998.

2. H. Zhang, J.V.R. Prasad, D.N. Marvis (School of Aerospace Engineering-Georgia Institute of Technology). *Ship air wake effects on helicopter rotor aerodynamic loads.* AIAA, 1994.

3. D.N. Marvis, J.V.R. Prasad, D.P. Schrage (School of Aerospace Engineering-Georgia Institute of Technology). *A Simulation Methodology for Modelling Ship-Air wake Turbulence.* 25th Annual International Symposium of the Society of Flight Test Engineers, Washington Aug. 1-5, 1994.

4. M. Shinozuka (Columbia University, New York), C.-M. Jan (Gibbs and Hill Inc. New York). *Digital simulation of random processes and its applications.* Journal of Sound and Vibration (1972) 25 (1), 111-128.

5. P. Eglin (Eurocopter). *Aerodynamic Design of the NH90 Helicopter Stabilizer.* 23rd European Rotorcraft Forum, Dresden, Germany, September 1997.

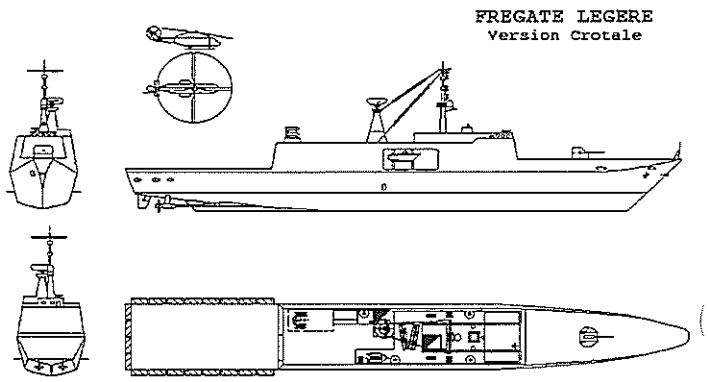

Figure 1: Frigate La Fayette 1/50th model

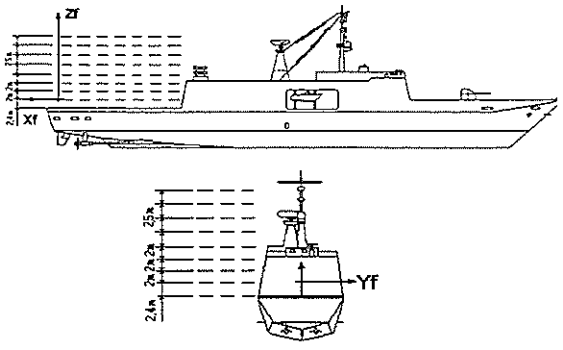

Figure 2 : Test planes position

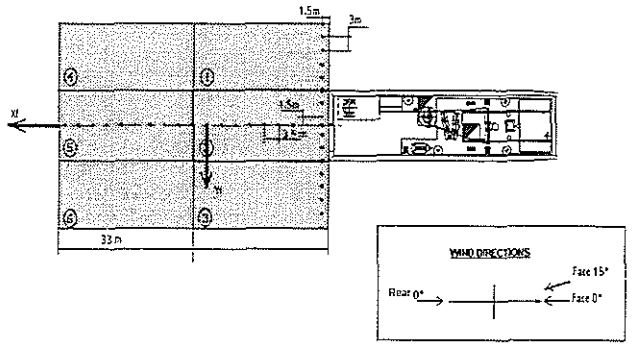

Figure 3 : Test points position

Test Configurations

Ship bank angle (ϕ) = 0°

- Frwd wind 0° (50 and 25 kts) : Areas 1 to 6 2*2584 points
- Frwd wind 15° (50 kts) : Areas 2, 3, 5 and 6 1824 points
- Rear wind 0° (50 kts) : Area 1 and ½ Area 2 720 points

Ship bank angle (ϕ) = 10°

- Frwd wind 15° (50 knots) : Areas 2, 3, 5 and 6 1824 points

Planes height to the deck

2.4 m / 4.4 m / 6.4 m / 10.9 m / 13.4 m / 15.9 m / 18.4 m

Figure 4 : Summary of test configurations

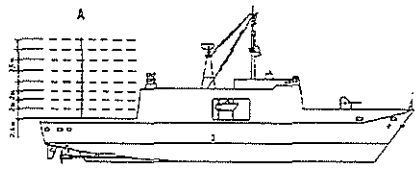

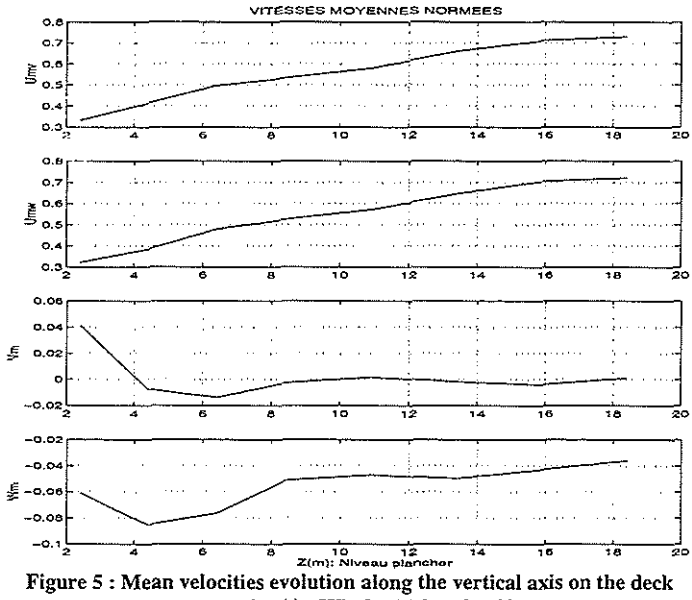

Figure 5 : Mean velocities evolution along the vertical axis on the deck centre (pt A) - Wind = 50 kts, ß = 0°

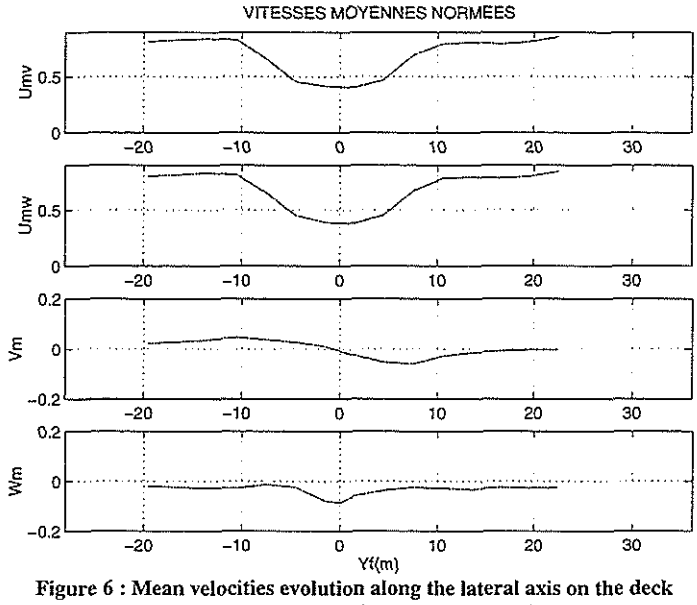

Figure 6 : Mean velocities evolution along the lateral axis on the deck centre (pt A, height=4.4m) - Wind = 50 kts, ß = 0°

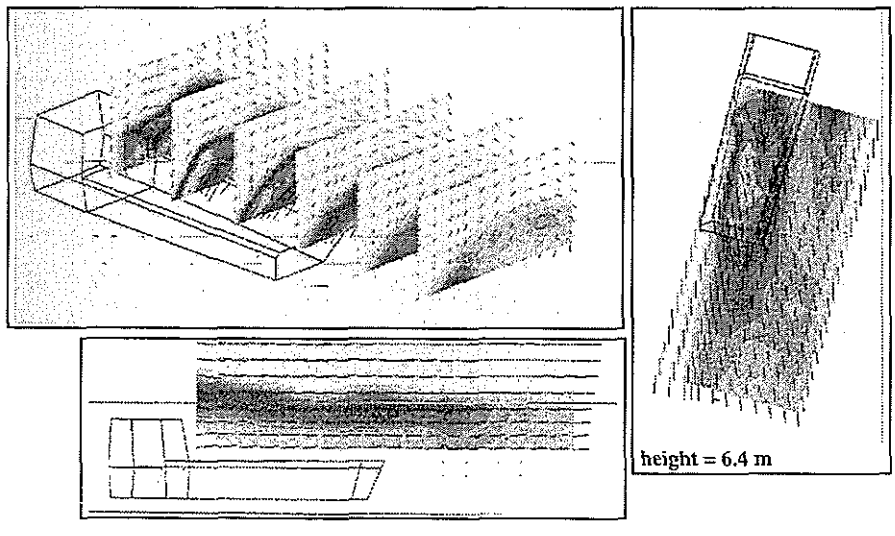

Figure 7 : 3D visualisation of tests at 50 kts ; ß = 15° ; ϕ = 0°

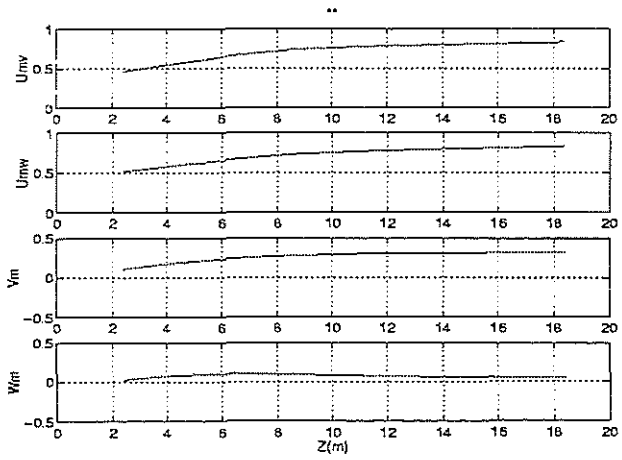

Figure 8 : Evolution of mean velocity components along the vertical axis on point A

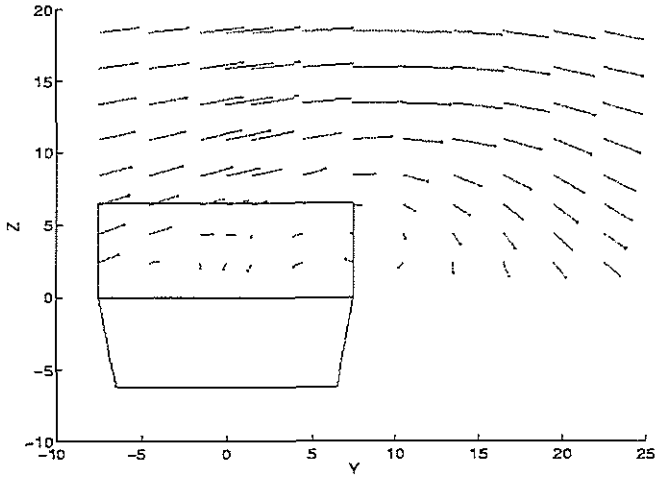

Figure 11 : Lateral section of the flow on plane n° 8 Wind =50 knots, β = 15°, ϕ = 10°

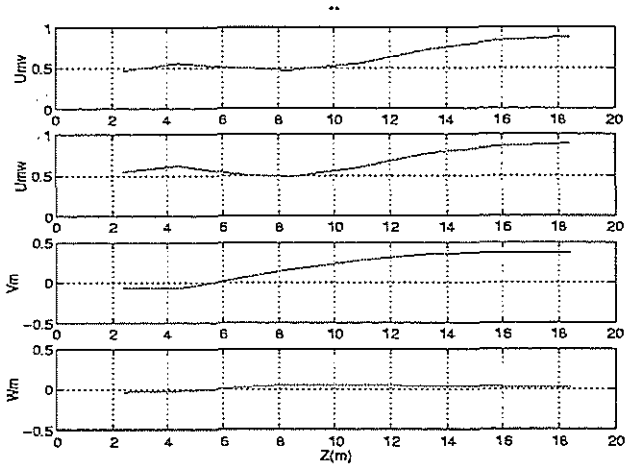

Figure 9 : Evolution of mean velocity components along the vertical axis on point B

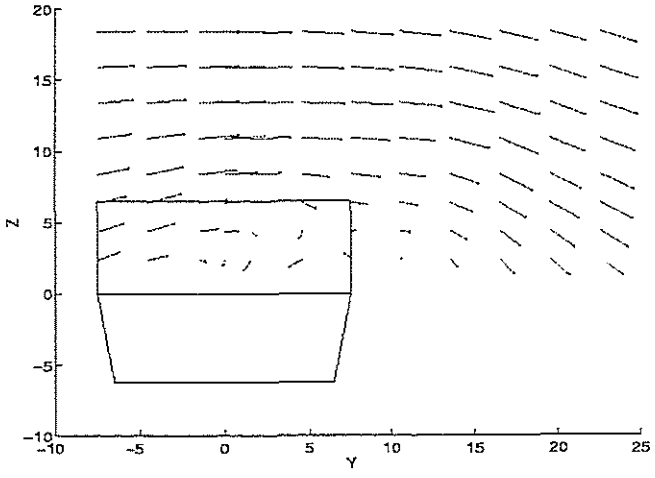

Figure 12 : Lateral section of the flow on plane n° 3 Wind =50 knots, β = 15°, ϕ = 10°

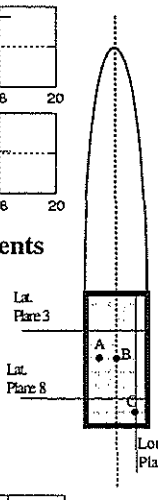

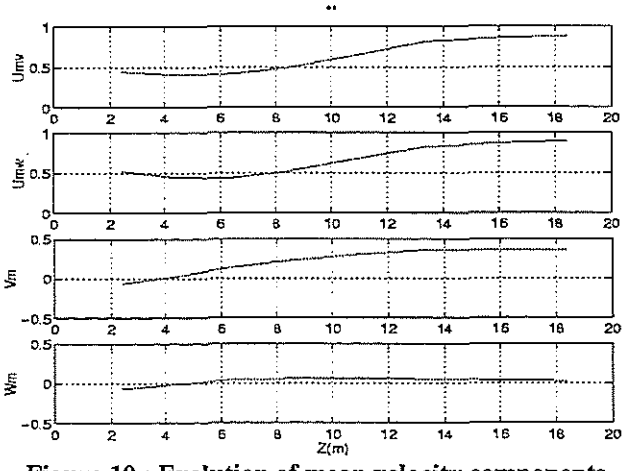

Figure 10 : Evolution of mean velocity components along the vertical axis on point C

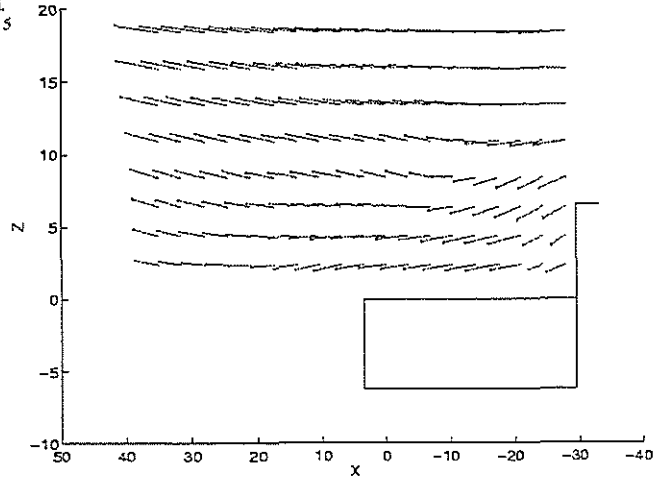

Figure 13 : Longitudinal section of the flow on plane n° 5 Wind =50 knots, β = 15°, ϕ = 10°

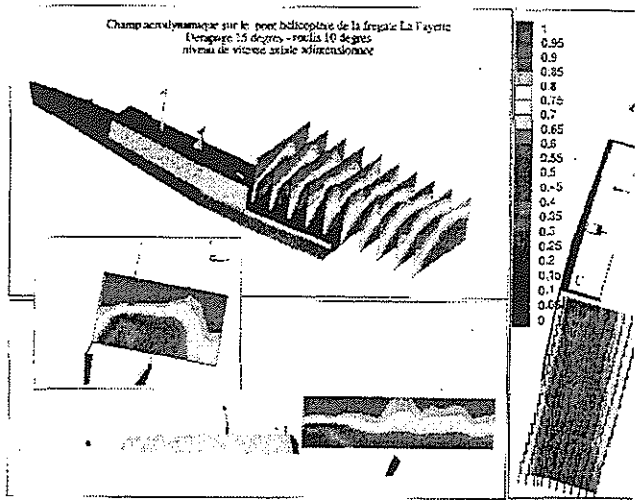

Figure 14 : 3D flow visualisation
Wind = 50 knots, $\beta = 15°$, $\phi = 10°$

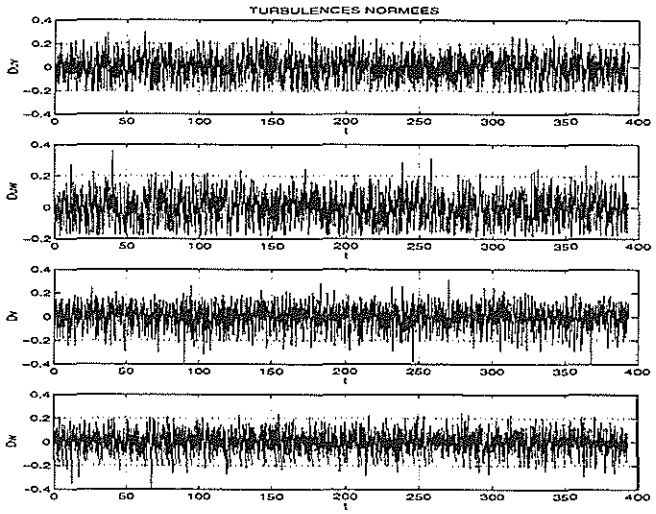

Figure 15 : Example of normalised velocity fluctuations, on the deck centre. Wind = 50 kts ; ß = 0° ; ϕ= 0°

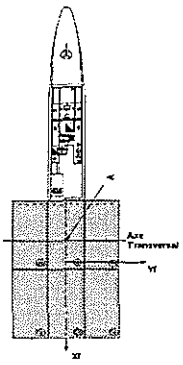

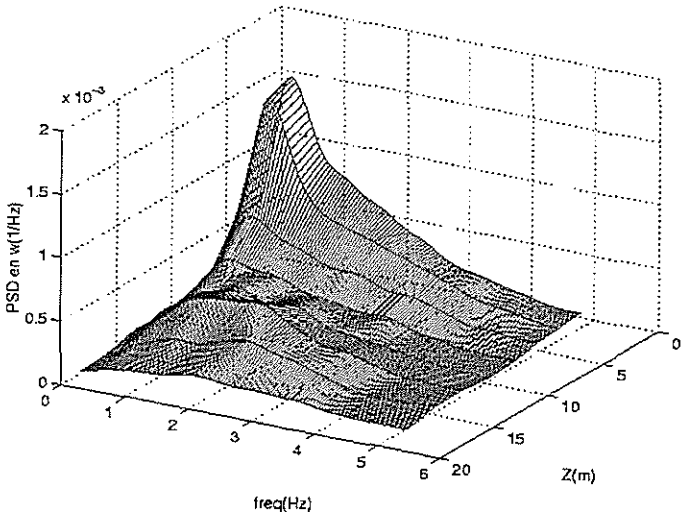

Evolution with altitude above the deck centre

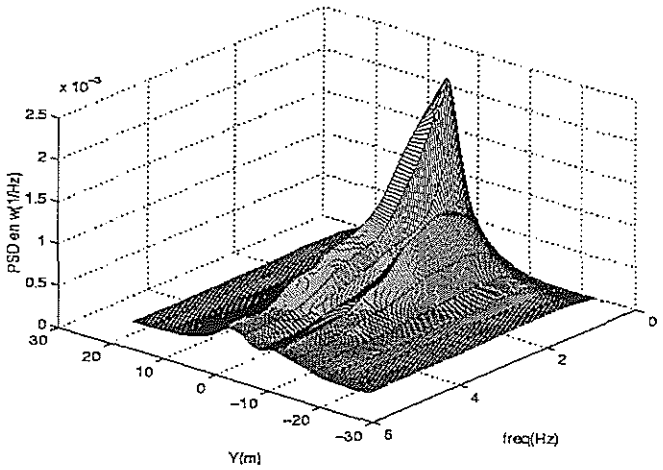

Evolution along the lateral axis on the deck centre (height 2.4m)

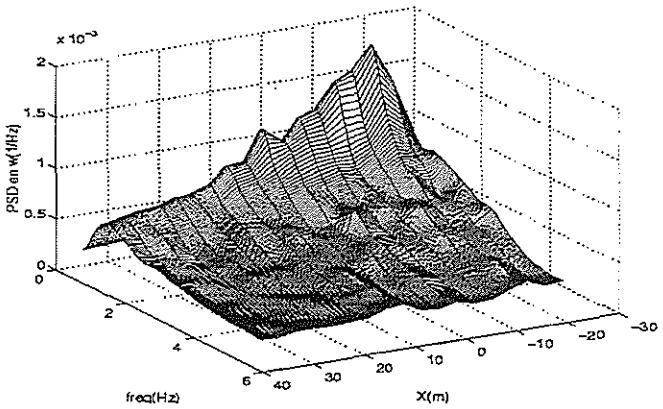

Evolution along the deck median axis (height 2.4m)

Figure 16 : Vertical velocity PSD evolution along the vertical, the lateral and the logitudinal axis.
Wind = 50 knots, $\beta = 0°$, $\phi = 0°$

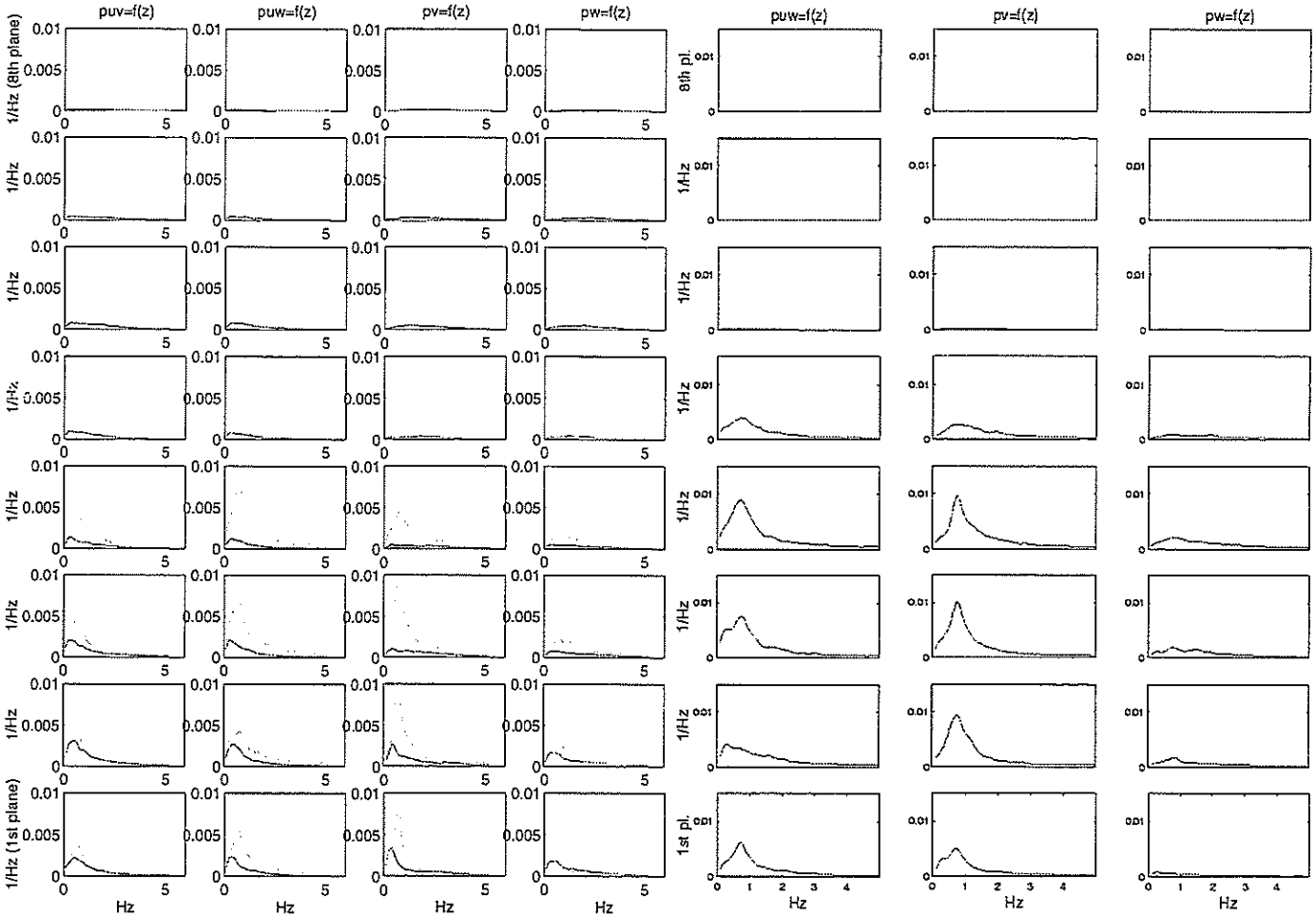

Figure 17 : Comparison of u, v, w PSDs evolution in altitude on the deck centre. wind = 50 kts ; side-slip 0°/15° ship bank angle = 0°

Figure 18 : u, v, w PSDs evolution in altitude on the deck centre. wind = 50 knots, side-slip = 15° ship bank angle = 10°

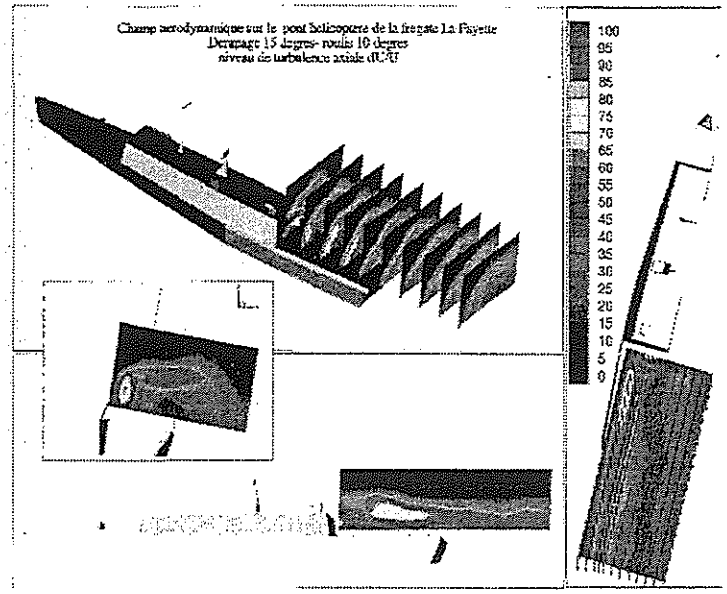

Figure 19 : 3D visualisation of longitudinal turbulence levels. wind = 50 knots, β = 15°, ϕ = 10°

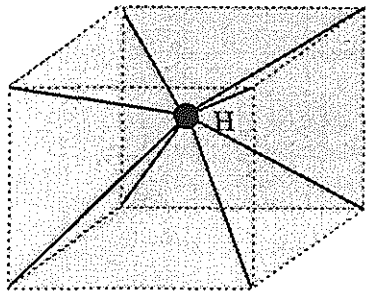

Figure 20 : Test area elementary parallelepiped

Objective :
Avoiding velocity discontinuity when entering the test area

Method :

1- Creation of a transition area.

2- Interpolation of air-wake mean velocity between the test area and infinite free stream.

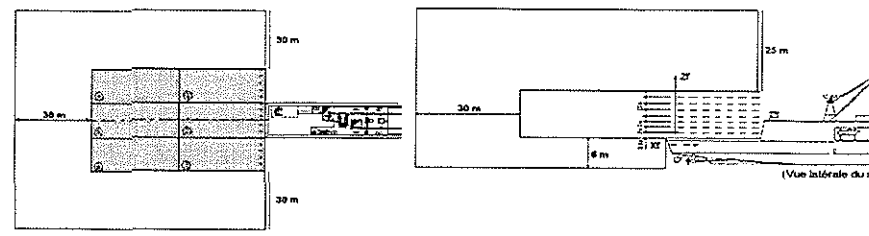

Figure 21 : Model limit conditions

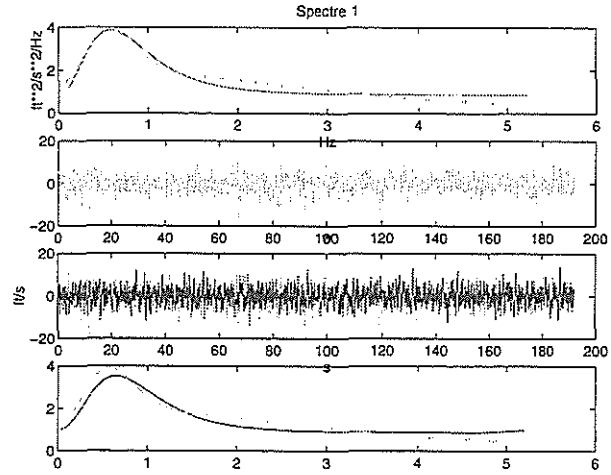

Figure 22 : Example of vertical velocity turbulence generation on the deck centre

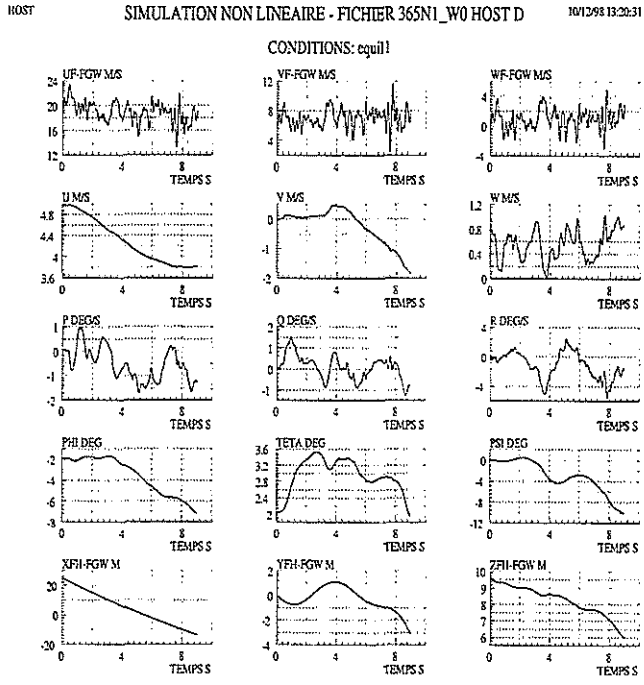

Figure 23 : HOST simulation – Helicopter parameters
Flight above the deck at 10 knots ; slope angle = -1°
Relative wind = 50 knots ; β = 15°
frigate in sinusoidal roll motion

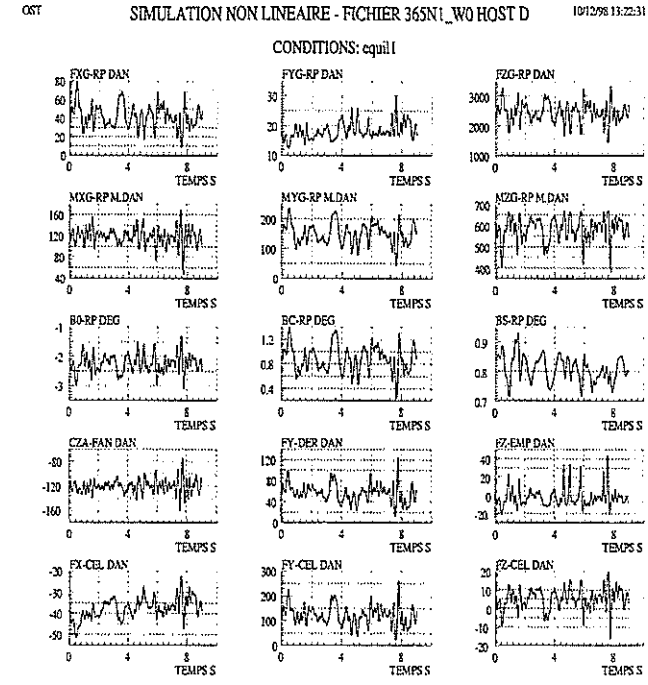

Figure 24 : HOST simulation – Helicopter forces and moments
Flight above the deck at 10 knots ; slope angle = -1°
Relative wind = 50 knots ; β = 15°
frigate in sinusoidal roll motion

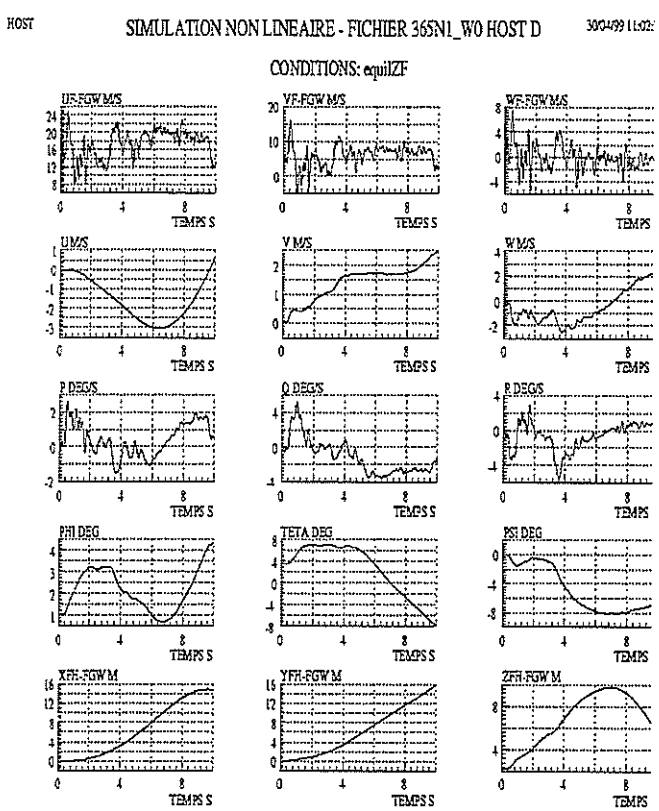

Figure 25 : HOST simulation (multi-element model)
Helicopter parameters
Hover flight above the deck
Relative wind = 50 knots ; β = 13° ; frigate still

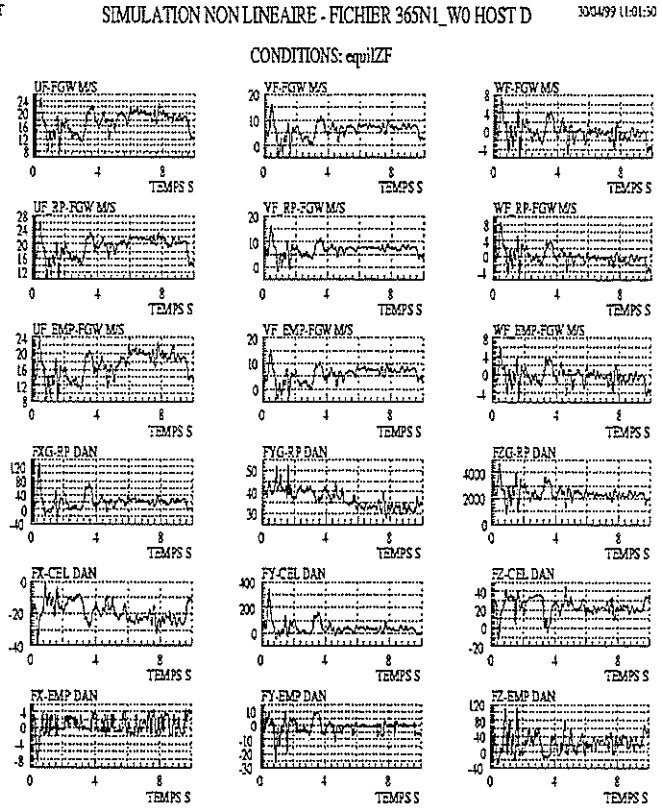

Figure 26 : HOST simulation (multi-element model)
Helicopter forces and moments
Hover flight above the deck
Relative wind = 50 knots ; β = 13° ; frigate still

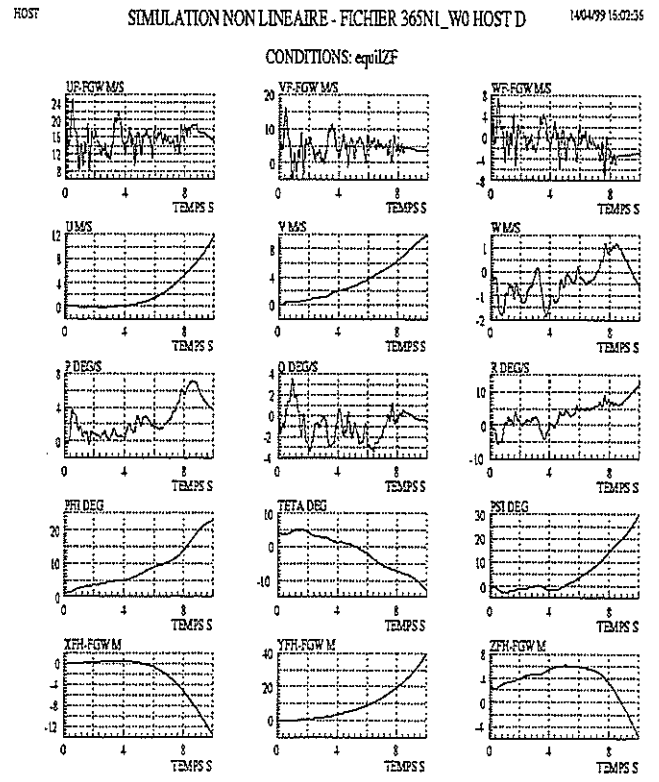

Figure 27 : HOST simulation (mass point model) Helicopter parameters. Hover flight above the deck. wind = 50 knots ; β = 13° ; frigate still

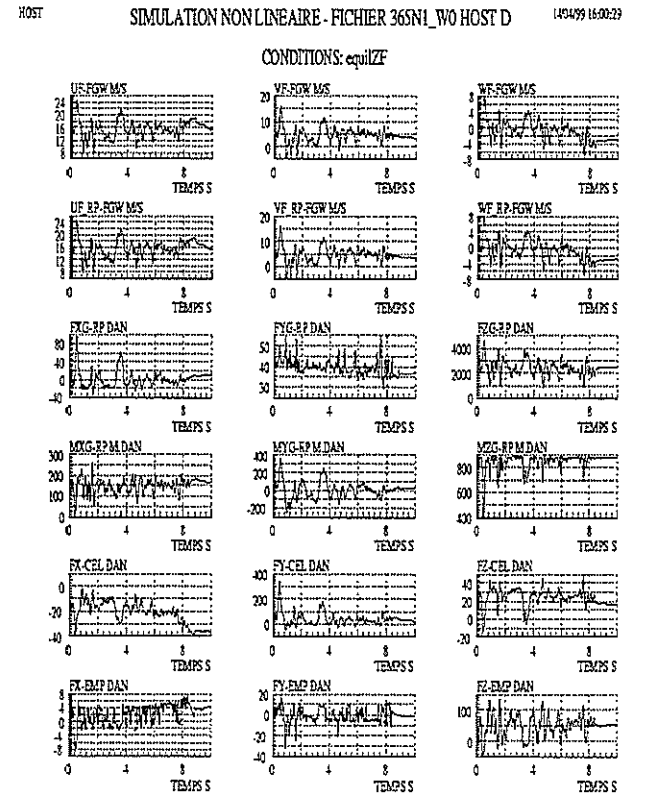

Figure 28 : HOST simulation (mass point model). Helicopter forces and moments. Hover flight above the deck. Relative wind = 50 knots ; β = 13° ; frigate still

TWENTYFIFTH EUROPEAN ROTORCRAFT FORUM

Paper D1

A GENERIC COMPOUND HELICOPTER MODEL

BY

M. ORCHARD, S. NEWMAN
DEPARTMENT OF AERONAUTICS AND ASTRONAUTICS,
UNIVERSITY OF SOUTHAMPTON, ENGLAND

SEPTEMBER 14-16, 1999
ROME
ITALY

ASSOCIAZIONE INDUSTRIE PER L'AEROSPAZIO, I SISTEMI E LA DIFESA
ASSOCIAZIONE ITALIANA DI AERONAUTICA ED ASTRONAUTICA

A Generic Compound Helicopter Model

M. N. Orchard

Spitfire Mitchell Memorial Research Scholar, Department of Aeronautics & Astronautics,
University of Southampton

S. J. Newman

Lecturer in Helicopter Engineering, Department of Aeronautics & Astronautics,
University of Southampton

1. Introduction

The desire to significantly expand the flight envelope of rotorcraft, on a cost-effective basis, has led to the reinvestigation of concepts that had been previously discarded. The compound helicopter configuration is one of these concepts, which has been shown to be technically successful in the past, through the development of aircraft such as the Lockheed AH-56A Cheyenne and Fairey Rotodyne, if not financially and politically successful. The compounding of a helicopter originally evolved as a method of increasing the forward velocity potential of the conventional helicopter. However, it also offers the potential for improved manoeuvrability, greater service ceiling, range and productivity. These benefits, through the use of additional propulsion and lift for the aircraft, come at the cost of increasing the level of complexity of the design and with hover penalties though. These are unavoidable due to the interactions between the various aircraft components and the redundancies in the provision of lift and propulsion inherent in the configuration.

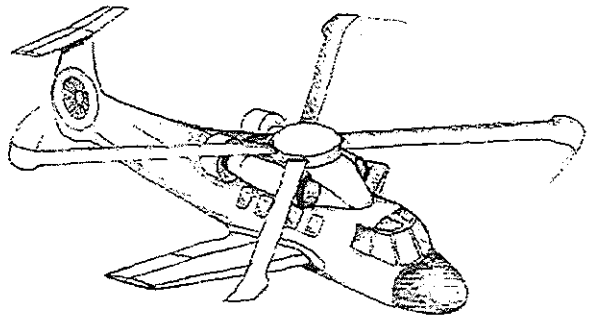

Figure 1: The Compound Helicopter

There is a seemingly endless number of variations in the configuration possible for a compound helicopter, a typical configuration type being shown in figure 1. Part of the designer's difficulty lies in determining which of these choices are worthy of further investigation and, conversely, which should be discarded. While many aspects of the design of such an aircraft seem intuitive, the purpose of this work was to develop a systematic means of eliminating unrealistic configurations and identifying those that hold the most potential for development. The intention was to devise a simple theory that could be implemented with minimal computational complexity, thereby allowing a wide range of configurations to be investigated in a short period of time. Once this had been completed then the configurations that had been selected as having greatest potential could be analysed using a more detailed and intensive simulation. This methodology also has the advantage that it highlights the trends involved with any change made to the configuration, which may be lost in an optimisation routine. The designer will therefore have an understanding of the effect of any modification forced on an aircraft design after the initial configuration has been chosen.

2. Design Issues

Whilst compounding the helicopter offers many advantages, there are many hurdles that must be overcome before the aircraft's full potential will be realised. From an aerodynamics point of view there are the difficulties encountered with the blockage caused by the wing in hovering flight, which reduces the thrust available from the rotor. There is also the detrimental effect that the wing and rotor have on each other's lifting capability when flown in close proximity to one another during forward flight. Whilst the wing is necessary to alleviate the onset of retreating-blade stall on the rotor, it also comes at a weight penalty that restricts the payload of the

compound helicopter in comparison to a conventional one. Weight growth, compared with a helicopter, to meet a common mission has been a consistent finding amongst compound helicopter configuration studies and this will call for speed increases to maintain a similar productivity level to the conventional helicopter. The other main addition to the compound helicopter is that of supplementary propulsion, which also adds to the weight difficulties, not to mention the cost of the aircraft. Increased power requirements of the compound helicopter will necessitate that not only does the aircraft outperform the conventional helicopter in terms of speed, but that it also has a productivity advantage to make its cost premium worthwhile.

3. Development of the Generic Model

To meet the need for computational simplicity and enable the analysis of a large selection of configurations to be achieved quickly and efficiently, a closed form solution for the aircraft trim attitude and rotor thrust requirements was devised. The need for a mathematically tractable solution, due to the high level of interdependency between aircraft components, simplifications, such as the use of a point source model, small angle approximations and the neglect of the rotor drag force, had to be made. A series of simultaneous equations were derived which enabled the goal of a closed form solution to be achieved. The inclusion of a wing to the model also brought its own problems with interdependencies that could only be solved by eliminating some of the smaller terms in the simultaneous equations relating to the wing induced drag. This caused difficulties later on with an underestimation of the forward trim tilt of the non and partially thrust compounded aircraft.

As the developed wake of a rotor at high speed begins to approximate that of a circular wing, the interference effects of the rotor on the wing were calculated using a horseshoe vortex representation of the rotor-wake. The reduction in wing incidence that the rotor wake caused was found by performing a standard integration of the vortex-induced downwash across the wing using the Biot-Savart law. The resulting definite integral, relating the incidence change to the wing geometry and rotor thrust, was included in the trim analysis.

The trim analysis did not make any allowance for the impact of compressibility effects on the advancing blades or the influence of retreating blade stall, so practical limits were applied, after solving the trim equations. To account for the compressibility effects a simple restriction of the advancing blade tip to a Mach number below 0.92 was applied. Aircraft that operated with the wing stalled were eliminated immediately, even if the configuration was feasible, as this is inefficient and would require an inappropriate degree of freedom in the design process. The rotor thrust limit caused by retreating-blade stall was determined by forcing the first three terms of the Fourier series for the aircraft's rolling moment to zero. Should a particular configuration be deemed feasible, then the power requirements were found using actuator disc theory, including Stepniewski's factor. For some analyses take-off limitations were applied including an estimation of the wing blockage in hover, derived from the work of Lynn [1], and the ability to hover at 5000ft with one engine inoperable. Further limits were applied to account for the gust response problems that may occur for an unloaded rotor, 10 percent of the aircraft MTOW being the lower limit of the rotor thrust imposed. So that unrealistically low rotor speeds would not appear in the results from the analysis, another limit was applied, to ensure the aircraft retained a minimum of a third of the lateral control travel in hovering flight, so that manoeuvring flight remained possible.

To analyse the productivity of the different configurations, it was necessary to know the relative empty weights of the various aircraft. This was achieved by taking the baseline helicopter to have an empty weight of half the MTOW. To this weight was added the weight of the wing, power plant and transmission using, as a basis, the results of the statistical analyses of Torenbeek [2] and Tischenko, *et al* [3]. The results of the latter study were modified to include the findings of Lastine [4], regarding the weight penalty incurred by a compound helicopter transmission. Once the weights of these components were known, not only could the payload, and hence productivity, of the aircraft be determined, but using this weight break down and the power requirements, the cost was estimated using the results of Harris and Scully's study of the cost of rotorcraft [5]. This was then linked to the productivity as a cost-

effectiveness measure, the productivity estimate simply being the payload multiplied by the maximum velocity of the aircraft, in order to maintain the results in a generic format rather than tying them to a specific mission.

The final performance measure included in this paper was that of manoeuvrability. The maximum load factor was determined at the bottom of a symmetrical pull-up manoeuvre, to avoid the need for a new trim solution, for the various configurations. This simply took the maximum lift that could be generated by the rotor and wing and related it to the aircraft's weight. This assumed that the aircraft would be flown in a similar manner to a fixed wing aircraft, and unfortunately, due to the nature of the trim models used, could not account for the change in rotor inflow and the wing and stabiliser offsets from the aerodynamic centre of the aircraft.

4. Configuration Analysis Work

In keeping with the goal of finding generic configuration trends, the analysis was not tied to any specific mission, rather it was used to investigate the general performance parameters of power requirements, velocity capability, manoeuvrability, productivity and cost-effectiveness. The closed form trim model and actuator disc theories are intrinsically limited in the configuration variables that can be examined. Those studied in this work were therefore restricted to the wing span, wing setting angle relative to the fuselage, wing aspect ratio, supplementary thrust ratio to aircraft drag in the direction of flight, wing location, rotor speed and supplementary propulsion efficiency. Secondary variables such as blade number, fuselage drag and additional aircraft geometry are necessary to enable the calculation of the performance parameters. However, the significance of their influence is better investigated with higher fidelity simulations, and much work along these lines has already been completed for the conventional helicopter, so these were felt of lesser import for this study.

To best observe the trends, the analysis was used to produce 3-D surface plots, representing the effect of varying two aircraft parameters on a single performance attribute. This was achieved using Matlab® software, the effect of modifying the remaining primary variables being found by creating a series of plots and cross-referencing between them. While the model can be utilised for any aircraft size and geometry, a 4 ½ tonne aircraft using a 4 bladed rotor and of similar dimensions to the Sikorsky S-76 was used for the analysis contained herein.

5. Model Limitations

In order to achieve the aim of a closed form trim and rotor thrust solution the assumptions made have imposed some limitations on the model. The elimination of some of the smaller wing induced drag terms resulted in a minor underestimation of rotor thrust, but more significantly this created a underestimation of the forward trim tilt of the aircraft when combined with the small angle assumption. This latter effect was most noticeable for the winged helicopters that did not use thrust augmentation. The underestimation was of the order of three degrees for aircraft using extremely large wings. This did not affect the fully thrust compounded aircraft, due to its level fuselage attitude (the rotor disc attitude and fuselage attitude were linked for simplicity), so more confidence can be placed in these results.

The interference model assumed that the rotor wake is fully formed and approximates to that of a circular wing. At lower velocities this assumption will begin to break down, hence the configurations with which this model has been analysed have been limited to velocities above 100 knots. Also restricting the analysis were the rudimentary boundaries used for the compressibility and retreating blade stall limits on the rotor, due to the use of actuator disc theory and the closed form trim solution. The former simply constrains the tip speed below a set Mach number and does not take account of the critical drag rise on the power of the aircraft, or the effect that the reduced blade incidences of the unloaded rotor have on the local Mach numbers on the blade. Dynamic stall has been included through a quasi-static estimation, but the effect of the changes in the rate of pitch change with reduced rotor speed could not be included.

6. Maximising the Velocity Potential

The conventional helicopter is limited in velocity by the boundaries of retreating-blade stall and compressibility effects on the

advancing blade. The addition of supplementary thrust and a wing to the helicopter allows these boundaries to be manipulated, but also brings a new restriction in the form of the problem of rotor gust-response. Whereas the conventional helicopter power requirements are set by the hover condition, the compound helicopter's power requirements are set at the maximum velocity.

Looking at figure 2 of the maximum velocity capability of a range of configurations, varying the supplementary thrust ratio and the wing area, all of the limits mentioned in the preceding paragraph become apparent. With a reduced rotor speed to show the benefits of compounding, the point representing the conventional helicopter and a large portion of the aircraft utilising only a small amount of thrust compounding, on the left-hand side of the figure, are constricted by retreating-blade stall. The higher plateau, which represents the aircraft attaining the compressibility limit, is notably only reached by aircraft using both thrust and lift compounding, hence overcoming retreating-blade stall. The addition of thrust or lift compounding separately does not benefit the aircraft in speed potential significantly. The third boundary that of rotor gust-response, is denoted by the large drop off in velocity capability of the configurations to the right of the plot, and the chamfer formed in the compressibility plateau is caused by the power limit of 3000-hp imposed on the program. There is a fifth limit that of the supplementary wing stalling, but this was avoided throughout the analysis for the reasons noted in section 3.

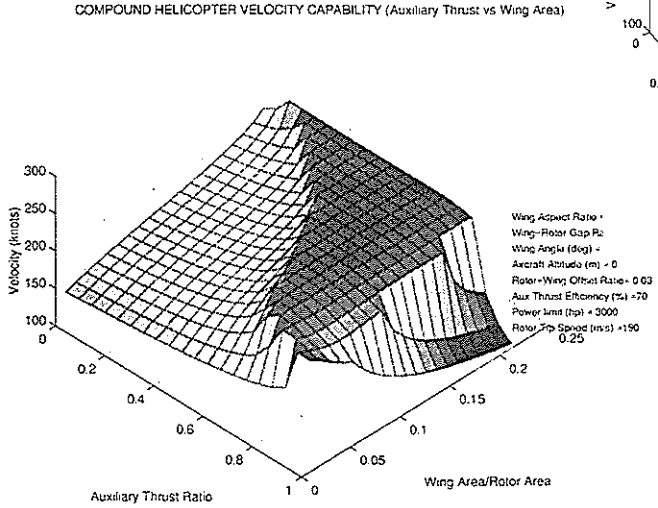

Figure 2: Velocity Capability – Varying Supplementary/Auxiliary Thrust and Wing Area

A point highlighted by this velocity analysis and previous work has been the need to reduce the rotor speed to realise the full velocity advantage of the compound helicopter. Past research has suggested the use of variable speed rotors, but these can create difficulties in avoidance of resonant conditions. The analysis conducted to produce figure 3, however, indicates that the full velocity potential of the compound aircraft could be utilised with a constant reduced rotor speed, while still maintaining a control margin for low speed manoeuvrability. This can be achieved because of the retreating-blade stall avoidance afforded by the wing in forward flight and the excess power a compound helicopter will have in hovering flight. It will however, necessitate the use of high inertia blades, for safety reasons, and assumes that the majority of the compound helicopter's power is available to the rotor during hover. The three main features of this plot are the curved surface representing the intrusion of the gust-response limit on the rotor, the flat slope to the left, being caused by the basic compressibility limit applied. The partially hidden limit towards the peak is that of retreating-blade stall. Of note is the small wing area necessary to achieve the maximum velocity potential of the aircraft.

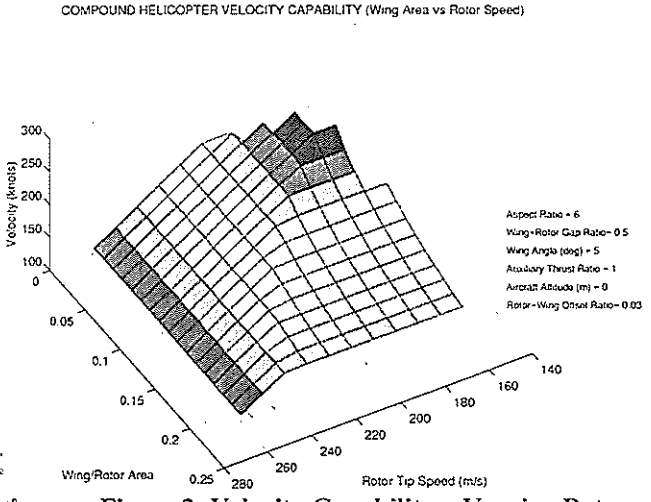

Figure 3: Velocity Capability – Varying Rotor Speed and Wing Area

7. Aircraft Power Requirements

One of the main results highlighted by the analysis was that some aircraft parameters were found to be performance determining, such as the wing angle and wing area, whereas others such as the wing location and wing aspect ratio only had a major influence at

extreme locations or aspect ratios. Examining the effect of the wing location in figure 4, it can be seen that when the wing is in close proximity to the rotor the effective wing incidence is greatly reduced, although increasing the rotor-wing gap to a distance of half the rotor radius, the interference effects are reduced to negligible proportions. A major feature of this plot is the significant minimum just below and behind the rotor, which is caused by the use of a single horseshoe vortex to represent the rotor wake. A more uniform interference effect would be expected in real life. Away from this region it does, however, give a reasonable comparison to flight test data, full thrust compounding being used in this particular plot to eliminate the influence of fuselage trim attitude changes.

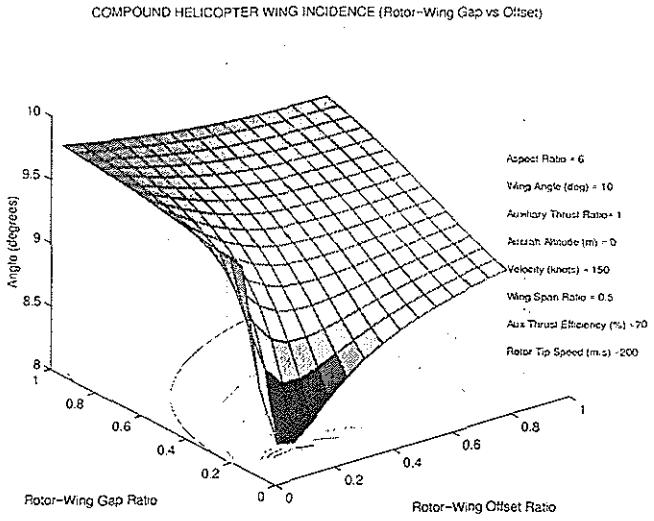

Figure 4: Wing Incidence – Varying Rotor-Wing Gap and Rearward Offset

The wing aspect ratio was also found to be of secondary importance to the design of the aircraft, figure 5; the benefits of an 'optimum' aspect ratio only being of the order of 50-hp. Conventional fixed wing aircraft wisdom states that increased aspect ratio will improve the efficiency of the aircraft, although there are structural and manoeuvre constraints that must be applied. In the case of the compound helicopter there is the added difficulty of the rotor wake. As the wing aspect ratio is increased, not only does it position the tip further into the high-energy hover downwash, but it also incurs greater interference from the 'trailing-vortex' portion of the rotor's wake in high-speed forward flight. For this reason interference effects largely negate the increase in wing efficiency gained by increasing the aspect ratio. As long as the worst inefficiencies are avoided, the aspect ratio should be chosen for other practical reasons such as minimising the hover download and structural requirements.

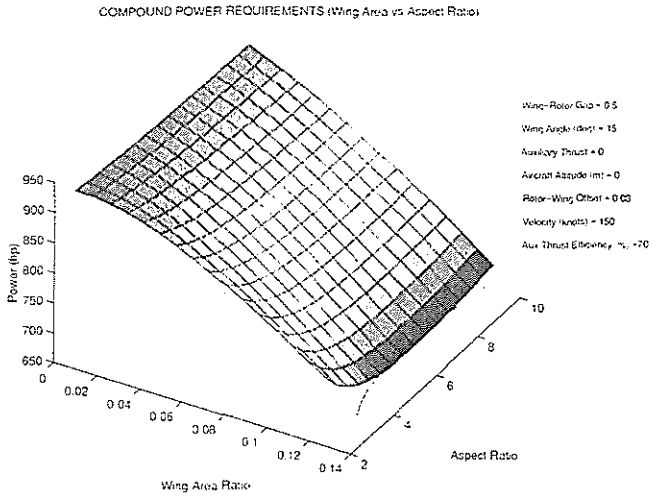

Figure 5: Power Requirements – Varying Wing Aspect Ratio and Area

Of the parameters investigated, the supplementary thrust ratio to drag, the supplementary propulsion efficiency, the wing area and wing angle relative to the fuselage were found to be performance determining. In terms of the power requirements, the addition of supplementary thrust to the aircraft will not be beneficial if the rotor is capable of supplying all of the aircraft's thrust requirements, unless the supplementary propulsion is extremely efficient, due to the increased ram drag it will have in comparison to the rotor. That thrust compounding is power intensive can be seen in figure 6, but it does come with the advantages of increased wing effectiveness and can eliminate the need for changes in fuselage tilt.

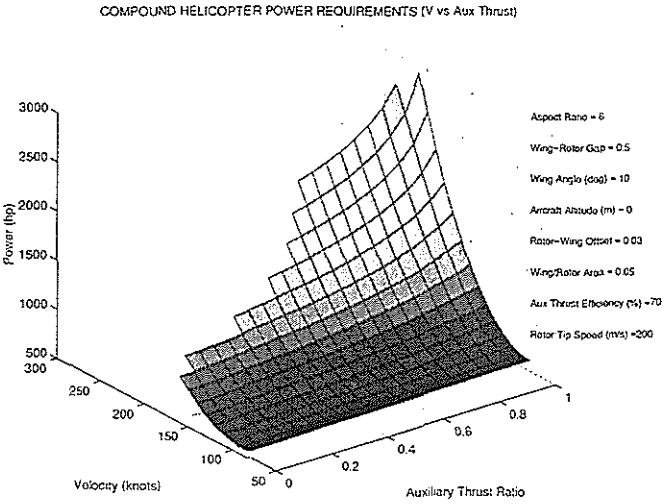

Figure 6: Power Requirements – Varying Velocity and Supplementary Thrust

The addition of the wing is necessary if the limit of retreating-blade stall is to be overcome and greater velocities attained, but it does not necessarily produce reduced power requirements. In figure 7 a small reduction in total aircraft requirements is gained by using a wing of small area and angle, probably due to the reduction in rotor thrust necessary. As more wing area and incidence is added then the greater profile and induced drag incurred by the wing raise the total power requirements, as the supplementary propulsion's higher parasite power outstrips the reductions made in the rotor induced power level. The cut away region at large wing areas and angles represents the limit imposed on the rotor by gust-response considerations.

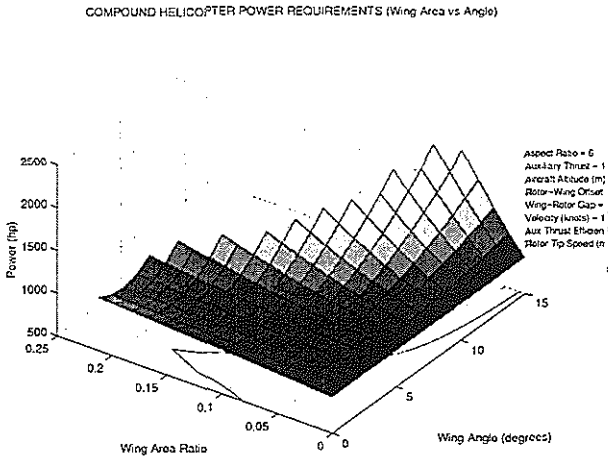

Figure 7: Power Requirements – Varying Wing Area and Aspect Ratio

A further feature of note is the positioning of the trough in the total power requirements, which appears to reduce in wing incidence as the wing area is increased. This suggests that there is an optimum ratio of wing lift to rotor lift, which seems to be reinforced by the similar shapes of figures 8 and 9, of the effect of varying the wing angle and the wing area respectively, against the aircraft velocity. Any distinct mathematical relationship for the rotor to wing lift ratio though will be disguised by interference effects and inefficiencies of the two lifting devices. The viable configurations of both of these plots are bounded on the right hand side by rotor gust response limits and retreating-blade stall limits to the left.

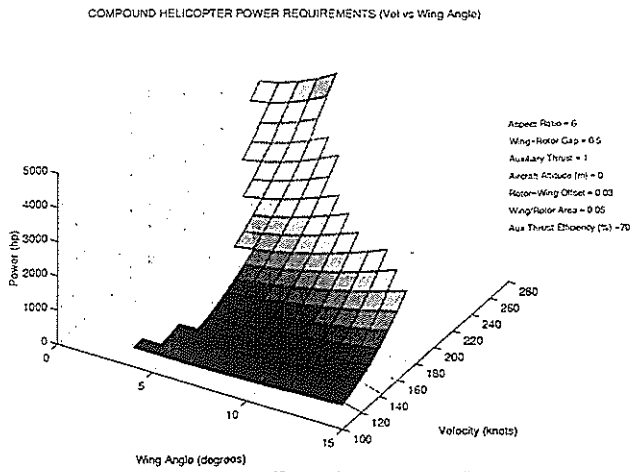

Figure 8: Power Requirements: Varying Wing Angle and Velocity

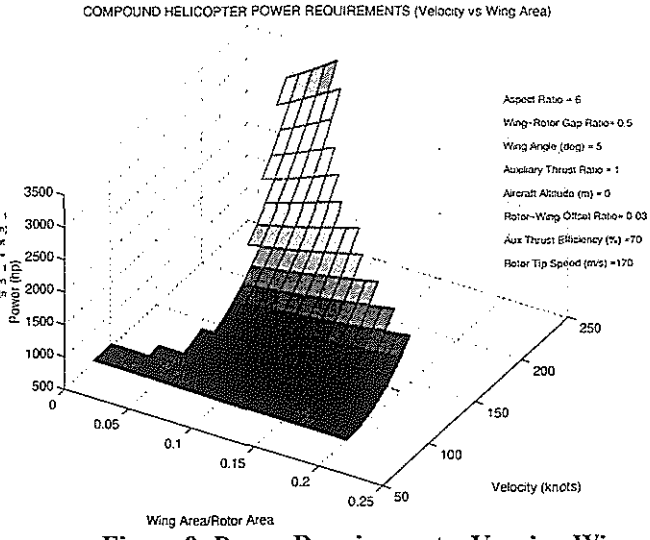

Figure 9: Power Requirements: Varying Wing Area and Velocity

8. Productivity

The productivity of a compound helicopter is potentially degraded in comparison to a conventional helicopter, despite the increase in speed capability, through the addition of the wing, extra transmission and larger power plant(s), as the weight of these items reduce the payload that can be carried. The analysis, used within, simply determines the productivity of the aircraft using the product of the payload and the aircraft's maximum velocity, a fixed upper power limit being imposed. This gives a good generalised indication of the relative productivity of the various configurations, but should be taken with some caution. The reason for this caution is that a configuration with excellent speed capability and poor payload may come across with the same productivity as one with poor

speed perfromance and excellent payload, although the usefulness of these two contrasting aircraft will come down to the specific mission to be performed. The generalised productivity analysis does, however, give the designer an idea of the type of configuration, which they should be aiming for.

Figure 10, shows the productivity when varying the supplementary thrust ratio and the wing area. It shows the main features found when analysing the productivity of the various compound helicopter configurations. An interesting outcome was that certain fully thrust compounded configurations, utilising a small wing area to avoid retreating-blade stall, sufficient power and a reduced rotor speed to off-set the compressibility limits on the advancing blade, could exceed the productivity of the conventional helicopter by up to 30 percent. The productivity of the fully thrust compounded aircraft with a small wing area in the figure comfortably surpasses that of the conventional helicopter, which is limited, along with many of the partially thrust compounded aircraft by retreating-blade stall. This was found to be the case even when both aircraft employ an optimum rotor speed, despite the conservative nature of the analysis, which favours the conventional helicopter.

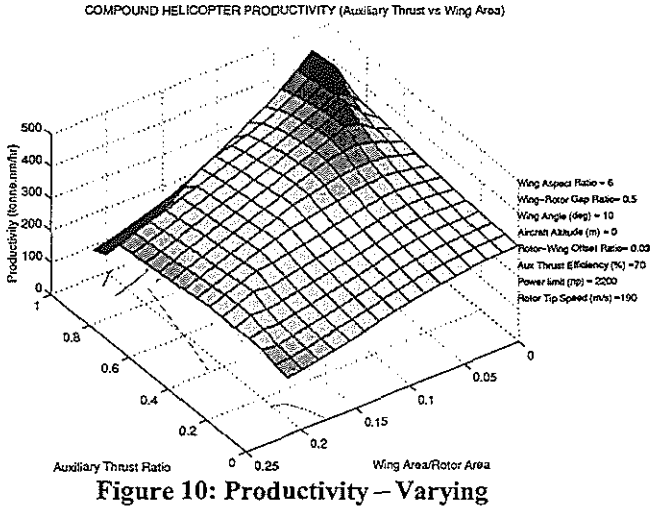

Figure 10: Productivity – Varying Supplementary Thrust Ratio and Wing Area

Figure 10 can be compared with figure 2, portraying the velocity limits, where the same four regions are apparent. Aircraft limited by gust-response, to the left of the plot, have a significant productivity penalty due to the reduction in velocity potential caused by the gust response restrictions combined with payload reductions. The central region of an almost constant upward slope represents the aircraft limited by advancing blade compressibility limits, the upward slope being a result of the payload penalty imposed on the aircraft by the addition of larger wings. The addition of more wing area to the aircraft, after the retreating-blade stall limitations have been overcome, being detrimental to the productivity. A slightly concave portion of the slope is evident just before the peak, which is due to the speed of the aircraft being power limited below that imposed by the rotor limitations. High power levels and/or high supplementary propulsion efficiencies are required to overcome the power limitations of the fully compounded aircraft and obtain its full productivity capability. Beyond the peak and to the right of the Mach limited configurations, the aircraft are constrained by retreating-blade stall. Thrust compounding on its own has a neutral or slight benefit on the productivity of the aircraft due to the slight unloading benefit it allows the rotor for the avoidance of retreating-blade stall. Although when combined with the wing the improved wing effectiveness, and stall alleviation, it brings gives the substantial productivity benefits seen.

9. Cost Effectiveness

While it is important to have a highly productive aircraft, the aircraft's initial cost has to be reasonable, otherwise the customer will not be in a position to purchase it, despite the benefits it provides. Simply the benefits of its productivity have to be affordable. Previous portions of this analysis have shown the fully compounded helicopter to be potentially more productive than the pure helicopter, however the fully compounded aircraft is more power intensive. This latter point is potentially detrimental to the compound helicopter's overall viability, since the power plant is probably the most expensive component of the aircraft.

Using the same geometry and aircraft parameters as for the productivity plot of figure 10, a plot of the initial cost of the aircraft divided by the productivity is given in figure 11. Interestingly a trough forms where a configuration moves from being limited by retreating-blade stall to where it is fully alleviated and compressibility becomes the limiting factor, which corresponds to the ridge in the previous figure between these two

limitations. The most cost-effective aircraft on this trough are those that have the smallest wing-area, and therefore the greatest thrust compounding ratios. The addition of wing area, apart from that required to alleviate retreating-blade stall is again shown to be detrimental, partly due to the cost, but mainly due to the reduced productivity outlined in the previous section. Gust-response limits again form a region of poor worth on the right-hand side of the plot.

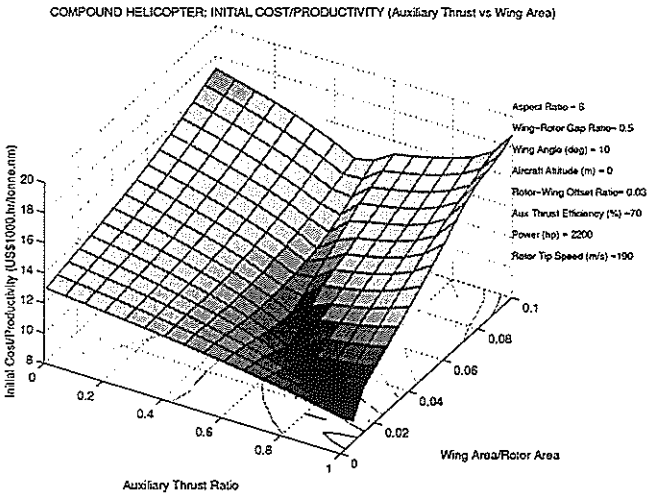

Figure 11: Initial Cost/Productivity

Altering other parameters for this analysis such as the rotor speed can have a significant effect on the cost effectiveness of the aircraft. Increasing the rotor speed improves the velocity capability and hence the productivity of the, previously retreating-blade stall limited, aircraft to the left of the trough, which improves their cost/productivity ratio. Increasing the power limit is advantageous to the productivity of the aircraft to the right of the trough, although the large cost of this additional power exceeds the benefit gained from the increased productivity, unless the supplementary propulsion efficiency is sufficiently high

10. Manoeuvrability

As a conventional helicopter increases in forward velocity, the increase in collective blade incidence required reduces the incidence available to trim and manoeuvre the aircraft before the retreating-blade will stall. This not only places a limit on the velocity of many of the potential compound helicopter and conventional helicopter configurations, but it also restricts the rotor thrust available at any set velocity, hence limiting the manoeuvre loads that can be supported by the aircraft. The addition of a wing, however, endows the aircraft with a second source of lift that incidentally increases in lifting effectiveness with increasing forward velocity, in contrast to the rotor. For this reason the compounded aircraft is expected to have greater manoeuvrability at high speed than the conventional helicopter.

Of particular interest in figure 12 is the low manoeuvrability of the conventional helicopter at the relatively high speed and the limited effect that thrust and lift compounding give when applied separately. This plot, of the load factor that can be maintained in a sustained symmetrical pull up manoeuvre, for varied wing area and supplementary thrust, shows only minor manoeuvre benefits for the winged helicopter, as the increased fuselage tilt required when the rotor thrust is reduced limits the effectiveness of the wing. Similarly the addition of supplementary thrust separately provides little additional manoeuvre capability, due to the low level of rotor unloading it enables. It is when these two compounding components are combined, however, that the full manoeuvre benefit of the compound helicopter is shown. The addition of supplementary thrust to the winged helicopter enables it to be 'flown' in a similar manner to a conventional fixed wing aircraft through the manoeuvre maximising the effectiveness of the wing, as can be seen most notably with a full thrust compounding ratio. The addition of the moderately sized wing and auxiliary thrust in figure 12 improves the load factor capability by 2g, but there is a conspicuous area past the peak in this figure that is cut away. This area represents configurations that would be limited by rotor gust response difficulties in level flight, however, this does not preclude the following of the favourable manoeuvre trends to a much greater load factor through the use of a mechanism such as variable incidence wings or flaps to improve the wings lifting ability.

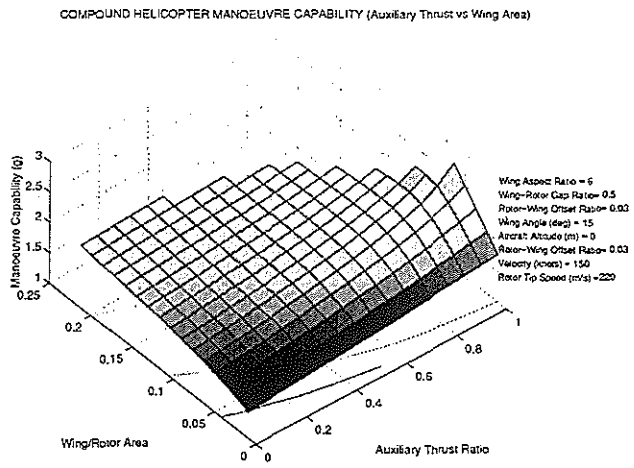

Figure 12: Manoeuvre Capability – Varying Supplementary Thrust and Wing Area

The final points highlighted by the manoeuvre analysis, not shown, are the ability of the fully compounded helicopter, using both thrust and lift augmentation, to maintain its manoeuvrability to high speed, unlike the helicopter. This is mainly as a result of the increase in wing effectiveness as the aircraft velocity increases, supplementing the rotor's decrease in effectiveness. The same effect enables a compound helicopter utilising a reduced rotor speed to have a much superior manoeuvre envelope at high speed compared to the conventional helicopter despite the reduction in rotor thrust available.

11. Conclusions

The results of this closed form analysis show that a computationally inexpensive theory such as this can give a good insight into the problems and trends with designing a complicated aircraft such as the compound helicopter. It does have some drawbacks, however, with inaccuracies in the trim estimation and the rudimentary nature of the boundaries that have to be applied to account for rotor compressibility, dynamic stall effects and gust response.

The trends revealed by the analysis show that there are certain performance driving parameters, such as wing area and the auxiliary thrust ratio, whilst others, such as wing location, only significantly influence the performance at certain extreme conditions. An additional point highlighted by the analysis is that the optimum aircraft configuration will vary somewhat depending on what performance parameter the designer is trying to extend. From a productivity perspective, a wing of small area is beneficial, whereas if manoeuvrability or altitude is the designer's goal, a greater wing area is advantageous. Full thrust compounding on the other hand was important in boosting the velocity capabilities of the aircraft and improving its manoeuvrability, but incurred a large power penalty unless the efficiency of the supplementary propulsion device was high, to negate the disadvantages of its high ram drag.

The analysis highlighted the benefits possible through fully compounding the helicopter of increased velocity, increased productivity and increased manoeuvrability. Apart from the need for a highly efficient supplementary propulsion device, the other main conclusion of this work is that the development of a variable incidence wing or efficient flaps will be needed to fully exploit the compound helicopter's promise. This is necessary to avoid rotor gust response difficulties, minimise the power requirements of the aircraft throughout the speed range and to realise the aircraft's exceptional manoeuvre potential.

References

1. R. Lynn, Wing-Rotor Interactions, Journal of Aircraft Vol.3, No.4 Jul. 1966.
2. E. Torenbeek, Synthesis of Subsonic Aircraft Design, Kluwer Academic Publishers 1982.
3. M. Tishchenko –A. Nekrasov -A. Radin, Helicopters – Selection of Design Parameters, NAS2-10062 Apr. 1979.
4. J. Lastine, Advanced Technology VTOL Drive Train Configuration Study, USAAVLABS-TR-69-69 Jan. 1970.
5. F. Harris –M. Scully, Rotorcraft Cost Too Much, Journal of the American Helicopter Society, Vol. 43, No. 1, Jan. 1998.

25th EUROPEAN ROTORCRAFT FORUM

PAPER No. D-2

EC 120 DESIGN

by Jean-Claude BOUVIER

Head of Eurocopter Design

September 14 - 16, 1999

Rome, Italy

ASSOCIAZONE INDUSTRIE PER L'AEROSPAZIO, I SISTEMI E LA DIFESA
ASSOCIAZONE ITALIANA DI AERONAUTIC ED ASTRONAUTICA

EC 120 DESIGN

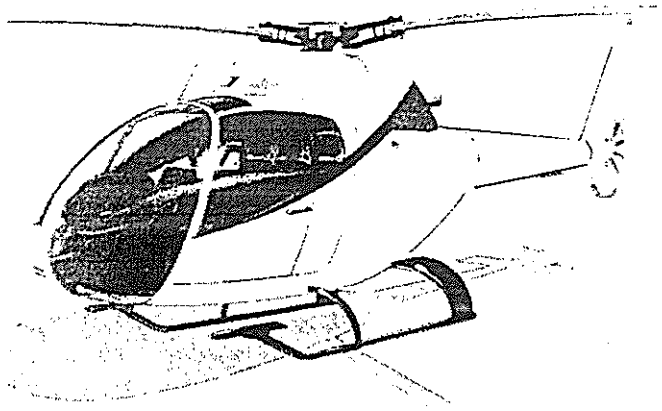

Our new helicopter, the EC 120, is the first EUROCOPTER · helicopter to have incorporated an industrial design process from the time the general specifications were drawn up.
As a discipline, industrial design helps improve man/machine interfaces and is dedicated to users' satisfaction.

At the end of the eighties, Eurocopter, then Aérospatiale Helicopter Division, initiated the P120 study i.e. a four-blade helicopter with high engine power. The Pre Project unit of the Engineering Department consulted two agencies in Paris, Volanis design and Picard IDEI, to assist Aérospatiale with the shape and outfitting studies.
This first contact between company and industrial design helped sensitize the Engineering Dept. to this field associated with human factors.
The projects were presented as 1/5th-scale models and perspective drawings of the helicopter fuselage and cockpit internal outfitting; they proved really helpful and were highly appreciated by the Engineering Dept.

This design gave personality to the helicopter as it was being thought out. A designer's drawing is both a synthesis of the engineering work and a projection for new proposals. Marketing analyses are also facilitated by the designer's suggested changes.
Since he is not necessarily an aerospace specialist, the designer will naturally come up with innovating ideas showing the helicopter in a different and unusual light. Innovation is playing a significant role from the conceptual and commercial standpoint when manufacturers may come up with the same type of product over a short period of time. Originality is today increasingly based on the services helicopters do offer and it is those novelties that underline the competition's obsolescence.
Twenty years after the Ecureuil, Eurocopter elected to integrate industrial design in the Engineering Dept.and the work that was done on the P120 demonstrated that a specialist in this field could become a full time member of the engineering team.

P120 is now, for strategic and commercial reasons, a simpler, lighter and cheaper EC120, and EUROCOPTER DESIGN has been integrated as a company unit.

The EC 120 program was started in 1992 and our first job was to put this new helicopter into shape.
Interior design is obviously the field in which the industrial designer must focus the most attention and numerous elements connected to passenger comfort were studied. All layout proposals must however match with the general shape of the aircraft and correspond to the prevailing character of the helicopter. One consideration took precedence with regard to the outline of the EC120: this aircraft had to be esthetically pleasing for the next 30 years. The direct consequence of this requirement was to refuse any concessions to fashion; nothing changes more quickly than fashion.

The shape of the EC120 seems to have been sculptured as it moves through the air and at the same time, it conveys the traditional brand image of EUROCOPTER products.
The drawing below is the first rough sketch of the EC120.

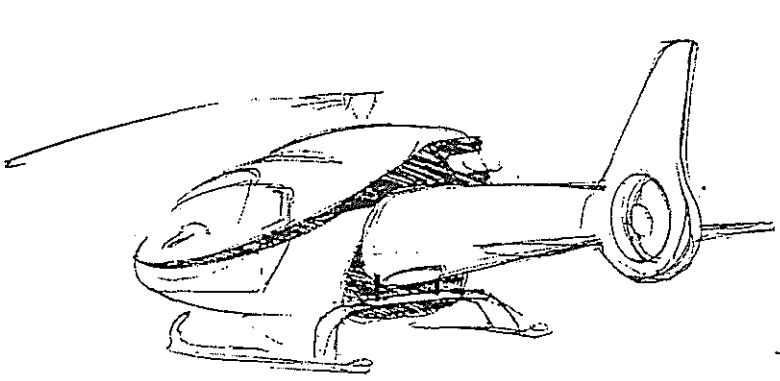

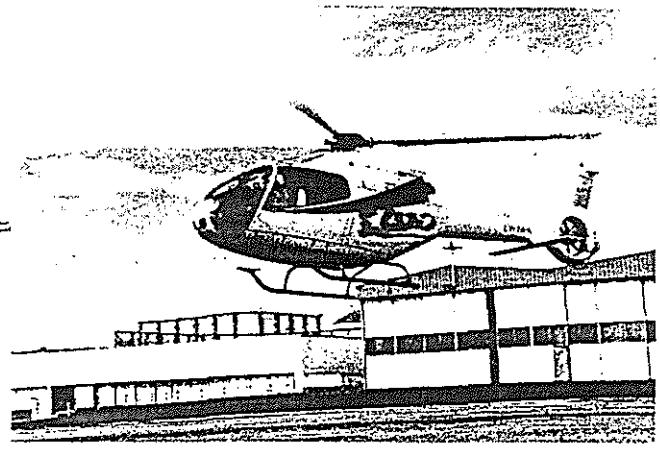

Well before the interior drawings were started, the design work consisted in visiting several small helicopter operators in the area.

About twenty operators, pilots, mechanics and passengers were met and we have had very opened discussions. Dozens of photos were taken. The photos and the operators' comments were analyzed and this analysis became the database that the designer used to make his suggestions for the EC 120.

Before analyzing the EC 120 in more detail, let's take a quick look at what had happened in the past.

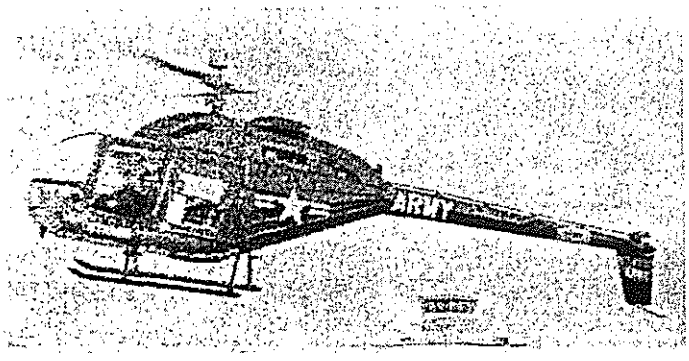

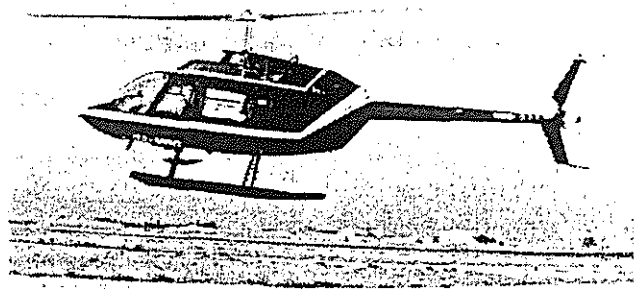

When the BELL engineers decided to put in a proposal to the MOD invitation for bids, they presented the OH4, which was not particularly adapted for a commercial market. Convinced that they had a good helicopter, BELL called in an industrial design consultancy to improve the helicopter in all the areas where it wasn't up to standard, without modifying the very satisfactory technological aspects. The Jet Ranger took form from this design study and went on to become the best selling turbine helicopter world-wide.

The first known experience in this field in France was the study conducted by Raymond Loewy on the Alouette II. Unfortunately this "Governor" Alouette was not a true industrial design study in that Raymond Loewy proposed a simple styling, decorating study, which had for first consequence to make the helicopter a lot heavier.

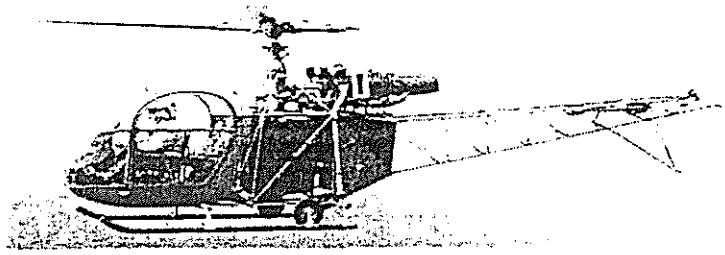

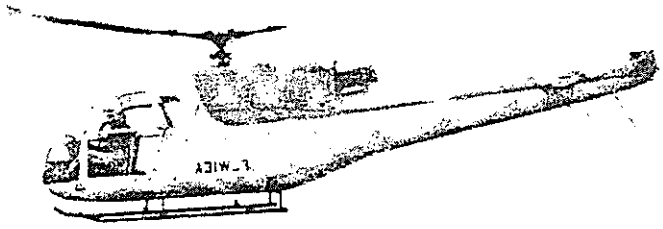

Now to come back to our EC 120, EUROCOPTER wanted the design to be part of the work covered by the Preliminary Design Department, which was tasked with drawing up the general specifications and the initial dimensioning studies, before it was handed over to the Design Office. This study should also be useful for other programs in any case.

Using the reports of findings on existing helicopters, the designer first concentrated on the weak points which operators put up with, either consciously or unconsciously.

This is how the scope of the industrial design stage went much further than simply drawing the general silhouette of the helicopter.

Creativity is offering users what they need, before they know they need it!...this means that there is no chance that it will come out of clinical tests.

An enthusiastic acceptation comes from a good surprise, and a surprise will never come out of a Gallup Poll, because the average of any opinions will always give an average opinion. It is up to the designer to analyze human behavior and to draw from it the lessons that will generate **innovating proposals**.

When a designer realizes that nothing has been provided to carry the mandatory documents that are just as indispensable for each flight as the main rotor, i.e.: the Flight Manual, the Aircraft Log Book, the insurance certificates, the weight sheet, the maps and, for public passenger transport, the Operating Manual and the safety directives, and, consequently, that the owners of new helicopters end up by making cases themselves out of plywood with a hammer and nails, then he does not think of styling nor is his aim to catch the eye; he does his job as a designer and proposes rational solutions, using all the typical aeronautical parameters. His answer must be a certifiable product that takes into account the ergonomic aspects as well as the weight, cost and industrialization requirements. Hence the first thing we did was to identify the largest possible number of anomalies.

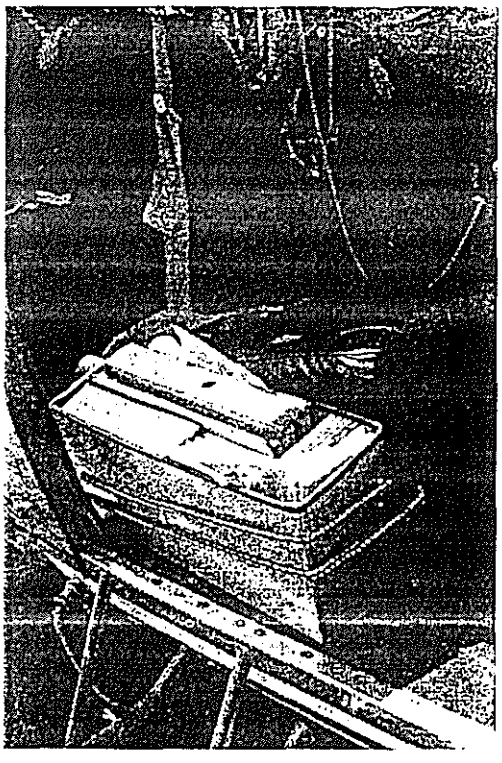

Observing, on the spot, the way in which human beings behave is far more effective than anonymous answers to a questionnaire.

The designer applies behavioral ergonomics, semiology ; in other words, he tries to identify problems by noting attitudes that he considers to be abnormal. When he discovers that three out of ten passengers fall when embarking or disembarking, he tries to find out why this happens. His findings will have immediate effects as regards to the size and the position of the footsteps, as well as the number and locations of the hand grips.

Let us analyze this slide together:

This gentleman is a business man, who is not used to traveling in a helicopter. As he approaches the helicopter, he is either a little anxious or enthusiastic, in any case he is inevitably already stressed when he arrives with his attaché case. Now he must pass under the rotor, which is spinning. A flight line technician has placed some steps in front of the door and he is ready to help our friend to board.

Nevertheless, if we take a closer look, his left foot misses the step and he desperately gropes for a non-existent handgrip with his left hand. He hits his shim harshly, then as he straightens up he hits his head on the top of the door opening. What a welcome on board!

The designer's aim is to produce the stimulus that makes people want to become owners.

TECHNICAL ASPECTS

GENERAL CONCEPT:

Because the general outline of the helicopter had to remain ageless over decades, the design department chose the following principles: natural balance of volumes, harmonious interaction of shapes and extreme simplicity of lines. These considerations had an immediate consequence: good aerodynamic integration. The first reduced scale model tested in the wind tunnel gave excellent results and nothing has had to be modified subsequently.

EC120 structure is a novelty for EUROCOPTER. Human factors imposed as much space as possible for passenger's luggage and that lead to the split fuel tank concept.
The fuel tanks were divided into two units offering a large cargo space with a rear access thus improving the helicopter's comfort and efficiency for the users.

The wide canopy surrounding the crew is an industrial design decision, which is apparently running against recent developments favoring composite nose cones. However, this choice was based on the need to enhance pilots and passengers visibility, this requirement is particularly well adapted to the missions conducted by such a light helicopter.
It is also with daily usage in mind that industrial design recommended two different cabin openings, with a flap door on the right hand side and a sliding door on the left one to meet every expectation.

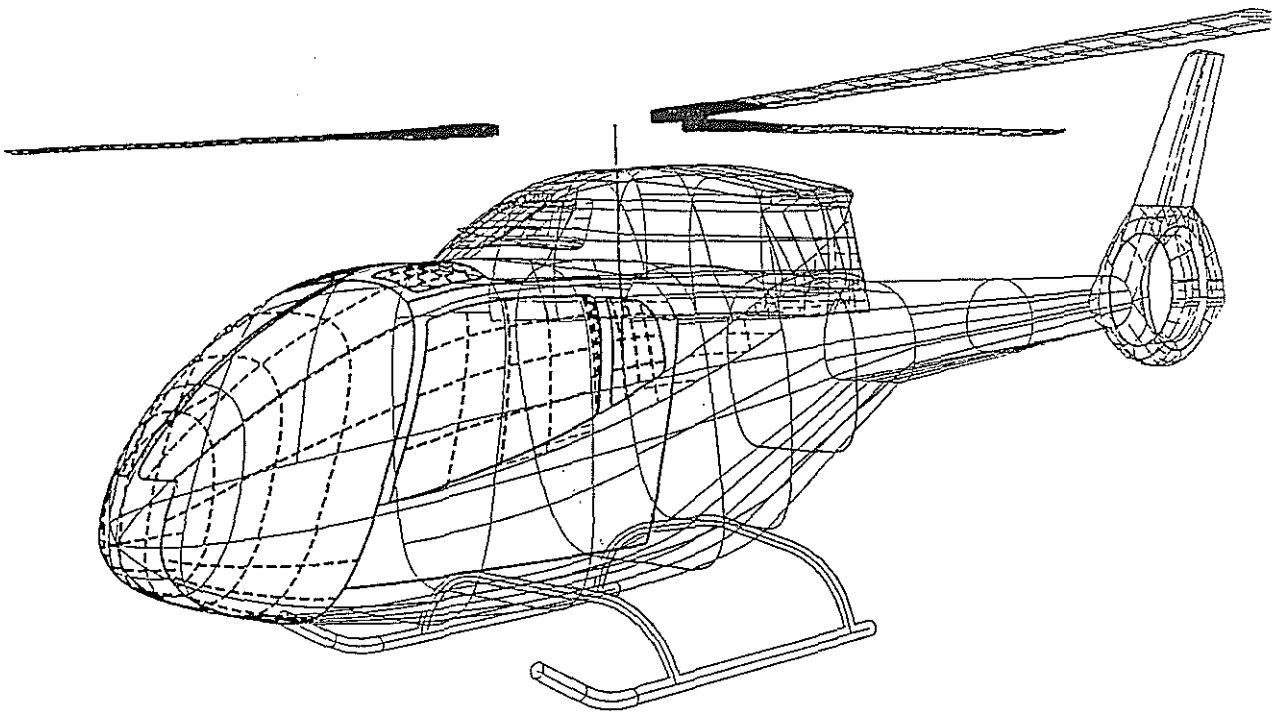

SEATS

The seat is the interface through which the cockpit is adapted to the anthropometric and physiological characteristics of the pilot.

Nowadays pilots count their flying time in thousands of hours and they are more sensitive to the discomfort of their seat, which can cause backache, lumbago, stiff necks and other traumatisms.

The EC120 seat was also drawn to harmonise with the helicopter's soft shapes and everything was done to integrate this seat secondary fonctions. The side bar, for example, is an integral part of the back and its role is to facilitate passengers access to the rear seats. The headrests are also part of the back and they contribute to the aesthetics of the whole. The legs made of mass machined aluminum include attachment points for the future optional items. Even highly technical concepts such as energy absorption with leg deformation were integrated by the designer and these legs, a very novel concept in themselves, were deliberately left as visible structural parts.
The seat bucket is designed to follow the body shapes as closely as possible, in order to optimises crew comfort and preserves the aft passengers' visibility.
These minimal principles naturally helped reduce the seat's cost and weights.

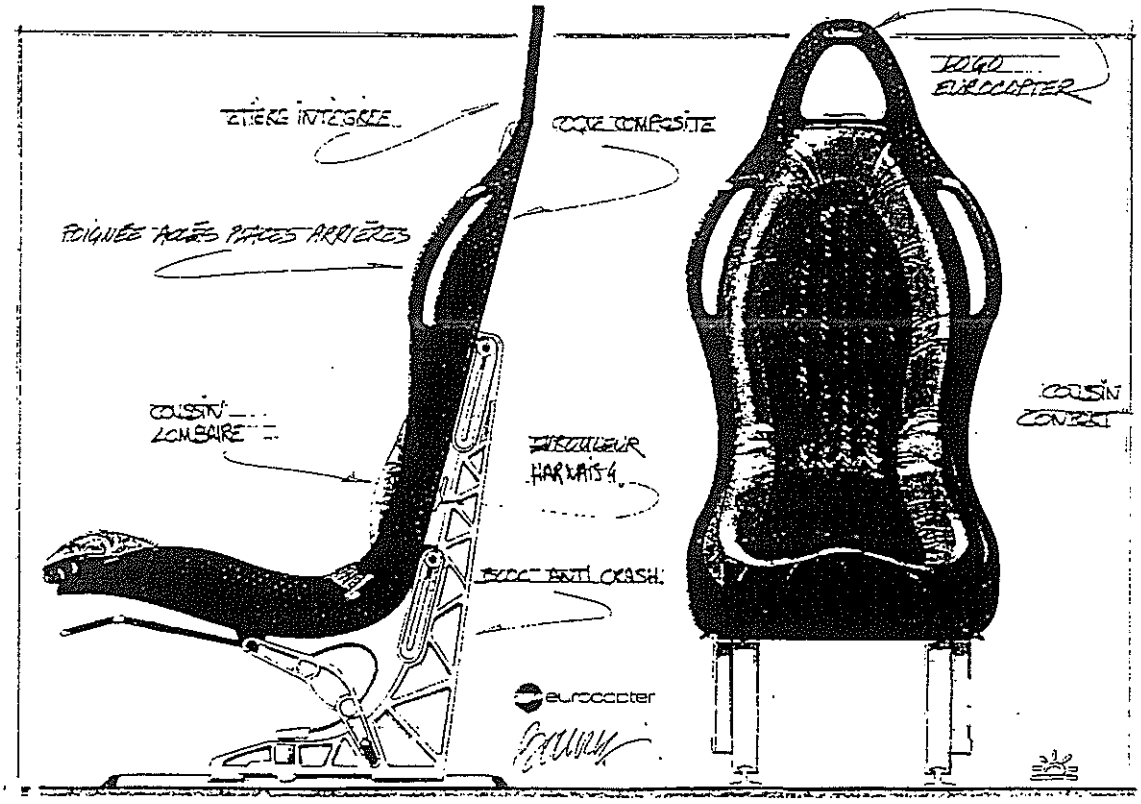

The EC 120 seat must be considered from three essential aspects: immediate environment (including accessibility), comfort of the cockpit and man-machine interface.

A helicopter must be a uniform whole. Skipping over areas that are not considered to be particularly "noble" such as stowage space or handles could be detrimental to a helicopter and cancel out considerable efforts that may have been made elsewhere.

All our actions and aspirations are directed towards finding the happy medium, harmony, and equilibrium. The helicopter is no exception.
The EC 120, and particularly its seat and its accessories must reflect the rigorous thought whose aim is to satisfy all those whose lives are organized in, around, for or are dependent on this helicopter.

POSSIBLE FUTURE EVOLUTIONS:

The design work done on the EC120 is obviously a first step in this field, and the proposals we made can be useful on any other machine.

When we met light-weight helicopter operators, we noted that they were really concerned about the quality of the cabin appearance and that it was absolutely necessary to have a multipurpose cabin.

Both these considerations lead us to the same answer: functional modules fitted into the pilots' seats.

We owe it to our customers to offer them the guarantee that when they buy an helicopter, they will have a pleasant, attractive and functional cabin, whatever types of missions the helicopter will be carrying out.

The differences between the helicopters will only be created by the different FUNCTIONS, hence MODULES that correspond to specific missions.

The interchangeability of functional modules will no doubt be one way of making the tool even more suitable for the requirements.

Let us take as an example the optional intercom system.
At the present time, if a customer wants to fit an intercom system on his helicopter, he must first refer to a specialist in this type of installation, take the helicopter to his facilities and have it grounded for several days. When he collects his helicopter, he will, of course, have paid for the intercom system, plus the installation, plus the transfer, plus the grounding. He will have a costly installation permanently installed but he will only use it for certain specific missions.

Now let's imagine that EUROCOPTER offers an "*Intercom System Module*", which is in fact a compact component that can be installed in just a few seconds on the back of the pilot's or copilot's seat and powered by plugging it in to the center console.

The customer would have the equipment he wanted without having the inconvenience of transferring his helicopter for the installation and the grounding period and he would be able to purchase this equipment directly from EUROCOPTER.

He would be able to install his module only when it was needed, so he would add extra weight to the helicopter only when the FUNCTION was required. Moreover, an operator with several helicopters would only need to buy one intercom system, which he could install on any one of his helicopters at any time.

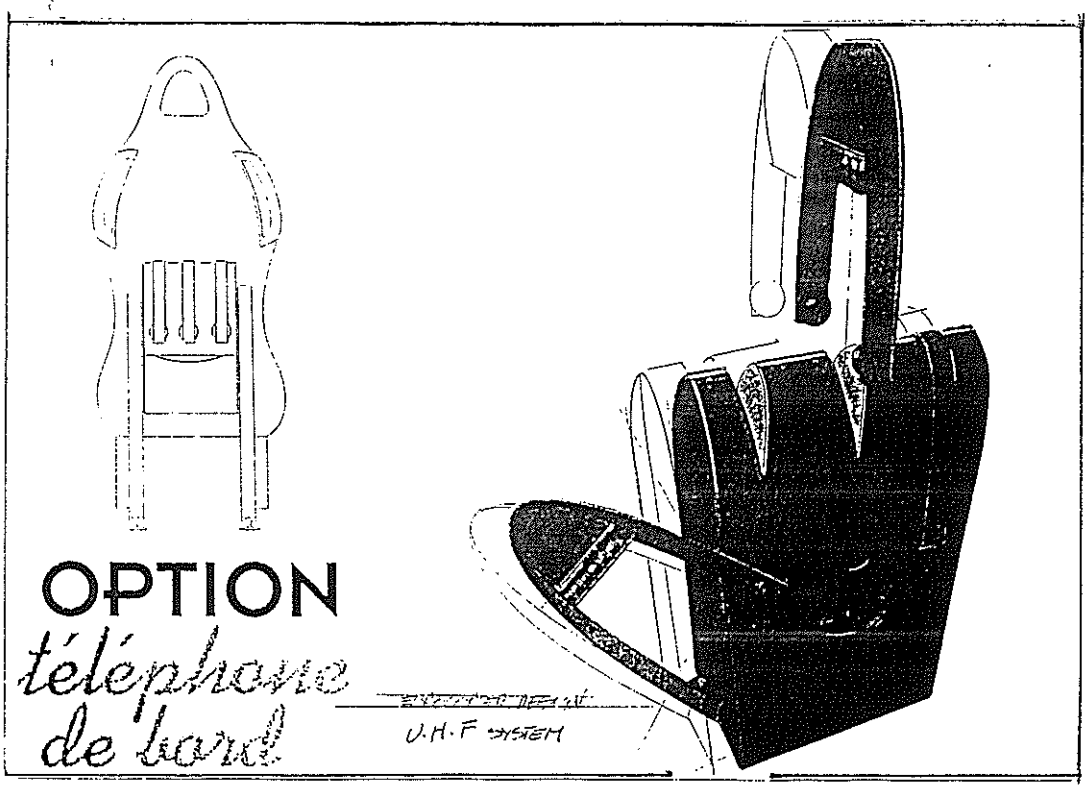

The same could be true for a large number of equipment items such as the Public Transport kit, the radio-telephone or the mini bar, a whole host of optional equipment that the operator could instantly install and remove, thus adapting his helo to the requirements of the moment.

Nowadays we deliver a significant part of light helicopters "green", that is to say with very little or no equipment. This is a problem that concerns the design department directly. It would be very interesting to follow up some of these helicopters that are sold unequipped to find out what happens to them afterwards and why we couldn't provide these aircrafts with a complete equipment.

The interchangeable module could be the answer.

Example of proposals:

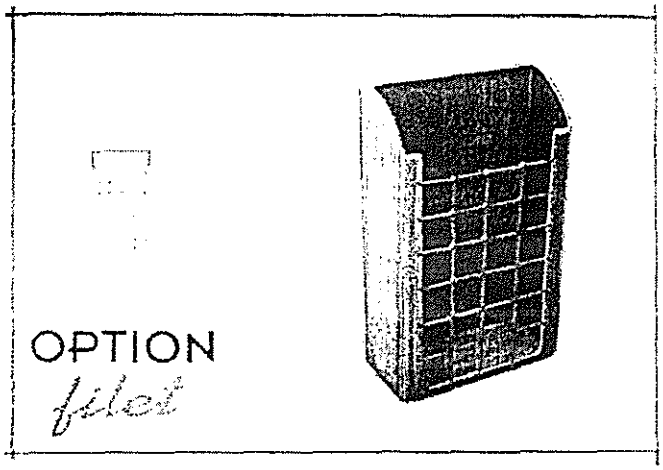

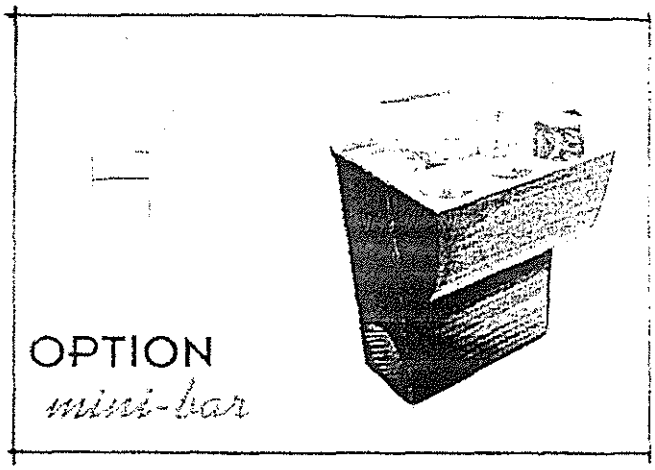

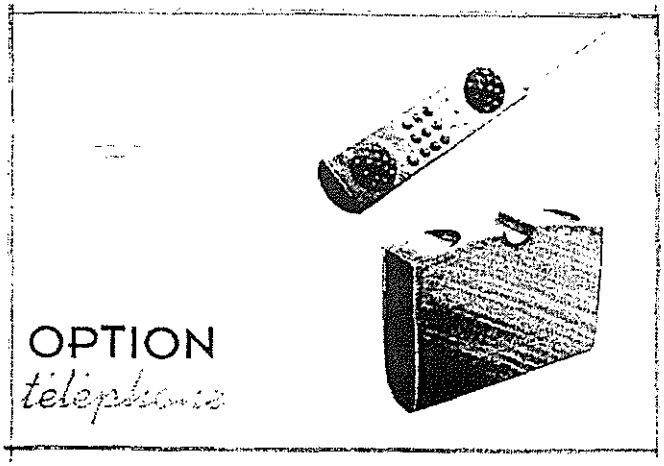

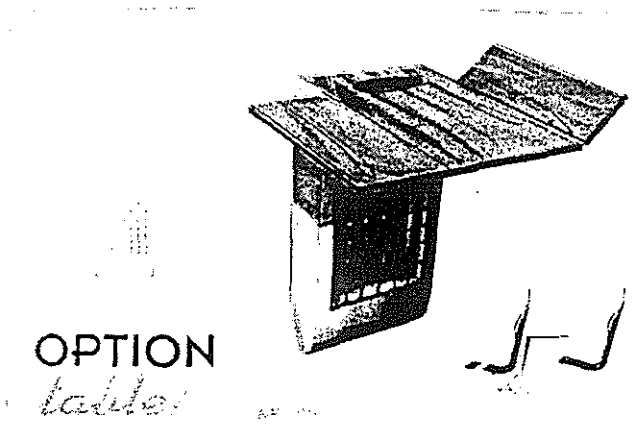

eurocopter
d-e-s-i-g-n

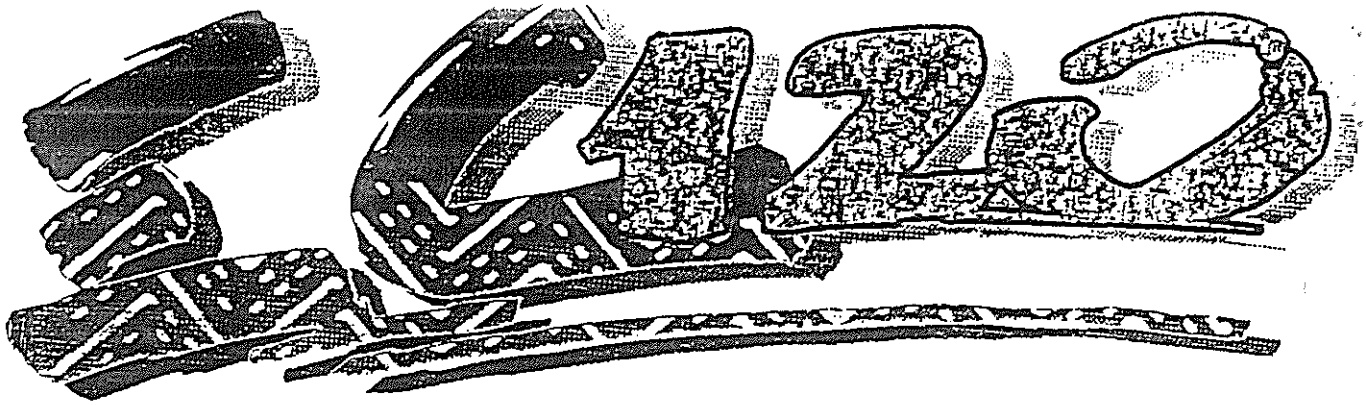

IN CONCLUSION

Technology for technology's sake is not only tremendously expensive, it is also a self-perpetuating quest that puts off what should be done today in the pursuit of what may be possible tomorrow ... or the day after. We now have an opportunity to adapt our ways of working to the changes in our civilization, which, day after day, are redefined around a production process that combines techniques, culture, usage value analysis and sociology of life styles.

Designing a product implies making a multitude of choices and "micro decisions" which give rise to an optimized industrial and commercial reality. The challenge consists in designing helicopters with such choices of compromise that the resulting aircraft prove to be the best solutions for the largest number of **customers**... therefore operators and manufacturers.

The designer refuses all dogma and constantly fights against generally accepted ideas.

The EC120, because of it size and the market it is aiming at, has been a great opportunity to develop new industrial design concepts. This EUROCOPER light single carries some specific thoughts that may open a new era for helicopters at the begining of the millennium to come.

If we are not careful, very rapidly we could find ourselves with two types of helicopters: on one hand, the best machines, those that fly fastest and highest; on the other, those that sell because they are more functional, easier to live with and better suited to the passengers' everyday interests.

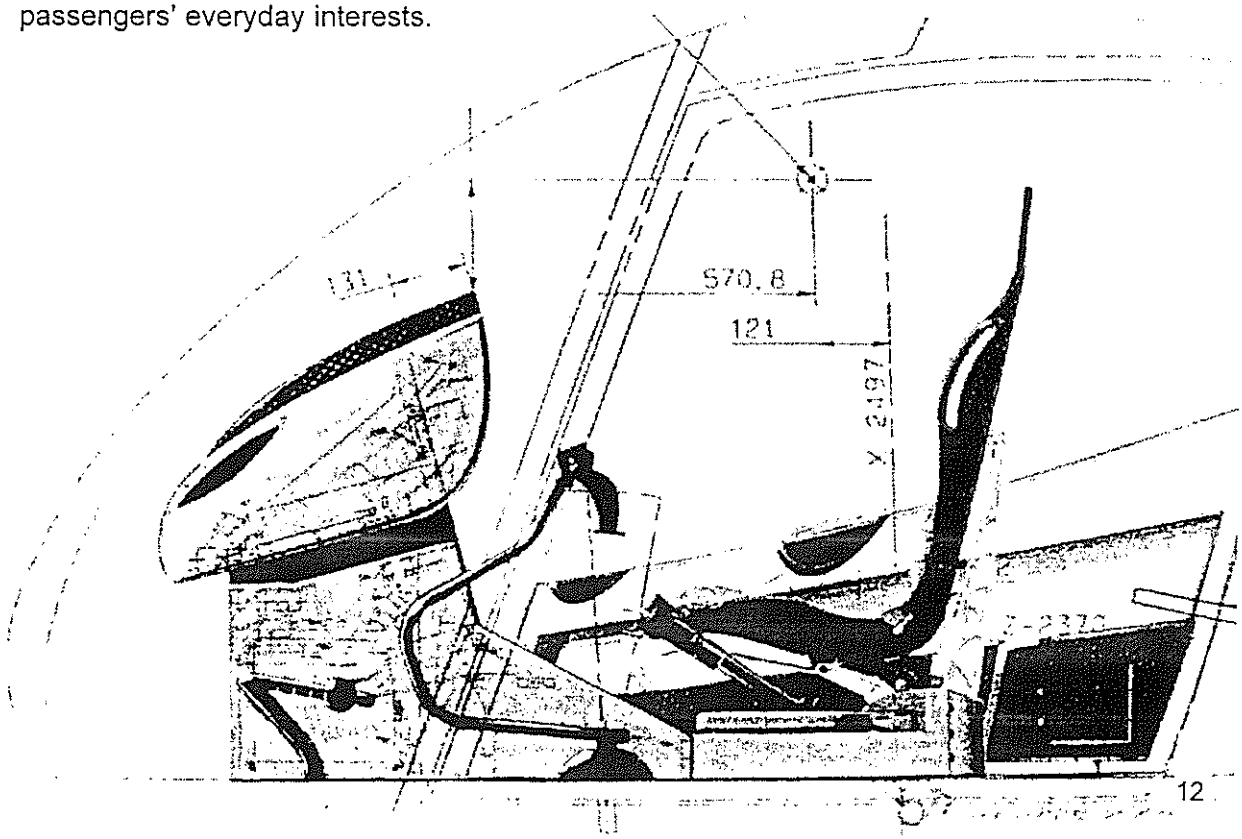

TWENTY FIFTH EUROPEAN ROTORCRAFT FORUM

Paper n° D3

BUILDING THE CONCURRENT ENTERPRISE – THE CE-NET INITIATIVE

BY

ROBERTO SANTORO, ESOCE ITALIA PRESIDENT
MARC PALLOT, ESOCE

SEPTEMBER 14-16, 1999
ROME
ITALY

ASSOCIAZIONE INDUSTRIE PER L'AEROSPAZIO, I SISTEMI E LA DIFESA
ASSOCIAZIONE ITALIANA DI AERONAUTICA ED ASTRONAUTICA

INDEX

INTRODUCTION 3

1 - AREAS FORMING THE CONCURRENT ENTERPRISING DOMAIN 3

1.1 - CONCURRENT ENGINEERING (CE) 3
1.2 - VIRTUAL ENTERPRISE (VE) 3
1.3 - ELECTRONIC COMMERCE (EC) 4

2 - CONCURRENT ENTERPRISE 4

2.1 - DEFINITIONS 4
2.2 - CONCURRENT ORGANISATION - A UNIVERSAL MODEL 4
2.3 - CONCURRENT ENTERPRISE - A SCENARIO 5
2.4 - REQUIRED R&D ACTIONS FOR CONCURRENT ENTERPRISING 6

3 - CE-NET OVERVIEW 6

3.1 - OBJECTIVES AND RESULTS 7
3.1.2 - Long Term Goal *7*
3.1.3 - Objectives of this first phase *8*
3.2 - ORGANISATION AND PROJECT MANAGEMENT 8
3.2.1 - Network organisation *8*
3.2.2 - Network Nodes *9*
3.2.3 - Network Co-ordinator *9*
3.2.4 - Management Structure *10*
3.3 - HOW TO PARTICIPATE 11

APPENDIX A 11

PROFILE OF THE AUTHOR 11

Introduction

The main objective of CE-NET is to provide an infrastructure to support the shaping of the Concurrent Enterprise as being a full scale Concurrent Engineering implementation across partners' organisation boundaries within the Extended/Virtual Enterprise and a combination with Electronic Commerce area for trading models.

CE-NET is characterised by a multisectoral nature, with the involvement of different industrial sectors to promote cross-fertilisation of efforts dedicated to industrial competitiveness, exploiting the opportunities of re-using experiences and technological solutions deriving from different contexts, based on the sharing of general cultural features of the CE working environment. Bilateral confidential Benchmarking and CE Best Practice activities are essential part of the CE-NET operations and nodes interaction, especially between industrial manufacturing oriented nodes.

1 - Areas forming the Concurrent Enterprising domain

The following areas are not considered as a sequential progression but rather as a potential combination for generating a better comprehensive approach, defined as the ultimate type of operating environment, where synergy and complementarity between RTD projects of the areas mentioned below appears more evident and coherent.

1.1 - Concurrent Engineering (CE)

Definition:

"Concurrent Engineering is a systematic approach to the integrated, concurrent design of products and their related processes including manufacturing and support. This approach is intended to cause the developers from the outset to consider all elements of the product life cycle from conception through disposal, including quality, cost schedule and user requirements" [IDA88].

The manufacturing industries will gain enhanced competitiveness through the exploitation of CE technology, including the following benefits:

- Greater productivity and improved quality.
- Flexibility and improved collaboration with partners, suppliers & clients / customers i.e. no IT restriction on the choice of business partners if CE technologies are universal.
- Improved price - performance.
- Greater ability to respond to change.
- Improved Information management tools & enhanced working environment.
- Unlocking potential for growth & generating new business.

1.2 - Virtual Enterprise (VE)

Definition:

"A Virtual Enterprise (VE) is a temporary business organisation set up between trading partners, operating from geographically dispersed sites, for the duration of a common project. A VE is not a joint venture physically collocating the necessary resources on a same geographical site for achieving its business goals but rather a distributed organisation using remote resources. Multidisciplinary team members are electronically collocated and operating together through computer networks such as Intranet or Extranet".

Importance of VE technology to industry can be summarised as follows:

- Capacity of using remote resources
- Pooling of core competencies
- New way of organising operations across dispersed geographical sites, IT-enabled, customer initiated and solution oriented
- Remote collaboration and resource utilisation.

Virtual Enterprise concepts have been widely studied in the **VIVE** (**VI**rtual **V**ertical **E**nterprise) Project which addresses the creation of networks of companies co-operating on specific business opportunities. Further information is available at the URL *http://www.ceconsulting.it/VIVE*

1.3 - Electronic Commerce (EC)

Electronic Commerce is a wide domain from buying goods on the Internet up to business collaboration between trading partners.
The intersection between Virtual Enterprise and Electronic Commerce (Concurrent Enterprise) only concerns inter-enterprises electronic trading of models and collaboration across trading partners. Virtual models placed on the Business Network could be considered as trading knowledge objects.
EC has a deep impact in the business, such as:

- Speed up access to electronic catalogues
- Facilitate and accelerate sales and buying procedures
- Globalise the market
- Provide an opportunity to access the global market when appropriately organised

Concerning inter-enterprises relationships, the use of EDI can lead to

- Accelerates orders to be placed to providers
- Help to reduce stock
- Contribute to reduce cost to buy

2 - Concurrent Enterprise

Applying Concurrent Engineering and Electronic Commerce in the context of inter-enterprises business collaboration within the Virtual Enterprise is named Concurrent Enterprising. See the definition below for Concurrent Enterprise.

2.1 - Definitions

Concurrent Enterprise:
"A concurrent enterprise is a boundarylessness organisation operating concurrently with the market, trading partners, and users in a reactive and flexible way for improving creativity aptitude and innovation potential to meet the ever changing market demand". (M.Pallot, V. Sandoval, 98)
Concurrent Enterprises are able to trade product models on a Business Network.

Engineering:
Engineering is a discipline aiming at defining the way of developing a product.

Enterprising:
Enterprising is a discipline aiming at defining the way of doing business with trading partners.

2.2 - Concurrent Organisation - a universal model

"Enterprises are made of people whose individuality has a piece of the necessary knowledge, and altogether they constitute a new entity that is not only a juxtaposition of knowledge pieces but much more a puzzle where the symbiosis process helps to have pieces at the right place like a kind of sum.
A concurrent organisation is characterised by a system having a main conducting flow or stream where all existing entities belonging to that system are contributing to this flow in a complementary harmonised way (symbiosis).
An enterprise should be organised around a specific flow. This is a knowledge flow, which starts by needing understanding and then continues by creating ideas that are transformed into solutions

satisfying the needs. Concurrent organisations are multidimensional where different systems can contribute to another one, from infinitely small toward infinitely large or vice-versa. To understand how a concurrent organisation operates it is necessary to know interdependencies between its constituting entities. Here it might be helpful to explain to decision makers, such as politicians, and managers, that before undertaking any decision, they should try to simulate its impact in running a model made of interdependencies just to check whether it will be consistent or not." (M. Pallot, V. Sandoval, 98)

"A concurrent enterprise operates concurrently with the market, trading partners and users. To build a concurrent enterprise we need the concurrent engineering as normal engineering practices and the advanced know-how in virtual enterprise building, application and management. This new type of enterprise encompasses the electronic commerce Era. So every company must do any effort to adopt the new approach following a concurrent enterprising process, that means the process enabling the building of this kind of enterprise. Nevertheless, there are many factors, constraints and problems that need to be overcome before to set up concurrent enterprises.

First of all, the lack of adequate infrastructures in a wider sense. Within this context, one important point concerns concurrent systems technologies and tools for the sharing and interactive use of remote resources and concurrent activities in geographically dispersed locations, in the context of heterogeneous hardware and software architectures and systems. This point is a fundamental one to allow the concurrent enterprising process. Other points are interoperability and interworking particularly at the network management and service levels, to increase capacity, flexibility, reactivity and functionality and to promote the introduction of new services (including the evolution of the Internet) ; technologies for network integration (fixed and mobile, including satellite links) and new service independent architectures and systems, to ensure all users will have affordable access to broadband multimedia services; basic technologies and tools supporting real-time embedded systems applications and services." (M. Pallot, V. Sandoval, 98)

2.3 - Concurrent Enterprise - a scenario

The following is a description of a potential scenario for Concurrent Enterprises developing new products. Concurrent Enterprises are trading models on a business network constituted of potential providers.

Enterprises send information about their future or available models on the market that could be used in a business project (a kind of electronic catalogue) to a business network When a participant of the business network place a call for models (specific call for proposals), through its Virtual Buying Office, it automatically filters answering models that could be appropriate to the request. When there are several answers for designing a future model, an assessment of capabilities for operating in this virtual environment could help to select the most appropriate provider. Otherwise, parts of the models could be used by the Virtual Design Office for simulating its appropriateness within the targeted product or processes.

As soon as models are selected and contracts established, the real product and processes development starts in identifying the necessary interactions between trading partners. A Virtual Interaction Room support electronic collocation of people where constraints could be demonstrated in order to undertake the best decision for the product and processes architecture. In case of conflicting situation, a Virtual Negotiation Room provides the necessary tools for demonstrating any potential solution to the appropriate experts of trading partners. Finally, a Virtual Project Office facilitates the management and administration of the project across trading partners.

Concurrent Enterprising constitutes a strong opportunity for developing new telecom technologies, applications and services such as Telepresence or Telecooperation (P.Pulli, T. Pyssysalo, K.Kuutti, J.Similä, J.P. Metsävainio, O.Komulainen)

2.4 - Required R&D actions for Concurrent Enterprising

A life-cycle thinking of knowledge should be the basic framework behind the thematic network, i.e. the development stages: research, development work, dissemination and exploitation including deployment. From a planning viewpoint this is in line with a top-down identification of visions and needs, and a bottom-up initiation of projects/activities in the different phases of the life-cycle of concurrent enterprise knowledge – visions and short term as well as long term actions have to be integrated and attuned. Therefore, this is an iterative continuos improvement or learning process open for refinements and a corresponding initiation of new or modified initiatives to fulfil the goal of realising the concurrent enterprising concept.
The life-cycle approach can be illustrated in the following way.

Research:	**Development:**	**Deployment:**
Create visions	Define specific application areas based on basic research	Collect and categorise existing knowledge
Defining research purposes/areas	Define thematic oriented technology projects	Develop dissemination, exploitation and deployment channels and methods
Proof of Concepts projects	Develop technologies	Develop training programs
Development and elaboration of basic concepts	Examine organisational preconditions	Broadcast training programs
Thematic scope and framework description	Forecast and evaluate societal consequences	Find best practice and related technologies

3 - CE-NET Overview

It is widely accepted that for the effective advancement of the integrated product development environment within the overall context of concurrent enterprise there is a clear need for different organisations to continuously communicate with each other in order to exchange and share the latest developments/information. However, currently there is a lack of coherent infrastructure or mechanisms for the effective and constant cross-fertilisation of the research effort undertaken by various bodies whether they are in industry, academia or software vendors. Many of these organisations and institutes are involved in a range of concurrent engineering related projects both at European and National level.
Due to the lack of effective co-ordination of these developments one is not able to fully exploit the potential benefits from the output of the RTD efforts currently in progress Thus, the prime aim of the Concurrent Engineering Network of Excellence (CE-NET) is to establish a well co-ordinated and effective support infrastructure throughout Europe in order to share and exchange the latest developments in the concurrent enterprise domain.
However, specific objectives are:

- To provide the means for effective communication of tool and techniques available for the implementation of CE
- To integrate better the work undertaken in different national and European RTD projects
- To provide means for better cross-fertilisation of CE practices across different industrial sectors
- To raise level of awareness of potential benefits accruable by applying CE approaches
- To develop and provide means for better exploiting the results of RTD projects

These will be achieved by undertaking the following activities:

- Collect information about the existing industrial experimentation on CE implementation, CE studies events and reports for further utilisation and to avoid overlapping

- Cross-fertilisation by increasing awareness of CE concepts, approaches, technologies, implementation practices and their impact
- Provide concepts and guidelines to implement and apply CE between trading partners in a concurrent enterprise especially within the SMEs

The CE-NET consortium consists of some 26 organisations representing 12 countries. All members of the consortium, except ESoCE, will be involved as Associate partners. Each member of the network is positioned according to its specific skills in order to contribute to and to reap the benefits from the network most effectively. ESoCE will be the co-ordinator for the network.

EsoCE is an independent technical and non-profit society. Its mission is to promote the adoption and application of CE approach in industry and SME environment.
It has a networked structure, gathering similar organisations from all the European countries
Main objectives of ESoCE are:

- Improve and spread knowledge on CE point of view
- National and international exchange on information regarding CE initiatives
- Promote the participation of Industry to CE projects

3.1 - Objectives and Results

The CE-NET partners, large industrial companies such as Daimler-Benz Aerospace, Nokia, Odense Steel Shipyard, Signaal, Taylor Woodrow, and Thomson-CSF, are recognised as major players in the domain of CE implementation as well as SME's organisations such as Adepa, ATM, BCM, CCC, FIMET and InfoCom. Furthermore, academia is also very well represented by active research institutes in different fields related to CE such as Ecole Centrale Paris, Ladseb-CNR, PAKT, SISU, Tampere University of Technology, University of Bremen, University of Nottingham, University of Twente and VTT. So far, CE-NET partners are involved in a lot of initiatives and RTD projects related to CE.
Otherwise, there are a lot more organisations (large industrial companies, SMEs and research institutes) involved in CE related initiatives and projects as well as simply interested by the implementation of CE that represents a good potential to rapidly increase the number of participants to the network.

3.1.2 - Long Term Goal

Today, around the globe, there is an increasing pressure from the market forces to design and develop products with an increasing level of in-built complexity in the shortest possible time within a multi-company collaboration framework (providers often represent a large part of project success).
The complexity includes: the product itself: references, functionalities, security, technology, materials, integration, processes etc.

The global market and business environment requires European industry to increase its competitiveness and its ability to:

- manage multinational consumers, suppliers and corporate sites;
- establishing profitable consortia to cope with requirements and feature of large multinational programmes.

This increasing level of complexity can be best managed through the provision of an adequate integrated product/processes development environment which allows each individual participating company to concentrate to its core expertise and so contributing the global solution. The new shared

business process will be the heart of the Concurrent Enterprise through the full scale CE implementation within an Extended/Virtual Enterprise.
The main long term goal is to support the creation and functioning of the Concurrent Enterprise through the following three different phases:
1. Awareness and Foundation : define the concepts and processes for the Concurrent Enterprise.
2. Development and experimentation elaborate the functions of the Concurrent Enterprise, experiments IT solutions, specify the needs & requirements, and develop necessary technology in deploying R&D projects collaboration between nodes.
3. Training/education and technology transfer: identifying training and education requirements, and elaborate related programme and technology transfer activities.

3.1.3 - Objectives of this first phase

The prime aim of the CE-NET IS to establish a well co-ordinated and effective support infrastructure throughout Europe in order to share and exchange the latest developments in the broadest scope of CE implementation. Nowadays, the ultimate level of CE implementation IS represented by the Concurrent Enterprise paradigm (which is the implementation of CE within the Extended/Virtual Enterprise) that is often called Collaborative Engineering in US.

The overall duration of this phase is 18 months, and the allocated budget is 392 KEURO. The main tasks are:

- Build up a CE information database
- Develop and edit a CE newsletter
- Organise CE events: Conferences & workshops
- Build up a CE tools & techniques database
- Best CE practices and benchmarking

3.2 - Organisation and Project Management

3.2.1 - Network organisation

The CE Network is composed of Nodes and a Network Co-ordinator and has a Management Board and a Technical Committee. Nodes are also members of external organisations such as industry sectoral associations, research networks, SME's associations, working groups, user's groups and related initiatives. All those connections will be used as channels of dissemination and for collecting user's needs and market trends as well as the newest technology (see figure 3.1).

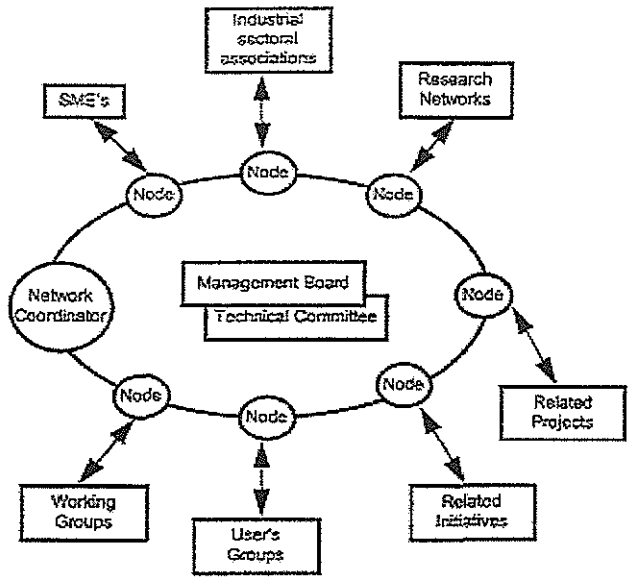

Figure 3.1 - The CE Network

3.2.2 - Network Nodes

Members of the network form nodes which can be a corporation or a part of it like a corporate's research centre, an independent research centre, an industrial company, an university or an industrial association. A national node can also be a co-operative group of these.

Each node will carry out the following tasks:

- To follow and collect information about its own, national, and regional R&D projects and activities on CE.
- To set up an Internet Server, based on CE-NET 's common taxonomy to disseminate information
- To measure, how effectively the information distributed by the node is exploited by potential users
- To identify needs and technologies for coming research projects and themes for workshops organised by the Network.
- To report its experiences to the Network

3.2.3 - Network Co-ordinator

The Network Co-ordinator (NC) is globally responsible for the overall administration of the network and act as the Network Secretary in the Management Board (MB).

The Network secretary (Network Co-ordinator) will be nominated by the MB and will have the responsibility to:

- Co-ordinate the overall contractual, financial and administrative aspects, including the reporting of the Network financial and budgetary status to the MB.
- Collect and submit to the CEC of cost statements for the project
- Draft the quality plan of the project
- Found and maintain the project archive

- Co-ordinate communication between the consortium and the European Commission or any external organisations
- To organise meetings of the Management Board and Technical Committee
- To support nodes arranging conferences or workshops
- To co-ordinate events and work between the nodes

The Network Secretary (Network Co-ordinator) will prepare the MB meetings that will be synchronised, when possible, with the TC meetings and Network events (conference and/or workshops) in order to have more efficient co-ordination and to reduce the travelling costs.

3.2.4 - Management Structure

The management of the Concurrent Engineering Network of Excellence (CE-NET) will be organised on two levels:

1. Network management level will be carried out by the Management Board (MB).
2. Technical management level will be carried out by the Technical Committee (TC).

In order to reduce the management overhead, the same representative of a project member may fill several positions in the management organisation.

Management Board

The MB will have the responsibility for the financial, administrative and exploitation aspects of the Network and will supervise the technical decisions. The MB will be chaired by an elected chairman who will act as chairman of the Network, seconded by a vice-chairman and they will be assisted by the Network secretary (filled by the Network Co-ordinator).

The MB will in particular:

- Decide the overall strategy for conducting the Network
- Review the progress of the project according to the strategy
- Review the policy and strategy for exploitation and publicity, authorise external presentation in meetings according to the information sensitivity classification level
- Assess any change to the procedures and contracts
- Elect the chairman and the vice-chairman of the Network and approve the nomination of the Network secretary
- To review the Network expansion policy
- To oversee the administration carried out by the Network Co-ordinator
- To accept new members and nodes
- To approve the actions plan

Technical Committee (TC)

The TC will have the responsibility of the technical decisions. The TC will be leaded by the Network Co-ordinator. It will be composed of the technical representatives of the project members.

The TC will in particular:

- Decide the technical directions according to the strategy defined by the MB.
- Assess the progress of the project, commission the corrective actions if necessary and authorise appropriate amendments to the work plan according to the recommendations of WP leaders in order to meet the project objectives.
- Approve the Quality Plan submitted by the Network Co-ordinator.
- Assess any change to the work programme and any technical recommendations to the MB.

- To define the action plans according to the long term strategies.
- To develop the information infrastructure (Internet CE-NET Web server).
- To define and update the Network common taxonomy for the CE reference database.
- To prepare the Conference and workshops themes.
- To review the working groups reports.
- To prepare recommendations and future directions.
- To assess the project proposals for the second phase.

The TC will normally meet three times during the first phase in a synchronised way with the MB meetings. The Network Co-ordinator will prepare the TC meetings that will be synchronised, when possible, with the MB meetings and Network events (conference and/or workshops) in order to have more efficient co-ordination and to reduce the travelling costs.

3.3 - How to participate

To join CE-NET a web site is available at the following URL

http://esoce.pl.ecp.fr/ce-net/

It is possible to take part to ESoCE initiatives. Further information available at

http://www.ceconsulting.it/ESOCE/default.html

APPENDIX A

Profile of the Author

Roberto SANTORO, CE Consulting-Italy

Mr. Santoro is directly involved in the development and dissemination of Electronic Commerce and Concurrent Engineering methodologies for adoption by European Industry, and has been acting for several years as expert reviewer of EU financed RTD projects within the ESPRIT programme. He is the promoter and co-ordinator of the European Society of Concurrent Engineering in Italy and the representative of Italian Confederation of Industrial Employers in the UNICE (Union of European Industrial Employers) CALS/Electronic Commerce Group.
Mr. Santoro is managing director of CE Consulting, an engineering service Company devoted to the development of advanced engineering methods and of the associated Information Systems, enabling integrated product development.
Mr. Santoro is providing business and technical leadership to a number of innovative European projects for which CE Consulting is the co-ordinating partner. Major examples include: VIVE (Virtual Vertical Enterprise), which addresses the constitution and operation of Virtual Enterprises specially devoted to Small and Medium Enterprises (SMEs) for the general market and in particular for responding to the new supply infrastructure requirements by Large Enterprise; CEPRA (Concurrent Engineering in Practice), which provides best practice tools and techniques to SME in the Aeronautics sector for adopting Concurrent Engineering.
Mr. Santoro is participating to the ESPRIT Project WeCAN (Wide Electronic Commerce Awareness Network of Excellence) dealing with awareness issues for the adoption of Electonic

Commerce by Small and Medium Enterprises. WeCAN supports Organizers of awareness activities by providing Best practice examples and case studies.

Mr. Santoro has been earlier leading, within the Datamat Group, the development of advanced Information Technology Systems and Engineering Services for the Industrial Sector.

Until 1988 Mr. Santoro has dedicated his professional activity to the design, licensing and operation of Nuclear Power Plants. As Managing Director of NUTECH European Operations since 1982, he provided management and technical direction to a variety of engineering projects for the European Nuclear Industry, requiring the integration of multiple engineering disciplines.

Born 1952 in Bari, Italy. Doctor in Mechanical Engineering, University of Genoa, Italy - 1976. Highest grade with Honours.

Contact information:

Roberto Santoro
CE Consulting Managing Director
Piazza Ungheria, 6
00198 Rome – Italy
Phone: +39.0684405713
Fax: +39.0684405721
Email: rsantoro@iol.it
URL http://www.ceconsulting.it

TWENTYFIFTH EUROPEAN ROTORCRAFT FORUM

Paper n° D5

ACT/FHS FOR THE NEXT GENERATION TECHNOLOGIES EVALUATION AND DEMONSTRATION

BY

HEINZ-JÜRGEN PAUSDER, DLR, INSTITUT FÜR FLUGMECHANIK, GERMANY
ULRICH BUTTER, EUROCOPTER DEUTSCHLAND, GERMANY
FRANK STEINMAIER, LIEBHERR AEROSPACE, GERMANY

SEPTEMBER 14-16, 1999
R O M E
ITALY

ASSOCIAZIONE INDUSTRIE PER L'AEROSPAZIO, I SISTEMI E LA DIFESA
ASSOCIAZIONE ITALIANA DI AERONAUTICA ED ASTRONAUTICA

ACT/FHS for the Next Generation Technologies Evaluation and Demonstration

Heinz-Jürgen Pausder, DLR, Institut für Flugmechanik, Braunschweig, Germany
Ulrich Butter, Eurocopter Deutschland GmbH, München, Germany
Frank Steinmaier, Liebherr Aerospace GmbH, Lindenberg, Germany

Abstract

An advanced flight research helicopter, the Active Control Technology Demonstrator and Flying Helicopter Simulator (ACT / FHS) is being developed by DLR (Deutsches Zentrum für Luft- und Raumfahrt) and industry (Eurocopter Deutschland and Liebherr Aerospace). The development program is commonly funded by the German Ministry of Defense, the DLR and the industry partners. Using an EC 135 helicopter as a baseline vehicle, the ACT/FHS is designed as a flying laboratory capable to be used as a flying simulator and to support the research and development requirements of major programs of DLR, industry, and test centers. These programs will focus on the technology concepts for extended operational flight envelopes of the future helicopters, the man vehicle interface and cockpit technologies, and the safety concepts for digital control system design. The ACT/FHS system architecture reflects the envisaged broad application range. The hierarchically structured system includes a reliable quadruplex 1:1 fly-by-light control system with smart actuators and a modular experimental system which will be realized as a simplex system but can be extended into a redundant system. The test bed will be flown by a safety pilot from the left hand seat and an evaluation pilot from the right hand seat. The modular experimental system provides the evaluation pilot with the capabilities needed for in-flight simulation and for demonstration of digital control, sensor, display, and cockpit technologies. The development of the ACT / FHS was started in 1995. The first flight is scheduled for 2000 and first application programs are planned in 2001 after achieving the test certification. The development approach, the status, and selected features of the scheduled application programs are described.

1. Introduction

Over the last decades, piloted simulators and demonstrators have emerged as recognized and widely accepted tools to support the research and development approach for future control and cockpit technologies. In the preamble to the proceedings of an international symposium on "In-Flight Simulation for the 90's" (Ref. 1) the following evaluation of flying simulation and its incorporation into the overall design process has been expressed:

> "Within the aerospace community flight simulation has become virtually synonymous with the reproduction of the cockpit flight environment in a ground-based flight simulation facility. As this discipline has matured and assimilated the advanced in digital processor and electronic imaging technologies, ground-based flight simulation has found its legitimate domain of pilot-in-the-loop investigations both as research and development and as a training aid. Nevertheless ground-based flight simulation does have limitations related to incomplete – and sometimes conflicting – nature of visual and motion cues which are presented to the evaluation pilot.
>
> In-Flight Simulators and Variable Stability Aircraft have played an unique role in aerospace research, development and for test training by providing the proper environment and immersing the pilot in a real flight situation."

In the fixed wing aircraft industry and research, the value of piloted flight demonstration and flying simulation has been exploited more extensively compared to the rotorcraft community. For helicopters, flying test beds become increasingly important as fly-by-wire/light control systems are considered within the overall design and as autonomous systems are integrated to support the pilot and the crew and to reduce the extensive workload within delicate and critical flight phases. Indeed, the crew station design undergoes fundamental changes with the availability of advanced cockpit technologies.

In (Ref. 2), Huber and Hamel overviewed the status and the future directions for helicopter flight control design including the ground based and airborne simulation facilities. Extensive experience with the development and the operation of flying helicopter simulators and demonstrators have particularly been made in the United States, in Canada, in Germany, and also in France.

The major forces impacting on the a/c overall system design can be classified as external or internal factors to the design process. Primary external factors are the mission and mission environment. The next generation of helicopters, both civil and military, will have to meet extended operational requirements including operation close to the ground with high agility and high precision maneuvers, in extremely bad visual environment at night and in adverse weather, and over unknown terrain and obstacles. In addition, the flight safety must be guaranteed and the operational and development costs have to be reduced.

The operational demands dictate the functional requirements which can be allocated to the human element (pilot) capabilities, the vehicle (baseline helicopter) characteristics, and the integrated system elements. Figure 1 sketches these internal elements and the areas of interfaces. The design of a well balanced integrated system has to consider the limitations of the baseline helicopter, the probability of degradation due to failures of integrated systems, and the workload of the pilots. Indeed, it is necessary to use the full capabilities offered by the technologies for active control, digital cockpit equipment, and intelligent sensors which support the pilot to improve the performance in current missions and to accomplish new complex missions. To meet the operational demands for future rotorcraft, advanced guidance systems, high authority and high bandwidth control systems, active controllers, and sensor systems combined with enhanced visual information for the pilot's tasks have to be integrated. Much of the work is needed to develop practical pilot-vehicle systems that allow to make full use of the adaptive human pilot without exceeding his capabilities. With modern technologies it will be possible to partly or fully transfer pilot tasks to automatic intelligent systems such as guidance and control of the aircraft, navigation, system monitoring, and mission planning. With the digital systems taking major steps forward, helicopters become highly complex and there may be concerns that development time, technological risks, and costs will be increased.

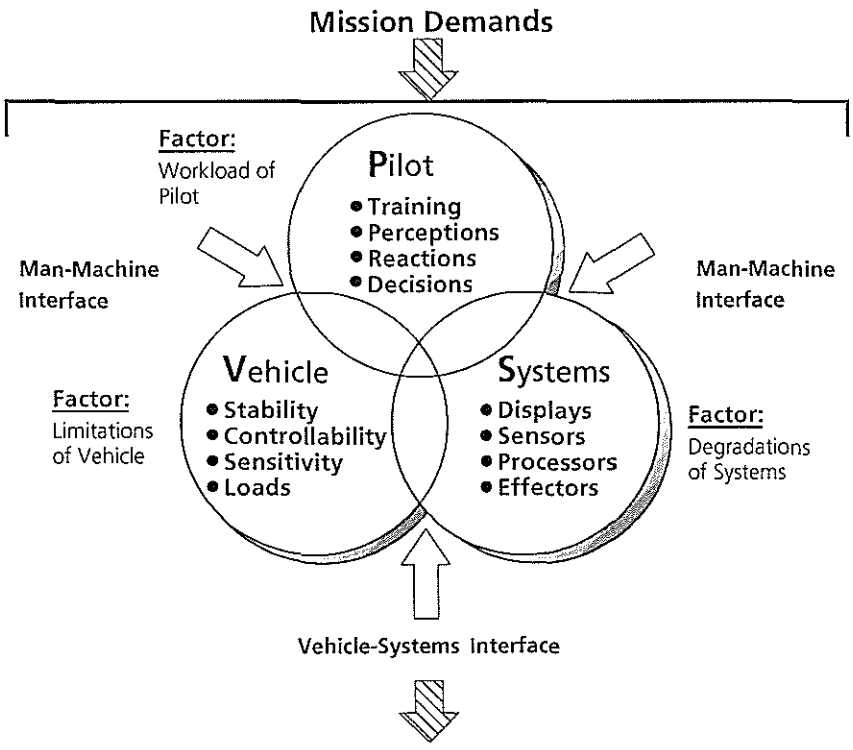

Figure 1:
Integrated System Aspects

For the effective realization of the envisaged benefits from these technologies, the use of flying simulators / demonstrators is required. Recognizing the demands for a flying test bed, the program for the development of the Active Control Technology Demonstrator / Flying Helicopter Simulator (ACT / FHS) was launched (Ref. 3).

2. Background and Project Objective

DLR's Institute of Flight Mechanics has gained international reputation in the field of in-flight simulation, covering the methodology and the simulator flight vehicle development and operation (Ref. 4). The fixed wing test bed ATTAS, based on the VFW 614 aircraft, has been used successfully as a flying simulator since 1986. Until 1995, DLR has operated the in-flight simulator ATTHeS (Advanced Technology Testing Helicopter Simulator) which was based on a BO 105 helicopter (Ref. 5). ATTHeS was equipped with a full authority, but non-redundant digital flight control system. Applications of the airborne test facility covered a wide variety of pilot-vehicle topics like handling qualities research, test pilot training, helicopter simulation in flight, control system design, and active controller evaluation. ATTHeS was used in research and industry programs, many of them performed within international cooperations. A summary of the application programs is given in the statistics of Figure 2.

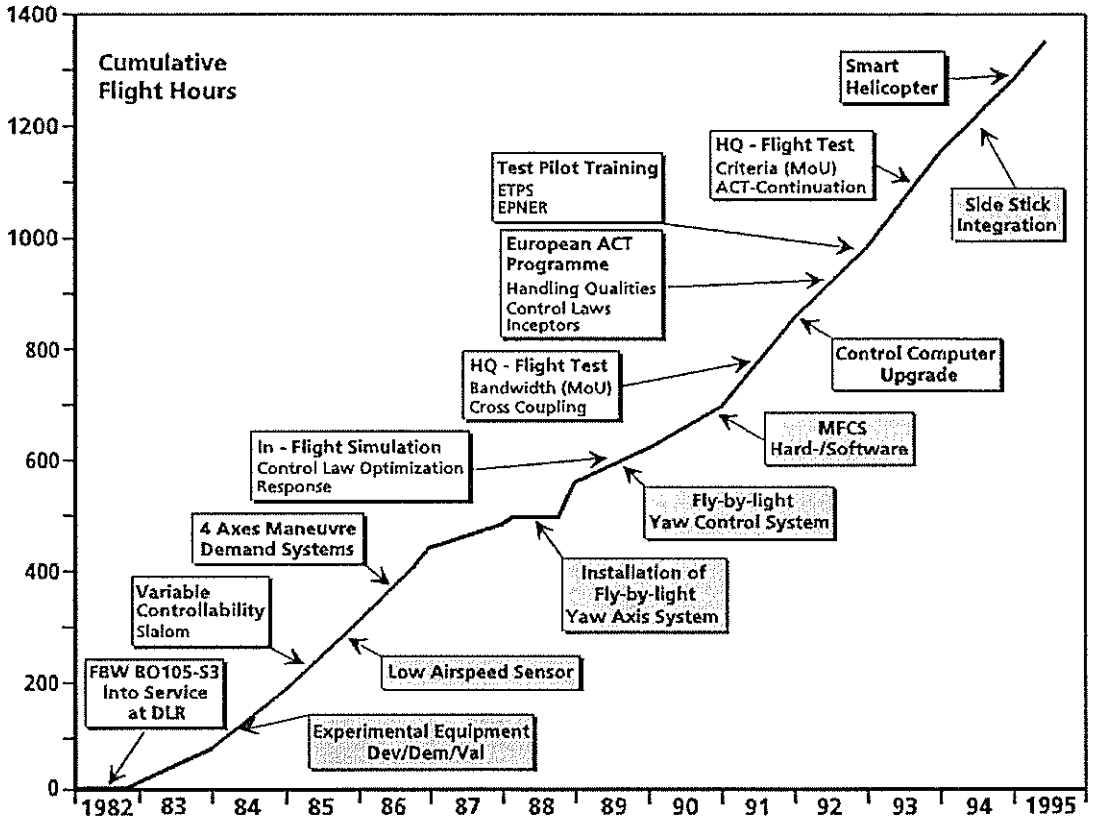

Figure 2: ATTHeS Flight Test Statistics

In 1995, the German Ministry of Defense, German helicopter industry and DLR has launched the program for the development of an advanced flying simulator called Active Control Technology Demonstrator / Flying Helicopter Simulator (ACT / FHS).

The overall objective of the ACT / FHS project is the development of an airborne test bed which will meet the various application requirements from industry, DLR, and official test centers. The use of the ACT / FHS will concentrate on the investigation and assessment of the technical feasibility and operational benefit of key technologies for future helicopter systems and the establishment of the design criteria for the integrated systems. The major applications, as specified by the main users, are:

- In-flight simulation;
- System development and integration;
- Technology demonstration.

The ACT/FHS in-flight simulation capability will be used to support the development of advanced systems and to adapt them to the pilot and the baseline helicopter. A primary objective of an ACT/FHS simulator will be the simulation of the dynamics of future helicopters with high fidelity and the evaluation of the performance and flying qualities of future helicopter designs to establish a basis for the specification and certification of tomorrows technologies.

The field of system development and integration requests specific capabilities and provisions for the integration of new active control and intelligent crew station functions. New concepts, including high authority control systems, active controllers, advanced display systems and modes, vision enhancement concepts, and mission packages have to be validated in flight as integrated part of the complete system and with specific emphasis on an improved mission effectiveness and on an optimized interface to the human pilot.

The third area of application of the ACT/FHS will be the demonstration of the functionality with respect to the operational benefits of new technologies. The technology demonstration shall be possible up to the certification tests for the new technology systems.

The specified different areas of use require the ability to integrate in ACT/FHS and evaluate hardware and software systems with various safety standards depending on whether experimental or operational equipment shall be tested. In-flight simulation and system development need an adequate flexibility to allow configuration changes, hardware and software modifications, and system upgrades. Systems and software have to be tested, which did not go through a safety examination in any detail. A slight reduction of the flight envelope can be accepted for these tests. The flight demonstration of technologies has to be performed in the full envelope. For the evaluation of the operational benefits and a pre-certification assessment, an operational standard with a proof of the failure probability of the integrated hardware and software must be provided.

An additionally indispensable fact for the accomplishment of the two-edged demands on safety and flexibility for modifications is that the test helicopter will be flown by a two-man crew. A safety pilot on the left hand seat is the pilot in command. The right hand seat is equipped for the evaluation pilot. Both pilots have access to the basic flight control in the ACT/FHS. When the evaluation pilot is flying, the experiment configuration mode can be switched on. However, access priority to control the helicopter is assigned to the safety pilot who can take over the control from the evaluation pilot at any time.

Application	Standards	Criticality Level	Safety Requirements	Failure Characteristics
In-Flight Simulation / System Development	Experimental Standard	Non Essential	Safety Pilot Reduced Flight Envelope	Fail-Safe
System Development / Technology Demonstration	Development Standard	Essential	Safety Pilot Full Envelope	Fail-Operate Fail-Safe
Technology Demonstration	Operational Standard	Critical	No Back-Up Full Envelope	(Fail-Operate)[n] Fail-Safe

Figure 3: Required System Standards

With these concept features, it will be possible to test non-redundant, non-qualified experimental equipment with non-validated software (experimental standard), partly redundant equipment (development standard), or fully redundant, highly reliable equipment (operational standard) (Figure 3).

3. Baseline Helicopter

As a result of an assessment using technical evaluations and the operational costs the EC 135 helicopter was selected to be the appropriate vehicle as a baseline for the in-flight simulation facility (Figure 4). For the selection of the aircraft, a representative test configuration was defined:

- 250 to 500 kg of payload
- 3 men crew (2 pilots, 1 flight test engineer)
- Fuel for 2 flight hours with maximum continuous power

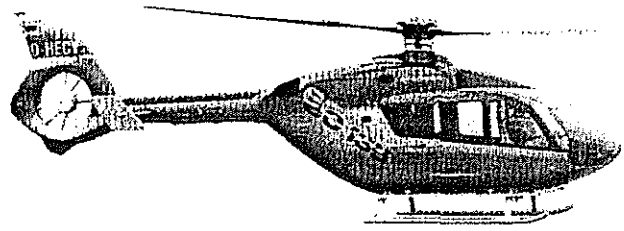

Figure 4: EC 135 Helicopter

The EC 135 is a light twin-engined multi-purpose helicopter with space for two pilots and five passengers. The EC 135 was selected in particular because it shows a very homogeneous, well balanced assessment result without significant weaknesses. Its bearingless main rotor and digital engine control represents modern helicopter technology. Furthermore, the EC 135 has low operating costs.

4. System Architecture

A hierarchical system architecture of the control system provides the pilots to fly the ACT/FHS in four different modes. The system is designed in a modular structure and with standardized interfaces and consists of the two interwoven technology units (see Figure. 5)

- a core system and
- an experimental system.

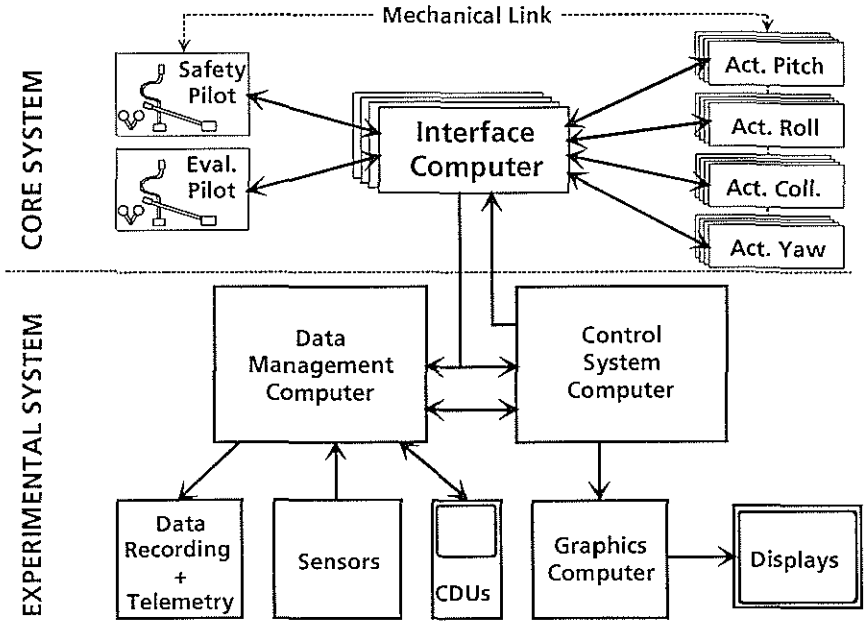

Figure 5: System Architecture

The mechanical control is used as a backup system.

Core System: The core system is the direct link (1:1) fly-by-light control system (more details in Ref. 6). It is the primary flight control system of ACT/FHS for the safety pilot and the evaluation pilot. The core system is designed in a rigid architecture according to the high safety standards for civil certification. In this 1:1 mode the pilot commands are directly processed through an interface computer to the actuators. The system consists of the inceptors with position transducers and trim actuators, the interface unit, optical data links to the actuators, and the smart actuation system with integrated actuator control electronics. It is a digital system with four-times redundancy and dissimilar hardware and software. The mechanical part of the actuators is designed as a duplex system. Built-in test functions provide continuous monitoring as well as pre-flight check and diagnostic tests for maintenance. The architecture of the core system is presented in Figure 6.

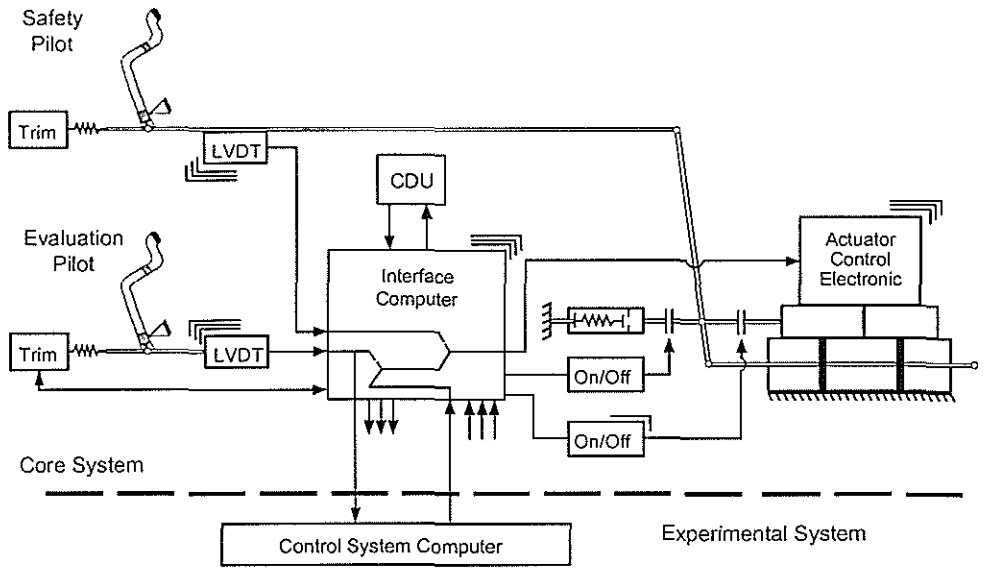

Figure 6: Core System

Experimental System: The evaluation pilot can switch to an experimental system with a flight control system computer which is interfaced into the direct link control path of the core system via the interface computer. The experimental system is designed with an open architecture and provides the level of flexibility to modify, to add, and to upgrade the test-software/ hardware which is needed to achieve the capability for in-flight simulation and in-flight technology demonstration. The experimental system is a simplex system but provision are provided for an upgrade to a duplex or a duo-duplex system. Well spread standards for the elements and standard interfaces are used to be prepared for system modifications and upgrades. The experimental system contsists of the following elements:

- The control system computer with a hardware/software architecture necessary for the computational requirements of the different application programs. It is connected to the interface computer in the core system by a bidirectional highspeed optical link and a standard ARINC system.
- A sensor package and a data acquisition system suitable for the acquisition of the experimental data. This includes sensors for fixed body, flight state, rotor state, and positioning.
- A data management computer which distributes data to the on-board telemetry, the data recording and the display system. With the data management computer it is possible to operate parts of the experimental system (e.g. display system) without the installed control system computer.
- A programmable cockpit display system for the evaluation pilot with an extensive computational capability for real-time data processing. The display system can be used as a multifunction-display and for the presentation of guidance information, digital maps, and test specific information.
- A test engineer's keyboard and display system for monitoring and managing the experiments.
- The control system computer is equipped with additional standard interfaces which allow to integrate additional experimental equipment (e.g. mission equipment or active controllers).

Mechanical Control System: During the operation in the evaluation pilot's modes, where the evaluation pilot has the full authority of the controls, the safety pilot's controllers are backdriven by the actuators which enables the safety pilot to monitor the actuators motions. If malfunction of the core control system should cause the loss of fly-by-light control the safety pilot can activate the mechanical back-up through an emergency cut off switch on the cyclic stick. The fly-by-light control can only be activated or reactivated on the ground. The principle of the transitions between the different modes are presented in Figure 7. More details about the signal processing within the core system are given in Ref. 7.

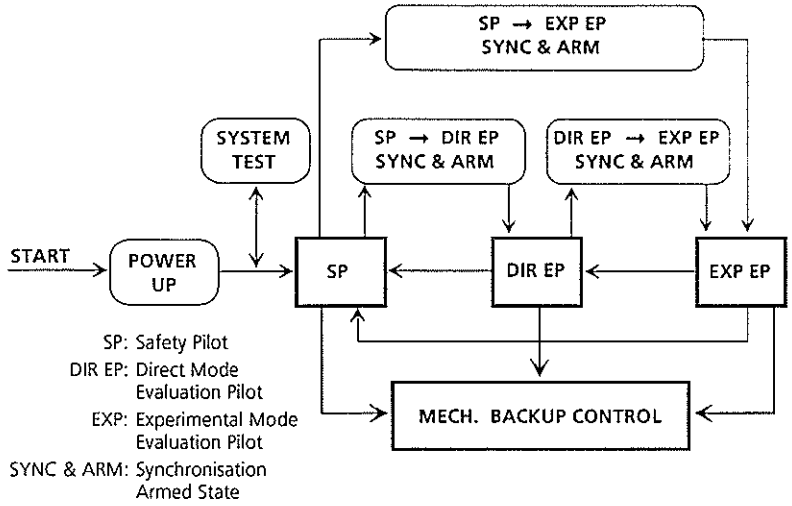

Figure 7: Modes and Transitions

Ground Stations: As an integrated part of the overall ACT/FHS facility, DLR's telemetry and engineer's ground station is adapted to the specific ACT/FHS utilization requirements. In addition, a ground based system simulator will be used for the training of the pilots and their familiarization with the ACT/FHS and for the pre-flight and compatibility testing of hardware and software modifications. Consequently, the simulator cockpit layout for the two pilots is equivalent to the cockpit environment of the flying test bed. An extended nonlinear model of the EC 135 and the coresystem is implemented. Hardware components of the experimental system are integrated which are identical to the onboard equipment.

5. Safety Concept

Functionality and reliability requirements for the two system units, the core system and the experimental system, are quite different. The core system, which is the backbone of the flight control system, has to fulfil civil certification safety requirements. For the experimental system, which shall provide a maximum of flexibility, reliability is not an explicit requirement.

Fault Tolerant Design: The complete functional chain of the core system from the position transducers to the direct drive control valves is designed as a quadruplex redundant system. In-lane monitoring within each of the four individual control channels is performed to detect and isolate component failures and deactivate faulty channels. The pure fly-by-light link of the core system has been designed in view of a catastrophic failure probability with less than 10^{-9} per flight hour.

Electrical power supply for the core system is provided by duplex essential bus bars. Transient power interrupts, which might occur due to short circuits or power switch-overs, are backed off by two buffer batteries. Hydraulic power is supplied by a duplex hydraulic system.

Dissimilar hardware for the active electronic components combined with dissimilar software is used to avoid that a generic design error would cause the the break-down of the complete system. The fail safe architecture of the control electronic is supplied by software monitoring as well as by hardware based watchdog circuits. The actuator command signals are consolidated in the actuator control electronics. The consolidation is designed in such a way that a generic failure, which is supposed to affect only one channel, would be compensated by the remaining healthy control channels.

Safety Functions: Beside the inherent integrity and reliability, the core system has to protect the aircraft against imported failures. Actuator commands, generated by the experimental system, are processed through the interface computer. Although these signals are monitored with respect to validity, parity, and update, the experimental system is able to produce runaways which must be stopped from being passed to the actuators to avoid that the aircraft is endangered. For this reason the incoming signals are processed through a runaway limiter, which can be distinguish between runaways and aggressive maneuvers. The limiter cuts off actuator commands exceeding certain combinations of signal rate and time of duration (Figure 8). Pilot

control commands are processed through a phase compensation filter to avoid pilot induced oscillations, which might occur due to actuator rate saturation. Resistance against electromagnetic interference is achieved with shielded electronic equipment and optical signal transmission. Figure 9 shows a schematic signal flow within the interface computer unit, including the runaway limiter and the phase compensation filter.

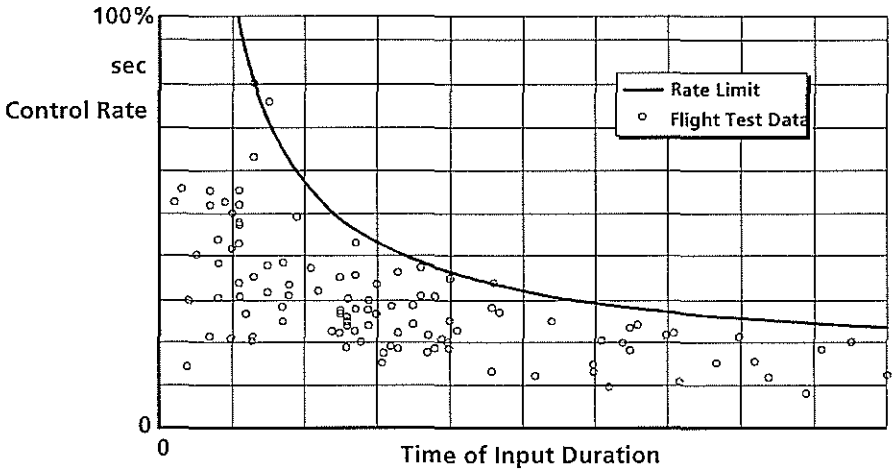

Figure 8: Rate Limitation

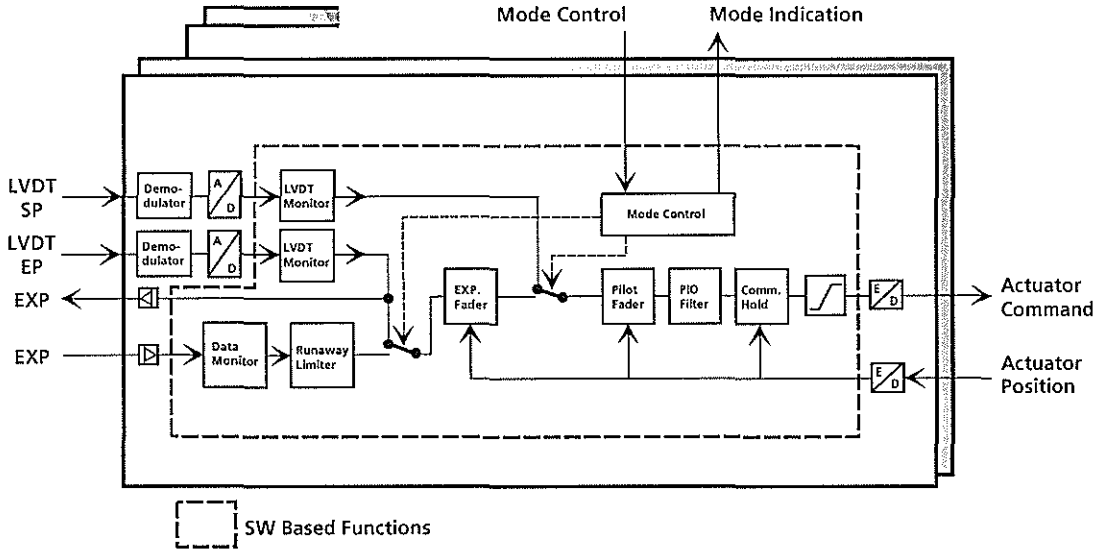

Figure 9: Interface Computer Signal Flow

Backup System: In addition to the electronic flight control system, a mechanical backup provides aircraft control in case of a total failure of the electronic system.

Safety Pilot: According to the safety philosophy adopted for the ACT/FHS, the safety pilot is the pilot in command and he has the responsibility for mode switching under normal operating conditions and a system reversion in case of failures. Switches for passing the control authority from the safety pilot to the evaluation pilot and back to the safety pilot are installed on the safety pilot's collective grip. The switches for the evaluation pilot for changing between the direct and the experimental modes are placed at the same positions at his collective grip. Switches for emergency cut-off of the experimental system as well as emergency cut-off of the complete electronic system and reversion to the mechanical backup are installed on the safety pilot's stick (Figure 10).

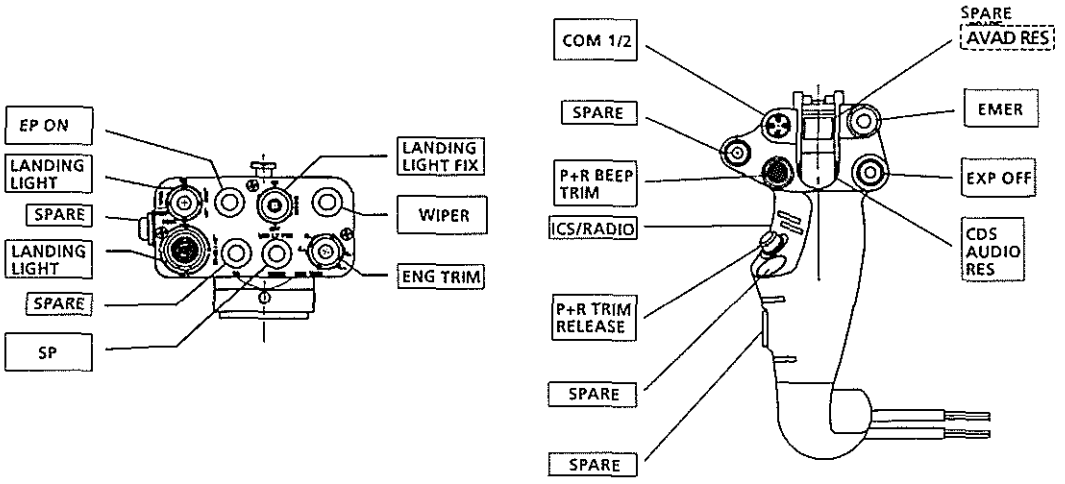

Figure 10: Safety Pilot's Controllers

In the evaluation pilot's modes, the motions of the actuators in all four axes are backdriven to the safety pilot's controllers which allows the safety pilot to monitor the activity of the actuators and enables him to quickly react in case of a failure. The safety pilot gets immediately control by applying a specified control force in any of the control axes.

In the case of any failure within the flight control system the safety pilot is alerted by a master caution indicator. Detailed failure information is displayed on the pilot's control panel. Reset switches on the panel allow the pilot to reconfigure the system after a transient failure. In the case of a severe system failure, e.g. three channels lost, a red warning light combined with an audio tone appears.

In summary, the safety philosophy for the ACT/FHS is based on a three level concept:

- The aircraft is automatically protected against system failures by a variety of safety features implemented in the system.
- The safety pilot is permanently aware of the operational situation and can take control at any time
- A mechanical backup control is available in case of emergency.

6. Schedule and Development Status

The development project was started mid 1995. The baseline helicopter was modified to provide structure, electric, cooling, hydraulic, and data link provisions for the integration of the ACT/FHS specific components. The mechanical control links have been replaced by a flexball link system. Prototypes of the core system elements are manufactured and tested. The integration of the core system has been started. Figure 11 overviews the system integration. As examples the main rotor actuator triple with the electronic control units is shown in Figure 12 and the cockpit interface unit for two lanes is shown in Figure 13. The first flight with the core system installed is scheduled for the second quarter of year 2000.

Extended component and overall system testing on the ground are performed. The flight tests needed for certification and performance evaluation in the mechanical mode and in the direct link mode for both pilots including the mode transfer procedures will be conducted following the first flight. The integration of the experimental system and the flight tests for the overall system are scheduled for the second half of 2000. The flight tests also include the final adaptation of the parameters implemented in the filters, limiters, mode transfer functions, and override forces and the pilots' evaluation of the transient behavior and the degradation characteristics after system failures. These tests will be performed with the similar software type for the core system. The development of the dissimilar software can be started after the final definition of the parameters.

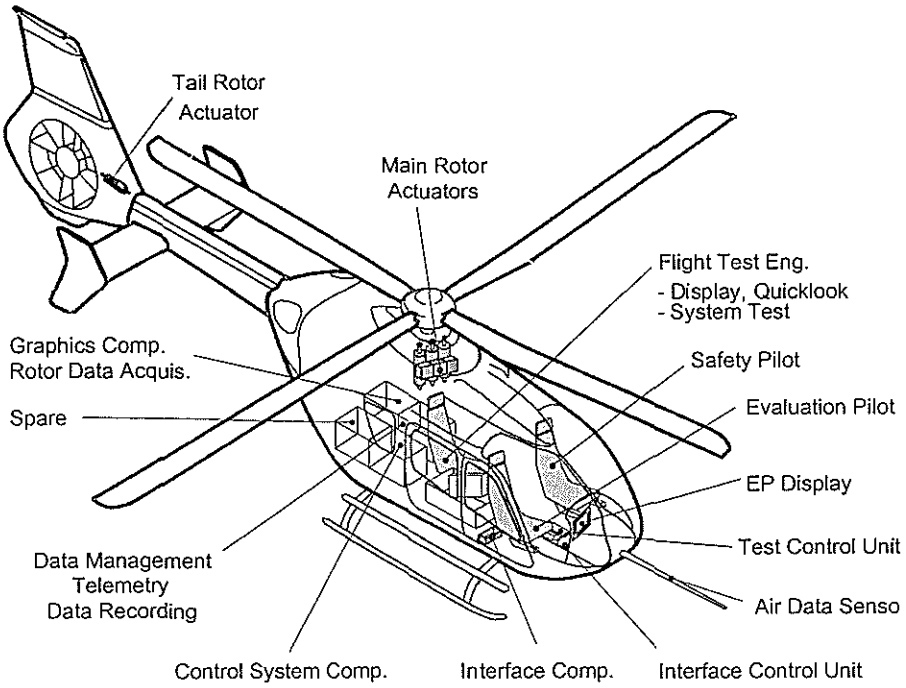

Figure 11: System Integration

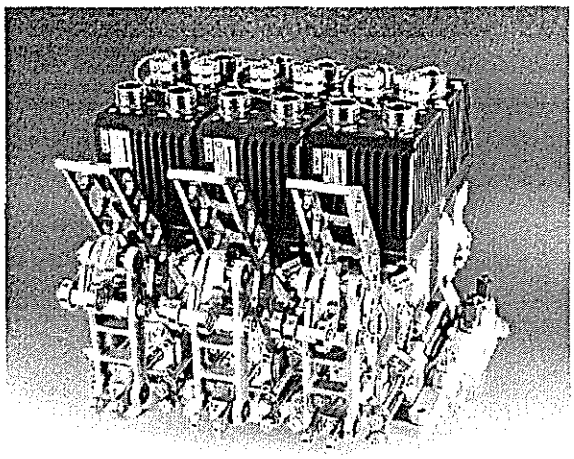

Figure 12: Main Rotor Actuator Triple

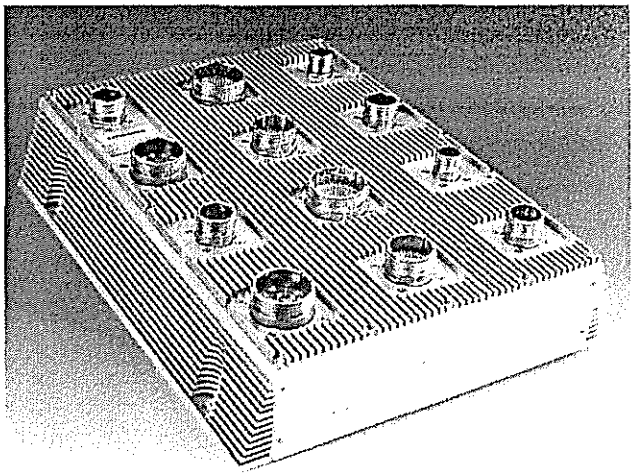

Figure 13: Interface Computer (2 Lanes)

Having considered the demands on the experimental system it was decided to use a VME bus architecture for the processing hardware. Future modifications and upgrades ask for a well established processor family with an availability of all standard interfaces. The graphics processor is an O2 machine from Silicon Graphics. Other components like the 10in flat panel displays and the control display units are off the shelf components for airborne use. The data recording is based on a silicon disk with SCSI interface. The sensor package includes the basic helicopter sensors and is completed by an attitude and heading reference system, DGPS, rotor data acquisition system, accelerometers at the pilot's seat, and an air data sensor. The swivel head air data sensor is mounted on a noseboom, specifically designed for the EC 135 (see Figure 14). All the experimental systems are ruggedized versions or have been ruggedized for the airborne environment. Most of the systems will be installed in equipment racks located in the baggage compartment, the flight engineer's panel and the evaluation pilot's panel. At present, the experimental system components are preintegrated in a mock up and are ground-tested in the ACT/FHS ground simulator.

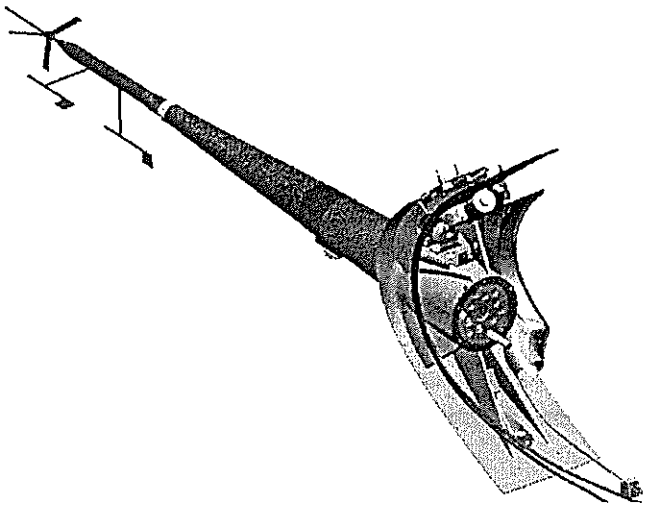

The certification for the expe-rimental aircraft with the fully developed dissimilar software type will be applied for mid 2001 which marks the end of the development program and the beginning of the user phase of ACT/FHS. During the first half of 2001 the ACT/FHS will be used with the similar software which slightly restricts the flight envelope.

Figure 14: Noseboom with Swivel Head Air Data Sensor

7. Research Use Strategy

At first, the flying simulation capability has to be realized for the ACT/FHS. Therefor, the first research efforts will be the flight validation of linear and nonlinear mathematical models of the EC 135 helicopter. They are needed for an adequate simulation fidelity of the ACT/FHS ground based system simulator. In addition, they are the fundamental prerequisites for the design of high bandwidth control systems. To achieve the required simulation fidelity in flight, an explicit model following control system (MFCS) has to be implemented. The MFCS forces the basic helicopter to respond to the pilot's inputs as an explicitly calculated command model which is useful when a high flexibility is required to vary the commanded model without any changes of the control system. DLR has a long expertise in the field of flying simulation based on the MFCS performance with the formerly operated ATTHeS simulator. The principle of the model following control design and the achieved simulation fidelity is described in Ref. 8. DLR started the MFCS design for the ACT/FHS in a simulation environment with the aim to have the full in-flight simulation capability available when the ACT/FHS will be delivered for full operation use in mid 2001.

After the completion of the development program DLR will be the owner and the main operator of the airborne test bed. Special priorities of use are assigned to the partners which have shared the work in the development phase and the financial budget for development.

The strategy of ACT/FHS utilization considers the following common long term goals with the key aspects which should contribute to improve the overall helicopter efficiency:

- development of 24h all weather helicopter capability,
- development of autonomous helicopter capability,
- qualification and certification of new technologies related to the active control of the helicopter,
- improvement of weapon efficiency and mission equipment, and
- overall optimization of the helicopter platform with advanced control and pilot assistant systems related to performance and cost trade offs.

In order to meet these objectives the partners have agreed upon an integrated approach which will be followed within the research and development activities of research centers, test centers, and industry. The evaluation of key technologies will include the interactions between flight control laws, man machine interface aspects, navigation systems, actuators, processors, sensors and has to consider the respective environmental conditions.

Studies are performed for preparing the first research user program addressing the generation of handling qualities data bases to fill identified gaps in the existing specification documents. Here emphasis is placed on the specific relation to transport type helicopter, the integration of active sticks, the investigation of advanced controller features, and pilot assistant functions. In the first phase, industry will concentrate on carefree handling features, advanced and mission oriented control laws, and the demonstration of full fly-by-light technology. The main interests of test centers are the evaluation of performance and compatibility of mission equipment.

8. Concluding Remarks

The ACT/FHS development program has been launched in 1995. The certification for the experimental aircraft will be applied for in 2001, which marks the end of the development program and the begin of the ACT/FHS use in the full test bed envelope

The ACT/FHS is designed as a multi purpose test bed for research, industry, and test centers for

- In-flight simulation,
- System development and integration, and
- Technology demonstration.

A hierarchical system architecture will allow to integrate and evaluate hardware and software components in an airborne environment. The standard of these components can range from experimental to operational. The ACT/FHS system is based upon the technology units:

- A core system, which is the primary flight control system for both pilots (safety and evaluation pilot) designed in a rigid, quadruplex structure in accordance to operational safety standards.
- An experimental system for the evaluation pilot, designed with an open structure, providing the required level of flexibility for test modifications.
- An engineer's and telemetry ground station and a system simulator for hardware and software in-the-loop testing and crew training.

The realized safety concept is primarily based on the two pilots crew and a hierarchical architecture.

The ACT/FHS will be used in an integrated approach of research, industry, and test centers considering the improvement of the overall helicopter efficiency. The objectives are to contribute to

- the development of future 24h all weather capability,
- the development of future autonomous flight capability,
- the optimization of the overall helicopter system related to the operational requirements.

9. References

1. NN, „Proceedings of the International Symposium on In – Flight Simulation", DGLR, RaeS, AAAF, AHS, AIAA Conference, Braunschweig, Germany, July 91.
2. Huber H., Hamel P., „Helicopter Flight Control State of the Art and Future Directions", 19th European Rotorcraft Forum, Cernobbio (Como), Italy, September 1993.
3. Pausder H.-J., Butter U., and Gollnick V., „ACT-Demonstrator / Flying Helicopter Simulator - An Airborne Testbed Development Project",22nd European Rotorcraft Forum, Brighton, UK, September 96.
4. Buchholz, J.J., Bauschat, J.-M., Hahn, K.-U., and Pausder, H,-J., "ATTAS and ATTHeS In-Flight Simulators" AGARD CP-577, Paper No. 31, 1996.
5. Pausder H.-J. et al, „Helicopter In-Flight Simulator ATTHeS - A Multipurpose Testbed and its Utilization", AIAA/AHS Flight Simulation Technologies Conference, Hilton Head Island, SC, USA, Aug. 1992.
6. Steinmaier, F., Bickel, N. , Pausder, H.-J., "Survivable Fly by Light Control System, ACT/FHS", RTO/SCI Symposium on Flight in Hostile Environment, Solomons Island, MA, USA, Oct. 1999.
7. Bickel, N., Steinmaier, F., „Design of a Primary Fly-by-Light Control system with a Dissimilar Redundant Architecture", 54th Annual AHS Forum, Washington, D. C., USA, May 1998.
8. Grünhagen von, W. et al "A High Bandwidth Control System for the In-Flight Simulator ATTHeS-Modeling, Performance, and Applications", in "Advances in Aircraft Flight Control", Taylor & Francis, London, UK, 1996.

TWENTYFIFTH EUROPEAN ROTORCRAFT FORUM

Paper n D7

THE MODERN HELICOPTER DESIGN CRISIS. ITS DISTINGUSHING FEATURES, CAUSE AND DEVELOPMENT

BY

THE CIBERNATIC INSTITUTE OF NAS OF UKRAINE

SEPTEMBER 14-16, 1999
ROME
ITALY

ASSOCIAZIONE INDUSTRIE PER L'AEROSPAZIO, I SISTEMI E LA DIFESA
ASSOCIAZIONE ITALIANA DI AERONAUTICA ED ASTRONAUTICA

I. Introduction.

The analysis of helicopter industry for last 50 years, i.e. from time of occurrence of the first generation of helicopters and beginning of their practical application, result in that unfavourable conclusion, that now rates of development of the given area of engineering considerably have decreased, it is possible even to speak about its begun degradation.

Speaking about the analysis, the author of the report means the not traditional analysis of statistics helicopter industry, and system historical-scientific analysis. The traditional analysis, which among other things seldom covers more than 10-15 years, would show certain growth of the majority of parameters of the aircraft, that could create impression of steady progress helicopter industry, while the historical-scientific analysis with sufficient evidence speaks, that this impression is deceptive. The historical-scientific research has other methodological basis and pursues other purposes, it examines object not by itself, and in interaction with other objects and phenomena, in which environment it arises, develops, functions. The purpose of such research to define the forms, logic and laws of development of object to find system of the factors, causing them, and also to establish, as the named system functions. (When the question is designing, which is the creative process initially focused on the account " of social aspect of the received result realisation "[1], the researching object is examined in interaction with social environment.)

Such tasks can not be solved, if the analysis covers only separate historical piece of life of the object, - it is necessary to consider its development during all time of its existence from the moment of origin of idea.

In due time author has carried out detailed multidimensional research of such kind which has captured all history of helicopters design up to middle of the 1980-Th. years [2]. By continuing it in some aspects till now, he has come to the above mentioned conclusions. Some of the received results are stated in the given report, they should be considered as preliminary, they will be specified in process of a deepening of the research and the increases of quantity of the used information (today's opportunities of the author in this respect objectively are limited). However and the received picture gives rather clear idea about a modern condition of helicopter industry, and also about the nearest prospects of its development.

The specified analysis is carried out in frameworks of wider research in the field of methodology of systems designing, which is carried out now in The Cybernetics Institute of NAS of Ukraine. In case of successful end it will allow not only to explain the reasons of the generated crisis in helicopter industry, but also to find ways of an output from it.

II. Features of modern crisis in the helicopter industry.

In the brief generalised form the essence of a today's situation in the helicopter industry can be formulated as follows: *a helicopter ceases to correspond to the public role*. Any technical system, especially vehicle, is a part of public life, and the requirements to it reflect public need for the given technical system, and concerning quality of performance its particular purposes by it, and concerning its ability to be entered in bio- and technosphere, not putting them damage. During public development under influence of a number of the factors the requirements change [2,3].

In methodology of designing requirements to system generated by public development and reflecting practical need for it, are determined as *the goal of its designing* [f.ex.4,5], or the fore seeing greatest possible effect [4, p.26]. In this case we consider purpose of designing of not concrete particular variant, and all given class of systems. If in required system this purpose is not realised, depending on a degree of a divergence of parameters of system with the requirements, or the interest of a society to it is reduced, or the system in general can be thrown out from public life as useless or even harmful. Just it has taken place in due time with dirigible balloons and autojiros.

To answer on question, in what condition is helicopter industry today, the author has analysed the modern goal of designing, and also the most specific characteristics of the newest helicopters and has compared them. In result the following picture has turned out.

General goal of helicopters design, as the earlier carried out historic-scientific analysis [2], has shown at an initial qualitative level was completely generated in 1970s . Since that time it includes three basic groups of the requirements: functional - technical, economic, ecological. Naturally, inside each of groups the development of the requirements proceeds and qualitatively and quantitatively. In Fig.1 most convenient for tasks of our research graphic model of the design goal is shown, i.e. constructed with appropriate by the character and degree of detailed elaboration.

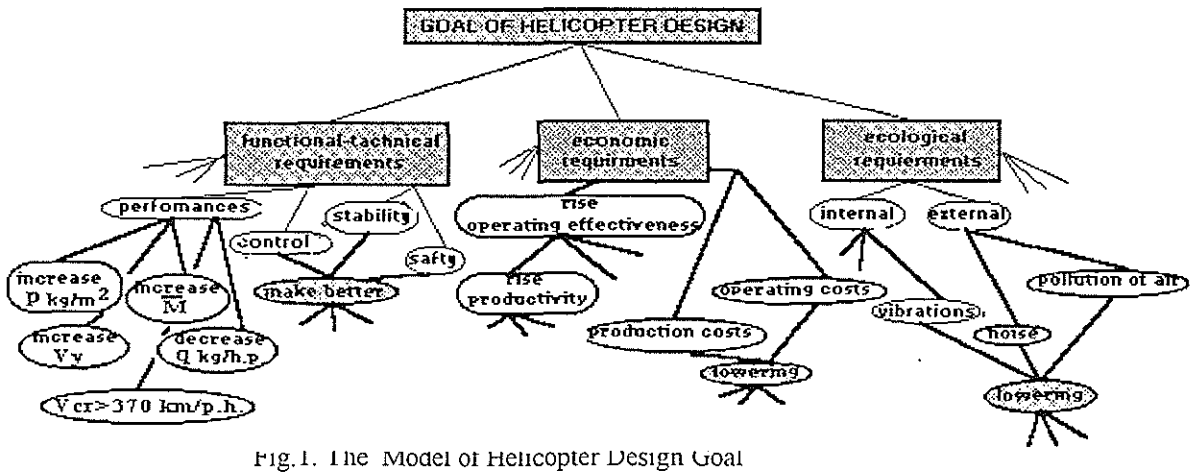

Fig.1. The Model of Helicopter Design Goal

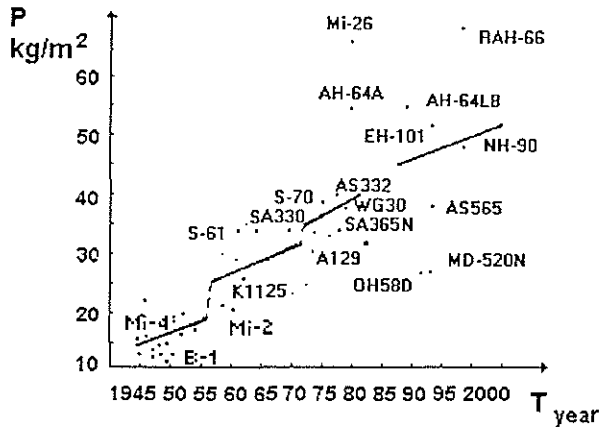

Fig.2

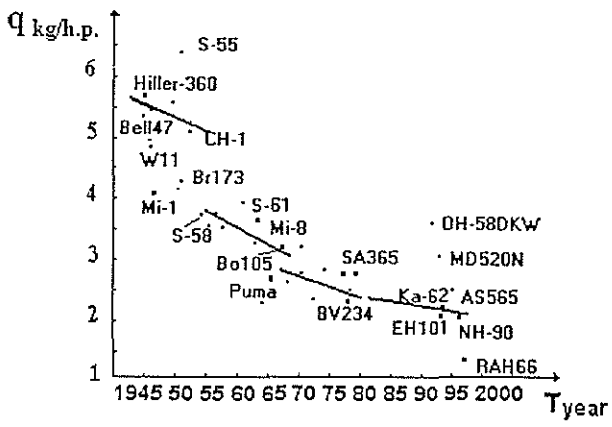

Fig,3

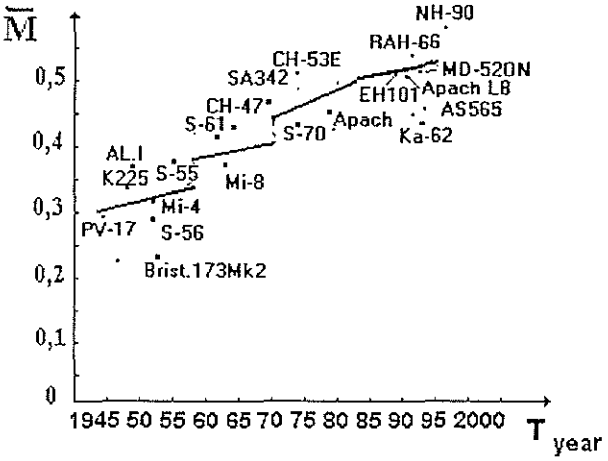

Fig.4

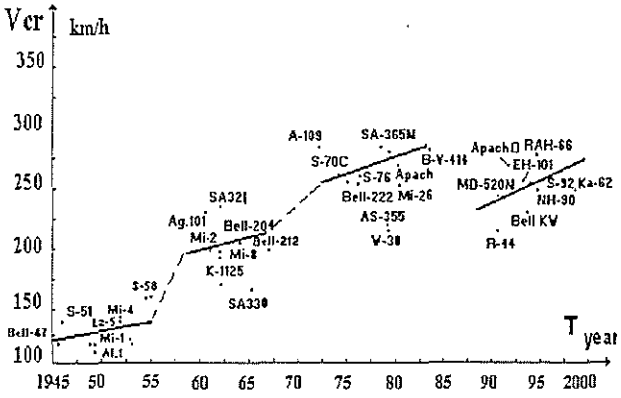

Fig.5

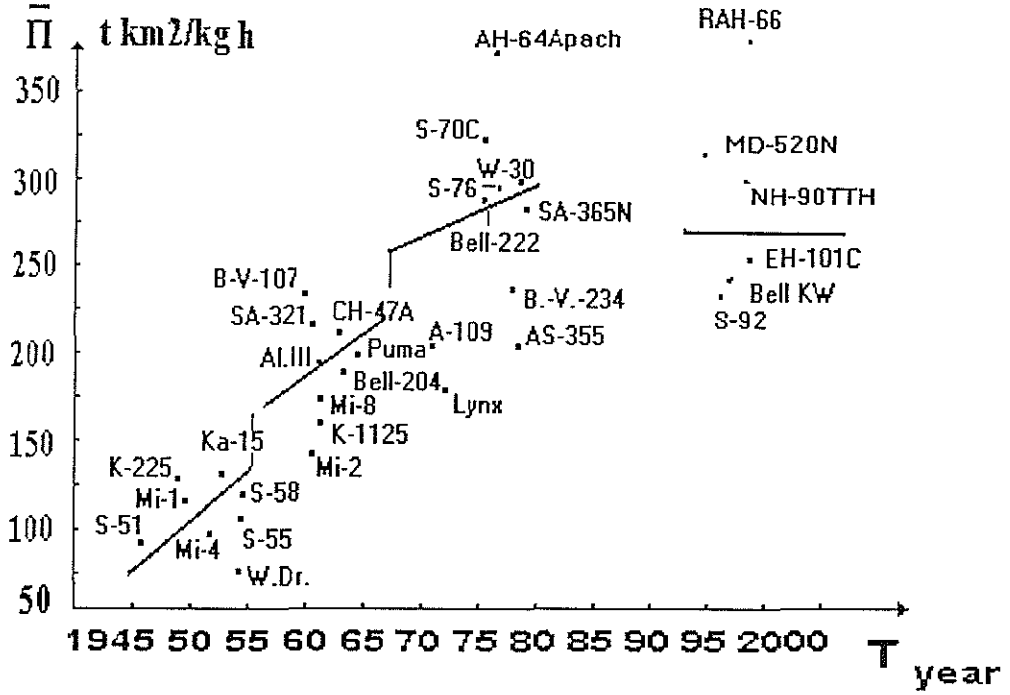

Fig. 6

Tab. 1

HELICOPTER	$\overline{M}$	p kg/m^2	q kg/h.p.	V cr.	$\overline{\Pi}$
3-d generation 1970 s					
W-30	0,44	40,3	2,5	222	307
AS-355C Super Puma	0,51	45	2,4 -	280	289
SA - 365N Dauphin	0,5	35,8	2,8	280	200
Bell 222	0,42	29,6	2,8	250	290,6
S-76	0,48	33,07	3,6	269	297
S-70C	0,48	43,7	2,9	268	324,2
1990 s					
AH - 64 Apach D	0,44	60,12	2,8	274	386
NH - 90 TTH	0,4	41,7	3,78	250	316,5
EH- 101 C	0,51	53,8	2,06	259	258
S - 92	0,38	47,97	2,88	259	229,
RAH - 66	0,46	69.5	2,87	260	385,2
Ka - 62	0,486	47,13	21,53	260	313,8
Bell KW (OH058D)	0,4	22,84	5,82	219	240,57
MD - 520 N	0,51	27,68	1,8	249	324,9
R - 44	0,416	13,7	4,18	209	214,4

It means, that in it parameters reflecting a perfection level of a helicopter as just the aircraft, in particular, such as cruising speed (V cr km / hour), rotor-loading (p êg/i2), power loading (q kg/ h.p.), over-all-payload ratio (m) are shown. Just these parameters also were analysed first of all. The results of this analysis are submitted on the diagrams, Fig.2 - 5, which reflect their development during 50 years.

Besides these parameters the operational effectiveness of helicopters by complex criteria used in practical designing was analysed. In Fig.6 changing of one of them, in particular, given reducing productivity [6] - Ï òêì2/êg h = GuVcr L / G fuel graphically is shown., where

Gu - payload weight, Vcr - cruising speed, L - range, G fuel -fuel weight.

From the diagrams it is visible, that for last 50 years in development of helicopters three characteristic periods appropriate to three generations of helicopters are possible to allocate. These periods are differ from each other by spasmodic changing of parameters, i.e. spasmodic increasing of a level of aircraft perfection. The time
interval before occurrence of the next generation is equal to approximately 10 years. However after the third generation, which has appeared in 1970 s, the jump in changing of parameters is absent, the area of a variation of their meanings for helicopters of last twenty years practically coincides with area of the third generation, tab.1.

Or else, for past 20 years the helicopter as just aircraft essentially has not changed. - Obvious delay of its development is present.

It is especially necessary to emphasise a situation with speed, so far, as it is known, development of air engineering (helicopter not the exception) goes on two basic directions: increase of speed and increase of carrying capacity.

Concerning carrying capacity it is possible to tell, that here progress is absent at all. Mi-26 constructed in 1976, and today is the heaviest helicopter which is taking place in operation. Since the 80-Th. years there is no almost mention about increase of carrying capacity as about a priority direction of development of helicopters in the special literature , i.e. in an obvious kind this requirement as if is absent, though objectively it always costs(stands) before designing. For example, in 1988-89 the information about Air Forces of USA together with firms Boeing, Lockheed and Douglas have defined necessity of development of the heavy helicopter by carrying capacity up to 22,5 tons and about works, conducted in this direction, in special literature have flown[7]. However in the literature of the next years the author did not meet the information on progress of these works, and while the promised helicopter has not appeared.

At the same time requirement of increase of speed was never removed from the agenda as one of basic for perspective rotary-wing aircraft. And since the 60-Th. years as desirable the figures compared to speeds of planes, i.e. 500, 700 and even 900 km/ p.h. were referred. And that the speed of helicopters for past 20 years practically has not changed, is a serious attribute of the crisis phenomena in designing.

Today helicopters on speed have appeared are comparable not to planes, and with modern automobiles and high-speed trains, thus conceding them in profitability and ecological acceptability (internal comfort and negative influence on an environment), already does a

helicopter uncompetitiveness, for example, in the interurban communication. And if for automobiles and trains the achievement of such speeds is the certain progress, for the helicopter a twenty years' delay on these figures - an attribute of degradation. Not casually a years, and in 50-Th. years, and in 60s. Then in development of helicopters there was a jump, and the interest to the combined aircraft died away. Today this interest again is high.

Thus, as actually aircraft the helicopter for two decades has changed insignificantly. Progress is the reduction of structure weight at the expense of application of composite materials and more careful constructive working up of subsystems and separate elements, and also decrease of drag at the expense of improvement of external aerodynamics. However, the decrease of structure weight has not resulted in increase of over-all-payload ratio, since the "vacated" weight has occupied the constantly becoming complicated onboard equipment. The improvement of the onboard equipment is, as a matter of fact, main direction of development of modern helicopters, at the expense of that their reliability, safety of flight, all-wetherability, quality of making certain special tasks.

At the same time the operating effectiveness as a whole remains former, and the economic parameters are worsened.

Cost of helicopters first of all grows. For 20 years, since 1973 for 1991 the average procurement price of a helicopter has grown from $400 000 up to $10 000 000 [8], and the growth of this parameter proceeds. For example, cost of the American helicopter AH-64 Apach in 1980 was defined as $ 4 210 000 [9], and as 1983 - already in $7 200 000 [10], now - as $ 7 700 000.

Constant care of the designers and consumers of helicopters is the decrease of the aircraft operation cost, but if within the limits of one generation it is possible with the help of some particular measures [F.Ex.11] to achieve relative progress in this question, as a whole from generation to generation the operating revenues grow. So for example, in 1967 cost of flight hour of the second generation helicopter S-61 (Mt.-o = 8,3 ò) made $ 234 [12], and in 1998 cost of flight hour of the third generation helicopter S-76Ñ (Mt.-o. = 5,3 ò) made already $ 669 [13].

The situation with conformity of helicopters to the ecological requirements is even more difficulty. These requirements officially are set from a beginning of the 1970s. To that time the rough development of aircraft, particularly civil, including helicopter industry, has made its coexistence with a man and as a whole with biosphere problematic. In 1971 the first restrictions on air noise [14] - from 86 up to 106 EPN dB were introduced, depending on take-off weight of the aircraft. However, in 1988 norms were reconsidered [15] in the party of some easing, approximately on 3 EPN dB, that was the compromise with opportunities of designing, but also has increased harmful influence of aircraft by an environment.

Accordingly in 1997 the new, more strong norms on noise were produced. They should enter action this year [16]. In helicopter industry the introduction of these norms has caused an alarm, since it threatens with serious restrictions on operating of helicopters and economic losses. The votes about 'necessities of balance between noise, safety of flight and economic

question on the combined aircraft as to alternative to the helicopter is keen again. It is necessary to note, that this question roses always, when helicopter industry appeared in crisis: and at the end of 20-Th. - beginning of the 30-Th.

opportunities' [f.e.17] are distributed. If to recollect, that biologically allowable noise level for the man - 55 dB, it is natural to assume, that society objectively can not allow spreading of the given mean.

In other words, given requirement of a society helicopters can not to satisfy, and, moreover, in connection with it is more strong the divergence between it and opportunities of helicopters has increased. The existing norms on engine emission now do not carry categorical character and on various parameters are exceeded by the different marks of helicopters. For example at norm of the contents of nitric oxide NOx - 40 g/kg in exhaust gases at some helicopters contains and 45, and 52, and 65 g/kg [18]. Though and at existing norms the pollution of an environment is great, and in process of increase of vehicles number the norm will have become stronger, also as well as norm on noise, about what already there is a speech in the documents ICAO [19].

Thus, the level of perfection achieved by helicopters for last twenty years, does not allow to name the newest modern helicopters as next generation, which occurrence in the near future with enthusiasm was predicted in 1980 s. The designing of helicopters for a past interval of time has not offered any essentially new revolutionary decisions which could cardinal change the basic characteristics of the aircraft, and have faster innovation character. It is possible to assert that the helicopter does not satisfy to the modern requirements of the society to technical system of the given class and the divergence with the requirements in due course is increased. Last speaks about certainly begun degradation of the aircraft, that entails decrease of demand on it and decline of all branch.

Already now unsatisfactory characteristics had an effect on scales of operating and manufacture of helicopters. In 1992-1993 began appreciable reduction of sales of helicopters, restriction of flights and even closing of helicopter airlines, in particular of urban and interurban communication [F.Ex.17,20,21].

Now in the literature the assumption of possible increase of demand for the aircraft and increase of helicopter sales. Reasons for such forecasts are increase of purchases of easy engines and hope for the opened markets of the countries former USSR and China. It is impossible to tell, that it is convincing arguments, as others, above analysed factors do not confirm optimism of these assumptions. If temporary revival caused by any circumstances of short-term action (for example, demand for military helicopters will take place in connection with a war-political situation in the world), it will carry short character and the general tendency of decrease of interest to the helicopter will not change.

In what, in opinion of the author, it is necessary to search for the reason of crisis and, accordingly, way of an output from it?

The historical and scientific and methodological analysis of designing of helicopters allows to assert, that in a basis of crisis helicopter industry the crisis of methods of designing lays. The essence of such crisis is detailed stated by the author in [3]. Briefly it can be formulated as inadequate of methods to design goal, i.e. complexity of a design task.

Modern crisis not first in a history of helicopter industry, and fourth. They always developed under one circuit: in process of accumulation of practical experience - or experience of tests (at early stages of historical development), or experience of operating of the aircraft - the goal of designing became complicated. The used methods came with it in the contradiction. Development of the helicopter was hampered, that

resulted in restriction of its using, or - at early historical stages - to complete refusal of the helicopter as of unpromising idea. Then owing to the certain reasons there was a radical transformation of methods, and the development of the helicopter was advanced in steps. The general methodological approach to solving of a design task was exposed usually to transformation, i.e. essentially sight on organisation and contents of all process of designing as a whole varied. The display of the previous crises in helicopter industry is in detail described in [2].

Attributes of modern crisis of methods was planned at the end of the 70-Th. years, when the helicopter industry experienced the certain boom in connection with occurrence of the third generation. 1960 -1970s were marked by burst of designer thought, occurrence of ideas of revolutionary scale: the new types of lifting and tail rotors, new types of main rotor hubs, new materials and so on. And nevertheless, the crisis of methods was generated and in 1990s was showed by natural braking of helicopter development. Modern helicopter industry uses just the same ideas of 60 - 70-Th. years, there was the stagnation planned in it.

The research devoted to the methodological analysis of designing of systems, which is carried out now in the Cybernetics Institute of NAS of Ukraine, considers as one of itself tasks to establish the contents of methodological mistakes made by modern designing, and to determine, in what particularly discrepancy of the methodological approach to design goal consists. The situation in helicopter industry is not of inherent extremely given area of engineering. General crisis of the technoshere was planned now, in a basis of it the crisis of methodology is. In different areas of engineering the crisis is shown with a different degree of an acuteness, but it is possible to tell, that general degradation of engineering, i.e. increase of break between its opportunities and requirements of public development began.

It is explained by a complex of the socio economic and scientific and technical reasons, which at the end concentrate in the methodological approach to designing of technical system.

The designing of helicopters is one of the main objects of our research, and as preliminary conclusions it is possible to make the following remarks.

The basic tendency of historical development of process of designing - transformation it from empirical designing, inventing in research process. In due time the author established this tendency, and also the direct forms for helicopter design [2], which it is possible to consider as an initial illustration of logic of systems designing development. The helicopter - artificial system, in a basis of its idea the natural analogues do not are, and until setting up of design process was not finished as research process, that has taken place in 1930 s, the problem of creation of a helicopter did not find the solution, in difference, for example, from the plane, which, having natural analogues, was created as the efficient aircraft practically still by methods of empirical designing [2]. And every time, when in development of the helicopter the crisis was formed to leave from this condition it was possible, reducing a spontaneous - heuristic part of designing and expanding analytical, its research part.

The development of designing of helicopters, as well as any modern science, is gone to the direction of more and more integrated, complex, or system, examination of natural phenomena and public life.

According to the basic tendencies of development, it is necessary to change the modern methodological approach to

First, of more complete account of the factors forming the goal of designing, i.e. to expand definitely frameworks of the system analysis carried out during designing;

Secondly, of inclusion in structure of researched system process of designing to make it according to again generated goal;

Thirdly, of using for solving particular scientific and technical problems of designing interfering perfection of the helicopters basic characteristics, methods of the organised heuristics. In that time to use besides transforming methods [23], containing an essential elements of spontaneous and more effective, based on the morphological approach [23].

The detailed ground of the offered conclusions will be given by the author in the subsequent works.

Summarising all is higher stated, it is possible to tell, that in helicopter industry obvious crisis have developed, continuing to progress. In its basis the reasons of methodological character are. It is necessary to search output from crisis, in opinion of the author of the report, in change of the general methodological approach for a choice of the design solution.

REFERENCES

1 .Диксон Д.. Проектирование систем. - М.:Мир,1969,- 440 с. (J.Dixon. Design engineering. -N.Y.-London,1966).

2.Болиева Т.Ч... Развитие методов проектирования вертолетов .Дисс.на соискание степени к.т.н. - М.:ИИЕТ АН СССР.-1987.(T.Ch.Bolieva. Razvitie metodov proektirovanija vertoljotov).

3.Bolieva T.Ch.. Characteristic Fceature of the Goal and Method Used for Helicopter Design as an Object of System Analysis. - 24- th European Rotorcraft Forum, Marseilles, France - 1998.

4.Гаспарский В..Праксеолигический анализ проектно-конструкторских разработок.- М.:Мир.1978.-172 с (W.Gasparsky . Kriterium metoda wyboru rozwazania technicznego w ujenciu prakseolometrycznym . Warsawa, 1970).

5. Дитрих Я. Проектирование и конструирование. Системный подход – М.:Мир, 1981.

6. Тищенко М.Н., Некрасов А.В., Радин А.С.. Вертолеты: Выбор параметров при проектировании. - М.:Машиностроение,- 1976.

7. Designe consepts for an advanced cargo rotorcraft./Shrage D.P.,Costello M.F., Mittleider D.N.// AIAA Paper.- 1988,-N4496, - P.1-10.

8. Перспективы развития зарубежных ВКЛА (обзор иностранной печати)./ сост. Е.И.Ружицкий, И.Г.Косарева. - М.:ОНТИ ЦАГИ. (TSAGI).

9. Brown says no major changes in Advances Attack Helicopter /Def.Space Bus.Daily. - 1980. - 109, N33. - P.246.

10. Flying the Hughes AH-64 Apache. / Lambert Mark // Interavia. - 1983. - 38,N 8, - P.833-836.

11. Reducing helicopter operating costs./Olson John R. //Vertiflite. - 1993.- 39, N1.- P.10-16.

12. Advent of the economic helicopter./Austin R.J.// Flight International.- 1967.- 92, N3045,- P.107-III.

13. S-76C.Powerful performe./ Graup. //Flight Int.- 1998.-154,N4642, - P.47-51.

14. ICAO/ 8.16.2.(1).- Montreal, 1971.

15. ICAO/ 8.16.2.(1).- Montreal, 1988.

16. JAR OPS 3. - 1997.

17. Helicopters for buisness./Sarsfield K.// Flight Int.-1998.- 154.N4641,- P.130-131.

18. ICAO/8.16.2.(2).- 1993.

19. ICAO. Circular 270-AT/111.- Montreal, 1997.

20. Groupe aerospatiale 1991: croissance de 16% du chiffre d' affaires 213 millionce de francs de benefice// Deron. et astronaut.- 1992. N2. - P.52.

21. Ventes d'helicopteres: la reprise se fait affendre// Air et cosmos/ Aviat. mag. - 1992. - N1382.- P.27-28.

22. Healthy helicopter market forcast /Proctor Paul// Aviation Week and Sp.Techn.- 996.- 144,N14.- P.42.

23. Одрин В.М. Метод морфологического анализа технических систем.- М.:ВНИИТИ,1989.- 310 с.

24. Jane's all the World' s aircraft. - Lnd. - 1985- 1998.

25. ICAO. Digest of statistics. - 1970-1997.

26."Flight","Aviation Week", "Aeroplane", "Air et cosmos" and other periodoca l editions.

SESSION
TESTING Flight Mechanics

P6

(Abstract submitted for consideration for presentation at the 25th European Rotorcraft Forum, September 14-16, 1999, Rome, Italy)

Flight Evaluation of an Adaptive Neural Network Flight Controller of an Uninhabited Helicopter

A. J. Calise, J.V.R. Prasad,
Georgia Institute of Technology
School of Aerospace Engineering
Atlanta, GA 30332, USA

J. E. Corban
Guided Systems Technologies, Inc.
P.O. Box 1453
McDonough, GA 30253, USA

Abstract

This paper presents recent results from our experimental flight controls research program, whose main focus is aimed at flight evaluation of a neural network based adaptive flight controller. A description is given of the uninhabited helicopter flight controls research testbed and associated avionics package. This is followed by a detailed description of our adaptive neural network based flight control architecture for attitude and trajectory control. Next, a description of the integration of the inertial measurement unit (IMU) with the onboard global positioning system (GPS) is presented. The paper concludes with results from our simulation and flight experiments.

Introduction

Traditional methods of flight control design consist of gain scheduling many linear point designs across the flight envelope using a high fidelity dynamic simulation. Continued reliance on these (albeit proven) methods contributes greatly to the expense associated with producing a new flight vehicle, and also limits achievable system performance. This is especially true when the flight system dynamics exhibit strong nonlinearities or are uncertain.

As an alternative, nonlinear techniques such as feedback linearization and dynamic inversion have been developed. Despite the power of these techniques, they fail to produce truly significant economic or performance-based improvements due to continued dependence on precise knowledge of the system dynamics. Research at Georgia Tech has recently demonstrated a direct neural network based adaptive control architecture that can compensate for unknown plant nonlinearities in a feedback linearizing setting. These neural network based controllers look very much like traditional adaptive control elements. Neural networks are viewed as highly nonlinear control elements that offer distinct advantage over more conventional linear paramter adaptive controller in achieving system performance.

In order to experimentally validate our research, and to support other activities in the area of autonomous flight vehicles research, we have developed an experimental flight controls research facility using a Yamaha R-50 uninhabited helicopter. The objective of this paper is to present an overview of our neural network based adaptive control methodology, describe the integration of IMU with the onboard GPS, and then summarize some of our flight test results.

Uninhabited Aerial Vehicle Research Facility

The UAVRF was initiated in June of 1997. This facility is dedicated to flight testing of advanced control algorithms on model helicopters. It presently contains two Yamaha model R-50 helicopters, each having 12 HP liquid cooled engines, a payload capability of 44 pounds and endurance of approximately 30 minutes.

The on-board system consists of a 200 Mhz Pentium based flight control processor with 32 Mb RAM and an R-1 integrated avionics system. The list of on-board sensors includes: BEI motion pack 3-axis gyro and accelerometer package, NovTel RT-2 differential GPS with 2 cm accuracy, 3-axis magnetometer, and 8 channel ultrasonic ranging system. A wireless modem digital data link is used to provide a two way communication link with a mission cntrol ground station. In addition, an on-board multiplexer switch allows a human safety pilot to engage the system, and to over-ride the flight control system in the event of an emergency. The control actuators consists of 3 linear servos for cyclic and collective control, and 2 rotary servos for yaw and throttle control. The UAVRF also houses two 300Mhz PCs that are used for hardware in the loop simulation, which permits accurate simulation and hardware testing of each mission prior to flight test.

Simulation Model

A nonlinear simulation model of the R-50 helicopter has been developed based on the math model given in Ref. 1. The model of Ref. 1 includes, in addition to a six degrees-of-freedom fuselage, a first-order representation of main rotor flapping and quasi-steady representation of main and tail rotor inflows. This model has been modified to include a simplified control rotor model developed in Ref. 2, a pilot's radio controller model and simplified engine and RPM governor models. Initial estimates of the aerodynamic data are adjusted using flight test data.

Adaptive Nonlinear Flight Control

This section presents an overview of the control system design. The interested reader is referred to Refs. 3 through 7 for more background on the subject approach to direct adaptive control of nonlinear systems, additional design details, derivation of the neural network update law, and a proof of stability.

The controller can be configured in each of the three rotational axes independently as either a rate or attitude command system. Handling qualities are prescribed by the use of a command filter which serves both to limit the input rate, and as a model for desired response. Specification of "good" handling qualities is not yet well defined for unmanned helicopters, and is the subject of future research. Figure 1 presents a block diagram of the control system architecture for the longitudinal channel when this channel is configured for rate command. The lateral and directional channels are identical in form. The construction of this block diagram is discussed in the following.

The design starts with an approximate linear model of the rotational dynamics of the helicopter which is to be inverted at a nominal operating condition.

$$\dot{\omega} = A_1 x_1 + A_2 \omega + B\delta \qquad (1)$$

In Equation (1), $\omega = [p, q, r]^T$ is the vector of angular rates about the body fixed axes [3], and A_1, A_2 and B represent matrices of the aerodynamic stability and control derivatives at the nominal operating point, respectively. The vector of standard helicopter control inputs, δ, is employed. It contains lateral and longitudinal cyclic pitch, δ_{LAT} and δ_{LON}, main rotor collective pitch, δ_{COL}, and tail rotor collective pitch, δ_{DIR}. In this formulation, the main rotor collective control position is treated as an additional translational state (i.e. it is assumed relatively slow), so that $x_1 = [u, v, w, \delta_{COL}]^T$.

The methodology assumes the 'pseudo control' vector, U, to be of the form

$$U = U_c + \dot{\omega}_c - U_{AD} \qquad (2)$$

The elements of U_C are the outputs of independent linear controllers, each operating on its corresponding error signal. The linear controller designs are used to specify the tracking error transients in each channel. Typically the transient is designed to be fast relative to the dynamics of the command filter but slow relative to the actuator dynamics. In the example of Figure 1, the pitch channel is configured as a rate command system. Integral action is added to provide for attitude retention giving it the designation Rate Command, Attitude Hold (RCAH).

In some piloting tasks, one may prefer instead an attitude command system. In such case the linear controller for the pitch channel example is designed as

$$U_c = K_p(\theta_c - \theta) + K_d(\dot{\theta}_c - \dot{\theta}) \qquad (3)$$

where θ denotes the pitch Euler angle. In this case a second order command filter is employed, and the second, rather than the first, time derivative of the command is fed forward. An outer loop trajectory controller can be set up with the attitude command system performing the inner loop function and using a methodology similar to Ref. 8.

Returning to the case of rate commands in all three axes, the commanded angular accelerations are constructed by the command filters as

$$\dot{\omega}_c = [\dot{p}_c, \dot{q}_c, \dot{r}_c]^T \qquad (4)$$

The left hand side of Equation (1) is set equal to the desired angular accelerations, the elements of which (in the case of rate command systems) are identically the pseudo controls constructed for each channel. The result, after substituting using (2) and (4), is then solved for the vector of helicopter controls

$$\delta = B^{-1}\{U - A_1 x - A_2 \omega\} \qquad (5)$$

Note that the linear model being inverted is only an approximation to the true helicopter dynamics, and that inversion error will therefore result in each channel. This inversion error can be expressed as a function of the states and pseudo controls.

The neural network output, U_{AD}, serves to adaptively cancel these inversion errors through on-line learning. The learning is accomplished by a simple weight update rule derived from Lyapunov theory, thus assuring the stability of the closed-loop system. The subject design employs a multilayer neural network with sigmoidal activation functions in the hidden layer. A neural network of this type is capable of approximating any smooth function to any desired accuracy, provided the number of hidden layer neurons is sufficiently large. Inputs to the neural network in each channel are taken as the rotational states, pitch and roll Euler angles, and the corresponding pseudo control.

Control System Implementation

For the purpose of real-time simulation and flight test, the control system formulation presented in the previous section has been coded in the C programming language. It runs in real-time in double precision with an update rate of 100 Hz on a 200 MHz Pentium-based Single Board Computer (SBC). The SBC is interfaced via shared memory to a previously developed commercial-grade flight control system known as the R1. The R1 provides for collection and management of sensor data, hardware and software interface to both the actuators and the pilot, and management of all telemetry links to a ground control station. For the current program, the R1 flight control system with SBC has been integrated on a Yamaha R-50 industrial unmanned helicopter, which is a 150 pound gross weight production vehicle designed for agricultural spraying. The result is a very capable unmanned helicopter testbed. Features of the R1 flight control system and its sensor suite are discussed in the following.

The R1 system is designed to support the integration of independent functional modules in order to accommodate a wide variety of research needs. Up to four Motorola 68332 processors communicate using high speed serial data transmissions (Motorola Queued Serial Peripheral Interface, QSPI). There are two 16 channel 12 bit analog to digital conversion boards interfaced to the primary 68332 via the QSPI. The four 68332s provide a total of 64 digital input/output channels with precision timing control functions for tasks such as generation and reading of pulse code modulated signals.

The R1 card cage also houses driver circuitry for an eight channel ultrasonic ranging system. This system is used to measure range to the ground over prepared surfaces during take-off and landing sequences. The card cage also accommodates a spread spectrum digital data link and a Rockwell MicroTracker differential GPS receiver (3-5 meter accurate sensing of position in differential mode with updates once per second). The original sensor suite included an Attitude and Heading Reference System (AHRS) based on the Systron Donner Motion Pak coupled with a Honeywell 3-axis magnetometer. The Motion Pak is a 3-axis cluster of solid state rate sensors and linear accelerometers. The AHRS provides measurements of angular rates, linear accelerations, and magnetic field strength from which magnetic heading and the pitch and roll attitude angles are derived.

Alternate sensor suite modules include an upgrade of the GPS receiver to either the Novatel RT-20 or the RT-2 (20 and 2 cm accurate positioning solutions respectively in differential mode with carrier phase lock and 5 Hz update rates), and substitution of the AHRS with a complete GPS-aided inertial navigation solution. Planned flight tests will employ the inertial navigation solution aided by the RT-2. The system has a 12 channel interface to standard pulse width modulated radio control equipment for the pilot interface, and sensors for measuring the rotational rates, temperatures, etc. The system operates on a 12 to 28V DC input power supply.

Hardware-in-the-Loop Testing

Figure 2 presents a block diagram of the real-time, hardware-in-the-loop test facility developed to prepare for flight evaluations of the controller. The right half of the figure represents the flight control system hardware and software described in the previous section. The left half of the figure represents elements introduced in order to conduct simulation studies. Only the Flight System elements depicted on the right are employed when flying the aircraft. In such case the actuator movements result in the true dynamic response of the aircraft. This response is characterized by the sensor suite and digitized at regular sampling rates. This sensor data is used for feedback control, and the traditional helicopter control deflections are computed.

Simulation and Flight Test Results

Preliminary flight test results for the pitch channel RCAH are presented in Figures 3 and 4 for the cases without and with adaptive neural network, respectively. It is clear from these figures command tracking is significantly improved with the adaptive neural net controller. The final paper will include additional flight test results for attitude and trajectory command tracking.

Summary

Design of a helicopter control system using a combination of feedback linearization and a neural network-based technique for on-line adaptation is presented. Hardware and software implementation of the controller on an unmanned helicopter testbed is then discussed. Simulation as well as flight test evaluation results are presented to illustrate the ability of the neural network controller to perform to specification in a real application environment. The final paper will include a detailed description of the IMU integration with the onboard GPS and simulation and flight test results of the attitude and trajectory controller.

References

1. Heffley, Robert K., "Minimum-Complexity Helicopter Simulation Math Model," NASA CR 177476, April 1988.
2. Perhinschi, M. and Prasad, J.V.R., "A Simulation Model of an Autonomous Helicopter," Proceedings of the RPV/UAV Systems 13th Bristol International Conference, April 1998.
3. Kim, B.S., Calise, A.J., "Nonlinear Flight Control Using Neural Networks," AIAA J. of Guidance, Control, and Dynamics, Vol. 20, No. 1, 1997.
4. Leitner, J., Calise, A.J. and Prasad, J.V.R., "Analysis of Adaptive Neural Networks for Helicopter Flight Control," J. of Guidance, Control, and Dynamics, Vol. 20, No. 5, Sept. – Oct., 1997.
5. Calise, A. J. and R. T. Rysdyk, "Nonlinear Adaptive Flight Control Using Neural Networks," IEEE Control Systems Magazine, 1998.

6. McFarland, M. B., and A. J. Calise, "Multilayer Neural Networks and Adaptive Nonlinear Control of Agile Anti-Air Missiles", Presented at the August 1997 AIAA Guidance, Navigation and Control Conference, Paper No. 97-3540.
7. Corbanm E., Calise, A.J. and Prasad, J.V.R., "Implementation of Adaptive Nonlinear Control for Flight Test on an Unmanned Helicopter," CDC, December 1998.
8. Prasad, J.V.R. and Lipp, A.M., "Synthesis of a Helicopter Nonlinear Flight Controller Using Approximate Model Inversion," Mathematical and Compter Modelling, Vol. 18, No. 3-4, pp. 89-100, 1993.

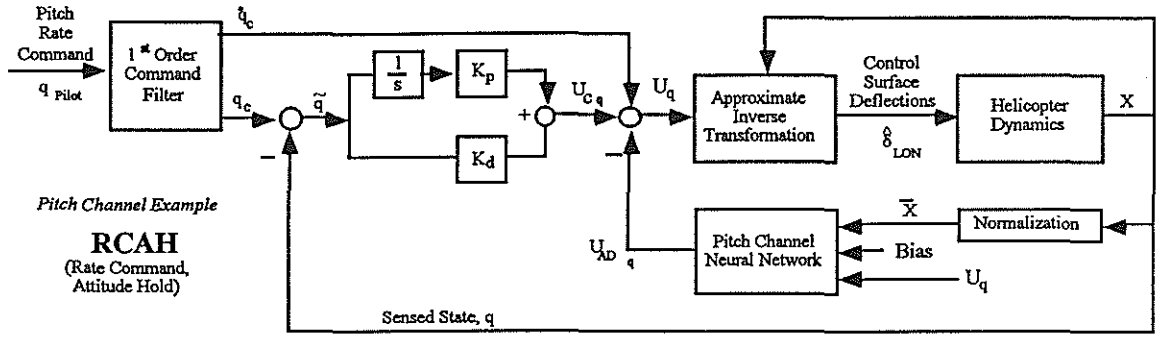

Figure 1. Block diagram of Rate Command, Attitude Hold System for Pitch Channel.

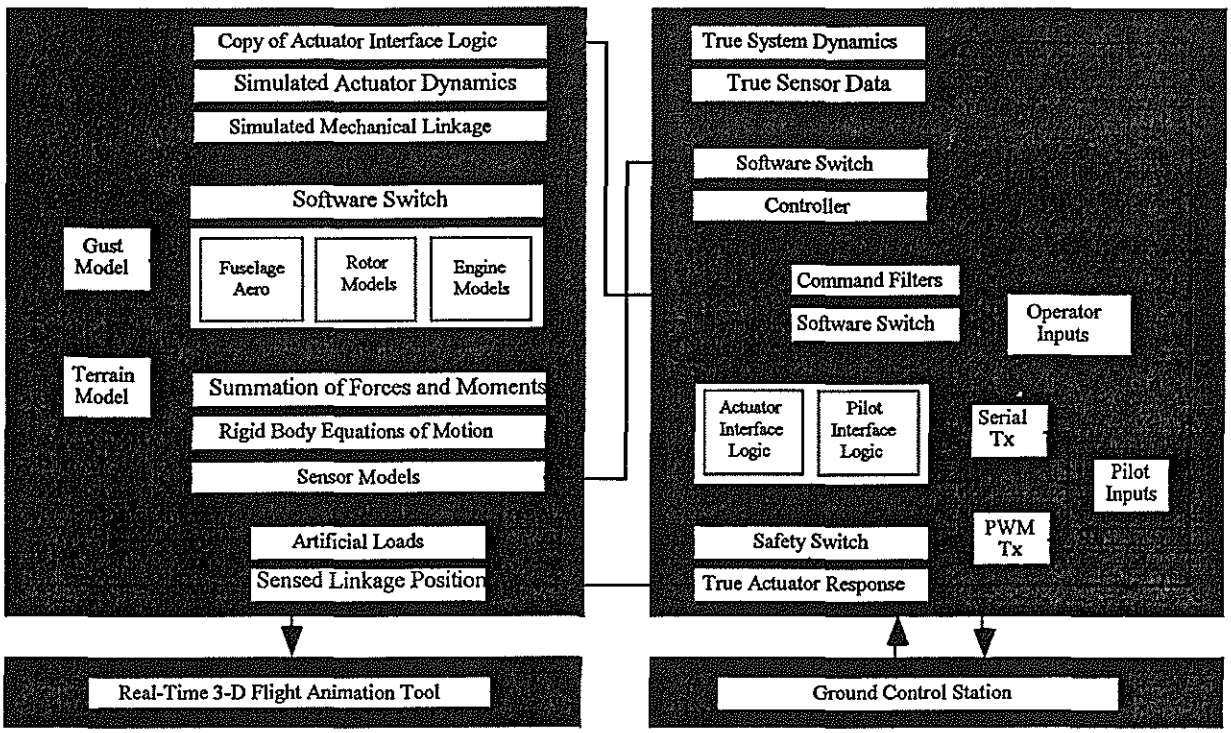

Figure 2. Joint GST/Ga Tech Real-Time Hardware-in-the-Loop Simulation Facility

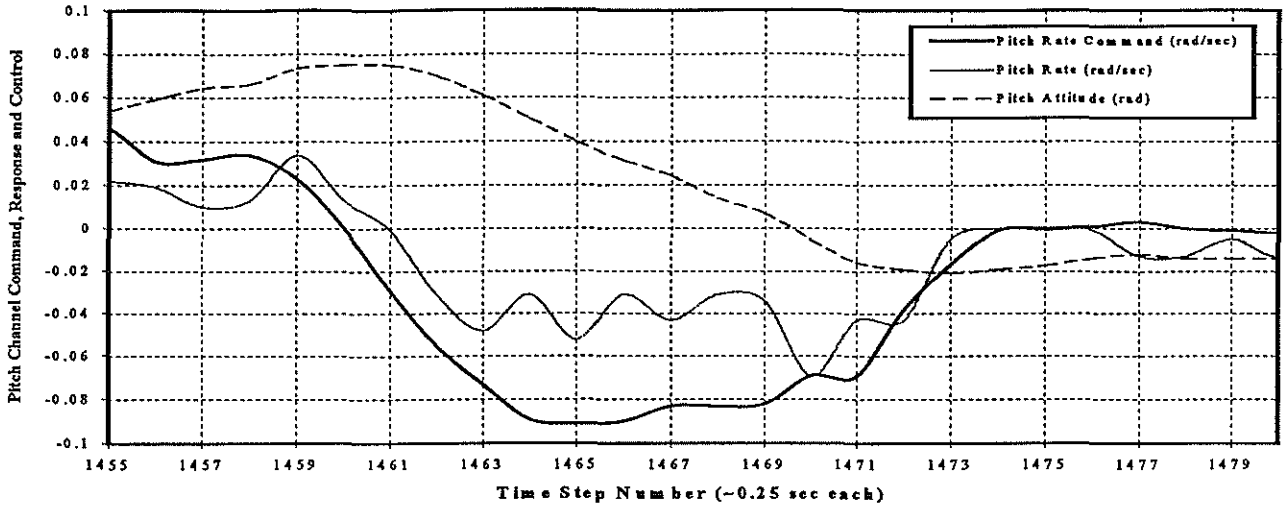

Figure 3. Preliminary Flight Test Results for Pitch Channel RCAH, No Adaptation

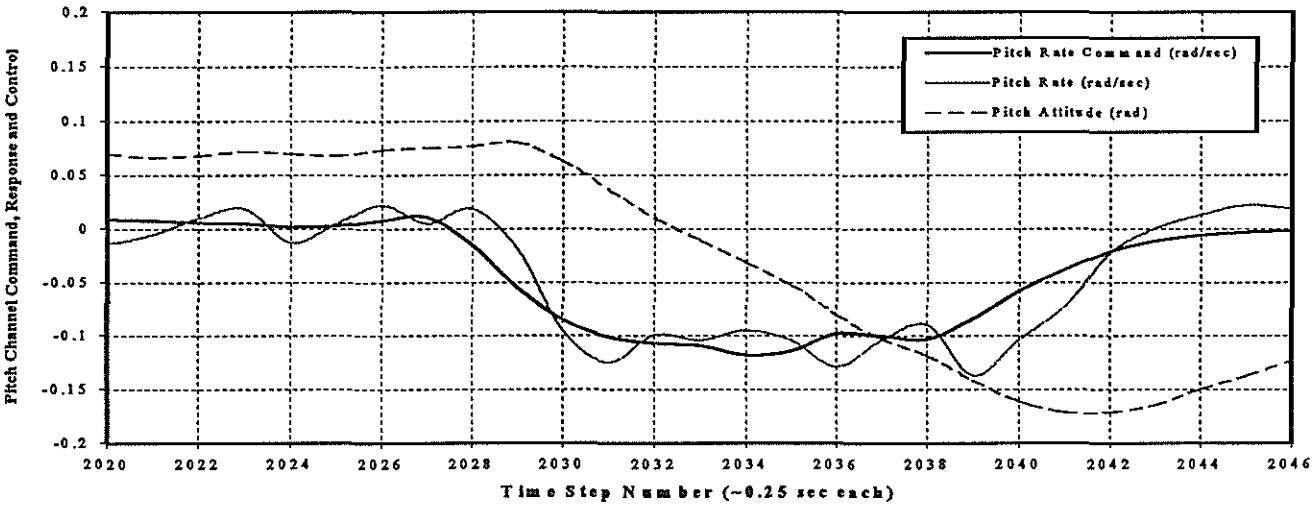

Figure 4. Preliminary Flight Test Results for Pitch Channel RCAH, with Neural Net Controller.

TWENTYFIFTH EUROPEAN ROTORCRAFT FORUM

Paper No: E1

THE DEVELOPMENT OF AIRWORTHINESS REQUIREMENTS FOR CIVIL NIGHT VISION GOGGLE (NVG) HELICOPTER OPERATIONS

BY

K. M. DODSON, N. TALBOT
FLIGHT DEPARTMENT
SAFETY REGULATION GROUP, CIVIL AVIATION AUTHORITY
GATWICK, UNITED KINGDOM

SEPTEMBER 14-16, 1999
ROME
ITALY

ASSOCIAZIONE INDUSTRIE PER L'AEROSPAZIO, I SISTEMI E LA DIFESA
ASSOCIAZIONE ITALIANA DI AERONAUTICA ED ASTRONAUTICA

THE DEVELOPMENT OF AIRWORTHINESS REQUIREMENTS FOR CIVIL NIGHT VISION GOGGLE (NVG) HELICOPTER OPERATIONS*

K. M. Dodson & N. Talbot
Flight Department, Civil Aviation Authority, UK

Abstract

Night vision enhancing technology has been used by pilots in military aircraft operations for many years. Steady development and refinement of the technology, together with the availability of associated equipment at reducing cost, has resulted in increasing interest in the use of Night Vision Goggles (NVGs) for specialist civilian aircraft operations. This paper briefly summarises the operating principles of NVGs and outlines the development, by the UK Civil Aviation Authority (CAA), of Airworthiness Requirements for civil NVG operations, following the findings of a proof of concept trial. The need for the requirements and the background to their development is explained, together with the main issues that the requirements need to address. An overview of the requirements is provided in Section 5 and the requirements are reproduced in full in Appendix 1. Finally, an international perspective is provided by describing ongoing activity within the Joint Aviation Authorities (JAA) and the Federal Aviation Administration (FAA) with the objective of producing harmonised requirements for civil NVG operations.

1. Introduction

There is increasing interest in using Night Vision Goggles (NVGs) for specialist civilian tasks; most notably for Police and Emergency Medical Services (EMS) operations. In January 1995, the UK CAA gave approval, on a trial basis, for one Police Constabulary Air Support Unit to undertake an evaluation of NVG operations using a BO105. The Devon & Cornwall Constabulary Air Support Unit believed the trial to be a great success, claiming safety and operational benefits for night operations. Consequently, other police forces are becoming increasingly interested and it was considered appropriate to develop formal requirements to support the use of civil helicopter NVG operations. Clearly, particular safeguards must be in place since there are potential hazards when the pilots view of the outside world is maintained solely by Night Vision Goggles. The military use of NVGs, over many years, has resulted in considerable experience of the benefits and hazards of their use. This experience was given due consideration by reviewing available military documents including, for example, any relevant Military Specifications (Mil Specs). The paper describes the background to the development of the civil requirements and the significant airworthiness issues that need to be addressed. The resulting requirements are presented in full in Appendix 1 to the paper.

The Devon & Cornwall Police Constabulary NVG trial came to an end when the BO105 was retired from service in 1998. The same Constabulary now operate a BK117 and the newly developed NVG requirements are currently being used to approve a full NVG modification to this aircraft.

Police and Emergency Medical Service NVG helicopter operations are being conducted in some other Joint Aviation Authority States and the FAA in the US have recently certificated civil NVG operations. Consequently, the JAA and FAA are discussing NVG requirements with the intention of producing harmonised airworthiness and operational rules. Information on the progress of these discussions is also reported.

2. Principle of NVG Use and Potential Airworthiness Problems

In the electromagnetic spectrum, the human eye responds to wavelengths between 400 and 700 nanometres (nm) which we normally see as colours. However, as light levels reduce, the human eye is less able to distinguish colour and detail. On a dark night, colour perception is lost entirely and objects become shadowy, dim shapes. Night vision can be improved by increasing the amount of light reaching the eye, as with a torch for example, or by imaging technology by creating a visible phosphor-screen image from normally imperceptible radiation, as in a Night Vision Imaging System (NVIS). NVIS goggles consist of two image intensifier tubes and look much like binoculars mounted to a helmet. They operate by the amplification of light in the far red and near infra-red (IR) section of the electromagnetic spectrum (600 to 1000 nm). The two main types of intensifier tube in use are classified as Generation II, which uses a multialkali photocathode, and Generation III which uses the far more sensitive gallium arsenide photocathodes. Even at low light levels, a Gen III tube produces a very sharp image on the phosphor screen with little loss of resolution.

The basic principle of the use of modern Night Vision Goggles is that the outside world is viewed through the goggles and the cockpit is viewed by looking "under" the goggles using the naked eye. The main way of meeting these differing requirements is to provide cockpit lighting that contains no infra-red. The use of the unaided eye to monitor the cockpit instruments requires them to be illuminated by acceptable amounts of visible light. If any illumination in the cockpit emits energy within the response range of the IR-sensitive photocathode, it may degrade the performance of the goggles since they have a built in automatic gain device which reduces their sensitivity and resolution as the level of IR energy is

* Paper presented at the 25th European Rotorcraft Forum, Rome, Italy, September 1999

increased. Therefore, to operate the goggles at maximum efficiency, IR energy must as far as possible be eliminated from cockpit illumination systems. This non IR lighting has a characteristic blue/green colour and is achieved by the use of filters. Standard tungsten filament light bulbs produce approximately 95% of their energy in the infra-red wavelengths and hence will cause major interference with the performance of NVGs unless filtered. This includes warning lights, since a single unfiltered warning light illuminating at a critical phase of flight could cause loss of all external view, with the resulting obvious hazard.

It could be argued that loss of external view through the goggles would not be a problem as a reversion to conventional (non-NVG) flight could be carried out. Although this would be the case in some flight regimes, it is likely that NVGs will be used to manoeuvre the aircraft into situations that would be difficult to get out of without continued use of the goggles. Examples of this might be flight into a cloud topped valley or other operations close to obstacles. It would be potentially dangerous to provide the pilot with a piece of equipment that could be used to fly into difficult situations without also providing a reasonable expectation of adequate integrity and continued availability. For the purposes of drafting airworthiness requirements it is considered that a loss of external view for whatever reason in the critical flight condition should be classified as Hazardous, in accordance with the guidelines of JAR 29.1309 (Ref 1) and associated Advisory Material. This classification implies that the possibility exists for damage to the aircraft and for injury or loss of life, but falls short of the Catastrophic classification of JAR 29.1309, which implies total loss of the aircraft and occupants.

A classification of Hazardous seems appropriate for the critical flight phase, and drives provision of a defined degree of integrity for both goggles and cockpit compatibility through the mechanism of a System Safety Assessment.

3. BO105 Civil NVIS Proof of Concept Trial

A proof of concept trial was carried out by the Devon and Cornwall Constabulary Air Support Unit, with the objective of establishing the benefits, if any, to Police operations from the use of Night Vision Goggles. The aircraft used was the Air Support Unit's BO105, modified for NVG use and operated with GEC Ferranti NiteOp Gen III goggles. The initial phases of the trial involved the CAA, from both Airworthiness and Operational points of view. A CAA Test Pilot and a Flight Operations Inspector were involved in initial approval of the cockpit modifications and early operational use. The early, joint part of the trial was flown using two pilots.

Approval of the cockpit modifications was done without the benefit of formal airworthiness requirements, purely on an 'engineering judgement' basis, which was deemed adequate within the context of a limited trial closely controlled by the operational procedures applicable to police operations. Nevertheless a subjectively good standard of cockpit compatibility was achieved but the process was lengthy and involved considerable discussion, highlighting the need for Airworthiness Requirements to simplify both design and certification of such systems.

Initial operating rules and crew training and qualification standards were established as a result of the initial joint CAA/Police part of the trial. These, combined with the airworthiness approval of the cockpit, allowed Devon and Cornwall Constabulary to continue the trial on an operational basis to assess fully the benefits of NVG use to their type of operation over a prolonged period of time without direct CAA involvement. The basic operational/airworthiness framework that was agreed had the following features:-

- Operations covered by Police Air Operators Manual, i.e. some alleviation and special provisions given against normal Public Transport provisions.
- Permissible crew compliment of one pilot and one specially trained police observer with crew duties defined.
- Agreed standard of pilot/observer training.
- Minimum Transit Height for NVG use of 500 feet above ground level.
- No reduction in weather minima already established for normal night operations.
- No take off and landing permitted using NVGs.
- Mandatory Radio Altimeter, with low height warning system.
- Flight Manual Supplement to detail limitations and procedures, e.g. NVG failure.
- Specified type of Night Vision Goggle.

The trial amassed a significant amount of NVG experience throughout the Devon and Cornwall geographic area. This area consisted of a mix of urban and rural areas, including very dark areas with little cultural lighting and also a considerable amount of coastline. Varied mixes of light conditions, both natural and cultural, and of ground texture were experienced within the context of a variety of police operational tasks. The types of task carried out included training, transit, location of 6 figure grid reference points, orbiting for search purposes, high (500 – 800ft) hovering and vehicle following. This experience allowed Devon and Cornwall Police to write a report assessing the benefits to police operations and to identify any issues associated with NVG operations.

The report concluded that the use of NVGs provided a benefit to Devon and Cornwall Police operations. It is beyond the scope of this paper to present the benefits to police operations but the general experience gained relevant to airworthiness issues is described below.

3.1 Cockpit Lighting/Compatibility

The cockpit lighting was found to be generally satisfactory. Particular points identified were the importance of the additional low height warning light coupled with the radio altimeter, some difficulty with

differentiation of colour on gauges and the need to fit removable Fire Warning Light filters for NVG use. The latter was because it had not been possible to achieve adequate daylight readability with NVG filtered Fire Lights, resulting in the filters having to be removed for day use. A longer term solution of possibly combining filtered lights with audio fire warning was suggested, to avoid the configuration change.

3.2 Night Vision Goggle Equipment

The NVGs used had proven to be reliable. Attention was drawn to the need for separate battery power supply for each tube, to reduce the probability of total goggle failure. Battery management was highlighted as an important issue to avoid in-flight failures and a method for recording operating time for individual batteries was suggested.

The importance of correct helmet fitting and use of a counterbalance in order to provide a stable platform for the goggles were points highlighted, together with the importance of correct pre-flight goggle adjustment.

3.3 Crew Compliment

It was considered that the combination of pilot and specially trained police observer was appropriate and that Crew Resource Management had been an important part of training.

3.4 Hazards

Some potential hazards were identified with suggestions to minimise these.

Depth Perception was a problem in areas of poor texture, highlighting the importance of the radio altimeter and low height warning system. Judging horizontal clearance was also difficult, e.g. when operating close to cliffs. A means around this was to use a horizontal reference such as the tide line on the beach but the problem was perceived as being similar to the difficulty with depth perception.

In the event of a partial, i.e. single tube, goggle failure, continued flight was considered acceptable although uncomfortable, but would be an adequate means to fly the aircraft to an area 'where conventional night flight could be better carried out'.

To allow for continued flight in the event of goggle failure, it was emphasised that weather minima should not be reduced for NVG operations, although it was suggested that this might be possible in areas of high cultural lighting. The need for the pilot to continually make an assessment of the weather/visual cues that would be available for non-goggle flight was highlighted.

Some concern was raised about the effect of goggle and counterbalance weight on the helmet in the event of an accident. The need to be able to remove the goggles quickly was identified and it was recommended that this be done prior to an accident where possible. The problem with this action however, would be the consequent loss of vision that could make an accident more likely, i.e. in the event of total power loss and engine off landing. In this case, even though there would be the chance of a heavy landing, or roll over, with a likelihood of additional injury caused by the weight of the goggles/counterbalance, continued use of the goggles to touchdown could significantly increase the probability of a safe landing being achieved. The report concluded that any additional risks associated with the additional weight seemed acceptable in the context of other perceived safety benefits, but it does highlight the aeromedical issues of NVG use.

4. Background To The Development Of The Requirements

Some nations do not exercise control of police operations through their Civil Aviation Authority, using instead a system of "State" control which has more in common with military methods of control and approval. However, for nations who control such activities through their Civil Aviation Authority, including the UK, there is a need for appropriate Night Vision Goggle airworthiness and operational rules to be developed.

In the UK, the Civil Aviation Authority took the view that the NVG proof of concept trial, using the BO105, should be considered complete when the aircraft was retired from service in 1998. Consequently, any clearance of an NVG modification to any other aircraft, including the Devon & Cornwall Constabulary's BK117 to replace the BO105, should only be made against formally developed requirements. The trial had demonstrated a benefit to police operations and it was apparent that there was a continuing need for NVGs. Hence, it was considered appropriate to develop formal requirements to support the use of civil NVG operations.

Nevertheless, NVGs are highly specialised equipment and the CAA had no prior experience of their use by flight crew on civil aircraft. Although the CAA had some pilots with military NVG experience, the task of developing requirements was large and the likely timescale, due to other commitments, was inconsistent with the operational need.

However, the Police Constabulary Air Support Unit were able to enlist the support of the Home Office, the British Government Department responsible for the Police. The Home Office agreed to provide financial support to enable the CAA to contract an outside agency, with NVG experience, to provide advice on the development of the airworthiness requirements and thereby assist the Authority to produce appropriate requirements more quickly than would otherwise be possible.

Hence, the CAA prepared a project specification and invitation to tender and undertook to conduct a technical evaluation of the bids received, recommend who would be the most suitable contractor, manage the project and,

following its completion, review the project's findings and produce formal draft requirements.

The project specification outlined the objectives and scope of the project as follows:

- To determine the airworthiness and operational factors influencing the safe, reliable and effective use of NVGs and to evaluate their significance.
- To recommend airworthiness requirements and supporting guidance material for the approval of civil helicopter NVG operations.

Whilst the project would also identify the operational issues and risks of civil helicopter NVG operations, the primary aim was to develop *airworthiness* requirements, in the light of the operational issues identified.

The project was to include a search and review of all relevant literature, together with a review of the currently acquired experience of the use of NVGs to determine the factors pertinent to the formulation of the requirements and any necessary guidance material. A review of all available military certification requirements and an assessment of their applicability for civil operations was also to be included. One example of such a document is the US Military Specification "Lighting, Aircraft, Interior, Night Vision Imaging System (NVIS) Compatible" MIL-L-85762A (August 1988) (Ref 2) which addresses the issue of cockpit lighting compatibility.

Following the issue of an invitation to tender, five proposals were received and the contract was awarded to GKN Westland Helicopters Ltd. The study was duly completed and a number of findings and recommendations were made which covered the following main issues:

- Lighting Compatibility
- Low Height Warning System
- Equipment Specification
- Ergonomics
- Aeromedical Considerations
- Flight Manual Supplement
- Operational Considerations

These issues are described in more detail in the following section.

5. Outline Of The Draft Requirements

In order to maintain an adequate level of safety, it is essential that during NVIS operations, continued compliance with the existing Airworthiness Requirements JAR 29 & 27 (Refs 1 & 3) is demonstrated. The findings of the study described above were used to formulate additional airworthiness requirements and advisory guidance material to support the approval of civil helicopter NVG operations and maintain the levels of safety achieved during normal aircraft operation.

The findings and recommendations from GKN Westland Helicopters Ltd were reviewed and refined by the CAA Flight Department to produce "Draft Airworthiness Requirements For Aircraft Equipped For Operations Using A Night Vision Imaging System (NVIS)". This material specifies additional requirements and limitations for aircraft equipped with NVIS. The requirements are intended to be generic and apply to any NVIS. To date, however, their application has been limited to Night Vision Goggles and it is accepted that they may need to be expanded for some alternative NVIS types.

In keeping with the existing airworthiness requirements, the NVIS requirements are broadly objective, to encompass changing technology, whilst supporting advisory material is also provided that is more detailed and identifies an acceptable means of compliance. The advisory material is referred to as ACJ (Advisory Circular Joint) material in line with the typical Joint Aviation Requirement (JAR) format.

The NVIS Airworthiness Requirements(AR) 1-13 are presented in full in Appendix 1, but each rule is discussed briefly below. It should be borne in mind that these are draft requirements subject to further consultation and the content could change in the event of justifiable commentary on them and experience gained from their application.

AR1 General

(a) **This appendix specifies additional requirements and limitations for aircraft equipped with an NVIS.**

This rule is self-explanatory.

(b) **The minimum standard of aircraft to which an NVIS will be applied shall be multi-engined and certificated for single or dual pilot IFR, non-NVIS night operations.**

Because of the possibility of operations with very restricted visual cues, and taking into account as background information the generalities of the ADS33D type handling qualities criteria (Ref 4) developed in recent times, it was considered that an appropriate level of aircraft stability and control would be that required for IMC flight.

Multi-engined aircraft were considered appropriate to reduce the probability of a power off landing having to be carried out, and these aircraft being mostly Category A, have higher performance and systems integrity standards.

(c) **NVIS operations must not affect continued compliance with the basic aircraft certification basis.**

It was considered that there was no logical reason for compromising the basic airworthiness standards that would apply for normal night flying, when considering NVIS approval. The appropriate JAR, FAR and British

Civil Airworthiness Requirements (BCAR), Section G (Ref 5) should continue to be met, e.g. colour differentiation of gauge markings.

(d) **NVIS operations must be possible without exceptional pilot skill or alertness.**

This rule is intended to avoid unusual complexity or difficulty in carrying out normal and emergency tasks whilst using NVIS.

AR2 **Lighting Compatibility**

(a) **Continued compliance with Paragraph .1381 of the appropriate JAR must be demonstrated, during NVIS operations.**

(b) **Any light emitted from equipment, in either the cockpit or the cabin, during NVIS operations, must be compatible with the NVIS.**

(c) **Any subsequent cockpit, cabin or external modification, including role equipment, involving a light emitting or reflecting device will require re-assessment.**

These rules are intended to ensure that there can be no light sources within the cockpit that could cause a degradation of NVIS performance. This is primarily to avoid a hazardous situation due to the illumination of unfiltered lights that could cause sudden loss of external view.

The Advisory Material suggests, in some detail, a possible test methodology that can be used to demonstrate compliance with these rules.

AR3 **Warning, Caution and Advisory Lights**

(a) **Continued compliance with Paragraph .1322 of the appropriate JAR must be demonstrated, during both NVIS and non-NVIS operations.**

This rule is intended to ensure that the pilot can still differentiate quickly and accurately between the Warning, Caution and Advisory lights displayed by the aircraft's warning system.

It is accepted that it may not be possible to use the original colours but nevertheless, reds and ambers must be identifiable as such, and clearly differentiated from each other and whatever advisory colour is used.

The overall attention getting capabilities of the warning system should not be degraded by the NVIS installation. Any degradation of the visual attention getting capabilities would need to be compensated by, for example, an audio warning system.

The guidelines of Military Specification MIL-L-85762A, Section 3.10.9.8 are suggested in the advisory material as a means of compliance.

AR4 **Instrument Lights**

(a) **Continued compliance of the NVIS compatible instrument lighting with Paragraph .1381 of the appropriate JAR must be demonstrated during non-NVIS operations.**

It would be possible that measures taken to ensure NVIS compatibility could affect adversely normal usage of the cockpit. This rule is intended to ensure that normal daylight and non-NVIS night use of the cockpit is not compromised. This would include the transition from day into night flight when it can be difficult to achieve an acceptable solution, e.g. for Central Warning Panel brightness.

AR5 **Dimming Levels**

(a) **The cockpit lighting must have a dimming range consistent with NVIS operations.**

The rule is self evident, but advice is given in the advisory material to help achieve an acceptable brightness level for day, non-NVIS night and NVIS operation. The advisory material assumes that conventional lighting will be available for non-NVIS night flying, however it is conceivable that only one lighting system would be fitted, i.e. an NVIS compatible system which, by definition, is viewed by the naked eye and also has to comply with normal night lighting standards. The advisory material is not intended to prevent the provision of an NVIS compatible lighting system only.

(b) **Inadvertent selection between Day, Night and NVIS modes must be prevented.**

The consequences of inadvertent selection of non filtered light could be severe. Again an assumption that there will be both conventional and NVIS compatible lighting in the cockpit is made, and equally, such provision is not mandatory. The advisory material suggests some means of switching which first requires a positive action, to minimise inadvertent selection.

AR6 **Chromaticity and Radiance**

(a) **The chromaticity of the light sources in the cockpit and cabin must be sufficiently separated to ensure colour coding discrimination is maintained.**

(b) **The radiance of the light sources in the cockpit and cabin must be compatible with the selected NVIS.**

These rules use the guidance of Sections 3.10.8 and Sections 3.10.9 and Appendix A of MIL-L-85762A to provide advisory chromaticity and radiance limits for cockpit and cabin light sources for a range of NVIS types. Using light sources which meet this standard is an acceptable means of compliance with the above requirement.

AR7 External Lighting

(a) External lighting systems must not unacceptably impair the performance of the NVIS.

This rule is self evident, but more relevant to civil operations than military. Civil aircraft are required to display the appropriate lights at all times whereas military aircraft will often operate lights-out for tactical reasons. The advisory material proposes a qualitative evaluation during flight trials.

(b) **Continued compliance with Paragraphs .1383 to .1401 of the appropriate JAR must be demonstrated.**

This rule requires that any external lights fitted, even though modified to minimise NVIS interference, must still meet the relevant existing requirements.

AR8 Low Height Warning System

(a) A radio altimeter display must be installed at every pilot's crew station from which NVIS operations are to be flown.

The fitted radio altimeter should have the following characteristics:

1) A display that is instantly visible and discernible during NVIS operations.

2) An expanded scale below 1000ft.

3) An integral fail/no track indicator.

4) An integral low height indicator light.

(b) If the cockpit has an EFIS or similar electronic displays, with an electronic radio altimeter presentation, then an additional visual low height indicator must be fitted to the instrument panel.

(c) An unambiguous supplementary visual low height warning, that is discernible during head-up NVIS operations, must be fitted at every pilot's crew station from which NVIS operations are to be flown.

(d) An unambiguous indication of radio altimeter fail, or no track within normal operating range, in addition to that provided by existing instrumentation, must be fitted at every pilot's crew station from which NVIS operations are to be flown.

(e) The luminous area of the supplementary low height repeater light, additional low height indicator light (EFIS if applicable) and radio altimeter fail/no track light (if applicable) must be such that each is clearly visible under all the conditions of flight in which the aircraft is cleared to fly.

(f) The operation of any repeater lights must follow the logic of the installed radio altimeter, and must not flash.

(g) An unambiguous low height audio cue must be fitted, which is readily cancellable.

Night vision systems do not currently give adequate height perception in all conditions of light and ground texture. There is a high probability of encountering conditions that will result in a lack of height awareness by the pilot and a real probability of the aircraft flying into the ground, even when operations are not intended to be carried out at very low heights. It can be very easy to lose 500ft from a nominal operating height (of say 500ft), either due to a descent, or more likely, featureless rising ground. For this reason, it is considered essential that an adequate height reference system, with associated unambiguous warnings of low height and system failure, is provided to ensure safety of flight using NVIS.

The importance attached to this is reflected by the detailed rules and associated advisory material. The effect of these rules is to require at each pilot's crew station an analogue radio altimeter with easily readable scale, repeater low height warning lights, radio altimeter no-track and fail warning lights and an unambiguous audio warning of low height.

AR9 Wire Strike Protection

(a) A wire strike protection system (WSPS) must be fitted to all helicopters cleared for NVIS assisted take-off and landing operations.

This rule could be considered to be operational rather than airworthiness, and may be removed from these airworthiness rules. Currently, no request has been received for NVIS certification for take-off and landing.

AR10 Equipment Specification

(a) The NVIS must be of a kind and design appropriate to its intended function.

This rule allows investigation of the suitability of any proposed NVIS. The advisory material makes recommendations as to NVIS characteristics, but rests heavily on MIL-L-85762A as being an established and accepted standard. Generation III, Type I or II Class B NVIS as defined in MIL-L-85762A, are proposed as the target standard equipment for civil applications.

It is arguable that a dedicated civil standard, such as a Technical Standard Order (TSO), should be created to define minimum NVIS standards, particularly in relation to reliability, as integrating military and civil requirements can be difficult and there is little control over any changes that might be made to military specifications.

(b) **The NVIS equipment and installation must comply with JAR 29.1309 Category A Requirements.**

This rule is intended to ensure that the view outside the cockpit through the NVIS is provided with an adequate certainty of being maintained. The advisory material states that "the NVIS equipment and installation should be subjected to a system safety analysis in accordance with AMJ 25.1309. The loss of external view due to either goggle failure or interference by cockpit lighting is potentially Hazardous and appropriate consideration must be given to this functional failure in the system safety analysis carried out".

(c) **Instructions for the Continued Airworthiness of the NVIS must be established.**

It is important that the originally certificated NVIS standard is maintained in service. Of particular importance is the management of battery life, if this is the chosen power source. Battery failure probably represents the highest risk of goggle failure in flight and adequate means must be proposed to ensure that the probability of failure is low enough to comply with AR10(b).

AR11 Ergonomics

(a) **The NVIS configuration must not compromise the wearer's ability to perform normal duties.**

(b) **Where the NVIS assembly constitutes an additional fit to the protective helmet (i.e. it is not integrated with the protective helmet) a fast removal mechanism must be provided.**

(c) **A fixed stowage receptacle, able to contain the NVIS and batteries (where applicable), must be provided within reach of the crew while strapped in.**

The ergonomics issues are fairly self evident but a requirement to cover these aspects helps to avoid unsuitable situations being presented for certification. A key issue here is the amount of available headroom to allow adequate head movement and the ability to hinge the goggles into the up position. The advisory material makes several recommendations on ergonomic issues to ensure easy operation when using NVIS.

The fast removal and goggle stowage requirements are intended to allow for the emergency landing case when the crew may wish to remove their goggles before landing. The stowage also prevents loose goggles becoming a hazard during normal (non-NVIS) operations.

AR12 Aeromedical Aspects

(a) **The NVIS configuration must minimise the risk of impact injury to the wearer.**

(b) **The total mass of the head-borne NVIS assembly must not exceed 3.0 kg. If the total mass of the head-borne NVIS assembly exceeds 2.5 kg, human factors monitoring will be required.**

(c) **The centre of gravity (C of G) of the total head-borne assembly must be as close as possible to the natural centre of gravity of the wearer's head.**

The aeromedical rules above are intended to minimise the probability of injury during accidents and also during normal NVIS use. The advisory material discusses the relative merits of frangible and non-frangible mounts for goggles but recognises that there is no clear answer on this subject. The head-borne weight limit is based on current military advice, as is the rule and advisory material relating to centre of gravity.

AR13 Flight Manual Supplement

(a) **A specific NVIS supplement must be incorporated into the appropriate Aircraft Flight Manual.**

It is considered that a Flight Manual Supplement must be provided to cover an NVIS modification and subsequent use. The Flight Manual Supplement should, as a minimum, address Limitations as specifically agreed between the Authority and the Operator such as minimum heights, types of operation, internal and external lighting configuration for NVIS operation, minimum equipment and minimum crew. Also included should be the procedures for emergencies and malfunctions, including NVIS failure, normal procedures and some descriptive material covering the NVIS and it's intended operation.

6. European/International Perspective

The NVIS requirements described above were prepared by the CAA in response to a specific and pressing need to generate requirements for the approval of aircraft and equipment for NVG operations in the UK. As a result, the UK CAA acted unilaterally in the first instance to produce NVG requirements. However, Police and Emergency Medical Service NVG helicopter operations are being conducted in some other JAA States and the FAA have also had a similar pressing need to approve NVG operations for EMS operators and have only recently certificated civil NVG operations.

Consequently, the JAA and FAA have now begun discussing the issue of NVG requirements in the Helicopter Joint Harmonisation Working Group with the intention of producing harmonised airworthiness rules.

The FAA have produced airworthiness material largely based on advisory circular (AC) material. An initial comparison of this material with the UK CAA requirements has shown a large degree of commonality in

objective, but with a different emphasis in the role of advisory material versus requirements. It is our intention that the requirements will ultimately form a Notice of Proposed Amendment (NPA) to JAR 27 & 29 but the precise method of promulgation has yet to be decided. A specific meeting to debate the issues and progress the task of producing harmonised NVG airworthiness material has been arranged with the FAA and is timed to coincide with a US Night Vision Conference to be held in October 1999. Significantly, this conference includes a civil night vision workshop which reflects the increasing interest now being shown in the application of night vision equipment for civil flying operations. Completion of the harmonisation process, in due course, will result in agreed airworthiness material available for use by both the JAA and FAA.

A parallel exercise is also ongoing to develop harmonised operational rules and it is intended that an appendix covering NVG operations will form part of JAR-OPS 3 (Ref 6).

7. Conclusion

In response to increasing interest in using Night Vision Goggles for specialist civilian tasks, the UK CAA has developed "Draft Airworthiness Requirements For Aircraft Equipped For Operations Using A Night Vision Imaging System (NVIS)". The requirements were produced following a proof of concept trial and a contracted study to determine all the factors influencing the safe, reliable and effective use of NVGs and their significance for the approval of civil helicopter NVG operations. Consequently, the requirements address the significant airworthiness issues and provide a firm framework for the assessment of aircraft equipped for NVG operations. The requirements are currently being used to approve an NVG modification to a BK117 for police operations. Police and Emergency Medical Service NVG helicopter operations are being conducted in some other JAA States and recently also in the US. Consequently, the JAA and FAA have now begun discussing the issue of NVG requirements with the intention of producing harmonised rules. The UK CAA draft airworthiness requirements will provide a significant input to this process.

8. Acknowledgements

The authors wish to acknowledge the valuable assistance provided by the following individuals and companies: Capt P. Hannant, formerly Air Support Manager of the Devon & Cornwall Constabulary Air Support Unit; Capt P. Ashby, Chief Pilot, Devon & Cornwall Constabulary Air Support Unit; Capt M. Kenworthy, Police Aviation Adviser, Home Office; Mr C. Kitchen, General Manager, Applied Military Optics (a Division of Mann Avionics Ltd); Mr A. Scott, Avionic Systems, Marconi Electronic Systems; Mr B. Thomson, Oxley Avionics (a Division of Oxley Developments Company Ltd); and GKN Westland Helicopters Ltd.

9. References

1. Anon, Joint Aviation Requirements, JAR-29, Large Rotorcraft.
2. Anon, US Military Specification "Lighting, Aircraft, Interior, Night Vision Imaging System (NVIS) Compatible" MIL-L-85762A, August 1988.
3. Anon, Joint Aviation Requirements, JAR-27, Small Rotorcraft.
4. Anon, Aeronautical Design Standard ADS-33D, Handling Qualities Requirements for Military Rotorcraft, USAATC, July 1994.
5. Anon, British Civil Airworthiness Requirements, Section G Rotorcraft, Civil Aviation Authority, August 1982.
6. Anon, Joint Aviation Requirements, JAR-OPS 3, Commercial Air Transportation (Helicopters), February 1999.

AIRWORTHINESS REQUIREMENTS FOR AIRCRAFT EQUIPPED FOR OPERATIONS USING A NIGHT VISION IMAGING SYSTEM (NVIS)

1. Assumptions

1.1 Whilst it is acknowledged that both safety and operational benefits can be derived during NVIS operations, nevertheless in some circumstances NVIS operations could carry an increased risk. These requirements have been written to minimise any potential risks. Employment of NVIS will enhance but not replace normal night VMC operations. In the event of a failure of the NVIS, a pilot must be able to revert to normal night VMC techniques.

1.2 "Lighting, Aircraft, Interior, Night Vision Imaging System (NVIS) Compatible" MIL-L-85762A (August 1988) guidelines will apply as a strategy to overall NVIS compatibility. This is a minimum requirement and if the applicant can demonstrate an improved capability this will be acceptable to the Authority.

1.3 These generic requirements are intended to apply to any NVIS. To date, however, their application has been limited to Night Vision Goggles (NVG) and the requirements may need to be expanded for some alternative NVIS types.

1.4 Pilots involved with NVIS operations will be qualified on type, and be current at non-NVIS night flying in accordance with current regulations.

1.5 NVIS operations may be approved for all flight regimes.

1.6 Exacting standards for all aspects of NVIS application, based on current military experience, will be applied to the civil regulations since safety is regarded as paramount.

2. Glossary of Terms

ACJ	Advisory Circular Joint
AMJ	Advisory Material Joint
AO	Atlanto Occipital
C of G	Centre of gravity
CWP	Central Warning Panel
EFIS	Electronic Flight Instrument System
EO	Electro-optic
GEN (I, II or III)	Generation (1, 2 or 3) of Night Vision Imaging System
JAR	Joint Aviation Requirements
NVG	Night Vision Goggles
NVIS	Night Vision Imaging System
Rad alt	Radio Altimeter
WSPS	Wire Strike Protection System

3. *Airworthiness Requirements*

AR1 General

(a) This appendix specifies additional requirements and limitations for aircraft equipped with an NVIS.

(b) The minimum standard of aircraft to which an NVIS will be applied shall be multi-engined and certificated for single or dual pilot IFR, non-NVIS night operations.

ACJ Material

The stability and control requirements for flight in IMC are required to be met. Under single pilot operations, the pilot must be able to remove his hands from the controls in order to be able to adjust or remove the NVIS, or change power sources in the event of a power failure. In the event of a failure of the NVIS, the pilot may require current instrument flying skills to maintain safe flight of the aircraft.

(c) *NVIS operations must not affect continued* compliance with the basic aircraft certification basis.

ACJ Material

Many of the existing basic airworthiness requirements are equally applicable to NVIS operations and compliance with these requirements must be maintained. Applicable paragraphs of the appropriate JAR include .771, .773, .1301, .1309, .1321, .1322 and .1381. FAA Advisory Circular AC 20-88 "Guidelines On The Marking Of Aircraft PowerPlant Instruments (Displays)" is also applicable.

(d) NVIS operations must be possible without exceptional pilot skill or alertness.

ACJ Material

Consideration should be given to the workload required to control the aircraft and it's systems during NVIS operations. Where possible, control functions associated with all other aircraft systems should be simplified to take account of NVIS operations.

AR2 Lighting Compatibility

(a) Continued compliance with Paragraph .1381 of the appropriate JAR must be demonstrated, during NVIS operations.

(b) Any light emitted from equipment, in either the cockpit or the cabin, during NVIS operations, must be compatible with the NVIS.

(c) Any subsequent cockpit, cabin or external

modification, including role equipment, involving a light emitting or reflecting device will require re-assessment.

ACJ Material

The applicant should ensure compliance by applying the NVIS test methodology described below.

NVIS Installation Test Methodology

Stage 1 Prior to fitting to an aircraft, any NVIS compatible equipment should be viewed in a dark room facility with the selected NVIS. During this assessment any unfiltered light will be detected and the effect of the lighting on the performance of the NVIS will be established. The testing should be carried out by suitably qualified engineers who have experience of NVIS compatible lighting and who are able to recognise the full range of effects due to unfiltered light sources.

Testing of permanently installed NVIS filtered equipment should include assessment of readability under simulated bright sunlight.

Stage 2 Following build of the aircraft, or modification, the aircraft transparencies are blacked out to simulate a dark night ambient lighting condition. The whole cockpit lighting installation, and where applicable, cabin/equipment lighting can then be assessed for:

a) readability of instruments, controls and displays.
b) lighting balance of self illuminated equipment panels and displays.
c) attention getting/brightness/balance of warning and caution indicators and the CWP.
d) the effect of reflections in the transparencies on the view out of the cockpit.
e) compatibility with the selected NVIS.
f) the effect of reflections on the selected NVIS.
g) cockpit ergonomics.

Stage 3 With the transparency blackouts removed, the readability of the permanently NVIS filtered equipment should be assessed under simulated bright sunlight or natural bright sunlight when available. (Bright sunlight equates to a level of 100,000 lux measured on the surface of the equipment under test).

Stage 4 To reduce the risk of failure during flight trials the installation should be assessed in accordance with the 'Lighting System NVIS Compatible Examination' methods specified in Sections 4.8.2 of MIL-L-85762A, August 1988 (or its successor, as agreed by the Authority).

Stage 5 The tests detailed in stages 2 and 3 should be repeated during day and night flight in the aircraft's typical operating environment over the extremes of range of natural light levels caused by cloud cover, sun elevation, moon phase and elevation.

For any 'additional' cockpit, cabin or external modification involving a light emitting device, reassessment should begin at the appropriate stage above. For all changes to the cockpit configuration which include the addition of, or relocation of any device including non light emitting devices, such as straps, fire extinguishers, upholstery, clothing, carry-on equipment, etc., the operator should be aware that there is a potential impact on overall night vision compatibility, and therefore should carry out a cockpit assessment, as in stage 2 above.

Within the process described at stage 4 above, the applicant should demonstrate that cockpit transparency transmissivity does not significantly impair the performance of the selected NVIS.

For aircraft types which make provision for light tight barriers between cockpit and cabin (eg. double curtains), NVIS incompatible lighting in cabin equipment may be permissible. In such cases it will be necessary for the applicant to demonstrate the effective nature of the barrier and that the operating procedures which cover movement between the cockpit and the cabin are adequate to ensure unfiltered light does not enter the cockpit. Equally it will be necessary to demonstrate that light escaping from cabin windows has no effect on the cockpit NVIS. Such provision should be demonstrated under stages 4 and 5 of the testing methodology above.

AR3 Warning, Caution and Advisory Lights

(a) *Continued compliance with Paragraph .1322 of the appropriate JAR must be demonstrated, during both NVIS and non-NVIS operations.*

ACJ Material

It may not be possible to obtain fully compatible warnings (red) and cautions (amber) captions without compromising sunlight readability. The lighting level defined in Section 3.10.9.8 of MIL -L -85762A, August 1988 (or its successor, as agreed by the Authority) is designed to achieve a slight measure of incompatibility or flare in the NVIS, which provides a positive attention getting benefit, whilst not compromising the view out of the cockpit.

The overall attention getting capabilities of the warning system should not be degraded by the NVIS installation. Any degradation of the visual attention getting capabilities would need to be compensated by, for example, an audio warning system.

AR4 Instrument Lights

(a) Continued compliance of the NVIS compatible instrument lighting with Paragraph .1381 of the appropriate JAR must be demonstrated during non-NVIS operations.

ACJ Material

The most common method of ensuring NVIS compatibility is to place filters over light sources to prevent emission of light from the portion of the spectrum which is visible to

NVIS. Where NVIS filters are used, it is preferable that they remain installed for day, night and NVIS flight, in order to simplify testing and subsequent operational management of the aircraft. This prevents problems associated with stowages, loose articles, aircraft departing without filters fitted and filters falling off during flight.

Other methods of achieving NVIS compatibility include the use of:

Light emitting diodes
Electro-luminescent panel floodlighting
Incandescent floodlighting.

The lighting installation for non-NVIS operation should not be degraded by virtue of NVIS compatibility.

AR5 Dimming Levels

(a) The cockpit lighting must have a dimming range consistent with NVIS operations.

ACJ Material

NVIS equipment presents an image to an observer by intensifying light that is beyond the part of the spectrum visible to the naked eye. The term used for emitted energy is radiance and is equivalent to luminance when referring to visible light emitted directly from a light source. The term for visible light reflected from a surface is illuminance and the equivalent for reflected energy beyond the visible spectrum is irradiance. The term brightness is generally used to describe luminance and illuminance. Radiance and irradiance cannot be termed brightness as they are invisible to the naked eye. It is true, however, that a non-NVIS compatible light, emitting excessive radiance, will cause the NVIS to overload and present a bright image to the NVIS user.

To ensure that an illuminated aircraft installation is compatible with NVIS equipment it is necessary to filter out that part of the spectrum that the NVIS is intensifying, i.e. Infra-Red. If this is not adequately achieved the NVIS will effectively overload and the definition of the view out of the cockpit will be significantly degraded. However, the visible luminance and illuminance of the aircraft installation should be such that the pilot can view the instruments and controls, etc. when looking into the cockpit, under the goggles, with the naked eye.

Day, Night and NVIS Modes are defined as follows:

Day: Warnings and cautions are presented at full brightness. Instrument and panel lighting are extinguished.

Night: Warnings and cautions are presented at a brightness clearly discernible for night operation. If a dimming capability is provided, all annunciators, including master warning and caution, may be dimmable as long as the annunciation is clearly discernible for night operation at the lower lighting level. Undimmed annunciations have been found unacceptable for night operation due to disruption of cockpit vision at the high intensity. Instrument and panel lighting is variable from extinction to full brightness.

NVIS: Warnings and cautions are presented at a fixed luminance of 15 footlamberts (fL) which maintains attention getting capabilities whilst not degrading the operation of the NVIS, in accordance with Section 3.10.9.8 of MIL-L-85762A, August 1988 (or its successor, as agreed by the Authority). Instrument and panel lighting is variable from extinction to full brightness and any non-NVIS filtered equipment lighting is extinguished.

(b) Inadvertent selection between Day, Night and NVIS modes must be prevented.

ACJ Material

Selection between Day, Night and NVIS modes should be by a locked toggle, guarded pushbutton switch or any other mechanism which requires positive action.

AR6 Chromaticity and Radiance

(a) The chromaticity of the light sources in the cockpit and cabin must be sufficiently separated to ensure colour coding discrimination is maintained.

ACJ Material

If NVIS compatibility is being achieved by filtering existing light sources, then filters should be selected to ensure the desired colour separation. If NVIS compatibility is being achieved by installing intrinsically compatible light sources then the chromaticity co-ordinates need to have similar colour separation.

Sections 3.10.8 and Appendix A of MIL-L-85762A, August 1988 (or its successor, as agreed by the Authority) provides guidelines for the chromaticity of all cockpit and cabin light sources for a range of NVIS types. Using light sources which meet this standard is an acceptable means of compliance with the above requirement.

NVIS Class B standard cockpit lighting (as defined in MIL-L-85762A, August 1988 or its successor, as agreed by the Authority) is aimed at NVIS equipment with 665nm filters and will cause flaring of NVIS equipment filtered to a 645 nm cut off. However, experience has shown that this degree of NVIS flare has little effect on flight safety and therefore may not, as an isolated feature, render non compliant an applicant's solution to NVIS compatibility based on 645nm cut off filters.

(b) The radiance of the light sources in the cockpit and cabin must be compatible with the selected NVIS.

ACJ Material

Sections 3.10.9 of MIL-L-85762A, August 1988 (or its successor, as agreed by the Authority) provide the radiance limits for cockpit and cabin light sources for a range of

NVIS types. Using light sources which meet this standard is an acceptable means of compliance with the above requirement.

AR7 External Lighting

(a) External lighting systems must not unacceptably impair the performance of the NVIS.

(b) Continued compliance with Paragraphs .1383 to .1401 of the appropriate JAR must be demonstrated.

ACJ Material

If, during night flight assessment, as part of the NVIS installation test process, it is found that the performance of the NVIS is impaired by the external lights, it may be necessary to modify the external lighting installation to obtain compatibility.

External lights which are non-NVIS compatible are increasingly likely to cause unacceptable flaring as height is reduced. The lighting of ground support vehicles should be assessed if appropriate.

The addition of external reflective surfaces, such as a white aerial on a skid, may also affect NVIS performance and may be subject to flight test.

AR8 Low Height Warning System

(a) A radio altimeter display must be installed at every pilot's crew station from which NVIS operations are to be flown.

The fitted radio altimeter should have the following characteristics:

1) A display that is instantly visible and discernible during NVIS operations.

2) An expanded scale below 1000ft.

3) An integral fail/no track indicator.

4) An integral low height indicator light.

ACJ Material

Compliance with AR8(a)(1) would normally be expected by virtue of an analogue display giving both position and rate information.

(b) If the cockpit has an EFIS or similar electronic displays, with an electronic radio altimeter presentation, then an additional visual low height indicator must be fitted to the instrument panel.

ACJ Material

The visual low height annunciation provided by an EFIS display is unlikely to be as obvious as a discrete incandescent lamp. The additional visual low height indicator is intended to provide an equivalent standard to that provided by an analogue altimeter with integral low height indicator light.

The additional visual low height indicator should be fitted as close to the electronic radio altimeter presentation as possible, and in clear association.

The additional low height indicator is considered cautionary and should therefore be coloured amber accordingly. The NVIS YELLOW colour as defined in Appendix A of MIL-L-85762A, August 1988 (or its successor, as agreed by the Authority) is the closest approximation to this which retains a measure of NVIS compatibility.

(c) An unambiguous supplementary visual low height warning, that is discernible during head-up NVIS operations, must be fitted at every pilot's crew station from which NVIS operations are to be flown.

ACJ Material

A low height repeater light should be fitted on the instrument panel coaming, on the edge of the coaming closest to the pilot. It's position should be such that the pilot can always see the visual low height cue from the full range of seating positions and during all phases of flight.

The low height warning light is considered cautionary and should therefore be coloured amber accordingly. The NVIS YELLOW colour as defined in Appendix A of MIL-L-85762A, August 1988 (or its successor, as agreed by the Authority) is the closest approximation to this which retains a measure of NVIS compatibility.

(d) An unambiguous indication of radio altimeter fail, or no track within normal operating range, in addition to that provided by existing instrumentation, must be fitted at every pilot's crew station from which NVIS operations are to be flown.

ACJ Material

The warning(s) may be provided, depending on the aircraft configuration, by visual and/or audio means.

The rad alt fail/no track indicator is considered cautionary and therefore any visual indications should be coloured amber accordingly. The NVIS YELLOW colour as defined in Appendix A of MIL-L-85762A, August 1988 (or its successor, as agreed by the Authority) is the closest approximation to this which retains a measure of NVIS compatibility.

If the rad alt fail/no track indicator incorporates a light, then it should be co-located with the low height indicator on the instrument panel coaming in front of the pilot.

Confusion with the low height repeater should be avoided. This could be achieved by providing dedicated audio cues.

(e) The luminous area of the supplementary low height repeater light, additional low height indicator light (EFIS if applicable) and radio altimeter fail/no track light (if applicable) must be such that each is clearly visible under all the conditions of flight in which the aircraft is cleared to fly.

ACJ Material

Since viewing distances in cockpits vary, the size of an object is defined in terms of angle subtended at the eye. The accepted acuity angle subtended at the eye for warning indicators, based on human factors research and used to define MIL STD 1472D character sizes, is 6 milliradians. Allowing for the degraded vision offered by NVIS equipment, 10 milliradians is probably acceptable, but no data is available to prove it. Low height repeater lights fitted to current helicopters cleared for NVIS operations subtend up to 22 milliradians at the eye datum position.

(f) The operation of any repeater lights must follow the logic of the installed radio altimeter, and must not flash.

(g) An unambiguous low height audio cue must be fitted, which is readily cancellable.

ACJ Material

The pilot should be able to cancel the audio cue to allow crew inter communication. Cancelling the audio cue should not extinguish any low height visual indications.

Audio cues should be designed to be consistent with the overall aircraft audio cueing philosophy.

AR9 Wire Strike Protection

(a) A wire strike protection system (WSPS) must be fitted to all helicopters cleared for NVIS assisted take-off and landing operations.

ACJ Material

The most common form of wire protection system fitted to existing helicopters consists of an arrangement of wire deflectors and cutting devices such that wires are deflected to a cutting blade and severed before they can damage critical aircraft components. A general specification for a WSPS does not currently exist. The system selected should be based on a consideration of the wire threats within the intended sphere of operations.

AR10 Equipment Specification

(a) The NVIS must be of a kind and design appropriate to its intended function.

ACJ Material

Generation III, Type I or II Class B NVIS as defined in MIL-L-85762A, August 1988 (or its successor, as agreed by the Authority) should be the target standard equipment for civil applications. Class B NVIS equipment allows red to be used in the cockpit.

It is recognised that some commonly used NVIS do not comply with Class B requirements; however, experience of aircraft modifications has shown that a satisfactory level of compatibility can be achieved with such equipment. Where a class B NVIS is not available, compatibility with the cockpit installation should be demonstrated as acceptable by following the NVIS Installation Test Methodology as described under section AR2.

If an NVIS with combining optics is chosen, then no cockpit lighting to which the NVIS is sensitive should be visible when the pilot looks inside the cockpit. This may be achieved through the use of a head position sensor to occult the light sources when the pilot looks into the cockpit. The inter-ocular spacing and location of the Electro-optic (EO) sensors will be different from those of the pilot's eyes and will cause the EO image to appear displaced from the natural image. Alternatively, a means to automatically 'stop down' the NVIS when the pilot looks into the cockpit could be provided.

(b) The NVIS equipment and installation must comply with JAR 29.1309 Category A Requirements for helicopters (or JAR 25.1309 for aeroplanes).

ACJ Material

The NVIS equipment and installation should be subjected to a system safety analysis in accordance with AMJ 25.1309. The loss of external view due to either goggle failure or interference by cockpit lighting is potentially Hazardous and appropriate consideration must be given to this functional failure in the system safety analysis carried out.

(c) Instructions for the Continued Airworthiness of the NVIS must be established.

ACJ Material

Maintenance procedures should be specified and observed e.g. battery checks etc. The maintenance tasks should be included in the maintenance schedule of the aircraft as appropriate. General procedural instructions for equipment testing should be provided to prevent performance degradation which may become a source of hazard.

Appendix material to the appropriate JAR gives guidelines on the Continued Airworthiness information that should be determined.

AR11 Ergonomics

(a) The NVIS configuration must not compromise the wearer's ability to perform normal duties.

ACJ Material

The applicant should provide details of pilots' normal duties

and demonstrate that they can be carried out safely, with emphasis on the considerations listed below:

a) The NVIS configuration should allow full head movement commensurate with all aspects of anticipated operation. If a goggle type NVIS incorporating a hinging mechanism is used, this should include the case of the NVIS hinged into the up position. In order to ensure free head movement, adequate clearance with all structure, with the pilot sat at the eye datum position should be demonstrated. The applicant should ensure that pilots are able to locate and operate from the eye datum position defined by the aircraft manufacturer such that they are able to consistently repeat the same seat adjustment position. If this is not possible, or if specific pilots choose to fly from an alternative seating position, then the applicant should ensure that minimum clearances are not compromised for each pilot and that these pilots are able to consistently repeat the same chosen seat adjustment position.

b) The NVIS, should not impede the pilot's ability to scan the cockpit instruments.

c) The NVIS configuration should not prevent the pilot viewing the outside world with the un-aided eye.

d) The NVIS should not require continual adjustment in flight.

e) The NVIS should be easily removed and refitted during flight.

(b) Where the NVIS assembly constitutes an additional fit to the protective helmet (i.e. it is not integrated with the protective helmet) a fast removal mechanism must be provided.

ACJ Material

In the event of an emergency, the pilot may wish to remove the NVIS assembly to minimise the risk of injury in the event of a hard landing. The emergency removal method should facilitate this with a single action requiring one hand only.

(c) A fixed stowage receptacle, able to contain the NVIS and batteries (where applicable), must be provided within reach of the crew while strapped in.

ACJ Material

When the NVIS is carried in the aircraft but is not being used for NVIS operations, then it should be restrained in the event of an accident. The restraining system should meet the general specification for crash protection specified for that aircraft. A dedicated stowage is recommended, since it is more likely to remain uncluttered by other items. The design of the stowage receptacle should be commensurate with the need to protect delicate optical equipment but should also enable the NVIS to be quickly stowed. It should be possible to open and close the stowage compartment with one hand, using a single action.

If the pilot elects to remove the NVIS in an emergency situation, then locating the NVIS in a stowage receptacle is a reliable means of ensuring that the NVIS does not become loose in the cockpit. Since under emergency conditions, time and convenience are of the essence, the stowage receptacle should be positioned for easy access. Good accessibility will also benefit general usage under normal conditions.

AR12 Aeromedical Aspects

(a) The NVIS configuration must minimise the risk of impact injury to the wearer.

ACJ Material

The main form of impact injury will be to the face if the head-borne assembly rotates forward on the head as a result of an accident or hard landing. Other forms of injury could be incurred by a loose object in the cockpit in the event that the NVIS becomes detached from the helmet.

In selecting the NVIS type the applicant should consider the following factors:

Protective polycarbonate visors worn between the eyes and the NVIS lens are commercially available and will provide added protection to the pilot's eyes in the event of an accident. A protective visor should be considered for the selected NVIS where damage to the eyes or face is possible due to the NVIS design, and if used, should be worn at all times during NVIS operation.

If users are unable to wear a protective visor because of spectacles, the spectacles should be fitted with safety lenses.

The applicant should ensure that helmet fittings are performed with the NVIS attached, in order to minimise NVIS movement relative to the pilot's eyes.

The relative safety merits of frangible and non-frangible NVIS mounts used on NVG types are difficult to determine. There are differing perspectives on the subject. Military users in the UK wear non-frangible types which have the benefit of being less likely to be accidentally knocked off, as well as reducing the likelihood of a loose object hazard in the cockpit following a hard landing. Frangible types are used in the US, and US studies reviewing historical accident data claim evidence for reduced risk of neck injury with frangible mounts. The applicant is advised to consider these issues, particularly with respect to NVIS stowage if the pilot elects to remove the NVIS.

(b) The total mass of the head-borne NVIS assembly must not exceed 3.0 kg. If the total mass of the head-borne NVIS assembly exceeds 2.5 kg, human factors monitoring will be required.

ACJ Material

Any additional weight over and above that of the helmet is undesirable because of the muscular and skeletal loads

imposed on the neck in maintaining control over the head. These loads can result in both short and long term medical problems. Total head-borne mass is linked with weight distribution on the head as covered under requirement AR12(c). The aeromedical impact of increased weight on the head in fixed wing applications particularly under "g" loads is well known and is the basis for the target figure stated.

The total head-borne mass is made up of the protective helmet, any additional electro optical equipment, the safety visor and counterweight.

In exceptional circumstances, where total head-borne mass is permitted to exceed 2.5 kg, an annual human factors review will be required, particularly with respect to continued acceptance by the pilots and reported instances of medical related problems.

(c) The centre of gravity (C of G) of the total head-borne assembly must be as close as possible to the natural centre of gravity of the wearer's head.

ACJ Material

Centre of gravity of the total head-borne assembly is the primary factor associated with both long and short term neck strain injuries and is linked with total head-borne weight as covered under requirement AR12(b). In order to minimise strain on the neck, it is necessary to balance the head-borne mass about the natural C of G of the head. The moment induced by the head-borne assembly under static cases should not exceed 90 Newton.centimetres measured relative to the AO (Atlanto Occipital) complex. (Ref. US Army Aviation Life Support Equipment Retrieval Program: Head and Neck Injury Amongst Night Vision Goggle Users in Rotary Wing Mishaps. US Army Aeromedical Research Laboratory (USAARL), Fort Rucker (Report No USAARL 98-02, October 1997.)

In exceptional circumstances, where the above maximum is permitted to be exceeded, the situation should be periodically reviewed, particularly with respect to continued acceptance by the pilots and reported instances of medically related problems.

AR13 Flight Manual Supplement

(a) A specific NVIS supplement must be incorporated into the appropriate Aircraft Flight Manual.

ACJ Material

The Flight Manual Supplement should, as a minimum, address the following issues:

a) General.

b) Limitations: as specifically agreed between the Authority and the Operator.

1) Minimum heights.
2) Weather minima.
3) Internal lighting.
4) External lighting.
5) Minimum equipment.
6) Minimum crew

c) Emergency and malfunction procedures.

d) Normal procedures.

e) Manufacturer's supplementary information.

1) Technical description of the NVIS.
2) Operating procedures for the NVIS.

TWENTYFIFTH EUROPEAN ROTORCRAFT FORUM

Paper n° E3

A Study of the Flight Safety under IMC

BY

Y.KUMAMOTO, H.FUJIMOTO, T.AMANO, K.KOBAYASHI

ADVANCED TECHNOLOGY INSTITUTE OF COMMUTER HELICOPTER

SEPTEMBER 14-16, 1999
R O M E
ITALY

ASSOCIAZIONE INDUSTRIE PER L'AEROSPAZIO, I SISTEMI E LA DIFESA
ASSOCIAZIONE ITALIANA DI AERONAUTICA ED ASTRONAUTICA

A Study of the Flight Safety under IMC

Yuichi Kumamoto
Guidance Research Engineer

Hajime Fujimoto
Guidance Research Engineer

Takaki Amano
System Research Engineer

Keiji Kobayashi
Control Research Engineer

Advanced Technology Institute of Commuter helicopter LTD.
Kakamigahara City, Gifu-Pref. 504 Japan

1.ABSTRACT

Recently, accidents of small aircraft, especially that of helicopters, have been increased in Japan. The various reasons for that are supported. One of the most attractive and most important causes is an operation in bad weather (poor visibility). The cause can be divided into two cases, one is the loss of communications and his/her position during the unexpected rapid weather change, and the other one is the excessive workloads by the loss of visual cue (ex. Vertigo).

Under the above circumstances, the drastic improvement of the helicopter operations safety in bad weather has been researched and developed from 1994 to 2000 by ATIC (Advanced Technology Institute of Commuter helicopter Ltd.). Our goals are;

1. To improve the ability of instrument flight of helicopters.
2. To improve the ability of the IFR operations based on the future navigation systems with the Global Positioning System (GPS).

After introducing the outline of whole "Flight Safety study", this paper mainly describes the Automatic Flight Control System with DGPS helicopter precision terminal procedures to enable near zero-zero approaches to a hovering at heliports, including the recent result of flight simulation.

2.ABBREVIATIONS

ACAH Attitude Command Attitude Hold
ACC Actuator Control Computer
ADC Air Data Computer
AEO All Engine Operative
AI Attitude Indicator
ATC Air Traffic Control
ATIC Advanced Technology Institute of Commuter helicopter
BLD Balked Landing
CLD Continued Landing
CNS Communication, Navigation, and Surveillance
CP Collective Pitch
DGPS Differential GPS
DME Distance Measuring Equipment
FBW Fly By Wire
FCC Flight Control Computer
FD Flight Director
FMS Flight Management System
GPS Global Positioning System
IFR Instrument Flight Rules
IMC Instrument Meteorological Conditions
ILS Instrument Landing System
IRS Inertial Reference System
LDP Landing Decision Point
MFD Multi-Function Display
ND Navigation Display
OEI One Engine Inoperative
PFD Primary Flight Display
SID Standard Instrument Departure
SPICE Stick & Pedal Interface & Control Electronics
STAR Standard Instrument Arrival Route
TA Category A
VFR Visual Flight Rules
VMC Visual Meteorological Conditions
VOR VHF Omnidirectional radio Range

3. INTRODUCTION

3.1 Technical problem for helicopter IFR operation

Recently, though safety and dispatch reliability of the helicopter are taken seriously, the operation by the instrument flight is required in order to realize safety and reliability in which the helicopter is equivalent to the fixed wing aircraft. However, there is a CNS problem in present helicopter IFR system and especially, the technical problem have been left for the safe operation in bad weather.

1. It is difficult to operate IFR using the ATC from the ground in low altitude

because communication and radar system does not work at this region.

2. Present IFR systems and standards are for fixed wing aircraft, so they're not suitable for the IFR operation of the helicopter.
3. The IFR operation to a low altitude at the heliport is very difficult in present IFR system.

From such circumstances, the accidents also occur frequently because of sudden weather change in VFR operation (14 times for 12 years from 1985). Not only foregoing problem but also other problems such as noise and low dispatch reliability have been left in technical problem to be solved.

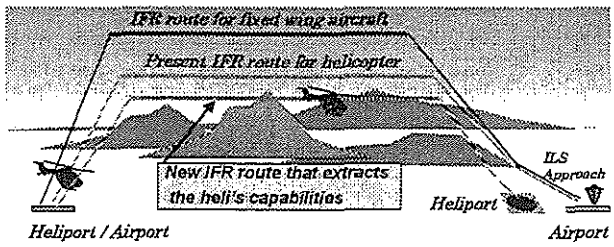

Fig. 1 Present helicopter IFR operation

3.2 Outline of ATIC

The Advanced Technology Institute of Commuter helicopter (ATIC) was established in March 1994 with investments from the Japan Key Technology Center (organization of the Ministry of International Trade and Industry and the Ministry of Posts and Telecommunications) to address these technical aspects of helicopter flight.

There are two research themes in the ATIC - noise reduction and flight safety improvement. ATIC Research Dept. No. 1 is undertaking research into external noise-reducing technology, while research into helicopter flight safety technology is being conducted by ATIC Research Dept. No. 2.

For flight safety, many researches have been executed and future air navigation system (FANS) using the GPS has been constructed in the world. The helicopter IFR operation using infrastructures such as GPS system has been also considered in Japan and it will be operated in early 21st centuries.

For the above circumstances, the ATIC research Dept. No.2 has studied the helicopter which can ensure safety and operation reliability under IMC by dividing the goal into two of "simplification of the navigation" and "simplification of the flight". In this paper, we describe mainly the simplification of the navigation.

We have studied the following technologies to reduce the pilot workload.

1. technology which accurately navigates the fixed flight path from the takeoff to the landing by manual operation and automatic operation.
2. technology that the pilot can intuitively recognize that the operation is rightly carried out.
3. technology which can display information effectively for pilot.

Research progress of the ATIC research Dept. No.2 is shown at table 1. The concept study was carried out in 1994, and the flight simulations were performed 8 times from 1995 to 1998. The ground test was carried out from 1998 to 1999 using hardware and software that will be actually used in flight test.

Table 1 ATIC schedule

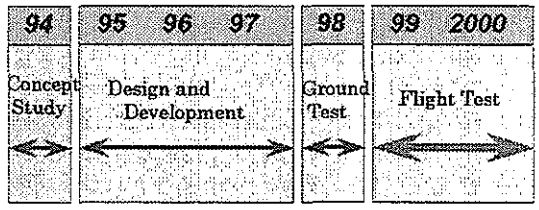

We briefly introduce the flight verification system, then describe the development of flight management system for civil helicopters, which reduce the pilot workload, including the results of the evaluations obtained using the latest flight simulations.

Fig. 2 The Flight Experiment Helicopter

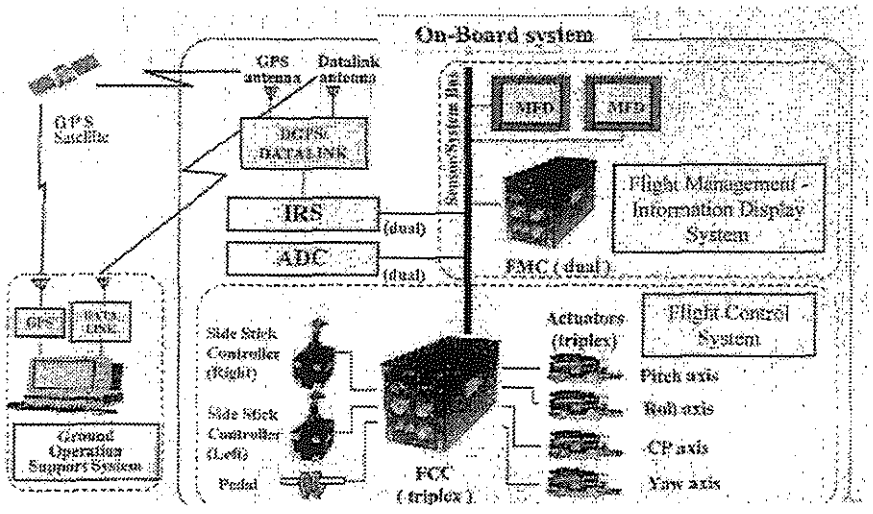

Fig. 3 Configuration of the On-board System

4. CONFIGURATION OF THE ON-BOARD SYSTEM

An overall configuration diagram for the on-board system is shown in Fig.3. The on-board system consists of a flight control system and a flight management - information display system. The flight control system is used to improve the flying qualities and simplify the control operation. This system utilizes a full-authority Fly-By-Wire (FBW) control system to achieve both the response required in Visual Meteorological Conditions (VMC) and high stability required for instrument flights under Instrument Meteorological Conditions (IMC). We can thus adopt sophisticated flight control laws, which enable great improvements in flying qualities. The flight management - information display system guides the helicopter and helps the pilot's judgments. The flight management computer guides the helicopter using positional information obtained from the Global Positioning System (GPS) receiver. In addition, during take-off and landing, the Differential GPS (DGPS) offers more accurate positional information by using compensation information obtained through a data link. With this information helicopter can track an accurate flight path that extracts the helicopter's capabilities, such as a curved approach and landing path. The automatic flight is carried out by linking the FMC and FCC. There are three flight control laws in FCC, RCAH (Rate Command Attitude Hold), ACAH (Attitude Command Attitude Hold), ACVH (Attitude Command Velocity Hold), and ACAH is used in automatic flight because it is the most stable control law in these laws. The navigation commands that calculated in FMC are transmitted to FCC and are transformed to the control commands. They're also transferred to SPICE for backdrive, the side stick moves under automatic flight as well as the case in which the pilot operates. So, the pilot can intuitively understand the condition of the control visually. And pilot can always do override under automatic flight when the pilot applies the force to the ASSC. The information display function helps the pilot make decisions by displaying information required during flight in an integrated and optimized form using two Multi-Function Display (MFD) units. Thus, the flight control system and the flight management - information display system together reduce the pilot workload in piloting and other non-piloting operations.

5. DEVELOPMENT OF FMS

5.1 Flight Management System

In the ATIC research Dept. No.2, the research has been studied on the problem of the navigation within the CNS problem. Concretely, the flight management system based on GPS or DGPS has been studied by changing system such as VOR/DME or ILS used at present. Especially, we have studied automatic flight to hovering and FD flight to LDP. The automatic flight is defined as a system for flying the designed flight path automatically by navigation command calculated in guidance function. In the meantime, the FD flight is

defined as a system for flying manually, while the pilot uses FD as a reference. The minimum height of FD flight is defined as a height of LDP considering the failures such as an engine failure under IMC. The minimum height of the automatic flight is defined as a height of hovering considering CAT III (near zero-zero approach) of fixed wing aircraft.

And we have researched not only flight management system, but also approach profile that extracts the helicopter's capabilities when the GPS is sanctioned as primary navigation mean.

5.1.1 Efficiency of FD flight and automatic flight

The effectiveness of these flights is divided into two cases whether the GPS is approved as primary navigation means or not.

The FD flight using the GPS is used as supplementary navigation means, when the GPS is not approved as primary navigation means, and the conventional route is used. The pilot workload is reduced, because a control is easier than usual method in this case. The flight safety is also improved by using the FD, because it is possible to move safely to the position where helicopter can be controlled from ground when weather changes rapidly from VMC to IMC. When the GPS is approved as primary navigation means in the FD flight, it is possible to reduce the pilot workload more and more in comparison with the case as mentioned by flying the GPS route and using DGPS on approach of which the high precision is required. Furthermore, it is possible to set the flexible flight route, because it is not necessary to use the ground navigation aids in the route setting. Operation reliability is also improved, because the navigation becomes possible to near LDP even in IMC. In addition, there is the possibility of the application by the low cost in comparison with the installation of the automatic flight, because there is no improvement of the flight control system such as the case of the automatic flight.

The advantage of the automatic flight in not approving the GPS as primary navigation means is equal to the application of the FD flight except that the navigational accuracy is improved.

Though it is also almost equal to the case of the FD flight in which the GPS is approved as primary navigation means, the operation reliability is improved more and more in comparison with the FD flight, because a helicopter is navigated to the hover in the automatic flight.

5.1.2 Details of the Flight Management System

Fig. 4 shows the block diagram of the flight management system. The guidance function is the most important in the flight management

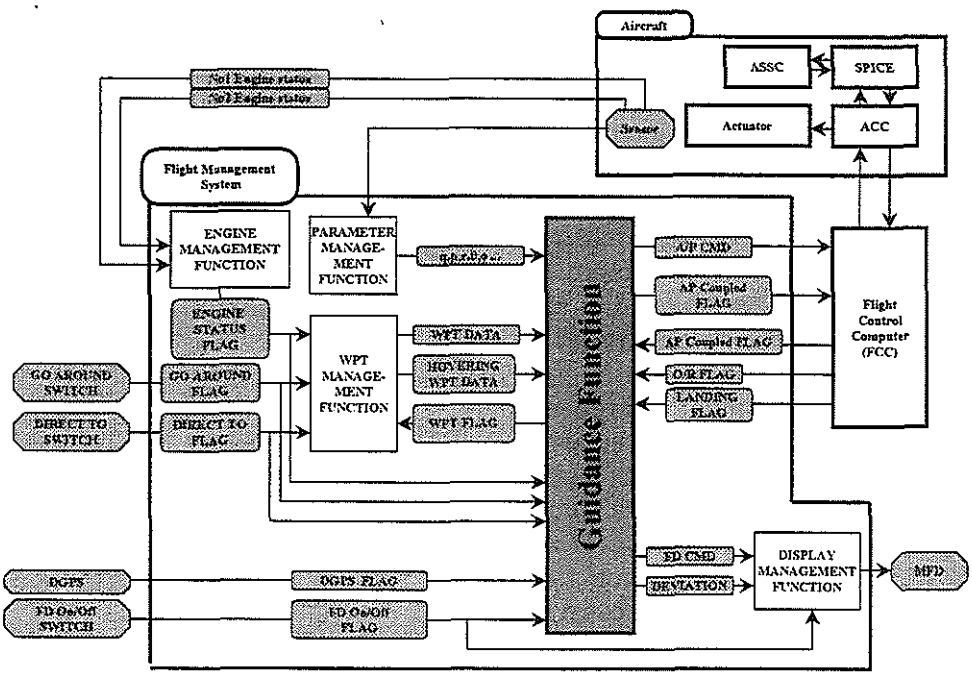

Fig. 4 Block Diagram of Flight Management System

system. And it is coupled to the flight control system, then FD flight and automatic flight are accomplished. There are four functions as other functions in flight management system. Engine failure control function watches the engine condition. Parameters control function watches the sensor conditions. Waypoint control function controls the waypoint used by the guidance function, and display control function controls outputs for display.

The guidance function judges the condition of the helicopter from the state flag (ex. Go Around flag) and waypoint data. And the guidance function adjusts the command gain necessary for calculating the navigation command. And the errors from the preset course are also calculated, and it is multiplied by command gain adjusted in advance, then the navigation command is created. The calculated errors are used for not only a calculation of the navigation command but also a decision of disengagement for automatic flight and changing the waypoint.

The guidance function is based on the traditional PID control to calculate the four axes navigation commands which are pitch attitude command (θ command), roll attitude command (ϕ command), yaw rate command(r command), and vertical speed command (H dot command) which are supplied to FCC (table 2). Those navigation commands are fed to actuators for automatic flight and to MFD for pilot FD manual flight.

Table 2 Navigation Command

Axis	Response Type	Reference		
		En-route Approach CLD	Hovering	BLD
Pitch	Attitude Command	Velocity Error	X Error	Velocity Error
Roll	Attitude Command	Lateral Deviation	Y Error	Lateral Deviation
Yaw	Rate Command	Heading Error		
CP	Rate Command	Height Error		Torque Error

5.1.3 Design of the approach profile

It is necessary to develop IFR operation ability by utilizing capabilities of the helicopter in order to improve the flight safety and dispatch reliability under IMC, and there are some problems to be solved for the IFR operation in approach and landing. These elements are concretely required.

1. It shouldn't interfere with the operation of fixed wing commercial aircraft around the airport, and it should be operated simultaneously.
2. The operation in the pinnacle heliport should be enabled.
3. Noise problem in the building roof operation in urban area or heliport operation should be overcome.

In this study, the course which combined an steep angle profile of 12 degrees considering low noise with the TA vertical take-off and landing approach profile was designed (Fig. 5).

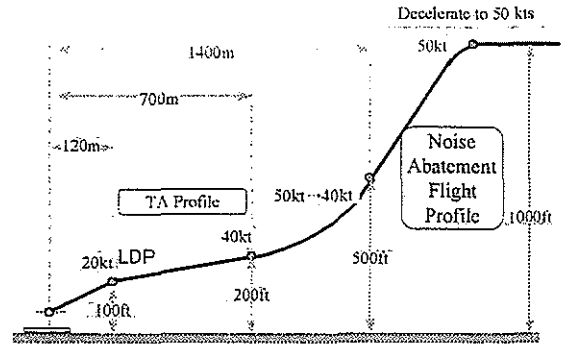

Fig. 5 Approach Profile

By flying at 50kt and -1000fpm, the region that is easy to generate slap noise is avoided under low-noise profile approach. The transition segment for connecting with the conventional TA profile is set after the low-noise profile end, and the speed is decelerated from 50kt to 40kt, and the height is also descended from 500ft to 200ft. It is similar to the TA profile after the transition segment end. This profile has been confirmed that it is available for the practical use by using actual helicopter (BK117).

Fig. 6 shows the comparison the above-mentioned flight path with the course in the ILS approach used in the conventional helicopter IFR operation. We see from fig. 6 that it is not necessary to operate in low altitude for long time if we use the new course, then it's possible to solve the noise problem very easily. And, it is also possible to prevent the interference of the fixed wing aircraft because the conventional ILS approach course can be avoided by flying this course. In addition, it is also possible to land on heliport and building roof in urban area where ILS has not been provided.

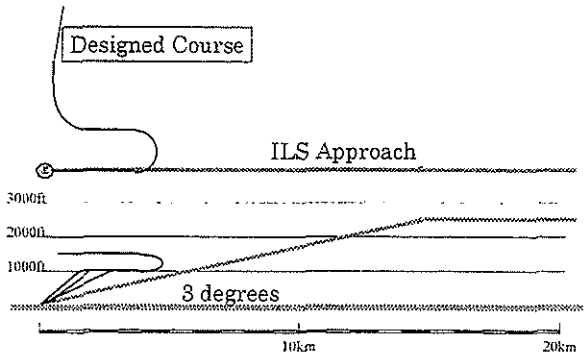

Fig. 6 Comparison with New App. and ILS

5.1.4 Design requirement of the guidance function

The design requirement of the guidance function for automatic flight is shown in table 3. These values are designed, as the error for automatic flights, without including the error of GPS and the accuracy of hardware. The flight path for the automatic flight is divided into three of en-route, approach and hovering. And requirements for height error, lateral deviation, speed error are set for each segment. En-route is defined as the segment from SID to STAR and approach as the segment to the hovering after the STAR.

Table 3 The Design Requirements for Automatic Flight

	En-route	Approach	Hovering
Herr[ft]	±30.0	±30.0	±5.0
Dev[ft]	±50.0	±50.0	±20.0
Verr[kt]	±10.0	±10.0	−

5.1.5 Override function

Fig. 7 shows the re-engage region for automatic flight. It has been designed in order to return automatically to the route when the pilot finished override if the helicopter is in the region.

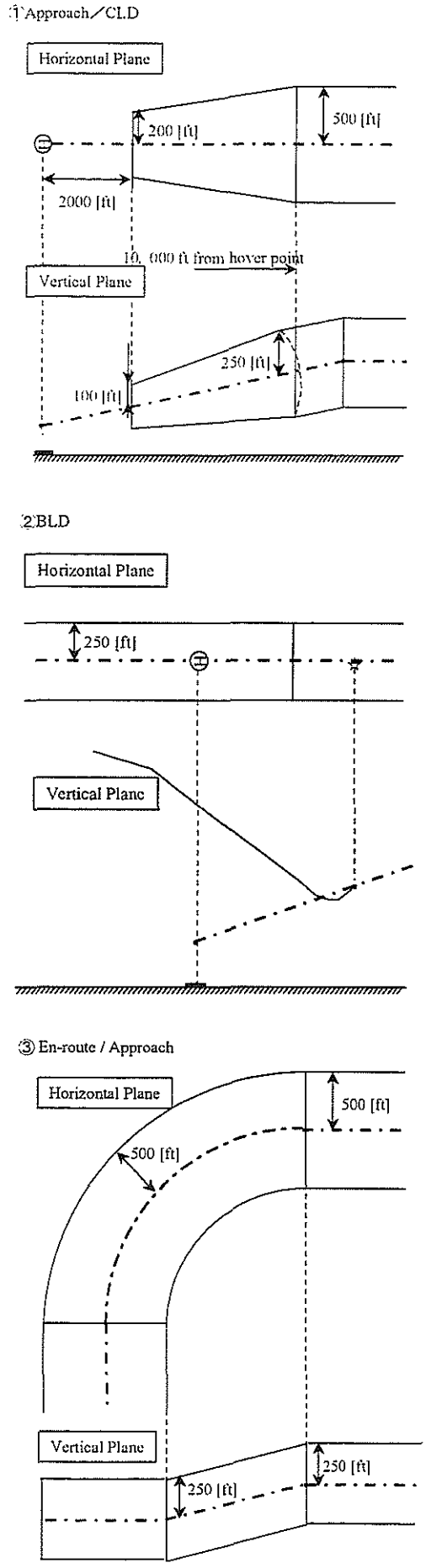

Fig. 7 Re-engage Region for Automatic Flight

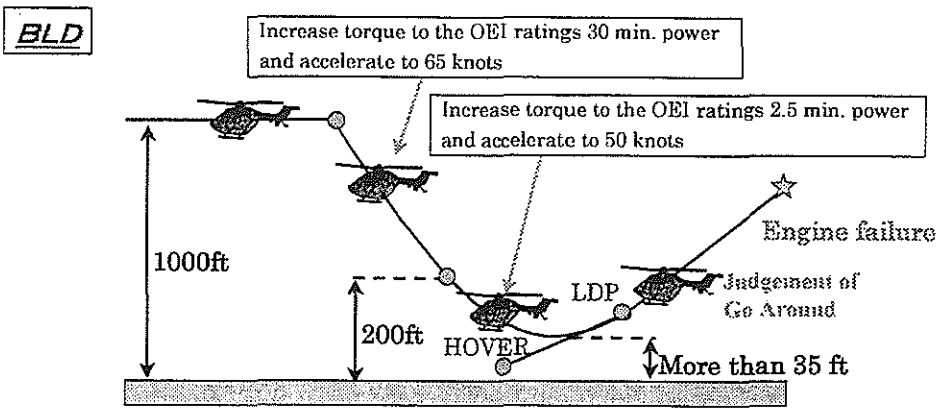

Fig.8 BLD Profile

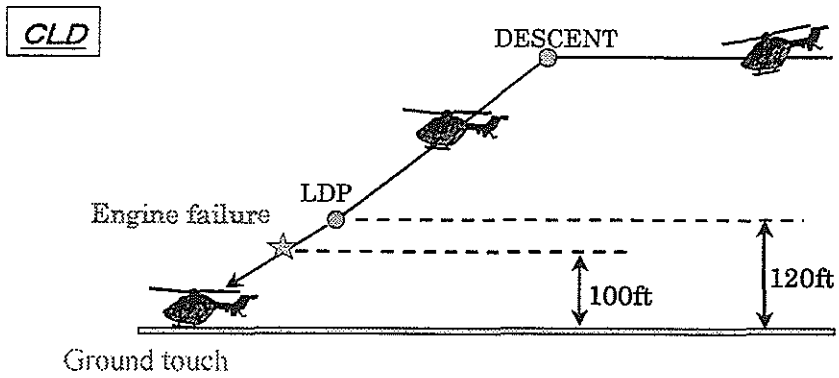

Fig.9 CLD Profile

5.1.6 One engine failure mode

We have also studied the guidance function for BLD and CLD in order to operate even one engine failure (fig. 8, 9). The BLD is executed by pushing the button as a pilot judgment.

5.2 Information – display system

Since visual cue is insufficient under IMC, the manual operation becomes very difficult. We have studied the presentation method, especially the display of the PFD for information display system that the pilot can easily acquire the attitude of the helicopter even in IMC.

The PFD that we designed for flight test is shown in fig. 10. The AI display changed at the MFD full size to recognize the attitude of helicopter with ease. And, the meter confirmation of the pilot was simplified by switching airspeed indicator to hover meter (horizontal velocity indicator) by airspeed.

Fig. 11 shows the ND that we designed for flight test. We see from fig. 11 that a pilot can intuitively recognize the circumstances around a helicopter because the ND shows an airway that is combined with topographic map. The conventional display of ND usually shows only a horizontal plane, but this ND also shows a vertical plane under the display of a horizontal plane, so a pilot can recognize the relation with a helicopter and the ground.

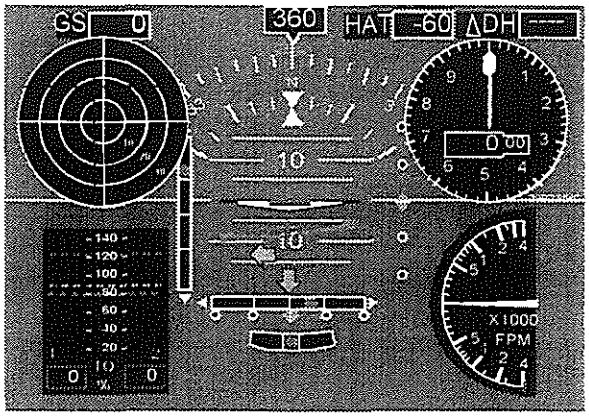

Fig. 10 Primary Flight Display

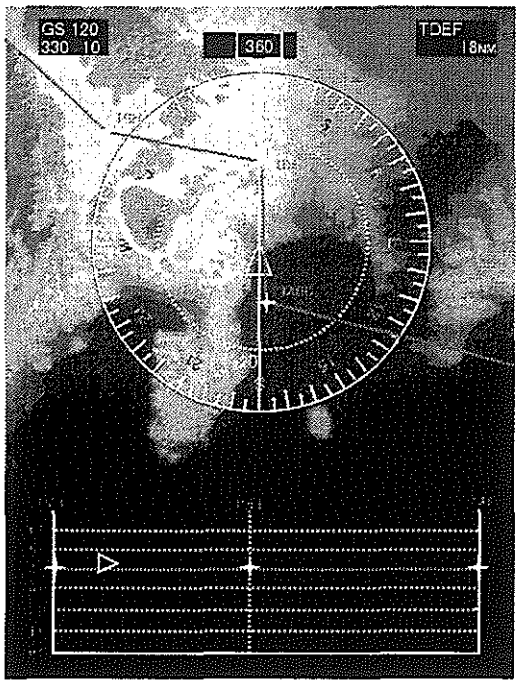

Fig. 11 Navigation Display

6. RESULTS OF THE FLIGHT SIMULATION

The flight simulations have been performed four times for this study, and the various data required to design the guidance function were obtained from the results of those tests. A simulated cockpit for the simulation was prepared and used in this study connected to a dome-type flight simulator of Kawasaki Heavy Industries, Ltd. (KHI)(Fig.12, 13).
Our primary evaluation results thus far are described below, based on the latest simulation.

Fig. 12 Simulated cockpit for simulation

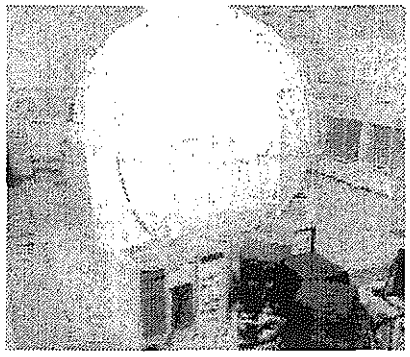

Fig. 13 KHI dome-type flight simulator

Fig. 14 shows the waypiont for flight simulation. The wind conditions were checked around the Gifu Air Base used by flight test carried out from the middle in 1999, we set wind direction 315°, steady wind of 20kt and gust.
The automatic flights were carried out from en-route to hovering in AEO and BLD/CLD in OEI. By performing sufficient flight simulations prior to a flight demonstration, satisfactory performance, reliability, and safety can be established before starting the flight tests.

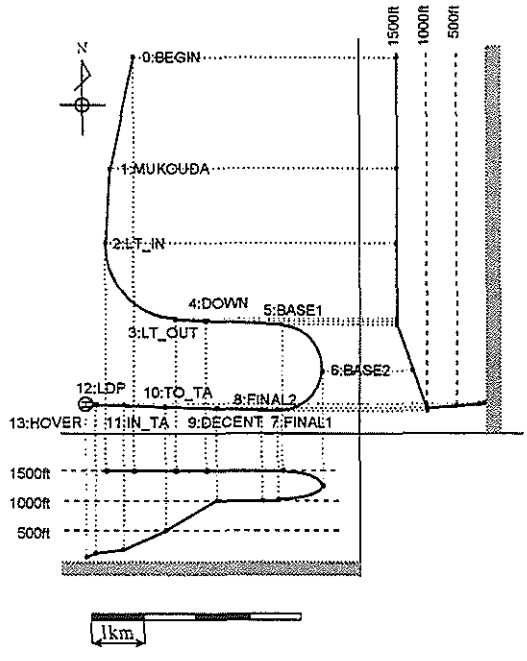

Fig. 14 Waypoint for flight Simulation

6.1 Results of the evaluation on en-route

Fig. 15 shows the time histories of the velocity error on en-route. We see from the graph (a) of fig. 15 that velocity error was within ±3 knots in no wind condition. It is satisfied with the design requirement for automatic flight that we established. On the other hand, the graph (b) of the velocity error in wind condition is not smoother than the result of the above. It is considered that it is based on the effect of the gust. There is a part that exceeds the design requirement in wind condition. But the design requirement has been established under no wind condition and the helicopter is controllable in this case, of course there is no tendency to diverge by gust.

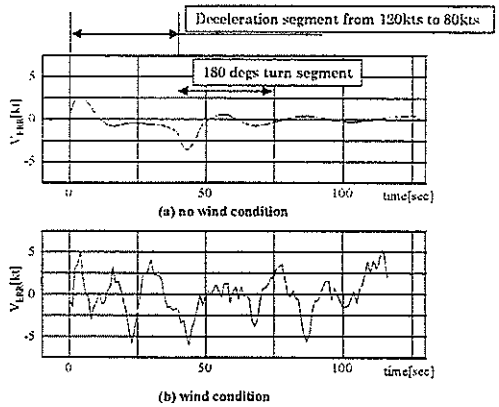

Fig. 15 V error (En-route)

Fig. 16 shows the graph of the deviation and height error on en-route. The frame in bold line in the graph shows the design requirement of the automatic flight set in ATIC.

In case of there being no wind, there is a part in which the height error deviates from the design requirement a little. It is occurred in the leg that decelerates from 120kt to 80kt. This cause is because the rate-of-climb arises in order to do the pitch-up in the deceleration. And, it is equal on the height error in case of the no wind condition and wind condition. On lateral deviation, there is a part that deviates from the design requirement. It is occurred near the changeover from the turning descent leg to the level straight-line leg.

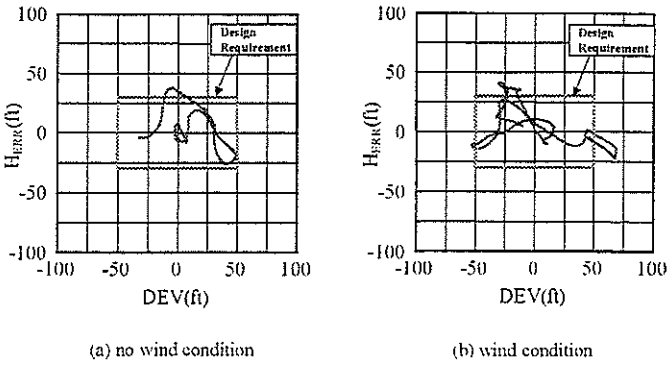

Fig.16 Results of Evaluation (En-route)

6.2 Results of the evaluation on approach

Fig. 17 shows the time histories of the velocity error on approach. We see from the graph (a) of fig. 17 that the velocity error was within ±3 knots in no wind condition and it was satisfied with the designed requirement. Attitudes of the helicopter were changed so frequently by deceleration and descent that the velocity error fluctuated frequently in comparison with the case of en-route. The graph (b) of fig. 17 shows the velocity error in the case of wind condition. We see from the graph (b) of fig. 17 that the motion of the velocity error calmed down from about 120 seconds. The wind condition causes this result. At the beginning of the evaluation, though the helicopter was under the influence of gust because airspeed was used for reference speed, reference speed was changed to the ground speed by height of helicopter (about 500 ft), then the helicopter was out of influence of gust. It is clear that the velocity error was satisfied with the design requirement because it was within ± 5 knots in both cases.

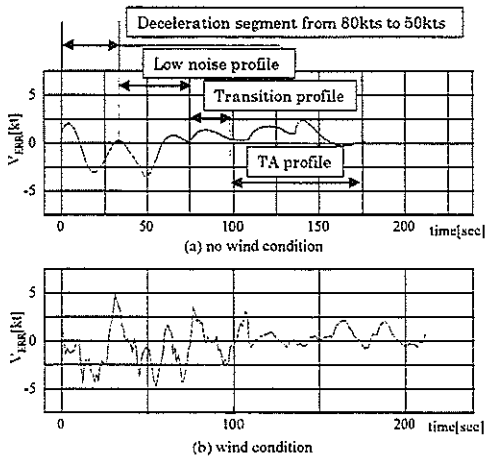

Fig. 17 V error (Approach)

Fig. 18 shows the graph of the deviation and height error on approach. We can see from fig. 18 that both deviation and height error were satisfied with the design requirements. The accuracy on the approach is better than that on en-route, because by using the gain scheduling by the airspeed, it becomes higher gain as lower speed.

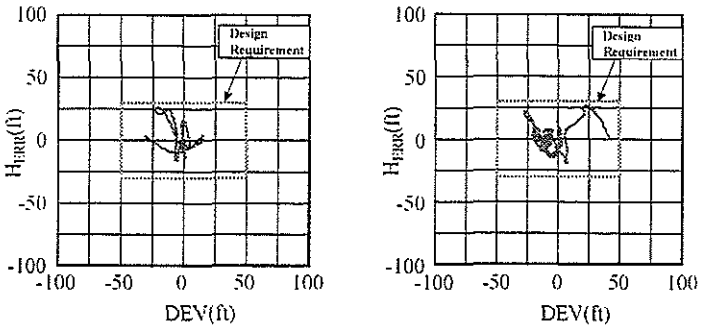

(a) no wind condition (b) wind condition

Fig. 18 Results of Evaluation (Approach)

6.3 Results of the evaluation for BLD

The results of the evaluation for BLD were satisfied with requirements of torque and velocity that were designed by the flight manual. In this paper, we show the most important factor, height loss. Fig. 19 shows the graph of height loss at BLD. The height loss was 60 ft in the case of no wind condition, and it was 7 ft in the case of wind condition. This is because the wind direction becomes head wind at 315 degrees. We see from fig. 19 that BLD is safely realizable.

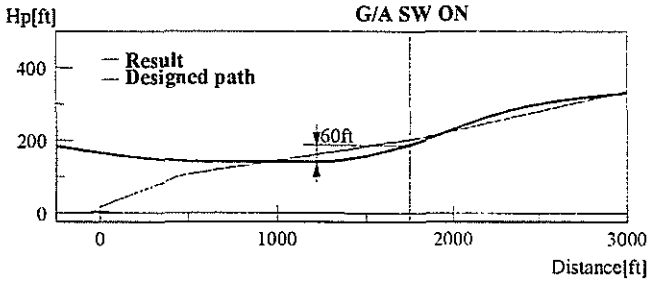

(a) no wind condition

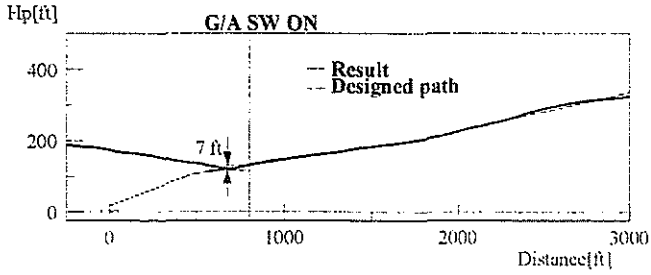

(b) wind condition

Fig. 19 Height Loss at BLD

6.4 Results of the evaluation for CLD

Fig. 20 and fig. 21 show the results of evaluation at CLD. The rectangle near the 0ft of the Hp graph shows the skid height. We defined landing time that the time when the helicopter touched this rectangle. And, ±100ft Square that shown near the 0ft of the deviation graph shows the size of the landing area of the roof top heliport.

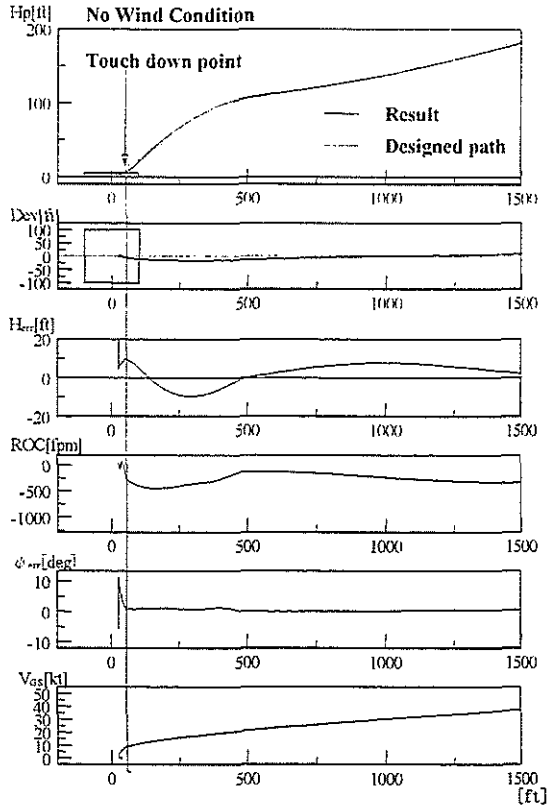

Fig. 20 Results of CLD (no wind)

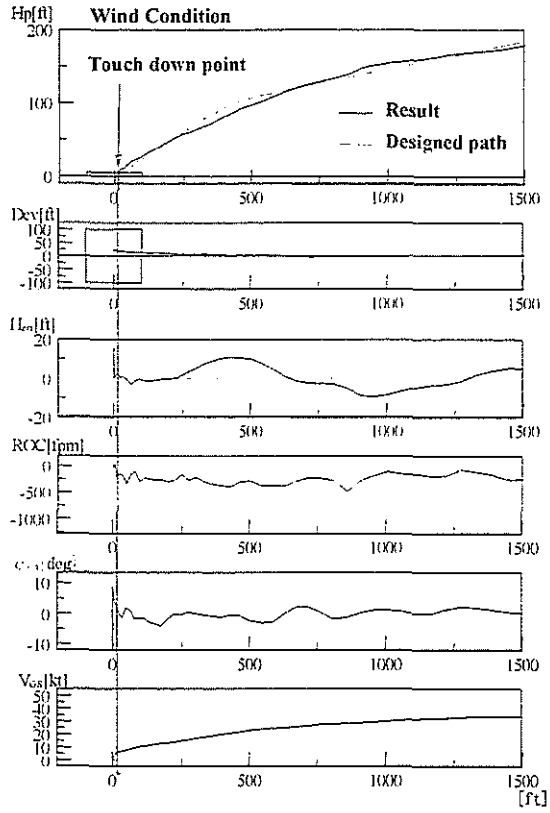

Fig. 21 Results of CLD (wind)

We see from fig. 20 that;

1. It can be grounded without going out from the heliport.
2. The deviation was within ± 20 ft after LDP.
3. The height error was within ± 15 ft after LDP.
4. Rate-of-descent at the ground touching was about 300 fpm, so it was satisfied with the requirement of the rate-of-descent (480 fpm) of the skid (BK117).
5. The direction error was within ±1 degree at the ground touching.
6. The ground speed was under 10 knots at the ground touching.

We see from the above results that automatic flight of CLD is possible in both conditions.

7. CONCLUSIONS

In this paper, the development of a flight management system especially automatic flight for civil helicopters being undertaken by ATIC to reduce pilot workloads has been described. The design requirements are established, considering the operation of civil helicopters, designed a guidance function based on those requirements, and evaluated the results of our design through flight simulations. The following results were obtained:

1. We designed the approach profile that could solve both of "noise problems at heliport or building roof in urban area" and "interference with the fixed wing aircraft operation in the airport" and we examined the profile for automatic flight.
2. The guidance function in the engine failure was examined. And two logic of go around mode and continued landing mode were established.
3. Then, we confirmed through the flight simulation that the guidance function was satisfied with our design requirements.

The results of override function were omitted by circumstances of the space this time,

4. We also examined the override function by flight simulation, and we confirmed that the function was very useful to the automatic flight.

We established the automatic flight, the flight simulation test for FD flight will be carried out at least 3 times in future, and pursue to establish the logic for FD flight.

The flight test is also started from July 1999, and about 100 flights have been scheduled including the evaluation of the automatic flight and FD flight.

9. REFERENCES

1. S.Tanase, H.Nagamori and T.Taira, Flight Test of BK117 Fly-By-Wire Research Helicopter of the 19th Congress of the International Council of the Aeronautical Science Sep. 1994.
2. T.Amano, A.Fujiwara and T.Akita, A Study on Pilot Support Display System for Helicopters of the 35th Aircraft symposium Oct. 1997.(in Japanese)
3. N.Kuraya, Current and Future Application of GPS on Civil Helicopters of the 35th Aircraft symposium Oct. 1997.(in Japanese)
4. H.Fujimoto, M.Takasaki, T.Amano, K.Kimura, Automatic Flight Control and Flight Director Systems of the Heli Japan 98 Paper n. T7-2 Apr. 1998.
5. Y.Kumamoto, H.Fujimoto, M.Takasaki, K.Kobayashi, *A Study of the Guidance* function for Commuter Helicopter of the 36th Aircraft symposium Oct. 1998.(in Japanese)

TWENTYFIFTH EUROPEAN ROTORCRAFT FORUM

PAPER E4

"IMPROVED METHODOLOGY FOR TAKE-OFF AND LANDING OPERATIONAL PROCEDURES

THE RESPECT PROGRAMME"

Authors: C. Serr[♦], J. Hamm[✧], F. Toulmay[♦], G. Polz[■], H.J. Langer[♦], M. Simoni[□], M. Bonetti[□], A. Russo[✧], A. Vozella[✧], C. Young[●], J. Stevens[○], A. Desopper, D Papillier[☆]

Organisations: Eurocopter[♦], GKN-Westland[✧], Eurocopter-Deutschland[■], DLR[♦], Agusta[□], CIRA[✧], DERA[●], NLR[○], ONERA, CEV[☆]

SEPTEMBER 14-16, 1999
ROME –ITALY

ASSOCIAZIONE INDUSTRIE PER L'AEROSPAZIO, I SISTEMI E LA DIFESA
ASSOCIAZIONE ITALIANA DI AERONAUTICA ED ASTRONAUTICA

ABSTRACT

In passenger transport missions, rotorcraft are operated in accordance with air traffic procedures which have been established essentially for the needs and performance capabilities of fixed wing aircraft, i.e. which incorporate trajectories with long rectilinear legs, moderate turns and shallow slopes in climb or descent. The specific ability of rotorcraft to take-off and land vertically, and to perform terminal manoeuvres in a confined space, following routes which do not interfere with the other air traffic, makes much more efficient operations possible. Nevertheless the potential benefit of revised flight procedures (in terms of better integration with other air traffic and reduced noise impact) and the consequent development of intercity connections, will materialise only if such procedures can be shown to preserve or improve flight safety without degrading the vehicle performance in terms of its payload capability.

Since the end of 1997, all of the European helicopter manufacturers together with experts from European aerospace research establishments have been working on a joint programme supported by the European Commission in an effort to develop improved take-off and landing procedures for a wide spectrum of field configurations and operating conditions. The programme, called RESPECT, standing for Rotorcraft Efficient and Safe Procedures for Critical Trajectories, will demonstrate the feasibility and safety of the proposed manoeuvres, addressing in particular those critical flight conditions during which an engine failure could endanger the passengers and/or population on ground. A methodical approach is being pursued, with the three following major steps:

1. establish a common performance simulation code and validate it using existing flight data,
2. use this code to analytically optimise trajectories and propose improved manoeuvres,
3. substantiate the practical feasibility and usefulness of these new procedures by means of piloted simulations and demonstration flight tests.

This methodology and the first year activity is presented

A109K

BO105

W30

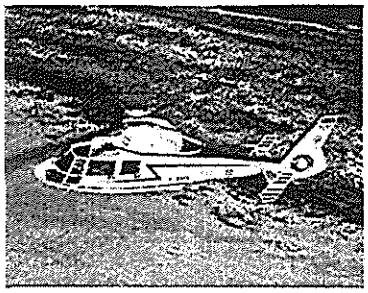

365N

1 THE RESPECT PROJECT

1.1 Industrial Objectives

The main objectives of the RESPECT project (Rotorcraft Efficient and Safe Procedure for Critical Trajectory) are:

- To determine for existing helicopters, how and by how much, terminal manoeuvres can be modified to improve mission effectiveness in terms of allowable payload and in terms of time necessary to take-off and depart or to approach and land whilst maintaining or improving the level of safety.
- To demonstrate the feasibility and error-tolerance of these manoeuvres taking into account all of the practical difficulties such as pilotability, crew field of vision, altitude and position cues, transient engine and rotor speeds, etc.., addressing in particular those critical flight conditions during which an engine failure could endanger the passengers and/or the population on the ground.

The helicopter industry as a whole would profit from the market growth triggered by improved flight procedures and by quieter heliport neighbourhoods, if it can be shown that flight safety is preserved or improved without degrading helicopter payload performances.

The time-to-market for the project results exploitation could take up to three years since it would be first necessary to convince the helicopter community (operators, airfield authorities, airworthiness authorities) of the advantages offered by the new approach.

These ambitious industrial objectives are naturally widely exceeding the framework of a 3-year programme. This complex problem must therefore be broken down to optimise the advantages of this co-operation and obtain results that are immediately applicable.

1.2 Partnership

This research programme is partially funded by the European commission and includes the following European manufacturers: Eurocopter (EC) - Eurocopter Deutschland (ECD),
GKN-Westland (GWHL) - Agusta (Ag)

As well as the following research agencies:

ONERA (associated to CEV for flight testing), DLR, CIRA, DERA and NLR.

These agencies have been working for many years with the industrialists on rotary wings. The breakdown is presented in Fig. 1.

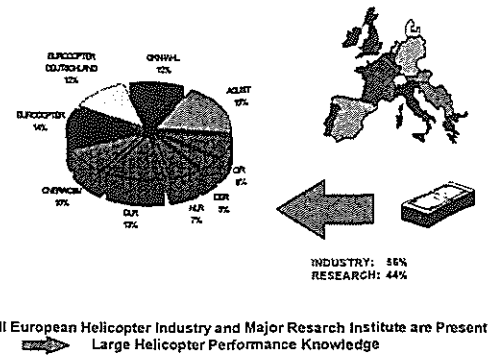

Figure 1

RESPECT is really close as a research programme to the product in the wide sense of the word. It includes main helicopter operations and covers operating improvements by retaining or enhancing the safety levels that are accepted by the Airworthiness Authorities today.

1.3 Methodology: The RESPECT Project

The RESPECT programme is intended to set up a study framework which will help to improve helicopter safety and performance for a wide range of helicopter weights and an extensive range of operations. The study topics and the helicopters types are listed in Fig. 2 below:

Operation	Helicopter	Max. Weight (kg)
Unprepared and confined area EMS/SAR	BO105	2500
	A109K	2720
Restricted Helipad	BO105	2500
	A109K	2720
	365N	3850
	W30	5800
Elevated Platform	365N	3850
	W30	5800
Clear airport City heliport	365N	3850
	W30	5800

Figure 2

The methodology that will be derived from the RESPECT programme is also the main thrust of this project and, in some respects, its first application. In applying the results of study, the RESPECT partners will work alongside helicopter operators as well as some European government agencies. In fact, a part of the programme is naturally dedicated to contacts with the operators' flying personnel as well as the agencies e.g. DGAC, CAA, LBA, JAA, EHA, IFALPA.

This methodology is well illustrated in Fig. 3 presenting the different tasks included in the RESPECT programme.

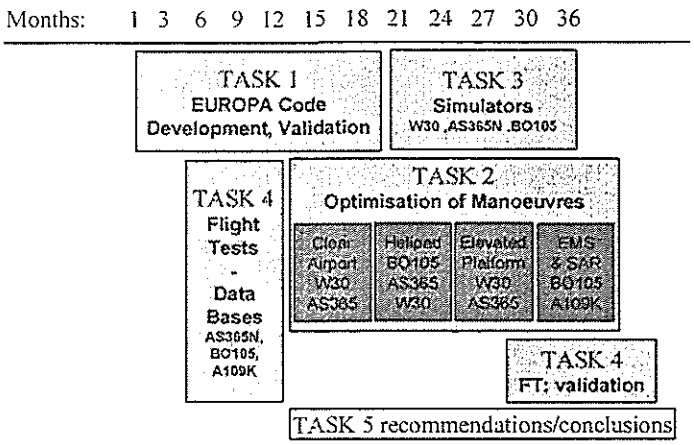

Figure 3

Task 1: Specification and development of a common computer code for the calculation of stabilised and non stabilised performance.

Task 2: Optimisation of procedures applicable for those cases and helicopters quoted.

Task 3: Piloted simulations to verify the optimised procedures for the respective helicopters.

Task 4: Flight testing: This part includes 'preliminary' as well as 'confirmatory' flight tests after the phase optimising procedures for the operations considered.

Task 5: Circulation of results. This involves not only communicating information regarding the RESPECT programme but also feeding this study with concrete cases close to the daily operating realities of the helicopters.

Most of the effort expended to data has been devoted to the development of a performance calculation code common to every partner.

2 EUROPA: PERFORMANCE COMPUTATION CODE – TASK 1

This chapter gives the design specification for the EUROPA (EUROpean Performance Analysis) software and the status of development achieved. The EUROPA code essentially consists of two elements: a helicopter performance simulation and the control logic required to run multiple performance simulations for:

1. manoeuvre optimisation,
2. research,
3. calculation of performance data for the generation of aircraft performance charts.

2.1 Uses for the code.

EUROPA is used in the BRITE EURAM "RESPECT" project, as a research tool for predicting the take-off and landing performance of helicopters operating in a variety of complex situations. The code is capable of accurate performance prediction and is suitable for the task of finding the optimum piloting strategy for each manoeuvre. The flight conditions which the model is able to analyse and the modelling accuracy are described.

Once fully developed, the code will be used by some of the partners (and possibly by other parties) for the estimation of helicopter performance for research, and the calculation of performance for certification and flight manual chart production. In this role the code must be capable of finding the limiting performance of a helicopter at each point in its operating envelope (both steady-state and dynamic performance).

Other uses of the code are:

- To define the **safety criteria** (necessary performance margins) for existing and future procedures.
- Analysis of manoeuvres and modelling of flight test events for parameter identification.

The validation of the model for each task will always be the responsibility of the user.

The work required to create this useful tool falls into two categories:

- Creation and validation of an accurate vehicle performance simulation.
- Development of an easy to use performance prediction tool, which uses

the vehicle simulation as a "performance calculation engine".

2.2 The EUROPA model.

The code includes models for the vehicle, the pilot, the environment and the control logic. For some helicopter components, there are several models or options from which the most appropriate to a given helicopter type can be selected. For example, a conventional rotor or a shrouded fan of the "fenestron" type can be used for the tail rotor. For the main rotor, a blade element integration, an analytical model in closed form and a flight test power identification can be selected according to the available aerodynamic data and the constraints on computation time. Engine models range from elementary time constant response to a thermodynamic description of engine components. A specific helicopter model is constructed by specifying appropriate modelling options as part of the input data files.

The pilot model and the control logic allow off-line simulation of various piloting strategies, generating realistic flight control activity and following a pre-selected schedule of fuselage attitude, airspeed, engine limitation, RPM, etc... according to the procedure under study. The effect of pilot abuse and errors such as reaction times, overreaction, etc... and the repeatability of manoeuvres can be parametrically investigated, making it possible to assess precisely the safety margins.

The required features of both elements of the model, their validation method and the accuracy requirements are outlined below:

2.3 Accuracy requirements.

The accuracy requirements can be divided into several categories:

Firstly the vehicle simulation is able to predict both the power required and attitude required to trim, to a high degree of accuracy. Although "factors" can used to refine the power match these factors are small. Users have a high degree of confidence in the fidelity of the basic aircraft model.

The accuracy of the vehicle manoeuvre simulation is also be of a high order. With any performance model, it is normally not possible to match any one flight test event to a high degree of fidelity due to un-modelled factors, such as small variation in the wind speed etc. However if a number of similar events are matched, the performance simulation must not show any trend in the errors (i.e. the predicted height loss during a hover flyaway may sometimes be less than measured, sometimes more, but a consistent trend is not acceptable).

When run to produce data for flight manual charts, the scatter between the predicted and measured performance is a combination of the accuracy of the simulation, and the repeatability of the manoeuvre. Margins are required to account for the worst possible combination of piloting errors. One of the uses of the code will be to predict the consequences of piloting abuse on performance. The Task 2 work to optimise performance must bear this in mind. If the optimum manoeuvre is difficult to fly, and the worst of the likely abuse cases is found to seriously degrade the performance, then the margins required to ensure safety may overwhelm the performance gains which accrue from optimising the technique! The accuracy of the code (in this case the modelling of the piloting technique) is verified by confirming that there is no consistent error, that is to say, the predicted performance should lie close to the centre of any measured performance scatter.

2.4 Development status

The EUROPA code has been compiled and run at each of the partner sites (on a variety of types of computer) and the same benchmark results have been obtained.

The EUROPA vehicle simulation has been shown to predict both the steady-state (trim) and dynamic (manoeuvre) performance of variety of helicopter types to a good degree of accuracy.

We have demonstrated that performance data can recorded for each simulation run (or trim condition) and that the output can be plotted to produce performance charts (H/V diagram, takeoff and landing charts (WAT) etc.).

To speed up the production of performance data, the simulation is able to iterate manoeuvres (e.g. critical engine failure point) and is able to cycle through multiple cases (i.e. run a series of cases automatically, varying the aircraft mass, pressure altitude, OAT, wind speed, etc.).

2.4.1 Steady-state (trim):

The code is capable of being run in a "trim only" mode. The utility of the code is of course improved by the addition of a "cycle" subroutine which permits the user to run multiple cases, for example over a range aircraft weights and speeds, so as to automatically produce a "predicted" power carpet. For validation purposes the performance-simulation output is stored in a file for comparison with flight test data.

The ability to run multiple cases is used to produce the stabilised performance data found in the Rotorcraft Flight Manual.

For performance prediction work, the basic power prediction is refined by the use of small "correction factors", which are normally applied to the predicted profile power, in order to produce a perfect match to the measured aircraft power carpet. The basic helicopter performance-simulation is made as accurate as possible, so that the factors required to produce a perfect match are small.

EUROPA can be run in the "trim only" mode to predict the ability of the helicopter to hover in winds from any quarter. For this, an accurate tail rotor model and control position prediction capability were developed both for Fenestron and classical tail rotor.

The good level of correlation with flight test is illustrated in fig. 4 for hover and fig.5 for forward flight. Figure 6 shows the differences between predictions and measurements from figure 5.

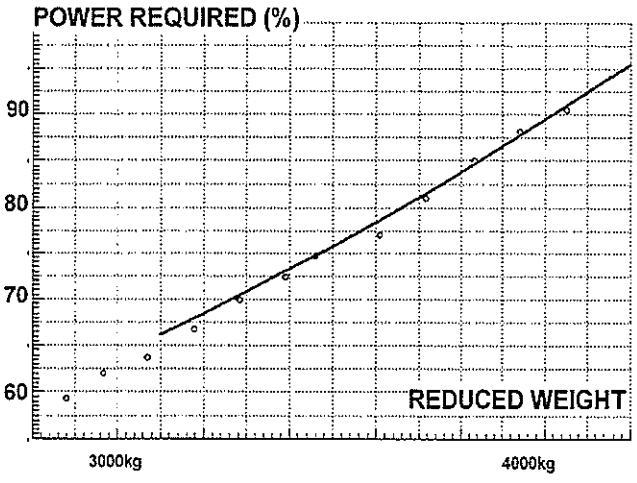

Figure 4: Hover out of ground effect

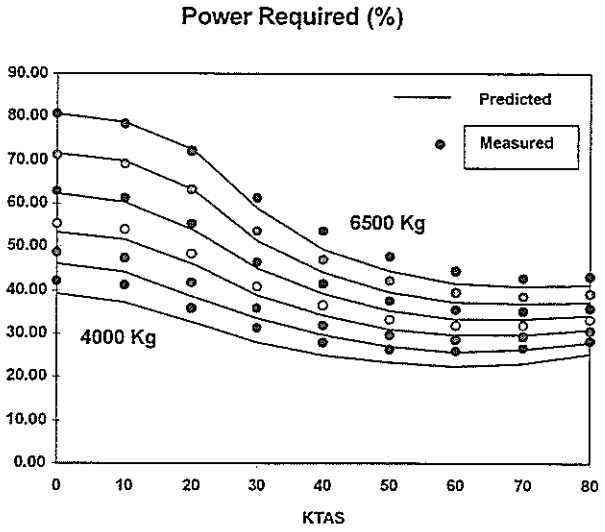

Figure 5: EUROPA/flight test comparison

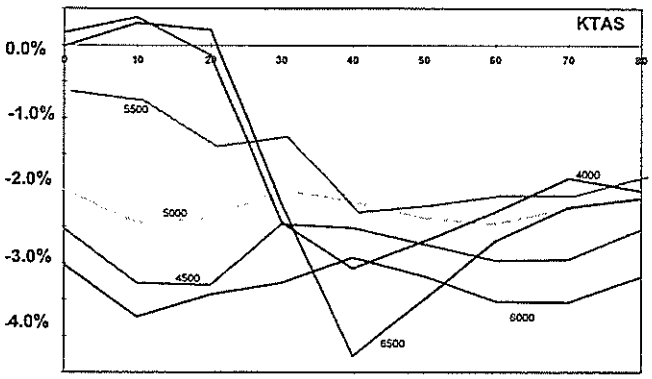

Figure 6: EUROPA/flight test - Accuracy

2.4.2 Dynamic performance (manoeuvre simulation)

Once the steady state performance of the simulation had been verified, the model was validated for the prediction of manoeuvres. As this is not a handling qualities code, only performance criteria are considered. To validate the vehicle model a "flight test manoeuvre matching" subroutine was created. The pitch and roll attitude time history from a measured flight test event is used as the "target attitude" and feedback controllers are used to generate the control inputs required to make the performance-simulation follow the measured aircraft attitude traces. Similarly, the collective is adjusted either to "follow" the flight test height trace or to match the measured movements of the collective stick. The yaw pedals are moved either to match the

heading (low speed) or centre the slip-ball (high speed).

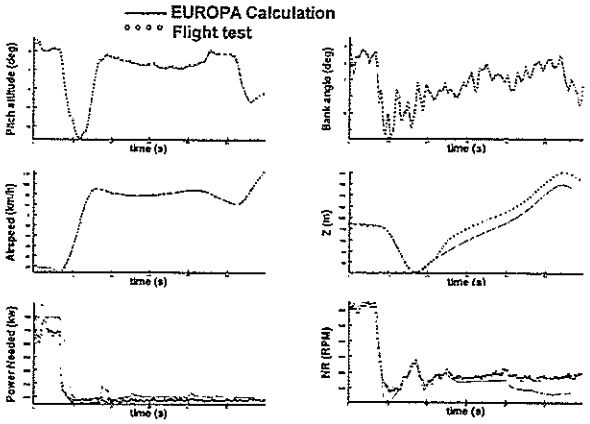

Figure 7 : Matching logic – Engine failure in descent flight 9° slope

The accuracy of the performance simulation is checked by comparing the "free" simulation parameters with flight test (torque, rotor speed, control positions, airspeed, aircraft position, etc.).

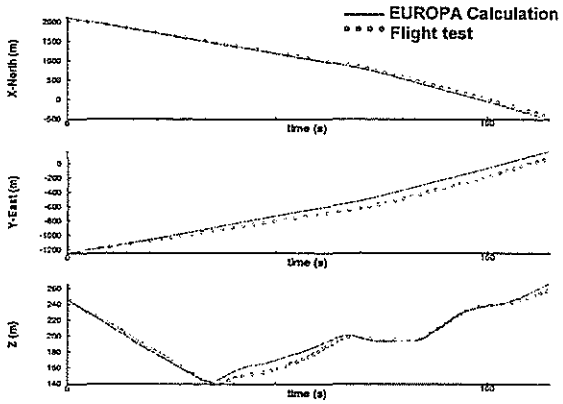

Figure 8 : Matching logic – Aircraft position (X,Y,Z)

Because some flight test parameters are not modelled (e.g. variations in vertical air mass motion and wind speed), validation tends not to be an exact science! It is normally necessary to model a number of similar flight test events and look for trends. The performance simulation is deemed to be valid if all of the predicted parameters sit close to the centre of the flight test "scatter".

When the basic vehicle model has been validated, the ability of the code to generate accurate performance predictions is checked by programming the performance-simulation to "fly" an idealised version of a number of measured events. The code is validated by comparing the predicted performance with the measured performance (e.g. rejected takeoff distance, distance to Vtoss, H-V limits, etc.).

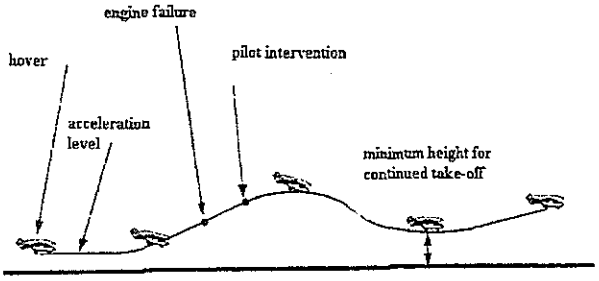

Figure 9 : Continued take-off scheme

In order to "fly" many of the critical flight manual manoeuvres, an "automated iteration" method is required. For example, when flying a Category A takeoff, the takeoff decision point (TDP) may be defined in terms of radar altitude (e.g. 35 ft). The critical continued takeoff case is an engine failure recognised by the pilot at the TDP. But, if the engine failure recognition time is one second, it will be necessary for the simulation to iterate on the engine failure time so that the required TDP is reached one second later.

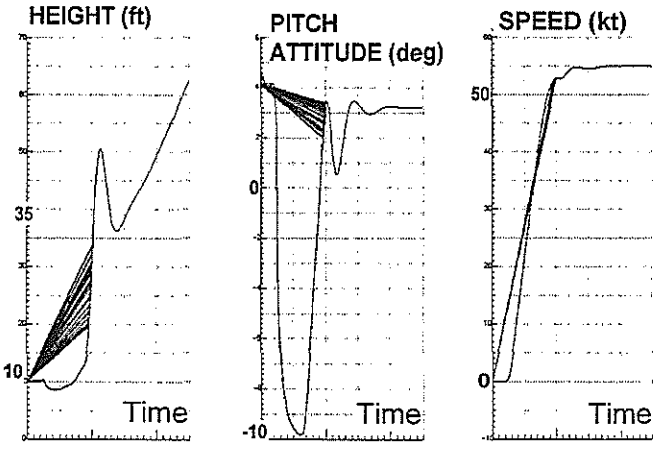

Figure 10 : Take Off Decision point calculation

Similarly, the limiting altitude for a vertical reject can be found only by iteration; starting at a low altitude and working up in height until a

touchdown is made at the limiting rate of descent and Nr.

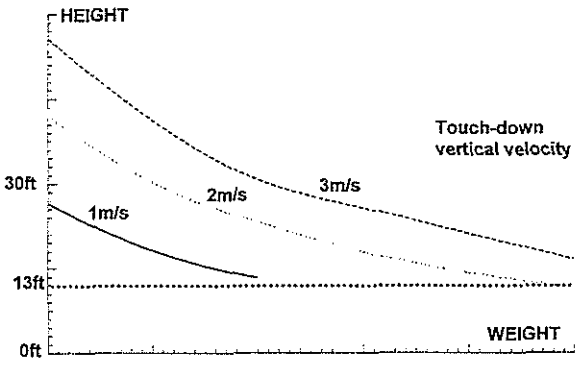

Figure 11 : H/V Diagram Low point calculation

The same type of "automated iteration" may also be used to vary the piloting technique, so as to achieve the optimum performance. The optimisation logic and the feedback parameters required, are the province of the RESPECT Task 2 partners, but the ability to undertake this type of modelling has been built in from the start.

To turn the simulation into a useful performance prediction tool, the "cycle logic" must allow a number of events to be simulated and the required performance data to be recorded and output. For example, the variation of the limiting vertical reject height with aircraft weight and wind speed; or the data required for the production of a Category A takeoff distance chart as a function of aircraft weight, pressure altitude, OAT, and wind speed. The accuracy of the performance output will be checked by comparison of the predicted "chart data" with measured flight test data.

At the end of RESPECT, EUROPA will only be a useful tool if the charts which are produced from the simulation output can be used to predict performance.

In practice, EUROPA must be able to quickly and accurately generate all of the dynamic performance data which is normally found in a Rotorcraft Flight Manual.

2.4.3 Visualisation

A visualisation post processing software using the VRML language is being developed in order to check the pilot visual cues with glazing surfaces corresponding to the actual cockpit.

This software provides animated visualisations of the particular helicopters used in the project and shows manoeuvres calculated by the EUROPA code. The results of off-line computations are easily interpreted and this visualisation technique will be used for the briefing of crew before piloted simulations and flight tests.

2.5 Conclusions.

A new code has been developed in common: EUROPA (European Rotorcraft Performance Analysis). Written in FORTRAN and meeting stringent standards for documentation and software quality, the code runs on desktop computers. Good portability has been shown. It can simulate steady state performance and complex 3D manoeuvres, such Cat A take-off and landing with lateral offset and turns with effects of wind. Manoeuvres can iterate for optimisation or chart production, so as to generate H-V diagrams, take-off decision point, exposure time, etc...

The EUROPA code is more than just a helicopter performance simulation. It is also a performance prediction tool which is quick and easy to use, and which produces output that can easily be plotted to produce accurate performance charts.

EUROPA can be run in two modes.

1. The steady-state (trim only) is used to produce power carpet data, and to analyse hover performance in any relative wind conditions.
2. The dynamic performance (manoeuvre) is used to analyse engine failure, takeoff, landing, and other such cases.

The EUROPA code is being validated in several stages. First the steady state trim has been validated by comparing performance-simulation with flight test. Next the manoeuvre capability of the vehicle model was verified by matching flown events, i.e. by comparing predicted and measured time history traces. Then the ability of the simulation to predict performance was confirmed by using EUROPA to predict the performance for a number of specific flight test events, and checking that the predicted performance is close to the centre of the flight test scatter. Finally the ability of EUROPA to produce valid charts will be checked by producing example "flight manual" charts and seeing how well they predict the performance flown during the RESPECT piloted simulation and flight trials.

3 ANALYSIS AND OPTIMISATION OF MANŒUVRES – TASK 2

Based on existing rules, recommended practise, flight manuals or information collected from operators, unambiguous and simple criteria are being defined in order to provide either objective functions or constraints for optimisation. They fall into four categories:

safety criteria, esp. considering the consequence of engine failure and with provision for pilot abuse and obstacle avoidance in degraded visual conditions (when applicable);

performance criteria, which are combinations of the technical factors impacting profitability or efficiency of operations: payload, time...

noise criteria, which take into account the favourable or unfavourable flight conditions in the Vh-Vz diagram;

air traffic criteria, which indicate compatibility with alternate approach/take-off paths avoiding interference with fixed-wing airport traffic and the possibility of freeing runway slots for this traffic (applicable to airports only).

4 PILOTED SIMULATIONS DEMONSTRATION OF NEW PROCEDURES – TASK 3

An engineering department obviously does not have the same knowledge and appreciation as the crew. After the off-line studies, the optimisation manoeuvres established with the EUROPA code shall be applied to undertake piloted simulations to present and have the procedures evaluated by the pilots. It is evident that those procedures are set up in close co-operation with the test crew but the risks inherent to the flight testing for such procedures calls for preliminary evaluation in the simulator which could also be used as a training platform.

For the piloted simulations, three helicopter types will be implemented: AS365N, BO105C and Westland 30. Later, the new procedures developed during the RESPECT study will be demonstrated in flight on the AS365N, BO105C and A109K2.

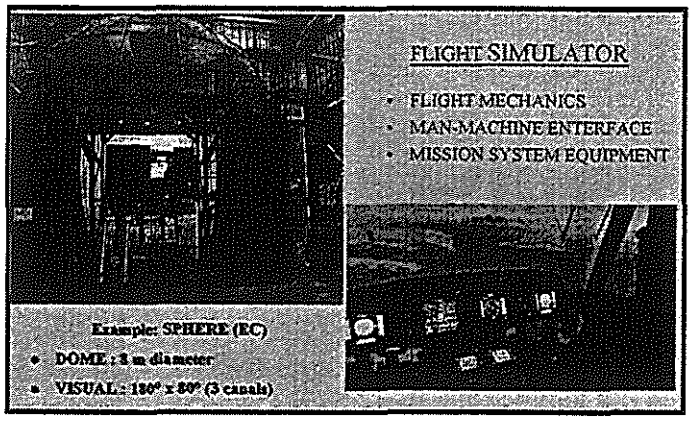

Figure 12

5 FLIGHT DATA - TASK 4

One needs reliable flight tests to validate or reject the analysis tool. These tests should be representative of the helicopter's behaviour in the emergency phases but shall not necessarily be performed in extreme conditions. The proximity to the ground or a rig , in particular, is not essential to compile the data bank needed to validate the helicopter's and/or the engines' behaviour in the acceleration, deceleration, climb or descent phase with or without engine failure. Some of these tests can be representative of the procedures scheduled but may also be limited to procedure sequences.

The dynamic performance studies are being conducted on a representative range of twin-engine helicopters: Dauphin AS365N, Westland 30, BO105C and A109K2 whose operations cover a wide spectrum of missions: passenger transport linking airports, heliports and offshore platforms; EMS to and from unprepared landing sites and hospital rooftop platforms; and mountain rescue.

Substantial data bases were available for all four helicopters. For the validation of the EUROPA code in manoeuvring flight, it was nevertheless found necessary to collect additional flight data: H-V diagrams, Cat A manoeuvres with simulated OEI situations. In 1998, complementary flight tests were performed with a Dauphin 365N operated by CEV and a BO105C operated by DLR. Similarly, tests with a A109K2 operated by Agusta were performed in 1999.

These tests were performed with well-instrumented helicopters. DGPS positioning is available for all manoeuvres.

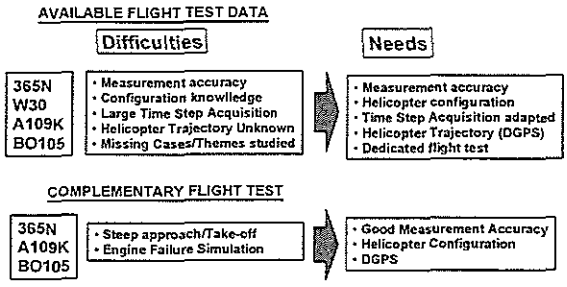

Figure 13

An additional flight test phase is scheduled for each of the 3 helicopters for which complementary flight tests have been performed in the second half of the RESPECT programme to check the results of the optimisation study off line and in the simulator.

Note that, for the RESPECT flight trials, there are likely to be various flight testing constraints (for example it may be necessary to use less than maximum engine power, etc). The flight trials will be used to check the optimised computed conditions, sufficiently far from the ultimate performance of the helicopter.

This involves performing the flight demonstration with an extensive knowledge of the safety procedures as well as a preliminary sensitivity study. The development efficiency shall be enhanced, the number of flying hours shall be reduced and so will the risks incurred by the aircraft and their crew.

6 RELATIONSHIPS WITH OPERATORS AND AUTHORITIES – TASK 5

The RESPECT team has established contacts with airworthiness authorities and operators, esp. via the JAA/OPS Helicopter Sub-Committee. HSC observers are invited to some RESPECT workshops and are scheduled to participate in piloted simulations. After thorough validation, the EUROPA code and the general methodology developed in RESPECT is expected to be used for developing operational procedures and limitations in a more accurate and less expensive way. On the other hand, the feedback from operators is helping RESPECT to concentrate on missions and operating conditions where the need for an improved methodology is most acute.

A web site is being maintained by the RESPECT team for the information of interested organisations. This site incorporates general information on the project and several pages for each active task, with a description of what is being done, photographs of the test helicopters and a short sample movie in synthetic images to illustrate one type of manoeuvre computed with the EUROPA code.

http://www.nlr.nl/public/hosted-sites/respect/

As the phases described above are completed, the safety procedures of each helicopter are extensively studied upon engine failure . The study and the related results are to be presented objectively to the certification agencies (European agencies first) as for a "conventional" certification process. Those products to which this process demonstrating safety margins or performances shall have been applied will naturally prove beneficial to the operators.

7 CONCLUSION

The RESPECT project aims to develop improved rotorcraft terminal procedures and airfield operations (i.e. take-off and landing manoeuvres) for a wide spectrum of field configurations, including, but not limited to, airports (freeing-up valuable runway slots), city centre heliports, and offshore platforms. The project will demonstrate the feasibility and safety of the proposed manoeuvres, with regard to the performance capabilities of existing helicopters, addressing in particular those critical flight conditions during which an engine failure could endanger the passengers and/or the population on the ground.

The approach to be used to reach this objective is threefold:

1. To establish a common performance simulation code and to validate it using flight data.
2. To use this code to analytically optimise trajectories and to propose improved manoeuvres.
3. To substantiate the practical feasibility and repeatability of these new procedures by means of piloted simulations and demonstration flight tests.

This paper reports on the work done and results obtained during the first project year. So far on-going activities concern the first step mentioned above, that is the development of a common simulation code named EUROPA (EUropean ROtorcraft Performance Analysis)

able to predict helicopter performances in typical take-off and landing conditions.

For most of the partners the EUROPA software developed provides a new tool for the analysis of helicopter flight and the prediction of dynamic performance. This is also the first time that all of the European helicopter manufacturers and many of the European helicopter research organisations have shared a common performance prediction computer code. This by itself is considered to be a significant achievement.

The performance/safety methodology to be developed and demonstrated in the project has a **prenormative character**: it is expected that future airworthiness or air traffic regulations, advisory circulars and local heliport rules will refer to the methodology developed during this study to quantify and validate the take-off and landing performance of rotorcraft, either as a complement to, or a substitute for, earlier less accurate methods.

For the project partners, the creation of a common European helicopter performance prediction tool will improve their ability to work together on future rotorcraft programmes.

For the helicopter manufacturing industry a potential improvement in the take-off performance, without any additional production cost, should result in a decrease of operational cost margins. A more rigorous assessment of safety margins and safety enhancements, without performance penalties, should also give a significant marketing advantage to European manufacturers before the new methodology can be fully recognised and applied by overseas competitors.

For helicopter operators, increased profitability can be expected from improved payload performance and a more general public acceptance of helicopter operation.

Concerning Safety and Environmental Impact, the outcome of the project will contribute to the development of the public transport helicopter as a dependable and safe vehicle which can effectively complement the existing transportation infrastructure by providing an air link to any medium size city within a range of 150 km of a major airport.

The main benefit will be to ensure a high standard of safety, both for the passengers, and for people living in the vicinity of heliports.

8 ACKNOWLEDGEMENTS

The authors wish to thank the European Commission for the partial funding of the RESPECT project.

9 REFERENCES

[1] P. Roesch, G Samoni, "Applications of Energy Concepts to the Determination of Helicopter Flight Paths", 5th European Rotorcraft Forum, Amsterdam, Sept 1979

[2] Okuno Y., Kawachi K., Azuma A., Saito S., "Analytical Prediction of Height-Velocity Diagram of a Helicopter Using Optimal Control Theory", Journal of Guidance, Vol. 14, No 2, 1991 (also published by AIAA in 1990)

[3] Vodegel H., Stevens J., "A Computer Programme for the Certification of Helicopter Vertical Take-off and Landing Operations and an Application to the S-76B Helicopter", 47th Annual Forum of the American Helicopter Society, Phoenix (Arizona), May 1991

[4] Tränapp N., Reichert G., Hepp H., "Maneuverability Aspects for Helicopter Take-Off and Landing ", Proceedings of the 18th European Rotorcraft Forum, Sept 1992

[5] Hamm J., "The Use of Pilot Models in Dynamic Performance and Rotor Load Prediction Studies", Proceedings of the 18th European Rotorcraft Forum, Sept 1992

[6] Langer H.J., Tränapp N., "BO105 Flight Test Data for a Wind Tunnel Test Program", DLR IB111-93/58

[7] Hamm J., "The Development of Helicopter Pilot Models to Control Engineering Simulations", Proceedings of the RAes/AHS Symposium on Rotorcraft Simulation, May 1994

[8] Morel F., "Multivariate Optimization Applied to Conceptual Design of High Capacity Long Range Aircraft", 19th ICAS Congress, Ahaheim (California), Sept 1994

[9] Grünhagen V. & al, "A High Bandwidth Control System for Helicopter In-Flight Simulator", International Journal of Control, Vol. 59, No1, 1994

[10] Basset P.M., Heuzé D., Taghizad A., Weinstock S., Desopper A., "Etudes hélicoptères en mécanique du vol et en qualités de vol à l'ONERA/DES", La Recherche Aérospatiale, 1995, N°3

[11] "Helicopter Performance Modelling", Final Report Action Group 07, 1996 (GARTEUR restricted distribution)

[12] Sharma V., Zhao Y., Chen R.T.N., "Optimal Sideways Operation of a Category-A Helicopter from an Elevated Platform", 52nd Annual Forum of the American Helicopter Society, Washington DC, May 1996

[13] Rollet P., "La simulation pilotée pour la conception et le développement des appareils à voilure tournante", AGARD FVP Symposium, May 1995 (published in CP-577)

[14] Steinke M.M. & al, "Airport/ATM Capacity Increase Through Rotorcraft Operation ", Final report of DG VII - Airport/4-Study, Sept 1995

[15] G. Padfield, "Flight mechanics"

TWENTYFIFTH EUROPEAN ROTORCRAFT FORUM

Paper No. F1

Honeywell Primus EPIC™ Integrated Avionics System

Larry Clark, Technical Manager
Next Generation Systems Team
Honeywell Inc.
Glendale, AZ USA

larry.clark@cas.honeywell.com

SEPTEMBER 14 – 16, 1999
ROME
ITALY

ASSOCIAZIONE INDUSTRIE PER L'AEROSPAZIO, I SISTEMI E LA DIFESA
ASSOCIAZIONE ITALIANA DI AERONAUTICA ED ASTRONAUTICA

Helicopter Industry Requirements

What are the requirements for a future helicopter avionics system? Honeywell talked with many helicopter manufacturers, operators, pilots and support personnel to get their inputs to this new avionics system design. Helicopter operators in all segements including military, EMS, offshore oil and corporate have different requirements and problems to be solved. Thus the system needs to be flexible and adapable.

Here are a few of the inputs that Honeywell received:

- Must be low cost, 30% lower in cost than today's avionics, for the same functions.
- Should be able to expand to host new functions of the future (CNS/ATM).
- One set of hardware that can be used across all models and versions of the helicopter (EMS, Corporate, SAR, utility, military, etc.).
- Should be able to integrate other federated functions including aircraft utilities, HUMS, etc.
- Easy to learn and to operate new functions, to reduce training of flight crews and maintenance personnel.
- Must meet the more harsh helicopter operating environmental conditions.
- More reliable, by at least 200%. MTBF measured in years, not hours.
- Easy to troubleshoot and return to service. Reduce helicopter down time (15 minutes).
- Reduced operating costs, spares costs.

Changes in Technology

Many of the things that customers wanted avionics to do in the past were not possible due to three limitations:

Display technology which used CRT devices that were limited in what they could display and still meet sunlight readability requirements.

Processor limitations which restricted the type of integration capabilities that the overall aircraft required.

Memory storage capacity to handle the vast quantities of data which included terrain, maps, charts, navigation data plus documentation such as aircraft manuals.

These limitations have been removed with the use of modern Commercial Off The Shelf (COTS) devices from the consumer PC industry. The challenge has been to take these COTS components and certify them to meet various FAA/JAA requirements. This involved development of a new operating system and data bus architectures.

Primus Epic, Honeywell's Next Generation Integrated Avionics System

The Honeywell design team that developed this new avionics architecture had several members with extensive helicopter experience. Thus it is no surprise that the design fits exactly what the rotary-wing industry required in a future avionics package.
This revolutionary new integrated avionics system is Honeywell's response to the industry's request for lower cost and higher reliability components as well as flexible architecture that easily permits customization to meet end user requirements.

Starting with a review of the entire end-to-end process of operating and servicing the aircraft, as well as mapping the information exchange that occurs between the entire flight team of pilots, dispatchers, air traffic controllers and maintenance technicians, Honeywell designed a system to provide seamless execution. Honeywell worked closely with Honeywell's Technology Center, the FAA, NASA and many operator advisory boards to ensure that the design utilized the latest concepts that addressed specific issues with today's and the future operating environment.

Honeywell is in a unique position to take commercial off-the-shelf (COTS) devices and integrate them into the aircraft while meeting the exacting requirements of the aircraft environment and certification mandates. COTS devices, such as processors, LCD flat panels, and high speed bus hardware, ensure that the latest technology is available at the lowest cost. The design of the Primus Epic system permits upgrades to the system hardware or software, with no impact or re-certification of other elements in the future.

Primus Epic is an open architecture design, with Honeywell providing both software and hardware development kits to outside parties to integrate their functions into the system. Already several companies have developed functions for Primus Epic system applications. For example, a supplier of fuel quantity systems has developed a module that takes the unique fuel sensor inputs and provides fuel quantity information to all the other Primus Epic functions in the aircraft for processing, display and other calculations.

A modular design permits the system to be configured to fit the turbine helicopter market as well as twin turboprop to regional jet commuter market, plus the entry level light jet up to the new long range global business jet segment. This is the first time that the helicopter segment has been able to take full advantage of the hardware and software available to other aircraft types. Any function available to the regional airlines or business jets, is now available to the helicopter operator. For example, up-linked weather information, electronic charts and maps, integrated maintenance and troubleshooting.

Modules have very high reliability goals and can be easily replaced by the operator in the field. Additional modules can be added when new functions or regulatory requirements exceed the current capability of the system. Modules and additional software functions can be added in the field to accommodate new mission requirements or assigning the helicopter to a new market. Common modules, with other Primus Epic systems, reduces the type and number of spares required. For example, any processor module can be used in a helicopter or fixed-wing installation.

The new Human Centered Cockpit Design uses a Cursor Control Device and pull down on screen menus to permit the crew to interface and control the aircraft at a higher level of interaction that in today's cockpits. Displays are LCD "flat panels" that provides new capabilities not previously available in today's civil aircraft. The aircraft can be configured with a few as two or as many as six displays.

Safety enhancements include better situational awareness by providing aircraft present position integrated on an electronic chart which includes terrain avoidance information. Weather images, from ground based radar or from satellite sensors, provides the crew information about conditions far ahead of the aircraft along the planned route. This electronic data link with the ground is only the first step toward CNS/ATM, and Free Flight that can easily be accommodated in the new Primus EPIC system.

Currently the Primus Epic hardware and software continues in development. First deliveries of prototype units has started, and flight testing on Honeywell's company aircraft has been ongoing for more than two years. Some elements, such as the unique DEOS operating system have already been certified by the FAA and other agencies. Environmental testing, including HIRF levels has

started. All of the Primus Epic hardware was designed to the helicopter environmental requirements from the very beginning.

Primus Epic, soon to be flying on the AB-139 helicopter, Fairchild-Dornier 728 and Embrarer 170 regional jets and the Raytheon Hawker Horizon.

TWENTYFIFTH EUROPEAN ROTORCRAFT FORUM

Paper n° F3

EUROPEAN FRAMEWORK FOR THE DESIGN OF INTELLIGENT TRAINING AIDS

BY

F. HERAN
SOGITEC, FRANCE

P. LE LEYDOUR,
THOMSON TRAINING & SIMULATION, FRANCE

P. MEYER zu DREWER
CAE, GERMANY

S. SIRIGNANO
AGUSTA, ITALY

SEPTEMBER 14-16, 1999
ROME
ITALY

ASSOCIAZIONE INDRUSTRIE PER L'AEROSPAZIO, I SISTEMI E LA DIFESA
ASSOCIAZIONE ITALIANA DI AERONAUTICA ED ASTRONAUTICA

EUROPEAN FRAMEWORK FOR THE DESIGN OF INTELLIGENT TRAINING AIDS

F.Heran, P.Le Leydour, P.Meyer zu Drewer, S.Sirignano

Mr François D. Héran
SOGITEC Industries
4, rue Marcel-Monge 92158 Suresnes Cedex
FRANCE
Fax 33 1 41 18 57 18
Tel 33 1 41 18 57 23
fheran@sogitec.fr

Mr Patrice Le Leydour
THOMSON TRAINING & SIMULATION
1, rue du Général de Gaulle Z.I. Les Beaux Soleils Osny
BP 226 95523 CERGY PONTOISE CEDEX
FRANCE
Fax 33 1 34 22 81 49
Tel 33 1 34 22 82 52
patrice.leleydour@tts.thomson.fr

Mr Peter Meyer zu Drewer
CAE Elektronik GmbH
Postfach 12 20
D-52201 STOLBERG
Fax 49 24 02 106 270
Tel 49 24 02 106 252

Mrs Susanna Sirignano
AGUSTA
Via G. Agusta 520 21017 Cascina Costa di Samarate (VA)
ITALIA
Fax 39 03 31 711 627
Tel 39 03 31 711 584
critias@tin.it

ABSTRACT

After a general presentation of EUCLID and CEPA 11, this paper presents the scope and some considerations of EUCLID CEPA 11 RTP 11.9 "Intelligent Training Aids", a project which started in January 1998.
The first phase of the study was focused to provide the scientific and technical bases for the further developments, to analyse literature on military education and training, to assess and characterise existing training devices in the participating countries.
A global training model is proposed. The identified model allows to define the main concepts of interactions between the training system and the actors taking part in the training. The paper describes the model derived from works in the fields of human engineering and psychology. The model is adapted from what has been developed to model the operator monitoring a complex system.
An analysis of general instruction tasks found in military training systems is then described.
Lastly, possible applications of ITA are deducted from this cognitive approach, as well as from the survey of fielded systems and the Consortium's experience.

This work is partially funded by the MoDs of France, Germany and Italy, in the framework of the EUCLID CEPA 11 program.

INTRODUCTION

This paper presents the scope and some initial considerations of EUCLID CEPA 11 RTP 11.9 "Intelligent Training Aids".
The first goal of the study is to provide the scientific and technical bases for the further developments, by researching literature on military education and training, assessing and characterising existing training devices in the participating countries.
During the genesis of this project, two opposite approaches were considered.
The first approach was technology driven; it would have led us to answer questions such as: what can Artificial Intelligence, Fuzzy Logic, or other techniques, offer ?
This method would have revealed to be well suited if the goal of the study had been to improve existing training aids by automating some of the instructor's tasks, but the aim of the Management Group was more ambitious.
To imagine new, intelligent training aids, it has been deemed necessary to identify which cognitive processes take place among the actors of the training, and to analyse the nature of the interactions between these actors and the training systems.
This led to the selection of a cognitive approach, complemented by field surveys, which are presented in the following sections.

EUCLID BACKGROUND

European Co-operation for the Long-term in Defence (EUCLID) is a structured approach to European defence technology development which started in 1988 and is now conducted under the aegis of WEAO by the WEAO Research Cell (WRC) in Brussels.
EUCLID consists in eleven Common European Priority Area (CEPA). Among these, CEPA 11 addresses Defence Modelling and Simulation Technologies. It defines priority subjects which are being addressed in Research and Technology Projects (RTPs).
CEPA 11 is comprised of the following bodies:

- the Steering Committee, chaired by the Netherlands, has members belonging to the MoDs of twelve European Nato countries, and a secretary, Mr Sten Jensrud, WRC,
- Management Groups (MoD representatives) manage the RTPs and report to the Steering Committee,
- the CEPA 11 Industrial Group (CIG 11), representing EDIG (European Defence Industry Group), advises the Steering Committee and reports to EDIG and to the companies belonging to national CIGs.

More detailed information can be found in Merison (1998).

PRESENTATION OF CRITIAS

CRITIAS, Co-operative Research in Intelligent Training and Instructional AidS, officially known as RTP 11.9 "Intelligent Training Aids", is a 3-nation project undertaken by France, Germany and Italy, France being the leading country. The contract has been awarded on 26 Jan 1998 and the duration of the project is three years.
The industrial Consortium is led by the French company SOGITEC, with the participation of CAE Elektronik GmbH for Germany, AGUSTA SpA and EIS SpA for Italy, and Thomson Training & Simulation (TT&S) as the other French partner.

Expected results of CRITIAS

The main results of CRITIAS will be the following:

- a formally defined set of Intelligent Training Aids which are coherent and applicable to many training systems,
- presentation and evaluation of Intelligent Training Aids demonstrators developed for specific training devices, for which users have a significant interest,
- a rationale supporting the above definition and developments.

What are the benefits of Intelligent Training Aids ?

Intelligent Training Aids are methods and tools for military training systems that will:

⇒ improve the quality of instruction,
⇒ provide the instructor with means of better preparing and following the training session, and preparing and executing briefing and debriefing,
⇒ support standardised instruction, and objective assessment and documentation,
⇒ reduce instructor workload and avoid distraction from the pedagogical tasks,
⇒ provide effective scheduling guidance within a set of training means and their sequential use,
⇒ include specialised expertise where necessary or needed for instructor support,
⇒ support self training and/or instructor-controlled training.

Application domain of Intelligent Training Aids

Intelligent Training Aids will effectively support technical and tactical control of military training devices which may be:

- Computer Based Training systems,
- individual or crew simulators of various complexity (PTT, FMS),
- tactical team training systems and simulator networks.

Training requirements of Air Force, Army and Navy will be addressed.

Structure of CRITIAS

CRITIAS is divided into four work packages:

WP1 Analysis of different training devices and their instructional use
WP2 Definition of Areas for Intelligent Training Aids Application
WP3 Definition of Requirements and Specification of Intelligent Training Aids
WP4 Development, Integration and Demonstration of Intelligent Training Aids

The following sections present some insight gained during the first stages of WP 1 and WP 2.

MODELLING TRAINING

The study focuses on the military training of a person or team through an initial (CBT) or advanced (PTT, FMS) training system. In order to build a theoretical framework for the study, we have investigated existing training models in the literature and designed a general training model as a baseline.

This model, depicted in figure 1, is comprised of the training system, which we define as a technical system encapsulated by training aids, interacting with the training actors. The technical system can be the real system or a simulation of the real system. Examples are a simulated cockpit, or a manual presented in a digital form (for CBT). The actors are the following:

- a trainee, who has to learn the use (for operation or maintenance) of a complex system,
- an instructor who is interacting with the trainee, mainly to help or assess the trainee,
- an expert (usually not present during training, so shown in a dotted line rectangle), who brings expertise to the training aids or to the instructor, as well as benefit from the experience gained by the instructor (and to a lesser extent by the trainee, this is not represented in the figure).

Interactions of the instructor with the system are possible, for example through the use of an IOS for a simulator or through a lesson planning system for a CBT. Interactions of the trainee with the system can also be enhanced, as for example if hypertext is used to read the computerised manual mentioned earlier or in a CBT lesson. In this latter example, the instructor may be virtual.

The knowledge that the instructor and expert possess pertains to three areas:

- System (how to operate the training system)
- Pedagogical (how to transfer knowledge to the trainee in an efficient way)
- Operational (how to use or maintain the "real" complex system)

We now can define an Intelligent Training Aid (ITA) as a function resulting from the transfer of a cognitive process from the instructor or the expert to the training aids.

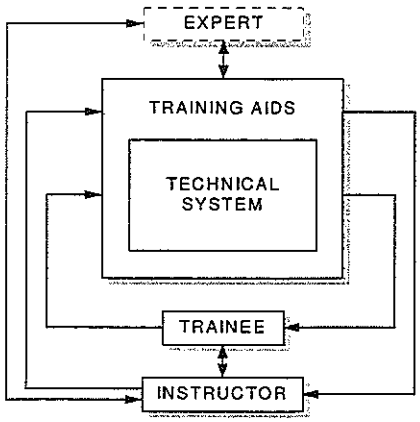

Figure 1: General training model

A trainee model

In this section, we are interested in modelling the trainee learning to operate a complex system. We take as a representative example the training of the operational activity for a military aircraft pilot, who has to achieve the goals of his assigned mission while maintaining a relative safety.

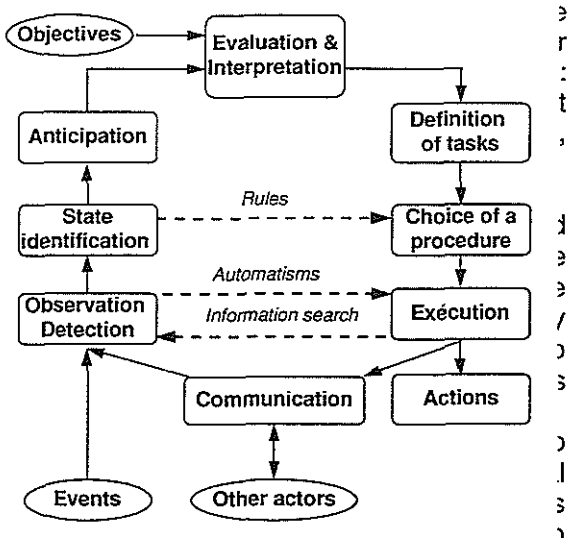

a complete revision.
The analysis of the representation, the objectives and the constraints results in a ***planning*** of the actions to undertake, in the determination of the relevant ***procedure***, then finally in the action itself. This action can be:

- an action resulting in an evolution of the state of the piloted system itself (modification of trajectory, use of the weapons...); in the following, this last concept will be termed ***action***,
- a ***communication*** with the other actors with whom the pilot co-operates,
- or finally a new ***search for information***.

In addition, this process is permanently simplified by many "short-cuts", which decrease the total workload of the pilot. An observation can start an execution quasi immediately: this happens for phenomena which, to respect strong temporal constraints, are treated on a reflex mode, or for routine activities which can be ***automated***.

A new state of the process may not require to reinterpret or re-evaluate the situation as a whole: the solution to this evolution is perfectly known, and is treated by the application of more or less formalised ***rules***.

The suggested model, illustrated by figure 2, is very largely inspired by the work of Rasmussen (1987), already adapted by Van Eslande (1997).

Figure 2: A trainee model

During the execution of a mission, the pilot is confronted with difficulties which can disturb the above-described process and generate abnormal operations.

A somewhat abstract and theoretical definition of the role of the instructor would consist in affirming that his objective is to modify the behavioural model of his trainee.
In a more concrete way, this means that it is necessary that the trainee acquires:

- the theoretical prerequisites, to be able to create a mental representation of the system,
- elementary skills necessary to action,
- elementary skills necessary to observation,
- elementary skills necessary to communication,
- reflexes,
- procedures,
- the capacity to create, to share, and to call into question, a representation of the situation,
- capabilities for planning,
- and finally, a capability to distribute his tasks, i.e. to treat at the procedure level what pertains to procedures, at the reflex level what pertains to reflexes.

Lastly, these abilities must be used in an increasingly complex environment.

Such a framework of training is more ambitious than a conventional definition, which is only concerned into directly observable results of the actions of the trainee.
In practice, innumerable difficulties may be encountered; by way of illustration:

- the already quoted example, on the rules applied in low altitude flight, shows that the "good procedure" concept relates to expertise, which is only exceptionally formalised; this remark also applies to "good planning",
- how to check the application of a procedure?
  On this subject, the above mentioned example on low-altitude flying is enlightening. Amalberti (1996) points out that the trainee pilot applies a method which is mostly relative to planning, in the sense that he tries to continuously correct an error whereas an expert pilot would react to thresholds. An analysis of the results of the two control strategies (threshold based process or continuous regulation) should be very sensitive if indications are to be deduced on the pilot's level of expertise.
- Generally speaking, how to observe the pilot's behaviour ? What are his intentions ? What information is he looking for ?

This stresses the fact that an instructor may need a wide range of aids, with various objectives, which have to be assessed in relation to the instructor's tasks, as developed in the following sections.

We have also investigated **Team Training**, for which Silverman, Spiker, Tourville, and Nullmeyer (Silverman et al., 1996) have proposed a conceptual model, which includes operational definitions for aircrew co-ordination, team performance and mission performance models.

INSTRUCTION TASKS

We first went through a *review of existing literature and practices* on instructional and pedagogical issues of military education and training. Focusing on instruction tasks, most of the findings related below come from the EUCLID CEPA 11, RTP 11.1 (MASTER) and RTP 11.3 projects.

Field Orientation findings

The instructor is considered the "heart" of the training programme. He is the link between theoretical knowledge and the real world. Six different instructor profiles can be deduced from the tasks instructors have to fulfil during a training session. These are:

- planning instructor,
- test instructor,
- briefing instructor,
- exercise instructor,
- analyst instructor,
- debriefing instructor.

It is assumed that a team of instructors can perform all above mentioned tasks. During an exercise one or several instructors may play the role of participants in the scenario, co-ordinated by *a chief instructor.*

An important instructor's function is to help the trainee to transform the skills learned on a training system onto the actual device. This transfer is greatly improved by the instructor's experience and his capability to advise trainees.

Instructors then build up a lot of expertise while teaching with the simulator. In most cases such expertise is not recorded anywhere and get lost when the instructor leaves, which, due to the job rotation system used in most military services, occurs rather frequently.

Often instructors are not involved in mission and task analysis, but usually they are the ones with relevant knowledge. Usually the specification of a training programme is system-driven, not training driven.

Furthermore learning goals are adjusted to the possibilities provided by the training system, not from a mission and task analysis. This might be the reason why so little facilities are available to support the instructor in evaluation of performances and provision of effective feedback.

Prior to focusing on *classifying the instructor's tasks* we felt the need to fix the process of instruction design within a *theoretical framework.*

An Instruction Design Framework

Instruction can first be defined as the provision of information extrinsic to the (training) task in order to enhance/induce learning in trainees.

An *instructor* is then an individual engaged in/assigned to delivering instruction.

Each time he (or she) prepares for the instruction a teacher has to determine what, when and how to teach, i.e. what a trainee has to accomplish, what the objectives are, what the teaching behaviour will be, what the schedule is, how to arrange the instructional material, how to motivate the trainee, how to provide appropriate feedback and how to evaluate the trainee's work.

Approaches to achieve these tasks are called "*teaching styles*".

The design of the instructional system includes definition of the events that take place during the instruction, and the sequence of these events.

Based on a cognitive model of a human's learning process, the proposed set of instructional events consists of nine activities (Gagne, 1985). These are:

- gain the attention of the trainee,
- Inform of the objective,
- stimulate recall of prior learning,
- present the information,
- provide learning guidance,
- elicit performance,
- provide feedback,
- assess the performance,
- and enhance retention and transfer.

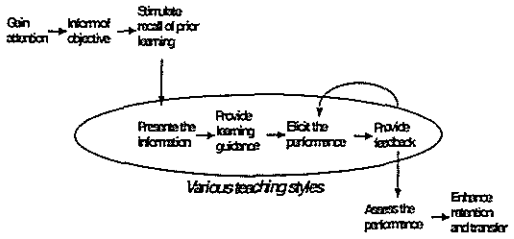

Figure 3: instructional events

The oval set reflects a particular approach to present information (a teaching style).
When followed, these events are intended to promote the transfer of knowledge from perception through the stages of memory.

Towards a Classification of Instructor's tasks

Instructors are usually considered as teachers whose primary task is to provide instruction to the trainees, before, during and after training. However, in most cases the instructor is also responsible for administrative and operational duties that are part of designing and maintaining a training programme, but also to run and to maintain the training system itself. All these responsibilities and duties combined result in a wide range of tasks of today's instructors.
To classify the instructor tasks five categories were defined.

Administrative and organisational tasks

General organisational and administrational tasks related to the training and training programme. This includes the design of scenarios, but also the management of the trainee database.

Pedagogical tasks

Tasks that especially involve the pedagogical knowledge of an instructor, e.g. to help the trainee to transfer the skills learned on the simulation system onto the actual device.

Instructional tasks

Tasks to execute a training session, e.g. to change display/instrument settings available to the trainee.

Additional tasks

All tasks that can't be assigned to one of the above categories, e.g. to play the role of an active participant in the scenario (like an opponent, a wing-man or a co-pilot).

Above tasks have not necessarily to be fulfilled during all training sessions and from all instructors. The tasks an instructor has to perform will vary depending on the kind of training device, the training objectives, the characteristics of the trainee, the number of trainees, the number of instructors, etc.
Whatever the kind of knowledge involved, any of the above mentioned tasks can, to a certain extent, cause distraction from the actual task of an instructor: *to provide an optimum training to the trainees.*

INTELLIGENT TRAINING AIDS

The first step is to review *existing training devices and training aids* used within military organisations in order to focus on significant areas of improvement related to possible Intelligent Training Aids. Focusing on different domains, most of the findings below come from a survey of in services training systems and interviews to instructor conducted for RTP 11.9.

Possible expert ITA

Bringing some expertise to the training aids requires modelling knowledge and skills possessed by a subject matter expert. Expert training aids encompass the different kinds of knowledge involved in training and instruction activities, which can be summarised in four different areas (Orey and Nelson, 1991; Orey, 1993; Mitchell, 1993) as illustrated in figure 4.

An expert training aids is based on knowledge about what is being taught, the *domain knowledge*, knowledge about the level, the strengths and weaknesses of a particular trainee at a particular moment, the *trainee knowledge*, knowledge about instructional strategies, the *pedagogical knowledge*, knowledge about the way to present information to and get information from the trainee, the *instructional knowledge*.

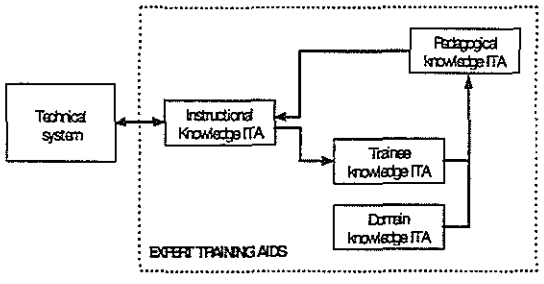

Figure 4: expertise areas

Domain knowledge

Expert domain knowledge addresses the behaviour (in terms of both actions and reactions) expected from an experienced trainee/crew in a given situation.
In conventional PTT and FMS training systems, such expertise remains the property of

instructors and is not transferred to the system. The expertise is built up while teaching with the simulator and it often is lost when the instructor leaves.
A possible axis of development for ITA is then to provide the training system with a formalised representation of the domain knowledge, e.g. a set of «fuzzy logic» rules that reflect a reference behaviour extracted from subject matter experts.

Trainee knowledge
Trainee knowledge addresses the representation of what the trainee knows about the domain and what he/she does not know, just like a human teacher being able to monitor the trainee's knowledge status. Such knowledge has then to be updated continuously by the instructor.
Monitoring and updating the trainee's knowledge remains however a difficult task, a possible axis of development for ITA is at least to provide the training system with the entrance and expected levels of proficiency of the trainee and with data computed from the trainee's behaviour for a further comparison with the expert domain knowledge model.

Pedagogical knowledge
Expert pedagogical knowledge addresses the expertise needed to teach the domain knowledge in an efficient and adequate way.
In conventional training systems (e.g. CBT) most of these decisions are taken beforehand by scenario designers. Decisions are pre-programmed and the way of teaching is usually not adapted during the lessons to a particular trainee's performance.
A possible axis of development for ITA is then to provide the training system with capabilities to adapt its teaching strategy dynamically, and to react or to help the instructor to react adequately to the performance of the trainee.

Instructional knowledge
Expert instructional knowledge addresses both the presentation to the trainee of the task environment, the exercises and the instructional interventions by the system or the instructor, as well as the recording of the trainee's responses and other performance variables.
A possible axis of development for ITA is then to provide the trainee with augmented cueing and feedback tutoring facilities, as well as inclusion of functional explanations in the technical system based as much as possible on self-explaining interfaces.

Levels of expertise for ITA
During the course of RTP 11.9 different levels of expertise for Intelligent Training Aids were defined. The definition follows the idea of increasing complexity of an intelligent system and increasing abstraction of the inputs into the system, thus reducing the instructor's workload during training level by level.

Intelligence can be defined as the ability to learn, to reason and to understand. For a technical application this means that an intelligent system itself has to have the ability to analyze data, to understand the data, to find commonalities and to draw conclusions from this point.

Figure 5 shows an intelligent system, it is possible to recognize that the main elements are the database and the rule base. The rule base determines how new data and rules have to be acquired. The significant part is the intelligent system's ability to change its data base and rule base by itself. That means the system will be able to learn.

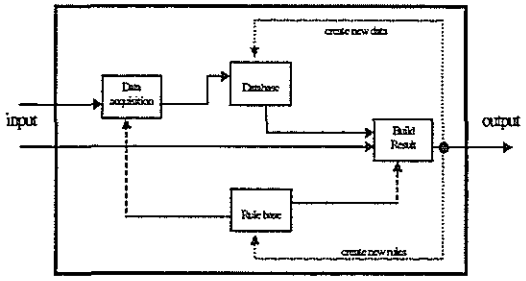

Figure 5: Intelligent System

Transferring this model to the application of an optimum intelligent training aid, the system must have the expert knowledge of an instructor which was described above: domain, trainee, pedagogical and instructional knowledge.

In respect to training the gathered knowledge will allow the intelligent system to analyze, to understand and to assess previous and current training situations and to foresee upcoming situations.

The figure shows an intelligent system at its full extent, and - following the definition of intelligence given above - it is the only system that can be strictly called intelligent. However, for the specification of ITA, the following levels were defined to individuate increasing complexity of an ITA application and discriminate on technological efforts capable to sustain them. The different levels represent different achievable levels of ITA. The levels are:

0) Ergonomic design of a man-machine-interface
1) Applying simple and static rules to the input
2) Increased flexibility by taking into account information from the data base
3) The system supports automatism to select compound actions from a database
4) The system is able to expand its database by means of fixed rules
5) The system is capable to analyze its database, find commonalities and expand it, creating new data
6) The system is capable to create new rules

In respect to the expert knowledge that is involved in training and instruction activities (see expert ITA described above), the intelligent system has at least to incorporate expert knowledge starting from level 2. Beside the instructional knowledge, which is needed to present information to and get information from the trainee, the ITA has to have knowledge about the actions and reactions expected by the trainee (domain knowledge). As these actions can depend on the trainee's representation of the domain, trainee knowledge has to be incorporated into the ITA for a more precise and adequate assessment. The pedagogical knowledge, which addresses instructional strategies, has to be transferred to an ITA to promote the ability of automatic and intelligent intervention or to provide training systems with the capability of automatic and dynamic adaptation of teaching strategies.

Toward a classification of ITA

In today's training systems, there is a distinct need for improved tools supporting the instructor in all the training phases that for our study have been distinguished in preparation, briefing, supervision, assessment and debriefing.
These training phases are common to every type of existing training devices (e.g. CBT, PTT, FMS, C3I) and consequently a classification of ITA can be proposed.

For the purpose of ITA classification we found a global approach would be more suitable to reach a comprehensive definition, being the analysis based on detailed investigation to find out either instructor's expectation inside the military organisations or known possible areas of technological research to support enhanced tool functionalities for the technical system. Following that approach General Areas of Interest have been identified for the ITA. Common aspects in the instructional needs respect to the training phases were logically grouped into GAoI software components. General Areas of Interest ITA are respectively:

⇒ Training Design
⇒ Automatic Intervention Support
⇒ Scenario Design
⇒ Assessment Support.

As first consequence of the above definition we recognised common instructional needs, i.e. "user requirements" to be supported by a GAoI ITA, covering more than one instructional phase whenever the instructor's tasks are correlated. As an example having an intelligent tool to author a scenario taking into account the specific training objectives (e.g. procedural, combat, tactical) could be also of interest for assessment/debriefing purposes and support the programming of assessment criterias/rules during the early stage of training design.

Training Design

The training design GAoI ITA high level functional requirements are training program authoring, training program optimisation and training objectives authoring. That means an ITA tools in this case should be at least capable of all the following:

a) provide means to define training programs in terms of courses, subjects, training objectives, temporal data, scenarios, training devices
b) provide means to evaluate training programs and their constituent elements (training objectives, scenarios, trainee performance, training devices) in accordance with different instructional strategies
c) provide means to document instructor defined criteria into the training program definition
d) provide means to track current trainee performance and optimize training programs accordingly
e) provide means to suggest training programs modification in accordance with investigated trainee's performance deficiency
f) provide means to suggest training programs modification in accordance with inadequate training devices capabilities
g) provide means to validate the correctness of a training program
h) provide means to optimize training programs on an individual basis, if requested
i) provide means to manage trainee info into a centralized database
j) provide means to document trainee competence and skills into a centralized database

k) provide means to import/export data from the training design data base to/from the training devices scenario and trainee DBs.

Automatic Intervention Support

The automatic intervention support GAoI ITA high level functional requirements are automated briefing, augmented feedback and intervention support. That means an ITA tools in this case should be at least capable of all the following:

a) provide means to support augmented feedback to trainee in accordance with the specific difficulties
b) provide means to modify training environment accordingly to current trainee skills
c) provide means to support tutor training environment
d) provide means to adapt level of training on current trainee performance and learning acquisition
e) provide means to support augmented feedback to instructors on current training situation for conditions/procedures evaluated of relevance for instructor's intervention
f) provide means to support automated briefing on training objectives using functions embedded within the training system itself
g) provide means to support instructor intervention mainly on critical situation
h) provide means to support analysis of the current training situation and tracking of instructor choices
i) provide means to record feedback to trainee as a way to maintain awareness of current trainee's performance
j) provide means to analyse and classify the errors made by the trainee.

Scenario Design

The scenario design GAoI ITA high level functional requirements are scenario authoring, scenario testing and evaluation, interpretation of external (intelligence) data, import/export of data. That means an ITA tools in this case should be at least capable of all the following:

a) provide means to define/design a scenario using an high-level hierarchical tool that does not require specific programming competencies
b) provide means to test and evaluate a scenario using a dedicated expert tool
c) provide means to define and program assessment criteria and/or automatic actions/events
d) provide means to support analysis and evaluation of scenario situation with particular relevance to prediction of possible scenario evolution
e) provide means to support analysis of the current scenario situation to support possible instructor's intervention and supervision
f) provide means to design a new scenario using collected data from debriefing
g) provide means to support briefing/debriefing and generate briefing and debriefing materiel
h) provide means to generate take home packages
i) provide means to import/export of external data.

Assessment Support

The assessment support GAoI ITA high level functional requirements are relevant to a more objective and standardised trainee evaluation, training programs/scenario re-authoring on the base of assessment results. That means an ITA tools in this case should be at least capable of all the following:

a) provide means to re-design a new scenario using assessment results
b) provide means to support assessment on the base of rules/criterias for different type of training (i.e. initial/advanced/tactical/team)
c) provide means to program assessment rules/criterias
d) provide means to support instructor assessment by means of specific contextual info pages
e) provide means to support automatic evaluation of procedures
f) provide means to support instructor in the analysis of assessment data by means of specific expert tool for different type of training (i.e. initial/advanced/tactical/team)
g) provide means to correlate assessment results on subsequent steps of a training program
h) provide means to identify relevant sequence of a training session for debriefing
i) provide means to generate debriefing materiel
j) provide means to optimise training program on the base of assessment results.

The functional requirements stated above for each GAoI ITA were being detailed into software requirements and general specifications in the next project steps.

CONCLUSION

We discovered the cognitive approach fully addresses the core of the problematic. Regrettably, doing the literature survey for this first task of the study, we found that there are few papers on military training addressing the instructor, the trainee and the training system

with a systematic approach, which is what we have tried to achieve.
Notably, the contribution of RTP 11.1 to CRITIAS has proved to be a major one for it has allowed to build the foundation of the framework the Consortium will use and enrich throughout the study.
The cognitive approach also helps to zoom out the idiosyncratic features of existing training aids and/or instructors' praxis, analysed in RTP 11.2 and RTP 11.3, and then makes it possible to formalise a more general framework of modern military training.
This framework provides guidelines to imagine innovative Intelligent Training Aids, that will improve the efficiency and the standardisation of the whole training process. At that stage, state of the art technology can be brought in to design ITA.
It will then be left to the craftsmanship of the *Pedagogical Architect* (Mayou, 1998), mastering both the technological aspects and the pedagogical objectives, to design the training means in full coherence with the training course.

About the authors:

François Héran is the Programme Manager for RTP 11.9. He joined the Electronics Division of Sogitec in 1987 and is currently in charge of European studies. He holds an Engineer Degree from Ecole Centrale (Paris) and a Master degree in Aeronautics from Stanford University (USA).
Mr François D. Héran
SOGITEC Industries
4, rue Marcel-Monge 92158 Suresnes Cedex
FRANCE
Fax 33 1 41 18 57 18
Tel 33 1 41 18 57 23
fheran@sogitec.fr

Patrice Le Leydour is Training Means Product Manager for the Military Unit of Thomson Training & Simulation at Cergy-Pontoise, France. He currently works on Trainee Management Facilities. He spent the last 8 years working on several instructor and debriefing stations projects. He has a Computer Engineer degree from the Institut Industriel du Nord/Ecole Centrale, Lille, France.
Mr Patrice Le Leydour
THOMSON TRAINING & SIMULATION
1, rue du Général de Gaulle Z.I. Les Beaux Soleils Osny
BP 226 95523 CERGY PONTOISE CEDEX
FRANCE
Fax 33 1 34 22 81 49
Tel 33 1 34 22 82 52
patrice.leleydour@tts.thomson.fr

Peter Meyer zu Drewer is Software Development Engineer for CAE Elektronik GmbH, Germany. Joining CAE in 1994, he was involved in the design of instructor stations for military flight simulators and a nuclear power plant simulator. For the latter project he spent 18 months at CAE Electronics Ltd. in Montreal, Canada. He holds a degree in Electrical Engineering from the Technical University of Aachen, Germany.
Mr Peter Meyer zu Drewer
CAE Elektronik GmbH
Postfach 12 20
D-52201 STOLBERG
Fax 49 24 02 106 270
Tel 49 24 02 106 252
pmeyer@cae-gmbh.de

Susanna Sirignano is Training System Engineer for the Training & Simulation Department of Agusta at Cascina Costa, Italy. She currently works on training systems definition and syllabi design for both Military and Civil market. She spent the last 8 years working on training analysis, syllabi trade-off and cost-effectiveness evaluation and on several trainers and simulators projects. She has a Nuclear Engineering degree from the Politecnico di Milano, Italy.
Mrs Susanna Sirignano
AGUSTA
Via G. Agusta 520 21017 Cascina Costa di Samarate (VA)
ITALIA
Fax 39 03 31 711 627
Tel 39 03 31 711 584
s.sirignano@agusta.it

References:

[Amalberti, 1996] Amalberti R. La conduite des systèmes à risques, Paris, P.U.F (1996)
[Gagne, 1985] Gagne R., (1985). Conditions of Learning.
[Mayou, 1998] Jean Mayou, Full and global approach paradigm: Fill the gap in the training process, *Procs* TRICON 1998
[Merison, 1998] Rudolf J.W. Merison, A European Technology Pillar in Creation, in Modern Simulation & Training, Feb. 98

[Orey, 1993] Orey, M. & Nelson, W. (1993). Development Principles for Intelligent Tutoring Systems : Integrating Cognitive Theory into the Development of Computer-Based Instruction. Educational Technology Research and Development, 41(1),59-72.
[Rasmussen, 1987]Rasmussen, J A framework for cognitive task analysis in system design, in E. Hollnagel, G. Mancini, D. D. Xoods (Eds) , Intelligent decision support in process environments, Berlin Springer-Verlag. (1987)
[Ruffel Smith, 1979], A simulator study of the interaction of pilot workload with errors, vigilance, and decisions, NASA TM-78482. Moffet Field, CA: NASA-Ames Reserach Center.
[Silverman et al., 1996] Denise R. Silvermann, V. Alan Spiker, Steven J. Tourville, Robert T. Nullmeyer, A combat mission team performance model: development and initial application, in: Interservice Industry Training Systems and Education Conference, Orlando 1996.
[Van Eslande, 1997] Van Eslande, Alberton L., Scénarios-types de production de l'erreur humaine dans l'accident de la route, Rapport INRETS n°218, juin 1997

TWENTYFIFTH EUROPEAN ROTORCRAFT FORUM

Paper No. F4

HELICOPTER MODULAR AVIONIC CONCEPTS

by

Alan Perkins
GKN Westland Helicopters Limited
Yeovil, Somerset, UK

SEPTEMBER 14-16, 1999
ROME
ITALY

ASSOCIAZIONE INDUSTRIE PER L'AEROSPAZIO, I SISTEMI E LA DIFESA
ASSOCIAZIONE ITALIANA DI AERONAUTICA ED ASTRONAUTICA

1. INTRODUCTION

GKNWHL have been conducting studies and assessments over a number of years concerning the development of flexible, integrated, modular helicopter avionic systems. Future avionic systems are expected to have evolved from the federated types, seen on platforms such as Merlin Mk1 and Heliliner, to integrated modular types in the next generation of future maritime, military transport and civil helicopters. This move is the result of a number of pressures on the aerospace and avionics industry to address issues such as controlling life cycle costs, overcoming obsolescence, and providing increased functional performance and flexibility within tight budgetary constraints.

Future developments in aircraft avionics also have to take into account the rapidly changing microelectronics market. Aircraft in service now and those due to enter service in the near future are faced with the prospect of electronic component obsolescence and subsequent supportability problems. The problem is made worse by semiconductor manufacturers withdrawing specialist support for the small volume market that avionics represents to concentrate on the high volume commercial markets driven by the expansion of personal telecommunications and computing. This paper examines some of the key issues that GKN Westland Helicopters (GKNWHL) have been addressing in their efforts to understand the changes that will be necessary for future systems and to identify an effective solution. Like many other companies in the aerospace community, GKNWHL are looking at the concept of modular avionics for the solution. This paper considers how the modular avionic concept could be applied to future versions of the EH101 helicopter.

2. MODULAR AVIONICS

Modular avionics promotes the use of common, standard components. The concept involves defining standard software components and a limited range of common hardware modules. The modular approach encourages the use of "open standards" which are expected to come from the commercial market and are ideally long lived. The standards are required to fit in a framework, see Figure 1, with well defined hardware and software interfaces as appropriate between the application, operating system, hardware drivers and hardware. These open standard interfaces enable elements of the system, in particular the hardware, to be replaced by newer designs and thus deal with obsolescence.

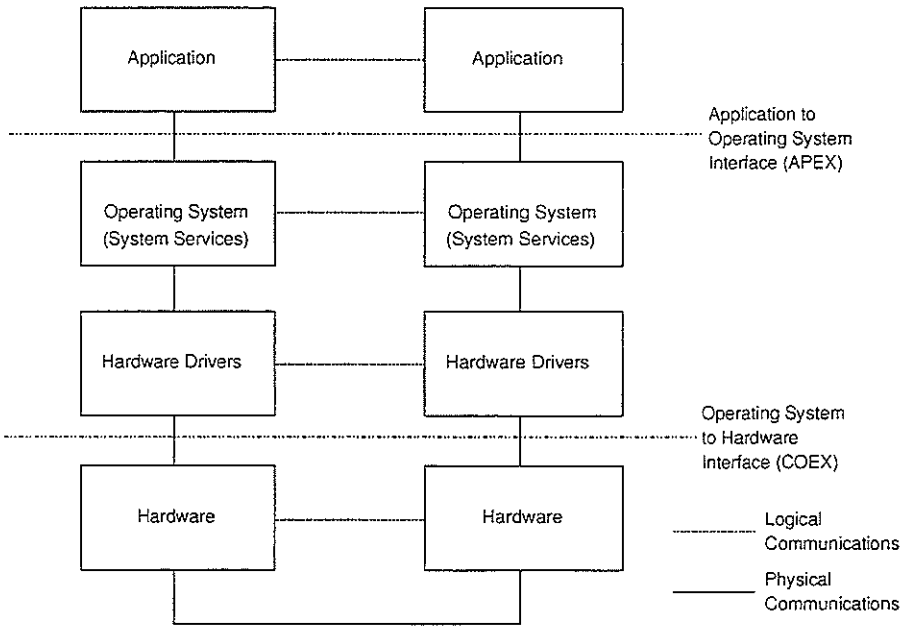

Figure 1 Framework for Open System

The standard components are designed for use across a range of platform types and are thus interchangeable and reusable. This is of particular benefit to a multi-role platform such as the EH101 where a number of versions could be in service with the UK armed services and civil operators. For a platform that may be in service for up to 30 years, the flexibility offered by a system that conforms to the open system framework is particularly important.

Modular avionics means different things to different people, it not only promotes the concept of common hardware and software with established interfaces defined by the framework, but presents a number of other options and challenges as well. These include:

- greater functional integration – requiring techniques to protect functions from each other if they are running on the same hardware module.
- mixing solutions from different vendors – the infrastructure created for the modular system should enable software functions from different vendors to be hosted on the same hardware module, or at least in the same enclosure.
- reconfiguration – enabling the introduction of maintenance free operating periods.
- new packaging concepts – enabling space and weight to be minimised.
- the use of "smart" localised resources – taking the digital domain out to sensors and effectors.
- incremental qualification and certification – allowing changes such as the addition, modification or removal of functions to be achieved without having to undertake significant re-test of the system.

The above list, the framework and the "openness" are the key elements of a modular system. The problem faced by aerospace companies is how to realise a modular system and which of the modular features listed above should be implemented. The drivers for this are cost and ability to meet operational requirements. The usual model for this position is represented by the cost versus capability curves as shown in Figure 2.

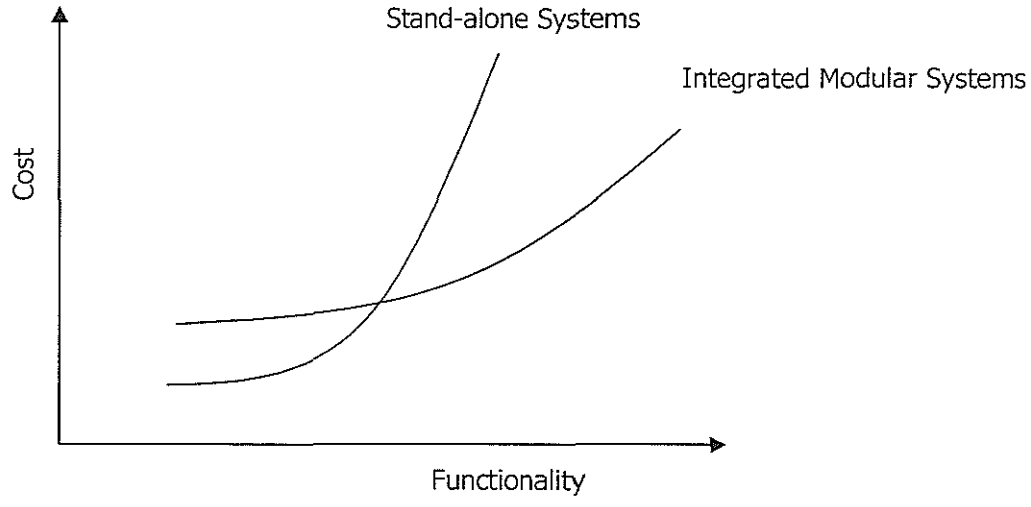

Figure 2 Cost Versus Capability Curves

The curves suggest that investment in moving from a non-modular system to a modular system will result in cost savings in the longer term as capability can be enhanced in the modular system at less cost than in a non-modular system. GKNWHL, through their studies, have been testing this relationship to understand whether the promised advantages will be realised.

3. BACKGROUND

An example military EH101 system is shown schematically in Figure 3. It comprises a core element which is broadly common to both civil and military variants and features:

- Aircraft Management System
- Electronic Instrument System
- Automatic Flight Control System
- Navigation System
- Communication System

These core systems are interconnected in military variants using a combination of MIL-STD-1553B and ARINC 429, and in civil variants using ARINC 429.

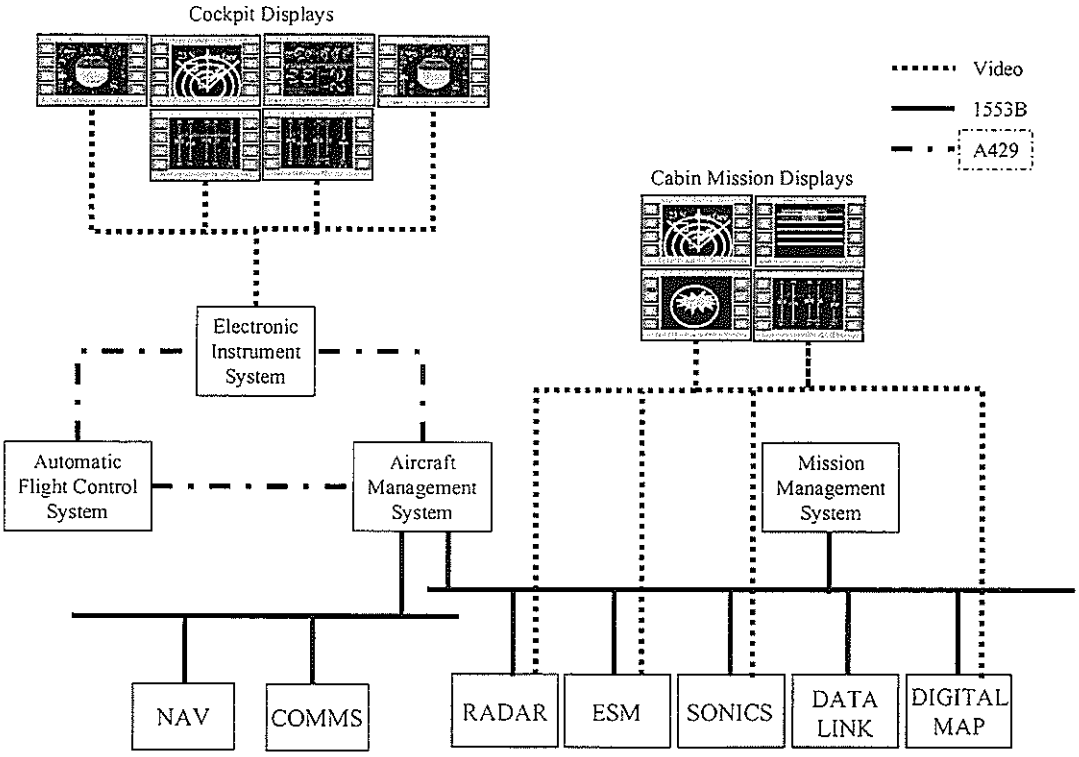

Figure 3 Current EH101 Architecture

Some of the variants, principally the military, feature a mission system fit. It is conceivable that a non-military variant could have a mission system of some form, perhaps a radar console in support of fisheries protection for example. The two EH101 variants entering service with the UK armed forces are the Merlin HM Mk1 and HC Mk3.

The Merlin HM Mk1 mission system features:

- Mission Management System
- Radar System
- Active Dipping Sonar
- Sonics System
- Data Link
- Digital Map
- Electronic Surveillance Measures

The Merlin HC Mk3 mission system features:

- Forward Looking Infra-red
- Defensive Aids

These mission systems are interconnected using a combination of MIL-STD-1553B and ARINC 429.

All EH101 variants feature complex video distribution systems managed by the Electronic Instrument System for the flight displays in the cockpit and from mission related graphic generation devices for the mission displays in the cabin and the cockpit, these can be seen in Figure 3.

3.1. FUNCTIONAL INTEGRATION

Avionic systems have become evermore sophisticated, with aircraft such as the Royal Navy's Merlin HM Mk1 incorporating radar, sonics (both active and passive), electronic surveillance measures, digital map and data link in the mission system. The task of managing these resources requires careful system design to ensure that workload is manageable, both in the cabin and the cockpit. For future systems with greater functionality, it is expected that the crew interface and support systems will develop to ease the workload. The result is functional development which requires ever closer integration of the various systems, particularly through the mission management system. GKNWHL's aim is to ensure that the functional integration is achieved in a cost effective manner and is supportable in-service, accommodating changes as a result of customer desires and technological development.

3.2. FLEXIBILITY

Flexibility is a key requirement for future aircraft, and this is particularly the case for helicopters. Customers are looking for products that are:

- Cheaper to acquire and operate.
- More flexible in use, to maximise the return on a relatively expensive asset.
- Easy to modify and adapt to take on new roles and satisfy changing requirements.
- More effective, without increased cost.

GKNWHL perceive the EH101 as providing a very flexible yet adaptable asset. Avionic system development towards a modular avionic solution is seen as potentially enhancing the flexibility by enabling rapid changes of role with the removal of equipment when the role change requires it, even with the higher level of functional integration expected of future systems. An IMA system would support this change in configuration through the developments in the software architecture with well established interfaces, particularly between the application and operating system, and with configuration management functionality within the operating system. Thus a change from an anti-submarine warfare role to a search and rescue role would see the removal of equipment from the cabin to provide additional space. The reversal of the role would involve re-instatement of equipment. In both cases there would be a need to run quick and effective test routines to validate system operation in the changed role.

The flexibility required of the avionic system extends to the sensor equipment fit itself. There is the need to be able to offer customers the option of fitting their preferred sensor systems, while retaining the overall integration and ultimately performance of the complete platform. The choice of sensor fit is very often driven by the desire to support specific industrial organisations and to provide a degree of offset that will help secure the sale of the helicopter. Once again, the software architecture will play a key role in enabling application software to be readily adapted.

4. SOFTWARE ISSUES

The framework for open systems shown in Figure 1 supports a software architecture that encourages the development of applications which exhibit independence from the hardware platform. The key feature of such a software architecture is the application interface, as shown in Figure 4. There has been much work to develop this application interface which in the long term will enable software re-use. The operating system that underlies the interface is also expected to support multiple applications in protected partitions, ensuring that at run-time, memory protection is achieved which guarantees the integrity of the applications.

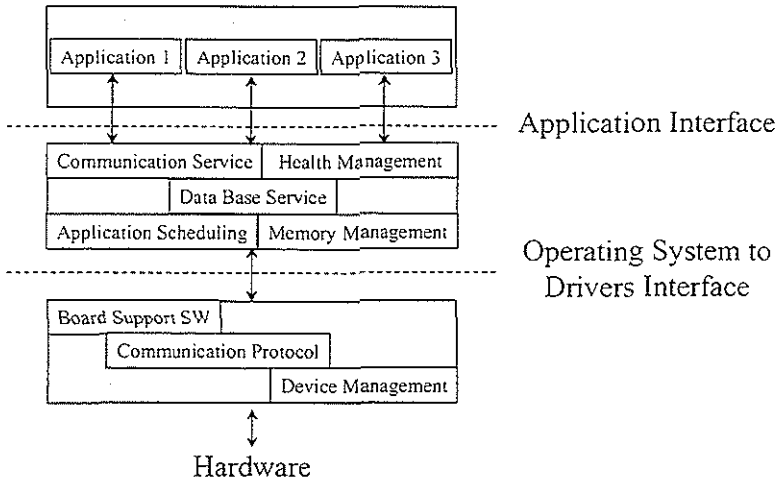

Figure 4 Example Software Architecture

5. MODULAR AVIONIC SYSTEM PROJECTS

Integrated modular avionics has been the subject of much study and some trials, with efforts taking place in the UK supported by the Ministry of Defence and by the Department of Trade and Industry through the CARAD budget. There have also been considerable efforts in the US, where platforms such as the F-22 Raptor the RAH-66 Comanche and the Boeing 777 have led the way with modular avionic systems. The key elements of these modular systems are:

- Common modules – both hardware, software and communication
- Common interfaces – ideally conforming to an open standard
- Functional integration
- Reconfiguration
- New packaging concept

The various modular avionic system projects present a number of options to the avionic system designer, making the task more difficult in determining the route to implementing a modular system from the currently available systems or those under development. Some of the options include the adoption of truly commercially derived technology (i.e. VME), the US military modular technology as proposed for F-22 and RAH-66 (although the commonality between these two platforms has been difficult to maintain), civil IMA as defined in ARINC 651 and its associated documentation and the European military solution being pursued through the Allied Standard Avionics Architecture Council (ASAAC).

5.1. US PROGRAMMES

The US military technology, based around the Standard Electronic Module type E (SEM-E) supports the key elements of an IMA system, but is based around two data bus standards that are unlikely to find continued support beyond the F-22 and RAH-66 programmes. These standards are the AS4704, High Speed Linear Data Bus and the AS4711, PI-Bus, both developed through the Society of Automotive Engineers. Developments in support of the Joint Strike Fighter will determine the long term viability of these bus standards, but it seems unlikely that they will feature in that programme.

5.2. ARINC EFFORTS

ARINC standardisation of IMA through the 600 series has not yet provided the infrastructure to fully support the development of IMA for civil aerospace systems. The Boeing 777 took the first step, but again the use of two data buses, ARINC 629 and ARINC 659, bespoke aerospace

solutions, has not been followed by other aerospace companies. The cost to connect to ARINC 629 is considered by many to be prohibitive and neither are truly open standards.

5.3. ASAAC

The work being undertaken as part of the second phase of the ASAAC programme is focussing on making best use of commercial technology and is therefore hoping to ensure that elements that will be "standardised" are effectively already open standard solutions for which an avionic variant can be easily defined. The only drawbacks with the ASAAC solution are target platform and timescale. The target in the UK is the Future Offensive Airborne System (FOAS) and its in-service date is 2018. GKNWHL perceive the need to employ IMA in the nearer term and need to ensure that any solution adopted is not at variance with the developments in the ASAAC programme.

5.4. COMMERCIAL VME

Finally, VME and supporting commercial software is being given some impetus through two UK aircraft programmes, - both the RAF's Harrier GR7 and the RN's Harrier FRS2 are receiving mission system upgrades which will see the introduction of ruggedised VME and commercial operating systems. This is an interesting first step to an integrated modular system, enabling additional functions to be brought into the mission computer, but does not introduce other features of a modular system such as reconfiguration and a new packaging concept.

5.5. GKNWHL PROGRAMMES

GKNWHL have recently completed one and are involved in a second programme which focuses on the concept of Integrated Modular Avionics. The first programme, supported by a grant from the UK Department of Trade and Industry, was the PACTS-21 (Platform Applications for Commercial aircraft Transport Systems for the 21st Century) programme, involving collaboration with key UK aerospace companies including BAe Airbus, Smiths Industries Aerospace, Marconi Electronic Systems and Lucas Varity Aerospace. The second is a UK Ministry of Defence supported programme called ReACH (Realisable modular Avionics Common across Helicopters) which is being conducted in collaboration with the Defence and Evaluation Research Agency (DERA) based at Farnborough together with Marconi Electronic Systems (MESL).

5.6. PACTS-21

The PACTS-21 programme had a civil aircraft focus, for which GKNWHL chose to examine the civil variant of the EH101, Heliliner. Through this work, GKNWHL examined a number of key issues and developed a simple commercial based modular rig. The key elements of study were:

- Asynchronous Transfer Mode,
- Future Avionic Architectures,
- the Systems Engineering process for complex systems and
- a Case Study to bring the elements together.

It has already been suggested that one of the problem areas for future modular systems is to adopt a data communication network that is an open standard solution and is long lived. Added to these the data communication network should also provide growth in terms of bandwidth and connectivity. Asynchronous Transfer Mode (ATM) is seen as a potential solution to the communication problem, providing a packet switching technique which has been devised to support a range of services including video, audio and data. GKNWHL have used ATM as the transfer mechanism between single board computers in their modular rig.

A packet switching network provides the opportunity to unify the network type within the avionic system, removing the need for separate backplane, data and video interconnects. The designer has the option of segmenting the system into different functional areas. Thus an ATM switch could provide circuit switch type operation (still using packets) in support of video data transfer and pure

packet switch operation within the core of the system, as shown in Figure 5. In the mission area, which was not studied in the PACTS-21 programme, mixing the high bandwidth segmented data with lower bandwidth messages is a possibility.

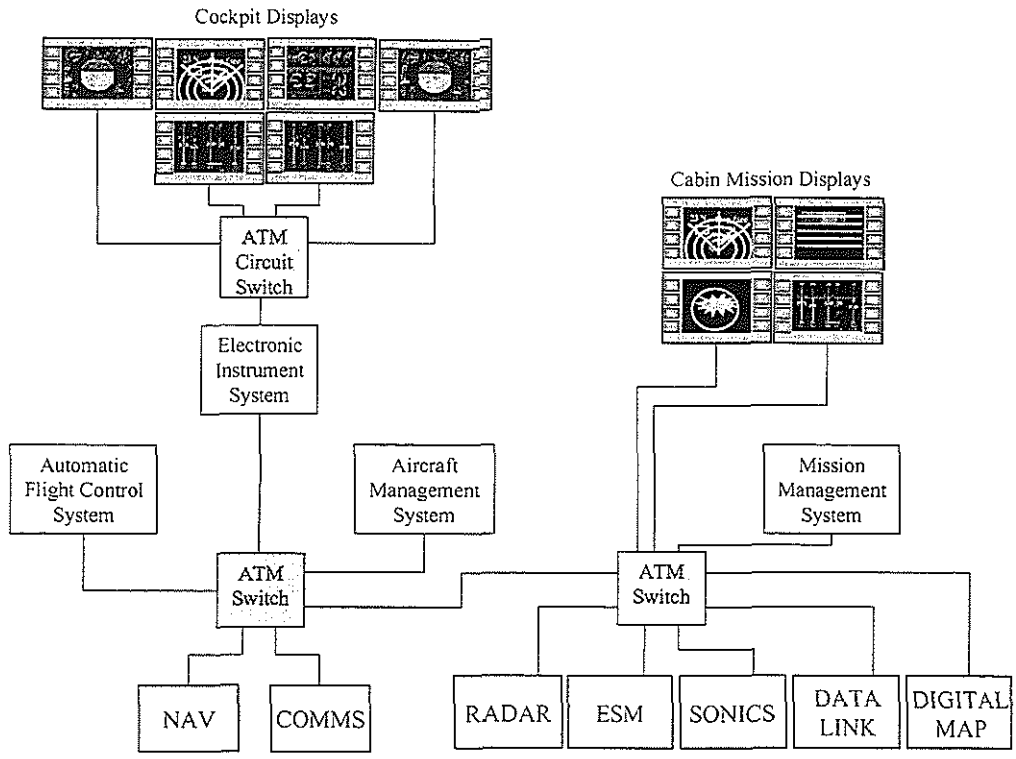

Figure 5 ATM Connected Architecture

ATM is not the only data communication systems option, alternatives are switched ethernet variants, Fibre Channel and Scalable Coherent Interconnect. It is likely that the first aerospace project to choose one of these networks will drive others to follow suit.

The PACTS-21 programme also enabled GKNWHL to examine the use of computer aided system engineering tools to support the systems engineering process in the development of complex systems. It is clear that if system designers are to succeed in their task with ever more integrated systems that good requirements management, function definition, design analysis and test/certification tools are necessary to manage the programme. GKNWHL were able to:

- capture and analyse requirements and link them into a functional definition using tools such as System Architect and RDD100.
- to analyse elements of the design using tools such as BONeS and Statemate and
- to implement the behaviour of a chosen function (the Communication-Navigation-Surveillance/Air Traffic Management described in ARINC 660A) in Statemate and use its autocode facility to produce an application onto the modular rig. An integrated software development environment, Rational Apex was used to support this process.

One of the important lessons learned from this exercise is that much work is needed to improve the flow of information through the set of tools that can support the systems engineering process for modular systems. This flow of information is important to record and trace design decisions and to support the certification process.

5.7. REACH

The ReACH programme has a military focus, taking Merlin HM Mk1 as the baseline helicopter and Merlin Mk2, Future Amphibious Support Helicopter (FASH) and Future Light Battlefield

Helicopter (FLBH) as the future target platforms. The main objective of the programme is to measure the worth of introducing IMA into these target platforms. The key stages of the programme are:

- Requirements and functional definition of the various platforms.
- Definition of ***realisable*** technology and architecture.
- Assessment of performance and costs of the system.

GKNWHL are responsible for the requirements and functional definition for which RDD100 is being used to manage the process. The tool is being used to capture the baseline requirements for Merlin HM Mk1 and then to record changes that are required in the form of additional, modified or removed functions.

Marconi Electronic Systems (MESL) have undertaken the technology and architecture scheme study which has identified technology that is realisable now or in the near term. The term realisable is specifically used as the aim is to understand what could be used in aircraft in the next few years and to understand how it will develop with time. One of the important goals is to ensure that the ideas developed in ReACH are not out of step with those of ASAAC. MESL's work in ReACH has involved defining the modules for a near term system and expanding upon their use within a processing group. This would for example, take the architectures shown in Figure 3 and Figure 5 to that of Figure 6 which shows a simplified form of the architecture with modular processing groups.

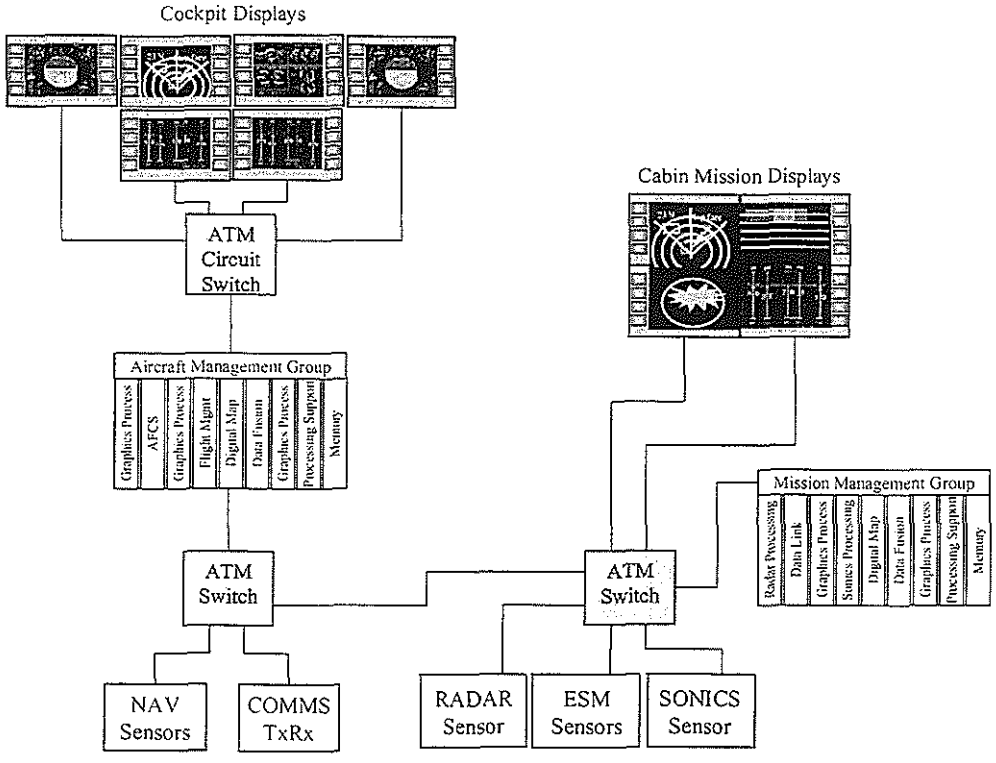

Figure 6 Architecture with Modular Processing Group

DERA and GKNWHL will take the functional definition and map the functions to the architecture scheme devised by MESL (not necessarily using ATM as the interconnect). The fully mapped architecture is then in a position to be analysed using tools available at DERA, in the form of performance models developed for SES Workbench, and at GKNWHL using Price H™ and S™ as well as Arena® to determine development and manufacturing costs as well as life cycle costs.

The architecture shown in **Figure 6** is not special to helicopters The area that requires specific attention for helicopters is that of packaging of the new modular elements.

6. NEW PACKAGING CONCEPT

There has been much work on the various modular avionic programmes to devise methods to package and install the common modules, providing the necessary infrastructure to connect, remove heat and protect the module from the environment. The heat removal requirements of some module designs has led to the proposed use of liquid cooling via heat pipes. The modules also rely on edge ribs to remove the heat from the components and wedge locks to hold the module in place. Wedge locks are a hindrance to the removal of heat. By looking at the uses that the sides of module are put to GKNWHL have identified an alternative approach to packaging – the clamp stack approach.

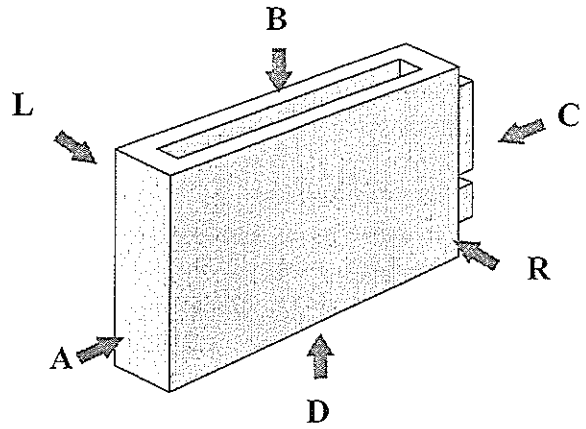

Figure 7 Module Side Names

Side **A** gives access for inserting and extracting the module to the rack.

Sides **B** and **D** provide access for the coolant.

Side **C** is taken up by the connectors.

This leaves sides **L** and **R** to be used for mounting.

The clamp stack modules are held in place by clamping forces applied at either end of the module set. The resulting arrangement frees the path for heat flow, removes heavy heat sinks and wedge locks and edge ribs and has a reduced parts count. The modules rely on float mounted connectors.

This module packaging arrangement has considerable advantages for helicopter systems as it is expected to be up to 50% lighter than conventional packaging designs.

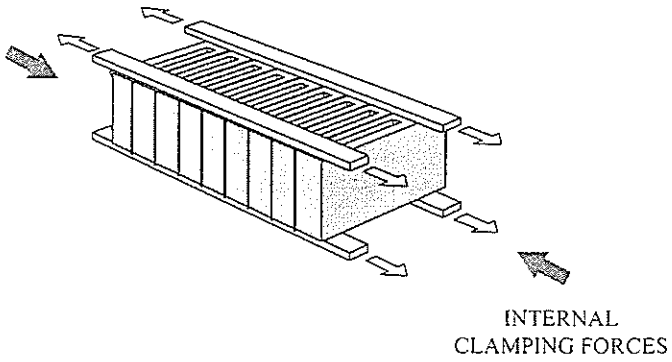

Figure 8 Clamp Stack Arrangement

7. RECONFIGURATION

It was suggested in Section 2 that with a modular system it is possible to introduce the concept of maintenance free operating periods (MFOP), that is the avionic system is able to tolerate faults and hardware failures for specified periods of time. These periods of time are designed to align with major maintenance activities of other aircraft systems. The MFOP is achieved by providing spare resources, common modules, within the avionic system that are available to a number of the avionic functions. This is in contrast to current practice where duplicate, complete line replaceable units (LRU) are provided one as a backup for another. In this case, the resources in the spare LRU are not available to other functions in other LRUs.

The technique of using spare, unassigned resources in a modular system is generally termed reconfiguration, see Figure 9. Two distinct forms of reconfiguration can be considered, static and

dynamic. Dynamic reconfiguration is designed to occur during avionic system operation in flight while static is targeted at recovering the functional capability of the aircraft on the ground.

Developments in the performance of built-in-test systems, enabling accurate fault detection, identification, location and isolation are vital. Work at GKNWHL has involved identifying techniques that can be applied at the various layers of the system framework, at the application, the operating system, drivers and hardware.

Some of the built-in test techniques identified included:

- syndrome pattern matching; the use of diagnostic look-up tables derived from failure mode and effect analyses, modified to include environmental information from temperature and stress monitoring devices and operational experience.
- boundary scan testing; a well established technique for testing digital circuitry which relies on the components embodying boundary scan facilities.
- n-version programming; where multiple variant versions of a software application are used to detect the failure of a software function by the comparison of the outputs of the different versions.

The application of reconfiguration, particularly in its dynamic form is considered high risk, and will probably be limited initially to non safety critical systems, specifically in the mission system. The action of reconfiguration must be pre-defined at the design stage in order that the appropriate test and validation of the effect can be fully determined.

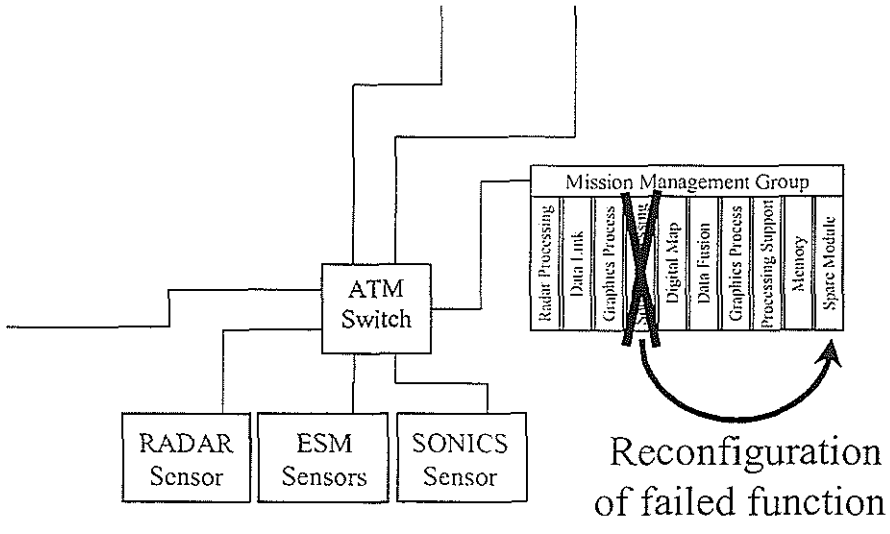

Figure 9 Reconfiguration of a Processing Group

8. EXTENDING THE DIGITAL DOMAIN

There is an opportunity with the introduction of modular avionics to extend the digital domain to all parts of the aircraft. The modular approach seeks to bring processing functions to the centre of the system enabling resources to be shared effectively between these functions and take advantage of spare modules to support the reconfiguration strategy. On the other hand, the placement of a particular modular component away from the centre of the system is designed primarily to reduce weight, but also improve system reliability. This component is termed a remote data concentrator (RDC) and has a number of specific uses. As its name suggests, it provides a means to gather up sensor data, normally of a low bandwidth, in a remote part of the aircraft and transmit it in digital form over a data network to the central processing resource. The RDC can also contain functionality which can provide local control of a system element and thus becomes a "smart" RDC.

Work by Lucas Varity within the PACTS-21 programme was particularly concerned with the use of smart RDCs in fly-by-wire actuator control architectures. Lucas focused upon the use of a generic smart actuator controller which was designed to be fitted to the secondary actuators of a fixed wing aircraft offering a light weight, low cost solution to the control of these systems.

GKNWHL's work on the use of RDCs in helicopters has not shown their use to be beneficial for sweeping up low bandwidth sensor signals. This is partly because there are actually few remote locations on a helicopter and the weight of an RDC is currently expected to be greater than the amount of wiring it is likely to replace. GKNWHL are likely to retain low bandwidth sensor interfacing within a modular rack. Efforts to reduce the number of types of analogue and discrete signal through standardisation may make the use of RDCs in helicopters more attractive.

9. QUALIFICATION AND CERTIFICATION

The topics of qualification and certification are important issues to be addressed when proposing a change in avionic system design from a federated avionic system, characterised by strict functional and physical partitioning to an IMA system with complex integration. The expectation that an IMA system can simply be implemented with common hardware and software from different vendors is obviously a naïve one. It is important to consider the route to qualification and certification from the outset of the design process, making use of computer aided system engineering tools to manage the process and show traceability of requirements and design decisions to the tested article and providing support for safety analysis.

There is a change in philosophy required to certificate future IMA systems. It is unlikely that the current safety analysis techniques associated with federated systems will be appropriate to IMA technology in particular when the issue of commonality raises the probability of common mode failure. It follows that a significant advance in the certification process is required to enable the exploitation of this technology. The term "incremental certification" is being associated with the process by which certification may be achieved for highly-complex systems. This will allow elements of an IMA system to be certified in isolation, for example the hardware and application software would be certified as independent components. This approach aims to limit the cost of re-testing a complete system that has been modified, for example with the introduction of a new processor to replace an obsolete one or a new avionic function. Any enhancements to the certification process will need to address the following issues:

- Software portability; application and operating systems,
- Software partitioning; integrity of multiple applications (e.g. navigation, communication) being performed on the same processing module,
- Configuration control; the run-time allocation of functions to available resources,
- Mixing of applications with mixed criticality.

The Society of Automotive Engineers has produced aerospace recommended practice, ARP4754, titled Certification Considerations for Highly Integrated or Complex Aircraft Systems which discusses the subject from a total life cycle aspect.

10. CONCLUSIONS

This paper has addressed a wide range of topics concerned with modular avionic systems and what is particularly important for its introduction in helicopters. Obviously, the fundamental principles behind IMA for helicopters does not vary from that of fixed wing aircraft, either military fast jet or civil airliner. However, the helicopter is renowned for its flexibility and presents particular challenges for IMA if this flexibility is to be fully exploited. GKNWHL are continuing to develop their understanding of IMA principles in collaboration with other UK companies and research organisations and are also looking forward to working with Agusta and other European companies on the forthcoming Framework 5 programme, PAMELA.

TWENTYFIFTH EUROPEAN ROTORCRAFT FORUM

Paper n° F6

SOFTWARE PARTITIONING FOR SAFETY-CRITICAL AIRBORNE SYSTEMS IN PRACTICE

BY

M.F.R. KEUNING

NATIONAAL LUCHT- EN RUIMTEVAARTLABORATORIUM (NLR),
THE NETHERLANDS

SEPTEMBER 14-16, 1999
ROME
ITALY

ASSOCIAZIONE INDUSTRIE PER L'AEROSPAZIO, I SISTEMI E LA DIFESA
ASSOCIAZIONE ITALIANA DI AERONAUTICA ED ASTRONAUTICA

SOFTWARE PARTITIONING FOR SAFETY CRITICAL AIRBORNE SYSTEMS IN PRACTICE

M.F.R. KEUNING

NATIONAAL LUCHT- EN RUIMTEVAARTLABORATORIUM (NLR), THE NETHERLANDS

Abstract

Increasingly demanding helicopter operations lead to a higher workload on the pilot. To support these helicopter operations and relief the workload on the pilot more sophisticated avionics are incorporated. Many of the avionics' functional requirements are realized in software. This has induced a strong growth of the size and complexity of the used software.

Often this software contains safety critical components as well as less critical components. Because of economic pressure, techniques are needed to reduce the development effort of the less critical software components in these systems without compromising the functioning of the critical components and thus the airworthiness. One solution - as proposed by DO-178B: *Software Considerations in Airborne Systems and Equipment Certification* - is partitioning. A partitioning architecture is discussed which is successfully implemented and certified as a part of helicopter avionics. DO-178B categorizes software components into five criticality levels. The realized avionics contains software components of three different levels including the most critical level (i.e. level A).

The developed novel partitioning architecture is based on two hardware capabilities, a Memory Management Unit (MMU) and a processor with two protection levels. The hardware of the developed system contains a compliant processor with built-in MMU that supports both segmentation as well as paging as means of memory protection. Only paging is used because with the selected processor segmentation induces up to 50% performance overhead whereas the overhead of paging stays well below 5%.

Central to the partitioning architecture is a proprietary kernel that runs in a protected environment. The proprietary kernel manages all protections within the application. Like most operating systems, protection is provided between tasks. Furthermore protection is provided between components of different software levels (i.e. intra task and inter task) which is the most important protection support concerning safety.

A formal model of avionics partitioning defines three essential requirements for the kernel's access mediation functions, i.e. complete, tamper-proof and assured. All these essential attributes are met by the developed partitioning architecture. The developed partitioning architecture can be ported to other hardware and extended, with for example: support for Integrated Modular Avionics (IMA) and support for distributed and multi-processor systems.

The implemented partitioning architecture was successfully certified as a part of the helicopter avionics. The measured processor load overhead induced by partitioning is only about 1%. Memory usage increased by approximately 5%. These resource requirements are very acceptable considering the economic advantages gained. Consequently the developed partitioning architecture is very useful and can be reused in future applications.

1. Introduction

In the early 1980s, a new era for airborne systems and equipment began. Usage of software

incorporated in these systems started to increase with a dazzling speed. The amount of software used in civil aircraft has almost been doubled every two years and given this trend it is expected to grow with a factor of about 1000 over the next 20 years [Sto96]. An industry accepted guidance - DO-178 that is currently in revision B [RTC92] - was written. This guideline has the purpose: ``to provide guidelines for the production of software for airborne systems and equipment that performs its intended function with a level of confidence in safety that complies with airworthiness requirements".

In correspondence with FAR/JAR-25 [FAR] DO-178B [RTC92] identifies five levels of system failure conditions and associates herewith five software safety levels (hereafter simply referred to as levels). See Table 1 for the categorization of the software safety levels.

Software Safety Level	Failure impact
Level A	Catastrophic
Level B	Hazardous
Level C	Major
Level D	Minor
Level E	No Effect

Table 1

The highest level software - Level A - is considered to have possible catastrophic impact if the software fails to operate according to its requirements. The lowest level - Level E - is considered to have no impact on flight safety. The identification of multiple software levels within one application imposes the problem that components of different levels may interfere with each other. This problem can be overcome by developing all components according to the highest identified level. However, as easy as this solution may seem as costly can the realization thereof become. DO-178B [RTC92] proposes several architectural concepts to tackle this problem. One of these concepts is partitioning.

Partitioning is described by DO-178B [RTC92] as: ``Partitioning is a technique for providing isolation between functionally independent software components to contain and/or isolate faults and potentially reduce the effort of the software verification process".

The realization of a safety critical helicopter avionics application initiated the development of a proprietary partitioning architecture that conforms to the DO-178B [RTC92] guideline. A partitioning architecture was developed whose only hardware requirements are a processor with protection modes and a memory management unit (MMU). This partitioning architecture is presented in section, the realization in the avionics application is discussed in section.

2. A Partitioning Architecture for Safety-Critical Airborne Software

When using multiple levels of software - as defined by DO-178B [RTC92] - within a single hardware environment care has to be taken to prevent lower level components from influencing higher level components of the software. Faced with such a situation for a real application two options were considered:

1. To develop all software components according to the highest identified level (i.e. level A) even if a lower level would be sufficient for some components. This option was considered because the size of the components of another level than level A was relatively small.
2. To develop a partitioning scheme. Since the software is running on a processor with built-in MMU and protection mechanism (i.e. i386EX [Int87]) it is possible to implement a partitioning scheme without adding hardware requirements.

The main points of consideration were effort, flexibility and performance. Looking just at initial

effort would maybe have favored against partitioning but recurring effort because of modifications and extensions is very much in favor of partitioning. Flexibility is strongly related to the effort issues. In this sense, partitioning has a great advantage over the first option. With partitioning, it is easy to add a new extension at a lower level (e.g. new or enhanced maintenance or debug capabilities) whereas without partitioning a lot of effort could be induced. Performance however can be a big concern for partitioning. Experimental measurements on the real application pointed out that partitioning could add up to 50% execution time. This would have effectively eliminated the option to use partitioning if there were not a more efficient solution.

This performance overhead of partitioning is caused mainly by the usage of a memory management unit (MMU) which is needed to manage protection of memory and memory mapped hardware resources. The used processor has two basic approaches to memory management namely segmentation and paging (these two approaches can actually be combined into a hybrid form). Performance measurements greatly favored paging over segmentation. Whereas segmentation adds up to 50% overhead, the overhead of paging stayed well below 5%. Noted should be that all memory allocation is static and no swapping is performed.

Paging however has a fixed granularity (4Kb for the used processor) and that can become a problem in protecting small special purpose memories (e.g. special non-volatile or dual-ported memory). However, analysis of the memory usage of the real application - especially the usage of the small special purpose memories - indicated no serious problems concerning the paging granularity.

After evaluation it was decided to develop a partitioning scheme based on paged memory management. The performance overhead of segmentation is simply too large and the potential effort increase without partitioning is unacceptable.

The rest of this section will outline the general concepts of the developed partitioning architecture. The discussion focuses mainly on the protection issues of the partitioning architecture. In addition, issues like the incorporation of tasking on top of the partitioning architecture, reusability and extendibility are discussed.

Features and Goals

Following are the main features and goals of the practical general partitioning architecture:

- Compliance to the three essential attributes for an access mediation function provided by the kernel as defined by Di Vito [Vit98]:

  Complete

  There shall be no way for software running in any partition to bypass the kernel and access resources not under the kernel's control.

  Tamper-proof

  There shall be no way for software in any partition to tamper with the kernel or its data so as to subvert the kernel's control of system resources.

Assured

The kernel shall contain minimal functionality and shall meet all of the regulator's requirements for the criticality rating of the overall Avionics Computer Resource (ACR).

- Inter level protection support (i.e. inter and intra task).
- Multi-tasking and inter task protection support.
- Minimal extra resources requirements, notably performance overhead.
- Portability to similar hardware architectures (i.e. processor with protection levels and MMU).
- Shared memory support for inter level and inter task sharing.
- Static memory management (i.e. no swapping, no dynamic memory allocation).

Memory management is static because for dynamic memory management it is much harder to prove correct usage with respect to availability and access time. Therefore, if it is possible to use static memory management - thus no swapping and dynamic memory allocation - it is preferred above dynamic memory management for safety critical applications.

Partitioning Protection Architecture

The primary goal of the usage of a partitioning protection architecture in avionics is to ensure the safety of the people in the aircraft. This goal infers that it is most appropriate to use carefully chosen proven concepts for the partitioning architecture.

The partitioning protection architecture of this application is based on two concepts used in most operating systems:

1. The possibility to run partitioning management software - in the form of a kernel - in a protected environment.
2. Memory protection management through the usage of an MMU (paging).

However, the memory management of this partitioning architecture is not exactly as memory management used in other operating systems. Whereas most operating systems employ memory management mainly on a per task basis, memory management for this partitioning architecture is primarily based on a per software level basis (i.e. across tasks/threads).

Figure 1 shows the structure of the partitioning architecture. Each instantiation of a partition is assigned a level that is used to enforce access restrictions. Access to the partitions is controlled by defining execution environments with restricted access to the partitions. Six execution environments are defined: one for each of the possible software levels (i.e. A to E) and one for the kernel. Figure 2 shows the possible transitions between execution environments. How access to partitions is restricted within the six execution environments is defined as follows:

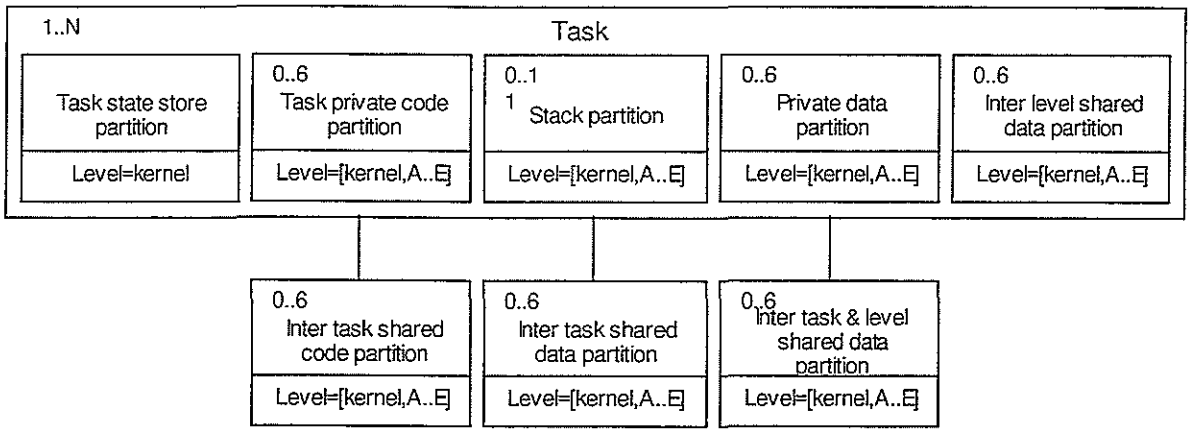

Figure 1

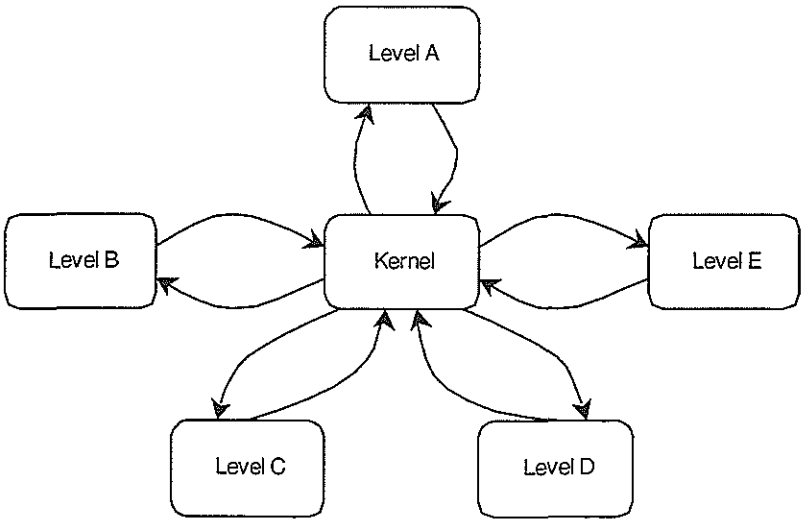

Figure 2

- Each task owns a partition to store the Task State. This partition is only readable and writable by the kernel.
- Each task owns one to eleven stack partitions. A kernel stack must always be provided. Furthermore, for each level of code executed by the task a stack partition must be provided. Finally, for each level of code involved in interrupt handling a stack partition must be assigned. Only one of the stack partitions is used at the same time by any task. Access to stack partitions other than the current stack partition is prohibited.
- Two types of code partitions exist:
    1. Task private code partitions.
    2. Inter task shared code partitions.

  Up to six code partitions of each type (task private partitions are counted per task) can exist, one for the kernel and one for each used software level. Within any execution environment, access to lower level code partitions is prohibited.
- Four types of data partitions exist:
    1. Private data partitions.
    2. Inter level shared data partitions.
    3. Inter task shared data partitions.
    4. Inter level and inter task shared data partitions.

Up to six data partitions of each type (task private partitions are counted per task) can exist, one for the kernel and one for each used software level.

This general structure can be seen as a meta structure of which actual instantiations can be made by defining the actual instances of the partitions that are needed for an application. Implementation of a partitioning protection architecture in this way can be done by implementing a specific instance of the general meta structure or by implementing support for the complete general architecture where an instantiation is realized through configuration. The second option will take more initial effort and will require more system resources but is flexible and far less effort is needed for reuse.

When actually implementing such a partitioning architecture an analysis should be done on what the maximum supported software level should be. The software level assigned to the partitioning management software must be at least the same as the maximum supported software level of the partitioned components. For maximum flexibility level A should be assigned to the partition management software. For the rest of this paper it is assumed that the software level assigned to the partition management software is level A.

Control Coupling

Control coupling is illustrated by Figure 3. Access to other levels of software is completely controlled by the kernel, which ensures secure control coupling. The kernel assures that on a change of software level appropriate measures will be taken. The state of the current execution environment will be saved before the execution environment will be changed and control is passed to the new software level. Upon return, the execution environment will be restored and control is passed back to the requesting software level.

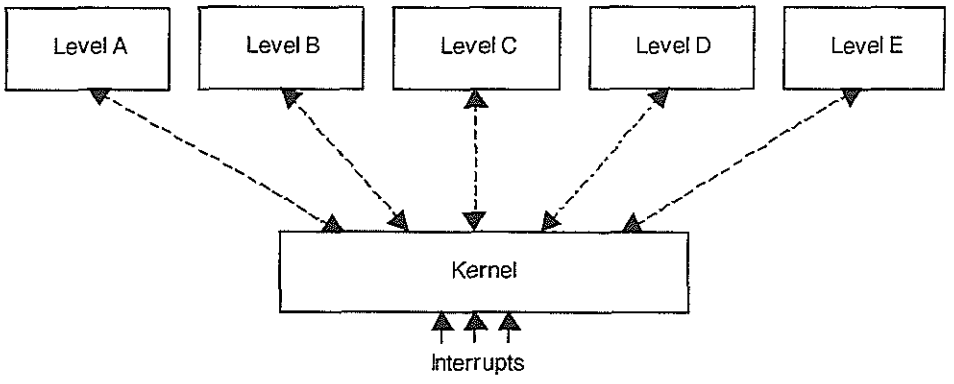

Figure 3

The following requirements can be postulated for secure control coupling:

- Control access to a higher level is not permitted in the sense that the kernel does not allow changing execution environment and passing control to a higher level.
- Control access to a lower level requires an execution environment switch to be done before actually passing control. Thus, every control access to a lower level must be controlled by the kernel that will perform the execution environment switch.
- Under no condition may lower level code be executed in a higher-level execution environment.
- Higher level code may be run within a lower-level execution environment. In this case, no kernel intervention is needed and can be statically realized through the MMU.
- Change of control to another task is allowed only by specially assigned scheduling code, which may be either part of the kernel or implemented as user code. In either case, the

scheduling code must be assigned at least the software level of the highest incorporated level of software in the application.

- Asynchronous control couplings (i.e. interrupt handling) are always handled by the kernel which however may dispatch actual handling to user level code after an appropriate environment switch.

Control couplings that require an execution environment change are serviced by the kernel by supplying so called call gates. Calls to the call gates can be completely controlled by the kernel, which can prevent any illegal control changes.

Data Coupling

For data coupling between levels and tasks, some frequently used techniques can be used. The focus is on the basic concept of shared memory usage. More advanced schemes - like message passing - can be easily incorporated as an extension.

Figure 1 shows four classes of data partitions. Three of these classes are shared data partition types enabling the usage of three different kinds of sharing:

- Inter level sharing (i.e. no sharing between tasks).
- Inter task sharing (i.e. no sharing between software levels).
- Inter level and inter task sharing.

Inter level sharing is of special interest with respect to safety critical software development. Access right restrictions must be enforced for inter level sharing which is not explicitly necessary for inter task sharing.

The following restrictions must be enforced on shared data between software levels:

- Execution environments with a level lower than the level assigned to the shared data partition may not have write access to that partition.
- Execution environments with a level higher than the level assigned to the shared data partition may read from that partition but this type of access has to happen in a controlled way. Design and verification must show that usage of this data will not degrade the safety level of the functionality under any condition. To ease design and verification this kind of access could be made available only through requests to the kernel.
- Other types of access to shared data cannot degrade the safety level; thus, they can be permitted without restrictions.

Reusability and Extendibility

The immense increase in quantity and complexity of software in airborne systems goes hand in hand with the increase and complexity of the hardware it runs on. Because of this growth reuse and extendibility of applied concepts in applications is also becoming increasingly important in order to save effort and cost. The partitioning architecture as discussed above is very capable of both being reusable as well as being extendable.

One easy extension is to support communication methods other than communication via shared memory. For example, a message-passing concept could be incorporated in the kernel. Messages have the advantage that they are inherently more controlled than shared memory access. This concept is used for example in a commercial operating system which is currently undergoing certification for DO-178B level B [OS98].

Current avionics development moves more and more towards the concept of Integrated Modular Avionics (IMA). The ARINC specification 653 [Aer97] specifies the baseline operating environment for application software used within IMA. One aspect addressed by the

ARINC 653 [Aer97] specification is partitioning. The developed partitioning architecture can be extended to an ARINC 653 [Aer97] compliant IMA system.

Another extension would be support for distributed systems. Take for example N processors - which are compliant with the requirements for this partitioning architecture - with communication channels to interconnect them. On each of these processors, the developed partitioning architecture could be used. The architecture could then be extended to incorporate inter processor sharing and protection.

3. Instantiation of the Partitioning Architecture in a Realized Certified Application

A dedicated instantiation of the partitioning architecture as discussed in section 2 was successfully implemented in a realized and certified application. The choice to implement a dedicated instantiation of the partitioning architecture instead of a complete configurable implementation was based on factors concerning development cost and resource usage. The realized application concerns an avionics device that manages the equipment of a flight display sub-system - which the device is part of - and all the data flows in the sub-system. This sub-system is designed to operate in all possible configurations of single/dual pilot (SP/DP) and visual/instrument flight rules (VFR/IFR). For IFR the management device is duplicated and is re-configurable by the (co)pilot. In addition, some of the most critical flight data equipment are duplicated and re-configurable for IFR. All reconfigurations are also managed by the realized application.

Corruption of some of the parameters handled by the flight control display management equipment is considered a catastrophic failure condition. Therefore the software components that handle those parameters are categorized as level A; other components of the software are categorized at lower levels (i.e. B and E).

Partitioning Protection Architecture

Figure 4 shows the dedicated instantiation of the general structure (see Figure 1) as it is implemented in the realized application. Four instead of six execution environments are implemented; transitions are the same as in Figure 2.

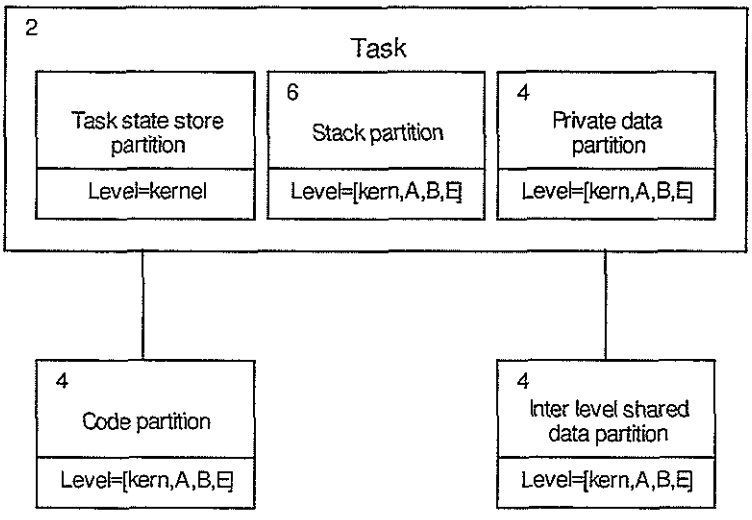

Figure 4

Control Coupling

The implementation of the partitioning architecture in the realized application has an additional restriction concerning control coupling. This restriction states that only the highest software level (i.e. level A) is allowed to initiate control change to another level. This restriction prevents the situation where e.g. a level A component calls a level B component which in turn calls a level E component. The latter call could be very well unwanted since one of the requirements states that no level E software shall be executed when the aircraft is in the air. Note however that enforcing this restriction is not necessary because the application design should not include these cases (they are in conflict with the requirements) and the verification process should identify these cases if the software would inadvertently include one.

Data Coupling

The partitioning architecture implemented in the realized application contains only one type of shared data partition namely: `Inter task & inter level shared data partition'. Access rights on shared data partitions are more restrictive then those defined for the general partitioning architecture:

- Write access is allowed only to data partitions with the same level as the level of the current execution environment.
- Read access is allowed to all data partitions. Access to data partitions of levels lower than the current execution level have been accounted for in the application design and it has been verified that invalid data cannot lead to an uncontrolled failure condition.

Overhead Assessment

After the realization of the partitioning architecture in this application, two assessments have been done concerning the introduced overhead.

1. Overhead in development effort.
2. Overhead in system resource usage.

The effort that has been put into the development of the partitioning architecture is about 1% of the total development effort put into the application. This effort is easily compensated for by the decrease in verification effort especially for modifications of the application.

The two main resources that are used by the partitioning architecture are processor capacity and memory. The partitioning architecture induces only about 1% performance overhead for the realized application. Concerning memory consumption it was determined that the usage of ROM increased by approximately 20KB on 496KB and the usage of RAM increased by about 20KB on 512KB.

4. Conclusions

This paper presented a partitioning architecture for safety critical airborne systems based on the usage of a processor with system/user protection and an MMU. With the incorporation of modern powerful processors in these systems, such a partitioning architecture can be ported to many different systems. The major benefits of this architecture are:

- Little performance overhead.
- Few memory resource requirements.
- No extra hardware requirements besides the processor protection facilities and MMU.
- Portability to a variety of systems.
- Flexibility to adjust to specific application requirements. It is even easy to adjust an existing application to incorporate this partitioning architecture.

- Easy extendibility with application specific requirements or with more general functional extensions. Among the possible extensions to this basic partitioning architecture are:
  - Support for more advanced data coupling techniques like message passing.
  - Support for Integrated Modular Avionics.
  - Support for distributed and multi-processor systems.

The partitioning architecture has been successfully implemented in a realized and certified avionics application with very reasonable resource usage. It can be concluded that this partitioning architecture is very useful and can be applied in future applications.

References

[Aer97] Aeronautical Radio, Inc., Annapolis, Maryland. *ARINC Specification 653: Avionics Application Software Standard Interface.* 1997.

[FAR] *Federal Aviation Requirements/Joint Aviation Requirements 25.*

[Int87] Intel Corp. *80386 Programmer's Reference Manual.* 1987. Order Number 230985-001

[OS98] Enea OSE Systems. *OSE addresses safety issues in embedded systems through certification.* Pressrelease – Dallas, TX, October 1998.

[RTC92] RTCA. *DO-178B; Software Considerations in Airborne Systems and Equipment Certification.* 1992.

[Sto96] Neil Storey. *Safety-Critical Computer Systems.* Addison-Wesley, 1996.

[Vit98] Ben L. Di Vito. A F*ormal Model of Partitioning for Integrated Modular Avionics.* Contractor Report 208703, NASA, 1998.

TWENTYFIFTH EUROPEAN ROTOCRAFT FORUM

Paper No. G1

MODAL ANALYSIS OF AEROELASTIC RESPONSE OF A HOVERING ROTOR – THE IMPACT OF THE MODE CHOICE

BY

M. GENNARETTI
University Roma Tre, Italy

A. CORBELLI, F. MASTRODDI, L. BALIS CREMA
University of Rome 'La Sapienza', Italy

SEPTEMBER 14–16, 1999
ROME
ITALY

ASSOCIAZIONE INDUSTRIE PER L'AEROSPAZIO, I SISTEMI E LA DIFESA
ASSOCIAZIONE ITALIANA DI AERONAUTICA E ASTRONAUTICA

MODAL ANALYSIS OF AEROELASTIC RESPONSE OF A HOVERING ROTOR – THE IMPACT OF THE MODE CHOICE

M. GENNARETTI
University Roma Tre
Dipartimento di Ingegneria Meccanica e Industriale, Rome, Italy

A. CORBELLI, F. MASTRODDI, L. BALIS CREMA
University of Rome 'La Sapienza'
Dipartimento Aerospaziale, Rome, Italy

ABSTRACT

The aim of this paper is the aeroelastic analysis of the elastic motion of a cantilever blade in flap-lag-torsion motion. Specifically, we investigate on the convergence behavior of the solutions obtained using different approaches for the elastic displacement description. Three different mode shape sets are used in Galerkin's method approaches, and their solutions are also compared with those obtained from a FEM approach. The aerodynamic model used in this work is the simple very-low frequency approximation of the pulsating-free-stream Greenberg extension of the Theodorsen theory. Numerical investigation is performed both for determining the aeroelastic stability boundaries of the blade and for analyzing the frequency response to a vertical pulsating free-stream velocity.

1. INTRODUCTION

The subject of this work is the aeroelastic stability and response analyses of hingeless cantilever rotor blades, with emphasis on the solution accuracy and convergence behavior, as a function of the approach used for the elastic-motion description.

In the aeroelastic analysis of helicopter rotors, the structural dynamics of the blades is often formulated in terms of a series of mode shapes whose coefficients (mode amplitudes) may be interpreted as the time-dependent Lagrangean variables (generalized coordinate) of the structure. This approach assures convergence of the solution in terms of stability analysis, faster than alternate descriptions of the elastic displacement (*e.g.*, finite elements, consisting of using non-orthogonal piecewise-defined shape functions). From a practical point of view, it means that if a certain level of accuracy of the stability analysis is obtained by using M linearly independent modes (and corresponding Lagrangean variables), the same level of accuracy may be reached by using a larger number $N > M$ of non-orthogonal shape functions (and corresponding Lagrangean variables). Nonetheless, it is possible to observe a different convergence behavior of the solution, if this is analyzed in terms of local stress levels. For instance, for a cantilever blade, if one considers the root elastic bending moment as the parameter to be studied in the aeroelastic analysis, then the convergence of the modal approach solution could be found to be slower than that obtained from a FEM approach (that uses locally defined shape functions). Therefore, the best choice for the description of the elastic displacement depends generally on the target of the performed aeroelastic analysis.

Several types of mode shapes may be used in rotor blade structural dynamic analysis. Among them, there are the set of eigenfunctions of the blade structural operator defined in the rotating frame (rotating free-vibration modes), and the set of eigenfunctions of the blade structural operator defined in the non-rotating frame (non-rotating free-vibration modes): the first set of eigenfunctions is influenced by the presence, in the structural operator, of the centrifugal and Coriolis inertial terms, whereas the second set of eigenfunctions does not consider the presence of these inertial terms, which are to be included in the analysis as forcing terms. However, the orthogonal shape functions to be used in the analysis, might also be unrelated to the blade structural operator: for instance, the uncoupled bending and torsion free-vibration modes of a non-rotating uniform beam, have been applied in Refs. [1] and [2] for aeroelastic analysis, whereas the modified Duncan polynomials have been used in Ref. [3]. Furthermore, some authors have also performed aeroelastic analysis of rotor blades applying FEM approaches, and among them Friedmann and Straub [4] developed a FEM formulation for the flap-lag aeroelastic analysis of hovering rotors, whereas Sivaneri and Chopra [5] examined the aeroelastic stability of flap bending, lead-lag bending and torsion of a helicopter rotor in hover using a finite element formulation based on Hamilton's principle.

The aim of this work is a comparison among helicopter-rotor aeroelastic solutions given by different mode-shape decompositions and the application of a finite element approach. Specifically, we wish to investigate about the advantages and disadvantages in using the mode shape approach, with respect to the finite element approach. The comparison will be presented in terms of aeroelastic stability analysis and stress levels prediction on the blade (particularly, at the root of a cantilever hingeless rotors). In performing the aeroelastic analysis, the unsteady aerodynamic loadings will be described by the simple quasi-steady approximation of the Greenberg formulation obtained extending the Theodorsen theory to pulsating free-stream velocity [6].

2. BLADE STRUCTURAL AND AERODYNAMIC MODELS

In order to achieve the purposes of the present work, we have chosen to use classical and quite simple models both for structural dynamics and for aerodynamic loadings acting on the blade.

The rotor blade considered here is a hingeless blade structurally modeled as a cantilever slender beam, undergoing flap bending, chordwise bending and torsion. A realistic hingeless rotor configuration is defined by lots of parameters that influence both the steady state blade stress distribution and the blade stability characteristics. Such parameters are precone, droop, torque offset and sweep that in this work, except for the precone angle, have been considered to be equal to zero. An additional fundamental element in a hingeless rotor description is the flexibility of the pitch link devoted to the actuation of blade motion controlled by the swash plate: it is a major factor in the structural coupling between flap bending, lead-lag bending and torsion, and hence influences the aeroelastic behavior of the blade. Furthermore, coupling between bending and torsion elastic deflections is strongly influenced also by parameters like the positions of the mass center, tension center, elastic center and the aerodynamic center. All these depend on the blade construction features and shape and have a great impact on its stability characteristics. For the sake of simplicity, in this work we have assumed no chordwise offsets of the elastic axis, tension axis and center-of-mass axis.

Under all the simplifying assumptions mentioned above and considering untwisted blades with uniform mass and stiffness spanwise distribution, the equations of motion governing the blade structural dynamics are those given in Ref. [1], that are the corresponding simplified version of those derived in Ref. [7]. These equations are a set of coupled integro-partial differential equations with unknowns the lateral in-plane displacement of the elastic axis, $v(x,t)$, the lateral out-of-plane displacement of the elastic axis, $w(x,t)$, and the cross-section elastic torsion deflection $\varphi(x,t)$. Their expressions are

of the following type (see Ref. [1] for details):

$$m\,\ddot{v} + \mathcal{O}_v[v, w, \varphi, \dot{v}, \dot{w}] = \mathcal{L}_v \tag{1}$$

$$m\,\ddot{w} + \mathcal{O}_w[v, w, \varphi, \dot{v}, \dot{w}] = \mathcal{L}_w \tag{2}$$

$$J_\varphi\,\ddot{\varphi} + \mathcal{O}_\varphi[v, w, \varphi] = \mathcal{M}_\varphi, \tag{3}$$

where m denotes the blade mass per unit length, J_φ denotes the cross-section torsional mass moment of inertia, $\mathcal{O}_v$ and $\mathcal{O}_w$ denote fourth-order in space, nonlinear, integro-partial differential operators, whereas $\mathcal{O}_\varphi$ denotes a second-order in space, nonlinear, partial differential operator. Furthermore, $\mathcal{L}_v$ and $\mathcal{L}_w$ are, respectively, the in-plane and out-of-plane aerodynamic forces per unit length acting on the blade, whereas $\mathcal{M}_\varphi$ is the aerodynamic pitching moment per unit length acting on the blade.

Observing equations (1)–(3) it is apparent that a very important role in rotor blade aeroelastic predictions is played by the aerodynamic model applied in describing the forcing terms $\mathcal{L}_v, \mathcal{L}_w, \mathcal{M}_\varphi$. This is true for fixed-wing aeroelastic applications, but its importance is further amplified in rotary-wing aeroelastic analysis due to the complexity of the unsteady aerodynamic field generated by the rotor blades. In particular, the shape of the vortical wake generated by the blades is such that the velocity that it induces on the rotor has a great impact on the unsteady aerodynamic loading distributions, and the accurate description of this velocity field is a fundamental requirement for a realistic aerodynamic field prediction. Furthermore, in rotor aerodynamics the effects due to the 3-D flow are much stronger than in the case of fixed-wing aerodynamics, and this is an additional element of complexity that generally makes unsatisfactory the application of two-dimensional analytical aerodynamic models. Nonetheless, in this work we have applied a very simple quasi-steady, two-dimensional aerodynamic model. This choice has been suggested by the desire of having a simple explicit expression of the aerodynamic loadings in terms of the structural dynamics unknowns of the problem, so as to concentrate the analysis on the role played on the solution accuracy and rate of convergence, by the type of spatial description used for the elastic displacement approximate expressions. Following the approach used in Ref. [1], $\mathcal{L}_v, \mathcal{L}_w, \mathcal{M}_\varphi$ have been obtained from the very-low frequency approximation of the pulsating-free-stream Greenberg extension of the Theodorsen theory for the prediction of unsteady lift and pitching moment on airfoil in unsteady motion [6], with the inclusion of the effects of the wake-induced velocity on the aerodynamic force direction. The resulting formulae for $\mathcal{L}_v, \mathcal{L}_w, \mathcal{M}_\varphi$ are explicit functions of $\varphi, v', w', w'', \dot{v}, \dot{w}, \dot{\varphi}$, and $\ddot{w}$, that combined with equations (1)–(3) yield the final closed-loop flap-lag-torsion aeroelastic equations of motion analyzed in this work.

3. MODAL-APPROACH SOLUTION

As mentioned in Section 1, the aeroelastic equations of motion described above have been solved following both a modal approach and a FEM approach, in order to compare their solutions accuracy, their rate of convergence, and then analyse advantages and disadvantages of the two. In this section we outline the solution scheme obtained by applying the modal approach.

The set of coupled integro-partial differential equations (1)–(3) has been transformed into a set of ordinary differential equations in time, by Galerkin's method. First, the elastic deflections have been expressed in terms of the following series

$$v(x,t) = \sum_{n=1}^{N} q_n^v(t)\,\Phi_n^v(x) \tag{4}$$

$$w(x,t) = \sum_{n=1}^{N} q_n^w(t)\,\Phi_n^w(x) \tag{5}$$

$$\varphi(x,t) = \sum_{n=1}^{N} q_n^{\varphi}(t)\, \Phi_n^{\varphi}(x), \tag{6}$$

where $q_n^v, q_n^w, q_n^\varphi$ denote the generalized coordinates of the problem, whereas $\Phi_n^v, \Phi_n^w, \Phi_n^\varphi$ are sets of linearly independent shape functions (mode shapes), whose choice influences accuracy and rate of convergence of the solution. Next, substituting equations (4)-(6) into equations (1)–(3), the Galerkin method yields a set of $3N$ nonlinear, ordinary differential equations in terms of the generalized coordinates of the problem. Then, the aeroelastic solution is determined from their linearized version for small perturbation motions about the equilibrium configuration. Specifically, expressing the generalized coordinates in terms of the steady equilibrium value and of a small perturbation quantity (*i.e.*, assuming, for instance, $q_n^v(t) = q_{0n}^v + \Delta q_n^v(t)$), a nonlinear algebraic problem with unknowns $q_{0n}^v, q_{0n}^w, q_{0n}^\varphi$ is first formulated and solved by the Newton-Raphson method, and then $3N$ linear differential equations for the small perturbation motion are determined, with coefficients depending on the equilibrium solution. The $3N$ small perturbation equations have the following form

$$\mathsf{M}\,\ddot{\mathsf{q}} + \mathsf{C}\,\dot{\mathsf{q}} + \mathsf{K}\,\mathsf{q} = 0, \tag{7}$$

where $\mathsf{q}^T = \{\Delta q_n^v, \Delta q_n^w, \Delta q_n^\varphi\}$ is the row matrix containing the small perturbation motion unknowns, M is a symmetric matrix containing structural and aerodynamic mass terms, C is an asymmetric matrix containing gyroscopic and aerodynamic damping terms, whereas K is an asymmetric matrix containing structural and aerodynamic stiffness terms.

In this work, three different sets of mode shapes have been employed: *i)* the first set is that given by the eigenfunctions of the cantilever, uniform beam, for which $\Phi_n^v \equiv \Phi_n^w$; *ii)* the second set of mode shapes used in equations (4)-(6), are the eigenfunctions of the rotating uniform beam (incidentally, in the case of the rotor blade considered in this work and for collective pitch angle set equal to zero, is governed by the (decoupled) integro-partial differential equations given by Houbolt and Brooks in Ref. [8]); *iii)* the last set of mode shapes used is that given by the eigenfunctions of the small perturbation equations (7) in vacuo and without gyroscopic terms (*i.e.*, those obtained neglecting both aerodynamic terms and Coriolis force contribution), and therefore is dependent on the steady equilibrium condition examined in the stability or response analysis. The analysis of the behavior of the solutions corresponding to these mode-shape sets is one of the goals of the present paper, and is performed in order to give an idea about how convenient is the use of simple mode shapes in the modal solution approach.

4. FEM-APPROACH SOLUTION

In this section we briefly outline the finite-element formulation used in this work for the aeroelastic analysis of the hingeless rotor blade described above.

For the sake of simplicity, in this phase of the work the finite element formulation has been applied to the elastic blade equations of motion presented in Ref. [8], which are applicable only to the quite narrow range of blade dynamic configurations consisting of both small steady equilibrium deflections, and small unsteady perturbation deflections. Therefore, following the expression of the Hamilton principle given in Ref. [8] (which the reader can also refere to for all the notations and symbols used in the following), and indicating with $\mathcal{U}$ the total strain energy and with $\mathcal{V}$ the work performed by the centrifugal body forces and the applied loading, we have

$$\mathcal{U} - \mathcal{V} = \frac{1}{2}\int_0^R \mathcal{F}(v, w, \varphi, v', w', \varphi', v'', w'', p_y, p_z, q)\, \mathrm{d}x \tag{8}$$

where $\mathcal{F}$ denotes the energetic functional whose expression is given Ref. [8], p_y, p_z, and q represent the applied loading given by the sum of the aerodynamic loadings, $\mathcal{L}_v$, $\mathcal{L}_w$, and $\mathcal{M}_\varphi$, and of the inertial loadings.

Next, we describe the finite element formulation that has been applied to equation (8). Let us divide the blade into a finite number, N_e, of beam elements located on the elastic axis, ξ, coinciding with the radial axis x starting from the shaft (η will denote the chordwise axis, and ζ the axis orthogonal to ξ and η). Therefore, $N_e + 1$ nodes are also defined and six degrees of freedom may be associated to each node: following the standard FE procedure, these are the three translations denoted with u^e, v^e, and w^e (in ξ, η, and ζ direction respectively), and the three rotations φ, r_w, and r_v around the ξ, η, and ζ axis, respectively.

Considering the generic beam finite element with nodes denoted by a and b, in the finite element formulation the displacement vector $\mathbf{u}^e$ (with components u, v, and w) is approximated as

$$\begin{aligned} \mathbf{u}^e(\xi,\eta,\zeta,t) &= u_a^e\Phi_1^e + v_a^e\Phi_2^e + w_a^e\Phi_3^e + \phi_a^e\Phi_4^e + r_{w_a}^e\Phi_5^e + r_{v_a}^e\Phi_6^e \\ &+ u_b^e\Phi_7^e + v_b^e\Phi_8^e + w_b^e\Phi_9^e + \phi_b^e\Phi_{10}^e + r_{w_b}^e\Phi_{11}^e + r_{v_b}^e\Phi_{12}^e, \end{aligned} \tag{9}$$

where the subscripts a and b indicate that the d.o.f.'s are referred to the node a and b, respectively, whereas vectors $\mathbf{\Phi}_i^e$ are the the standard finite element shape functions for a beam element. From equation (9), in terms of components, the elastic displacement vector may be expressed as

$$\mathsf{u}^e(\xi,\eta,\zeta,t) = \mathsf{A}^e(\xi,\eta,\zeta)\,\mathsf{x}^e(t) \tag{10}$$

where u^e is the column matrix containing the components of the vector $\mathbf{u}^e$, x^e is the column matrix containing the twelve element d.o.f.'s, and the matrix A^e contains the finite element shape functions, as described, for instance, in Ref. [9].

Next, considering all the finite elements of discretization of the blade and substituting for each of them equation (10) into equation (8), one obtains the discrete form of the energetic functional of the aeroelastic problem. Thus, requiring to the energy defined by equation (8) to be stationary with respect to the finite element d.o.f.'s, one obtains the following final finite element dynamic equation for the generic element

$$\mathsf{K}^e\mathsf{x}^e + \mathsf{K}_C^e\mathsf{x}^e = \mathsf{e}^e \tag{11}$$

where e^e is the column matrix containing the external loadings (aerodynamic forces and relative inertial forces), K^e is the (standard) stiffness matrix due to the elastic energy, $\mathcal{U}$, whereas K_C is the (equivalent) stiffness matrix taking into account the effects due to due centrifugal loadings, and obtained from the work $\mathcal{V}$.

Finally, following the standard FE procedure, the element consistent $[12 \times 12]$ mass matrix can be defined as:

$$M_{ij}^e = \int_{V^e} \rho\,\mathbf{\Phi}_i^e \cdot \mathbf{\Phi}_j^e\,\mathrm{d}V \tag{12}$$

where ρ denotes the structural density.

Once the stiffness and mass matrices are evaluated for each blade element, the global matrices can be assembled considering the elementary beam topology, and then, observing that $\mathsf{e}^e = -\mathsf{M}^e\ddot{\mathsf{x}} + \mathsf{f}^e$, with f^e denoting the aerodynamic loads, the final equations for the blade dynamics have the form

$$\mathsf{M}\ddot{\mathsf{x}} + (\mathsf{K} + \mathsf{K}_C)\,\mathsf{x} = \mathsf{f}. \tag{13}$$

with trivial meaning for the global matrix M, K, K_C, and C. As already outlined in Section 3, the aerodynamic loads, f, have been dermined from the quasi-steady approximation of the pulsating-free-stream Greenberg extension of the Theodorsen theory.

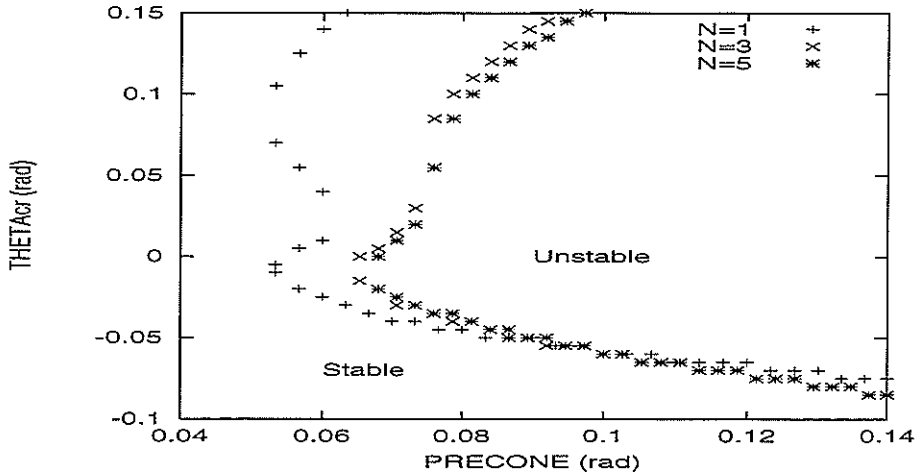

Figure 1: Stability Boundary due to precone angle for soft in-plane blade. Uniform-beam modes.

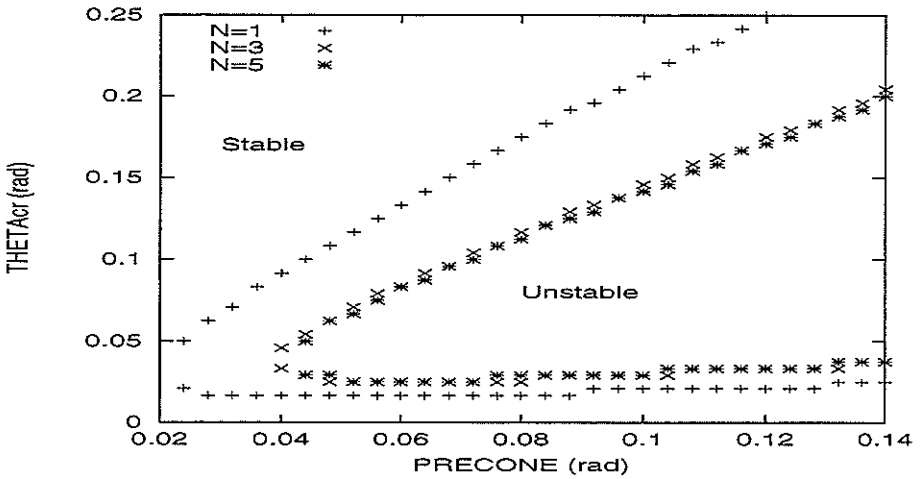

Figure 2: Stability boundary due to precone angle for stiff in-plane blade. Uniform-beam modes.

5. NUMERICAL RESULTS

In our numerical investigation, we have studied both the aeroelastic stability behavior of the hingeless blade considered, and its response to an external exitation caused by a vertical pulsating free-stream velocity.

For the stability analysis, we have determined the stability boundaries of a soft inplane blade and those of a stiff inplane blade, in terms of critical collective pitch angle *vs* the precone angle. In both cases, we have studied the convergence behavior of the solutions obtained using the three sets of mode shapes described in Section 3. The two blades considered have the fundamental flap natural frequency $\omega_w = 1.15\Omega$, with Ω denoting the angular velocity of the rotor. Furthermore, the soft inplane blade has the fundamental torsion natural frequency $\omega_\varphi = 2.5\Omega$, and the fundamental lead-lag natural frequency $\omega_v = 0.7\Omega$, whereas the stiff inplane blade has the fundamental torsion natural frequency $\omega_\varphi = 5\Omega$, and the fundamental lead-lag natural frequency $\omega_v = 1.5\Omega$.

Figure 1 depicts the stability boundaries of the soft inplane blade determined by the modal approach, with a different number of eigenfunctions of the nonrotating uniform beam. In this case, using 5 modes (per elastic displacement) seems to give a solution in terms of stability boundary that is very close to the converged one (*i.e.*, additional mode shapes do not alter significantly the

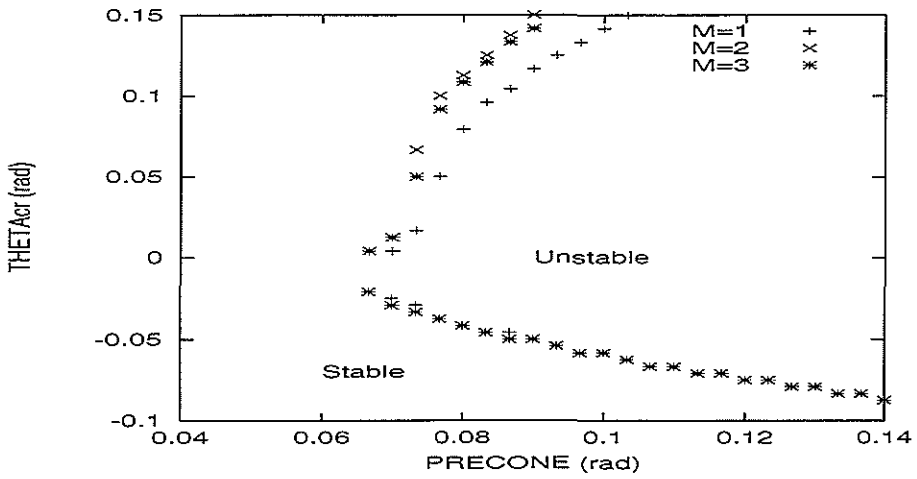

Figure 3: Stability boundary due to precone angle for soft in-plane blade. Equilibrium-independent rotating beam modes.

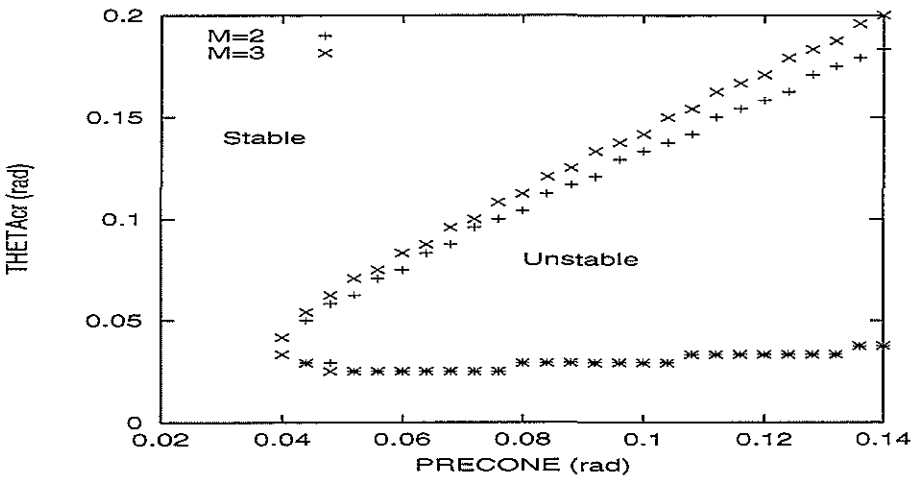

Figure 4: Stability boundary due to precone angle for stiff in-plane blade. Equilibrium-independent rotating beam modes.

stability boundary). A similar behavior of the solution is observed in Figure 2, where the stability boundaries are depicted for the stiff inplane blade, for elastic displacements expressed in terms of the eigenfunctions of the nonrotating uniform beam.

Then, Figure 3 and 4 illustrate, respectively, the stability boundaries of the soft and stiff in-plane blades, both obtained by the modal approach with mode shapes given by the eigenfunctions of the uncoupled-displacement rotating beam (*i.e.*, those independent on the steady equilibrium configuration). In this case, the convergence stability boundary appears to be determined using only 3 modes per elastic displacement.

Next, we have applied the modal approach by using the eigenfunctions of the coupled-displacement rotating beam, which depend on the steady equilibrium configuration. Figures 5 and 6 depict the soft inplane blade and the stiff inplane blade stability boundaries, respectively. In this case, the use of only one or two mode shapes seems to give a satisfactorily accurate prediction of the stability boundary.

Finally, we have studied the response of the blade to a vertical pulsating free-stream. Specifically, including in equations (7) and (13) the external aerodynamic forcing term due to the vertical

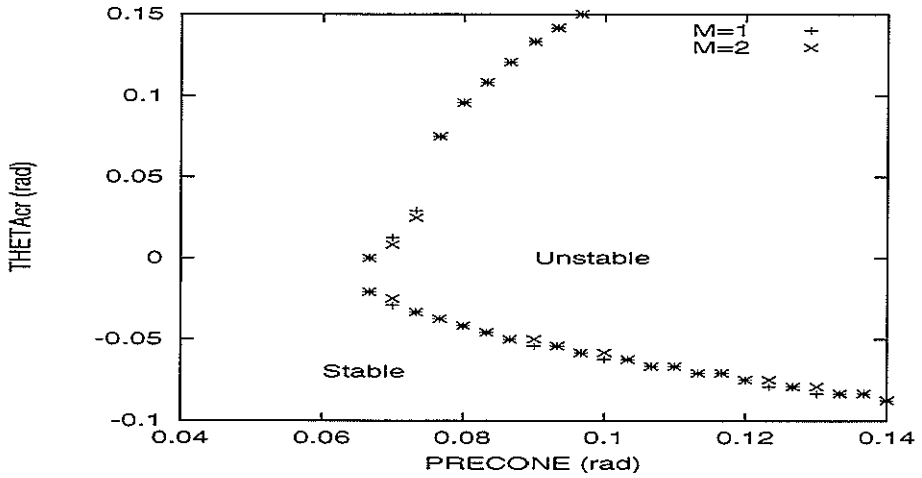

Figure 5: Stability boundary due to precone angle for soft in-plane blade. Equilibrium-dependent rotating beam modes.

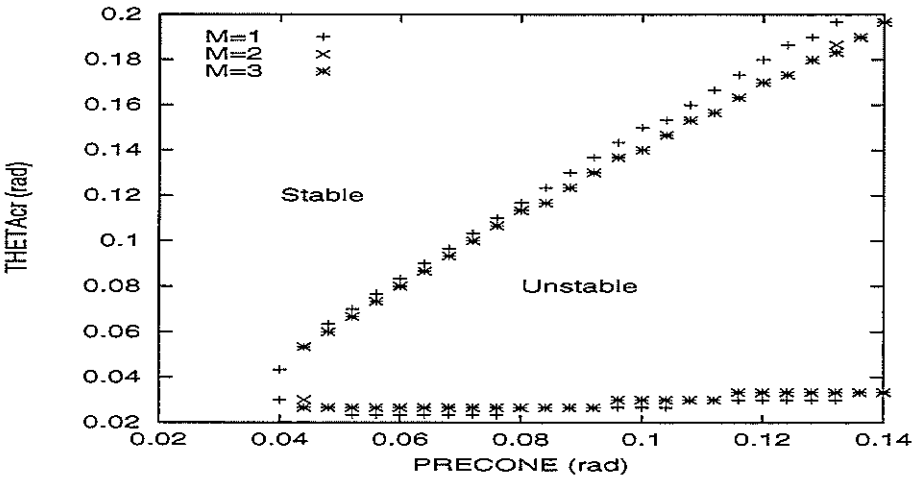

Figure 6: Stability boundary due to precone angle for stiff in-plane blade. Equilibrium-dependent rotating beam modes.

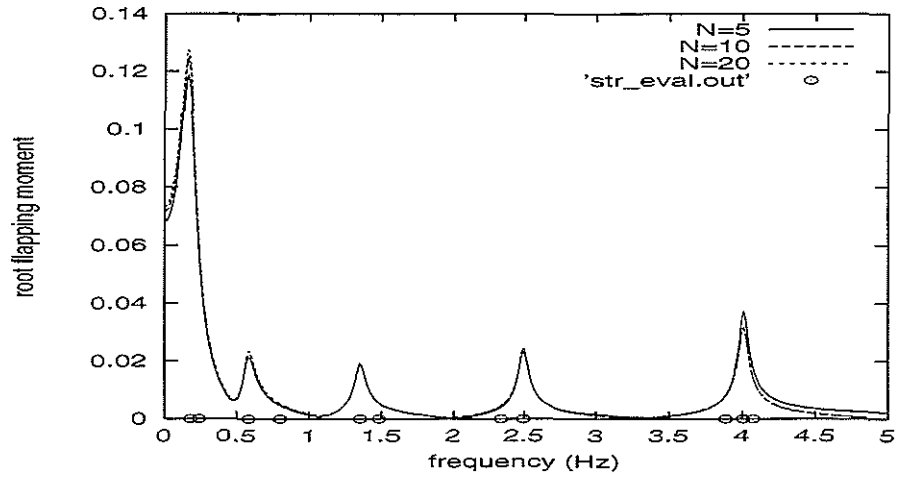

Figure 7: Amplitude of root-flapping-moment frequency response to a vertical pulsating free-stream. Modal approach using non-rotating uniform-blade modes.

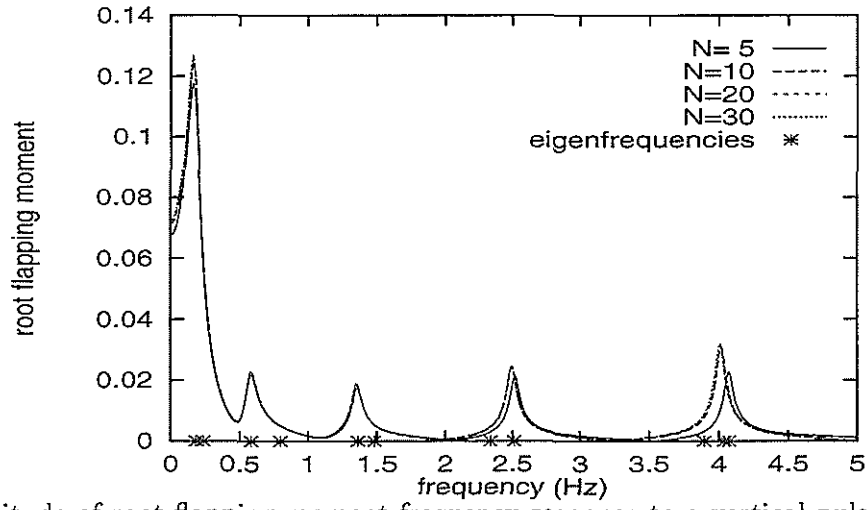

Figure 8: Amplitude of root-flapping-moment frequency response to a vertical pulsating free-stream. FEM approach.

free stream stemming from the quasi-steady aerodynamic theory considered, we have evaluated the spectrum of the unsteady elastic bending moment arising at the root of the cantilever blade with the collective pitch angle set equal to zero. The blade studied is the stiff inplane one, with $\omega_w = 1.15\Omega$ and $\omega_\varphi = 5\Omega$. In Figure 7 we depict the amplitude of the frequency responses obtained from the modal approach using different numbers of free-vibration modes of the nonrotating beam. In this case, the convergence of the response-peak values seems to be achieved with 20 modes, *i.e.*, with a very higher number of modes with respect to that needed for the stability-boundary convergence. The response analysis has been performed also using the FEM approach outlined in Section 4. The corrisponding results for different numbers of discretization elements on the blade, are illustrated in Figure 8 where the converged response appears to be achieved by the solution using 20 elements, although the 10-element solution gives a very accurate prediction of the root bending moment. From the comparison between Figures 7 and 8, one may observe that the two convergence histories reveal a similar behavior in terms of rapidity, and this demostrate that the use of modal approach is not more convenient with respect to the FEM one when local stress analysis is performed.

5. CONCLUDING REMARKS

The aeroelastic stability and response analysis for a cantilever flap-lag-torsion motion blade has been performed.

Specifically, we have analyzed the convergence behavior of solutions obtained using different mode shape sets in a modal approach, and using a FEM approach. As expected, in the stability boundary analysis (where the relevant contribution is given by low-frequency modes) the modal approach has demontrated to be a very efficient tool having a fast convergence behavior. However, in the frequency response analysis performed in terms of the root flapping moment, the convergence histories from modal and FEM solutions appear to have very similar behaviors and the very fast convergence rate of modal approach-solution seems to be deteriorated.

REFERENCES

1. Hodges, D.H., and Ormiston, R.A., Stability of Elastic Bending and Torsion of Uniform Cantilever Rotor Blades in Hover with Variable Structural Coupling, NASA TN D-8192, 1976.

2. Kwon, O.J., Hodges, D.H., and Sankar, L.N., Stability of Hingeless Rotor in Hover Using Three-Dimensional Unsteady Aerodynamics, J. of the American Helicopter Society, 1991.

3. Karunamoorthy, S., and Peters, D.A., Use of Hierarchical Elastic Blade Equations and Automatic Trim for Rotor Response, Vertica, vol. 11, 1987.

4. Friedmann, P.P, and Straub., F., Application of the Finite Element Method to Rotary Wing Aeroelasticity, J. of the American Helicopter Society, vol. 25, n. 1, 1980.

5. Sivaneri, N.T., and Chopra, I., Dynamic Stability of a Rotor Blade Using Finite Element Analysis, AIAA J., vol. 20, n. 5, 1982.

6. Greenberg, J.M., Airfoil in Sinusoidal Motion in a Pulsating Stream, NACA TN-1326, 1947.

7. Hodges, D.H., and Dowell, E.H., Nonlinear Equation of Motion for the Elastic Bending and Torsion of Twisted Nonuniform Rotor Blades, NASA TN D-7818, 1974.

8. Houbolt, J.C., and Brooks, G.W., Differential Equations of Motion for Combined Flapwise Bending, Chordwise Bending, and Torsion of Twisted Nonuniform Rotor Blades, NACA R-1346, 1957.

9. Przemieniecki, J.S., Theory of Matrix Structural Analysis, McGraw-Hill, New York, 1968.

ACKNOWLEDGEMENTS

This work has been supported by Centro Italiano Ricerche Aerospaziali (C.I.R.A.), grant NR. 007/99: *"Sviluppo di modelli dinamici ed aerodinamici per l'aeroelasticità dei rotori a mozzo non fisso"*.

The authors wish to acknowledge Dr. R. Bacchi and Mr. A. Bassetti for their help in obtaining some of the numerical results presented.

TWENTYFIFTH EUROPEAN ROTORCRAFT FORUM

Paper n° G2

UNDERCARRIAGE IMPEDANCE TESTING AND AIRCRAFT IMPEDANCE MODELLING FOR GROUND STABILITY PREDICTION

BY

I LYNDON, J TEDBURY, S AKBAR
GKN WESTLAND HELICOPTERS LTD,
YEOVIL, ENGLAND

SEPTEMBER 14-16, 1999
ROME,
ITALY

ASSOCIAZONE INDUSTRIE PER L'AEROSPAZIO, I SISTEMI E LA DIFESA
ASSOCIAZONE ITALIANA DI AERONAUTICA ED ASTRONAUTICA

Undercarriage Impedance Testing and Aircraft Impedance Modelling for Ground Stability Prediction

I Lyndon, J Tedbury, S Akbar

GKN Westland Helicopters Ltd.,
Yeovil, England

Abstract

The ground resonance clearance for the EH101 rotorcraft fitted with one high pressure tyre on each main landing gear was achieved many years ago. New variants of the EH101 rotorcraft fitted with low pressure tyres and twin wheels on each main landing gear are being introduced. Preliminary work showed that, for the new EH101 variants, the effect of fitting twin wheels is to reduce the landing gear bearing loads which will cause the landing gear oleo to stroke more than the single wheeled variant. This change will affect the stiffness and damping characteristics of the landing gears and thus new ground resonance clearance is required. This paper describes the landing gear impedance test and non-linear modelling which was used to replace the an expensive, and time consuming, airframe impedance test when predicting ground resonance stability.

1. Introduction

To prove the ground resonance stability of the EH101 rotorcraft in its early days of its programme, a series of analysis and tests were carried out which involved both theoretical analysis, airframe testing and rotorcraft testing. The original variant of the EH101 was fitted with high pressure tyres and single wheels on each main landing gears. New variants of the EH101 are fitted with low pressure tyres and twin wheels on each main landing gear and preliminary work showed that these changes would result in increased the movement of the main landing gears. Thus further analysis and testing was required to prove the ground resonance stability of the EH101 variants fitted with the low pressure tyres. Rather than repeat the original series of analysis and tests, a new series of analysis and tests are being used where the expensive, and time consuming, airframe test has been replaced by a cheaper landing gear impedance test combined with non-linear mathematical modelling. A comparison of the original and new methodologies are shown in figure 1. This original process was described in detail in a paper presented by A L Jordan of GKN Westland Helicopters at the thirteenth European Rotorcraft Forum (ref. 1) and the actual test rig with the airframe in place is shown in figure 2.

2. New Process

The demonstration of the ground resonance stability of the EH101 variant fitted with the low pressure tyres will be achieved using the new methodology where non-linear methods plus landing gear impedance test replace the linear methods plus airframe impedance test. The main components of this new methodology are the landing gear non-linear mathematical model, the theoretical analysis, the landing gear impedance test and the rotorcraft ground resonance test.

2.1 Single Leg Impedance Testing

The purpose of the impedance test is to determine the landing gear characteristics when subjected to the typical loads and motions that could occur in the fundamental modes of the airframe. For this test each type of landing gear was mounted vertically in a test rig as shown in figure 3. Each landing gear was loaded with a representative static weight and then oscillated at combinations of amplitude and frequency. When the gear had stabilised at each test condition the tyre closure, oleo closure, mass travel and ground force were recorded for approximately one minute. These series of tests were carried out with and without the tyres fitted and figure 5 shows the force -v- time recordings for one of these tests on the Main Landing Gear (MLG). There are two noticeable differences between the results for with and without tyres fitted as follows -

1) for the test without the tyres, there is a a step change in force whenever the oleo changes its direction of motion. This is caused by the hysteresis in the oleo due

to the seal and bearing friction. When the tyre is fitted, its flexibility masks the effect of this oleo hysteresis.

2) the variation in the force is smaller for the test with the tyres fitted. For a given amplitude of motion, the amplitude of oleo motion will be less when the tyre is fitted. Thus there will less flow of oil through the oleo damping assembly resulting in less oleo oil damping force.

For each test condition, the work done per cycle was calculated from the test results. To determine the equivalent linear stiffness and damping coefficients, the non-linear damping force is approximated to a linear viscous damping term that will dissipate the same amount of energy per cycle. For each test condition the impedance is calculated from the recorded force and displacement measurements. The linear stiffness is the real term of the impedance and the linear damping is the imaginary term divided by frequency. The force that this linearised system produces for a harmonic excitation with the same amplitude as in the test, is then calculated. The resulting force -v- closure curve is elliptical in shape and it is checked that this linear system dissipates the same amount of work per cycle as in the actual test (see figure 6). The linear stiffness and damping coefficients are used in the analysis that calculates the modes of the rotorcraft airframe on its landing gear in its six degrees of freedom. Figures 7 & 8 show the plots of stiffness and damping coefficients for the MLG test without the tyres fitted.

2.2 Modelling of Aircraft Responses

2.2.1 Airframe / Landing Gear Model

GKN Westland Helicopters has a three dimensional non-linear dynamic mathematical models using the MATLAB/SIMULINK software package. This model comprises of an aircraft body, rotor, landing gears and ground surface (or ship's deck). The rotorcraft motion is allowed in all six degrees of freedom and it has three identical landing gear modules. The rotorcraft initial conditions are defined at the rotorcraft centre of gravity and include position, velocity and attitude in all three axis. The model can cater with large translational and rotational displacements of the rotorcraft plus movement of the deck in all directions. The output from the model can be displayed as tables, graphs or as an animation. This model can also be used to simulate single leg drop tests by restricting the rotorcraft motion to the vertical axis only. A short description of the main modules in the mathematical model is given below –

Aircraft Body -

The aircraft body is assumed to be rigid body with its mass and inertia concentrated at the centre of gravity. The movement of the aircraft body in its six degrees of freedom are calculated from the forces and moments applied to it. The rotor and landing gears are assumed to be rigidly attached to the aircraft body and thus as the body moves their positions move so that in the body axis their positions relative to the centre of gravity remain unchanged. The body has its own axes system that uses the centre of gravity as its datum point. The initial conditions describe the position, attitude, velocity and acceleration of the centre of gravity and are defined in an input data file. The forces and moments about the centre of gravity as generated by the other modules are applied to the aircraft body and the resulting movement in the six degrees of freedom are calculated. When representing the single leg drop tests, five of the degrees of freedom are fixed leaving the body free to move in the vertical axis only, as if the landing gear where fixed in a drop test tower.

Rotor -

The forces and moments from the main rotor and tail rotor can be applied. An additional set of forces may be applied at any position, as defined in the input data file, which allows the model to caters for such things as loads due to the wind on the airframe.

Landing Surface -

The landing surface is assumed to be a flat plane that can move with six degrees of freedom. Thus it can simulate the flat stationary ground of an airport or the flat moving deck of a ship.

Landing Gear -

The same module is used for each landing gear although the input data used by each module can be different. It can accept both single and twin tyre arrangements, with the wheels set at any steer angle plus offset from the centreline of the oleo in any direction. The module includes a set of tyres, wheels plus axles, bearings, seals, air spring and oleo damping. The position of the tyres, bearings, airframe attachment point and angles of the oleo to the vertical are defined in the input data. The force in the oleo is determined by the oleo closure, oleo closure rate, friction force due to the load on the bearings and seal friction. Seal friction and bearing friction

constants, including the values for both static and dynamic friction, can be defined. The non-linear curves for the tyre deflection, air spring and oleo damping are defined as "lookup" tables and the effect of the axle stiffness is also included. Also tyre damping plus tyre lateral and fore/aft stiffness can be defined. The movement of the contact point between the tyre and the deck is also calculated, there being three basic conditions, with the transition between each condition being continually monitored. Different value of friction for a "stuck" and "sliding" tyre can be defined. The three conditions and their definitions are as follows -

Flying -tyre not in contact with the ground, thus no tyre forces can be generated. If at any time during the simulation the closure of the tyre reduces so that it cannot remain in contact with the deck then the condition reverts to "flying".

Stuck - tyre in contact with the ground. The contact point at touchdown is calculated as the point that is directly under the wheel hub and also at right angles to the deck. It remains as a fixed point on the deck surface until the sliding of the tyre is detected. Thus as the wheel hub moves relative to the contact point the force due to the tyre is calculated in all three axis. When sliding of the tyre is detected to have stopped, then the tyre contact point is again held stationary at the last calculated position on the deck surface prior to the sliding of the tyre ceasing.

Sliding -tyre in contact with the ground but sliding. When the lateral plus fore/aft tyre force exceeds the tyre limiting friction value times the tyre vertical force, then the tyre contact point is allowed to move (or skid) across the deck surface. The tyre contact point is placed in the opposite direction to the movement of the wheel at a distance calculated by diving the tyre friction value times tyre vertical load by the relevant tyre stiffness.

The equations of motion used for the landing gear models have been described in detail by other authors (ref. 2) and therefore will not be detailed in this document. One of the major requirements for this mathematical model was that it should be able to simulate aircraft and deck movements that last over a relatively long time. Therefore some mathematical refinements that could have been made to the model have not been included where the small increase in accuracy did not warrant the greater increase in computing time. An examples of this is the use of a lookup tables for the oil damping characteristic instead of calculating the characteristic based on the response of the valve components. However, if required, it is very easy to add further features the model at any time.

2.2.2 Verification of Data using the Single Leg Drop Testing Results

Compliance with the landing gear energy absorption requirements of the various certification requirements is usually demonstrated by Single Leg drop testing. During these tests, various landing gear parameters can be measured which can then be used to refine and verify the data used in the mathematical model of the landing gear. Before the drop testing is started, the gear is checked for correct filling and inflation by carrying out a very slow closure and extension of the gear over nearly its full stroke. The results of this test can be used to confirm if the air spring data used in the landing gear model is correct. A typical load -v- stroke curve as obtained from a typical air spring curve test and as predicted by the mathematical model is shown in figure 9. This initial test can also be used to confirm the stiffness of the axle by comparing the difference in oleo and mass travel with the measured tyre deflection. Figure 10 shows the load -v- deflection curves for the tyre only and for the tyre plus axle.

The primary objective of the drop tests is to measure the maximum values of the forces at the ground and the maximum values of mass travel, oleo closure and tyre closure. However these parameters plus other requested parameters, such as oil and gas pressure, are recorded continuously during each drop test. Figure 11 is a typical example of the recordings taken during a drop test. Using the recordings of the oil pressure, gas pressure and oleo closure, the actual oleo damping characteristic can be determined and compared with the theoretical characteristic used in the mathematical model, as shown in figure 12. When deriving the actual oleo damping characteristic the effects of oil compressibility on the recorded measurements need to be taken into account. Also by using the recordings of gas pressure and oleo closure, the actual air spring curve under adiabatic conditions can be determined and compared with that used in the mathematical model, as shown in figure 13. Finally the accuracy of the model can be checked by comparing its predictions with the actual drop test results. This comparison should include such

parameters as mass travel, oleo closure as well as ground force. Figure 14 shows the ground force -v- time comparison between an actual drop test result and the model prediction, and it can be seen that the correlation is very good.

2.2.3 Complete Rotorcraft Model comparison with DTV Drop Test Results

During the development of the EH101 rotorcraft a Drop Test Vehicle (DTV) was built which was representative of the actual rotorcraft but used a simple steel frame in place of the actual rotorcraft airframe (see figure 4). The DTV was fitted with the actual landing gears, which were instrumented, and its weight and moment of inertia could be adjusted to represent any actual rotorcraft condition. One of the tests that the DTV was used for was to simulate landings of the complete rotorcraft onto a ship's deck, where the DTV could be set at any landing attitude and then dropped from a set height onto a flat surface set at any angle. To check that the complete rotorcraft model would give accurate predictions when using data derived from the single leg drop testing, some of the DTV drop tests were simulated with the complete rotorcraft model. These simulations included rotorcraft level landings, tail down landings and aircraft rolled landings onto both level and angled decks. Figure 15 shows the actual test recordings and figure 16 shows the model predictions for the DTV level landing test and as can be seen the correlation is very good. Further comparisons of the model predictions with the DTV test results for different cases also showed a good correlation and thus it was considered safe to use data derived for a single landing gear in the complete rotorcraft model.

2.2.4 Comparison of Model Prediction with Impedance Test Results

The same mathematical model of the landing gear, as used for the drop test predictions, was also used to predict the results for the impedance tests. Figure 17 shows the force -v- closure graph as predicted by the model compared to the actual test result for one particular test condition without the tyres fitted. As the predicted curve was a good match with the actual test result, the model was then used to predict the work done per cycle for all the test conditions. Figure 18 shows the comparison between the predicted work done and the actual work done for two of these impedance tests. Figure 19 shows the error between the predicted and actual results for all the test conditions and it can be seen that as the amplitude increases the error bandwidth reduces very significantly. The total work done is basically from two sources, seal/bearing friction and oil damping. As the amplitude increases the percentage of the work done due to the oil damping also increases and therefore the percentage of the total work done due to the friction decreases. As the level of seal friction is likely to be very variable between tests, it was considered that the correlation between the between model prediction and actual test results was very good. The comparison between model prediction and actual test results was then repeated for all the MLG impedance tests with the tyre fitted. Again the correlation between the prediction and actual test results was good but it was noticed that the prediction tended to slightly overestimated the work done at the lower amplitudes and slightly underestimated the work done at the higher amplitudes. The process was then repeated for the NLG impedance test without the tyre fitted. The comparison of predicted to actual test results showed that the correlation was poor, as at the high amplitudes the predicted work done was significantly higher than that achieved in the tests. Comparison of the predicted and actual force -v- closure graphs showed that, on the gear extending part of the stroke, the predicted force was considerably lower than the actual force. By running the mathematical model with various levels of additional recoil damping we were able to determine that no significant level of additional recoil damping was being generated (see figure 20). Examination of the assembly drawings of the NLG damping arrangement (see figure 21) showed that the recoil plate was not spring loaded, as it is in the MLG damping assembly, but relied on the movement of the oil through it to open and close it. It became apparent that, under the test conditions, the rate at which this oil was moving was not high enough to quickly move this recoil plate from its open to closed position and thus full recoil damping was not being achieved. As the results for the MLG tests were in accordance with the model prediction, this indicated that a spring loaded recoil plate would work correctly under these test conditions. Thus to restore the required level of additional recoil damping, a modification has been introduced to spring loading the recoil plate in the NLG damper assembly.

2.2.5 Model Prediction Of Airframe Impedance Test

The complete rotorcraft mathematical model was used to simulate an airframe impedance test by carrying out a frequency sweep with an alternating force of fixed magnitude applied at the rotor head. For each case, the maximum amplitude of the airframe at each frequency can then be plotted for pitch and roll. The natural frequencies of the airframe occurs where the peak in each of the plots occurs.

The initial EH101 airframe impedance test, carried out in 1987 using the prototype aircraft airframe, was also simulated using the complete rotorcraft mathematical model and the procedure described above. The resulting plot of amplitude against frequency for each frequency sweep is shown in figure 22. It can be seen that as the force increases in magnitude the pitch natural frequency decreases. This is due to the fact that the lower forces produce lower pitch amplitudes and most of the movement is in the tyres with virtually no stroking of the oleos. As the force increases the pitch amplitude also increases and the oleos start to stroke. This reduces the overall stiffness, as the oleo stiffness is now in series with the tyre stiffness, thus reducing the pitch natural frequency. This change in pitch natural frequency, as the pitch amplitude increases and the oleo starts to stroke, is in general agreement with the change in pitch frequency predicted by the present linear methods.

The actual airframe test measured the force required to move the airframe at a constant amplitude with varying frequency with the lowest force occurring at the natural frequency. Therefore a graph of force -v- frequency at constant amplitude was constructed for two of the actual airframe impedance tests, using the results from the model prediction. The comparison of model prediction against actual test measurements is shown in figures 23. As can be seen the correlation is good although the natural frequencies do not exactly match, the model prediction being about 0.2 Hz below the test value in both cases. Another way to view the data is to plot natural frequency against the pitch amplitude as shown in figure 24. Again the correlation between the prediction and test results is good although the model slightly under predicts the natural frequency at the lower pitch amplitudes and slightly over predicts the natural frequency at the higher pitch amplitudes. The pitch and roll natural frequencies as predicted by the model, as predicted using the previous linear methods and as measured in the airframe impedance test are shown in table 1 below.

	model	linear methods	airframe test
Pitch Mode			
lower amplitudes	1.77 Hz	1.80 Hz (oleo locked)	1.9 Hz
higher amplitudes	1.40 Hz	1.36 Hz (oleo stroking)	1.3 Hz
Roll Mode			
lower amplitudes	1.37 Hz	1.04 Hz (oleo locked)	1.3 Hz
higher amplitudes	1.31 Hz	0.80 Hz (oleo stroking)	1.2 Hz

Table 1

As can be seen the agreement between the natural frequencies as derived by model and airframe test is very good. The linear method also gives very good correlation with the other two methods in the pitch mode but the agreement is as good in the roll mode. Both the model and the airframe test show only a small change in roll mode natural frequency for increasing roll amplitudes, whereas the linear method indicates that with the oleos stroking there should be a significant change in natural frequency. This small change in natural frequency is probably due to the high friction in the MLGs due to the single offset wheel which limits any significant increase in oleo movement as the roll amplitudes increase.

2.2.6 Prediction of Change in Airframe Modes for New EH101 Variants

The complete rotorcraft mathematical model was also used to predict the fundamental modes of the airframe with the low pressure tyres fitted to the landing gears. The predicted pitch and roll natural frequencies with low pressure tyres fitted and with the high pressure tyres fitted are shown in table 2 below. This shows that –

Pitch Mode – at lower amplitudes there is no significant change in natural frequency but at the higher amplitudes there is a noticeable change in natural frequency. Also there is a bigger change between the natural frequencies at lower and higher amplitudes when the low pressure tyres are fitted.

Roll Mode – at lower amplitudes there is a significant change in natural frequency. There is also a bigger change between the natural frequencies at lower and higher

amplitudes when the low pressure tyres are fitted.

	High Pressure Tyres	Low Pressure Tyres
Pitch Mode		
lower amplitudes	1.77 Hz	1.75 Hz
higher amplitudes	1.40 Hz	1.29 Hz
Roll Mode		
lower amplitudes	1.37 Hz	1.45 Hz
higher amplitudes	1.31 Hz	1.22 Hz

Table 2

This analysis has confirmed that the fundamental modes of the airframe will change for the new EH101 variants fitted with the low pressure tyres and has also indicated the size of that change.

3 *Conclusions*

The present series of tests and analysis, which are still ongoing, have already demonstrated that the non-linear mathematical model of the landing gear can accurately predict the results of the single leg landing gear impedance test. It has also been shown that the predictions using this model are in good agreement with the results obtained using the existing linear methods and the airframe impedance test results. Thus it is considered that this model can be used with confidence to predict the presence of changes in fundamental modes of the airframe when changes, such as the fitting of low pressure tyres, are made to the landing gears. The method of using the landing gear drop test results to confirm the accuracy of the data used in the mathematical model of the landing gear has also been demonstrated.

Therefore it is considered that the new procedure of landing gear impedance test combined with non-linear modelling of the rotorcraft can be used to replace the more expensive and time consuming airframe impedance test. The use of the landing gear impedance test and non-linear modelling will allow the characteristics of each item in the landing gear to be better identified and understood. Also the effect rotorcraft of changes to the landing gear arrangement on the ground resonance stability of the rotorcraft can quickly and easily be assessed with confidence.

4 Future Model Developments

It is planned to continue the development of the complete rotorcraft mathematical model. Planned modifications include the introduction of airframe flexibility plus a rotor so that the ground resonance behaviour of the complete rotorcraft, rather than just the airframe, can be predicted. An interface between this model and an existing aircraft model, that can be flown by a pilot, will also be added. Further analysis and comparison of the model predictions with the existing airframe test and forthcoming ground resonance tests of the new EH101 variants may identify further improvements that should made to the model.

It should be noted that use of this mathematical model is not restricted to just ground resonance predictions but includes other areas of rotorcraft performance. Another planned development is to use the model to predict the aircraft loads when it lands onto a ship's deck that is moving.

References

1 A L Jordan - Ground Resonance Clearance of Westland/Agusta EH101 Helicopter - paper 6.6 Thirteenth European Rotorcraft Forum

2 W A Welsh - Simulation and Correlation of a Helicopter Air-oil Strut Dynamic Response - 43rd Annual Forum of American Helicopter Society

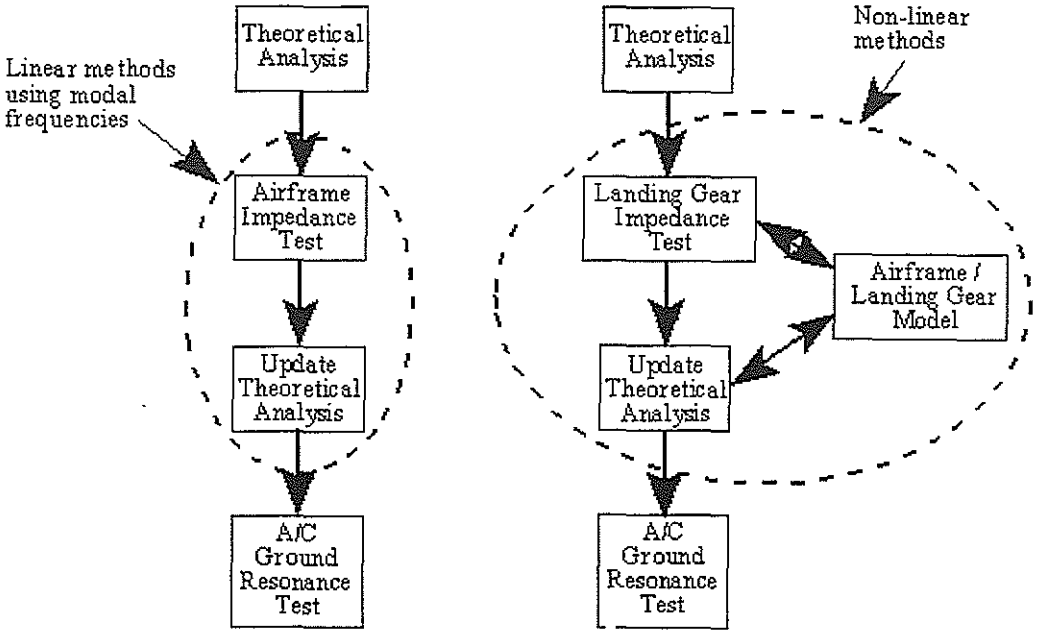

Original Process **New Process**

Figure 1

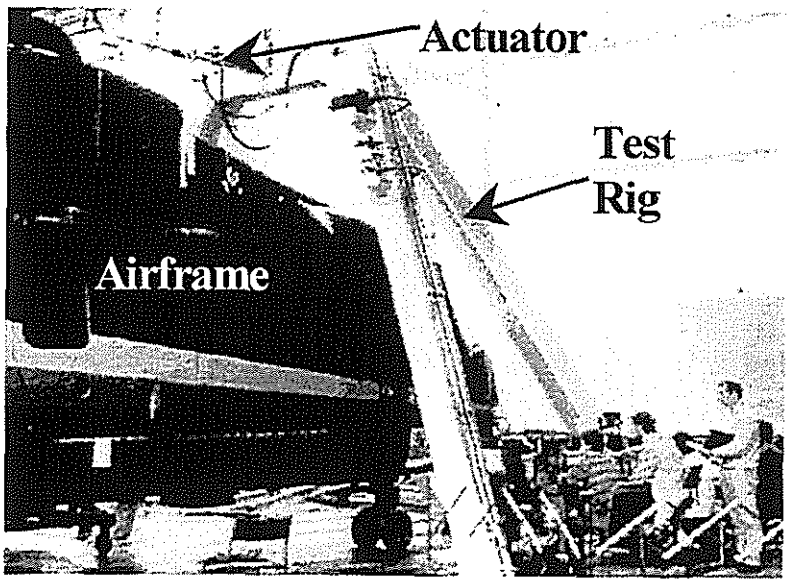

Figure 2 – Airframe Impedance Test

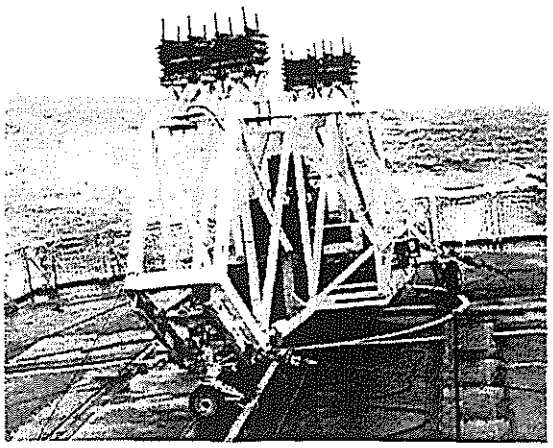

Figure 4 – Drop Test Vehicle (DTV)

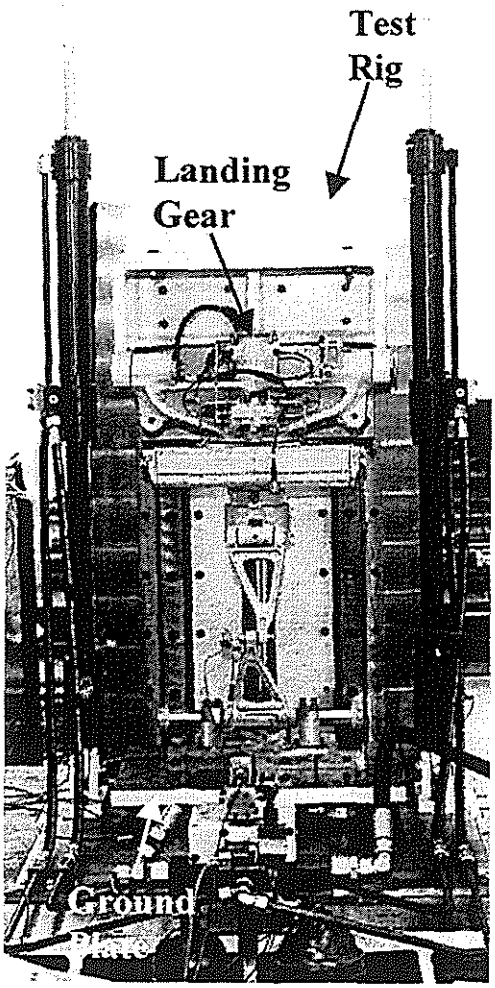

Figure 3 – Landing Gear Impedance Test Rig

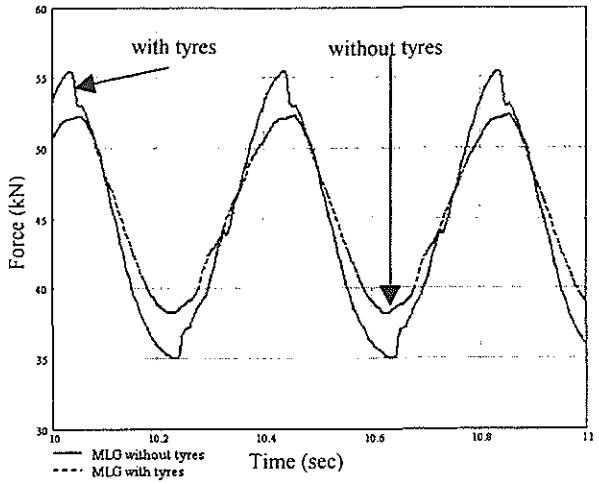

Figure 5 -
L/G Impedance Test Time Histories

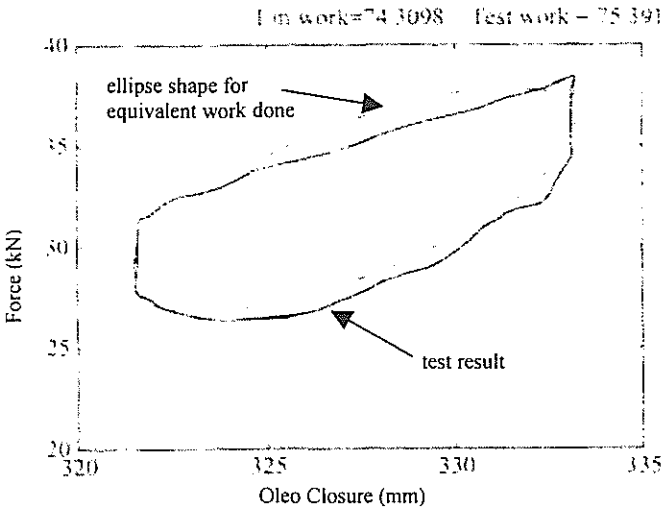

Figure 6 - Work Done per Cycle

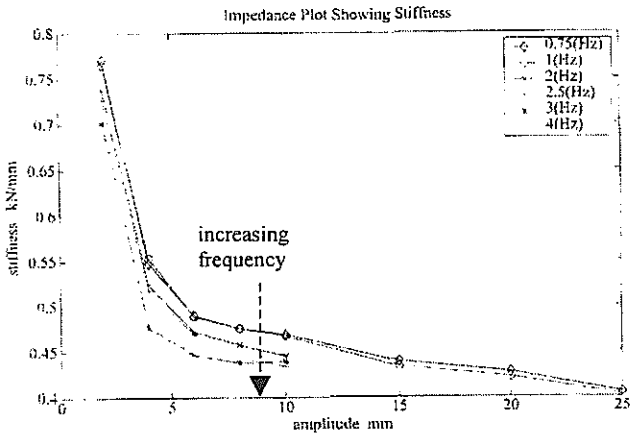

Figure 7 – Stiffness Plot

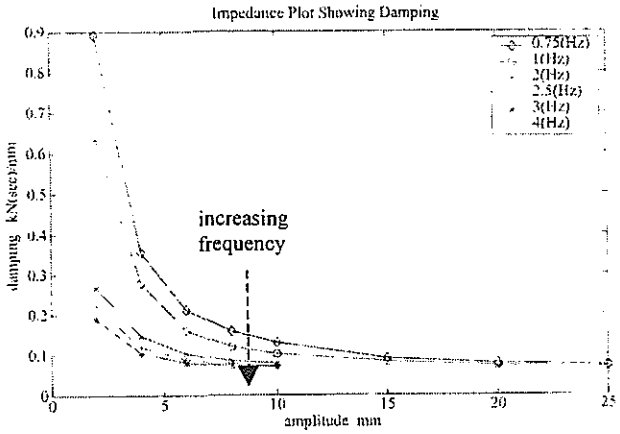

Figure 8 – Damping Coefficient Plot

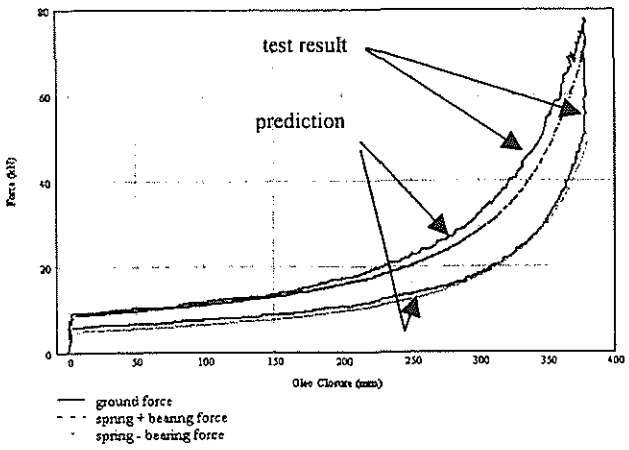

Figure 9 –
Landing Gear Isothermal Air Spring Curve

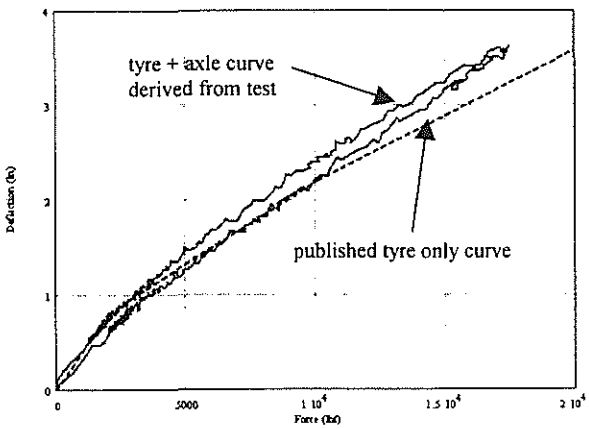

Figure 10 – Tyre Curves

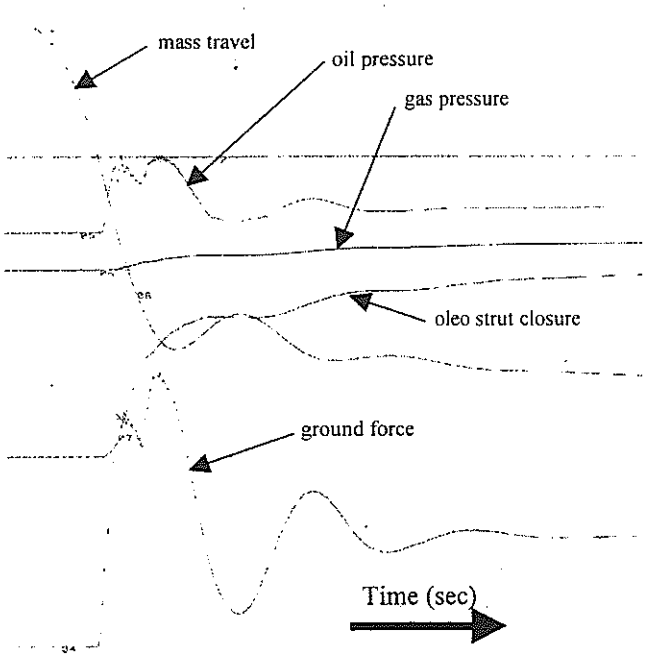

Figure 11 – Drop Test Recording

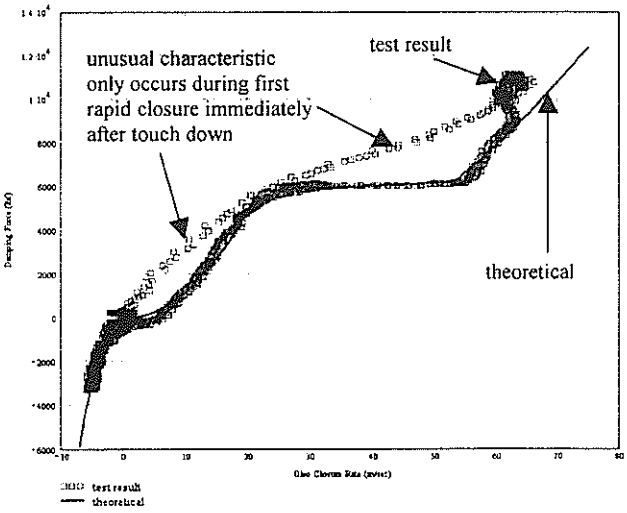

Figure 12 – Oil Damping Characteristic

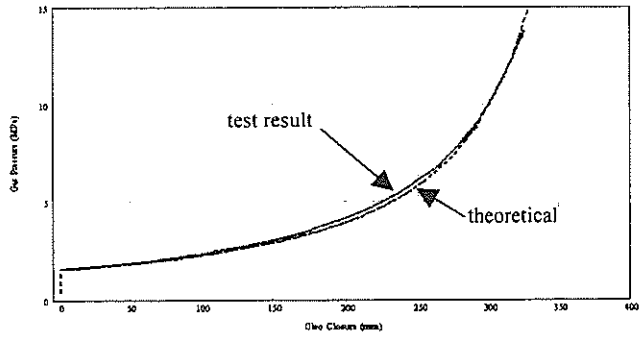

Figure 13 – Oleo Adiabatic Air Spring Curve

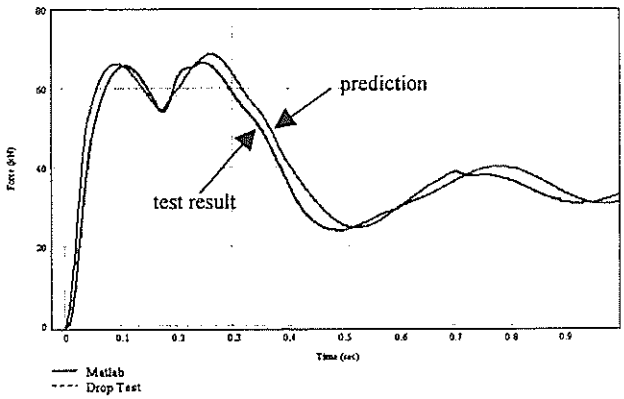

Figure 14 – Comparison of Actual and Predicted Drop Test Results

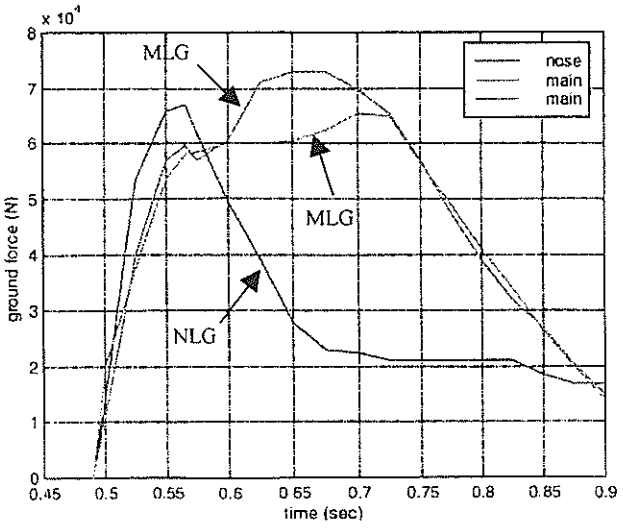

Figure 15 – DTV Actual Test Result

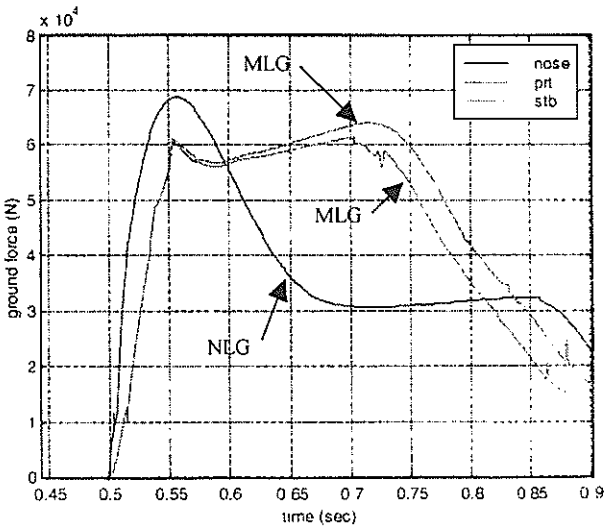

Figure 16 – DTV Predicted Test Result

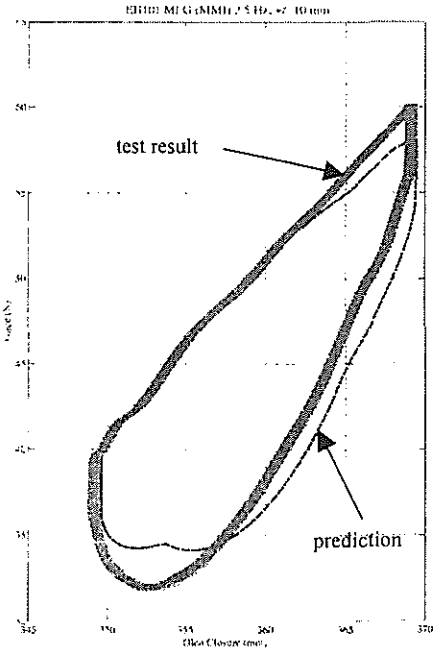

Figure 17 –
Landing Gear Impedance Test Comparison

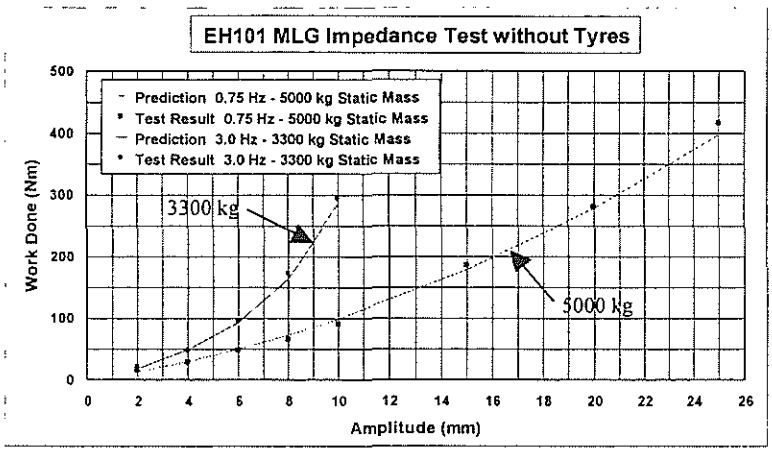

Figure 18 –
Landing Gear Impedance Test Comparison

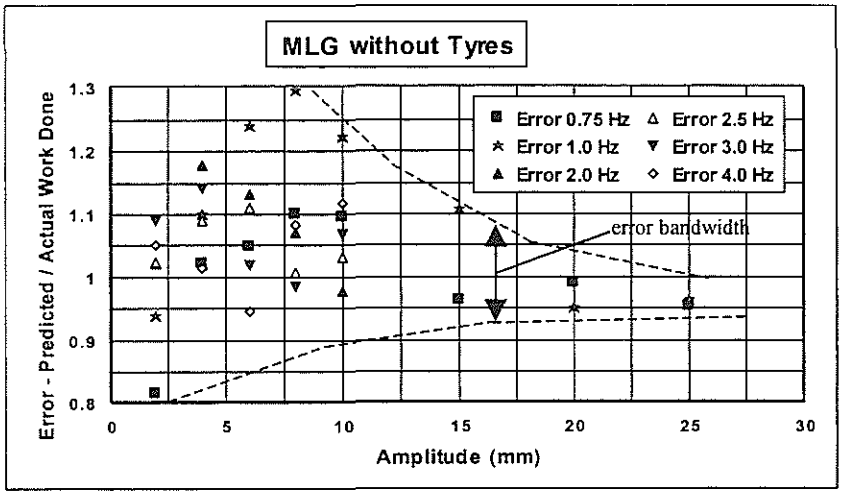

Figure 19 -
Landing Gear Impedance Test Work Done Comparison

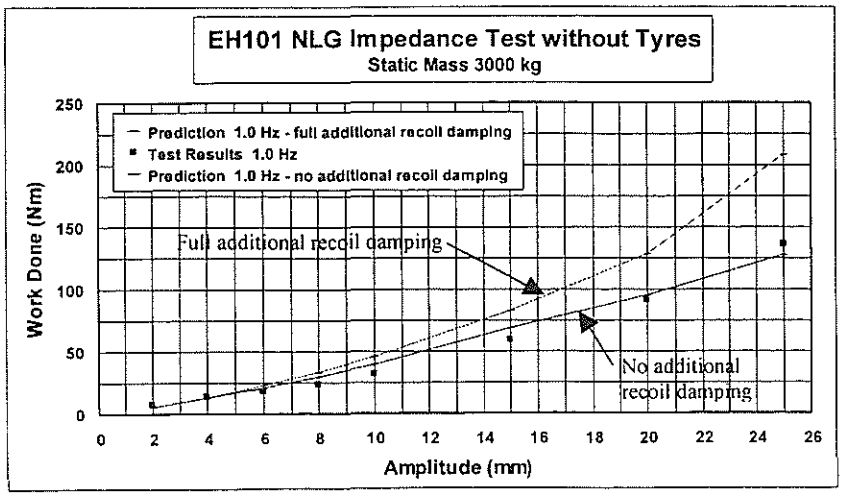

Figure 20 -
Landing Gear Impedance Test Work Done Comparison

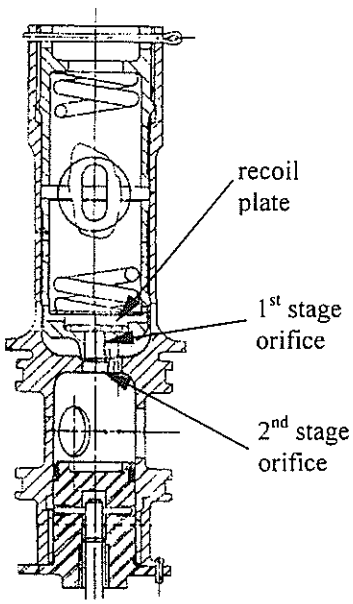

Figure 21 –
NLG Damping Valve

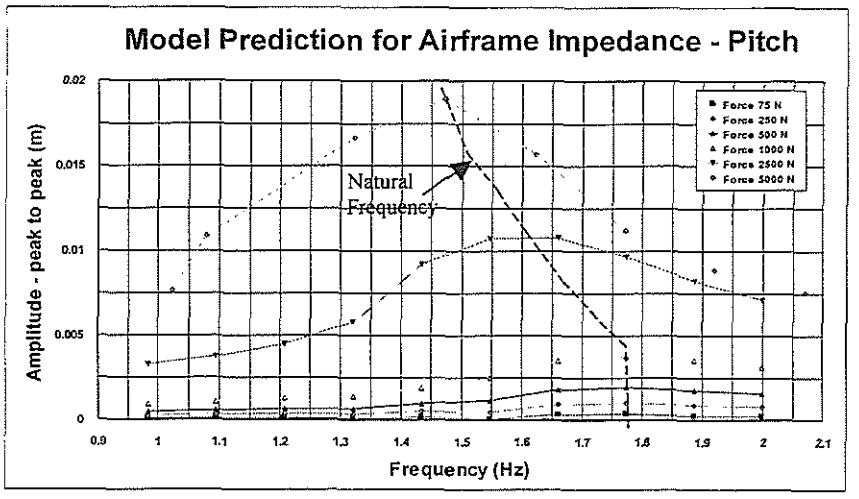

Figure 22 – Model Prediction of Airframe Impedance (Pitch)

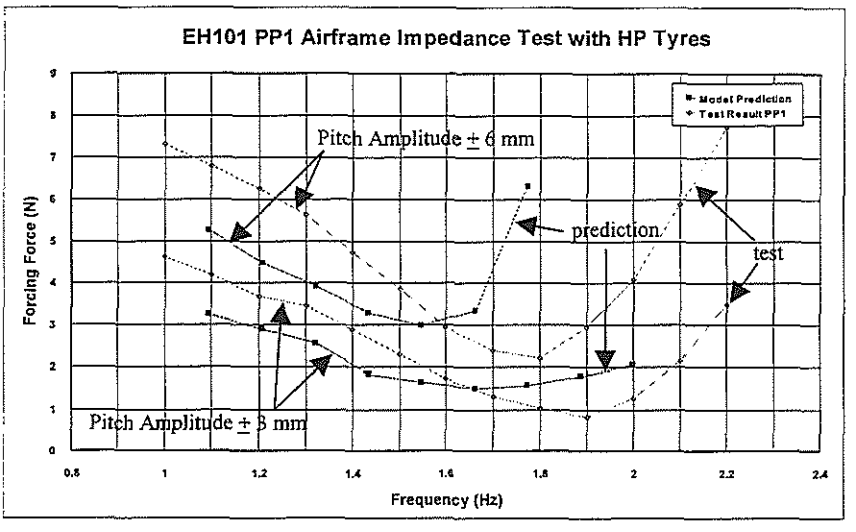

Figure 23 – Comparison of Model Prediction against Airframe Impedance (Pitch)

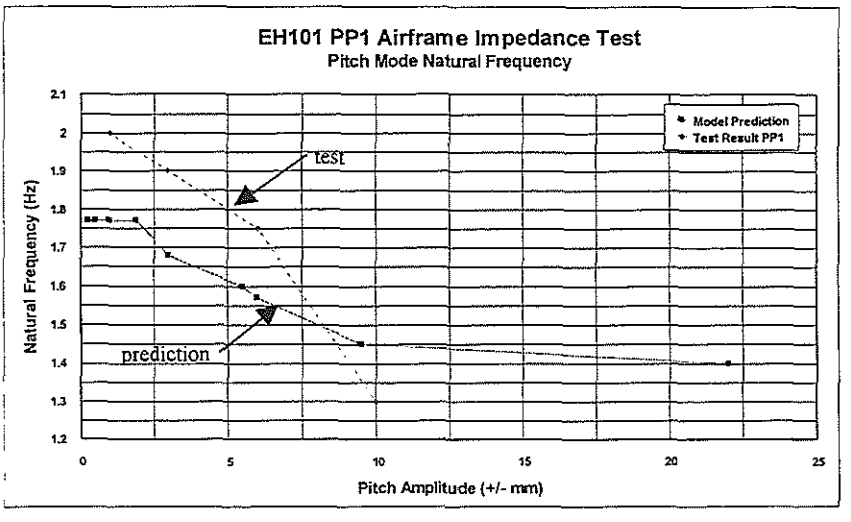

Figure 24 – Comparison of Model Prediction against Airframe Impedance (Pitch)

TWENTYFIFTH EUROPEAN ROTORCRAFT FORUM

Paper n° G3

AEROELASTIC AND AEROSERVOELASTIC STABILITY OF THE BA 609

BY

TOM PARHAM JR., LAWRENCE M. CORSO

BELL HELICOPTER TEXTRON INC., FORT WORTH, TEXAS, USA

SEPTEMBER 14–16, 1999
ROME
ITALY

ASSOCIAZIONE INDUSTRIE PER L'AEROSPAZIO, I SISTEMI E LA DIFESA
ASSOCIAZIONE ITALIANA DI AERONAUTICA ED ASTRONAUTICA

AEROELASTIC AND AEROSERVOELASTIC STABILITY OF THE BA 609

Tom Parham, Jr.
Lawrence M. Corso
Bell Helicopter Textron, Inc.
Fort Worth, Texas, U.S.A

1. ABSTRACT

The BA 609 is a nine passenger, 16,000 lb (7,250 kg) civil tiltrotor being designed by Bell Helicopter Textron, Inc. and Agusta, a Finmeccanica Company. The BA 609 design must meet all stability requirements specified in the civil certification basis. Based on analysis and Bell's experience with previous tiltrotor aircraft, the BA 609 will meet these requirements. The first tiltrotor developed at Bell was the XV–3. During the testing of this aircraft, a coupled rotor/wing whirl instability was encountered in airplane mode. The phenomenon is similar to propeller whirl flutter, except that rotor gimbal flapping and inplane mode coupling are important factors on tiltrotor aircraft. This proprotor stability phenomenon has been an important design consideration during the XV–15 and V–22 development. At Bell Helicopter Textron, Inc., analyses and methodology for the stability analysis of tiltrotors have been developed over the last 25 years. The U.S. Marine V–22 was developed using similar stability analyses and has demonstrated speeds of 379 knots (702 km/h) in airplane mode flight. To ensure that the stability requirements are met for these aircraft, their wing stiffnesses are designed to preclude proprotor stability. On the BA 609, the wing airfoil thickness-to-chord ratio is 23% thick to achieve the stiffness requirements. Once the basic airframe is designed, the effect of the flight control system is included in the analysis. Because the V–22 and BA 609 both use high-bandwidth digital control systems, these effects must also be considered in the stability analysis. The flight control system model used for stability analysis includes pilot biomechanical models to represent the pilot control inputs caused by cockpit accelerations of the structural modes. Filters are included in the flight control system, where needed, to reduce the coupling with the structural modes. Extensive correlation of analysis with model test data and flight test data yields high confidence that the BA 609 design requirements will be met.

2. INTRODUCTION

Currently Bell and Agusta are developing the BA 609 to be the world's first civil tiltrotor. Fig. 1 shows a full-scale mockup of the BA 609. The gross weight of this aircraft is 16,000 lb (7,250 kg), significantly smaller than the V–22, which has a nominal gross weight of 47,000 lb (21,315 kg). The BA 609 is designed to provide point-to-point transportation for up to nine passengers at cruise speeds up to 275 knots (509 km/h) and at ranges up to 750 nautical miles (1,390 km). There are significant challenges in designing a tiltrotor aircraft to meet these requirements. Aeroelastic and aeroservoelastic stability must be considered early in the design process to ensure that the stability requirements are met.

Tiltrotor aircraft can experience a wing/pylon/rotor whirl instability in high-speed airplane mode similar to the propeller-whirl flutter of conventional propeller aircraft. The proprotor stability problem is more complicated than conventional propeller-whirl flutter because of the additional flapping and feathering degrees of freedom, control system flexibility, and blade kinematic and elastic couplings. The proprotor stability phenomenon was first encountered on the XV–3 tiltrotor, as described in Ref. 1. Both propeller-whirl and proprotor instabilities are a result of precession-generated aerodynamic loads, but the flapping degree of freedom of the proprotor causes fundamental differences in the instability. Bell and NASA conducted joint research on the problem, studying it with analysis and model tests (Refs. 2 and 3). This research paved the way for the successful Bell/NASA XV–15 program (Ref. 4). The XV–15 aircraft, which is similar in size and weight to the BA 609, demonstrated that tiltrotor aircraft can be designed and built with proper wing stiffness to preclude proprotor stability. The proprotor stability phenomenon continues to be studied with analysis and tests to determine other design parameters that affect stability (Refs. 5, 6, and 7).

During the XV–15 flight test program, damping in one of the antisymmetric wing modes was less than predicted when the stability augmentation system (SCAS) was on. However, with the SCAS off, damping was much higher. The problem was traced to the roll rate feedback in the SCAS, which was degrading the stability of this mode (Ref. 8). A notch filter circuit was added to the SCAS to reduce coupling with this wing mode. With

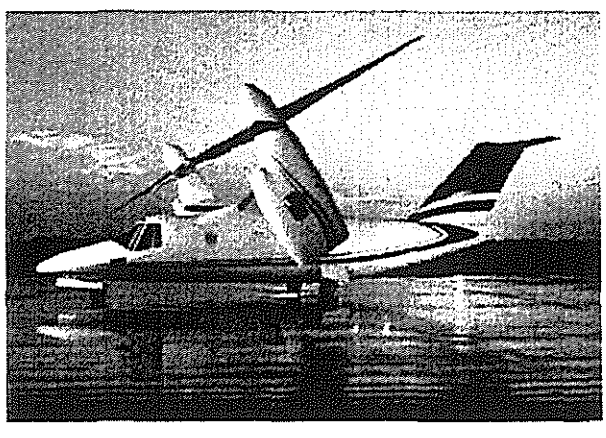

Fig. 1. BA 609 civil tiltrotor.

this filter, the damping SCAS on was similar to SCAS off. The BA 609 digital flight control system (FCS) is included in the stability analysis to ensure that the FCS does not degrade the stability of the wing modes.

In addition to the FCS, the pilot can respond at the structural mode frequencies and create an additional feedback path. Refs. 9 and 10 describe the pilot coupling phenomenon on helicopters. The pilot acts like a feedback path, causing control inputs due to cockpit accelerations of the structural modes. On large aircraft like the V–22, this can be a significant issue, because of the low-frequency structural modes. Refs. 11 and 12 describe pilot coupling on the V–22 and the design changes that reduce pilot biomechanical coupling.

3. PROPROTOR STABILITY

Airplane mode proprotor instability can be characterized as a whirl divergence as a result of precession-generated aerodynamic hub forces. The proprotor is destabilized by shear forces only, since the rotor is gimbaled to the mast. Due to the flapping degree of freedom, the proprotor destabilizing forces can create an instability in either the pitch or yaw degree of freedom alone. Ref. 13 provides a detailed discussion of this instability, which is briefly described below.

To understand the origin of the destabilizing forces, consider a proprotor and pylon undergoing a pitch oscillation. For the simplified case discussed here, the rotor consists of rigid blades with a gimbaled hub to allow rotor flapping. The swashplate, or control plane, is fixed relative to the mast. The pitch motion of the control plane will cause the rotor to process at the pylon pitch rate and assume a flapped position relative to the mast. The elemental blade forces cause an inplane shear force that causes proprotor/pylon instability at high speed. This instability is a significant design driver on tiltrotor aircraft. Specifically, the wing torsional stiffness requirements dictate that the wing be thick relative to comparable turboprop aircraft (23% for the BA 609). The high torsional stiffness associated with the thick wing design helps reduce the amount of pylon pitching motion in the fundamental wing bending mode, thereby minimizing the destabilizing effect.

4. ANALYTICAL METHODOLOGY

Fig. 2 is a flowchart showing the stability analysis methodology. Aeroelastic Stability Analysis of Proprotors (ASAP) is a linear eigenvalue analysis developed at Bell specifically for proprotor stability.

The stability analysis is first performed on the basic aircraft without including the FCS. The wing stiffnesses and pylon support and rotor properties are iterated until the requirements are satisfied. Then a linearized model for the FCS is added to the analysis to verify that the FCS does not significantly degrade the stability of the system. Structural notch filters are used to reduce FCS gain at the elastic mode frequencies as required. This methodology has been successfully used on the V–22 aircraft (Ref. 12).

The pilot can induce oscillations of the elastic modes of the aircraft through the cockpit controls. The flight control system and mechanical controls must also be designed to preclude these oscillations. In the stability analysis, the pilot/control system is modeled as a dynamic system that creates feedback paths from cockpit accelerations to control inputs. Because there is significant variability in the pilot/stick dynamic systems, the stability is evaluated with the highest gain that is expected for the pilot/control system.

5. ASAP MATH MODEL

ASAP is a linear eigenvalue stability and forced response analysis developed by Bell for tiltrotor aircraft. The analysis is based on constant coefficient differential equations. For helicopter and conversion mode, the analysis uses coefficient averaging (Ref. 14) to eliminate periodic coefficients. The analysis includes an elastic airframe, drive system, and rotor model, as well as a general FCS model.

ASAP uses discrete hinges and springs to represent the rotor system dynamics. The rotor is allowed a gimbal degree of freedom at the mast centerline, which includes

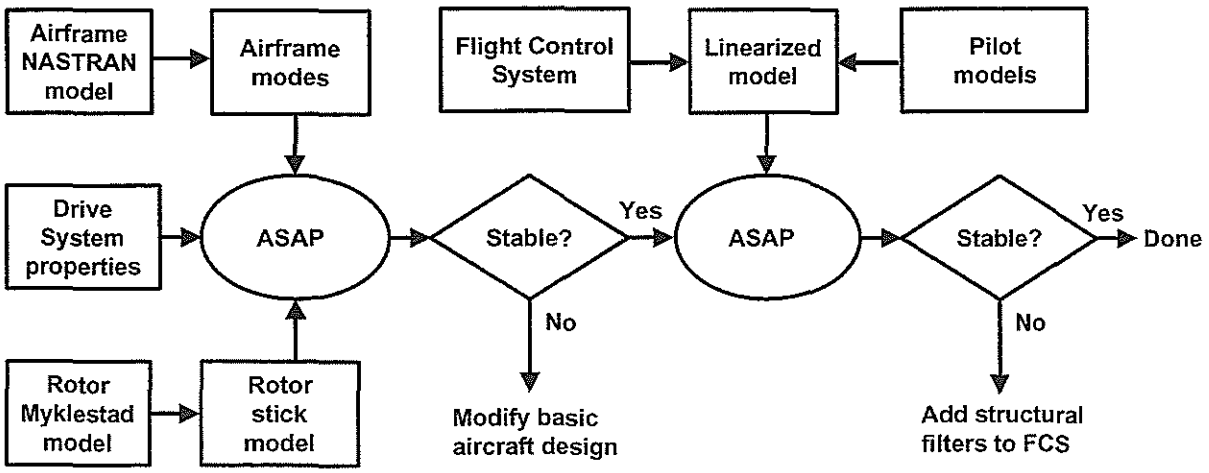

Fig. 2. Overview of tiltrotor stability methodology using ASAP.

the rotor underslinging dynamics. The analysis has provisions for discrete coning and lead-lag hinges along the blade. Fig. 3 shows the degrees of freedom for the ASAP rotor model, which allow ASAP to model the rotor cyclic flapping and inplane modes and the collective rotor coning mode. Kinematic pitch-flap, pitch-cone, and pitch-lag coupling are calculated external to the program and input in table form to represent the blade feathering motions. The blade static deformed position is represented by steady angles about the hinges, including coning at the coning hinge and prelag at the lag hinge. These steady deformations are also calculated external to ASAP and input in table form.

ASAP includes two rotor aerodynamic models. Rotor aerodynamics can be represented by a constant parameter or distributed parameter model:

1. The constant parameter model uses a constant chord blade with constant lift curve slope and assumes ideal twist. The blade lift curve slope is corrected for Mach number effects using an effective Mach number and the Prandlt Glauert correction. The rotor angle of attack at the 3/4 radius is defined in a table of angle of attack as a function of rpm and airspeed. While this rotor model is quite simplistic, it has worked well in correlation with measured stability data.
2. Alternatively, the distributed parameter aerodynamic model can be used. This model uses the actual chord distribution, twist, and airfoil tables. The blade aerodynamic coefficients are linearized about the trim position at each blade segment. Rotor trim parameters are calculated external to the analysis and input in tabular form. Typically, high-speed airplane mode stability is less sensitive to the trim condition than is helicopter mode stability.

The airframe is represented by up to twenty-five symmetric or antisymmetric airframe modes. The modal frequency, damping, and mode shape are input to the analysis. The rotor hub, control plane, control surface, and aircraft center of gravity (cg) mode shapes are provided to include coupling with the rotor forces and airframe control surface aerodynamic forces. The airframe control surfaces are represented by linear aerodynamic derivatives that act as concentrated forces on effective mode shapes for the control surfaces.

The ASAP math model includes a representation of the rotor control system geometry to model pylon/swashplate control system coupling. Blade feathering with respect to the mast is input to the rotor to account for the mast bending in the elastic mode shapes. This feathering includes the effect of rotor system phasing and geometry.

ASAP includes a drive system dynamic model with the shafts represented by torsional springs and the rotor, engine, and gearboxes represented by inertias (Fig. 4). The model includes the four torsional springs (mast, proprotor gearbox drive shaft, engine drive shaft, and interconnect drive shaft) and four inertias (rotor, engine, proprotor gearbox and tilt-axis gearbox. These degrees of freedom are adequate to represent the first symmetric and first two antisymmetric drive system modes, which can be important in calculating stability. The drive system model also includes a perturbation engine torque, so that the model can be used for torsional stability.

A general FCS model is included in ASAP for aeroservoelastic stability analysis. The FCS model has a library of linear transfer functions, which can be arranged with inputs, outputs, and summing junctions to model any linear control system. Any of the system degrees of freedom can be used as sensors to the control system. Mode shape locations are provided so that the airframe response at any point can be used as an input to the FCS. The rudder, aileron, elevator, rotor collective, rotor cyclic, and engine torque are possible control outputs. The pilot biomechanical feedback is modeled as an additional feedback in the FCS. Any nonlinear elements in the FCS are

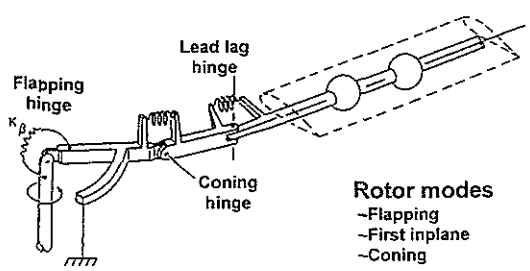

Fig. 3. ASAP rotor model.

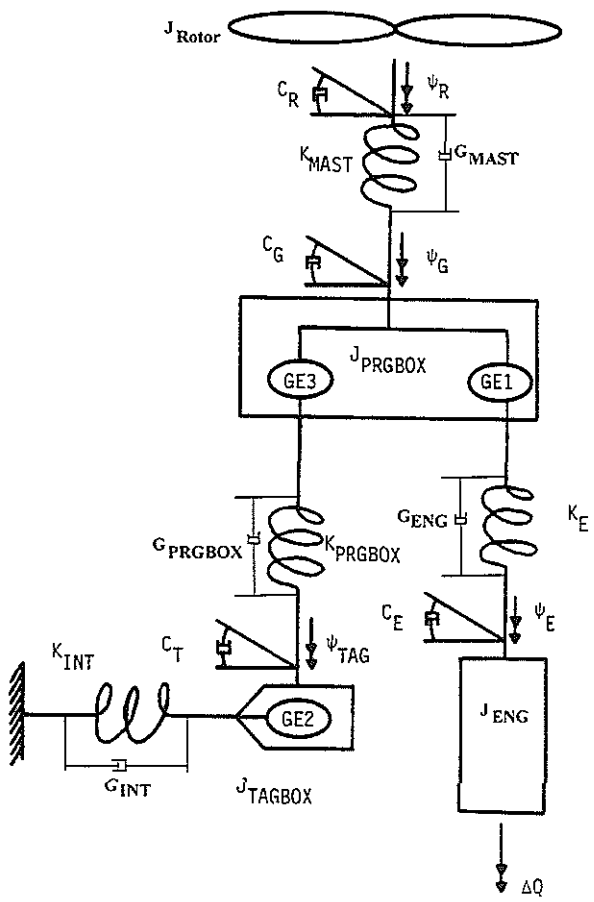

Fig. 4. ASAP drive system model.

represented by their linear equivalent. For example, digital delays are represented by second order Pade approximations.

Using the ASAP rotor, airframe, and FCS math models, several stability problems can be analyzed. The coupled rotor/airframe math model allows rotor flap/lag and wing/pylon/rotor stability to be analyzed in airplane and helicopter modes. The FCS model allows aeroservoelastic stability to be analyzed. Root locus plots as well as frequency and damping versus airspeed plots can be generated by the analysis. For control system analysis, Bode plots are generated to calculate the gain and phase margins in the FCS.

Fig. 5 shows correlation of ASAP analysis with measured stability data from Ref. 13. This data is for an early V–22 wind tunnel model and verifies that the simple ASAP rotor model is adequate for proprotor stability predictions. Ref. 12 describes the correlation of ASAP with V–22 measured stability data, including the effects of the FCS and pilot biomechanical coupling.

6. BA 609 AIRFRAME DYNAMIC PROPERTIES

Airframe dynamics are represented by a detailed NASTRAN finite-element model. The normal modes of the airframe are calculated by NASTRAN and input to ASAP. The BA 609 NASTRAN model is shown in Fig. 6. This model has approximately 38,700 grids and over 232,000 degrees of freedom. Most of the aircraft structure is modeled by plate and bar elements. CONM2 elements are used to distribute the mass and inertia properties over the structural model. Modes are generated for stability analysis at various nacelle angles and gross weight configurations.

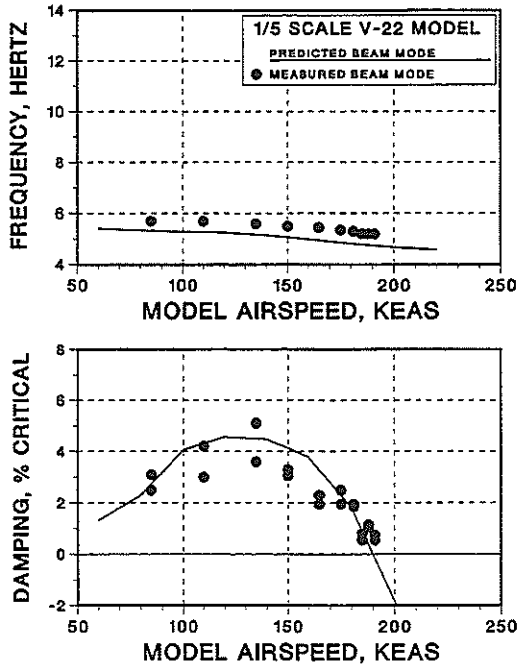

Fig. 5. Correlation of ASAP with model test data.

The airframe frequencies for airplane and helicopter modes at 16,000 lb (7,250 kg) gross weight are shown in Table 1. The six rigid body modes are calculated by NASTRAN, but are not included in the table. Each mode has a name that describes the fundamental motion. For example, the "symmetric wing beam" mode primarily involves symmetric beamwise bending of the wing. In airplane mode the pylon cg is forward of the wing elastic axis, so there is wing torsion motion in this mode also. Because of the complexity of the structure, none of the modes are purely vertical or lateral, even though they may be labeled as such. NASTRAN models the coupling between the degrees of freedom, and all mode shapes include motion in all three translation and rotation degrees of freedom.

The NASTRAN model is also used for vibration predictions and predicts the higher frequency modes up through 6/rev. For proprotor stability analysis, only the fundamental wing modes below 1/rev are important and Table 1 lists only these modes. The BA 609 FCS operates at 50 Hz, so the FCS Nyquist frequency is 25 Hz. For stability analysis including the FCS, the modes up to the Nyquist frequency are included, although the fundamental wing modes are still the critical modes.

7. BA 609 DRIVE SYSTEM DYNAMIC PROPERTIES

The drive system in the BA 609 includes engines mounted in the pylons and an interconnect drive shaft between the two rotors. The long interconnect drive shaft causes the first antisymmetric drive system frequency to be in the frequency range of the fundamental wing modes, so the drive system can be important for stability. Table 2 lists the BA 609 drive system natural frequencies.

8. BA 609 ROTOR DYNAMIC PROPERTIES

The rotor used on the BA 609 is a three-bladed, stiff-inplane rotor. The blades are tapered and highly twisted (47.5 degrees) to achieve low-speed and high-speed performance. The rotor has a constant velocity gimbal at the mast centerline to allow rotor flapping. A relatively small hub spring is used to reduce flapping

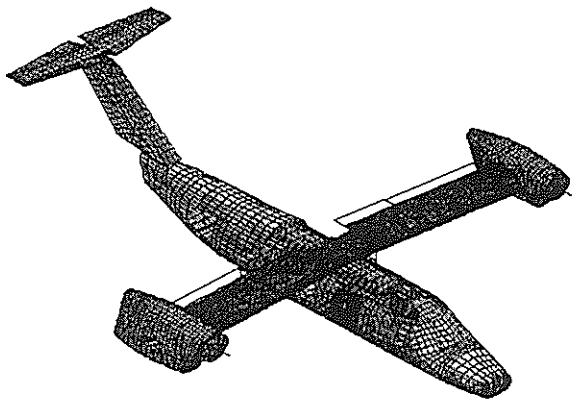

Fig. 6. BA 609 NASTRAN model in airplane mode.

Table 1. BA 609 airframe properties.

Airplane Mode (478 rpm)	Frequency		Helicopter Mode (569 rpm)	Frequency	
Mode name	Hz	*x*/rev	Mode name	Hz	*x*/rev
Symmetric wing beam	3.35	0.42	Symmetric wing beam	3.02	0.32
Antisymmetric wing chord	3.76	0.47	Antisymmetric wing chord	3.68	0.39
Symmetric wing chord	5.31	0.67	Symmetric wing torsion	4.29	0.45
Antisymmetric wing beam	5.87	0.74	Antisymmetric wing torsion	4.78	0.50
Symmetric wing torsion	6.10	0.77	Antisymmetric wing beam	6.05	0.64
Antisymmetric wing torsion	6.36	0.80	Antisymmetric pylon yaw	6.30	0.66
Fuselage lateral bending	7.35	0.92	Symmetric wing chord	6.62	0.70
Symmetric pylon yaw	10.66	1.34	Symmetric pylon yaw	6.94	0.73
Antisymmetric pylon yaw	10.88	1.37	Fuselage lateral bending	7.51	0.79
Fuselage vertical bending	12.05	1.51	Fuselage vertical bending	11.31	1.19

Table 2. Drive system natural frequencies.

Mode	Frequency (Hz)
1st antisymmetric	3.27
1st symmetric	6.70
2nd antisymmetric	9.07

Table 3. BA 609 rotor frequencies.

	Airplane Mode 478 rpm; $\theta = 87.5$ deg		Helicopter Mode 569 rpm; $\theta = 75$ deg	
Mode	Rotating system (*x*/rev)	Fixed system (Hz)	Rotating system (*x*/rev)	Fixed system (Hz)
Flapping	1.005	0	1.002	0
In-plane	1.300	2.391	1.255	2.419
Coning	1.188	9.468	1.15	10.911

during rotor startup. The constant velocity gimbal is used to reduce the drive system 2/rev torque when the rotor flaps. The design uses negative δ_3 (flap up, pitch nose up) to reduce flapping and keep the rotor flapping mode below 1/rev to eliminate the possibility of flap/lag instability (*Ref. 15*). For proprotor stability, only the fundamental rotor modes are significant, and only these modes are modeled in ASAP. Table 3 shows the fundamental rotor frequencies (no aerodynamics or airframe coupling) at two different rotor speeds. The BA 609 operates at 569 rpm (100%) in helicopter and conversion modes. Once fully converted to airplane mode, the rotor speed is decreased to 478 rpm. The flapping frequency is slightly above 1/rev in a vacuum, although the rotating system frequency is about 0.9/rev, when aerodynamics are included. The fixed system inplane frequency shown in the table is the regressing inplane mode. While the rotor is stiff-inplane to preclude ground resonance, the regressing inplane mode frequency is close to the airframe frequencies and is important for proprotor stability.

9. LINEAR FLIGHT CONTROL SYSTEM MODEL

The BA 609 utilizes a state-of-the-art digital fly-by-wire control system. The pilot has a conventional cyclic stick and pedals, as well as a collective/power lever that controls the vertical axis in helicopter mode and forward speed in airplane mode. The vertical axis control is similar to a conventional helicopter collective in that pulling on the handle increases rotor collective and engine power. The FCS includes rate, attitude, and linear acceleration feedback for handling qualities. Engine torque and rotor rpm feedback are used to maintain rotor speed and power setting. The controls include the two conventional fixed-surface controls (flaperon and elevator) as well as rotor collective, longitudinal cyclic, and engine power setting. The rotor controls can be moved symmetrically or antisymmetrically. Note that the aircraft does not have a rudder or rotor lateral cyclic control. The model includes sensor dynamics, digital delay approximations, and actuator dynamics to achieve good fidelity at the structural mode frequencies.

The FCS has airspeed and nacelle angle scheduling to change the control sensitivity and mixing with flight condition. Ref. 16 describes the development of the BA 609 control architecture and control laws. Structural notch filters are included in the FCS to reduce coupling with structural modes as required.

10. PILOT BIOMECHANICAL RESPONSE

On the V–22, the pilot biomechanical response created three separate divergent oscillations as described in Ref. 11. These oscillations were not anticipated on the V–22 and resulted in delays at flight test as design

solutions were developed and implemented. On the BA 609, the stability methodology has benefited from the V–22 experience and thus included pilot coupling from the start.

The primary difficulty is determining what the pilot biomechanical response will be for a given cockpit and control geometry. On the V–22, the response was measured on the actual aircraft with various pilots. On the BA 609, the pilot response is based on the measured V–22 response with some adjustments for differences in the control geometry.

Typically, pilot response is quantified in terms of inches of stick response per g of acceleration. Fig. 7 shows the V–22 longitudinal pilot model and the measured response data. The open symbols are the measured ground shake test response for two different pilots. As indicated by the response, the pilot biomechanical response can be characterized as a highly damped second order system with a natural frequency between 3 and 4 Hz. There are limited flight test data that support the ground shake test data. A second order transfer function was curve fit to match the measured pilot response, which is referred to as a pilot model. This model is only valid above 1 Hz and should not be confused with the low-frequency pilot models, which predict how the pilot flies the aircraft. On the V–22 and BA 609 there is a lateral control stick balance weight. Because these weights and their moment arms are different on the BA 609 and V–22, an analytical model was tuned to match the measured V–22 data and then modified to represent the BA 609 control properties. For the BA 609 longitudinal cyclic, lateral cyclic, and collective/power lever, pilot biomechanical models were developed and used in the stability analysis. The validity of these models will be verified during the BA 609 testing.

The three pilot models are included as additional feedback paths in the ASAP FCS model. Fig. 8 shows these feedback paths. The pilot models are formulated to represent a high-gain, worse-case pilot. Typically, the actual measured pilot gain will be less than predicted by the models.

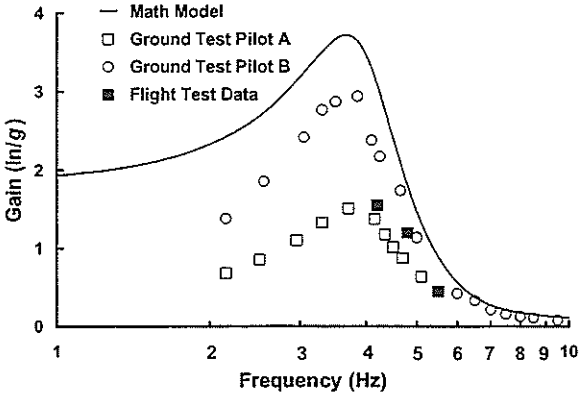

Fig. 7. Measured V–22 longitudinal cyclic stick pilot biomechanical response.

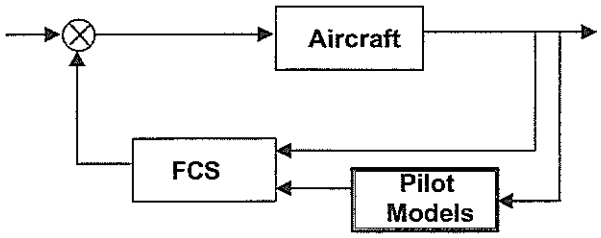

Fig. 8. Pilot feedback block diagram.

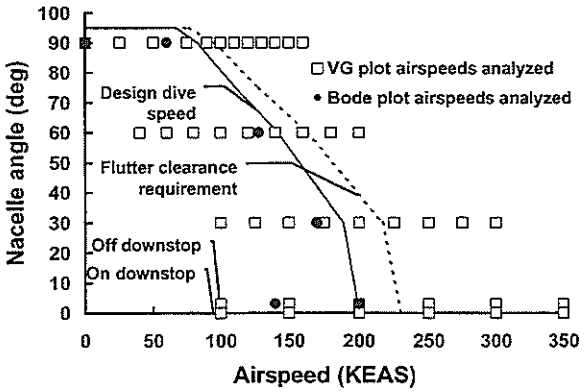

Fig. 9. BA 609 flight envelope at 569 rpm.

11. BA 609 FLIGHT ENVELOPE

The flight envelope for the BA 609 is typically specified separately for helicopter/conversion mode and airplane mode. As forward speed increases from hover, the pilot tilts the nacelles forward. Cockpit displays for the pilot show where the aircraft is within the conversion corridor. Fig. 9 shows the flight envelope for helicopter/conversion modes. Also shown are the stability analysis points. Altitude and gross weight restrictions also limit the conversion corridor of the BA 609. At maximum gross weight during helicopter/conversion mode, the flight envelope has a maximum ceiling of 8,000 ft (2,438 m). The aircraft is capable of flying to 14,000 ft (4,267 m) in conversion mode; however, this capability requires lighter gross weights.

When the nacelles are fully converted, the nacelles are preloaded into a downstop, which provides additional pylon stiffness for high-speed airplane mode flight. Once the downstop is engaged, the rotor speed is reduced from 569 rpm to 478 rpm. The airplane mode flight envelope versus altitude is shown in Fig. 10, which shows the operating ceiling of 25,000 ft (7,700 m). Also included in this figure are the stability analysis data points.

12. STABILITY PREDICTIONS

The analytical stability predictions for the BA 609 were obtained using the methodology described above. The flowchart shown in Fig. 2 summarizes the approach used to ensure that the stability requirements are satisfied. The ASAP computer code is used to calculate eigenvalues for coupled wing, rotor, and drive system as a function of airspeed. Several altitude and gross weight combinations are analyzed to ensure that the basic aircraft has sufficient

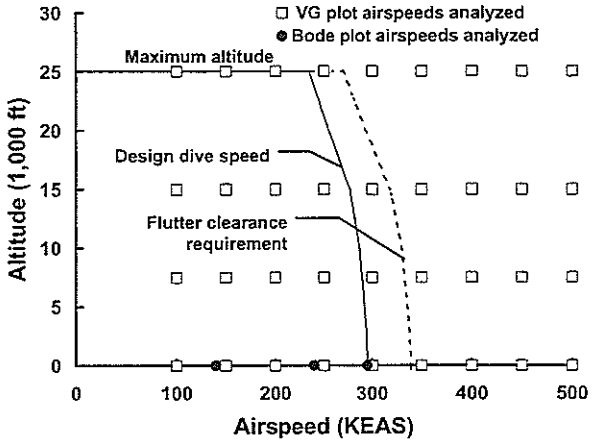

Fig. 10. BA 609 flight envelope at 478 rpm.

stability margins over the entire flight envelope. The basic aircraft frequency and damping versus airspeed for the critical 16,000 lb (7,250 kg) gross weight configuration at sea level standard condition are shown in Fig. 11. To verify that the aircraft is stable for the entire gross weight range, the stability is also verified at the empty gross weight of 11,000 lb (4,990 kg). The symmetric wing chord (SWC) is shown to be critical at 364 knots (674 km/h). The regulations require a 15% margin above the design speed for flutter clearance. Since the predicted point of instability (364 kn [674 km/h]) is greater than the flutter clearance speed (339 kn = 1.15 × 295 kn), the basic aircraft satisfies the stability requirement.

Fig. 11 does not show the frequency and damping for the rotor modes that are included in the analysis. Particularly in high-speed airplane mode, the rotor flap lag stability is important. Fig. 12 shows the rotating system stability for the rotor flapping and inplane modes. Note that the flapping mode is below 1/rev because of the negative spring effect of the negative δ_3. This reduces the flapping frequency to keep it separated from the inplane mode, but does not cause static divergence of the rotor. The damping plot shows that both modes are well damped.

With these requirements satisfied, the linearized flight control system model is then included in the analysis. The FCS bandwidth is high enough for the FCS to interact with the elastic modes of the airframe. Bode plots are generated for each path to verify that the system has acceptable gain and phase margins at the elastic mode frequencies. Although there are no certification requirements for gain and phase margins, 6 dB and 60 degree margins are maintained to ensure a robust design. If the margins are not acceptable, structural filters are added to attenuate the FCS coupling with the structural modes. A typical Bode plot for the aircraft roll rate path is shown in Fig. 13, which shows the gain in the aircraft open loop roll rate path before and after a filter was added. The AWC and AWT modes have gain margins above zero dB without the filter. Therefore, a structural filter is required to reduce FCS coupling to meet the gain margin requirement. The structural notch filter designed for the roll rate path is shown in Fig. 14. This filter reduces the gain at

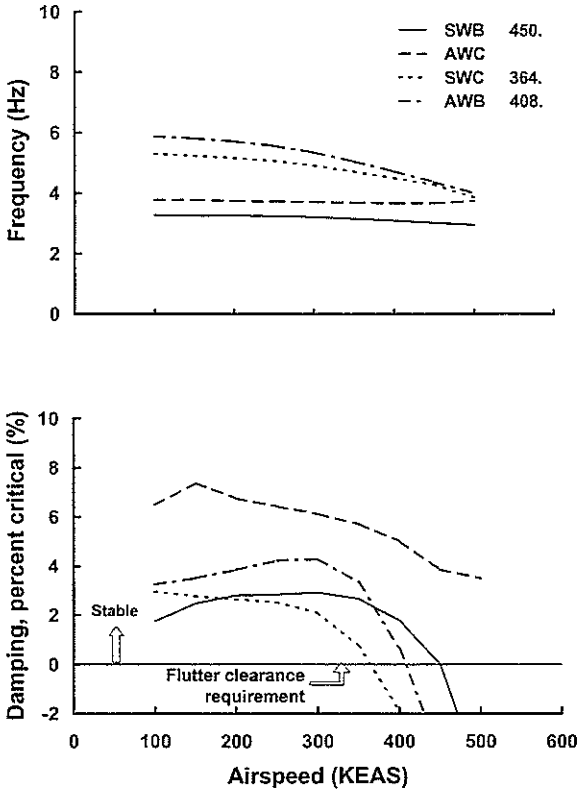

Fig. 11 Airplane mode frequency and damping versus airspeed at sea level standard.

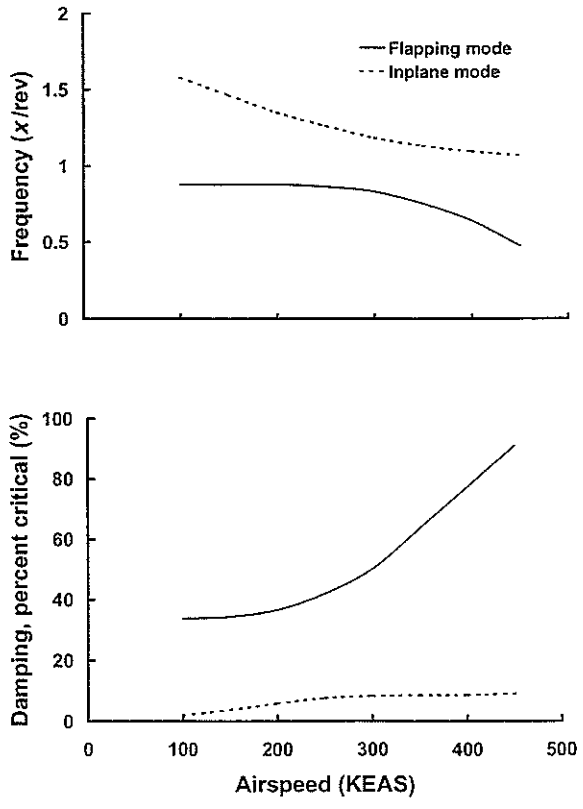

Fig. 12. Rotor flap/lag stability.

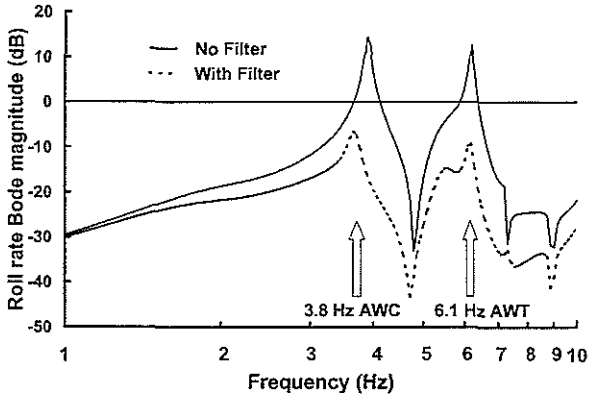

Fig. 13. Airplane mode roll rate Bode plot.

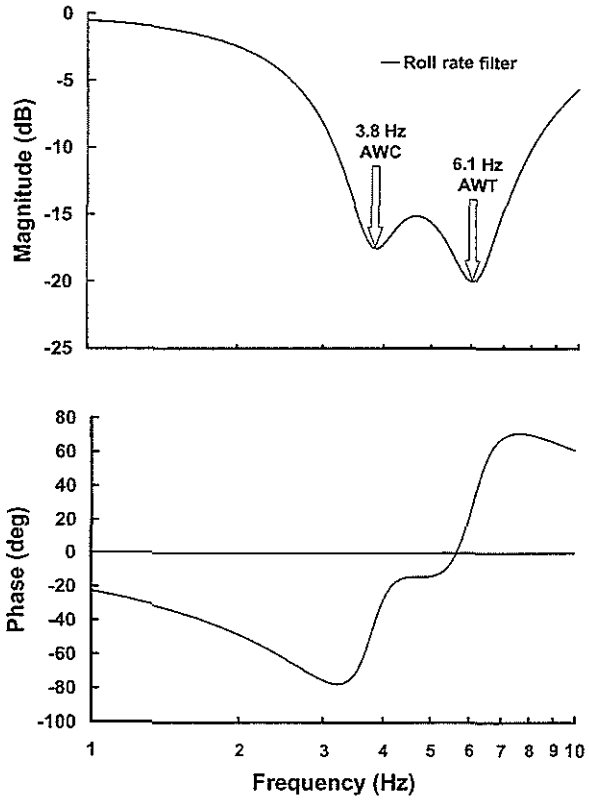

Fig. 14. Airplane mode roll rate filter.

the AWC and AWT mode frequencies by 17.5 and 20 dB, respectively. This filter consists of two second-order notch filters in series. Notch filters are used because they have less phase lag at low frequencies than a second order lag, for example. The phase lag at low frequencies will impact and degrade the handling qualities of the aircraft. Filters placed in the pilot feed forward path can potentially cause phase lags, which may increase the PIO tendency of the aircraft. Similar filters are designed for the other paths, which include

- Longitudinal cyclic stick
- Lateral cyclic stick
- Pitch rate
- Lateral acceleration

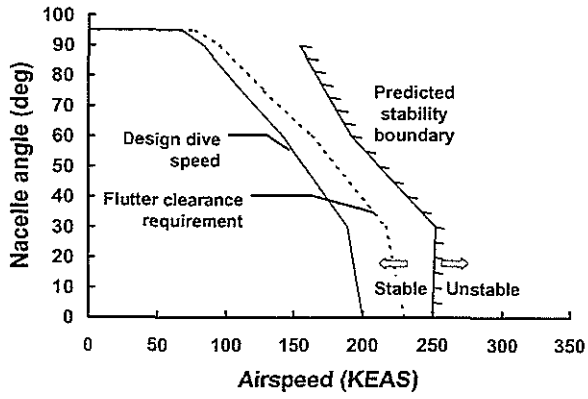

Fig. 15. BA 609 stability boundary and requirements at 569 rpm.

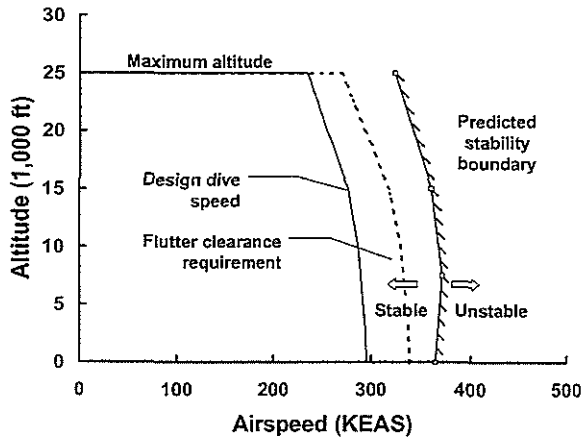

Fig. 16. BA 609 stability boundary and requirements at 478 rpm.

- Power lever
- Yaw rate
- RPM error

Once the filters are defined, the FCS paths are closed and the closed loop aeroelastic stability is evaluated with the effect of the FCS. Fig. 15 shows the helicopter/conversion mode stability predictions at sea level standard conditions and 100% rpm. Sea level standard condition was selected, since previous analysis showed this altitude to be critical. Similarly, closed-loop stability predictions in airplane mode are calculated and compared with the flutter clearance envelope. Fig. 16 shows the airplane mode stability predictions at various altitudes. Based on this analysis, the BA 609 meets all the stability requirements over the complete flight envelope.

In addition to the wing and rotor modes, the FCS can affect the symmetric drive system modes. The first symmetric drive system mode is at 6.70 Hz, which is within the bandwidth of the FCS. ASAP showed that the rpm governor degrades the stability of this mode (Fig. 17). While this mode is predicted to be stable, a filter was added to satisfy the open loop gain margin requirements. Because the filter reduces the coupling of the rpm

governor portion of the FCS, the damping with the filter is more like the basic system.

Classical ground resonance is avoided on the BA 609 by use of a stiff inplane rotor. However, the V-22 experienced a divergent oscillation on the ground caused by pilot biomechanical feedback (Ref. 11). Stability of the XV–15 has not been affected by pilot biomechanical coupling because it used mechanical control linkages instead of fly-by-wire controls. A separate stability analysis was performed on the ground to verify that the BA 609 does not have a ground oscillation like the V-22. On the ground, the airframe dynamics are represented by a rigid aircraft on flexible landing gear and tires. There are two lateral roll modes of the aircraft on its landing gear, and the second mode with a roll pivot point above the aircraft cg is a stability concern. This mode is referred to as the high-focus roll mode. The ASAP analysis has been correlated extensively with V–22 onground data to accurately predict the damping in this mode. Because this mode of the rigid aircraft on the gear and tires (1.82 Hz) is very low, it is difficult to stabilize this mode with only a notch filter without significantly degrading the aircraft handling qualities. Therefore, a lateral balance weight is used in the mechanical controls to reduce the sensitivity of the pilot lateral stick input to cockpit lateral acceleration. This allows a smaller filter to be used in the lateral stick feed forward path without degrading the handling qualities.

Fig. 18 shows the basic aircraft predicted damping for the onground, high-focus roll mode. The basic aircraft is stable as shown. With the FCS and pilot biomechanical feedback, the aircraft is unstable. The combination of a filter and balance weight stabilizes this onground mode.

13. SUMMARY AND CONCLUSIONS

Bell has developed a comprehensive methodology to evaluate aeroelastic and aeroservoelastic stability, which has been applied successfully to the V–22 and XV–15. This analysis shows that the BA 609 will satisfy all of the aeroelastic and aeroservoelastic stability requirements. Specifically for the BA 609, the following conclusions can be made:

1. Acceptable airplane mode proprotor stability speeds are met primarily because of the high torsional stiffness in the wing.
2. Ground resonance can be avoided by using a stiff-inplane rotor.
3. High-speed flap lag instability can be avoided by using negative δ_3.
4. Coupling of the flight control system with the structural modes can be reduced using notch filters without introducing unacceptable low-frequency phase delays.
5. The adverse effect of pilot biomechanical coupling on stability can be reduced by using notch filters in the FCS and a balance weight in the mechanical controls.
6. Torsional stability is maintained by appropriate filtering of the rotor rpm error feedback.

14. REFERENCES

1. K. G. Wernicke, "Tilt Proprotor Composite Aircraft, Design State of the Art," 24th Annual Forum of the American Helicopter Society, May 1968.
2. T. M. Gaffey, J. G. Yen, and R. G. Kvaternik, "Analysis and Model Tests of the Proprotor Dynamics of a Tilt-Rotor VTOL Aircraft," V/STOL Technology and Planning Conference, Las Vegas, Nevada, September 1969.
3. Raymond G. Kvaternik, "Experimental and Analytical Studies in Tilt-Rotor Aeroelasticity," AHS/NASA Ames Specialist Meeting on Rotorcraft Dynamics, February 1974.
4. Kipling Edenborough, Troy M. Gaffey, and James A. Weiberg, "Analysis and Tests Confirm Design of Proprotor Aircraft," AIAA 4th Aircraft Design, Flight Test, and Operations Meeting, Los Angeles, CA, August 1972.
5. Mark W. Nixon, "Parametric Studies for Tiltrotor Aeroelastic Stability in Highspeed Flight," 33rd Structures, Structural Dynamics, and Materials Conference, April 1992, Dallas, TX.

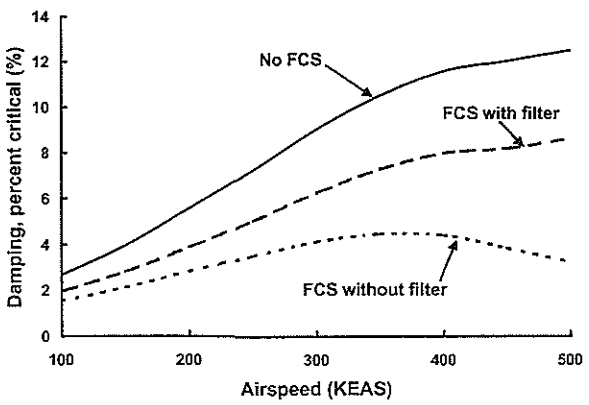

Fig. 17. First symmetric drive system mode stability.

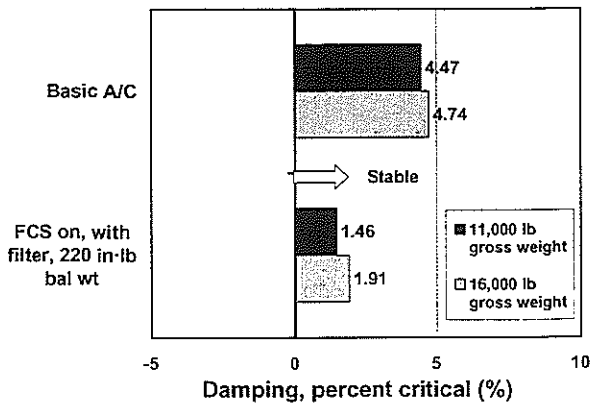

Fig. 18. Onground high-focus roll mode stability.

6. Michael J. Moore, et. al., "High Speed Tiltorotors: Dynamics Methodology," 49th Annual Forum of the American Helicopter Society, St. Louis Missouri, May 1993.
7. Lawrence M. Corso, et. al., "Design, Analysis, and Test of a Composite Tailored Tiltrotor Wing," 53rd Annual Forum of the American Helicopter Society, Virginia Beach, Virginia, April–May 1997.
8. J. M. Bilger, R. L. Marr, and Ahmad Zahedi, "Results of Structural Dynamic Testing of the SV–15 Tilt Rotor Research Aircraft," 37th Annual Forum of the American Helicopter Society, New Orleans, LA, May 1981.
9. Roman T. Lytwyn, "An Analysis of the Divergent Vertical Helicopter Oscillations Resulting from the Physical Presence of the Pilot in the Collective Control Loop," *Journal of the American Helicopter Society*, Vol. 12 (1), Jan 1967.
10. Thaddeus Kaplita, et. al., "Helicopter Simulation Development by Correlation with Frequency Sweep Flight Test Data," 45th Annual Forum of the American Helicopter Society, Boston, MA, May 1989.
11. Tom Parham, et. al., "V–22 Pilot-In-The-Loop Aeroelastic Stability Analysis," 47th Annual Forum of the American Helicopter Society, Phoeniz, AZ, May 1991.
12. Robert F. Idol and Tom Parham, "V–22 Aeroelastic Stability Analysis and Correlation with Test Data," 51st Annual Forum of the American Helicopter Society, Fort Worth, Texas, May 1995.
13. David Popelka, et. al., "Correlation of Stability test Results and Analysis for the 1/5 Scale V–22 Aeroelastic Model," 41st Annual Forum of the American Helicopter Society, Fort Worth, Texas, May 1985.
14. Wayne Johnson, *Helicopter Theory*, Princeton University Press, 1980.
15. Troy M. Gaffey, "The Effect of Positive Pitch-Flap Coupling (Negative δ_3 on Rotor Blade Motion Stability and Flapping)," 24th Annual Forum of the American Helicopter Society, May 1968.
16. R. L. Fortenbaugh, D. King, M. A. Peryea, and T. Busi, "Flight Control Features of the Bell Agusta (BA) 609: A Handling Qualities Perspective," 25th European Rotorcraft Forum, September 1999.

TWENTYFITH EUROPEAN ROTORCRAFT FORUM

Paper n° G4

ON THE IMPORTANCE AND EFFICIENCY OF 2/REV IBC FOR NOISE, VIBRATION AND PITCH LINK LOAD REDUCTION

BY

M. MÜLLER
U.T.P. ARNOLD
D. MORBITZER
ZF LUFTFAHRTTECHNIK GMBH, GERMANY

SEPTEMBER 14-16, 1999
R O M E
ITALY

ASSOCIAZIONE INDUSTRIE PER L'AEROSPAZIO, I SISTEMI E LA DIFESA
ASSOCIAZIONE ITALIANA DI AERONAUTICA ED ASTRONAUTICA

ON THE IMPORTANCE AND EFFECTIVENESS OF 2/REV IBC FOR NOISE, VIBRATION AND PITCH LINK LOAD REDUCTION

M. Müller
U.T.P. Arnold
D. Morbitzer

ZF Luftfahrttechnik GmbH, Germany

1. Abstract

This paper presents experimental and theoretical results that help to assess the importance and effectiveness of 2/rev IBC/HHC active rotor control. Wind tunnel and flight test results will be shown which clearly indicate the positive impact of the second rotor harmonic frequency for vibration reduction. Simple models will be used to explain two physical mechanisms of inter-harmonic coupling that are believed to be predominant in causing the 2/rev effects discussed in this paper. Beside the usefulness in reducing vibrations, 2/rev has also proven to be essential to reduce BVI noise and pitch link loads. Selected experimental results are presented to show the effectiveness with respect to these optimization goals.

2. Notation

A_n	deg	IBC/HHC control amplitude of n/rev harmonic component
a/R		relative (equivalent) hinge offset
$C_{(...)} = (...) / (\pi\rho R^4 \Omega^2 [R])$		thrust, moment coefficient
$I_\beta = \int r^2 dm$	kgm^2	blade flap momentum of inertia
M_x, M_y	Nm	rotor roll, pitch moments
N		number of blades
n		order of harmonic component
R	m	rotor radius
$\underline{S}$		IBC to vibration response transfer matrix (non-linear, steady-state)
$S_\beta = \int r dm$	kgm	blade static flap mass Momentum
T	N	rotor thrust
$\underline{T}$	N[m]/ rad	IBC to vibration response transfer matrix (linear, steady-state)
$\underline{u}$	rad	vector of higher harmonic control inputs (sin, cos compon.)
Z_s	N	blade root vertical shear force
$\underline{z}$	N[m]	vector of vibration components (sine, cosine components.)
β	deg, rad	flap angle
$\gamma = (\rho C_{l\alpha} c R^4) / I_\beta$		LOCK number
$\delta = (w_{Ro} - w_i) / (\Omega R)$	- , rad	inflow ratio/angle
$\underline{\vartheta}_{HHC}$	rad	vector of higher harmonic control inputs (sin, cos compon.)
ϑ_{twist}	rad	built-in blade twist
ϑ_{root}	deg, rad	blade pitch angle at blade root
$\mu = u_{Ro} / (\Omega R)$		advance ratio
ρ	kg/m^3	air density
$\sigma = cN / (\pi R)$		blade solidity
φ_n	deg	IBC/HHC control phase angle of n/rev harmonic component
ψ	deg	rotor azimuth angle (=non-dimensional time)
Ω	rad/s	rotor rotational speed
$(...)' = d(...) / d\psi$		first derivative with respect to rotor azimuth

3. Introduction

Active Rotor Control by blade root actuation has proven highly valuable and successful in reducing several negative effects associated with helicopter rotors operating in tangential flow. At high forward speed various problems arise due to the asymmetric flow condition, high MACH numbers, the large wake skew angle and the requirement to satisfy momentum trim. Figure 1 gives an symbolic overview of the more important ones of these effects.

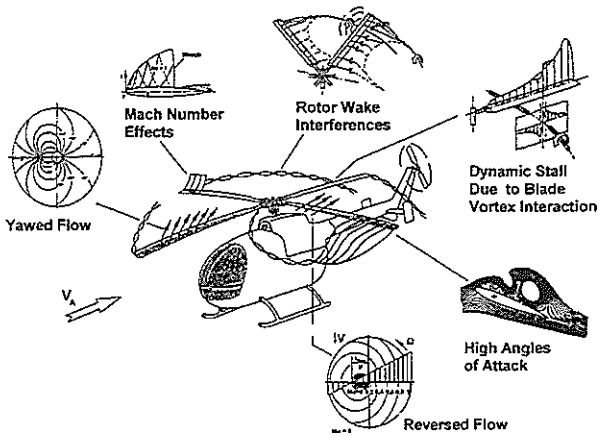

Figure 1: Negative Effects Associated with Helicopter Rotors in Tangential Flow

Two technical approaches of higher harmonic blade root pitch control have been developed and tested in the past, both competing with respect to the required effort and the gained benefit.

Company	ZFL			DLR	McDonnell Douglas	Sikorsky	Aerospatiale	Boeing Vertol	
Campaign	Flight Test	Wind Tunnel Test (NASA Ames)	Flight Test	Wind Tunnel Test (DNW)	Flight Test	Flight Test	Flight Test	Wind Tunnel Test	
Test Bed	BO105	1:1 BO105 Rotor	BO105	40% BO105 Model Rotor	OH-6A	S-76	SA-349	Model 179	1:6 CH-47D Model Rotor
Year	1990/91	1993/94	1998	1990	1982	1985	1985	1981	1985
Control Concept	IBC OL	IBC OL	IBC OL	HHC OL	HHC OL/CL	HHC OL	HHC OL/CL	HHC OL/CL	HHC CL
Control Parameter	3Ω 4Ω 5Ω +/- 0.16° +/- 0.40°	2Ω 3Ω 4Ω 5Ω 6Ω Max. +/- 2°	2Ω 3Ω 4Ω 5Ω 6Ω +/- 1.1°	3Ω 4Ω 5Ω +/- 0.8 +/- 1.2	3Ω 4Ω 5Ω +/- 2.00° +/- 0.33°	3Ω 4Ω 5Ω +/- 1°	2Ω 3Ω 4Ω +/- 1.0° +/- 0.8°	3Ω 4Ω 5Ω +/- 1.3°	2Ω 3Ω 4Ω +/- 3°
Advance Ratio μ	0.15 0.26	0.10 0.15 0.30 0.40 0.45	0.10 0.15	0.10 0.15 0.20 0.35	0.10 : 0.24	0.07 : 0.25	0.12 0.31	0.10 0.30	0.4
Noise Reduction	✓	max. 8dB	max. 6dB	max. 6dB			max. 6dB		
Vibration Reduction	50%-80%	max. 85%	50%-80%	30%	60%-70%	40%-60%	80%	90%	✓
Performance Improvement		max. 7%			NO	NO	✓	1,7% - 4%	✓
Load Reduction		✓							
Structural Blade Load	↗	↗ ↘			↗			↗	
Pitch Link Load		↗			↗			↗	
Critical Loads		NO			NO			NO	NO
References				[2], [3]	[4], [5]	[6]	[7]	[8], [9]	[10]

Figure 2: *Overview of Experimental Research Activities and their Results in the Field of HHC (Higher Harmonic Control) and IBC(Individual Blade Control)*

One system, commonly called HHC (Higer Harmonic Control), enables higher frequency motions of the swashplate to produce additional harmonic blade pitch variations. As result of the kinematic properties these systems are restricted to particular multiples of the rotor frequency, namely kN-1, kN and kN+1 for k=1,2,3...

The other system, denoted as IBC (Individual Blade Control), allows to control each blade individually without any restriction of the applied frequencies. Beside the deviations in the technical lay-out, the main difference is the possibility of the IBC-type systems to introduce 2/rev control in modern rotors having more than three blades. Figure 2 gives an overview over various experimental activities that were focused on the application of HHC or IBC. Since the majority of the test campaigns had to cope with the restrictions of HHC the question, how useful 2/rev control might be, did not actually arise. For details of IBC systems as designed and used by ZFL for several wind tunnel and flight test campaigns see Refs. [13], [16], [17] and [18].

Nevertheless, the value of 2/rev at least for reducing rotor power required is widely accepted. This particular application seems to have triggered the general interest in HHC as can be derived from early publications like Ref. [19]. The necessity of 2/rev for vibration reduction, however, is frequently questioned. The obvious properties of the transformation between rotating and the non-rotating frame are believed to imply that 2/rev has to be much less effective than (N-1)/rev, N/rev and (N+1)/rev inputs. As a matter of fact, even such sophisticated programs as CAMRAD clearly underpredict the 2/rev effect compared to wind tunnel and flight test results. By using the experimental IBC systems designed, manufactured and operated by ZFL it was possible for the first time to extensively investigate those 2/rev effects.

In the following sections the focus is solely put on the 2/rev results. For comparison with the proven effects of the HHC frequencies and for a comprehensive description of the test results gained with ZFL's IBC systems see Refs. [12], [13] and [15].

4. Noise Reduction through 2/rev IBC

One main application of higher harmonic blade pitch control is to reduce the BVI noise radiation. Therefore, ZFL, having participated in several national and international research programs, has conducted intensive experimental investigations of noise reduction through IBC. The 1993/94 full-scale wind tunnel tests at the NASA Ames research center led to promising results in this field, Ref. [18]. The RACT flight tests carried out last year were used to validate these impressive results. For noise measurements in the wind tunnel, the rotor operation condition was adjusted to a high BVI condition as usually encountered during landing approach. Therefore, the same flight conditions were investigated during the RACT flight tests. The ground based measurement hardware consisted of 3 microphones, one on

the advancing, one on the retreating side and the third one on the center line of the flight path, all of them located according to the ICAO regulations.

Figure 3 shows the maximum A-weighted sound pressure level L_{Amax} versus the single-harmonic 2/rev blade pitch control phase angle φ_2. Maximum noise reduction of more than 5dB was achieved at $\varphi_2 \approx 60$deg near the optimum phase angle expected according to the wind tunnel results, Ref. [12]. Given this considerable effect of 2/rev control on rotor noise it is of great interest what effect the same control inputs exhibit on the vibrations in the non-rotating frame. Former HHC results, Ref. [23], for the same type of rotor had shown that noise and vibration reduction could never be achieved simultaneously when using the HHC frequencies 3/rev, 4/rev and 5/rev. For details on the comparison between wind tunnel and flight test results see Ref. [12].

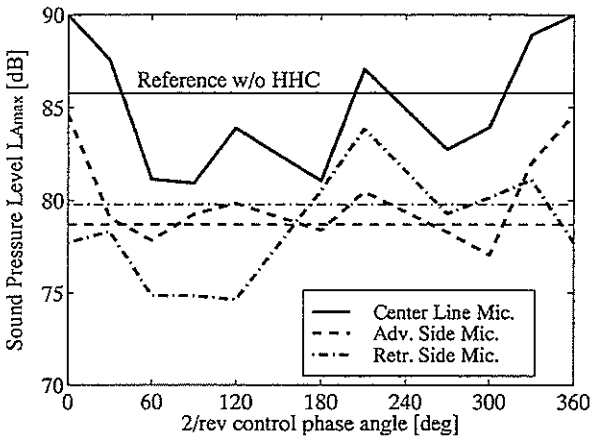

Figure 3: Rotor Sound Pressure Levels vs. IBC Phase Angle for Single-Harmonic 2/rev Control, A_2 = 1deg (RACT flight test results, BO-105S1, μ = 0.15, γ = -6deg)

5. Vibration Reduction through 2/rev IBC

The rotor induced vibrations of a helicopter originate from the unsteady aerodynamic forces acting on the rotor blades. They are caused by phenomena which can in many cases be associated with fixed rotor azimuth positions (see Figure 1). The resulting aerodynamic loads are of periodical type with the corresponding frequency spectra mainly consisting of so-called rotor harmonics $n\Omega$. They excite the rotor blades to oscillations in both flapwise and lead-lag direction. These blade motions combined with inertial and elastic forces finally determine the blade root loads. To obtain the resulting vibrations in the fixed frame the forces and moments of all blades have to be added and transformed into the non-rotating system. Due to this transformation several harmonics cancel each other and the resulting vibrations in the fixed frame only consist of frequencies which are integral multiples of the blade passage frequency $kN\Omega$ with k = 1,2,3... Out of these harmonic components, the lowest one is not only associated with highest amplitude but furthermore represents the most straining one for the passengers.

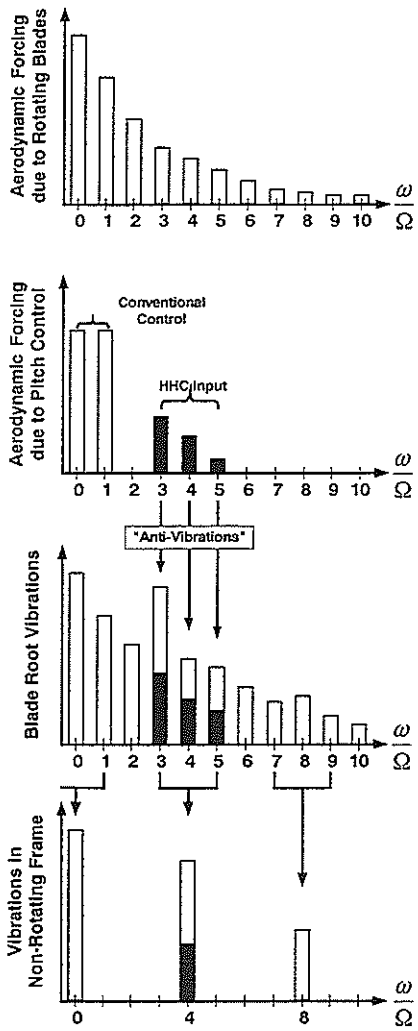

Figure 4: Transformation of Vibratory Loads from the Rotating into the Non-Rotating Frame and Application of HHC to Reduce Vibrations (4-Bladed Rotor)

It is caused by blade load components of the frequencies (N-1)/rev, N/rev and (N+1)/rev in the rotating frame, see Ref. [26]. These harmonics can be affected by controlled blade pitch changes of the same frequencies. With properly adjusted amplitudes and phases the blade oscillations can be controlled in a way that leads to a reduction of the resulting hub loads and subsequently to the desired minimization of the fuselage vibrations, see Figure 4.

Because of this correlation between blade loads in the rotating frame, vibrations in the non-rotating frame and the corresponding higher harmonic blade pitch control inputs, mostly (N-1)/rev, N/rev and (N+1)/rev control as can be provided by HHC systems has been considered for vibration reduction. Consequently, 2/rev control was not believed to be of great relevance for rotors with more than four blades, since blade pitch inputs with this frequency do not have the same direct feedthrough to vibrations in the fixed frame.

5.1 Experimental Results

Although the validation of the wind tunnel test results with respect to noise reduction was the main purpose of

the RACT flight tests, accelerations in the fuselage were measured and recorded, too. The highly sophisticated data acquisition system installed in the BO-105S1 (Ref. [13]) provided acceleration signals in three axis at the top of the main gear box, at the co-pilot seat and in the payload compartment. These vibration data have facilitated the extensive evaluation of the effect of 2/rev control on vibrations, compare Refs. [12] and [13].

5.1.1 Mathematical Description of IBC Transfer Behavior and Effectiveness Measure

Earlier evaluations of the helicopter vibrations had used measured 4/rev hub vibrations in the non-rotating frame, which were then analyzed in the sine/cosine plane. This method leads to the well-known ellipses that describe the linear, quasi-steady transfer behavior between the IBC inputs and the resulting vibrations. The model relates the cosine and sine components of the higher harmonic pitch control angles arranged in the vector $\underline{\vartheta}$ to the cosine and sine components of the 4/rev vibrations in the fuselage arranged in the vector $\underline{z}$ and can be written as the following linear transformation.

$$\underline{z} = \underline{\underline{T}}\,\underline{\vartheta}_{HHC} + \underline{z}_0$$

Such a model seemed to be appropriate for linear time-periodic systems. The shape and size of the ellipse depends on the $\underline{\underline{T}}$-matrix elements, see Ref. [12] for details. This linear mapping of the input $\underline{\vartheta}_{HHC}$ to the output $\underline{z}$ is well suited to describe the transfer behavior between 3/rev, 4/rev, and 5/rev inputs and the 4/rev vibratory response. For 2/rev inputs, however, this linear mapping does not provide an accurate representation of the transfer behavior to the measured 4/rev fuselage vibrations. Therefore the linear formulation has been extended by a quadratic term to

$$\underline{z} = \underline{\underline{T}}\,\underline{u} + diag(\underline{u})\,\underline{\underline{S}}\,\underline{u} + \underline{z}_0 ,$$

where the cosine and sine components of the 2/rev input now form the vector $\underline{u}$. It can be shown that this non-linear transformation represents the system behavior much better and provides an astonishing well suited means of interpolation for the measured data. The determination of the two transfer matrices is based on the least-mean square method. For a given number of measurements it yields the following set of equations.

$$\underbrace{\begin{bmatrix} \Sigma u_{1i}^2 & \Sigma u_{1i}u_{2i} & \Sigma u_{1i}^3 & \Sigma u_{1i}^2u_{2i} & \Sigma u_{1i} \\ \Sigma u_{1i}u_{2i} & \Sigma u_{2i}^2 & \Sigma u_{1i}^2u_{2i} & \Sigma u_{1i}u_{2i}^2 & \Sigma u_{2i} \\ \Sigma u_{1i}^3 & \Sigma u_{1i}^2u_{2i} & \Sigma u_{1i}^4 & \Sigma u_{1i}^3u_{2i} & \Sigma u_{1i}^2 \\ \Sigma u_{1i}^2u_{2i} & \Sigma u_{1i}u_{2i}^2 & \Sigma u_{1i}^3u_{2i} & \Sigma u_{1i}^2u_{2i}^2 & \Sigma u_{1i}u_{2i} \\ \Sigma u_{1i} & \Sigma u_{2i} & \Sigma u_{1i}^2 & \Sigma u_{1i}u_{2i} & \Sigma i \end{bmatrix}}_{\underline{\underline{A}}} \cdot \underbrace{\begin{bmatrix} s_{11} \\ s_{12} \\ t_{11} \\ t_{12} \\ z_{01} \end{bmatrix}}_{\underline{t}_1} = \underbrace{\begin{bmatrix} \Sigma z_{1i}u_{1i} \\ \Sigma z_{1i}u_{2i} \\ \Sigma z_{1i}u_{1i}^2 \\ \Sigma z_{1i}u_{1i}u_{2i} \\ \Sigma z_{1i} \end{bmatrix}}_{\underline{y}}$$

This can be solved by extending the input vector as follows.

$$\underline{u}_i^{\cdot} = \begin{bmatrix} u_{1i} & u_{2i} & u_{1i}^2 & u_{1i}u_{2i} & 1 \end{bmatrix}^T$$

With $\underline{\underline{A}} = \left(\underline{\underline{U}}^*\right)^T \underline{\underline{U}}^*$ and $\underline{y} = \left(\underline{\underline{U}}^*\right)^T \underline{z}^*$ the first column $\underline{t}_1$ of the non-linear mapping is given by

$$\underline{t}_1 = [s_{11} \quad s_{12} \quad t_{11} \quad t_{12} \quad z_{01}]^T = \left(\left(\underline{\underline{U}}^*\right)^T \underline{\underline{U}}^*\right)^{-1} \left(\underline{\underline{U}}^*\right)^T \underline{z}^* .$$

In the same manner the second column of the transfer matrix can be computed, where the related second input vector is now described by

$$\underline{u}_i^{\cdot} = [u_{1i} \quad u_{2i} \quad u_{1i}u_{2i} \quad u_{2i}^2 \quad 1]^T .$$

For quantitatively assessing the effect of different IBC frequencies on the vibrations a simple numerical measure was defined. The effectiveness for linear transfer behavior is given in [12] and is defined as the ratio of resultant vibration level to HHC input amplitudes. The mean vibratory response magnitude can be approximated by the radius E of a circle having the same area as the actual ellipse described by the T-matrix components. For the non-linear transformation which is applied to the transfer behavior between 2/rev control and 4/rev vibrations this method is no longer applicable, because this mapping does not have a finite area. Therefore, the effectiveness is now defined as the distance of the measurements in the sine/cosine-plane from the reference data point for unity excitations of 1deg. For k measurements the over-all HHC effectiveness is defined by

$$E = \frac{1}{k}\sum_{i=1}^{k} \left|\underline{Z}_i - \underline{Z}_0\right| .$$

One should note that this equation coincides with the former definition when applied to a linear system that shows a perfect circle in the cosine/sine-plane. All wind tunnel and flight test data presented in the following sections have been analyzed with this non-linear transformation method.

5.1.2 Flight Tests

The measured accelerations at the co-pilot seat are shown in Figure 5. The magnitude of the 4/rev accelerations versus the 2/rev IBC phase angle as well as the components in the cosine/sine-plane are plotted. In addition, the figure presents the interpolation that results from the non-linear mapping. As can be seen, the 2/rev input is able to reduce the vibrations by more than 60%. The identified transformation matches the measured data very well, which proves the suitability of the non-linear formulation.

In contrast to former HHC results, where noise and vibration reduction were never achieved simultaneously, Ref. [23], the evaluation of the 2/rev control data shows decreased vibration and noise levels for almost the same phase angle (Figure 3). The previously mentioned idea of vibration reduction by superposing "anti"-vibrations intentionally generated through HHC of the same frequency does not cover this effect of simultaneous noise and vibration reduction through 2/rev control. Consequently, the influence of 2/rev has to be based on another mechanism.

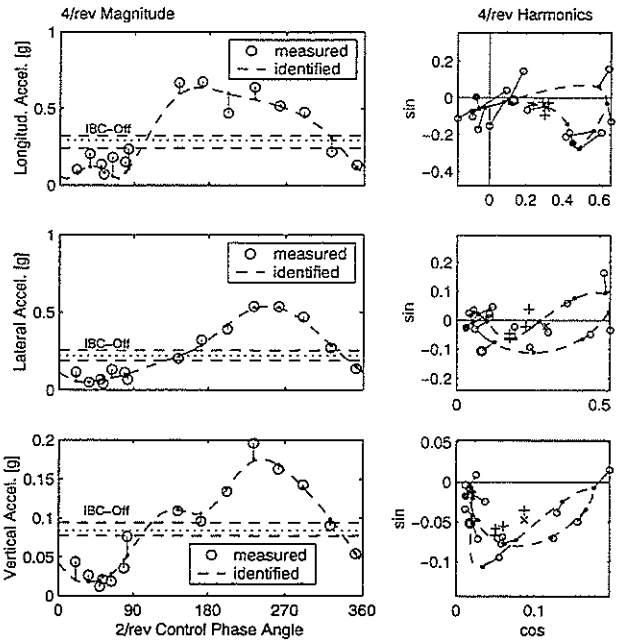

Figure 5: Accelerations at Co-Pilot Seat vs. IBC Phase Angle for Single Harmonic 2/rev Control, A_2 = 1deg (RACT Flight Test Results, BO-105S1, μ = 0.15, γ = -6deg)

5.1.3 Wind Tunnel Tests

The vibration results of the wind tunnel tests are presented in Figure 6 and Figure 7. The magnitudes of the 4/rev hub loads versus the IBC phase angle and the corresponding components in the cosine/sine-plane are plotted for two flight conditions.

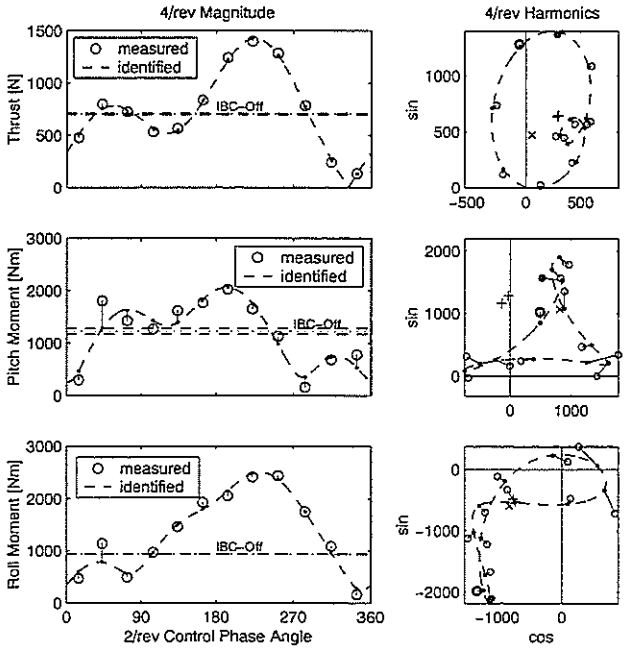

Figure 6: 4/rev Thrust, Roll and Pitch Moment at Rotor Hub (Non-Rotating Frame) vs. IBC Phase Angle for Single-Harmonic 2/rev Control, A_2 = 1deg (Wind Tunnel Data, Full-Scale BO-105 Rotor, μ = 0.15, α_{Ro} = 2,9deg)

Again, the figures contain the interpolation results from the identified transfer matrices and confirm the suitability of the non-linear mapping. Similar to the flight tests, 2/rev control has an considerable effect on the vibrations. Figure 7, however, also shows that applying a single control frequency alone does not provide the means to reduce vibrations in more than one axis simultaneously. In the example presented here, the amplitude was correctly set for optimum suppression of thrust vibrations, but was too small with respect to pitch and too large with respect to roll moments.

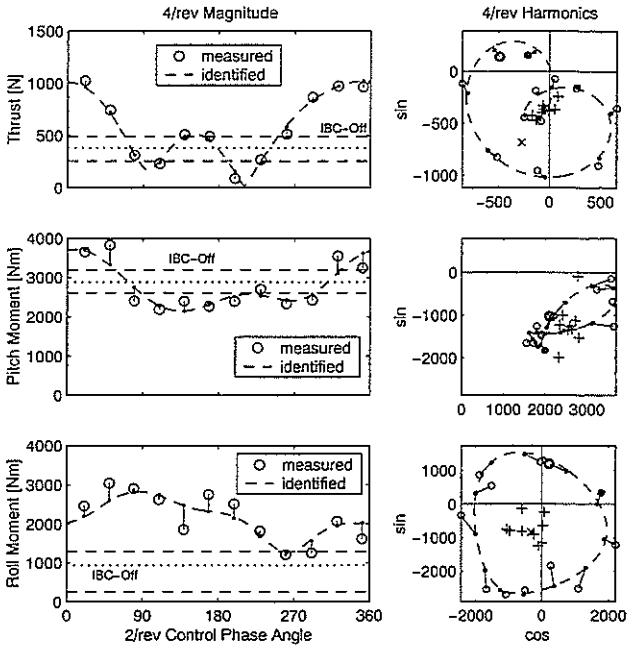

Figure 7: 4/rev Thrust, Roll and Pitch Moment at Rotor Hub (Non-Rotating Frame) vs. IBC Phase Angle for Single-Harmonic 2/rev Control, A_2 = 1deg (Wind Tunnel Data, Full-Scale BO-105 Rotor, μ = 0.4, α_{Ro} = -9deg)

5.1.4 Effectiveness Identified from Wind Tunnel Test Data

Figure 8 summarizes the wind tunnel evaluation concerning the IBC effect on vibratory loads. For all tested higher harmonic inputs Figure 8 presents the resulting effectiveness on thrust, pitch and roll moments based on 1deg higher harmonic blade pitch inputs. Although the effectiveness of 2/rev turns out to be smaller than it is for the other frequencies, 2/rev is still a valuable frequency. One has to keep in mind that (servo-) hydraulic IBC systems as they were used for the presented experiments are limited to a certain maximum travel velocity. This limit yields a hyperbolic characteristic of available control amplitudes over the control frequency, where 2/rev allows by far the highest amplitudes. As a matter of fact, the available 4/rev amplitude only reaches approximately 50% of the corresponding 2/rev authority. Thus, the lower effectiveness of 2/rev is compensated by the availability of higher amplitudes at this frequency.

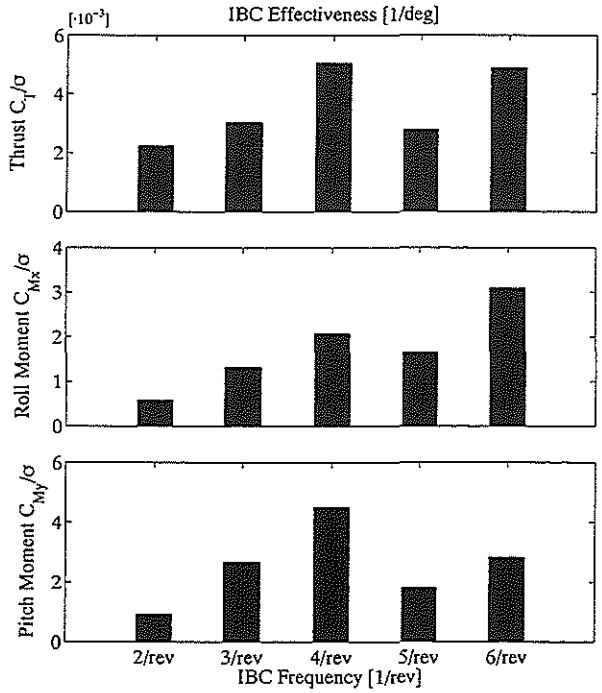

Figure 8: IBC Effectiveness on Thrust C_T/σ, Roll C_{Mx}/σ and Pitch Moment C_{My}/σ Coefficients Derived from BO-105 Rotor Wind Tunnel Data

5.2 Theoretical Explanations

As can be seen from Figure 4 there is no direct path between the 2/rev aerodynamic effects in the rotating frame to the resultant vibrations in the non-rotating frame. As we know, only (N-1)/rev, N/rev and (N+1)/rev blade forces contribute to the N/rev vibrations in the fuselage, whereas the remaining components cancel each other due to the rotor symmetry. This property holds as long as all blades are perfectly identical. Otherwise, residual vibrations of frequencies other than N/rev will additionally occur in the non-rotating frame. However, practical experience shows that for fairly well balanced and tracked blades these vibrations are of much smaller amplitude than those with blade-harmonic frequencies. Therefore, for the following discussions all blades are assumed to be identical. Moreover, all examples refer to a four-bladed rotor as obviously do all BO-105 test results.

The question left to be answered is, which mechanisms of inter-harmonic coupling exist in the rotating frame that link 2/rev IBC inputs to frequencies that finally make their way down to the fuselage.

5.2.1 Simplified Rotor Model

To answer the above question, a very simple rotor model was used for some theoretical investigations. The model only represents the first rigid flapping mode for each blade. Lead-lag motion as well as elastic bending modes of higher order are neglected. For small variations about a given rotor operating condition the following periodically time-variant linear differential equation was derived, which describes the flapping motion of an isolated blade.

$$\beta'' + \gamma D(\psi)\beta' + \left[\gamma K(\psi) + K_0\right]\beta = \gamma\left[E_1(\psi)\vartheta_1 + E_2(\psi)\vartheta_{root} + E_3(\psi)\delta\right]$$

The coefficients D, K and E which depend on the blade properties and the advance ratio can be found in Ref. [14]. In order to relate the flapping motion to those vibratory blade loads which finally propagate to the non-rotating frame, the vertical blade root shear force Z_s was considered a representative parameter. This blade root shear force directly depends on the state variables of the flapping equation and is given by

$$\frac{Z_s}{\Omega^2 S_\beta} = \beta'' + \gamma G(\psi)\beta' + \gamma H(\psi)\beta - \gamma\left[Q_1(\psi)\vartheta_1 + Q_2(\psi)\vartheta_{root} + Q_3(\psi)\delta\right]$$

5.2.2 Interharmonic Coupling of Periodic (Parameter Excited) Systems

It is well known that differential equations with periodic coefficients, even when linear from their structure, show certain behavioral similarities to nonlinear systems. The properties considered here concern the forced solution.

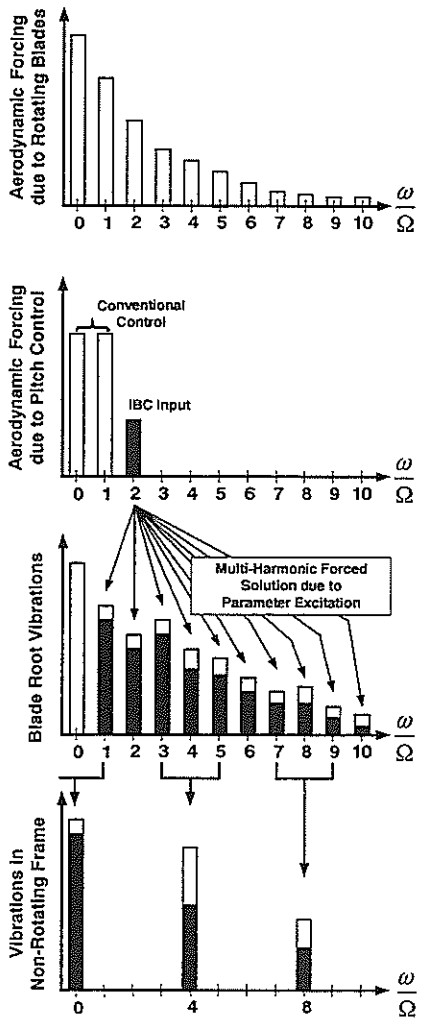

Figure 9: Application of 2/rev IBC to Reduce Vibrations, Effect of Inter-Harmonic Coupling due to Parameter Excitation (4-Bladed Rotor)

While linear time-invariant systems respond to any excitation only with the forcing frequency, the forced solution of periodic systems may contain other frequencies as well. In case of the flapping equation, where the forcing frequencies correspond to integer multiples of the basic period (i.e. the rotor frequency), the forced solution is composed of all integer multiples of the rotor frequency. Thus, even a single-harmonic 2/rev forcing function will produce a multi-harmonic system response containing all components 0/rev, 1/rev, 2/rev, 3/rev,... A more detailed description of the behavior of periodic systems can be found in Refs. [21] or [22].

In addition, any periodical input variable combined with the periodical character of the right hand side coefficients, which are given below for the approximation $a/R = 0$, leads to products of sine and cosine terms in the forcing function.

$$G(\psi) = \frac{1}{9} + \frac{1}{6}\mu\sin(\psi)$$

$$H(\psi) = \frac{1}{6}\mu\sin(\psi) + \frac{1}{3}\mu^2\cos(\psi)\sin(\psi)$$

$$Q_1(\psi) = \frac{1}{12} + \frac{2}{9}\mu\sin(\psi) + \frac{1}{6}\mu^2\sin^2(\psi)$$

$$Q_2(\psi) = \frac{1}{9} + \frac{1}{3}\mu\sin(\psi) + \frac{1}{3}\mu^2\sin^2(\psi)$$

$$Q_3(\psi) = \frac{1}{6} + \frac{1}{3}\mu\sin(\psi)$$

This in turn yields a multi-harmonic excitation even for single-harmonic control inputs through the usual effect of frequency splitting by $\pm\Omega$. Figure 9 summarizes the consequence of these mechanisms for the application of 2/rev IBC to reduce vibrations.

To give an impression of the quantitative relations, some simulations have been evaluated with respect to the spectra of β and Z_s provoked by 1/rev and 2/rev control inputs. The results are shown in Figure 10 and based on the two different configurations defined in Table 1. The cases A and B refer to an idealized rotor at $\mu = 0.5$ with all right hand side input parameters except the single harmonic pitch input set to zero. Both 1/rev and 2/rev inputs provoke response frequencies other than the exciting ones. The cases C and D reflect a more realistic condition at $\mu = 0.35$, where the rotor is loaded and the conventional 1/rev control is used to suppress the 1/rev flapping motion. Again, frequencies such as 3/rev and 4/rev are clearly affected by the 2/rev input. It is hardly necessary to mention that the described inter-harmonic coupling diminishes if the forward speed is reduced to smaller values. At $\mu = 0.1$ the effect has vanished almost completely.

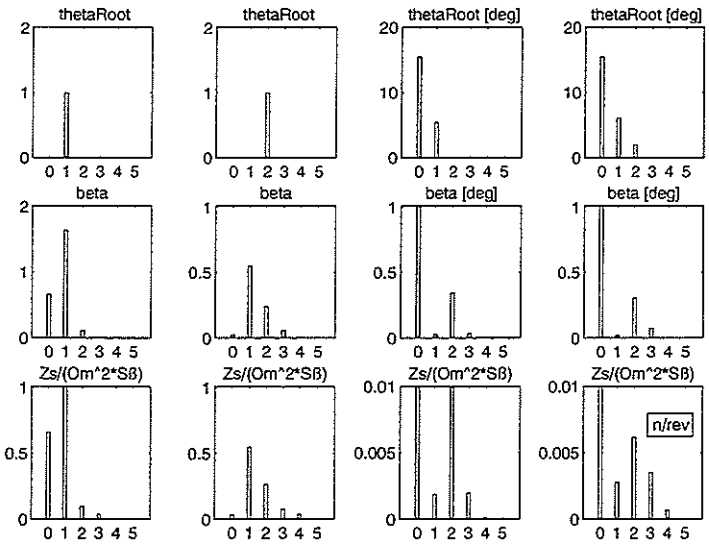

Figure 10: Multi-Harmonic Response (β and Z_s) to Single-Harmonic Forcing Function (A_0, A_1 and A_2) in Presence of Parameter Excitation (for Details See Table 1)

Case	A	B	C	D
Fig. 10	far left	mid left	mid right	far right
A_1	1rad	0	5.4deg	6.1deg
A_2	0	1rad	0	2.0deg
μ	0.5		0.35	
δ	0		-0.065	
ϑ_{Twist}	0		-8deg	
$\vartheta_{0\ root}$	0		15.5deg	
Blade Model	idealized unloaded rotor		≈ BO-105 level flight (re-trimmed for zero 1/rev flapping)	
γ	8			
a/R	0			

Table 1: Parameters Used for the Simulations Presented in Figure 10

5.2.3 Multi-Harmonic Blade Response due to Impulsive Forcing

Another attempt to describe the mechanism of inter-harmonic coupling relies on the idea of impulsive excitation. This description implies that a linear system which is excited through an impulsive but periodic input responds in multi-harmonic frequencies. Applied to the rotor this means that the blades excited by an impulsive disturbance respond with multi-harmonic oscillations. They in turn lead to the undesired vibrations in the non-rotating frame. If 2/rev control was able to affect the disturbance in some way, this input would subsequently have an indirect feed-through onto the vibratory loads in the non-rotating frame (Figure 11).

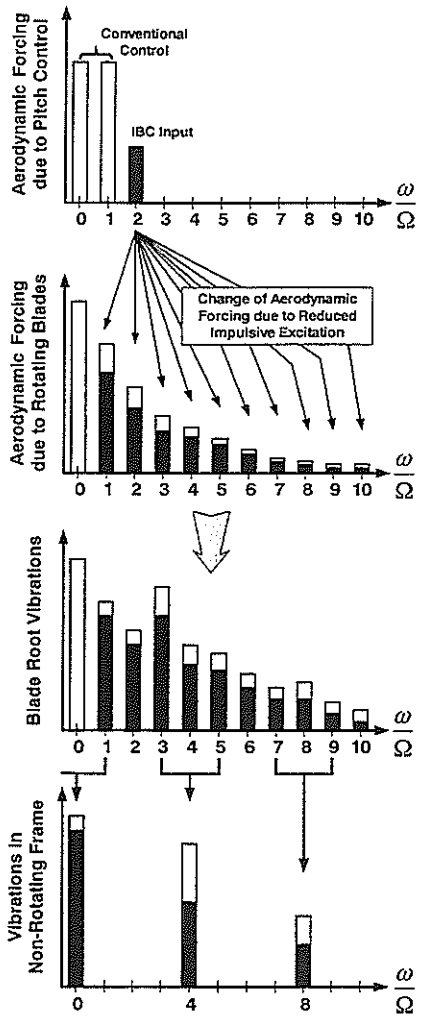

Figure 11: Application of 2/rev IBC to Reduce Vibrations, Effect of Avoiding Inpulsive Excitations in Order to Reduce Multi-Harmonic Forcing

Modeling the Rotor Blade Response to Impulsive Excitation

To investigate the above mentioned mechanism the simple rotor model of chapter 5.2.1 was used again. In contrast to the theoretical investigations there, now only hover i.e. $\mu = 0$ needed to be considered.

This yields to constant coefficients in the above ODE. Now, all four blades were actually modeled and simulated in parallel. The vibrations in the non-rotating frame were then calculated by applying the following summations and transformations to the individual blade components

$$T = -\sum_{i=1}^{N} Z_i \ , \ M_x = a\sum_{i=1}^{N} Z_i \sin\psi_i \ , \ M_y = a\sum_{i=1}^{N} Z_i \cos\psi_i \ .$$

The block diagram of Figure 13 gives an overview of the complete model used to investigate the effect of impulsive disturbances. The two input variables relevant for the following discussion are blade pitch and inflow angle. Their impact on the vertical blade root shear force is shown in the BODE plots of Figure 12.

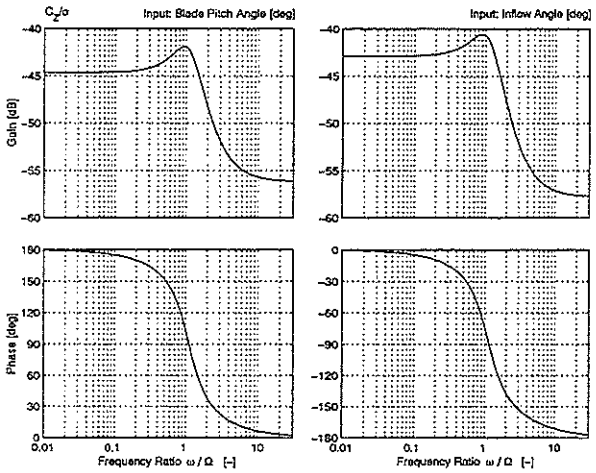

Figure 12: BODE Plot of Vertical Blade Root Shear Force due to Blade Pitch Input (Left) and Inflow Angle (Right)

The non-constant portion of the inflow was assumed to consist of discrete impulsive peaks of initially constant magnitude. In the presented example, two unequally spaced peaks were positioned over one rotor revolution. Figure 14 shows how in the reference case blade flapping responds to the impulsive inflow disturbances.

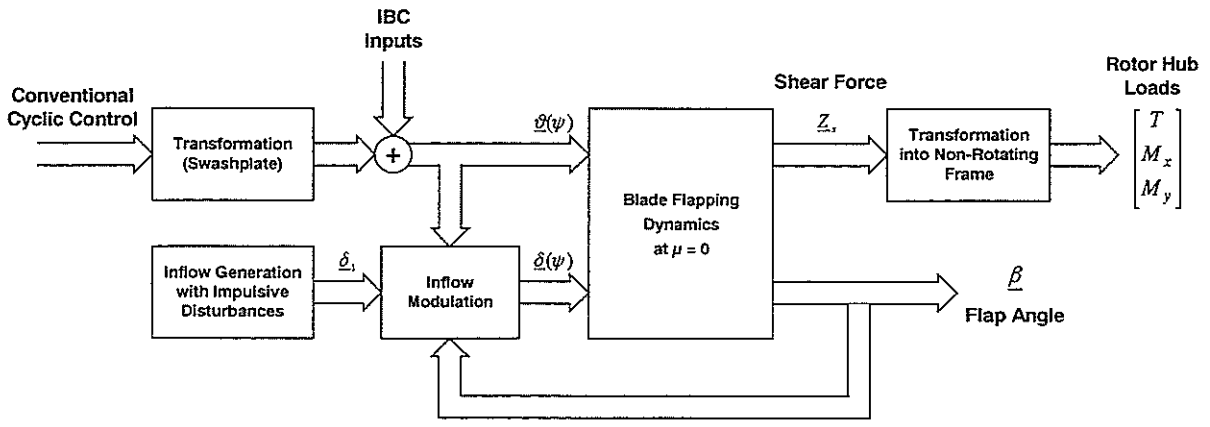

Figure 13: Block Diagram of Simulation Model Set Up to Investigate the Effect of Impulsive Inflow disturbances on Vibration Reduction Mechanism

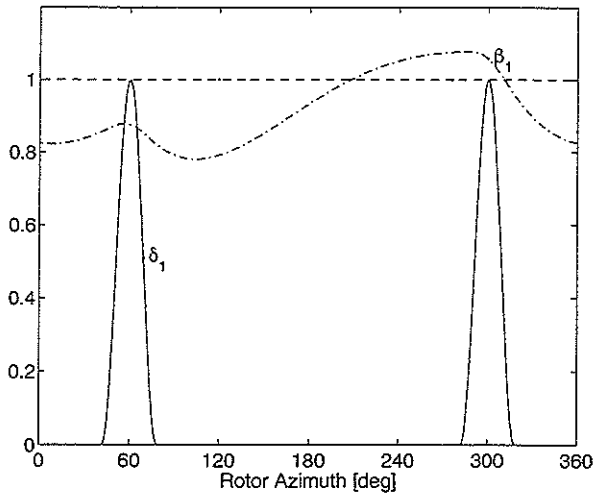

Figure 14: Assumed Inflow Peak Time History and Resulting Flap Angle Response (Reference Case without Inflow Modulation)

This type of impulsive but periodic excitation obviously causes a blade response that contains all frequencies $n\Omega$, which in turn produces the undesired vibrations in the fuselage as discussed before, compare Figure 15. The harmonic contents of the blade response gets richer, when the pulses are shortened in relation to the rotor revolution.

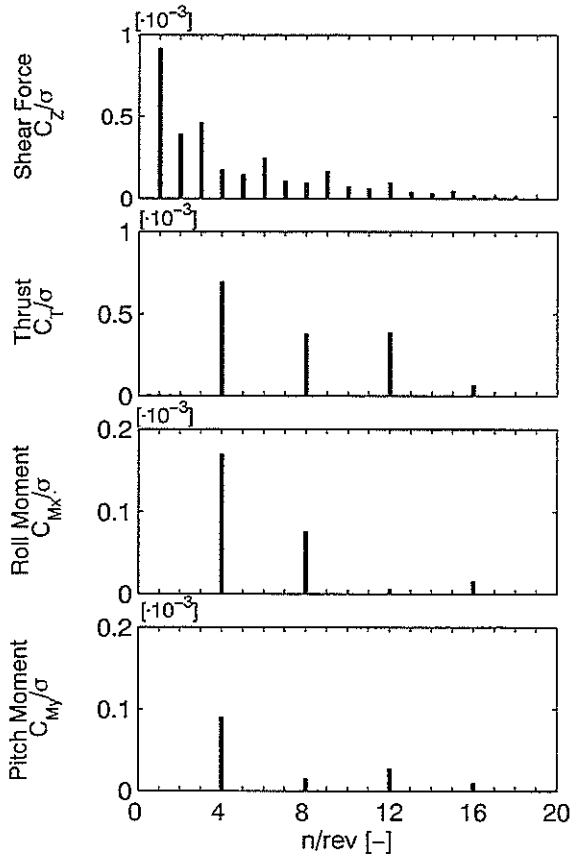

Figure 15: Spectra of Vertical Blade Root Shear Force (Top) and Thrust, Roll, Pitch Moment in the Non-Rotating Frame due to Impulsive Inflow Disturbances (Upper-Mid to Bottom)

One may think of these disturbances as being caused in some sophisticated manner by blade vortices or blade tailboom interference. It has to be stressed that the model was intended to capture only the basic effect and is of course not capable to provide any meaningful prediction.

The simple key idea is now that IBC and not least its 2/rev component directly or indirectly can influence the inflow disturbance strength. This is represented by the block "Inflow Modulation" in Figure 13. Since it was intended to show the principle mechanism only, a simple multiplication was chosen for this block. By no means it was attempted to model any realistic physical mechanism as for example the modulation of the blade vortex strength or the changing of the blade/vortex miss distance through blade pitch control.

Simulation Results

To demonstrate the 2/rev effect of IBC, two cases were investigated. First, the inflow peak intensity at a fixed rotor azimuth angle was assumed to be a direct function of the local blade pitch angle and second a function of the local flap angle. By properly tuning the 2/rev control phase angle, the inflow peaks could be attenuated and as a consequence the vibrations in the non-rotating frame. Figure 16 shows simulation results for various 2/rev control phase angles using the inflow modulation by ϑ. The ellipsoid graphs clearly show the expected influence of 2/rev control. This second explanation of the 2/rev influence seems to be an ideal complement to the first one, because it does not require those high advance ratios to become effective.

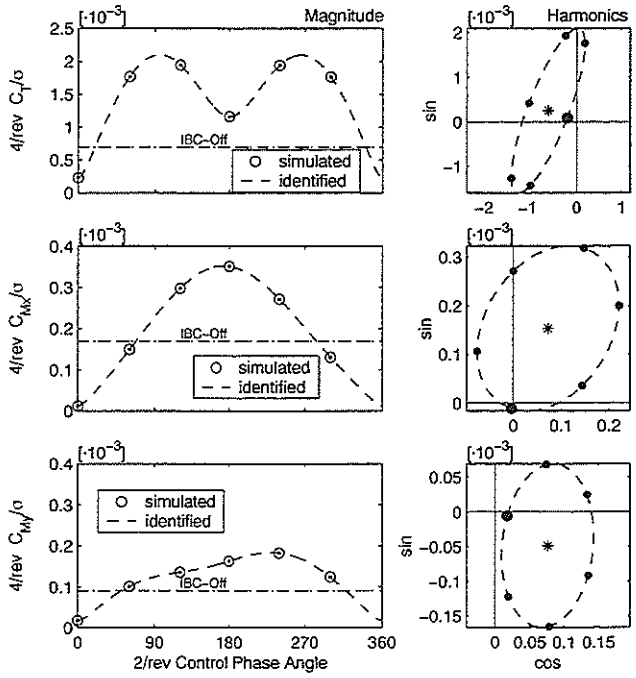

Figure 16: 4/rev Hub Loads in the Non-Rotating System vs. IBC Phase Angle for Single-Harmonic 2/rev control, A_2 = 2deg (δ Modulated by ϑ)

6. Effect of IBC on Pitch Link Loads

Beside the diminishing power efficiency of the rotor some other adverse effects put an upper limit on the maximum forward speed. One of these problems usually encountered at high speed concerns high pitch link loads. Note that the pitch link loads are taken representative for undesired high loads in the complete control chain, which may include much weaker elements than the push rods themselves. Figure 17 gives an impression of the harmonic contents of the pitch link loads as measured for the BO-105 rotor during the full-scale wind tunnel tests mentioned above. This picture shows clearly that the 2/rev components substantially contribute to the control force.

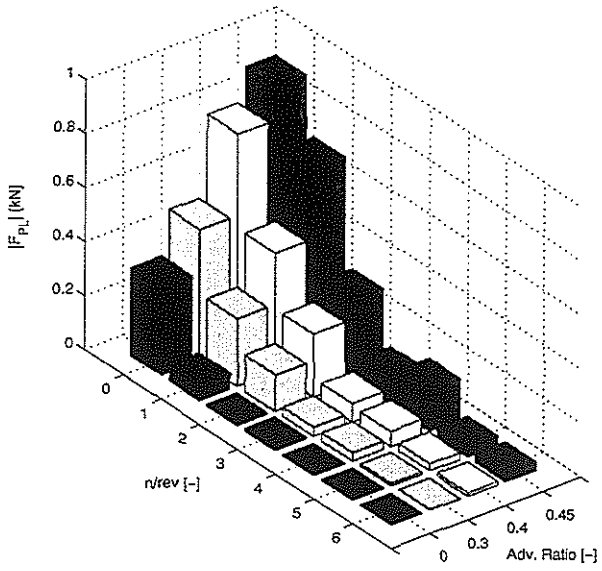

Figure 17: Harmonic Components of Pitch Link Load at Different Advance Ratios (Wind Tunnel Results with Full-Scale BO-105 Rotor)

As one would expect, introduction of 2/rev actuator motions in the rotating frame primarily changes the 2/rev component of the pitch link load. All secondary effects on adjacent harmonic components stay below approximately 30% of the 2/rev effectiveness.

Figure 18 shows how effective 2/rev control can be used to suppress the 2/rev component of the pitch link load. The presented example corresponds to an IBC amplitude of A_2 = 1deg with the best phase out of the 30deg increments investigated during that experiment. In this particular case, the change in the conventional 1/rev control necessary to re-trim the rotor had an additional positive effect on the 1/rev component.

The last set of diagrams in Figure 19 shows how favorable the influence of 2/rev can turn out. As can be seen from the upper two diagrams, the chosen amplitude of 1deg has almost exactly matched the optimal value, while the phase could have been adjusted slightly better for perfect suppression of the 2/rev force component. It should be noticed here that the nonlinear *T*-matrix approach again proves well suited to represent the recorded data.

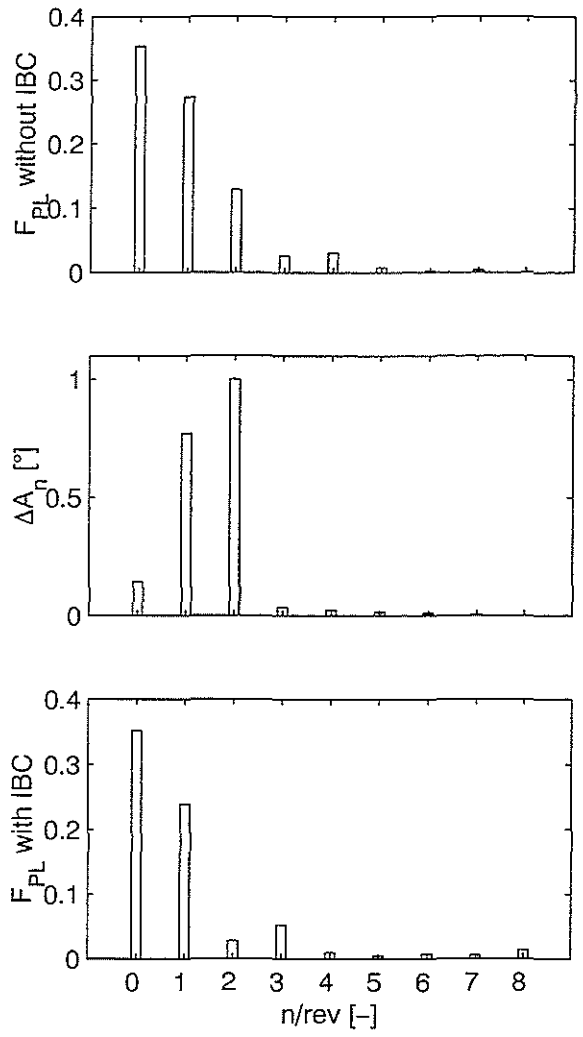

Figure 18: Change of Pitch Link Load Spectrum due to Single Harmonic 2/rev Control, A_2 = 1deg, φ_2 = 280deg (Wind Tunnel Results with Full-Scale BO-105 Rotor)

The time history given in the lower diagram, finally shows the optimum 2/rev control with respect to the peak-to-peak values. By slightly shifting the control phase it is possible to further fine-tune the amplitude and phase relations between the affected harmonic components. This improves the reduction of the peak-to-peak value from about 22% for the case with optimum 2/rev suppression Figure 18, to about 32%.

The application of higher frequencies becomes increasingly ineffective, because the positive effects from reducing the aerodynamic blade pitch moment is compensated by growing inertial moments.

It is worthwhile mentioning that for 2/rev control there exist control phases for which the averaged mechanical power to be provided by the IBC actuator to drive the blade becomes negative, see Ref. [15]. In these cases the phase relation between the controlled actuator motion and the resultant force is such that over one rotor revolution mechanical energy is exchanged but not dissipated.

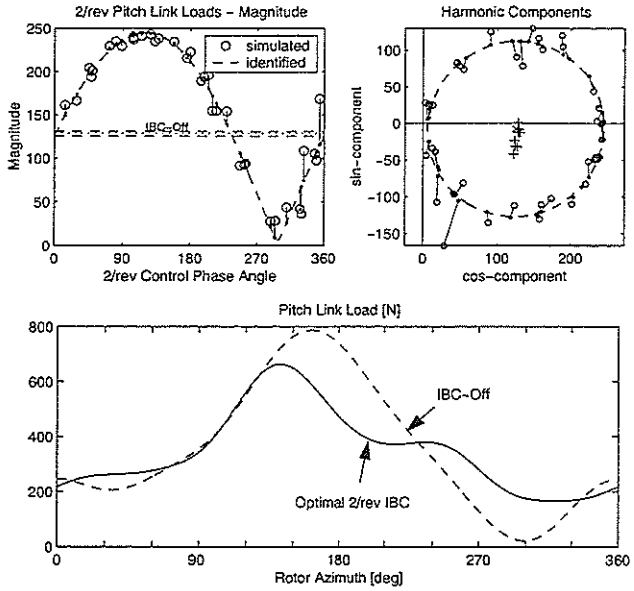

Figure 19: 2/rev Pitch Link Load Component vs. IBC Phase Angle φ_2 for Single-Harmonic 2/rev Control (Upper Diagrams) and Time History for Optimum 2/rev IBC, A_2 = 1deg, φ_2 = 340deg (Lower Diagram, Wind Tunnel Results with Full-Scale BO-105 Rotor)

From the recorded data it was found that the optimum control phases for this effect happen to match the control phases for minimum rotor power required. This would suggest that even passive systems might be considered for this particular application not discussed any further here.

7. Conclusions

In order to show the value of 2/rev harmonic control, various results from flight and wind tunnel tests have been presented. In addition, simple analytical models were used to support the conclusions drawn from the evaluated data. An extended non-linear $\underline{T}$-matrix formalism has proven useful in identifying and modeling the relation between 2/rev blade pitch inputs and the resultant 4/rev fuselage vibrations.

As far as vibrations are concerned, the effectiveness of 2/rev is indeed significantly smaller than it is for the HHC frequencies (N-1)/rev, N/rev and (N+1)/rev but it is still sufficiently high to be worthwhile considering.

Furthermore, inclusion of 2/rev as additional control frequency not only adds two more control inputs to the MIMO system but also offers a better chance to avoid negative side effects on secondary cost function parameters. It was shown, for example, that the optimization goals noise and vibration do not collide in the case of (even single-harmonic) 2/rev control. This is in sharp contrast to the observations made earlier during wind tunnel tests of HHC systems, see Ref. [23]. It is, however, quite clear that not all discussed improvements can be achieved simultaneously i.e. with one single set of control amplitudes and phases. On the other hand, applications like the reduction of control system loads will be of interest only during short periods of time, for example when during maneuver flight certain fatigue stress limits are about to be exceeded, which in turn would eat up precious component lifetime.

During the whole BO-105S1 flight test campaign none of the pilots has reported any noticeable impact of 2/rev control on the helicopter trim or handling qualities. Therefore, 2/rev is believed to be a valuable supplement to the classical HHC frequencies not only with respect to rotor power efficiency issues but also for the important optimization goals noise, vibration and pitch link load reduction.

Since the technical realization of 2/rev generally requires a system like IBC which is capable of controlling each blade individually, additional applications become feasible without any extra hardware. Examples are beside others automatic blade tracking, lag damping augmentation, artificial δ_3 or blade load alleviation, see [24]and [25].

8. References

[1] R. Kube, **Effects of Blade Elasticity on Open and Closed Loop Higher Harmonic Control of a Hingeless Helicopter Rotor,** DLR-FB-97-26, Deutsches Zentrum für Luft- und Raumfahrttechnik (DLR), Institut für Flugmechanik, Braunschweig, 1997 (in German)

[2] Yu, Gmelin, Heller, Philippe, Mercker, Preisser, **HHC Aeroacoustics Rotor Test at the DNW - The Joint German/French/US HART Project,** Twentieth European Rotorcraft Forum, Amsterdam, 1994

[3] Splettstoesser, Schultz, Kube, Brooks, Booth, Niesl, Streby, **BVI Impulsive Noise Reduction by Higher Harmonic Pitch Control: Results of a Scaled Model Rotor Experiment in the DNW,** 17th European Rotorcraft Forum, Berlin, 1991

[4] Straub, Byrns, **Application of Higher Harmonic Blade feathering on the OH-6A helicopter for vibration reduction,** NASA contractor report 4031

[5] Wood, Powers, Cline, Hammond, **On Developing and Flight Testing a Higher Harmonic Control System,** 39th Annual Forum of the American Helicopter Society, St. Louis, 1983

[6] W. Miao, S.B.R. Kottapalli, H.M. Frye, **Flight Demonstration of Higher Harmonic Control (HHC) on S-76,** 42nd Forum of the American Helicopter Society, Washington D.C., 1986

[7] Polychroniadis, Achache, **Higher Harmonic Control: Flight Tests of an Experimental System on SA349 Research Gazelle,** 42nd Forum of the American Helicopter Society, Washington D.C., 1986

[8] Shaw , Albion, **Active Control of Rotor Blade Pitch for Vibration reduction: A Wind Tunnel Demonstration,** Vertica, Vol. 4, 1980, pp.3-11

[9] Shaw , Albion, **Active Control of the Helicopter Rotor for Vibration Reduction**, JAHS, Vol. 26, No.3, July 1981, pp. 32-39

[10] Shaw, Albion, Hanker jr., Teal, **Higher Harmonic Control Windtunnel Demonstration of fully effective Vibratory Hub Force Suppression**, 41st Annual Forum of the American Helicopter Society, Fort Worth, TX, 1985

[11] R. Kube, K.-J. Schulz, **Vibration and BVI Noise Reduction by Active Rotor Control: HHC compared to IBC**, 22nd European Rotorcraft Forum, Brighton,1996

[12] D. Morbitzer, U.T.P. Arnold, M. Müller, **Vibration and Noise Reduction through Individual Blade Control,** 24th European Rotorcraft Forum, Marseille, 1998

[13] D. Schimke, U.T.P. Arnold, R. Kube, **Individual Blade Root Control Demonstration – Evaluation of Recent Flight Tests**, 54th Forum of the American Helicopter Society, Washington D.C., 1998

[14] U. Arnold, G. Reichert, **Flap, Lead-Lag and Torsion Stability of Stop-Rotors**, 19th European Rotorcraft Forum, Como, 1993

[15] U.T.P. Arnold, M. Müller, P. Richter, **Theoretical and Experimental Prediction of Individual Blade Control Benefits**, 23rd European Rotorcraft Forum, Dresden, 1997

[16] O. Kunze, U.T.P. Arnold, S. Waaske, **Development and Design of an Individual Blade Control System for the Sikorsky CH-53G Helicopter**, 55th Forum of the American Helicopter Society, Montreal, 1999

[17] P. Richter, A. Blaas, **Full Scale Wind Tunnel Investigation of an Individual Blade Control System for the BO 105 Hingeless Rotor**, 19th European Rotorcraft Forum, Como, 1993

[18] S. A. Jacklin, A. Blaas, S. M. Swanson, D. Teves, **Second Test of a Helicopter Individual Blade Control System in the NASA Ames 40- By 80-Foot Wind Tunnel,** 2nd AHS International Aeromechanics Specialists' Conference, 1995

[19] W. Steward, **Second Harmonic Control on the Helicopter Rotor,** R.A.E. Report Aero. 2472, November 1952

[20] P.R. Payne, **Higher Harmonic Rotor Control - The Possibilities of Third and Higher Harmonic Feathering for Delaying the Stall Limit in Helicopters,** Aircraft Engineering, August 1958

[21] G.H. Gaonkar, D.S. Simha Prasad, D. Sastry, **On Computing Floquet Transition Matrices of Rotorcraft,** Journal of the American Helicopter Society 3/1981

[22] U. Arnold, **Investigations on the Aero-Mechanical Stability of Stop-Rotors** (in German), Doctoral Dissertation, ZLR-Forschungsbericht 94-03, Technical University of Braunschweig, 1994

[23] R. Kube, K.-J. Schultz, **Vibration and BVI Noise Reduction by Active Rotor Control: HHC compared to IBC**, 22nd European Rotorcraft Forum, Brighton, 1996

[24] G. Reichert, U. Arnold, **Active Control of Helicopter Ground d Air Resonance**, 16th European Rotorcraft Forum, Glasgow, 1990

[25] N.D. Ham, **Helicopter Individual-Blade-Control Research at MIT** 1977-1985, Vertica 1-2, 1987

[26] R. Kube, **Effects of Blade Elasticity on Open and Closed Loop Higher Harmonic Control of a Hingeless Helicopter Rotor** (in German), DLR-Forschungsbericht 97-26, 1997

TWENTYFIFTH EUROPEAN ROTORCRAFT FORUM

Paper n° G6

ACTIVE CONTROL OF VIBRATIONS DUE TO BVI AND EXPERIMENTAL CORRELATION

BY

M. DE TERLIZZI, P. P. FRIEDMANN
UNIVERSITY OF MICHIGAN, USA

SEPTEMBER 14 - 16, 1999
ROME
ITALY

ASSOCIAZIONE INDUSTRIE PER L'AEROSPAZIO, I SISTEMI E LA DIFESA
ASSOCIAZIONE ITALIANA DI AERONAUTICA ED ASTRONAUTICA

ACTIVE CONTROL OF VIBRATIONS DUE TO BVI AND EXPERIMENTAL CORRELATION

M. de Terlizzi*and P.P. Friedmann†
Department of Aerospace Engineering
University of Michigan
Ann Arbor, Michigan 48109-2140

ABSTRACT

This paper describes vibratory load reduction due to blade vortex interaction (BVI) using an actively controlled trailing edge flap (ACF). Two aeroelastic models capable of simulating the vibration reduction process have been developed. The first uses quasisteady aerodynamics for the calculation of blade loads; the second employs a new compressible unsteady aerodynamic model. Both models are combined with a free wake simulation capability for capturing the effects of BVI. Reduction of 4/rev vibratory hub loads was studied in a four-bladed hingeless rotor. Results from the simulation were compared with experimental data. The vibration reduction study indicates that the ACF has remarkable potential for reducing vibratory hub loads induced by BVI. Good correlation with experimental results relative to 2/rev, 3/rev, 4/rev and 5/rev flap actuation was obtained.

LIST OF SYMBOLS

c_b	Blade chord
c_{cs}	Control surface chord
C_{d0}	Blade profile drag coefficient
C_f	Flap correction factor
C_W	Weight coefficient of the helicopter
$\mathbf{C}$	Assembled damping matrix
D_0, D_1	Generalized flap motions
$\mathbf{f}_b$	Vector of blade equations
$\mathbf{f}_t$	Vector of trim equations
EI_y, EI_z	Blade bending stiffnesses in flap and lead-lag, respectively
$\mathbf{F}$	Assembled load vector
J	Controller performance index
k_A	Polar radius of gyration of blade cross section, $k_A^2 = (EI_y + EI_z)/EA$
k_m	Mass radius of gyration of blade cross section, $k_m^2 = k_{m1}^2 + k_{m2}^2$ - per unit length
k_{m1}, k_{m2}	Principal mass radii of gyration of the cross section - per unit length
$\mathbf{K}$	Assembled stiffness matrix
l_e	Length of beam element
L_b	Blade length
L_{cs}	Control surface length
m	Blade mass per unit length
$\mathbf{M}$	Assembled mass matrix
n_b	Number of blades
$\mathbf{q}_b$	Vector of blade dofs
$\mathbf{q}_t$	Vector of trim parameters
R	Rotor radius
$\mathbf{T}$	Matrix of control sensitivities
u,v,w	Components of displacement
$\mathbf{u}$	Vector of control input harmonics
W_0, W_1	Generalized airfoil motions
$\mathbf{W}_u, \mathbf{W}_{\Delta u}, \mathbf{W}_z$	Control weighting matrices
x_{cs}	Distance from blade root to control flap midpoint
X_{FA}, X_{FC}	Horizontal offset of fuselage aerodynamic center and fuselage center of gravity from hub
$\mathbf{z}$	Vector of 4/rev hub loads
Z_{FA}, Z_{FC}	Vertical offset of fuselage aerodynamic center and fuselage center of gravity from hub
α	Amplitude of warping
α_R	Rotor trim pitching angle
β_p	Blade precone angle
γ	Lock number
$\gamma_{x\zeta}, \gamma_{x\eta}, \overline{\gamma}_{x\eta}, \overline{\gamma}_{x\zeta}$	Shear strain components, overbars denote strain at elastic axis
$\theta_o, \theta_{1c}, \theta_{1s}$	Collective and cyclic pitch components
θ_p	Tail rotor collective pitch
$\vec{\lambda}_i$	Induced velocity vector
Λ_a, Λ_s	Tip anhedral (positive up) and sweep (positive aft)
μ	Advance ratio
ϕ	Elastic twist angle of blade
ϕ_R	Rotor trim rolling angle
ψ	Azimuth angle
σ	Rotor solidity ratio
Ω	Rotor angular velocity

*Postdoctoral Scholar
†François-Xavier Bagnoud Professor of Aerospace Engineering

1 INTRODUCTION

An important source of higher harmonic airloads on helicopter blades, at lower advance ratios, is the phenomenon known as blade-vortex interaction (BVI) [1]. It consists of a vortex-induced loading due to the interaction of a blade with the wake tip vortex generated by the preceding blades. Blade-vortex interaction is important since it has a strong effect on vibratory response at low advance ratio descent. A number of analytical and experimental studies have been focused on the BVI phenomenon [2,3], and alleviation of BVI effects has been studied using higher harmonic control [4] and individual blade control [5]. A recent study by the authors [6–8] made an important contribution towards understanding the physical mechanism of BVI, and the potential for its alleviation using the actively controlled flap. The study concluded that alleviation of BVI-induced vibratory loads is more complicated than the reduction of vibratory hub loads due to high speed forward flight. Simulation of BVI requires a refined wake analysis tool for predicting the effects of the wake vortices on the inflow distribution at the rotor disk. This aerodynamic tool must be capable of an accurate prediction of the position of the tip vortices and the overall geometry of the helicopter wake with respect to the rotor blades. Moreover, it needs to be computationally efficient, since it must be combined with the helicopter aeroelastic response solver.

The desire to develop rotorcraft having "jet smooth" ride has shifted the emphasis in the area of vibration alleviation from traditional passive means of vibration reduction such as vibration absorbers and isolators to active control strategies [9]. Among the active control approaches the actively controlled flap (ACF) based on a controlled partial span trailing edge flap located in the outboard region of the blade has emerged as a leading candidate for practical implementation. Recent analytical [10–16] and experimental [17–19] studies have confirmed the potential of the ACF to reduce vibrations in forward flight and preliminary studies have also indicated a potential application to noise reduction [20, 21]. The experimental work by Fulton and Ormiston [18, 19, 22] has provided good quality experimental data on the practical implementation of the ACF and its application to fundamental vibration reduction in the open loop mode. The tests were performed on a small scale, 7.5-ft diameter rotor in the Army/NASA 7 x 10 ft wind tunnel.

Recently, Myrtle and Friedmann [13, 14] developed a new compressible unsteady aerodynamic model for the dynamic analysis of a rotor blade/actively controlled flap combination. In vibration control studies performed using the ACF with the new aerodynamic model [13–15], significantly higher average and instantaneous flap actuation power requirements were obtained when compared to those based on quasisteady aerodynamics. From these studies it was concluded that unsteady aerodynamics and compressibility effects need to be included in simulations of the ACF, so that more accurate specifications for flap actuation requirements is provided.

Despite the significant amount of analytical studies on the actively controlled flap, little work has been done on validating the theoretical models for the ACF versus experimental results. A comparison between analytical and experimental results is essential to validate the promising theoretical results for a real-world application. Milgram and Chopra performed a correlation study [23] between the UMARC [24] and CAMRAD/JA [25,26] analysis codes and the experimental data obtained in a wind tunnel test of the McDonnell Douglas Active Flap Rotor (AFR) conducted in the NASA-Langley 14 x 22 ft wind tunnel [21]. The results from the correlation were somewhat inconsistent, with some analytical results showing good agreement with experimental data and others exhibiting poor correlation. Ormiston and Fulton [19] presented comparisons between experimental data and results from two analytical models: a simplified rigid blade model [19] and an elastic blade representation modeled using the 2GCHAS code [27]. The primary purpose of the comparison was to interpret some dynamic phenomena observed in the experimental results therefore the variables compared were not directly related to the vibration control problem.

The overall goals of the study are: (1) the development of closed loop control strategies, in the time and frequency domain, for effective reduction of vibrations due to BVI, using an actively controlled flap, and (2) validation of the theoretical models developed versus the experimental results provided in Ref. 18. Two aeroelastic models have been developed for the purpose. The first model is employed for the aeroelastic analysis in the frequency domain using quasisteady aerodynamics to calculate the blade aerodynamic loads. The second model is used for the time domain analysis using compressible, unsteady aerodynamic theory.

The specific objectives of the paper are:

(1) Development of an aeroelastic response simulation capability both in the time and frequency domain suitable for representing BVI effects on helicopter rotors including the new unsteady compressible aerodynamic model developed in Ref. 13.

(2) Determine the effect of unsteady aerodynamics on BVI and its control by comparing the results

using quasisteady aerodynamics and the new unsteady model.

(3) Conduct active control studies for BVI alleviation using the ACF in closed loop mode.

(4) Correlate results from the aeroelastic model developed in the study with the experimental data obtained in Ref. 18.

2 WAKE MODEL

The aeroelastic models developed in this study are combined with a free wake analysis from which the nonuniform induced velocity distribution at the rotor disk is calculated. The rotor wake model used in the study has been extracted from the comprehensive rotor analysis code CAMRAD/JA [25, 26] distributed by Johnson Aeronautics. It consists of a wake geometry model, which determines the position of the wake vorticity in space, and a wake calculation model, which calculates the nonuniform induced velocity distribution given the wake geometry.

The wake geometry routine was developed by Scully [28]. The wake vorticity is created in the flow field as the blade rotates, and then convected with the local velocity of the fluid. The local velocity of the fluid consists of the free stream velocity, and the wake self-induced velocity. Thus, the wake geometry calculation proceeds as follows: (1) the position of the blade generating the wake element is calculated, this is the point at which the wake vorticity is created; (2) the undistorted wake geometry is computed as wake elements are convected downstream from the rotor by the free stream velocity; (3) distortion of wake due to the wake self-induced velocity is computed and added to the undistorted geometry, to obtain a free wake geometry. The position of a generic wake element is identified by its current azimuth position ψ and its age ϕ. Age implies here the nondimensional time that has elapsed between the wake element's current position and the position where it was created. By carrying out this procedure, the position of a generic wake element is written as:

$$\vec{r}_w(\psi,\phi) = \vec{r}_b(\psi-\phi) + \phi\vec{v}_W + \vec{D}(\psi,\phi) \qquad (1)$$

where $\vec{r}_b(\psi-\phi)$ is the position of the blade when it generates the wake element, $\vec{v}_W$ is the free stream velocity, and $\vec{D}(\psi,\phi)$ is the wake distortion, obtained by integrating in time the self-induced velocity acting on the wake element. The first term is the position at which the wake was created, the second term is the convection due to the free stream velocity, and the third is the distortion due to the self-induced velocity.

The wake calculation model, developed by Johnson [29], is based on a vortex-lattice approximation for the wake. The wake is composed of two main elements: the tip vortex, which is a strong, concentrated vorticity filament generated at the tip of the blade; and the near wake, an inboard sheet of trailed vorticity, which is much weaker and more diffused than the tip vortex. The tip vortex elements are modeled by line segments with a small viscous core radius, while the inboard wake can be represented by vortex sheet elements or by line segments with a large core radius to eliminate large induced velocities. The near wake vorticity is generally retained for only a number K_{NW} of azimuth steps behind the blade.

Figure 3 shows the wake module components and the uniform inflow calculation procedure. Given the blade displacements and circulation distribution, the wake geometry is calculated. Once the wake geometry has been determined, the procedure calculates the influence coefficients, which are stored in the influence coefficient matrix. The induced velocity distribution is obtained by conveniently multiplying the influence coefficient matrix times the circulation distribution.

3 AEROELASTIC MODEL FOR FREQUENCY DOMAIN ANALYSIS

3.1 Structural Dynamic Model

The structural dynamic model adopted has been developed in an earlier study conducted at UCLA [30]. The blade is modeled as an elastic rotating beam that consists of a straight portion and a swept tip, whose orientation with respect to the straight portion is described by a sweep angle Λ_s, positive aft, and an anhedral angle Λ_h, positive up. The blade configuration is shown in Fig. 1. The blade is modeled as a one-dimensional structure composed of a series of beam-type finite elements. A single finite element is used to model the swept tip. The model has provisions for arbitrary cross-sectional shape having multiple cells, generally anisotropic material behavior, transverse shear and out-of-plane warping. The general strain displacement relations for the beam are simplified by using an ordering scheme [31] allowing one to express the strain components in terms of seven unknown variables: the displacement components u,v,w, the elastic twist ϕ, the warping amplitude α, and the transverse shears at the elastic axis $\overline{\gamma}_{x\eta}$, $\overline{\gamma}_{x\zeta}$. Constitutive relations are introduced based on the assumptions of linear elastic and generally orthotropic material properties.

Hamilton's principle is used to formulate the blade dynamic equations. Hermite polynomials are

used to discretize the space dependence of the element generalized coordinates: cubic polynomials are used for v and w, quadratic polynomials are used for ϕ, u, α, $\overline{\gamma}_{x\eta}$ and $\overline{\gamma}_{x\zeta}$. The resulting beam element consists of two end nodes and one internal node at its mid-point, and has a total of 23 degrees of freedom, as shown in Fig. 2. Using the interpolation polynomials and carrying out the integration over the element length, the finite element equations of motion for each beam element are written. The nonlinear blade equations of motion are obtained from a finite element assembly procedure:

$$\mathbf{M}(\mathbf{q_b})\,\ddot{\mathbf{q}}_\mathbf{b} + \mathbf{C}(\mathbf{q_b},\dot{\mathbf{q}}_\mathbf{b})\,\dot{\mathbf{q}}_\mathbf{b} + \mathbf{K}(\mathbf{q_b},\dot{\mathbf{q}}_\mathbf{b},\ddot{\mathbf{q}}_\mathbf{b})\,\mathbf{q_b} + \mathbf{F}(\mathbf{q_b},\dot{\mathbf{q}}_\mathbf{b},\ddot{\mathbf{q}}_\mathbf{b}) = 0 \quad (2)$$

To be able to model the BVI control problem, an actively controlled trailing edge flap was incorporated in the blade aeroelastic model. The control surface is assumed to be an integral part of the blade, attached by hinges at a number of spanwise locations (Figure 1). The flap is assumed to rotate in the plane of the blade cross section. The flap deflection is considered a controlled quantity. It is also assumed that the presence of the small flap, located in the outboard region of the blade, has a negligible effect on the blade deformation. Thus, only the inertial and aerodynamic effects associated with the flap are included in the aeroelastic model, and the structural effects due to the flap are neglected. Two modules in the original aeroelastic analysis were modified to account for the presence of the flap, namely: (1) the free vibration analysis, that produces the mode shapes and frequencies, and (2) the aeroelastic response calculation. Additional details on the implementation of the flap in the structural dynamic and aeroelastic analysis can be found in Ref. 6.

3.2 Aerodynamic Loads

The aerodynamic loads are calculated from a modification of Theodorsen's quasisteady aerodynamic theory [10]. To account for the effect of reverse flow on the aerodynamic loads, lift and moment are set to zero within the reverse flow region, and the drag force is reversed in direction. The implementation of this aerodynamic model is based on an implicit formulation [32] where the expressions used in the derivation of the aerodynamic loads are coded in the computer program and assembled numerically during the solution process.

3.3 Method of Solution

A modal coordinate transformation is performed on Eq. (2) to reduce the size of the problem. A substitution approach [30] is used for the treatment of the axial degree of freedom, so as to properly account for the centrifugal force and Coriolis damping effects. In this approach, both the axial degree of freedom and the axial equation of motion are retained in the aeroelastic calculation. Three flap, two lag, two torsion and one axial mode are employed in the modal coordinate transformation.

The coupled trim/aeroelastic analysis in the model is based on the blade equation, corresponding to Eq. (2), which are rewritten as:

$$\mathbf{f_b}(\mathbf{q_b},\dot{\mathbf{q}}_\mathbf{b},\ddot{\mathbf{q}}_\mathbf{b},\mathbf{q_t};\psi) = \mathbf{0} \quad (3)$$

and the trim parameter vector is given by

$$\mathbf{q_t} = \{\alpha_R,\theta_o,\theta_{1c},\theta_{1s},\theta_p,\phi_R\} \quad (4)$$

The trim equations, representing the force and moment equilibrium of the helicopter in steady, level flight, can be written as

$$\mathbf{f_t}(\mathbf{q_b},\dot{\mathbf{q}}_\mathbf{b},\ddot{\mathbf{q}}_\mathbf{b},\mathbf{q}_t;\psi) = \mathbf{0} \quad (5)$$

Three force and three moment equilibrium equations are enforced.

The coupled trim/aeroelastic response solution is solved simultaneously using the harmonic balance method. The coupled trim/aeroelastic response problem is reduced to the solution of a nonlinear algebraic system for the unknown variables represented by the trim parameters $\mathbf{q_t}$ and the blade motion harmonics.

The combination of the aeroelastic model with the wake analysis required the implementation of a circulation iteration loop within the aeroelastic response procedure. In the circulation loop, the circulation distribution over the blade span at a number of azimuth stations is calculated and the induced velocity over the rotor disk is evaluated from the circulation. Once the blade motion has been calculated for the new induced velocity distribution, the circulation is reevaluated and convergence is tested. The iteration continues until the circulation has converged. The convergence criterion is based on the mean-square of the change in the peak bound circulation from one iteration to the next:

$$\frac{1}{J}\sum_{j=1}^{J}(\Delta Ga_j)^2 \le (\epsilon)^2 \quad (6)$$

where Ga_j is the bound circulation peak value at the azimuth station j, J is the number of azimuth station

at which the circulation is evaluated, and ϵ is the convergence tolerance.

The structure of the solution of the trim/aeroelastic response with the wake module is shown in Figure 4. Coupled trim/aeroelastic response calculation requires the simultaneous solution of the trim and blade equations in the same loop, so the circulation calculation has been moved inside the trim/structural response calculation loop. The wake geometry and influence coefficient calculation has been placed outside the trim/aeroelastic response iteration.

4 AEROELASTIC MODEL FOR TIME DOMAIN ANALYSIS

4.1 Structural Model

For the time domain analysis, a simpler structural formulation intended for the simulation of isotropic rotor blades has been included in the second model, to reduce the computational requirements required by the unsteady compressible aerodynamics.

The hingeless rotor blade is modeled as a slender beam composed of a linearly elastic, homogeneous material, cantilevered at the hub. The blade model is taken directly from Ref. 10 and describes the fully coupled flap-lag-torsional dynamics of an isotropic blade. Small strains and finite rotations (moderate deflections) are assumed, and the Bernoulli-Euler hypothesis is used. In addition, strains within the cross-section are neglected. The equations of motion for the elastic blade consist of a set of nonlinear partial differential equations of motion, formulated in the undeformed system, with the distributed loads left in general symbolic form.

The control surfaces are assumed to be an integral part of the blade, attached at a number of spanwise locations using hinges that are rigid in all directions except about the hinge axis, constraining the control surface cross-section to pure rotation in the plane of the blade cross-section. The control surface does not provide a structural contribution to the blade, and influences the behavior of the blade only through its contribution to the blade spanwise aerodynamic and inertial loading.

4.2 Aerodynamic Model

Aerodynamic loads are modeled using a blade element formulation, with sectional loads provided by a new two-dimensional unsteady compressible aerodynamic model [14] developed by Myrtle and Friedmann [13] for an airfoil/flap combination that includes unsteady freestream effects.

The aerodynamic model was developed using a rational function approximation (RFA) [33–35] approach based on the least squares, or Roger's approximation [33]. In this approach, oscillatory aerodynamic response data is used to generate approximate transfer functions that relate generalized motions to aerodynamic loads in the frequency domain.

Consider an aerodynamic system which is represented in the Laplace domain by the expression

$$\mathbf{G}(\bar{s}) = \mathbf{Q}(\bar{s})\mathbf{H}(\bar{s}), \tag{7}$$

where $\mathbf{G}(\bar{s})$ and $\mathbf{H}(\bar{s})$ represent Laplace transforms of the generalized aerodynamic load and generalized motion vectors, respectively. Using the Least Squares approach, $\mathbf{Q}(\bar{s})$ can be approximated using a rational expression of the form

$$\tilde{\mathbf{Q}}(\bar{s}) = \mathbf{C}_0 + \mathbf{C}_1\bar{s} + \sum_{n=1}^{n_L} \frac{\bar{s}}{\bar{s}+\gamma_n}\mathbf{C}_{n+1}. \tag{8}$$

By using rational expressions, the approximations can be easily transformed to the time domain to yield a state space model for the aerodynamic loads that is compatible with the structural equations of motion and commonly applied control approaches.

In the present research, a two-dimensional doublet lattice method [36] based on the Possio integral equation [37] is used to generate the necessary compressible flow oscillatory response quantities for a set of generalized airfoil and flap motions over range of reduced frequencies. In addition, the values of the poles γ_n have been optimized to produce a minimum error approximation.

A set of generalized airfoil and flap motions designated W_0, W_1, D_0, and D_1 were chosen which correspond to the normal velocity distributions shown in Figure 5. After defining the generalized motion vector $\mathbf{h}(t)$ and generalized force vector $\mathbf{f}(t)$ as

$$\mathbf{h}(t) = \begin{bmatrix} W_0(t) \\ W_1(t) \\ D_0(t) \\ D_1(t) \end{bmatrix}, \quad \mathbf{f}(t) = \begin{bmatrix} C_l(t) \\ C_m(t) \\ C_h(t) \end{bmatrix}, \tag{9}$$

the aerodynamic system in Eq.(7) can be approximated and transformed to the time domain to produce a state space aerodynamic model given by the expressions

$$\dot{\mathbf{x}}(t) = \frac{U(t)}{b}\mathbf{R}\mathbf{x}(t) + \mathbf{E}\dot{\mathbf{h}}(t), \tag{10}$$

$$\mathbf{f}(t) = \frac{1}{U(t)}\left(\mathbf{C}_0\mathbf{h}(t) + \mathbf{C}_1\frac{b}{U(t)}\dot{\mathbf{h}}(t) + \mathbf{D}\mathbf{x}(t)\right). \tag{11}$$

where $\mathbf{R}$, $\mathbf{E}$ and $\mathbf{D}$ are time invariant matrices obtained by the algebraic manipulation of Eq. (8). The

aerodynamic loads $\mathbf{f}(t)$ are given by Eq. (11), and are a function of a set of aerodynamic states $\mathbf{x}(t)$. These states are governed by the set of first order differential equations given in Eq. (10), and are driven by the generalized airfoil and flap motions contained in the vector $\mathbf{h}(t)$. Additional details on the derivation of the aerodynamic model can be found in Ref. 13.

In an aeroelastic simulation, the aerodynamic state equations become coupled with the structural equations of motion and must be solved simultaneously. To account for the effect of reverse flow on the aerodynamic loads, lift and moment are set to zero within the reverse flow region, and the drag force is reversed in direction.

4.3 Method of Solution

The solution of the rotary-wing aeroelastic response problem is carried out in two steps. First, spatial discretization based on Galerkin's method [38] is used to eliminate the spatial dependence, and subsequently the combined structural and aerodynamic state equations are solved in the time domain.

In this study, Galerkin's method is based on three flap, two lead-lag, and two torsional free vibration modes of a rotating beam. The free vibration modes were calculated using the first nine exact nonrotating modes of a uniform cantilevered beam.

The complete aeroelastic model for the blade and actively controlled flap consists of three sets of equations. The first two sets consist of nonlinear differential equations that describe the structural degrees of freedom and aerodynamic states. The equations of motion for the elastic blade are represented by the expression given in Eq. (3). The complete set of aerodynamic state equations are given by Eq. (10) and can be expressed as:

$$\mathbf{f_a}(\mathbf{q_b}, \dot{\mathbf{q}}_\mathbf{b}, \ddot{\mathbf{q}}_\mathbf{b}, \mathbf{x_a}, \dot{\mathbf{x}}_\mathbf{a}, \mathbf{q_t}; \psi) = \mathbf{0}. \tag{12}$$

A third set of equations represent the trim equations, representing the force and moment equilibrium in steady, level flight, which can be simbolically represented by the expression given in Eq. (5). To obtain the coupled trim/response solution, only the steady state response of the system is considered. In this case, the trim condition can be represented by the implicit nonlinear equations

$$\mathbf{f_t}(\mathbf{q_t}) = \mathbf{0}. \tag{13}$$

Evaluation of Eqs. (13) requires the steady state hub loads that correspond to the trim parameters $\mathbf{q_t}$. These are obtained by integrating Eqs. (3) and (12) numerically over time, until the response solution has converged to the steady state. The trim solution $\mathbf{q_t}$ is obtained using a simple autopilot type controller described in Ref. 14.

The circulation loop and the wake geometry calculation are performed at each rotor revolution until overall convergence is achieved.

5 CONTROL APPROACH

Reduction of the 4/rev hub loads is investigated using a control approach similar to that described in Ref. 10. In this approach, a linear optimal controller is obtained based on the minimization of a performance index J which is a quadratic function of vibration magnitudes $\mathbf{z}$ and control input amplitudes $\mathbf{u}$. At the *i-th* control step,

$$J = \mathbf{z}_i^T \mathbf{W_z} \mathbf{z}_i + \mathbf{u}_i^T \mathbf{W_u} \mathbf{u}_i + \Delta \mathbf{u}_i^T \mathbf{W}_{\Delta \mathbf{u}} \Delta \mathbf{u}_i, \tag{14}$$

where $\Delta \mathbf{u}_i = \mathbf{u}_i - \mathbf{u}_{i-1}$.

In this study, it is assumed that the control input and resulting vibration levels are known without error. Furthermore, a linear, quasistatic, frequency domain representation of the vibratory response to control is used [9,10], given by

$$\mathbf{z}_i = \mathbf{z}_{i-1} + \mathbf{T}_{i-1}(\mathbf{u}_i - \mathbf{u}_{i-1}), \tag{15}$$

where $\mathbf{T}_{i-1}$ is a transfer matrix relating vibratory loads to changes in the control input, taken about the current control $\mathbf{u}_{i-1}$:

$$\mathbf{T}_{i-1} = \frac{\partial \mathbf{z}}{\partial \mathbf{u}}\Big|_{\mathbf{u}_{i-1}}. \tag{16}$$

Substituting (15) into (14), and applying the condition

$$\frac{\partial J}{\partial \mathbf{u}_i} = 0, \tag{17}$$

yields the optimal local controller, given by

$$\mathbf{u}_i^* = -\mathbf{D}_{i-1}^{-1}\{\mathbf{T}_{i-1}^T \mathbf{W_z} \mathbf{z}_{i-1} - \mathbf{W}_{\Delta \mathbf{u}} \mathbf{u}_{i-1} - \mathbf{T}_{i-1}^T \mathbf{W_z} \mathbf{T}_{i-1} \mathbf{u}_{i-1}\}, \tag{18}$$

where

$$\mathbf{D}_{i-1} = \mathbf{T}_{i-1}^T \mathbf{W_z} \mathbf{T}_{i-1} + \mathbf{W_u} + \mathbf{W}_{\Delta \mathbf{u}}. \tag{19}$$

6 RESULTS AND DISCUSSION

The results presented in this section are divided in two parts: (1) closed loop vibration reduction results, and (2) results illustrating correlation with experimental data.

6.1 Vibration Control Studies

The variables plotted are expressed in nondimensional form, using the rotor angular velocity Ω, the blade mass per unit span m and the rotor radius R as dimensional parameters, which are combined in a suitable manner so as to nondimensionalize the pertinent quantities. The results from both aeroelastic models are obtained for a straight hingeless blade having the parameters given in Table 1.

Using the unsteady, compressible aerodynamic theory and the control law described, simultaneous reduction of 4/rev vibratory hub loads with the free wake model was examined. The results were compared with similar results obtained using quasisteady aerodynamics. Two advance ratios, $\mu = 0.15$ and $\mu = 0.30$, were considered. These two cases correspond to fundamentally different vibration phenomena. At $\mu = 0.15$ the effects of BVI are strong and represent the primary source of higher harmonic airloads, while at $\mu = 0.30$ BVI is less significant and vibratory loads are mainly due to the high speed forward flight. Figures 6 and 7 show the baseline and controlled vibratory hub shears and moments when using the unsteady, compressible aerodynamics, which is referred to as RFA aerodynamics, and the quasisteady aerodynamics, respectively, at $\mu = 0.15$. Figures 8 and 9 illustrate similar results at the higher advance ratio of $\mu = 0.30$. The baseline vibratory loads predicted by the two models differ as much as 50%. For the vibratory vertical shear FHZ, which is the largest vibratory component, the RFA aerodynamic model predicts a value approximately 50% higher than that obtained with quasisteady aerodynamics. For both cases, however, the local controller appears to be effective at reducing the vibratory loads at both advance ratios, but its performance at the low advance ratio, $\mu = 0.15$, is not as good as at $\mu = 0.30$. This is to be expected, since at $\mu = 0.30$ the effects of nonuniform inflow are mild, and earlier results [10] indicated that the actively control flap performed very well when uniform inflow distribution is assumed. Figures 10 and 11 illustrate the flap input for the two advance ratios obtained with RFA aerodynamics and quasisteady aerodynamics, respectively. The figures emphasize the differences between the flap input required for vibration reduction at these two advance ratios, indicating that the vibratory loads for the two cases are very different. It should be also noted that for $\mu = 0.15$ larger flap deflections are needed for vibration alleviation. Results with RFA aerodynamics show that flap input angles as large as 15 degrees are required. For such large flap deflections nonlinear aerodynamic effects will be significant, and will be incorporated in future simulations. Therefore, these results suggest that one flap might not be sufficient for controlling BVI induced vibrations, and a dual flap arrangement studied by Myrtle and Friedmann [15] could represent a better approach.

In figures 12 through 13 the baseline and controlled nondimensional rotating vertical shear at the root of the blade for the two advance ratios is compared. The oscillatory amplitudes of the loads in the rotating reference frame increase at $\mu = 0.15$ when compared to $\mu = 0.30$, indicating that the controller alleviates BVI effects at the expense of increased blade loading. A similar increase can also be observed for the root bending moment [6].

Finally, control power requirements during vibration alleviation for RFA aerodynamics are compared with those required when using quasisteady aerodynamics in Figs. 14 and 15. The instantaneous control power is calculated from:

$$P_{cs}(\psi) = -M_{\delta}(\psi)\,\dot{\delta}(\psi) \qquad (20)$$

where M_{δ} is the control surface hinge moment and $\dot{\delta}$ is the angular velocity of the control surface about its hinge. In these figures the results denoted by QS Aero - indicate quasisteady Theodorsen type aerodynamics and RFA Aero - indicate the new unsteady aerodynamic model. In Fig. 14 power requirements at the advance ratio $\mu = 0.30$ with RFA and quasisteady aerodynamics and the free wake model are compared with the results from the uniform inflow assumption. It is evident that power requirements are larger for the free wake case. Figure 15 compares power requirements at $\mu = 0.15$ from RFA and quasisteady aerodynamics with the free wake model. The power requirements at $\mu = 0.15$ are approximately one order of magnitude larger than the ones relative to advance ratio $\mu = 0.30$. This is due to the large amplitude of the flap control angles required for BVI-induced vibration reduction. The power requirement distribution at $\mu = 0.15$ exhibits several sharp peaks due to the higher harmonic content of the BVI-induced aerodynamic loads. Figure 15 indicates that higher average flap actuation power requirements are obtained using RFA aerodynamics.

6.2 Correlation with Experimental Data

The objective in this section is to validate the analytical simulation developed by comparing the results obtained from the simulation with the experimental data from Figs 8c - 8f of Ref. 18. In these plots, phase sweeps of elevon motion were performed to investigate the effect of the phase of flap motion on vibratory loads and to determine flap effectiveness at discrete elevon harmonics. The results from the phase sweeps were used in Ref. 18 to reduce root

out-of -plane bending moments based on a simple superposition model, and therefore they represent the most significant data on flap effectiveness for vibration reduction purposes provided in Ref. 18.

The flap motion employed in the phase sweep study can be analytically described as:

$$\delta(\psi) = \delta_{fi} \cos(i\psi + \phi) \qquad (21)$$

where ϕ is the flap motion phase and 2/rev, 3/rev, 4/rev and 5/rev harmonic motions were chosen for the flap actuation. The data points in the plots were obtained in the following manner. First, harmonic motion for the flap was chosen ($i = 2, 5$), then a phase sweep was performed, acquiring data points for a series of phase angles ϕ. Finally, the amplitude of the blade root flap bending moment at the frequency of the flap motion was calculated and plotted. The elevon angles in Ref. 18 are induced by a piezoelectric bimorph in which the voltage is controlled. The results in Ref. 18 indicate that the flap deflection amplitudes δ_{fi} in the phase sweeps varied between $4^o - 6^o$, depending on the specific harmonic being considered. Therefore, in the simulations the value of δ_{fi} was selected to be $\delta_{fi} = 5^o$ for all the phase sweep angles.

The results were obtained on a two-bladed rotor at the rotor speed of 760 RPM and an advance ratio of $\mu = 0.20$. The rotor main characteristics are presented in Table 2. The two rotor blades presented some slight differences in their construction, therefore two sets of data are presented in each plot, one relative to the first blade, referred to as Blade1, the other relative to the other one, named Blade2. In addition to the phase sweep results, the baseline (denoted in the plot as uncontrolled) values of root moment amplitudes are indicated in the plots by straight lines. It is worthwhile mentioning that some additional curves presented in Fig. 8c - 8f of Ref. 18, which were obtained by a curve fitting procedure, have not been reproduced here, since they have no bearing on the correlation objective of this paper. Two sets of results have been obtained in the course of the simulations performed. The first set has been obtained using quasisteady aerodynamics. The second set is based on the unsteady, compressible aerodynamic model, which will be referred to as the RFA model. The finite element-based structural representation described in Section 3.1 has been employed in the simulations, since it can reproduce more accurately the nonuniform spanwise structural and inertial properties of the blades used in the experiment.

The results using quasisteady aerodynamics are shown in Figures 16 through 19. The results from the simulation are compared with the experimental data points from Figs. 8c - 8f, taken from Ref. 18. Both the results for Blade1 and Blade2 are shown. Note that the blade structural and inertial parameters which have been used in the simulation represent a trade-off between Blade1 and Blade2 properties. Therefore, the results from the simulation are expected to fall somewhere between these two datasets. The baseline values of root moment harmonics have been predicted fairly well, with a maximum error of about 30% for the 3/rev root moment amplitude. Results from phase sweeps also show good overall agreement with experimental data. As expected, the results from the simulation show trends that are a trade-off between the results from Blade1 and Blade2. The larger discrepancies occur for the 2/rev moment amplitudes in Figure 16, where some data points show a difference as large as 50% from the experimental data. Furthermore, it is noteworthy that in this case a 90^o shift seems to be present between simulation and experimental data. Results for the 3/rev, 4/rev and 5/rev harmonics, shown in Figs. (17) - (19) indicate very good agreement. It is important to mention that simulations have been computed using a flap correction factor $C_f = 0.2$. This is a much lower value than $C_f = 0.6$ adopted in the control studies described in the previous section, as mentioned in Table 1. The implication of the low value of C_f is that the flap effectiveness has been overestimated in the control studies performed using quasisteady aerodynamics. Figure 20 shows the effect of the flap correction factor C_f on the 3/rev phase sweep results. In this plot, results for values of $C_f = 0.2$, $C_f = 0.4$ and $C_f = 0.6$ are compared with experimental data. With an increase in C_f, all the values in the distribution are increased by a constant term, and the value $C_f = 0.2$ provides the best fit with experimental data.

Results based on RFA aerodynamics are presented in Figs. 21 through 24. Similar to the quasisteady aerodynamics case, the baseline values of root moment harmonics have been predicted fairly well, with a maximum error of about 50% for the 5/rev root moment amplitude. Results from phase sweeps also show good agreement with experimental data except for the 5/rev case, where a discrepancy of 70% is evident when compared to the experimental results. The analytical results for the RFA aerodynamics have been obtained for the same value of the flap correction factor $C_f = 0.6$ as the one used in the control studies. Therefore the control studies performed with RFA aerodynamics represent a more realistic set of data than the one obtained from quasisteady aerodynamics, where the effectiveness of the flap has been overestimated. This also explains the higher flap displacement and flap actuation power requirements for the RFA control studies when compared to those ob-

tained from quasisteady aerodynamics. It is interesting to note that the flap correction factor C_f has a completely different physical meaning for the RFA model than it has for the case of quasisteady aerodynamics. In the RFA aerodynamic model C_f is a multiplicative factor that attenuates the amplitudes of the flap generalized motions, whereas in the quasisteady aerodynamics case it reduces the aerodynamic loads due to the flap. The effect of the flap correction factor C_f in the RFA model is shown in Fig. 25 for the 3/rev phase sweep results. In this plot, results for $C_f = 0.6$ and $C_f = 0.4$ are compared with experiment. Increasing the value of C_f results in an increase in the magnitude of the peaks and valleys of the distribution, leaving the average value unchanged.

7 CONCLUDING REMARKS

Two aeroelastic response models based on two different aerodynamic theories have been developed for the simulation of BVI on helicopter rotors with partial span trailing edge flaps. The models have been compared with experimental data. The results represent an important contribution towards understanding the mechanism of BVI and its alleviation by active control. The principal conclusions are summarized below:

(1) The mechanism of vibration reduction using the ACF is fundamentally different for BVI ($\mu = 0.15$) and vibrations due to high speed forward flight ($\mu = 0.30$).

(2) When using quasisteady or RFA aerodynamics, a reduction of approximately 80% was observed for BVI vibration, while at high forward flight vibration reduction in excess of 90% is obtained. The magnitude of control angles and the harmonic content are also substantially different between these two cases.

(3) Results from RFA aerodynamics indicate that flap input angles as large as 15 degrees may be required. For such deflections, one flap might be inadequate and a dual flap arrangement may be required.

(4) Alleviation of BVI due to ACF increases the oscillatory root bending moments and shears in the rotating system.

(5) Power requirements for vibration reduction in the presence of BVI are an order of magnitude higher than those needed for high speed forward flight, due to the larger magnitude of flap control angles for the $\mu = 0.15$ case.

(6) Higher average flap actuation power requirements for vibration reduction in the presence of BVI are obtained using RFA aerodynamics, when compared to quasisteady aerodynamics.

(7) Simulations of phase sweeps relative to 2/rev, 3/rev, 4/rev and 5/rev flap motion were performed and compared with experimental results from Ref. 18. Comparison between analytical and experimental data showed good correlation for most cases.

(8) Correlation study indicates that control studies performed using quasisteady aerodynamics have overpredicted the influence of the control flap, due to an excessive value of the flap correction coefficient C_f. By contrast, results from RFA aerodynamics provide more realistic information, since a more appropriate value of C_f was selected. The effect of the flap correction coefficient on the two aerodynamic models has been studied and clarified.

(9) The ACF displays exceptional potential for alleviating vibratory loads due to BVI, however this problem is more complex than vibration due to high speed flight. Refined control strategies for BVI alleviation need to be developed by incorporating information about the distance between blade tip and vortex in the objective function.

ACKNOWLEDGEMENTS

This research was supported by Army Grant DAAH04-95-1-0005 funded by the Army Research Office with Dr. John Prater as grant monitor. The authors wish to express their gratitude to Dr. Mark Fulton for his valuable assistance in providing data for the correlation studies.

References

[1] Johnson, W., Airloads, Wakes and Aeroelasticity, NASA CR 177551, 1990.

[2] Yu, Y. H., Rotor Blade-Vortex Interaction Noise: Generating Mechanisms and Its Control Concepts, AHS Specialist Meeting on Aeromechanics Technology and Product Design for the 21st Century, Bridgeport, CT, October 1995.

[3] Yu, Y. H., Tung, C., et al., Aerodynamics and Acoustics of Rotor Blade-Vortex Interactions, *Journal of Aircraft*, Vol. 32, No. 5, 1995, pp. 970 - 977.

[4] Kube, R. et al., HHC Aeroacoustic Rotor Tests in the German Dutch Wind Tunnel: Improving Physical Understanding and Prediction Codes, Proc. 52nd American Helicopter Society Annual Forum, Washington, DC, June 1996.

[5] Splettstoesser, W. R. et al., The effect of Individual Blade Pitch Control on BVI Noise - Comparison of Flight Test and Simulation Result, Proc. of the 24th European Rotorcraft Forum, Marseilles, France, September 1998, pp. AC07.1 - AC07.15.

[6] de Terlizzi, M. and Friedmann, P. P., Aeroelastic Response of Swept Tip Rotors Including the Effects of BVI, Proc. of the 54th Annual Forum of the American Helicopter Society, Washington, DC, May 1998, pp. 644 - 663.

[7] de Terlizzi, M. and Friedmann, P. P., BVI Alleviation Using Active Control, Proc. of the 40th AIAA/ASME/ASCE/AHS/ASC Structures, Structural Dynamics and Materials Conf., AIAA Paper 99-1220, St. Louis, MO, April 1999.

[8] de Terlizzi, M., Blade Vortex Interaction and Its Alleviation Using Passive and Active Control Approaches, Ph.D. Dissertation, University of California at Los Angeles, 1999.

[9] Friedmann, P. P. and Millott, T. A., Vibration Reduction in Rotorcraft Using Active Control: A Comparison of Various Approaches, *Journal of Guidance, Control and Dynamics*, Vol. 18, No. 4, 1995, pp. 664 - 673.

[10] Millott, T. A., and Friedmann, P. P., Vibration Reduction in Helicopter Rotors Using an Actively Controlled Partial Span Trailing Edge Flap Located on the Blade, NASA CR 4611, 1994.

[11] Milgram, J. H, A comprehensive Aeroelastic Analysis of Helicopter Main Rotors with Trailing Edge Flaps for Vibration Reduction, Ph.D. Dissertation, University of Maryland at College Park, 1997.

[12] Milgram, J. and Chopra, I., A Parametric Design Study for Actively Controlled Edge Flaps, *Journal of the American Helicopter Society*, Vol. 43, No. 2, 1998, pp. 110 - 119.

[13] Myrtle, T. F. and Friedmann, P. P., Unsteady Compressible Aerodynamics of a Flapped Airfoil with Application to Helicopter Vibration Reduction, Proc. 38th AIAA/ASME/ASCE/AHS/ASC Structures, Structural Dynamics and Materials Conf., AIAA Paper 97-1083, Kissimmee, FL, April 1997, pp. 224 - 240.

[14] Myrtle, T. F. and Friedmann, P. P., New Comprehensive Time Domain Unsteady Aerodynamics for Flapped Airfoils and Its Application to Rotor Vibration Reduction Using Active Control, Proc. 35th AHS Forum, Virginia Beach, VA, April 29 - May 1 1997, pp. 1215 - 1231.

[15] Myrtle, T. F. and Friedmann, P. P., Vibration Reduction in Rotorcraft Using the Actively Controlled Trailing Edge Flap and Issues Related to Practical Implementation, Proc. of the 54th Annual Forum of the American Helicopter Society, Washington, DC, May 1998, pp. 602 - 619.

[16] Friedmann, P. P., Myrtle, T. F., and de Terlizzi, M., New Developments in Vibration Reduction with Actively Controlled Trailing Edge Flaps, Proc. of the 24th European Rotorcraft Forum, Marseilles, France, September 1998, pp. DY07.1 - DY07.21.

[17] Straub, F. K., Active Flap Control for Vibration Reduction and Performance Improvement, Proc. of the 51st Annual Forum of the American Helicopter Society, Fort Worth, TX, May 1995, pp. 381 - 392.

[18] Fulton, M. V. and Ormiston, R., Small-Scale Rotor Experiments with On-Blade Elevons to Reduce Blade Vibratory Loads in Forward Flight, Proc. of the 54th Annual Forum of the American Helicopter Society, Washington, DC, May 1998, pp. 433 - 451.

[19] Ormiston, R. and Fulton, M. V., Aeroelastic and Dynamic Rotor Response with On-blade Elevon Control, Proc. of the 24th European Rotorcraft Forum, Marseilles, France, September 1998, pp. DY10.1 - DY10.22.

[20] Hassan, A. A.,, Charles, B. D., Tadghighi, H., and Sankar, L. N., Blade-Mounted Trailing Edge Flap Control for BVI Noise Reduction, NASA CR 4426, 1992.

[21] Dawson, S. et al., Wind Tunnel Test of an Active Flap Rotor: BVI Noise and Vibration Reduction, Proc. of the 51st Annual Forum of the American Helicopter Society, Fort Worth, TX, May 1995, pp. 631 - 648.

[22] Fulton, M. V. and Ormiston, R., Hover Testing of a Small-Scale Rotor with On-Blade Elevons, Proc. of the 53rd Annual Forum of the American Helicopter Society, Virginia Beach, VA, April 29 - May 1 1997, pp. 249 - 273.

[23] Milgram, J., Chopra, I., and Straub, F., Rotors with Trailing Edge Flaps: Analysis and Comparison with Experimental Data, *Journal of the American Helicopter Society*, Vol. 43, No. 4, 1998, pp. 319 - 332.

[24] Bir, G.,, Chopra, I.,, et al., University of Maryland Advanced Rotor Code (UMARC) Theory Manual, Technical report UM-AERO 94-18, July 1994.

[25] Johnson, W., A Comprehensive Analytical Model of Rotorcraft Aerodynamics and Dynamics, Vol. I: Theory Manual, Johnson Aeronautics, Palo Alto, CA, 1988.

[26] Johnson, W., A Comprehensive Analytical Model of Rotorcraft Aerodynamics and Dynamics, Vol. II: User's Manual, Johnson Aeronautics, Palo Alto, CA, 1988.

[27] Rutkowski, M. J., Ruzicka, G. C., Ormiston, R. A., Saberi, H., and Jung, Y., Comprehensive Aeromechanics Analysis of Complex Rotorcraft Using 2GCHAS, *Journal of the American Helicopter Society*, Vol. 40, No. 4, 1995.

[28] Scully, M. P., Computation of Helicopter Rotor Wake Geometry and Its Influence on Rotor Harmonic Airloads, Ph.D. Dissertation, Aeroelastic and Structures Research Laboratory, Massachusetts Intitute of Technology, 1975.

[29] Johnson, W., Wake Model for Helicopter Rotors in High Speed Flight, NASA CR 177507, 1988.

[30] Yuan, K. A., and Friedmann, P. P., Aeroelasticity and Structural Optimization of Composite Helicopter Rotor Blades With Swept Tips, NASA CR 4665, 1995.

[31] Friedmann, P. P., Helicopter Rotor Dynamics and Aeroelasticity: Some Key Ideas and Insights, *Vertica*, Vol. 14, No. 1, 1990, pp. 101 – 121.

[32] Celi, R. and Friedmann, P. P., Rotor Blade Aeroelasticity in Forward Flight with an Implicit Aerodynamic Formulation, *AIAA Journal*, Vol. 26, No. 12, 1988.

[33] Roger, K. L., Airplane Math Modeling Methods for Active Control Design, Structural Aspects of Active Controls, AGARD-CP-228, August 1977.

[34] Edwards, J. H., Ashley, H., and Breakwell, J., Unsteady Aerodynamic Modeling for Arbitrary Motion, *AIAA Journal*, Vol. 17, No. 4, 1979, pp. 365 – 374.

[35] Vepa, A., Finite State Modeling of Aeroelastic Systems, NASA CR-2779, 1977.

[36] Albano, E. and Rodden, W. P., A Doublet-Lattice Method for Calculating Lift Distributions on Oscillating Surfaces in Subsonic Flows, *AIAA Journal*, Vol. 7, No. 2, February 1969, pp. 279 – 285.

[37] Possio, C., L'Azione Aerodinamica sul Profilo Oscillante in un Fluido Compressibile a Velocita Iposonora, *L' Aerotecnica*, April 1938, (Also available as British Ministry of Aircraft Production R.T.P. translation 987).

[38] Friedmann, P. P., Formulation and Solution of Rotary-Wing Aeroelastic Stability and Response Problems, *Vertica*, Vol. 7, No. 2, 1983, pp. 101 – 141.

Table 1: Configuration for the Vibration Reduction Studies (Servo Flap)

Rotor Data	
$EI_y/m\Omega^2R^4 = 0.0106$	
$EI_z/m\Omega^2R^4 = 0.0301$	
$GJ/m\Omega^2R^4 = 0.001473$	
$L_b = 1.0$	$n_b = 4$
$(k_A/k_m)^2 = 2.0415$	$a = 2\pi$
$k_{m1}/R = 0.0$	$k_{m2}/R = 0.02$
$\gamma = 5.5$	$\beta_p = 0.0$
$\sigma = 0.07$	$c_b/R = 0.055$
Helicopter Data	
$C_W = 0.00515$	$C_{d0} = 0.01$
$Z_{FC}/R = 0.50$	$Z_{FA}/R = 0.25$
$X_{FC}/R = 0.0$	$X_{FA}/R = 0.0$
Flap Data	
$L_{cs} = 0.12L_b$	$c_{cs} = c_b/4$
$x_{cs} = 0.75L_b$	$C_f = 0.6$

Table 2: Configuration for the Correlation Studies (Plain Flap)

Rotor Data	
$N_b = 2$	$L_b = 1.0$
$\omega_{F1} = 1.11$	$e = 0.106R$
$\omega_{L1} = 1.08$	$c_b = 0.0756$
$\omega_{T1} = 4.6$	$\sigma = 0.048$
$\gamma = 6.95$	
Flap Data	
$x_{cs} = 0.75R$	
$L_{cs} = 0.12R$	$c_{cs} = c_b/10$

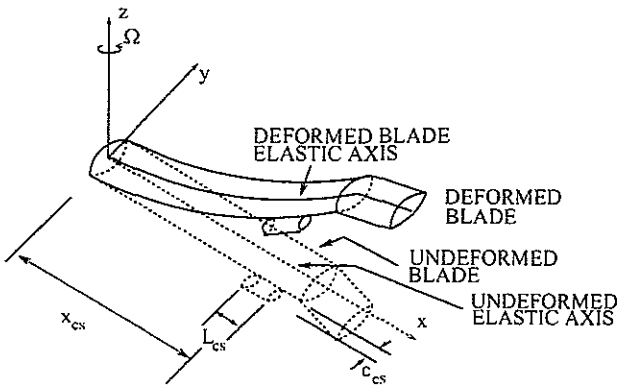

Figure 1: Schematic model of hingeless blade with actively controlled partial span trailing edge flap.

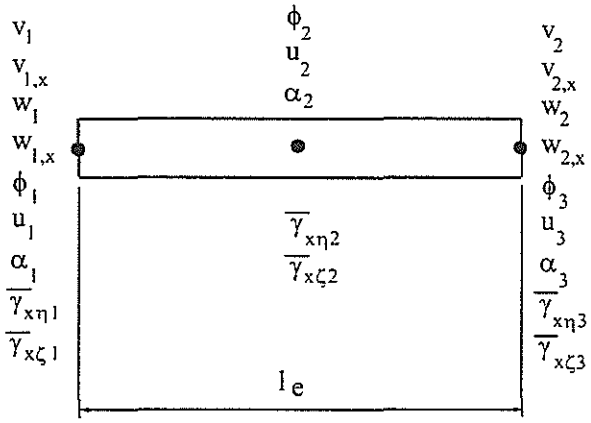

Figure 2: Finite element degrees of freedom.

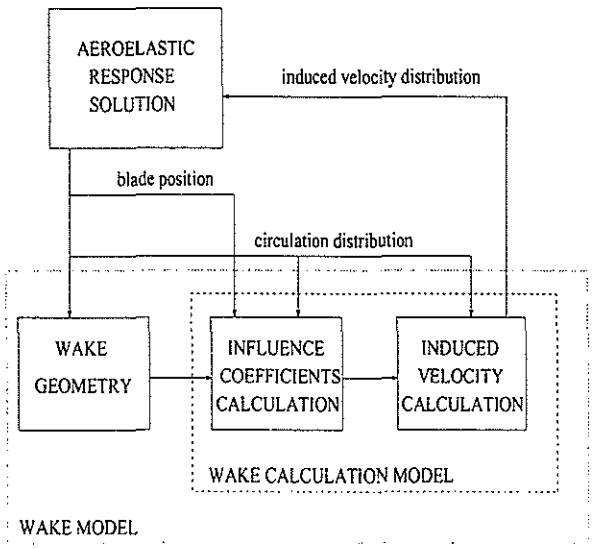

Figure 3: Wake model structure

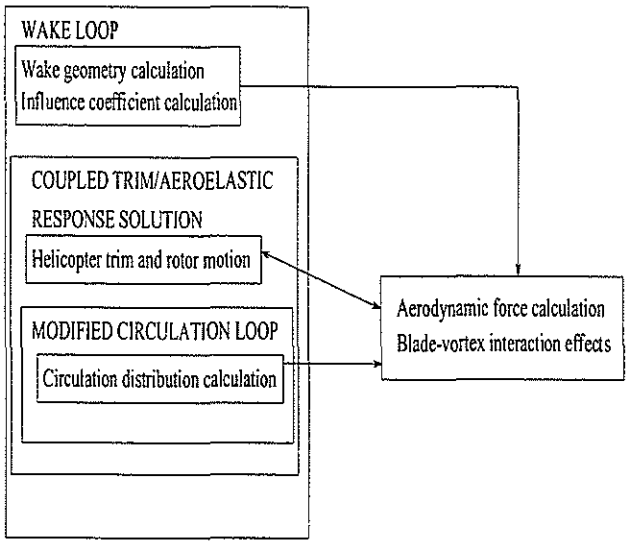

Figure 4: UCLA model: solution structure

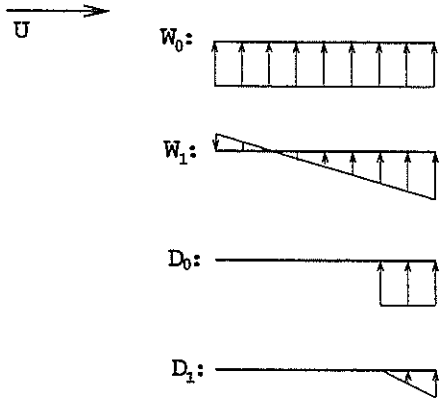

Figure 5: Normal velocity distributions corresponding to generalized airfoil and flap motions W_0, W_1, D_0, and D_1.

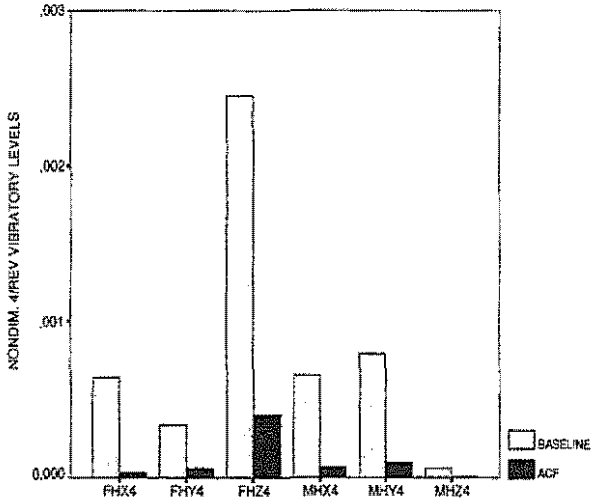

Figure 6: Simultaneous reduction of the 4/rev hub shears and moments, $\mu = 0.15$, RFA aerodynamics.

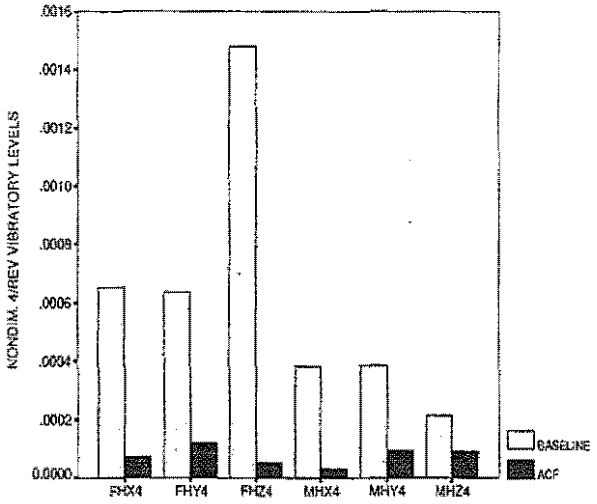

Figure 8: Simultaneous reduction of the 4/rev hub shears and moments, $\mu = 0.30$, RFA aerodynamics.

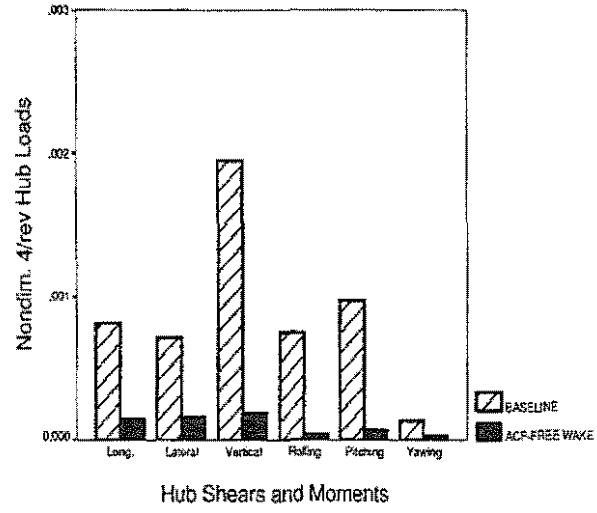

Figure 7: Simultaneous reduction of the 4/rev hub shears and moments, $\mu = 0.15$, quasisteady aerodynamics

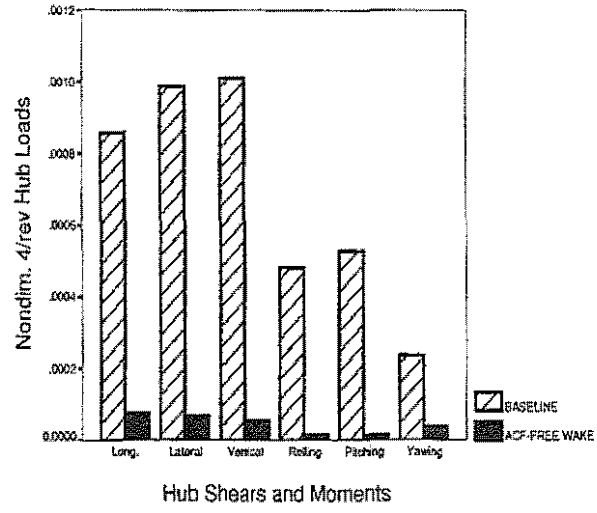

Figure 9: Simultaneous reduction of the 4/rev hub shears and moments, $\mu = 0.30$, quasisteady aerodynamics

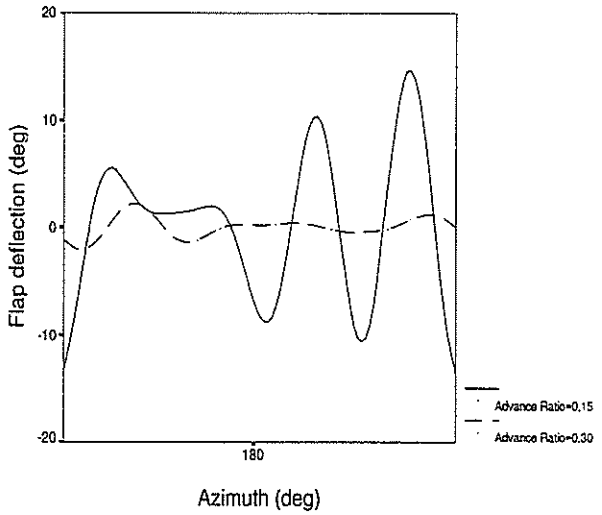

Figure 10: Flap deflection history at the advance ratios $\mu = 0.15$ and $\mu = 0.30$, RFA aerodynamics.

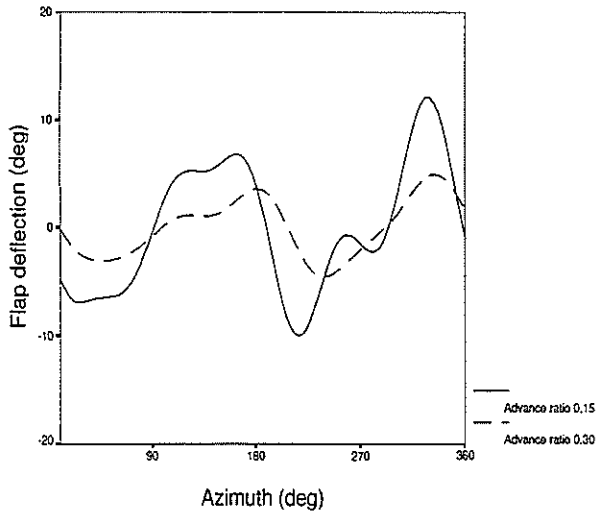

Figure 11: Flap deflection history at the advance ratios $\mu = 0.15$ and $\mu = 0.30$, quasisteady aerodynamics

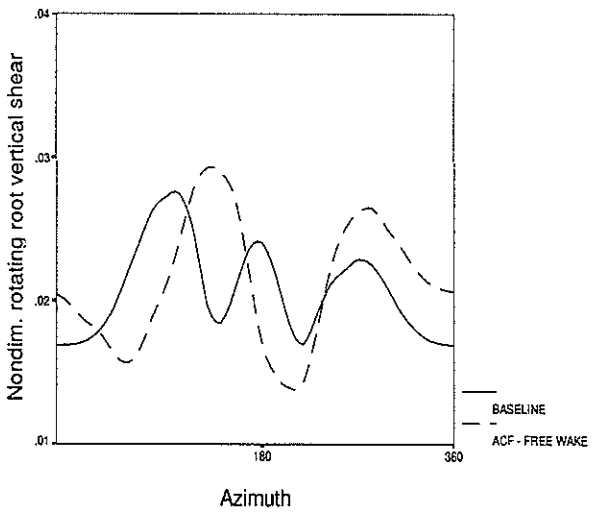

Figure 12: Nondimensional rotating root vertical shear, $\mu = 0.15$, quasisteady aerodynamics.

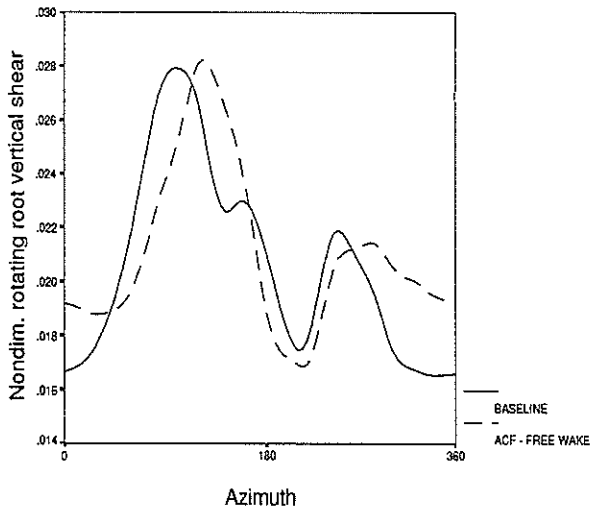

Figure 13: Nondimensional rotating root vertical shear, $\mu = 0.30$, quasisteady aerodynamics.

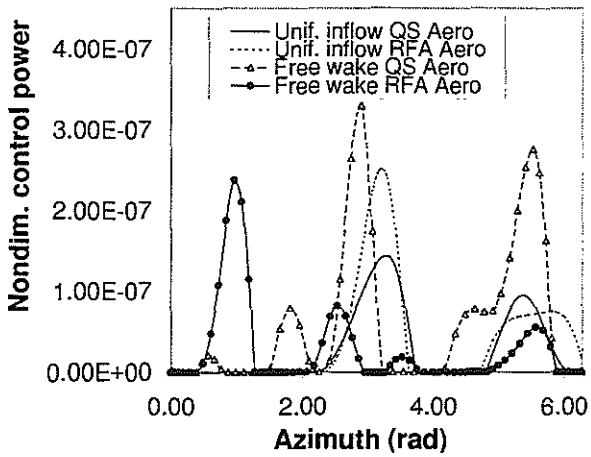

Figure 14: Control power requirements over one revolution, $\mu = 0.30$.

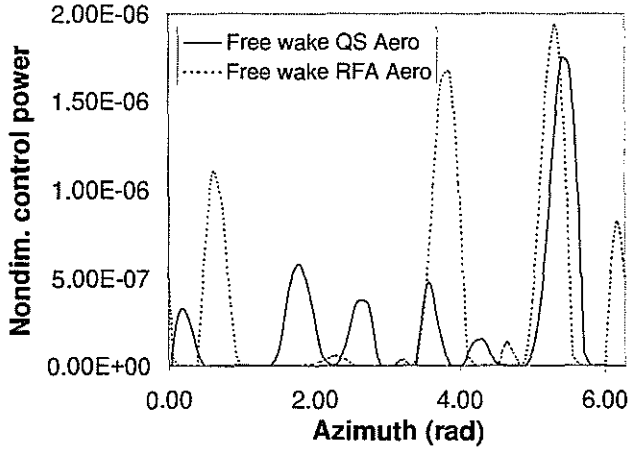

Figure 15: Control power requirements over one revolution, $\mu = 0.15$

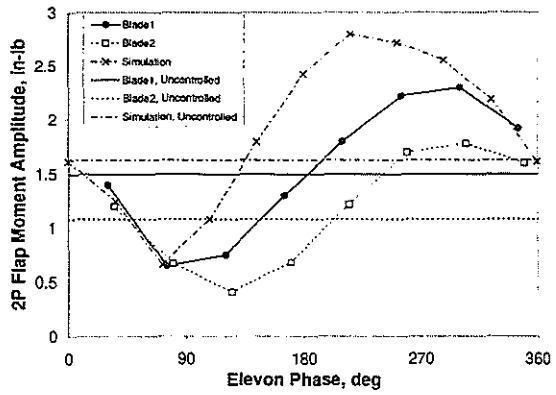

Figure 16: Variation of 2/rev flap bending moment with elevon phase (760 RPM, $\mu = 0.20$, quasisteady aerodynamics)

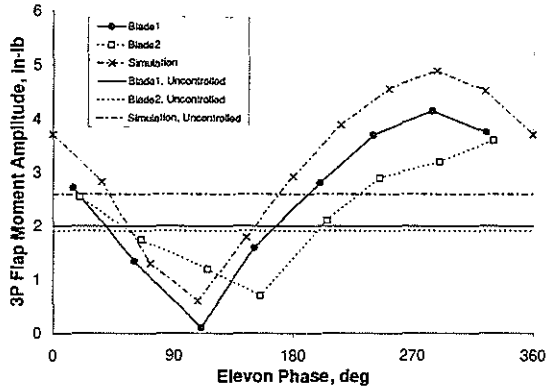

Figure 17: Variation of 3/rev flap bending moment with elevon phase (760 RPM, $\mu = 0.20$, quasisteady aerodynamics)

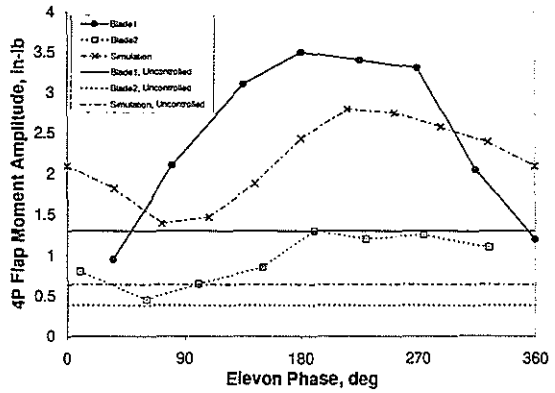

Figure 18: Variation of 4/rev flap bending moment with elevon phase (760 RPM, $\mu = 0.20$, quasisteady aerodynamics)

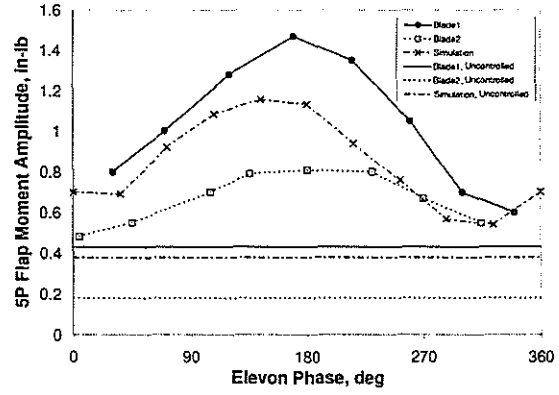

Figure 19: Variation of 5/rev flap bending moment with elevon phase (760 RPM, $\mu = 0.20$, quasisteady aerodynamics)

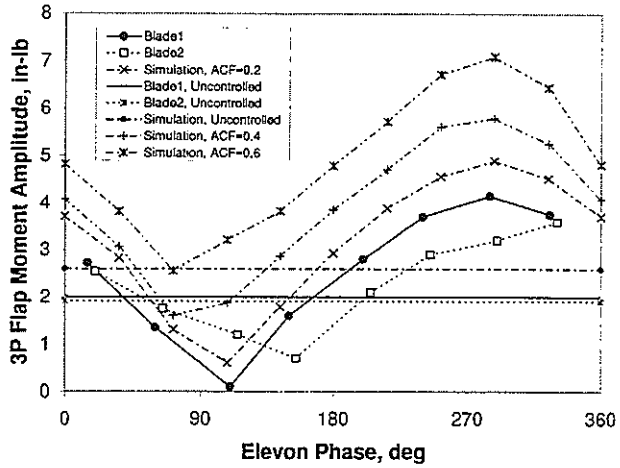

Figure 20: Effect of flap reduction coefficient C_f on 3/rev phase sweep (760 RPM, $\mu = 0.20$, quasisteady aerodynamics)

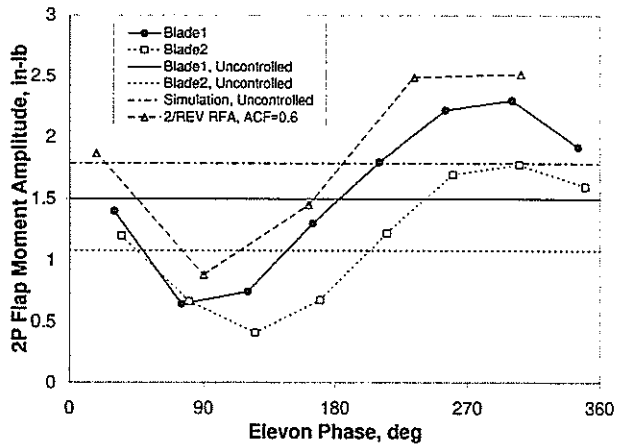

Figure 21: Variation of 2/rev flap bending moment with elevon phase (760 RPM, $\mu = 0.20$, RFA aerodynamics)

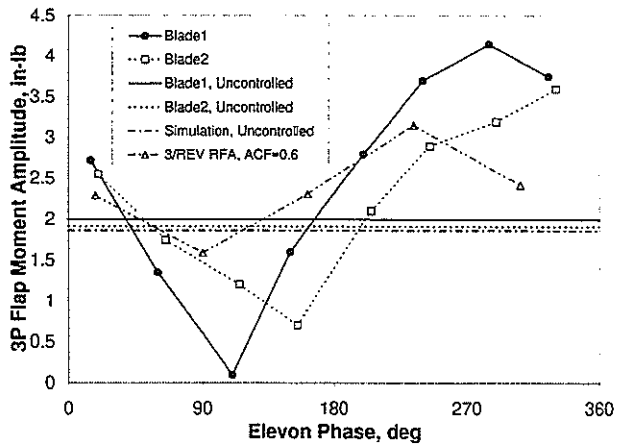

Figure 22: Variation of 3/rev flap bending moment with elevon phase (760 RPM, $\mu = 0.20$, RFA aerodynamics)

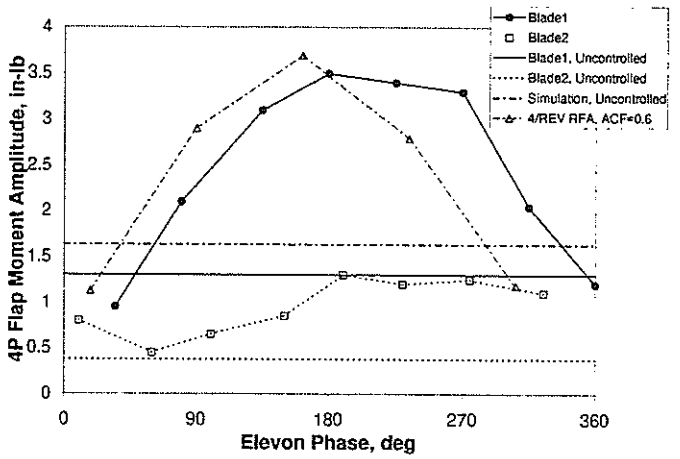

Figure 23: Variation of 4/rev flap bending moment with elevon phase (760 RPM, $\mu = 0.20$, RFA aerodynamics)

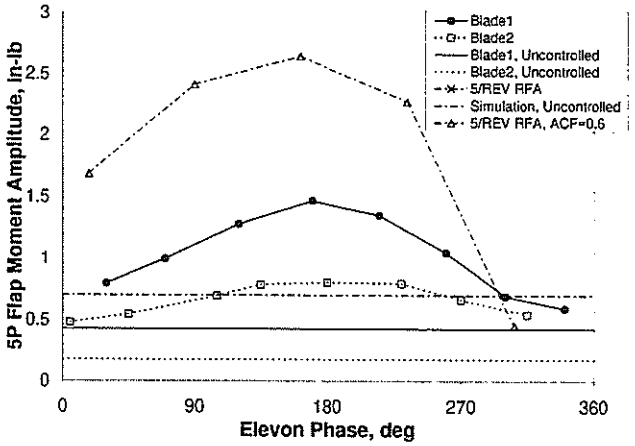

Figure 24: Variation of 5/rev flap bending moment with elevon phase (760 RPM, $\mu = 0.20$, RFA aerodynamics)

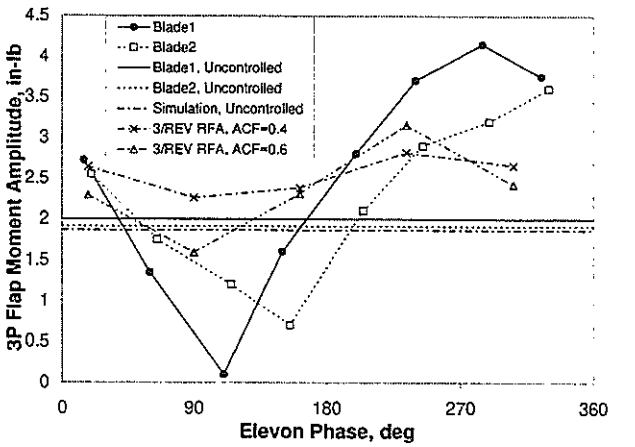

Figure 25: Effect of flap reduction coefficient C_f on 3/rev phase sweep (760 RPM, $\mu = 0.20$, RFA aerodynamics)

TWENTY FIFTH EUROPEAN ROTORCRAFT FORUM

Paper n° G – 7

G.A.H.E.L.
A NEW GENERAL CODE FOR HELICOPTER DYNAMICS
- CURRENT DEVELOPMENT STATUS -

BY

B. VIGNAL AND R. FERRER
EUROCOPTER, FRANCE

SEPTEMBER 14 – 16, 1999
ROME
ITALY

ASSOCIAZIONE INDUSTRIE PER L'AEROSPAZIO, I SISTEMI E LA DIFESA
ASSOCIAZIONE ITALIANA DI AERONAUTICA ED ASTRONAUTICA.

G.A.H.E.L.
A NEW GENERAL CODE FOR HELICOPTER DYNAMICS
- CURRENT DEVELOPMENT STATUS -

By

Berengere Vignal and Roger Ferrer

EUROCOPTER Dynamics engineers

Every new development program presents some difficulties in terms of dynamics. In fact, the general architecture of a new helicopter is decided during the project phase when the dynamic behaviour is not yet well known. This may have a high impact on the efficiency of the anti-vibration devices. Moreover, resolving dynamics problems during the development phase may impose fundamental modifications of the helicopter's geometrical design as well as costly delays.
The need for a general engineering code for helicopter dynamics that would provide simple answers is real.
G.A.H.E.L. (General Architecture of Helicopter) is meant to be an easy to use tool including a comprehensive database and simple models. It shall be used at the pre-project level to detect potential problems and give tentative solutions.
G.A.H.E.L. set-up begins with the creation of an updated database including the technical characteristics of every EUROCOPTER helicopter.
The parameters involved in the fundamental architectural selections as well as the optimisation of anti-vibration systems are then determined and a set of computing programs based on analytic models is developed.
These developments are validated with rig and flight-tests.
G.A.H.E.L. shall play a role in the virtual design and helicopters will thus be flown "*right from the drawing board*".
This paper presents a new generation tool that will help engineers in achieving dynamics during every development phase.

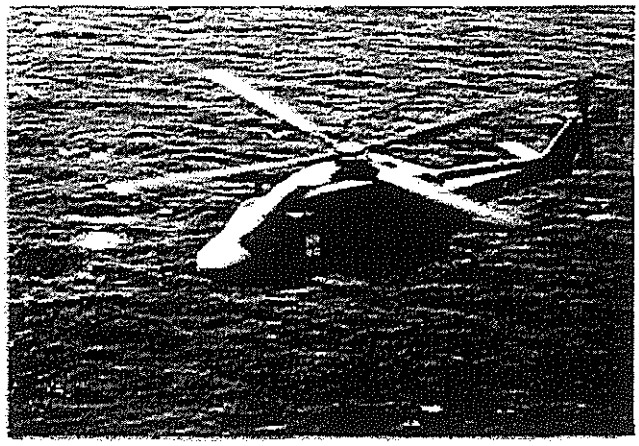

1. Introduction

Reducing vibrations is a fundamental step in the development of a new helicopter. But the general architecture of this helicopter is imposed during preliminary design in most new programs. The modifications needed if problems occur can be difficult to complete and generate costly delays in the development process.
This is why EUROCOPTER decided to develop a new engineering tool known as G.A.H.E.L. including basic analytic models that can provide general architecture parameters, help to avoid fundamental problems and are able to optimise the vibration reducing devices. This tool will play a role in a new generation of codes.

Different points are discussed in this paper:
- G.A.H.E.L. contents
- Validation method
- Development strategy

2. G.A.H.E.L. contents

G.A.H.E.L. (General Architecture of Helicopter) belongs to a new generation of computing tools which are simple and open, have already been updated and capable of describing a virtual optimised helicopter.
Developed in EUROCOPTER Dynamics Department, G.A.H.E.L. is organised along two lines: a technical database and a set of computing programs. Thanks to this approach, G.A.H.E.L. covers every need in terms of dynamics.

GAHEL general organisation is presented in Fig. 1

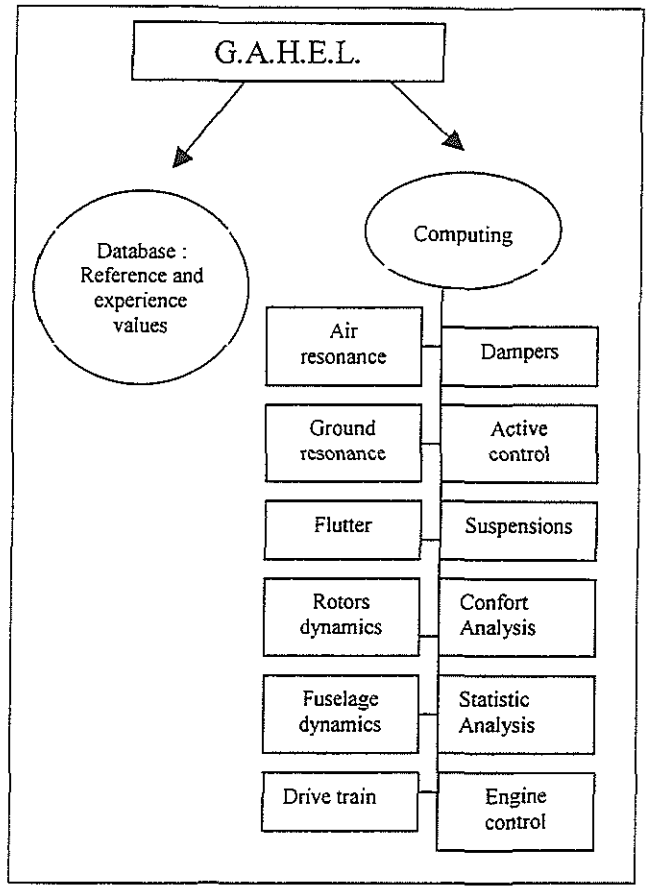

Figure 1 : G.A.H.E.L general organisation

2.1. Database:

The database includes technical characteristics for different helicopter sections:

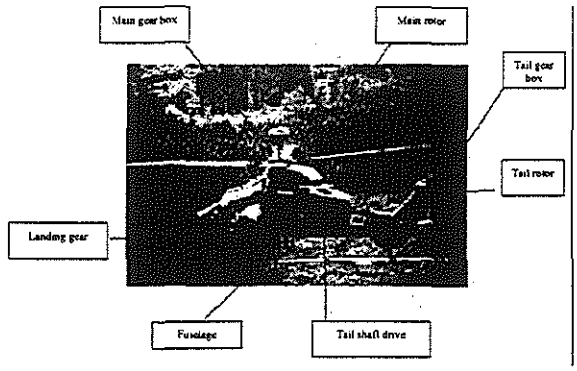

Figure 2: Helicopter sections included in G.A.H.E.L.

- The main rotor: type (hinged, Spheriflex, Starflex), nominal speed, idling speed, autorotation, number of blades, radius, blade mass, inertia, static moment and eccentricity, centrifugal load at the nominal speed, aerodynamics data, modal data (lead-lag and flapping modes), rig tests data.

- Ditto for the tail rotor.

- The fuselage : total mass, inertia in each direction, position of the centre of gravity and rotor hub, modal data.

- The landing gear: type (wheel or skid), geometric and material description.

- The main gearbox: power, geometrical characteristics.

- Ditto for the tail gearbox:

- and the intermediate gearbox:

- The tail rotor drive: shafts description : material (Young modulus and density), cross-section, length, number, tube description, bearings (distance and number), modal data (frequencies computed and measured).

- The suspensions: geometrical description, mechanical characteristics.

- The drive train : geometry, inertia, stiffness and damping.

The database includes reference as well as test results for EUROCOPTER production rotorcrafts.

2.2. Set of programs:

During the pre-project phase G.A.H.E.L. shall be used to detect potential dynamics problems and optimise the geometric parameters involved to improve dynamic characteristics.
The programs are based on analytic models computing the frequencies and vibration modes of a system, authorising stability studies and providing information for the selection of a basic architecture.

This set of programs can be divided into several sections:
- Stability programs.
- Natural frequencies and modes determination.
- Anti-vibration devices optimisation.
- Statistic analysis.

The different models are:

2.2.1. Stability programs:

Ground resonance stability:

In ground resonance mode, the body modes are generated by the structure proximal to the landing gear. Ground resonance occurs whenever the frequency of the fuselage on the ground is close to the lead-lag frequency in the fixed system (figure 3).

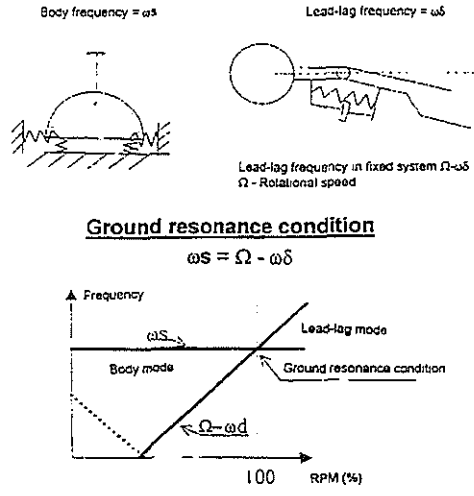

Figure 3 : Ground resonance phenomenon

Obtaining satisfactory stability margins is one of the prime concerns in the current helicopter design.

The main difficulty with this design is the non linearity of the lead-lag damper and the landing gear characteristics.

A stable helicopter can thus become unstable when the pilot excites ground resonance by precessing the cyclic pitch in the rotor's sense of rotation, due to the modification of dynamic characteristics with non linearity phenomena.

The basic ground resonance theory was originally developed by Coleman.
The first lead-lag mode and the hub in plane are the degrees of freedom taken into account in the analysis.
The helicopter fuselage is represented by a rigid body with pitch and roll rotations.

The system's equations are expressed by the Lagrange method. The linearized periodic coefficient perturbation equations are converted into a constant coefficient system with Coleman's transformation proceeding as follows (four bladed rotor):

$$\beta_i = \beta_0 + \beta_{1C}.\cos(\Omega t + (i-1).\frac{\pi}{2}) + \beta_{1S}.\sin(\Omega t + (i-1).\frac{\pi}{2})$$

$$\delta_i = \delta_0 + \delta_{1C}.\cos(\Omega t + (i-1).\frac{\pi}{2}) + \delta_{1S}.\sin(\Omega t + (i-1).\frac{\pi}{2})$$

$$\theta_i = \theta_0 + \theta_{1C}.\cos(\Omega t + (i-1).\frac{\pi}{2}) + \theta_{1S}.\sin(\Omega t + (i-1).\frac{\pi}{2})$$

The system is also expressed with:

$$M.(X_0).\ddot{X} + C(X_0).\dot{X} + K(X_0).X = F(X_0).\theta$$

where X is the co-ordinates vector, X_0 is the equilibrium position vector and θ are the control inputs.

X^T=[x y z α_x α_y α_z β_0 β_{1C} β_{1S} δ_0 δ_{1C} δ_{1S} θ_{MR} θ_{MGB} θ_{ENG1} θ_{ENG2} θ_{TR}]

θ^T=[θ_0 θ_{1C} θ_{1S}].

The equations are then transformed into a first order form:

$\dot{x}$=A.x+B.u
y=C.x
where x is the state space variable vector, y is the output measurements vector and u is the input excitations vector.

The rotor operating limits where the system is secure can easily be determined when studying two graphics describing the evolution in damping and the frequency of the modes involved.

Air resonance stability:

Air resonance is a coupling phenomenon between the rolling movement of the fuselage and the lag movement of the blade. It can be defined as an extension of ground resonance.
Several rotorcraft degrees of freedom are involved. Some displacement on roll axis induces a pitch increment on the back blade followed by a flap reaction generating a lag reaction.
Air resonance occurs when the rotor load factor is high or upon a turn at altitude, ...
This phenomenon generates instabilities and can jeopardise rotorcraft safety.
The model developed takes the degrees of freedom involved into account and studies stability with a Bode diagram.
Several gear train analytic models are being built to study air resonance.

Flutter:

Flutter phenomenon can be defined by a coupling of bending and twisting movements of the blades.
The first bending and twisting mode frequencies are computed and a graphic stability study is undertaken.

Drive train stability :

The helicopter drive train system is composed of rotors, engines, shafts and gears.

This system can generate different dynamic problems such as torque oscillations and rotor speed variations degrading handling qualities.

The dynamic analysis of the helicopter drive train is mainly focused on two points:

- suitable tuning of the system's torsional modes, providing a proper separation from bΩ as well as 2bΩ excitation frequencies. The lead-lag stiffness of the blades is often adjusted to raise this mode over bΩ and obtain a sufficient safety margin with respect to this excitation.

- adaptation of fuel controlling engine governor to the dynamic characteristics of the system in order not to decrease the natural damping of the first torsional modes.

High engine governor gains will ensure satisfactory accelerations but may lead to unstable coupling of the first drive train mode according to engine behaviour.

Finding a compromise between accelerations and drive train stability is a major problem, mainly as regards inter-blade technology because there is no damping of the lead-lag dampers on the 1st drive train mode.

The mathematical model representing the vibration behaviour of the helicopter in the [0 10 Hz] frequency range was designed from models describing ground or air resonance.
The fuselage is represented by a rigid body with yaw, pitch and roll rotation as well as vertical, lateral and longitudinal translation.
The landing gear is assimilated to perfect dampers and springs.
The blades are assumed to be rigid. The degrees of freedom taken into account are the pitch, lead-lag and flapping movements.
The torsional angles between the different components are defined .
The system's equations are determined with the Lagrange method.
The models help analyse the torsional dynamics of the drive train system as a whole.
The non-linear engine characteristics are linearized about a steady condition.
The stability margins are derived from a Bode diagram.

2.2.2. *Natural frequencies computation :*

Natural frequencies computation provides inputs for stability studies.

Determination of the fuselage natural modes:

Whenever a ground resonance study is undertaken, the fuselage modes are computed while assuming the rotorcraft is on the ground. Equivalent landing gear stiffness and damping are required to determine the modal deflections and frequencies of the fuselage.
This modulus computes modes for the wheel and skid landing gear.
The wheel landing gear is assimilated to perfect springs and dampers in the three axes for each wheel (figure 4).

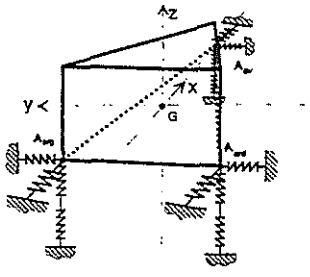

Figure 4 : Landing gear modelling

The optimisation procedure allows placing the frequencies in a specific area.

Determination of the natural blade modes:

The code computes the natural blade modes. The sensitive study is integrated and the optimisation procedure is made available.

Determination of the tail rotor drive natural frequencies:

The tail shaft can be classified in two categories:
- Sub-critical: Every natural frequency is superimposed to the speed of the tail rotor drive shaft.
- Super-critical: one of the frequencies is computed under the drive velocity.

The model computes the first five natural frequencies and modes and the margins are displayed with a graphic study taking the rotor bΩ frequencies and the tail drive speed into account.

2.2.3. *Anti-vibration devices:*

The anti vibration devices are broken down into 3 classes:

- rotor hub
- rotor-to-fuselage interface - upper deck
- fuselage.

Three categories (passive, semi-active and active systems) are distinguished in these three classes These technologies are described in figure 5.

	PASSIVE	SEMI ACTIVE	ACTIVE
ROTOR HUB	RESONATORS : -PENDULUM MASS -BIFILAR -HUB ABSORBER -ROLLER ABSORBER	Auto-tuned Hub absorber	HHC IBC
UPPER DECK	BBQ SARIB ARIS RESONATORS	Auto-tuned SARIB	ACSR
CABIN	MECHANICAL RESONATORS	Auto-tuned resonators	Cabin actuators

Figure 5 : Summary of anti vibration devices.

Dynamic absorbers :

Blade or hub-mounted dynamic absorbers (pendulum mass, bifilar, hub or roller absorber) are the most popular anti vibration devices used in helicopters. The resonance tuning of these dynamic absorbers must be close to the rotor harmonic to be reduced.
The code allows computing the characteristics of dynamics absorbers in terms of geometry and tuning characteristics.

Upper deck suspensions :

Eurocopter was one of the first helicopter manufacturers to offer a focal point suspension system, so-called "barbecue", on the market. This system was applied to the SA 330 Puma. The idea was to use soft elements to filter vibrations in the gearbox sump. The satisfactory results obtained in SA 330 boosted the development of several derivatives in AS 332, Dauphin and Ecureuil. A simplification is produced with the use of laminated elastomer mounts and flexible composite bars.

A new generation of suspension system so-called "SARIB®" was developed in recent years.
SARIB® is an anti-resonance isolation system, consisting, as shown in figure 6, of 4 individual units equi-spaced around the gearbox. One of those units

includes a leaf spring, the flapper arm and flapper mass. The leaf spring is designed with two parallel flanges at the stiff end. One bolt connects, through the outer bearing, the leaf spring, to a bracket on the gearbox deck and another bolt connects the leaf spring to a gearbox strut. Elastomeric bearings are provided at both connections.

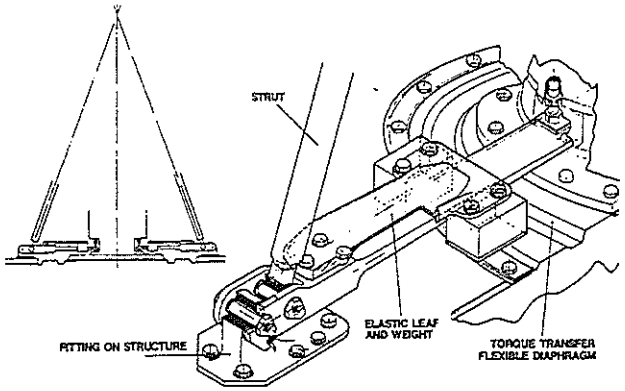

Figure 6 : SARIB Anti-Resonance isolation system

The elastic side of the leaf spring is supported at the bottom of the gearbox. The amplification needed for flapper mass oscillation is realised through the flapper arms and their connections to the stiff part of the leaf spring, close to the gearbox strut. A membrane provided between the bottom of the gearbox and the fuselage transmits the rotor torque. Excellent vibration levels were achieved with SARIB® isolation for different missions and weapon configurations.

The model allows optimising the basic architecture of this suspension and provides the necessary tuning.

These models help select the most suitable device for the application. Moreover the anti vibration system is optimised.

Active control :

The main idea behind the active control of air-mechanical stability is being able to use the hardware that is already available in the helicopter.

Air/ground resonance can also be achieved provided the proper compensation is introduced in a body state feedback loop.

The first step is to select parameters that are easily available in the helicopter (accelerations, angular velocities in the fixed system) as far as the observation variables of the phenomenon are concerned.

The helicopter is then identified for the observed phenomenon and the model can be generated. Control laws were developed with simulations at this stage.

Active control is based on the injection of a cyclic control into the rotor calculated from a parameter measured in the fixed datum.

Theoretical studies were also conducted for active stabilisation of the 1st drive train mode for inter-blade rotors, in particular.
The objective is the reduction of high resonance in the frequency areas where engine governor laws are still active and with sufficient gains to maintain satisfactory accelerations.

The theoretical model integrated in G.A.H.E.L. allows elaborating the control strategy and the control loop is made.

2.2.4. Statistical Analysis:

This part of G.A.H.E.L. computes similitude laws for several geometrical parameters of the helicopter.
The modulus designed with database figures and test results allows comparing rotorcraft; new helicopter architectures can then be defined from these laws.

These programs are set up for G.A.H.E.L. application, tested and validated on the rig and in flight as well as with a number of previous applications.

3. Validation method.

Each code developed and integrated in G.A.H.E.L. must be validated. The devices used to do this can be divided in two categories: the first involves using a previous computing tool provided to give satisfactory results. The second method involves using test results.
The same conditions are to be applied for both. Moreover, a non-regression of the codes must be demonstrated whenever modifications are made. Every option delivered must be tested.

The first case reported involves the vibration modes of a tail rotor drive.
This code was validated along two lines : a finite-elements model designed with SAMCEF software and a test performed in EUROCOPTER laboratories. The same tail rotor drive (Super Puma MK2) was used in every configuration.
The second case reported is the validation of the drive train simulation made on the Super Puma MKII.

3.1. Tail drive shaft:

3.1.1. G.A.H.E.L.:

This study is based on an analytic model made with finite elements. Beam elements are selected with displacement in two directions and bending rotation.
The mass and stiffness matrices are manufactured, the eigen values and vectors are computed. The first three bending frequencies are determined. Figure7 presents the architecture of the Super puma MKII tail rotor drive as used in G.A.H.E.L..

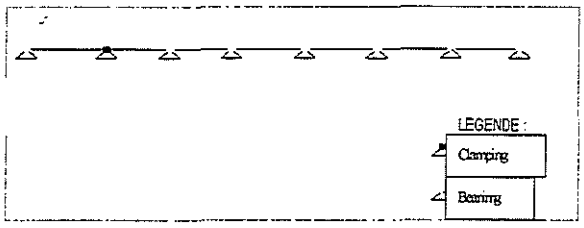

Figure 7 : Super Puma MKII tail drive architecture.

The first bending modes computed are:
1. 167.5 Hz : resonance of the first section
2. 171.5 Hz : resonance of the central section
3. 185 Hz.

The modal deflection of the second vibration mode is given on Figure 8.

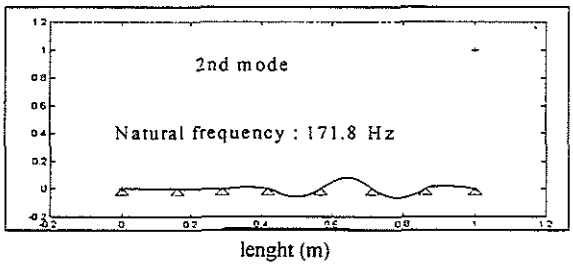

Figure 8 : 2nd modal deflection : G.A.H.E..L computation.

3.1.2. Test on the aircraft :

The purpose of the test is to identify the natural vibration modes of the tail rotor drive.
The study was limited to the second frequency: 170Hz, resonance on the central section.

3.1.3. F.E. model:

The F.E. model is embodied with SAMCEF application. The elements used are beams with displacement and rotation in all directions.

The displacement in the X (length) and Y (bending) directions are fixed on the nodes connected to a bearing element.
The results for the first bending frequencies are:
165.5 Hz: resonance of the first section.
170 Hz: resonance of the central section.
183.7 Hz.

The modal deflection of the second mode is presented in figure 9.

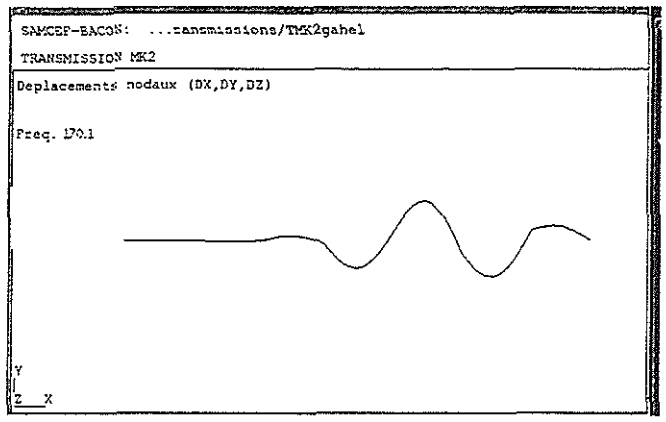

Figure 9 : 2nd modal deflection : SAMCEF computation.

3.1.4. Summary:

The results are summarised in the following table:

	FE model	TEST *	G.A.H.E.L.
1st mode			167.5 Hz
2nd mode	170 Hz	170 Hz	171.5 Hz
3rd mode	183.7 Hz		185 Hz

*: Only the second mode was measured during this test.

The correlation between the three values is satisfactory. The G.A.H.E.L. tail rotor drive model provides acceptable results.

3.2. Drive train :

The validation proceeds on the first drive train mode of the Super Puma MKII.
The simulations undertaken with the analytic model and flight test results in the prototype are compared.

The transfer function study shows that two modes of resonance are produced either when the rotor is excited with the collective lever (θ_0) or when the fuselage is

excited in yaw. Excitations with the cyclic stick do not produce any drive train / rotor / fuselage coupling.
The first mode frequency is 2.7 Hz and the second is 6Hz.

The parameters measured on the drive train already instrumented, are the main rotor mast and the engine shaft torque.
A preliminary study undertaken by Eurocopter shows that the engine governing system tends to amplify resonance in the 2.7 Hz but is insensitive to vibrations around 6 Hz.
The tests were thus intended to detect the 2.7 Hz mode.
Excitations were generated by the automatic flight control system with the collective lever. The excitation was sinusoid.

Figure 10 presents a comparison between the temporal responses for parameters measured and determined with a G.AH.EL. simulation throughout the mast torque excitation period.
The amplitudes are the same and a resonance occurs at the same frequencies.

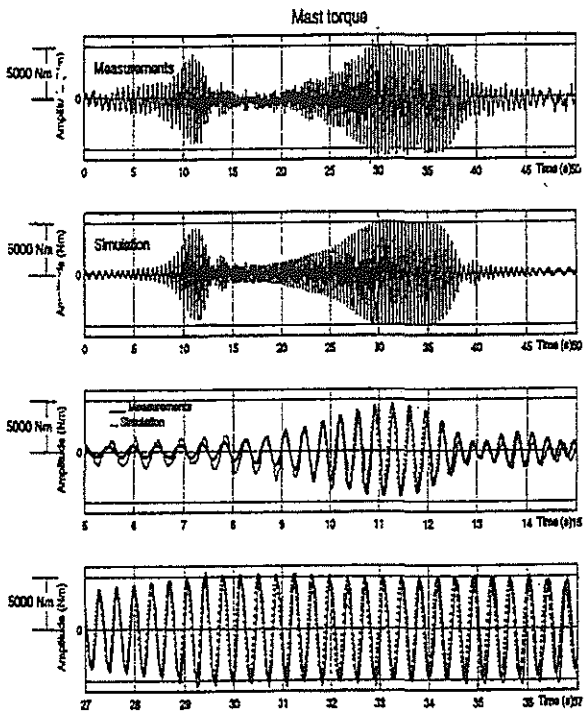

Figure 10 : Drive train identification : calculation/measurement comparison.

3.3. Conclusion:

The same method is applied for every computing program. The reference codes used for comparison purposes with G.A.H.E.L. can be programs that were validated in the past.
Many flight and rig test results are available in EUROCOPTER Dynamics Department for comparison with G.A.H.E.L. results.
Moreover, a model adjusting method is to be developed to limit the number of tests undertaken for G.A.H.E.L certification.

4. Development strategy

The objective is to create a simple standard tool which is easy to use, safe and cheap.

G.A.H.E.L. is developed in a unified environment.
MATLAB (version 5) application is used to generate the codes and Microsoft® EXCEL application to create the database. MATLAB is both an interactive environment and a language. It is technically highly efficient because of its high matrix computing capabilities. G.A.H.E.L. runs on a PC increasing facility of access and purchase.

The figures drawn from the EXCEL database are identified by their name rather than their values. The modifications made to the data base consequently have no impact on the validity of the programs.

Each program is validated and the non-regression code is provided for any modification.
The software is constructed program by program and this makes it easy to add a new model.

5. Conclusion

G.A.H.E.L. is a new general code for helicopter dynamics. It will include a set of computing programs and a technical database. Every development is validated with rig and flight tests.

Aeronautic tests are technically difficult to prepare and expensive to achieve.
The general trend is to develop a new generation of tools that will help certify a new aircraft or rotorcraft with a minimum of tests.
G.A.H.E.L. will play a significant role in this new approach.

G.A.H.E.L's future is the development of a link between codes to produce a software able covering every dynamic investigation.

6. REFERENCES:

1. **F. BEROUL - L. GIRARD - E. ZOPPITELLI, T. KRYSINSKI**
« Current state-of-the-art regarding helicopter vibration reduction and aeroelastic stability augmentation »
18th European rotorcraft Forum, 15-18 IX 1992 - Avignon

7. **M. ALLONGUE – T. KRYSINSKI**
" Validation of a new general aerospatiale aeroelastic rotor model through the wind tunnel and flight tests data".
46th Annual Forum of the American Helicopter Society, Washington DC, May 1990.

3. **T. KRYSINSKI**
"Active control of aeromechanical stability".
AGARG symposium, Ottawa Canada, May 1996.

1. **R.P. COLEMAN and AM INGOLD**
"Theory of self-exited mechanical Oscillations of rotors with hinged blades"
NACA report 1351, 1958.

2. **P. ALMERAS**
"Active control of aeromechanical stability applied by Eurocopter"
23th European Rotorcraft Forum, Dresden, Germany, September 1997.

TWENTYFIFTH EUROPEAN ROTORCRAFT FORUM

Paper n° G8

ROTARY WING AEROELASTICITY IN FORWARD FLIGHT WITH REFINED STRUCTURE MODELLING

BY

A. R. M. ALTMIKUS, B. BUCHTALA, S. WAGNER
INSTITUT FÜR AERODYNAMIK UND GASDYNAMIK,
UNIVERSITÄT STUTTGART, GERMANY

SEPTEMBER 14-16, 1999
ROME
ITALY

ASSOCIAZIONE INDUSTRIE PER L'AEROSPAZIO, I SISITEMI E LA DIFESA
ASSOCIAZIONE ITALIANA DI AERONAUTICA ED ASTRONAUTICA

ROTARY WING AEROELASTICITY IN FORWARD FLIGHT WITH REFINED STRUCTURE MODELLING

A. R. M. Altmikus, B. Buchtala and S. Wagner
Institut für Aerodynamik und Gasdynamik, Universität Stuttgart
Pfaffenwaldring 21, 70550 Stuttgart, Germany

1 Abstract

A modular approach for the numerical simulation of the aeroelastic behaviour of a multi-bladed helicopter rotor in forward flight is presented. For this purpose a new dynamic finite element model of the beam-like blade structure, DYNROT, is coupled with a three-dimensional finite volume Euler solver for unsteady compressible flows, INROT.

The Euler solver uses third order upwind discretization in the computational space for the convective terms and is second order accurate in time by using three point backward differences. Arbitrary, relative blade motion in the rotor reference system is enabled due to Chimera technique.

The dynamic behaviour of the various blades is simulated by a quasi one-dimensional Finite Element Method (FEM) using Timoshenko's beam theory. The dynamic blade model comprises calculation of coupled flap lag motion as well as coupled flap torsion. Blade deflections are directly solved in time by integrating the second order linear system of differential equations with the generalized-α algorithm.

The solution of the surface coupled two-field problem is found by the use of a staggered time-marching procedure. This procedure together with geometric conservative deformation of grids guarantees the high order accuracy of the overall method.

This new approach for simulation of blade dynamics is validated on experimental data achieved in flight tests with a *HUGHES-500* helicopter. Additionally it is compared with another method to describe the blade deformation, SIMPACK, which is based upon modal synthesis of the first natural modes of an Euler-Bernoulli beam model.

2 Introduction

The introduction of hingeless rotor blades to the helicopter has lead to improvements in important areas. The weight of the main rotor was reduced as well as its mechanical complexity leading to a decrease in maintenance expenditures and lower operational costs. Drawback was a risen vibration level due to momentum afflicted blade connection of hingeless blades. Vibration is considered a severe disadvantage with respect to passenger comfort and fatigue failure. This phenomenon is strongly determined by the aeroelastic interaction of the blade structure and the surrounding compressible, viscous flow.

In course of the development of suitable countermeasures, their efficiency within this interactive environment is examined with numerical simulation methods. Since the involved mechanisms take place in rather small scales referred to blade-length the correctness and reliability of results are highly dependent on the local accuracy of the applied simulation methods.

Modern aerodynamic methods inherently provide the demanded local accuracy but dependent on the underlying model equations, they are neglecting important physical properties of the rotor flow, which is charactarized by high instationarity, compressibility as well as viscosity. Today's Euler methods for inviscid rotor flows are widely used for simulation purposes and Navier-Stokes methods are under development.

The dynamic behaviour of rotor blades can be calculated with multiple rigid-body systems, finite beam elements, as well as shell elements and fully three dimensional finite elements. Nevertheless, a rotor blade can be regarded as a slender body, so that a beam-like representation serves as a sufficiently accurate simulation basis.

Recent research dealing with fluid-structure-coupling emphasises the importance of the fact that both, aerodynamic and structural model have to be thoroughly in tune with each other with, respect to spatial and time-wise discretization in order to simulate the observed aeroelastic phenomena.

3 Applied Solution Methods

3.1 Structure Dynamics

Physical Structure Model

The dynamic blade deformation is analyzed with the structure model DYNROT, which is based on a quasi one-dimensional finite element representation of a beam-like structure using Timoshenko's beam theory. In difference to Euler's beam theory, where cross-sections of the beam keep a perpendicular orientation to the bending axis, Timoshenko introduced shear deformation, thus allowing for an angle between tangential bending and cross-sectional normal direction. This model also accounts for rotational inertia.

Within the cross-section, tension centre [T] or shear centre [S] must not necessarily coincide with the centre of gravity [G]. Thus torsion and bending as well as axial strain and bending deformations are structure-sidedly coupled. Beyond that, the aerodynamic centre, i.e. the quarter chord line [Q], may have an offset to the other axes, thus allowing an aerodynamic coupling of the torsional and bending degrees of freedom.

The resulting differential equation for deflection of a simple fixed beam is of hyperbolic type, describing the transport of wave energy within the beam in a physically correct manner. Additionally, normal dispersion of wave velocities is ascertained [17] by Timoshenko's model.

The governing system of equations for the rotating beam was derived in the following way. The physical representation of the quasi one-dimensional beam is built up from infinitesimal thin cross-sectional layers. The deflection of each rigid slice is now formulated for its centre of gravity, relative to the undeformed centre of gravity line of the beam. The deflection is described by three rotational degrees of freedom and three translational degrees of freedom (Figure 1), subsumed in vector φ and vector $\boldsymbol{u}$.

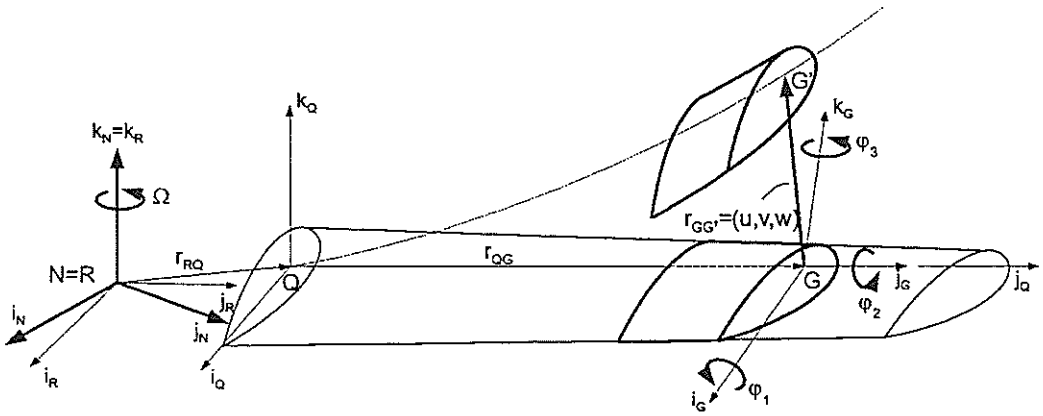

Figure 1: Finite element model of the rotor blade

Having a vector from the origin of the non-rotating reference frame [N] to the location of the centre of gravity [G'] in the deformed state of the beam, the corresponding velocities can be derived. With those entities, kinetic and potential energy of the cross-section can be formulated as length-related energy density functions in coordinates of the rotating reference system [R]. The energy terms can be further divided in translational and rotational kinetic energy and in elastic and gravitational

potential energy.

$$l = e_k - e_p = \frac{1}{2}(\rho A \dot{u}\dot{u} + \frac{1}{2}\omega\Theta\omega + EA\check{u}_{2B}^2 + \gamma^T G\gamma + \check{\varphi}^T T\check{\varphi} + N^0(\varphi_1^2 + \varphi_3^2)) + \rho A u g_{(R)} \quad (1)$$

Θ means the matrix of rotational inertias, G the matrix of shear stiffnesses and T the matrix of bending and polar stiffnesses. With

$$\check{u}_{2T} = \check{u}_2 - (z_{GT}\,\varphi_1)^{\check{}} + (x_{GT}\,\varphi_3)^{\check{}} \quad (2)$$

the spatial derivative ($\check{}$) of the axial strain deformation in the tension centre is yielded as a function of the DOF's. x_{GT} and z_{GT} are the distances between [G] and [T]. Timoshenko's theory delivers the shear angles as follows, with x_{GS} and z_{GS} as offsets of [S] from [G]:

$$\begin{aligned}\gamma_1 &= \check{u}_1 + \varphi_3 + (z_{GS}\,\varphi_2)^{\check{}} \\ \gamma_3 &= \check{u}_3 - \varphi_1 - (x_{GS}\,\varphi_2)^{\check{}}\end{aligned} \quad (3)$$

Dissipative energy is neglected in the first place but will be introduced later on by the mass and stiffness proportional Rayleigh-damping. Finally, N^0 represents the centrifugal force at the cross-section, which increases the elastic stiffness of the beam and causes an additional energy term in case of a rotating beam.

The complete Lagrange density function is obtained in dependence of time, radial position and generalized DOF's $q = (u, \varphi)^T = f(y,t)$, which are themselves a function of time and location along the beam axis

$$l = f(y, t, q, \check{q}, \dot{q}) \quad (4)$$

Assumed that the functional dependency of radial position is know, integration over beam length can be carried out for the Lagrange density so that the Lagrange function L is yielded. Further, nonconservative loads such as distributed aerodynamic forces acting on the system are written as virtual work. By Hamilton's principle the variation calculus of the time integral can be executed

$$\delta\mathcal{I} = \delta \int_{t=t_a}^{t_e} L\,Dt + \int_{t=t_a}^{t_e} \delta A\,Dt = 0 \quad (5)$$

so that the inhomogeneous system of differential is obtained:

$$\frac{D}{Dt}\frac{\partial L}{\partial \dot{q}} - \frac{\partial L}{\partial q} = F \quad (6)$$

Numerical Method

The previous formulation for the displacements is continuous in time and (1D) space. Only some rare problems can be fed into an analytical solution. For most arbitrary cases, solutions have to be found approximatively. Therefore the time and space dependent functions for the displacements are noted in a separation formulation as sum over finite elements

$$q(y,t) \approx \sum_{n=1}^{n_{el}} \left(h(y)_A\,\hat{q}(t)_A + h(y)_B\,\hat{q}(t)_B\right)_n \quad (7)$$

where $h(y)$ is only dependent on space and $\hat{q}(t)$ is only dependent on time. The nodal functions $\hat{q}$ serve as weighting functions for the normed form functions h and deliver the absolute amount of deformation at the element nodes. The functions h determine the form or devolution of the displacement within the element. These spatial functions were chosen linear over the element although there are proposals for

higher order Timoshenko beam elements [23, 7]. Since the fine spatial discretization of the aerodynamic grid will be used for the structure as well, linear functions turned out to be sufficiently accurate for the discussed problem. The negative side effect of shear locking is circumvented by reduced integration.

The finite element formulation is now introduced into the Lagrange density function. After spatial integration over the beam axis variation is performed for the whole equation. Thus leading to a linear system of ordinary differential equations

$$\boldsymbol{M}\ddot{\boldsymbol{Q}} + \boldsymbol{D}\dot{\boldsymbol{Q}} + \boldsymbol{K}\boldsymbol{Q} = \boldsymbol{G} + \boldsymbol{F}^{rot} + \boldsymbol{F} + \boldsymbol{M}^{c}\ddot{\boldsymbol{Q}}^{c} + \boldsymbol{D}^{c}\dot{\boldsymbol{Q}}^{c} + \boldsymbol{K}^{c}\boldsymbol{Q}^{c} = \boldsymbol{F}^{RHS} \tag{8}$$

$\boldsymbol{M}^c$, $\boldsymbol{D}^c$ and $\boldsymbol{K}^c$ are the coefficient matrices of the forced DOF movements, whereas $\ddot{\boldsymbol{Q}}^c$, $\dot{\boldsymbol{Q}}^c$ and $\boldsymbol{Q}^c$ are the accompanying column vectors of the time dependent constraints. Through such constraints cyclic and collective pitch as well as pre-cone and pre-lag are introduced.

This ODE-system is integrated in time by a generalized-α method presented by Chung and Hulbert [4]. This algorithm provides an optimal combination of high frequency and low frequency dissipation. It is implicit, unconditionally stable and of second-order accuracy. By appropriate choice of the underlying parameters it can be transfered into other α-methods like the Hilber-Hughes-Taylor or the Newmark algorithm. It can be further degraded with respect to frequency damping and phase error characteristics into the midpoint rule which still is second-order time-accurate.

3.2 Rotary Wing Aerodynamics

Physical Fluid Model

The three-dimensional, unsteady Euler equations are used to analyse the flow field around the helicopter rotor. They are formulated in a hub attached, non inertial rotating frame of reference with explicit contributions of centrifugal and Coriolis forces.

The computational grid of a rotor blade is supposed to have an arbitrary motion relative to the rotating frame of reference. This is due to the cyclic pitch control as well as to the actual blade degrees of freedom. Thus, the Euler equations are formulated using time invariant body fitted coordinates [2, 21]:

$$\frac{\partial \boldsymbol{\phi}}{\partial \tau} + \frac{\partial \boldsymbol{e}}{\partial \xi} + \frac{\partial \boldsymbol{f}}{\partial \eta} + \frac{\partial \boldsymbol{g}}{\partial \zeta} = \boldsymbol{k} \tag{9}$$

This so-called arbitrary Lagrangian-Eulerian (ALE) formulation allows each grid point to move with a distinct velocity in physical space, relative to the rotating reference system. The vector of the conservative variables, multiplied by the cell volume, is given by

$$\boldsymbol{\phi} = V \cdot (\rho, \rho\bar{u}, \rho\bar{v}, \rho\bar{w}, \bar{\bar{e}}) \tag{10}$$

Here the velocity and energy are given in terms of absolute quantities. Krämer [14] showed that using absolute quantities obviates systematic numerical errors and therefore preserves uniform flow when using a rotating frame of reference. The flux vector components of $\boldsymbol{e}$, $\boldsymbol{f}$, and $\boldsymbol{g}$ as well as the force vector $\boldsymbol{k}$ can be found in [21, 25].

For the finite volume cell-centred scheme, the flow variables are assumed to be constant within the cell. Since their values undergo a variation throughout the flow field, discontinuities arise at the cell boundaries. The evaluation of the fluxes at the cell faces is done by an approximate Riemann solver developed by Eberle [6]. The uniformly high order non-oscillatory (UNO) scheme [10] is used for the spatial discretization.

Geometric Conservation Law

Several sources [22], [5], [26], [15] point out, that the five conservation equations for mass, moment and energy on a moving grid does not automatically lead to a consistent approximation of the fluid flow,

because another numerical scheme – the "geometric conservation law" (GCL) – may not be fulfilled. This additional condition was incorporated in INROT by Hierholz [12], [11]. It is the conservation equation for the cell volume and states, that the volume change per time must equal the volume flux due to the moving cell boundaries. In time invariant body fitted coordinates it reads

$$\frac{\partial V}{\partial \tau} + \frac{\partial u_g}{\partial \xi} + \frac{\partial v_g}{\partial \eta} + \frac{\partial w_g}{\partial \zeta} = 0 \tag{11}$$

Here, V means the cell volume and $\boldsymbol{v}_g = (u_g, v_g, w_g)^T$ the grid velocity.

Since the cell volumes V are known geometric values, solely the grid velocities are the remaining entities to fulfill the GCL. Now it becomes clear, that the simple choice of grid deformation velocities which stem from external structure mechanic models might not determine the cell face velocities in a satisfying manner. But even these velocities can be obtained in a theoretically justified way if they are constructed with the known grid point positions at the actual and some former time steps.

Wake Capturing with Chimera Technique

The comprehensive simulation of multi-bladed rotors in forward flight has to take into account the reciprocal influence of the blades. The various blades affect themselves through their wakes, generated when lift is produced. Especially in flight situations with little down-wash like low-speed level flight or descend flight the rotor blades strongly interact with their own wake system. In such cases the distinct vortices of the flow field have to be resolved.

One possible approach is to implicitly capture the wake of a helicopter rotor by use of a sufficiently large computational domain which is able to resolve and transport the complete wake without further modelling. A separate grid is wrapped around each rotor blade. The individual blade grids are placed inside a base grid which covers the entire computational domain. The embedded grids exchange information at their boundaries with the base grid and hence with each other. Figure 2 shows the grid configuration of a five-bladed *Hughes 500* helicopter rotor.

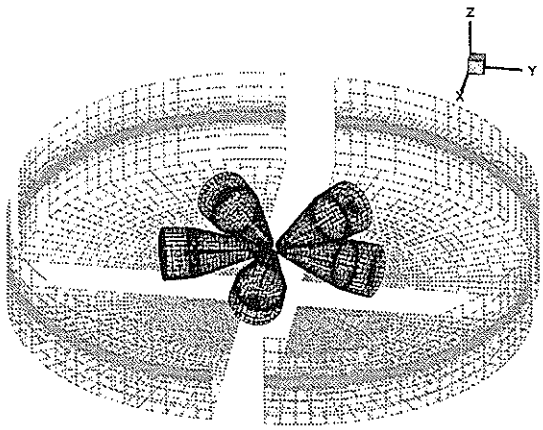

Figure 2: Chimera grids

The Chimera technique was incorporated in the flow solver INROT by Stangl [21]. Due to the large number of grid-points the computing time increases accordingly. Furthermore, additional time is needed for the search of transfer cells in the various grids. In order to minimize the required computing time, INROT was parallelized for shared memory architectures [25]. Each of the grids shown in Figure 2 is assigned to a processor. In order to achieve a good load balancing the base grid is divided into separate blocks, each with approximately the same number of grid points as the blade grids.

4 Fluid Structure Coupling

In very simple and small-scale structural problems the coupled system can be solved in a way that combines the fluid and structural equations of motion into one single formulation. This monolithic set of differential equations describes the fully coupled fluid structure system as a unity. However, we have to deal with the nonlinear Euler equations. The governing equations for the structure may be linear or non linear. It has been pointed out in [15] that the simultaneous solution of these equations by a monolithic scheme is in general computationally challenging, mathematically suboptimal and from the point of software development unmanageable.

Alternatively, the fluid structure coupling can be accomplished by partitioned procedures [3], [8], [15], [18]-[20], [24]. The fluid and structure partitions are processed by different programs with interactions only due to external input of boundary conditions, provided at synchronisation points. In the meantime the fluid and the structure evolves independently, each one of them using the most appropriate solution technique. This approach offers several appealing features, including the ability to use well-established solution methods within each discipline, simplification of software development efforts, and preservation of software modularity.

The exchange of boundary conditions – surface forces to the structural code and blade motion to the fluid solver – is best done consistent within the integration schemes used. Therefore, integrating from time level t^n to t^{n+1}, the implicit flow solver INROT is provided with boundary conditions at time level t^{n+1}. The implicit dynamic solver DYNROT obtains exchange data from time level t^{n+1} as well, but updates the structure consistently with a half time-step positive offset from $t^{n+1/2}$ to $t^{n+3/2}$. This is done by applying the above mentioned time integration method transforming it by appropriate parameter choice into the midpoint rule. An advantage of the midpoint rule is, that it allows the consistent construction, and not just the extrapolation of the structure displacement q at t^{n+1} with the structure state $Q = (q, \dot{q})^T$ at $t^{n+1/2}$

$$q^{n+3/2} = q^{n+1/2} + \frac{\Delta t}{2}(\dot{q}^{n+1/2} + \dot{q}^{n+3/2}) \tag{12}$$

$$\Longleftrightarrow \quad q^{n+3/2} - \frac{\Delta t}{2}\dot{q}^{n+3/2} = q^{n+1/2} + \frac{\Delta t}{2}\dot{q}^{n+1/2} \equiv q^{n+1}$$

Piperno proved in [19] that the inconsistent treatment of boundary conditions reduces the accuracy of the coupled system and eventually deteriorates the stability limit. Following his methodology Hierholz showed in [11] that 2nd order accuracy in time is maintained for the complete aeroelastic method using the depicted implicit-implicit staggered procedure.

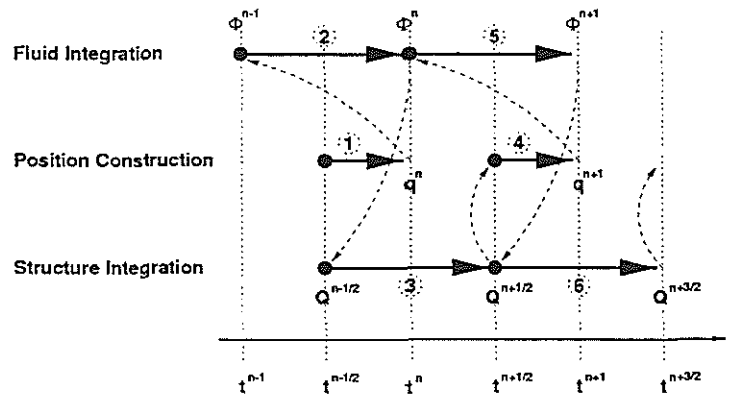

Figure 3: Implicit-implicit partitioned procedure

5 Results

5.1 Validation of Structure Method

The structure model was validated on numerous test cases. One shall be presented here, which is especially suited for rotor blade calculations. This test case described by Harris [9] gives an analytical function for the rotor flap bending deflection at realistic forward flight conditions and satisfies the boundary conditions of a pinned free beam. It is dependent on the azimuthal position of the blade and the radial position on the blade. This function is inserted in the governing differential equation for flap-wise bending of a rotating beam (e.g. see [13]) and the correlated aerodynamic force distribution is analytically derived.

Equivalently, the deflection function can be inserted into the differential equation for lag-wise bending [13]:

$$\rho A\ddot{u}_1 + EI_{33}\overset{\text{IV}}{\breve{u}}_1 - \frac{1}{2}\rho A\omega^2(R^2 - y^2)\breve{u}_1 + \rho A\omega^2 y\breve{u}_1 - \rho A\omega^2 u_1 = p_1 \tag{13}$$

As the given function for the blade deflection represents a pinned free beam, Coriolis forces would agitate rigid body motion about the lag hinge during simulation. Thus, as the numerical solution evolves during the calculation, it would be no longer comparable to the analytical solution. Therefore an analogous function was built up in order to conform with the boundary conditions of a fixed free beam. This was done by simply dropping the first order radial terms of the amplitude functions of the harmonic series given by Harris, obtaining:

$$\begin{aligned}
\frac{u_1}{R} &= f(\psi, Y) = f(\psi, \frac{y}{R}) \\
&= \cos(0\psi)\left(-\frac{4}{45}Y^{10} + \frac{8}{55}Y^{11} - \frac{2}{33}Y^{12}\right) \\
&+ \cos(1\psi)\left(+\frac{9}{160}Y^5 - \frac{3}{40}Y^6 + \frac{3}{112}Y^7\right) \quad + \sin(1\psi)\left(-\frac{1}{15}Y^5 + \frac{4}{45}Y^6 - \frac{2}{63}Y^7\right) \\
&+ \cos(2\psi)\left(-\frac{1}{30}Y^7 + \frac{1}{20}Y^8 - \frac{7}{360}Y^9\right) \quad + \sin(2\psi)\left(+\frac{1}{40}Y^5 - \frac{1}{30}Y^6 + \frac{1}{84}Y^7\right) \\
&+ \cos(3\psi)\left(-\frac{1}{108}Y^{10} + \frac{1}{66}Y^{11} - \frac{5}{792}Y^{12}\right) \quad + \sin(3\psi)\left(+\frac{1}{32}Y^8 - \frac{7}{144}Y^9 + \frac{7}{360}Y^{10}\right) \\
&+ \cos(4\psi)\left(-\frac{7}{330}Y^{11} + \frac{7}{198}Y^{12} - \frac{7}{468}Y^{13}\right)
\end{aligned} \tag{14}$$

Of course this test case is no longer related to real experiments but serves the purpose of verifying the inplane calculations of the structure code quite well. In consequence the derived analytic function of the resulting external load p_1 for the lagging-case is not a representation of any physical aerodynamic load either.

The underlying differential equations for lag bending and flap bending are based on an Euler beam. Otherwise the presented FEM falls back upon Timoshenko's beam theory. But the blade can be considered as slender so that the differences between both models are expected to be minimal in this case. Figures 4 and 5 confirm that assumption and further prove the accuracy of the structural model.

5.2 Hughes 500: Simulation versus Flight Test

A fully coupled aeroelastic simulation with both methods exchanging the determining boundary conditions at their common physical border, the blade surface, was compared against flight test results. These were gained by Lindert and described in [16]. In particular two measurements on the *Hughes 500* helicopter were chosen for comparison: a hover flight and a 100kt forward flight.

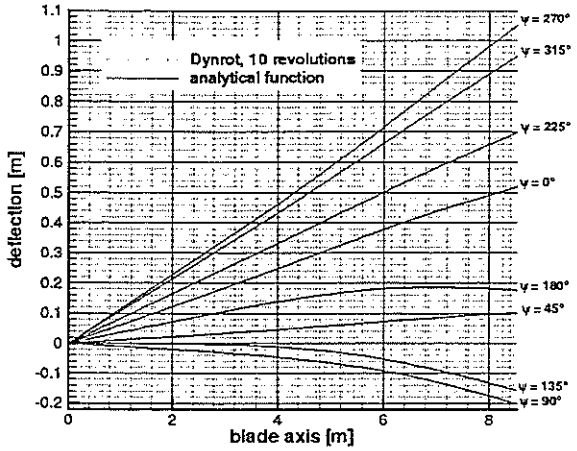

Figure 4: Analytical and numerical flap deflection

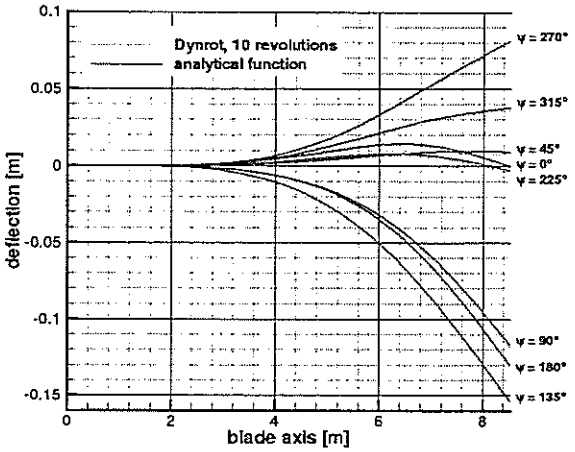

Figure 5: Analytical and numerical lag deflection

For this aeroelastic simulation the isolated rotor was considered fixed in space similar to a wind tunnel situation. The five-bladed Chimera grid system, depicted in figure 2, was used. 49 exchange points were used along thecentre of gravity line [G] of the blade matching the grid point distribution as well as the position of the structure nodes. Thus, any interpolation of boundary conditions was avoided.

The structure model was set up accounting for the special hinge construction of the *Hughes 500* rotor. Here the main rotor blades are connected to the rotor hub by a ball joint. Strap packs carry the centrifugal forces at the hinge, give the necessary high bending stiffness in lag direction and allow an unconfined flap movement. The blade has a rectangular shape and is equipped with a NACA 0015 profile of $0.18m$ chord length. It is linear twisted by $-9°$ and has an overall length of $3.5m$. The relevant parameter of both flight states are summarized in the following table:

		hover	forward flight
rotor radius	$[m]$	4.05	4.05
rotational speed	$[rad/s]$	51.836	51.836
helicopter velocity	$[kt]$	0	100
rotor advance ratio	$[-]$	0	0.25
speed of sound	$[m/s]$	340.4	340.4
rotor shaft angle	$[°]$	0	-4.0

Table 1: Parameter of both test cases

Measurements during this test campaign comprised flap angle β about the hinge but no control angles for collective and cyclic pitch. Therefore these had to be determined by a trim calculation, trimming for the observed flap angle. For the hover case the collective pitch angle has been used as trim parameter, to obtain a flap angle matching with the measured one. In case of the forward flight the triple of collective and both cyclic pitch angles has been trimmed to meet the measured flap angle considered approximately harmonic. The yielded values have been listed in table 2.

In the following the numerical simulations were confronted with the measurements. Additionally the results obtained with the previously described FEM DYNROT are compared with results which were delivered by Hierholz [12] who used the structure code SIMPACK. The latter method is based upon a multi-body-method where the dynamic system is composed of single rigid or elastic bodies,

		hover	forward flight
ϑ_0	[°]	7.3	8.33
ϑ_c	[°]	0.0	1.17
ϑ_s	[°]	0.0	−7.31

Table 2: Trimmed control angles

which are connected via joints. A modal formulation is used for the bending degrees of freedom of the blade which is approximated by a Euler-Bernoulli beam. The DOF's are structure-wise decoupled and torsion is neglected. For lag motion and flap motion the three first elastic modes are used. The rigid body motion about the flap hinge is represented by an additional rigid body mode. The linear system of ODEs is integrated in time by the Newton Method which is explicit and of first order accuracy.

5.2.1 Hover

For the hover test case the span-wise load distribution is presented in figure 6 and the elastic flap deformation is depicted in figure 7. Both are in pretty good agreement with the flight test measurements if one bears in mind, that first during a hover flight in opposite to a wind tunel situation a true steady flight condition can not be attained. Therefore the measurement data has been averaged over the azimuth. Second, air loads have not been gained by recording pressure values. Instead absolute forces have been reconstructed out of measured structural deformation and distributed loads have been derived under the assumption of piece-wise constant loads.

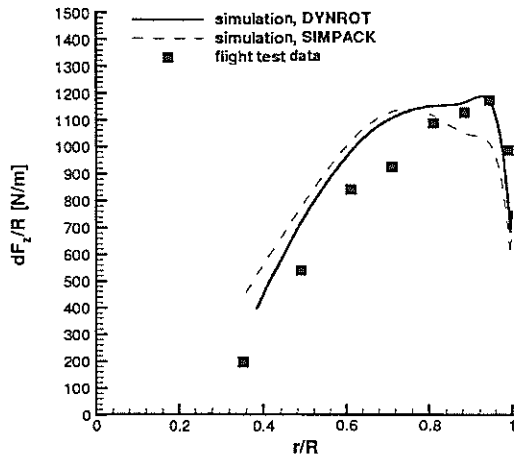

Figure 6: Distributed loads in hover

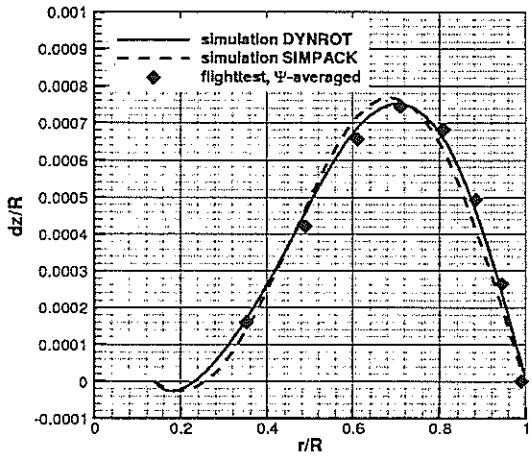

Figure 7: Flap bending deformation in hover

The flap deflection is slightly better represented by the DYNROT calculations. This is due to the included torsional degrees of freedom. A negative torsional moment which is caused by the dynamics of the rotating blade reduces the incidence angle along the blade thus reducing the lift forces especially at the outer diameters and allowing the centrifugal forces to curve the blade a little more.

5.2.2 Forward Flight

For the 100kt forward flight some elastic deformations of flap bending at various azimuth angles can be found in figure 8. Speaking of the elastic deformation a congruence of curvatures with flight test data could not be totally fulfilled. But the results obtained with DYNROT are better than those obtained

with SIMPACK. This is again related to the torsional degrees of freedom. Especially the form of the bending curve towards the blade tip at $\Psi = 315°$ proves that fact, although the line is quantitatively seen quite far away from the measurement values.

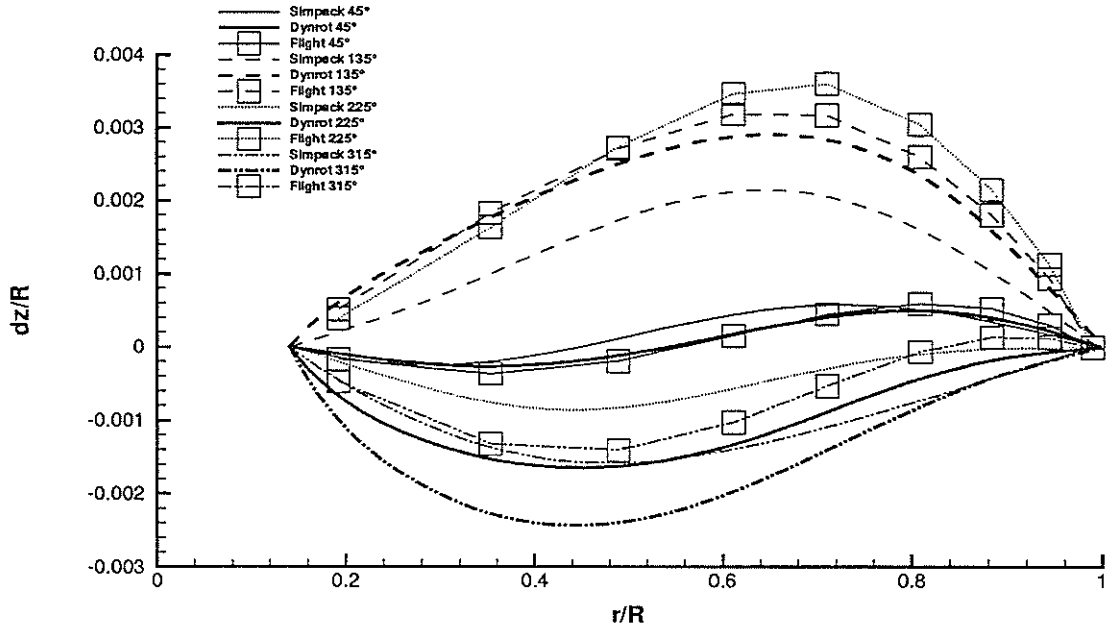

Figure 8: Flap bending deformation in forward flight

Generally, a direct comparison of isolated rotor simulation and flight test data for forward flight has to be handled with utmost care. First, a flight test does not guarantee a precise and well defined test environment as a wind tunnel does. Second, isolated rotor simulations neglect all occurring interaction of rotor flow with the fuselage and tail boom situated underneath.

Some other reasons concern this special test case. On the one hand the rotor shaft angle has not been measured during the flight test. Thus, a more or less reasonable value of $-4°$ had to be estimated. On the other hand the structure model has not been described precisely enough with respect to elastic properties of the blade like moments of inertia and offsets between the relevant axises. Furthermore, eigenfrequencies have only been given for flap bending but not for torsion or lag bending mode shapes. Here some assumptions had to be made as well, in order to construct a consistent structure model. The used properties are presented in table 3.

density	ρ	$[kg/m^3]$	2787.0
sectional area	A	$[m^2]$	$12.3 \cdot 10^{-4}$
Young's modulus	E	$[N/m^2]$	$7.31 \cdot 10^{10}$
shear modulus	G	$[N/m^2]$	$2.50 \cdot 10^{10}$
flap moment of inertia	I_x	$[Nm^2]$	$5.50 \cdot 10^{-8}$
polar moment of inertia	I_t	$[Nm^2]$	$2.68 \cdot 10^{-6}$
lag moment of inertia	I_z	$[Nm^2]$	$2.62 \cdot 10^{-6}$
axis distances from [Q]	x_G, x_S, x_T	$[m]$	0.0

Table 3: Structural properties

6 Conclusions

We presented a simulation method for the aeroelastic analysis of helicopter rotors. It allows to solve the highly demanding task of coupled aeroelastic calculation for any complex layout of multi-bladed helicopter rotors with arbitrary relative blade motion in a transonic, unsteady aerodynamic environment. A highly modular, partitioned approach could be realized using a time-marching staggered coupling scheme.

For the structure dynamics a FEM for a quasi one-dimensional beam based on the Timoshenko's beam theory has been developed for rotating applications. This method is especially suited for aeroelastic calculations, because it offers the possibility to introduce offsets between the aeroelastically relevant axises. Furthermore it enables appropriate control input at arbitrary hinge positions. The underlying ODEs are integrated directly in time by an implicit method of second order.

The fluid domain is described by the Euler equations in an ALE formulation. A finite volume upwind flow solver is used to solve the equations numerically. Inside the aerodynamic computation relative blade motion is gathered with the incorporated chimera technique. With an efficient and robust algebraic three dimensional grid deformation algorithm the elastic deformation of the blades was tracked inside the fluid domain.

Calculations of the aeroelastic behaviour of the five-bladed *Hughes 500* rotor in hover and 100kt forward flight were shown. These included flap bending, lag bending and elastic blade torsion. The results were compared with flight test data and a second coupled method. The importance of including the torsional degrees of freedom has been clearly shown. Excellent agreement of calculation with presented method and the flight test experiments could be shown for hover.

Although the forward flight comparisons have to be carried out with caution, they show a good qualitative and quantitative accordance with the experiment. Finally it has to be pointed out that a most comprehensive descriptions of the structure as it is offered by this new method is superior to a less refined method.

References

[1] Altmikus, A. R. M.: *Dynamikberechnung eines elastischen Rotorblattes unter Verwendung der Timoshenko-Balken-Theorie.* Master Thesis, Institut für Statik und Dynamik der Luft- und Raumfahrtkonstruktionen, Universität Stuttgart, 1998.

[2] Brenneis, A.: *Berechnung instationärer zwei- und dreidimensionaler Strömungen um Tragflügel mittels eines impliziten Relaxationsverfahrens zur Lösung der Eulergleichungen.* Ph.D. Thesis, Institut für Luftfahrttechnik und Leichtbau, Universität der Bundeswehr München, Neubiberg, 1989.

[3] Buchtala, B., Wehr, D. and Wagner, S.: *Coupling of Aerodynamic and Dynamic Methods for the Calculation of Helicopter Rotors in Forward Flight.* 23rd European Rotorcraft Forum, pp. 5.1-5.12, Dresden, September 1997.

[4] Chung, J. and Hulber, G. M.: *A Time Integrateion Algorithm for Structural Dynamics With Improved Numerical Dissipation: The Generalized-α Method.* Journal of Applied Mechanics, vol. 60, pp. 371-375 June 1993.

[5] Demirdzic, I., Peric, M.: *Space Conservation Law in Finite Volume Calculations of Fluid Flow.* International Jounal for Numerical Methods in Fluids, vol. 8, 1037-1050, 1988.

[6] Eberle, A.: *MBB-EUFLEX. A New Flux Extrapolation Scheme Solving the Euler Equations for Arbitrary 3-D Geometry and Speed.* Report MBB-LKE122-S-PUB-140, MBB, Ottobrunn, Germany, 1984.

[7] Friedman, Z. and Kosmatka, J. B.: *An Improved Two-Node Timoshenko Beam Finite Element.* Computers & Structures, vol. 47, no. 3, pp. 473-481, 1993.

[8] Guruswamy, G.P.: *Time-Accurate Unsteady Aerodynamic and Aeroelastic Calculations of Wings using Euler Equations.* AIAA paper 88-2281, 29th AIAA Structures, Structural Dynamics and Materials Conference, Williamsburg, Virginia, April 1988.

[9] Harris, F. D.: *The Rotor Blade Flap Bending Problem - An Analytical Test Case.* Technical Notes, Journal of the American Helicopter Society, pp. 64-67, October 1992.

[10] Harten, J. and Osher, S.: *Uniformly High-Order Nonoscillatory Schemes I.* SIAM Journal on Numerical Analysis, vol. 24, pp. 279-309, 1987.

[11] Hierholz, K.-H.: *Ein numerisches Verfahren zur Simulation der Strömungs-Struktur-Interaktion am Hubschrauberrotor.* Ph.-D. Thesis, Institut für Aerodynamik und Gasdynamik, Universität Stuttgart, 1999.

[12] Hierholz, K.-H. and Wagner, S.: *Simulation of Fluid Structure Interaction at the Helicopter Rotor.* Proceedings of the 21st ICAS Congress, Melboune, Australia, September 13-18, ICAS-98-2.9.4, 1998.

[13] Johnson, W.: *Helicopter Theory.* Princeton University Press, Princeton, New Jersey, 1980.

[14] Krämer, E.: *Theoretische Untersuchungen der stationären Rotorblattumströmung mit Hilfe eines Euler-Verfahrens.* Ph.D. Thesis, Institut für Luftfahrttechnik und Leichtbau, Universität der Bundeswehr München, Neubiberg, 1991.

[15] Lesoinne, M. and Farhat, C.: *Improved Staggered Algorithms for the Serial and Parallel Solution of Three-Dimensional Nonlinear Transient Aeroelastic Problems.* Fourth World Conference on Computational Mechanics, E. Onate and S.R. Idelsohn, editors, Barcelona, Spain, 1998.

[16] Lindert, H.-W.: *Anwendung einer strukturmechanischen Methode zur Rekonstruktion der Luftkräfte am rotierenden Rotorblatt aus Windkanal- und Flugversuchsmeßdaten.* Ph.D. Thesis, RWTH Aachen, VDI-Fortschrittsberichte, Reihe 12, Nr. 245, VDI Verlag, Düsseldorf, 1994.

[17] Nellessen, D. M.: *Schallnahe Strömungen um elastische Tragflügel.* Ph.D. Thesis, RWTH Aachen, VDI-Fortschrittsberichte, Reihe 7, Nr. 302, VDI Verlag, Düsseldorf, 1996.

[18] Park, K.C. and Felippa, C.A.: *Computational Methods for Transient Analysis.* In T. Belytschko and T.J.R. Hughes, editors, *Partitioned analysis of coupled systems*, pp. 157-219, North-Holland Pub. Co., 1983.

[19] Piperno, S., Farhat, C., and Larrouturou, B.: *Partitioned Procedures for the Transient Solution of Coupled Aeroelastic Problems, Part I: Model Problem, Theory and Two-Dimensional Application.* Computer Methods in Applied Mechanics and Engineering, vol. 124, no. 1-2, pp. 79-112, June 1995.

[20] Rausch, R.D., Batina, J.T., and Yang, T.Y.: *Euler Flutter Analysis of Airfoils using Unstructured Dynamic Meshes.* AIAA paper 89-13834, 30th AIAA Structures, Structural Dynamics and Materials Conference, Mobile, Alabama, April 1989.

[21] Stangl, R.: *Ein Eulerverfahren zur Berechnung der Strömung um einen Hubschrauber im Vorwärtsflug.* Ph.D. Thesis, Institut für Aero- und Gasdynamik, Universität Stuttgart, 1996.

[22] Thomas, P.D., Lombard, D.K.: *Geometric conservation law and its application to flow computations on moving grids.* AIAA Jourmal, vol. 17, pp. 1030-1037, 1979.

[23] Tessler, A. and Dong, S.B.: *On a Hierarchy of Conforming Timoshenko Beam Elements.* Computers & Structures, vol. 14, no. 3-4, pp. 335-344, Pergamon Press Ltd. 1981.

[24] Weeratunga, S.K. and Pramono, E.: *Direct Coupled Aeroelastic Analysis through Concurrent Implicit Time Integration on a Parallel Computer.* AIAA paper 94-1550, 35th AIAA Structures, Structural Dynamics and Materials Conference, Hilton Head, South Carolina, April 1994.

[25] Wehr, D.: *Untersuchungen zum Wirbeltransport bei der Simulation der instationären Umströmung von Mehrblattrotoren mittels der Eulergleichungen.* Ph.D. Thesis, Institut für Aero- und Gasdynamik, Universität Stuttgart, 1998.

[26] Zhang, H., Reggio, M., Trepanier, J.Y.: *Discrete Form of the GCL for Moving Meshes and Its Implementation in CFD Schemes.* Computers and Fluids, vol. 22, no. 1, pp. 9-23, 1993.

TWENTYFIFTH EUROPEAN ROTORCRAFT FORUM

Paper n^o G9

FUNDAMENTAL ISSUES RELATED TO THE PREDICTION OF COUPLED ROTOR/AIRFRAME VIBRATION

BY

Hyeonsoo Yeo, Inderjit Chopra
UNIVERSITY OF MARYLAND, COLLEGE PARK, USA

SEPTEMBER 14-16, 1999
ROME
ITALY

ASSOCIAZIONE INDUSTRIE PER L'AEROSPAZIO, I SISTEMI E LA DIFESA
ASSOCIAZIONE ITALIANA DI AERONAUTICA E ASTRONAUTICA

FUNDAMENTAL ISSUES RELATED TO THE PREDICTION OF COUPLED ROTOR/AIRFRAME VIBRATION

Hyeonsoo Yeo* Inderjit Chopra†

Alfred Gessow Rotorcraft Center
Department of Aerospace Engineering
University of Maryland, College Park, MD 20742, U.S.A.

Abstract

A comprehensive vibration analysis of a coupled rotor/fuselage system is carried out using detailed 3-D finite element models of the AH-1G airframe from the DAMVIBS program. Predicted vibration results are compared with Operational Load Survey flight test data of the AH-1G helicopter. Modeling of difficult components(secondary structures, doors/panels, etc) is essential in predicting airframe natural frequencies. Calculated 2/rev vertical vibration levels at pilot seat show good correlation with the flight test data both in magnitude and phase, but 4/rev vibration levels show fair correlation only in magnitude. Lateral vibration results show more disagreement than vertical vibration results. Accurate prediction of airframe natural frequencies up to about 38Hz(7/rev) appears essential to predict vibration in airframe. Second order nonlinear terms have an important effect on the prediction of vibration at high speed and high frequency. Third order kinetic energy terms generally have small influence(about 7% change) on the prediction of vibration.

Introduction

As helicopter crew and passenger comfort has gained increased emphasis, vibration requirements have become more stringent [1]. Even though there has been enormous progress with vibration suppression technology [2], cost and weight penalty has been excessive in part because of inadequate vibration prediction capability. To minimize the additional cost and weight penalty, accurate vibration prediction is necessary at the early design stage.

Even though considerable progress has been made to improve the mathematical analysis of rotors during recent years, reliable and accurate vibration prediction is still a challenging problem. In a recent validation study using the Lynx helicopter flight loads, it was found that most comprehensive analysis codes exhibit significant errors of as much as 60 percent from the measured vibratory loads [3]. Various analytical technologies were applied to evaluate their effects on vibration predictions. Of all the technologies, free wake models have been shown to have a dominant influence on vibration predictions at both low and high speed conditions([3] - [5]).

Airframe dynamics is also important in the prediction of helicopter vibration. NASA-Langley carried out a Design Analysis Methods for VIBrationS(DAMVIBS) program to establish the technology for accurate and reliable vibration prediction capability during the design of a rotorcraft [6]. Four major helicopter manufacturers(Bell, Boeing, former McDonnell Douglas, and Sikorsky) actively participated in this program. Systematic modeling and analysis techniques were investigated for the four technology areas: airframe finite element modeling, modeling refinements for difficult components(secondary structures, doors/panels, engine, fuel, transmission, cowlings, fairings, etc), coupled rotor-airframe vibration analysis, and airframe structural optimization. All participating companies developed state-of-the-art finite element models for the airframe, conducted ground vibration tests, and carried out comparisons of their predictions with test data. During this program, they improved the finite element modeling capability of both metal

* Research Associate, Member AHS
† Alfred Gessow Professor and Director, Fellow AIAA, Fellow AHS

Presented at the 25th European Rotorcraft Forum, Rome, Italy, September 14-16, 1999.

and composite airframes. In conventional finite element modeling of an airframe, only the primary load carrying structures were represented in terms of their mass and stiffness characteristics, and the secondary structures were represented only as lumped masses. Comparison of predicted frequencies with measured values showed that agreement is less satisfactory above about 20 Hz with conventional modeling. The study identified the critical role of difficult components for vibration prediction. It was shown that a detailed finite analysis of the airframe that included the effects of difficult components could predict frequencies with a deviation of less than 5% of measured values for modes with frequency up to 35Hz [7].

Under the DAMVIBS program, the four helicopter companies also applied their own methods to calculate the vibrations of the AH-1G helicopter, and correlated the predictions with an Operational Load Survey(OLS) flight test data. Most of the analyses were unable to predict vibration accurately for all flight conditions. These studies pointed out that the coupled rotor-fuselage vibration analysis should be improved in order to be useful for the design and development of a rotor-airframe system.

During the last two decades, coupled rotor-fuselage vibration analyses have been developed by many researchers using a variety of assumptions and solution methods (see reviews by Reichert [2], Loewy [8] and Kvaternik, et al. [9]). Simplified investigations such as those reported in Refs. [10] - [13] have made significant contributions to the understanding of the basic characteristics of rotorcraft vibration but are not sufficient for accurate predictions. Most analyses also incorporated highly idealized aerodynamics. For example, in Ref. [14] a coupled rotor/flexible fuselage model was developed for vibration reduction studies using 3-D fuselage. However, this analysis incorporated idealized aerodynamics such as uniform inflow and quasisteady aerodynamics so that vibration was substantially underpredicted. Helicopter vibration is due to the higher harmonic airloading of the rotor, thus nonuniform induced velocities caused by blade vortices can be a key factor in the prediction of vibration.

Recently, the present authors carried out a comprehensive vibration analysis of a coupled rotor/fuselage system incorporating refined aerodynamic models such as free wake and unsteady aerodynamics [15]. Predicted vibration results were compared with Operational Load Survey flight test data of the AH-1G helicopter. Modeling requirements for the vibration analysis of complex helicopter structures and rotor-fuselage coupling effects were identified. The importance of refined aerodynamic modeling was also addressed.

The non-linear equations of motion of a coupled rotor/airframe are quite involved. Often, an ordering scheme is used to systematically neglect higher order terms in the equations. Normally, third order terms(ϵ^3 terms) are neglected in rotor aeromechanic analyses, so that equations are manageable and retain enough accuracy. Many aeroelastic analyses of a rotor blades are focused to solve the aeromechanical stability that includes the calculation of blade steady periodic response and stability of linearized perturbation motion. These phenomena involve low frequency and retention of second order terms appears adequate. There are a few exceptions where higher order terms are included. For example, Crespo da Silva and Hodges [16], [17] derived equations of motion of a rotor blade retaining terms up to order of ϵ^3 and investigated equilibrium and stability of a uniform cantilevered rotor blade in hover. They emphasized the importance of higher order terms in the prediction of the behavior of blades with low torsional stiffness and at high thrust level. For aeromechanical stability, the rigid body modes appear adequate and the flexibility of fuselage is not considered. Since vibration analysis involves coupled rotor/fuselage equations, the modeling of both blades as well as airframe becomes important Since high frequency modes are involved in the vibration analysis, it may be possible that higher order terms may become important.

In this paper, the effect of higher order terms(especially third order) on the prediction of vibration is investigated. Since there are too many third order terms involved in the equations of motion, only higher order kinetic energy terms are investigated. Parametric studies are also conducted to examine the influence of several key factors on the prediction of vibration of a rotorcraft.

Vibration Analysis

The baseline rotor analysis is taken from UMARC(University of Maryland Advanced Rotorcraft Code). The blade is assumed to be an elastic beam undergoing flap bending, lag bending, elastic twist, and axial deformation. The analysis for a two-bladed teetering rotor is formulated and incorporated into UMARC. The elastic rotor coupled equations include six hub degrees of motion. The rotor vibratory loads are

transmitted to the fuselage through the hub and the effects of fuselage motion are included in the determination of blade loads.

The derivation of the coupled rotor/fuselage equations of motion are based on Hamilton's variational principle generalized for a nonconservative system.

$$\delta\Pi = \int_{t_1}^{t_2} (\delta U - \delta T - \delta W)\, dt = 0 \qquad (1)$$

δU is the variation of the elastic strain energy, δT is the variation of the kinetic energy, and δW is the work done by nonconservative forces which are of aerodynamic origin. The contributions to these energy expressions from the rotor blades and fuselage may be summed as

$$\delta U = \left(\sum_{b=1}^{N_b} \delta U_b\right) + \delta U_F \qquad (2)$$

$$\delta T = \left(\sum_{b=1}^{N_b} \delta T_b\right) + \delta T_F \qquad (3)$$

$$\delta W = \left(\sum_{b=1}^{N_b} \delta W_b\right) + \delta W_F \qquad (4)$$

where the subscripts b and F refer to the blade and fuselage respectively and N_b is the total number of rotor blades. For example, the variation of the kinetic energy for the bth blade is expressed as

$$\frac{\delta T_b}{m_0 \Omega^2 R^3} = \int_0^R m(T_{u_e}\delta u_e + T_v \delta v + T_w \delta w + T_{\hat{\phi}}\delta\hat{\phi} + T_{v'}\delta v' + T_{w'}\delta w' + T_F)\, dx \qquad (5)$$

The equation of motion for the teetering degree of freedom of a two-bladed rotor is obtained from the equilibrium of the flap moment about the teeter hinge.

The 3-dimensional NASTRAN finite element models of the AH-1G helicopter are used in the coupled rotor/fuselage vibration analysis. The airframe modal data(eigenvalues, eigenvectors, and generalized masses) are generated using NASTRAN and are used as an input to the coupled rotor/fuselage vibration analysis program. The couplings between rotor and fuselage are included in a consistent manner into UMARC.

Blade response equations, teetering motion equation, and fuselage response equations are solved simultaneously. To reduce computational time, the finite element equations are transformed into the normal mode space. Because the fuselage is in the fixed frame, the analysis is carried out in the fixed frame by transforming the rotor equations using a multiblade coordinate transformation. The nonlinear, periodic, coupled rotor/fuselage equations are solved using a finite element method in time.

Fuselage Models

First, the elastic line airframe structural modeling capability was incorporated into UMARC. The fuselage is discretized as an elastic beam using the same 15 degree-of-freedom beam element as that used for the rotor blade. Elastic line model of the AH-1G helicopter is shown in Figure 1. 39 beam elements are used in modeling main fuselage, tailboom, wing, and main rotor shaft. Second, the 3-D NASTRAN finite element model of the AH-1G helicopter airframe developed in the mid 1970s, shown in Figure 2, is included into UMARC. It consists of structural elements such as scalar springs, rods, bars, triangular and quadrilateral membranes. The total number of elements is 2965. The main rotor pylon is modeled as an elastic line using bar elements. The main rotor pylon(Figure 5) provides the structural tie between the main rotor and the fuselage. It is attached to the fuselage through the elastomeric mounts and a lift link. The lift link is the primary vertical load path and is very stiff in the vertical direction. The elastomeric mounts are designed to produce low pylon rocking frequencies to isolate the main rotor in-plane vibratory loads from the fuselage and to balance the main rotor torque. This model was used for the coupled rotor/fuselage vibration analysis to correlate with Operational Load Survey flight test data in the DAMVIBS program. Third, a modified 3-D finite element model of the AH-1G helicopter including effects of difficult components is included into UMARC. The earlier 3-D finite element model was modified by Bell Helicopter to achieve better correlation of natural frequencies with test data. These updates included replacement of the original elastic line tailboom with a built-up rod and shear panel tailboom and inclusion of fastened panels, doors, and secondary structure in the forward fuselage. However, this model could not be used directly for the validation study because the overall weight of the test vehicle was different from that of a OLS flight test vehicle. So, the NASTRAN model was modified to convert it to the OLS test configuration by updating the weight of fuel, ammunition, etc. The final refined 3-D airframe model is shown in Figure 3. The total number of finite elements used in this study is 4373. A comparison of NASTRAN and test natural

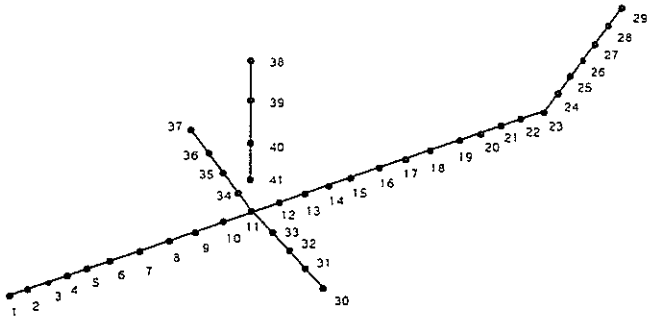

Fig. 1 Elastic line fuselage Model

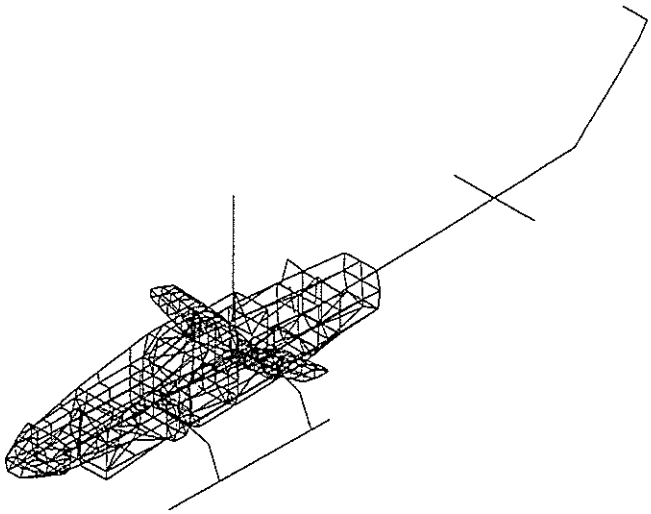

Fig. 2 3-dimensional finite element fuselage Model

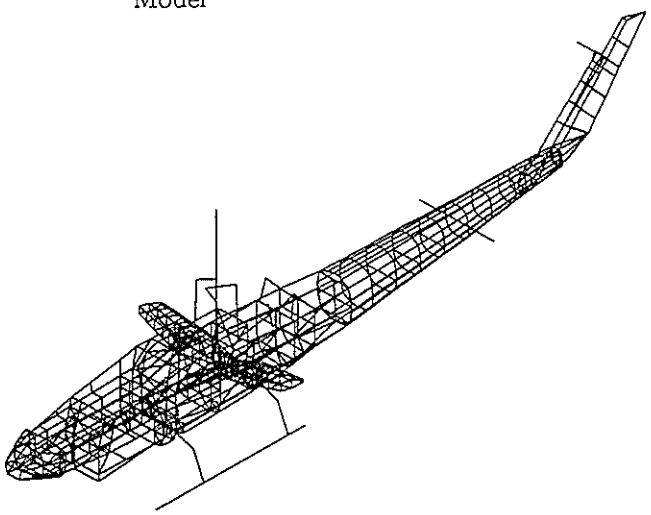

Fig. 3 Refined 3-dimensional finite element fuselage Model

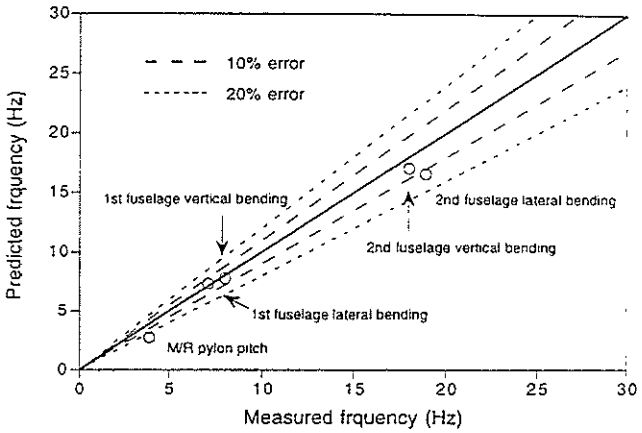

(a) Elastic line fuselage

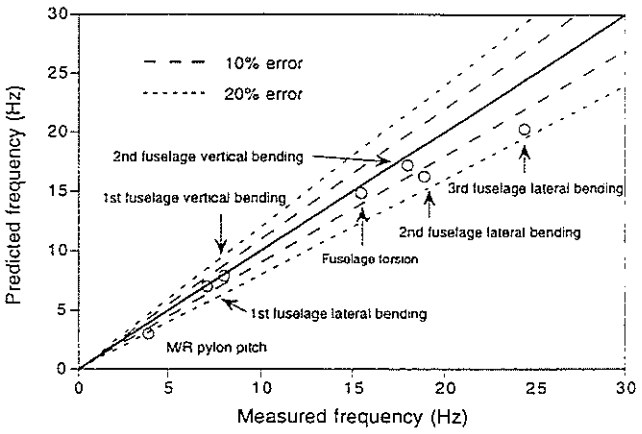

(b) 3-D fuselage

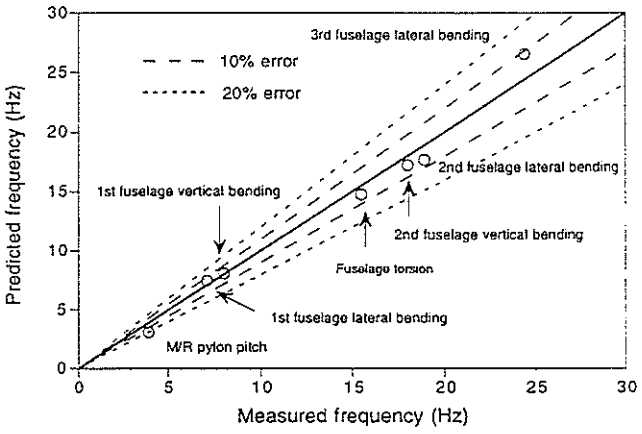

(c) Refined 3-D fuselage

Fig. 4 Frequency diagram

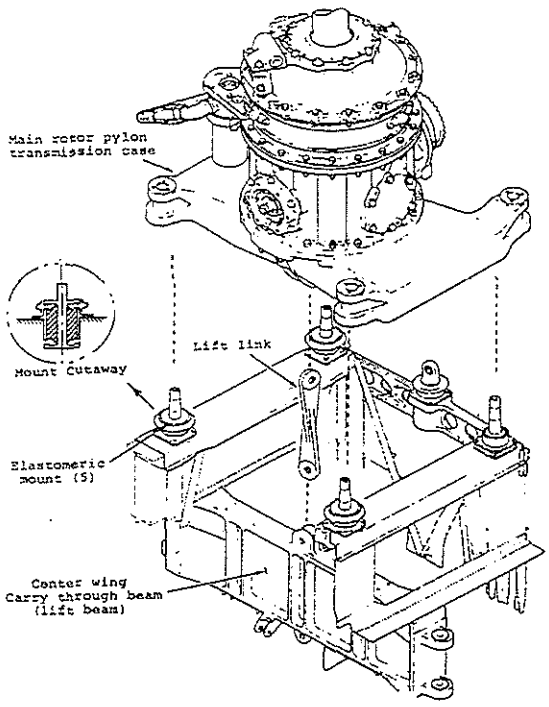

Fig. 5 Main rotor pylon of AH-1G helicopter

frequencies is presented in Figures 4. The diagonal line represents perfect match between predictions and test data. Percentage error bandwidths are included to indicate trends in correlation. The elastic line model shows fair correlation up to 20 Hz. But, fuselage torsion and third fuselage lateral bending modes cannot be found within the frequency range up to 30 Hz. 3-D fuselage model shows fair agreement with test data except for the second and third fuselage lateral bending modes. With the modeling of difficult components, the natural frequency correlation at the higher frequencies is improved from 20% error to less than 10% error for up to 30 Hz. In particular, the improvement of fuselage lateral bending frequencies is noticeable.

Results and Discussion

The two-bladed teetering rotor of the AH-1G helicopter and its NASTRAN airframe model are used to calculate vibratory hub loads and vibration levels at the pilot seat. Coupled rotor/fuselage equations are solved in straight and level flight conditions. Estimated vibration results are compared with OLS flight test data of the AH-1G helicopter. Detailed blade properties and test results are in Ref. [18]. For the calculation of inflow and blade loads, a pseudo-implicit free wake model [19] and a time-domain unsteady aerodynamics [20] are incorporated. The effects of compressibility(Prandtl-Glauert correction) and reversed flow are also included in the aerodynamic model. For normal mode analysis, thirty airframe modes(which covers frequencies up to 40 Hz(7.4/rev)) are used. Eight time elements with fifth order shape functions are used along the azimuth to calculate the coupled periodic response.

Effect of fuselage modeling

Vertical vibration levels at the pilot seat are presented in Figure 6 with airspeeds ranging from 67 knots to 142 knots. There is a good agreement of the magnitude of vibration level between predictions and test values and only slight differences exist between 3-D fuselage and refined 3-D fuselage results. Rotor/fuselage coupling reduces 2/rev vertical vibration by more than 50% and has a small effect on 4/rev vibration. Estimation of vertical vibration with the elastic line model has a negligible effect on 2/rev vibration, but underpredicts 4/rev vibration. Lateral vibration levels at the pilot seat are shown in Figure 7. Since there was a more scatter in the prediction of fuselage lateral bending frequencies from measured values among fuselage models, significant improvement in the calculated lateral vibration levels was expected with modeling refinements. Estimation of 2/rev lateral vibration with the elastic line model shows large deviation from test results. However, the elastic line model shows fair correlation of 4/rev vibration. Lateral vibration levels with refined 3-D fuselage model are larger than those with regular 3-D fuselage model. Refined model improves somewhat correlation of 2/rev vibration but, correlation becomes worse for 4/rev vibration. Both models overpredict 4/rev vibration.

Correlation of phase

For a systematic validation study of predicted vibration, both magnitude and phase of the hub loads should be compared. Hub vibratory loads, however, were not measured in the OLS flight test. Hence predicted vibration vectors(magnitude and phase) are correlated with measured vibration vectors.

Figures 8 and 9 show the effect of fuselage modeling on the phase of vibration at 101 knots. 2/rev vertical vibration results, shown in Fig. 8(a),

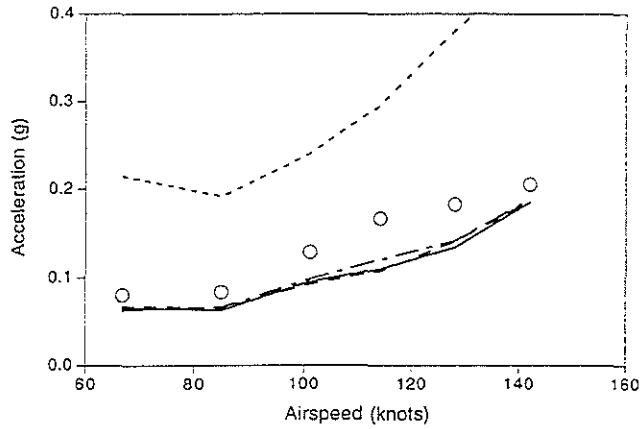

(a) 2/rev vertical vibration

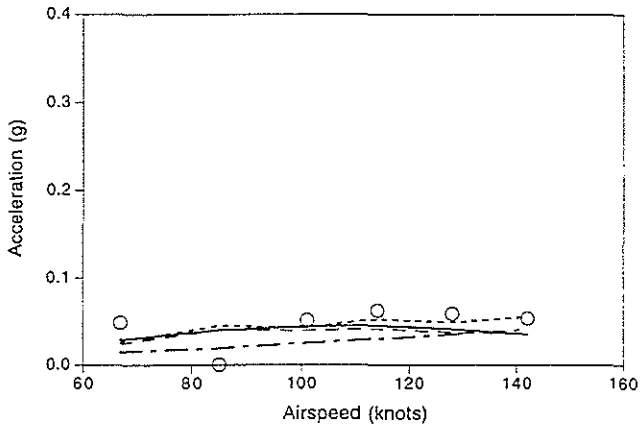

(b) 4/rev vertical vibration

Fig. 6 Vertical vibration level at pilot seat

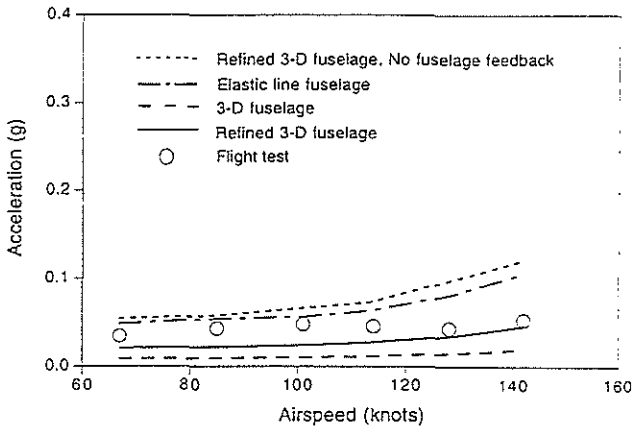

(a) 2/rev lateral vibration

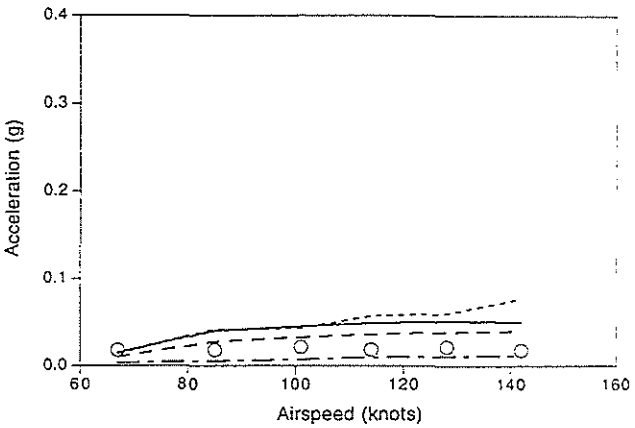

(b) 4/rev lateral vibration

Fig. 7 Lateral vibration level at pilot seat

show that detailed structural modeling helps to improve the correlation of phase angle even though the magnitude is unchanged. The effect of difficult component modeling on the phase of this component is negligible. 2/rev lateral vibration estimated using elastic line model shows a significant difference in both magnitude and phase from those using the detailed models(Fig. 9(a)). Significant difference of phase between an elastic line model and detailed airframe models is also observed in the 4/rev vibration. 4/rev lateral vibration results, shown in Fig. 9(b), show that difficult component modeling has an influence on the phase of this vibration component, and changes the phase angle by 9 degrees.

Predicted and measured vibration vectors(magnitude and phase) are correlated using refined 3-D fuselage model for three different speeds(67, 101, and 142 knots) which respectively represent low speed, moderate speed, and high speed flight conditions. The 2/rev vertical vibration result, shown in Figure 10(a), shows good correlation for both magnitude and phase at low and moderate speeds. At high speed, there is significant phase difference(about 20 degrees) between predicted and measured values. The 4/rev vertical vibration result, shown in Figure 10(b), shows considerable deviations for all speeds. For low frequency vibration, vertical hub loads seem to be modeled accurately up to moderate speed and fuselage model appears adequate in the vertical direction. The difference of 2/rev vibration at high speed is probably due to hub loads since the fuselage model is not expected to change with speed. For high frequency vibration, both hub loads and fuselage model may have errors. There is a large deviation in predicted and measured phase angles.

Figure 11(a) shows 2/rev lateral vibration result. Even though there is more disagreement

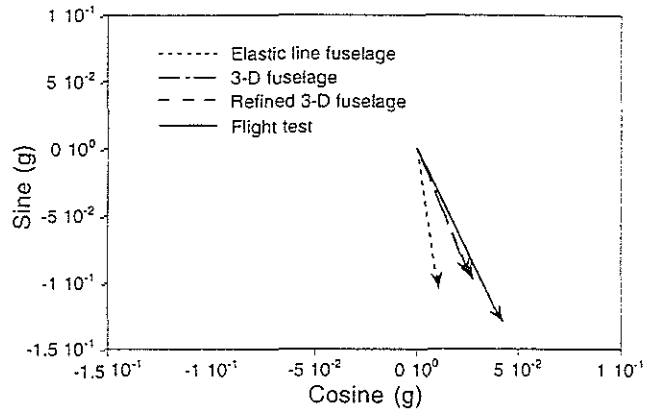

(a) 2/rev component

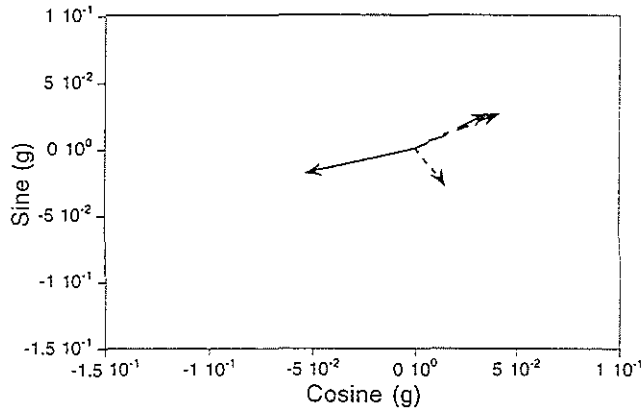

(b) 4/rev component

Fig. 8 Effect of airframe modeling on vertical vibration at pilot seat at 101 knots

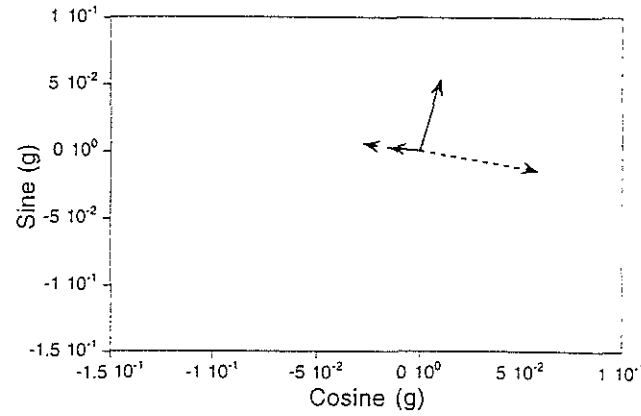

(a) 2/rev component

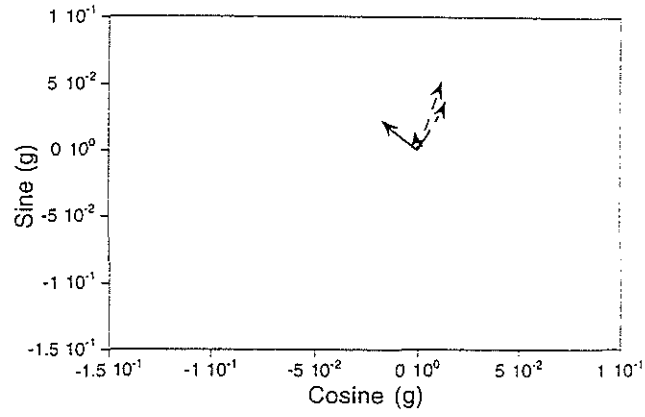

(b) 4/rev component

Fig. 9 Effect of airframe modeling on lateral vibration at pilot seat at 101 knots

between measured and calculated results than corresponding 2/rev results in the vertical direction, the trends appear quite consistent. Estimation shows the same phase angle at 67 and 101 knots as observed in the flight test data. At 142 knots, the test data shows a phase shift but the prediction does not show such a change. The measured phase difference at high speed differed about 19 degrees from those at low and moderate speeds. In Figure 11(b), 4/rev lateral vibration results show good correlation at low speed and the difference between predictions and test data increases with speed.

Contribution of airframe modes

The contribution of different airframe natural modes to vibration at the pilot seat is investigated next for a better understanding of airframe dynamics and its role in the prediction of helicopter vibration. Figures 12 through 19 show contributions of different airframe modes in vertical and lateral vibration at the pilot seat at 101 knots. Both a refined 3-D fuselage model and old 3-D fuselage model are used for the calculation of vibration. The contribution of each mode is presented in terms of magnitude of vibration nondimensionalized by the total vibration at the prescribed frequency.

Figure 12 shows that only four low frequency modes (M/R pylon pitch and roll, and 1st and 2nd fuselage vertical bending) have a dominant effect on the prediction of 2/rev vertical vibrations. The contribution of the M/R pylon pitch mode is due to the longitudinal hub force excitation. The contribution of fuselage vertical bending modes (primarily first and second modes) shows that the effect of vertical hub force on the pilot seat vibration is about 20% of total level. The dominant effect of M/R pylon roll mode (about

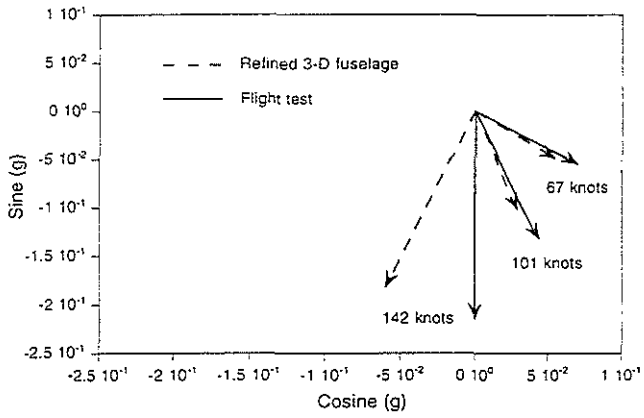

(a) 2/rev vertical vibration

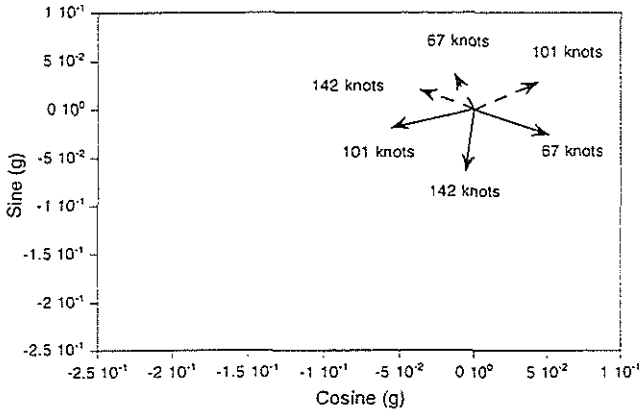

(b) 4/rev vertical vibration

Fig. 10 Vertical vibration at pilot seat

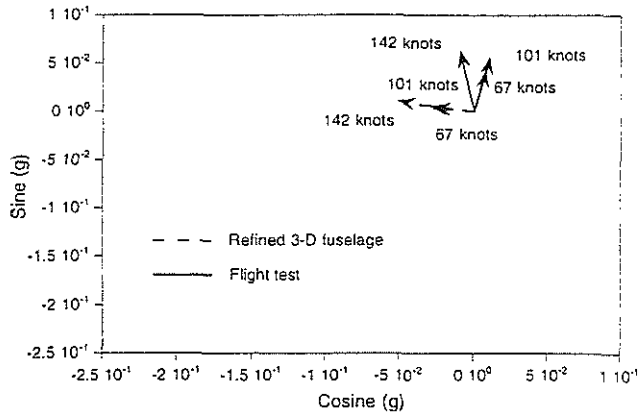

(a) 2/rev lateral vibration

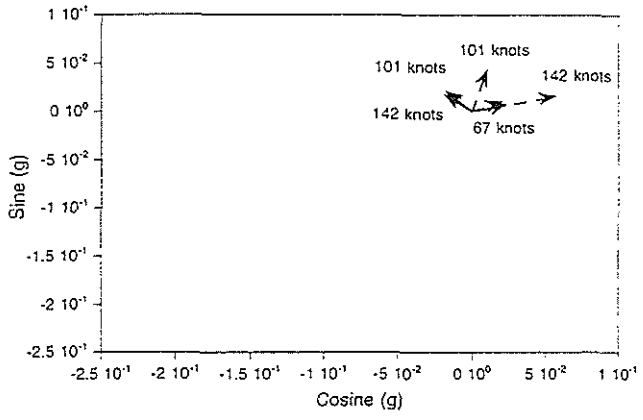

(b) 4/rev lateral vibration

Fig. 11 Lateral vibration at pilot seat

40%), which is related to the lateral motion, on 2/rev vertical vibration shows that the coupling between modes may have an important influence on vibratory response. For this roll mode, the vertical deflection at the pilot seat has almost same magnitude as the lateral deflection at this position. Thus, lateral hub force produces large vertical vibration as well as lateral vibration. Figure 13 shows 2/rev vertical vibration using an old 3-D NASTRAN model. Again, the main rotor pylon roll mode has the most dominant effect on the prediction of 2/rev vertical vibration. However, its contribution to total vibration is reduced to about 30% compared to 40% in the refined 3-D fuselage model. The contribution of pylon pitch mode remains same at about 18%. The contributions of 3rd fuselage vertical bending and main rotor mast fore-and-aft (F/A) bending modes increase to twice compared to those of the refined 3-D fuselage model.

For the 4/rev vertical pilot seat vibration prediction using a refined airframe model, shown in Figure 14, several modes have similar contributions and most of them are high frequency modes. Since there is more error in the prediction of high frequency modes, prediction of vibration at this frequency is likely to be less accurate. The coupling between modes can be clearly seen in this 4/rev vibration too. The contribution of M/R mast lateral bending and 3rd fuselage lateral bending modes to the 4/rev vertical vibration shows that lateral hub force produces vertical vibration and its contribution is also important. The modes whose frequencies are above 33 Hz (6/rev) have a negligible effect on the vertical vibration. Figure 15 shows 4/rev vertical vibration at pilot seat at 101 knots using an old 3-D NASTRAN model. Main rotor mast F/A bending and 3rd fuselage vertical bending modes have a dominant effect on this vibration. Unlike the refined 3-D fuselage model which shows the important effect of 3rd fuselage lateral bending

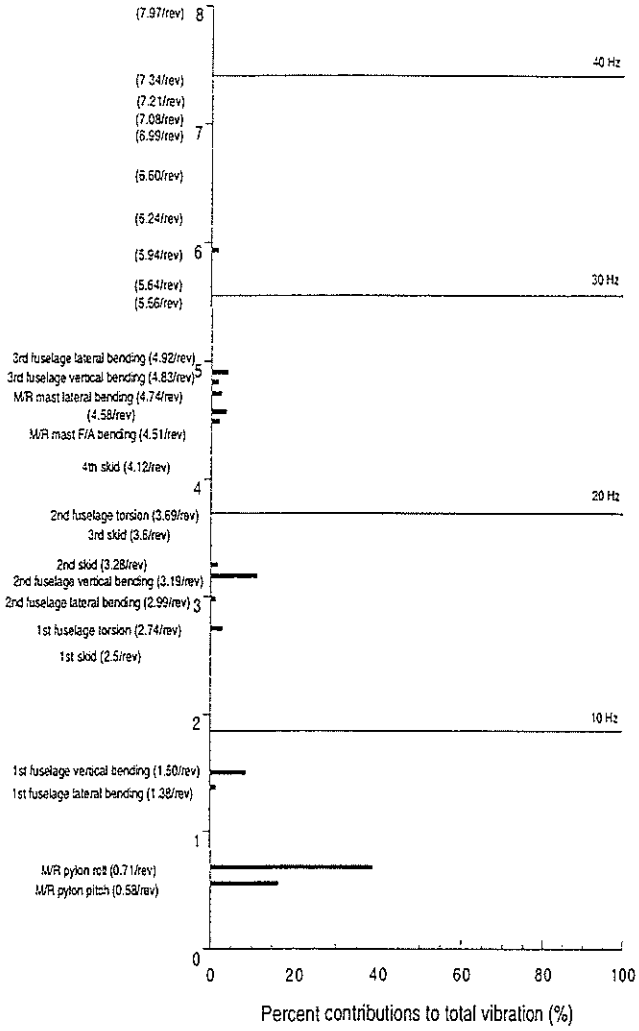

Fig. 12 Contribution of refined 3-D airframe natural modes to 2/rev vertical pilot seat vibration at 101 knots

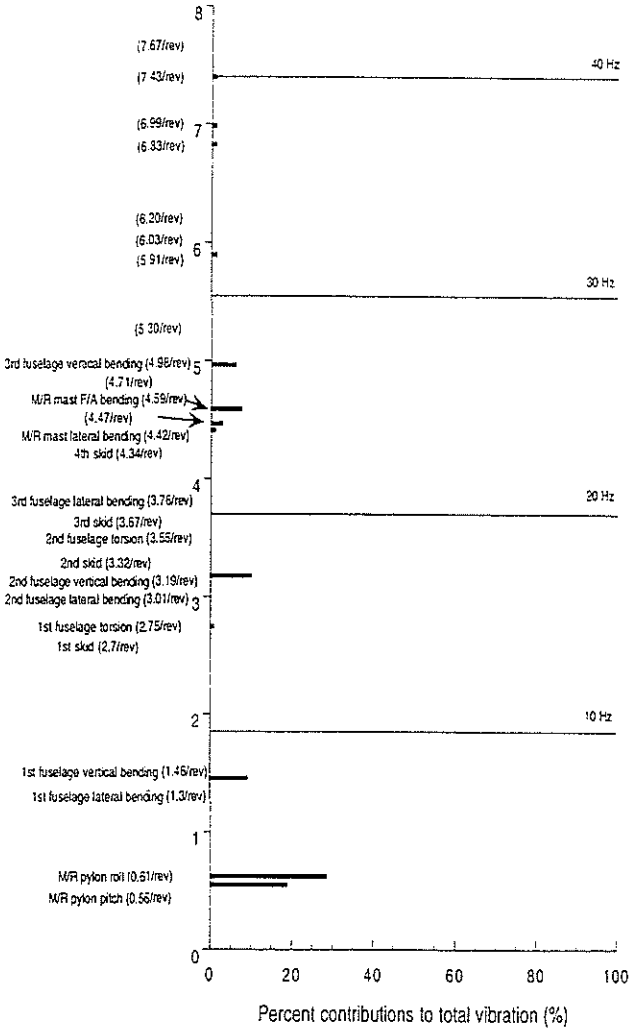

Fig. 13 Contribution of old 3-D airframe natural modes to 2/rev vertical pilot seat vibration at 101 knots

mode on the prediction of 4/rev vertical vibration, an old 3-D fuselage model does not show such a coupling effect. The modeling of difficult components appears to produce the coupling between modes.

As shown in Figure 16, the M/R pylon roll mode of a refined airframe model has a dominant effect on the prediction of 2/rev lateral vibration at the pilot seat. High frequency modes such as M/R mast lateral bending and 3rd fuselage lateral bending modes also have an important influence on the low frequency vibration. For an old airframe model(Fig. 17), M/R pylon roll, 2nd fuselage lateral bending, and M/R mast lateral bending modes have almost same contribution on the prediction of 2/rev lateral vibration.

For the 4/rev lateral pilot seat vibration prediction, shown in Fig. 18, high frequency modes have a larger influence and the contribution of the low frequency modes is small. The lateral vibration due to longitudinal and vertical hub forces is small. For the prediction of the lateral vibration, airframe modes whose frequencies are up to 38 Hz(7/rev) should be included. 4/rev lateral vibration results using an old 3-D airframe model, shown in Figure 19, show a dramatic difference from those using a refined 3-D fuselage model. M/R mast lateral bending mode of a 3-D fuselage has a significant contribution (about 50%) and 3rd fuselage lateral bending mode has an important contribution (about 10%) on the prediction of 4/rev lateral vibration. Compared to a refined 3-D fuselage model, the contribution of M/R mast lateral bending mode increases by more than 2.5 times and the contribution of 3rd fuselage lateral bending mode reduces by less than half. This shows that the airframe modeling appears to cause

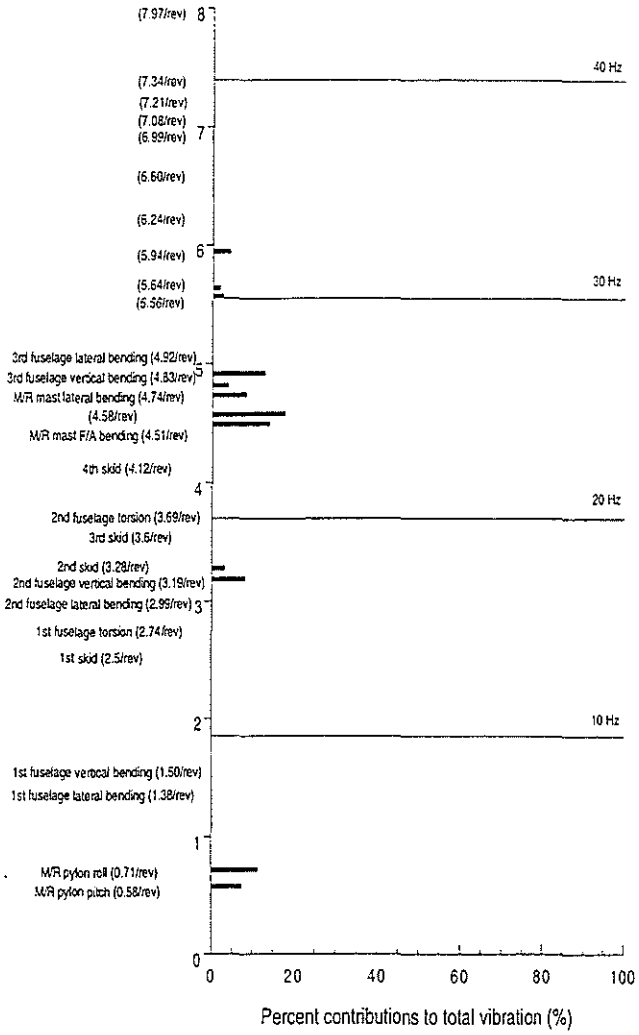

Fig. 14 Contribution of refined 3-D airframe natural modes to 4/rev vertical pilot seat vibration at 101 knots

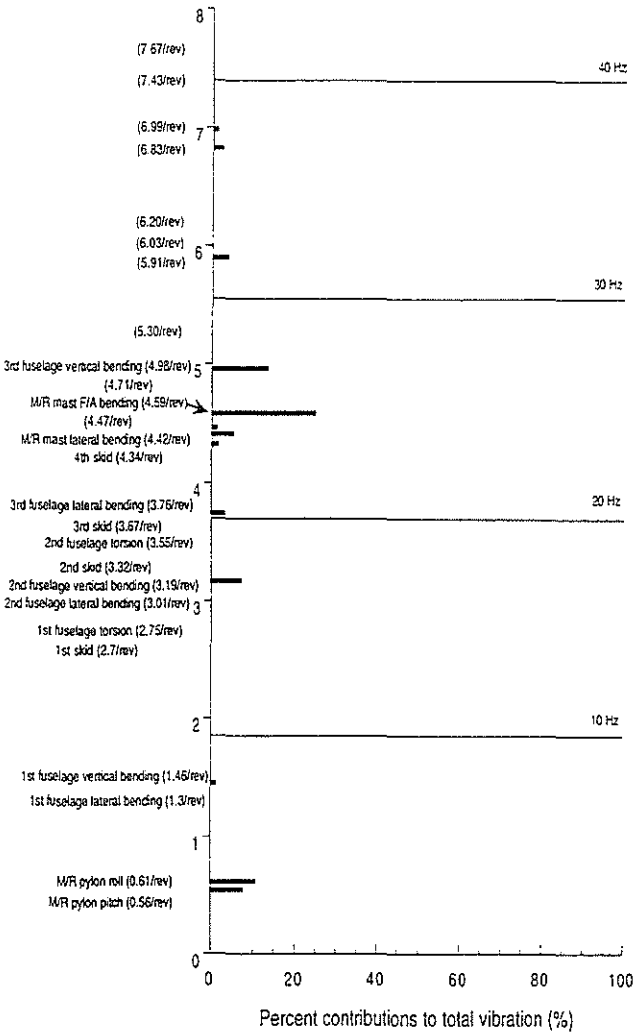

Fig. 15 Contribution of old 3-D airframe natural modes to 4/rev vertical pilot seat vibration at 101 knots

the differences of both magnitude and phase of the 4/rev lateral vibration prediction between two airframe models (Figure 9(b)). For the accurate prediction of vibration using 3-D fuselage model, airframe modes whose frequencies are up to 40 Hz (7.4/rev) should be included. This is similar to the conclusion with the refined 3-D fuselage.

Effect of Aerodynamic Coefficient

The section lift, drag, and pitching moment coefficients used in the present analysis are expressed as

$$C_l = c_0 + c_1\alpha \tag{6}$$

$$C_d = d_0 + d_1|\alpha| + d_2\alpha^2 \tag{7}$$

$$C_m = f_0 + f_1\alpha = c_{m_{ac}} + f_1\alpha \tag{8}$$

where $c_0, c_1, d_0, d_1, d_2, c_{m_{ac}}$, and f_1 are airfoil section coefficients. The effects of these coefficients on the prediction of vibration at pilot seat are investigated. The baseline and modified values of these coefficients are given in Table 1. The

Table 1 Aerodynamic coefficient variation

	Baseline value	Modified values	
c_0	0.0	0.05	0.1
c_1	6.16	5.7	6.28
d_0	0.0068	0.0	0.01
d_1	0.0	0.1	0.3
c_{mac}	0.0	-0.01	0.01
f_1	0.0	-0.1	0.1

zero angle pitching moment coefficient, c_{mac}, has the most dominant effect on the prediction of vibration among aerodynamic coefficients and the effects are shown in Figures 20 and 21. Negative pitching moment coefficient increases

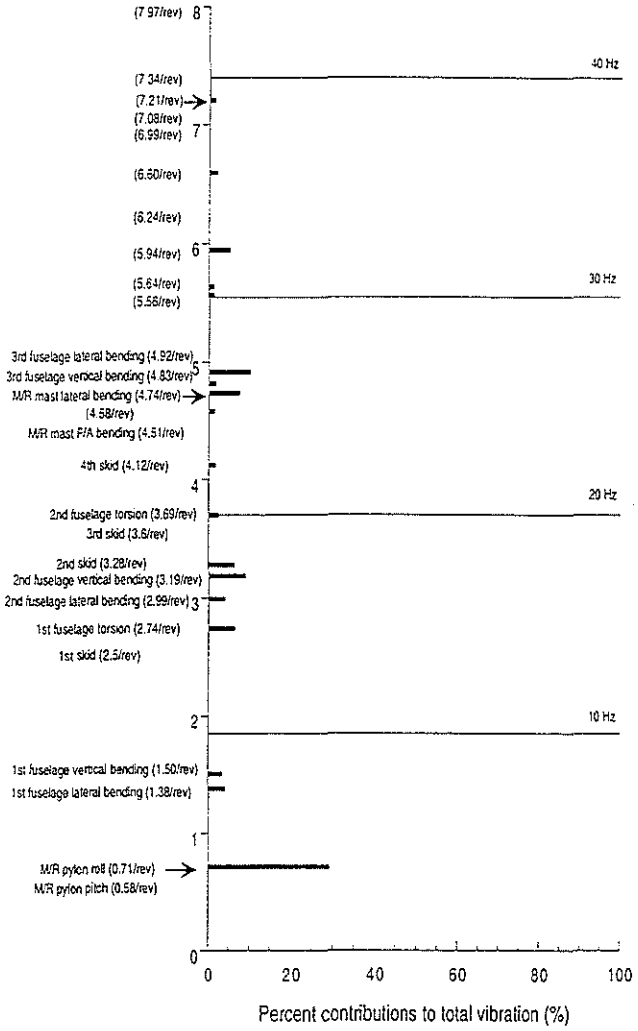

Fig. 16 Contribution of refined 3-D airframe natural modes to 2/rev lateral pilot seat vibration at 101 knots

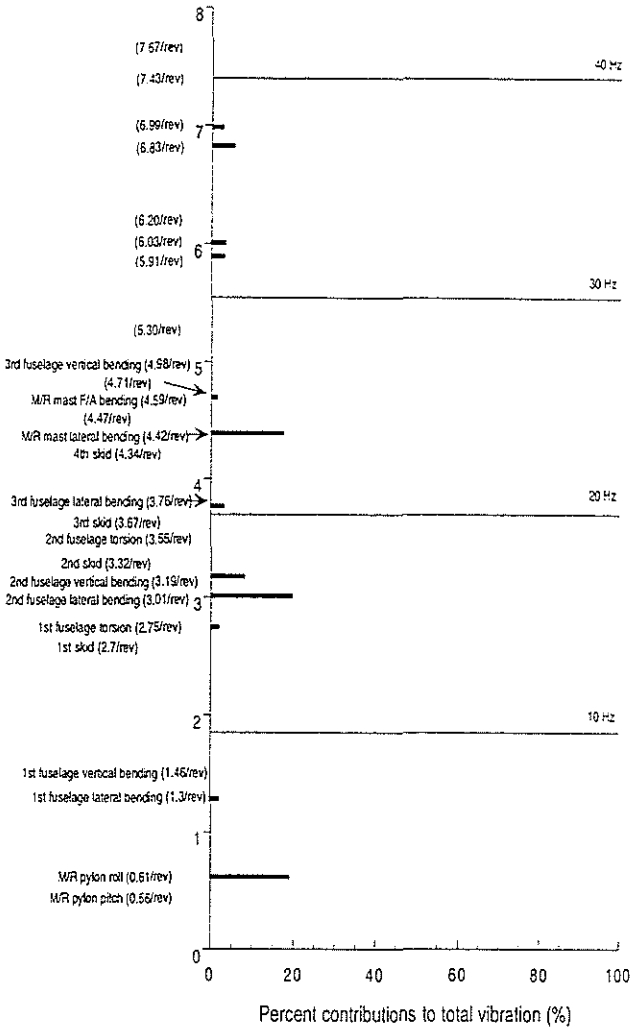

Fig. 17 Contribution of old 3-D airframe natural modes to 2/rev lateral pilot seat vibration at 101 knots

the magnitude of 2/rev vertical vibration level and slightly improves the correlation with test data. However, the difference of phase with test data increases. Negative pitching moment coefficient reduces 4/rev vertical and 2/rev lateral vibration and has a small effect on the phase of these vibrations. Pitching moment coefficient has a large influence on the phase of 4/rev lateral vibration (Figure 21(b)). Modified pitching moment coefficients change the phase by 15 degrees and negative pitching moment coefficient improves the correlation of phase with test data.

Effect of second order nonlinearities

Figures 22 and 23 represent 2/rev and 4/rev vertical vibration levels at the pilot seat respectively. First, second order structural and aerodynamic terms are neglected. Second, only second order aerodynamic terms are included. Third, only second order structural terms are included. And fourth, all second order nonlinear terms are included. Second order nonlinear terms have more influence on the prediction of vibration at high speed and high frequency. Second order nonlinear terms increase the magnitude of 2/rev vertical vibration by 5% and change the phase by 4 degrees at 142 knots. Nonlinear terms have a significant effect on both magnitude and phase of 4/rev vertical vibration. Second order nonlinear terms decrease the magnitude of 4/rev vertical vibration by about 60% and change the phase by almost 70 degrees. Figures 24 and 25 represent 2/rev and 4/rev lateral vibration levels at the pilot seat respectively. Especially nonlinear terms have an important influence on both magnitude and phase of 4/rev lateral vibration. Second order nonlinear terms decrease the magnitude of 4/rev

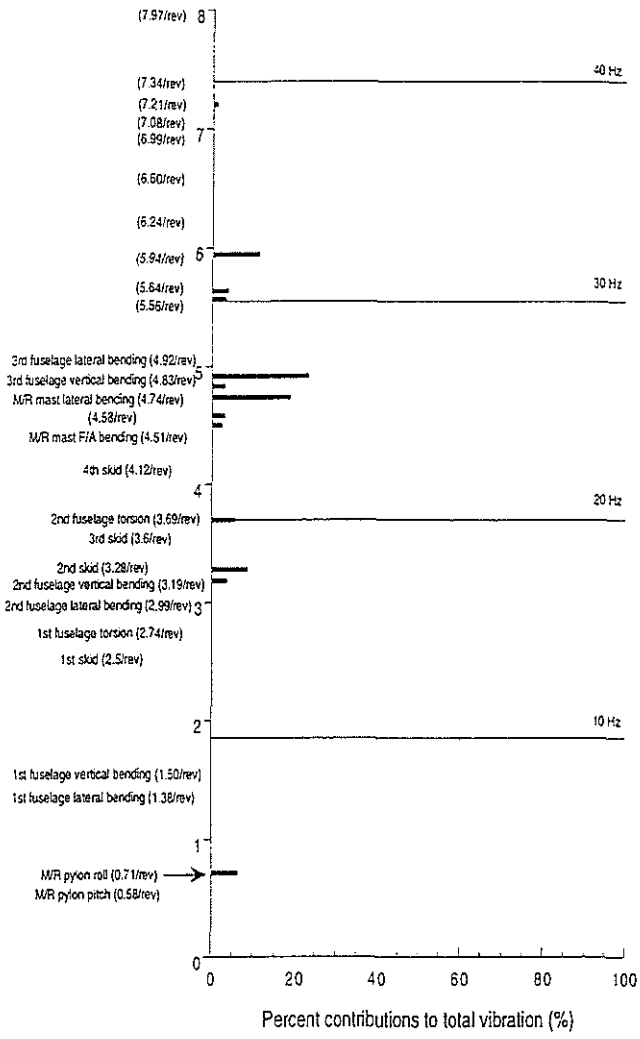

Fig. 18 Contribution of refined 3-D airframe natural modes to 4/rev lateral pilot seat vibration at 101 knots

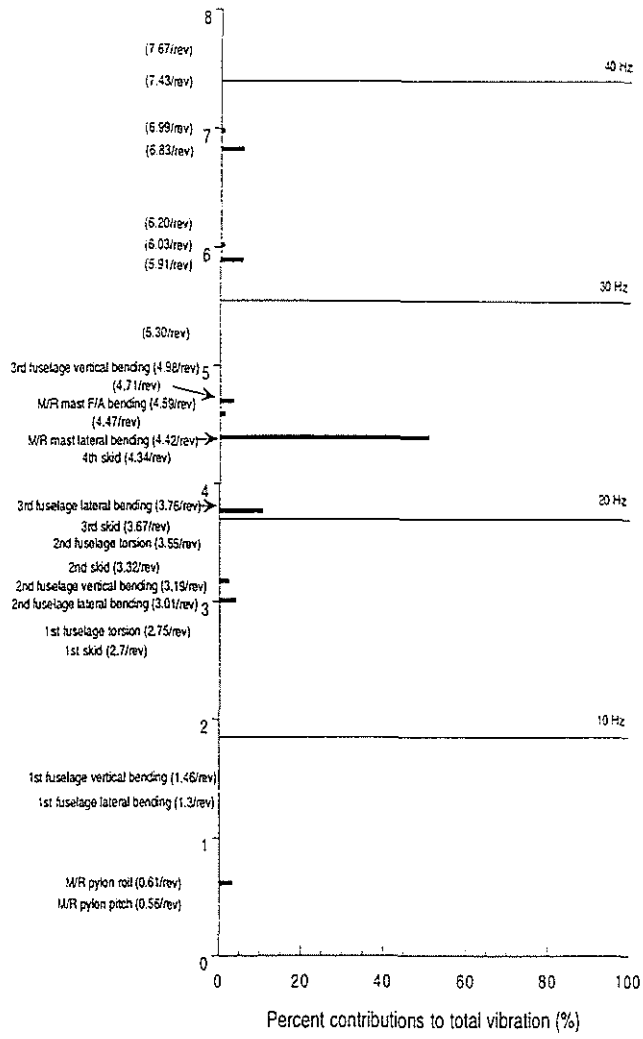

Fig. 19 Contribution of old 3-D airframe natural modes to 4/rev lateral pilot seat vibration at 101 knots

lateral vibration by 65% and change the phase 35 degrees at 142 knots.

Effect of third order kinetic energy terms

Kinetic energy of a blade retaining terms up to third order($O(\epsilon^3)$) is derived and then higher order terms are selectively included in the equations of motion to examine their effect separately. Table 2 shows third order kinetic energy terms investigated. When each term is added in the blade equation, its effect on the fuselage is also included.

Figure 26 shows the effect of third order terms on the magnitude of vibration at the pilot seat. Since higher order terms have negligible influence on the 2/rev vibration level, only 4/rev vibration results at 142 knots($\mu = 0.32$) are shown. Magnitude change of acceleration in the vertical direction is calculated as follows

$$\frac{\|\ddot{z}_{F(Case\ i)} - \ddot{z}_{F(Baseline)}\|}{\ddot{z}_{F(Baseline)}} \times 100 \qquad (9)$$

Baseline vibration level is calculated using terms up to second order. Generally, third order kinetic term has a very small effect on the prediction of vibration(less than 1%). Linear lag-torsion coupling term(Case 3) changes 4/rev vertical vibration by 4.3% and linear flap-torsion coupling terms(Case 14 and 15) change 4/rev lateral vibration by 7.6% and 5.9% respectively. Figure 27 represents the effect of third order terms on the phase of 4/rev vibration at the pilot seat. Third order linear flap-torsion coupling term(Case 14) changes phase angle of 4/rev vertical vibration by 7 degrees and third order linear lag-torsion coupling term(Case 3) changes phase angle of 4/rev vertical vibration by 5.3 degrees. The other

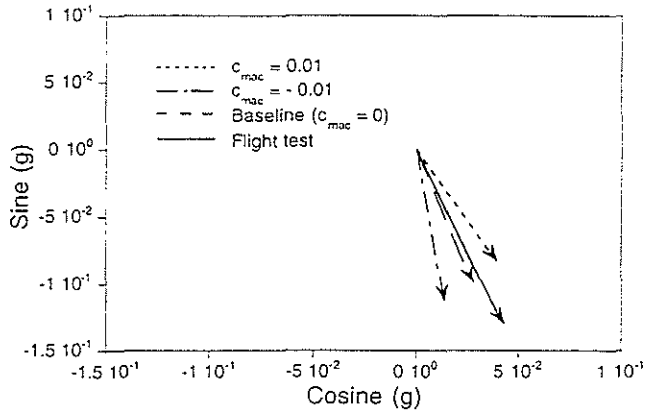

(a) 2/rev vertical vibration

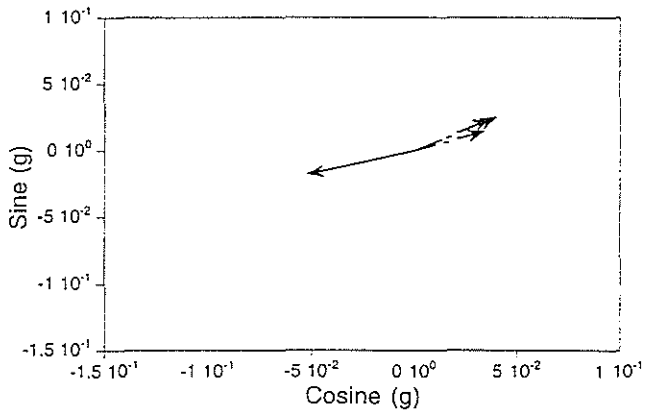

(b) 4/rev vertical vibration

Fig. 20 Effect of zero angle pitching moment coefficient (c_{mac}) on vertical vibration at pilot seat at 101 knots

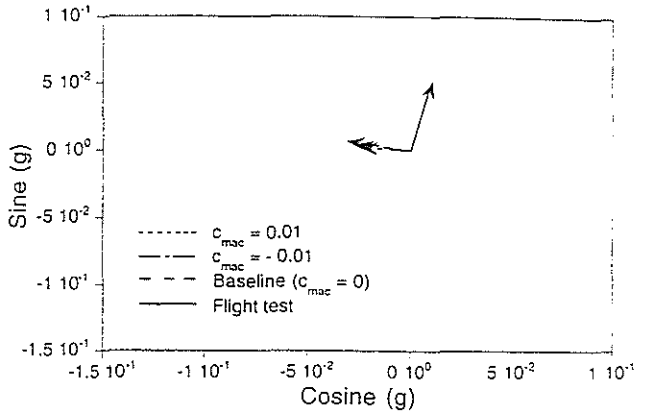

(a) 2/rev lateral vibration

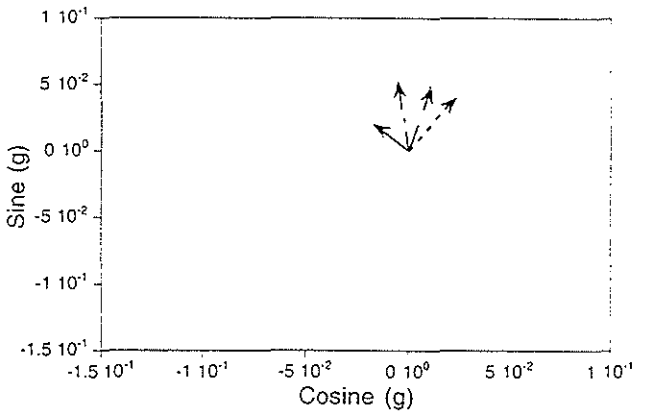

(b) 4/rev lateral vibration

Fig. 21 Effect of zero angle pitching moment coefficient (c_{mac}) on lateral vibration at pilot seat at 101 knots

terms have a negligible effect on the phase of 4/rev vertical vibration. For the 4/rev lateral vibration, all higher order terms have a small effect.

Figure 28 shows the consolidated effect of third order kinetic energy terms on the 4/rev vibration. Third order kinetic energy terms decrease the magnitude of 4/rev vertical vibration by about 7% and change the phase by 10 degrees. Their effects on the lateral vibration are smaller than those on the vertical vibration because the effects of Case 14 and Case 15 are canceled out.

Conclusions

From the validation and parametric studies, the following conclusions are obtained.

1. Modeling of difficult components is important for the accurate prediction of airframe natural frequencies, especially for high frequency modes.

2. The correlation between calculated 2/rev vertical vibration at the pilot seat and measured data shows good agreement in both magnitude and phase, except at high speed where the phase discrepancy is as large as 20 degrees.

3. Estimated 4/rev vertical vibration at the pilot seat shows good correlation with test data only in magnitude. At 142 knots, there is a phase deviation of 115 degrees.

4. The correlation of 2/rev lateral vibration at the pilot seat is generally fair(less than 0.02g difference), while calculated 4/rev lateral vibration is overpredicted at all speeds(maximum 0.03g).

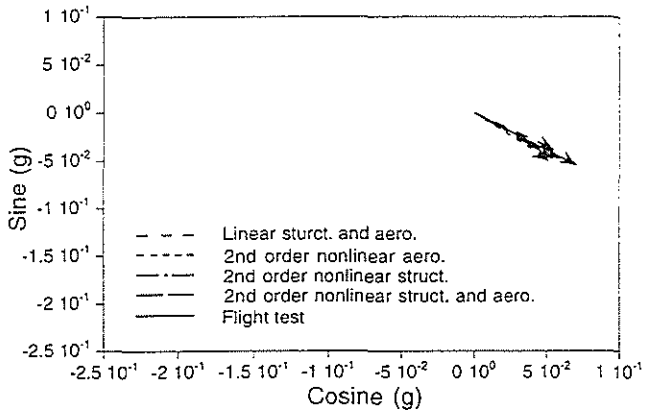

(a) 67 knots

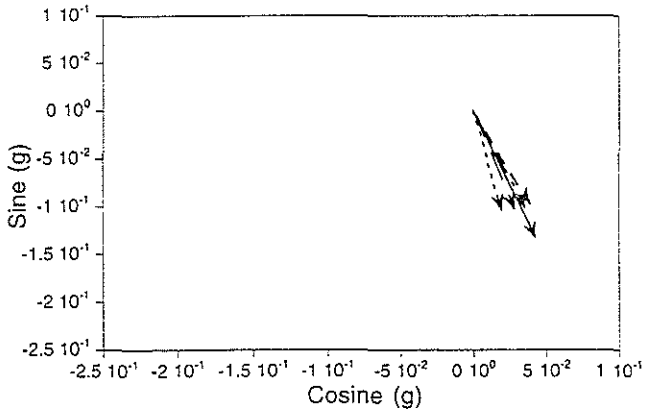

(b) 101 knots

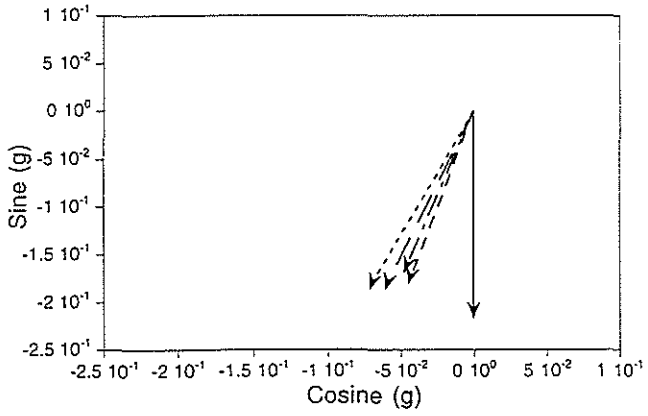

(c) 142 knots

Fig. 22 Effect of second order nonlinearity on 2/rev vertical vibration

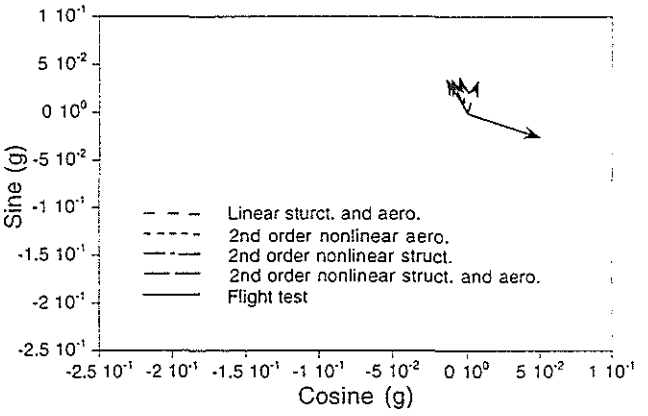

(a) 67 knots

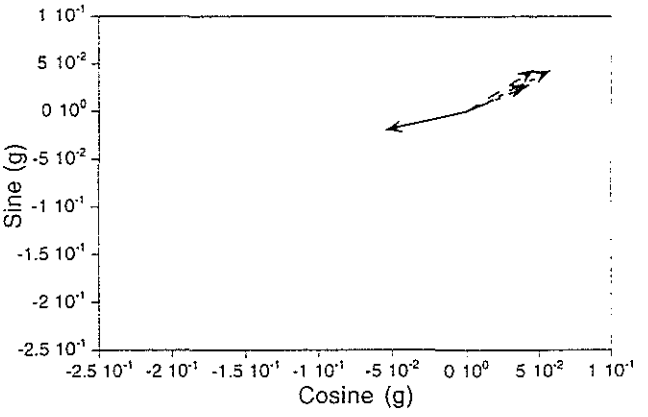

(b) 101 knots

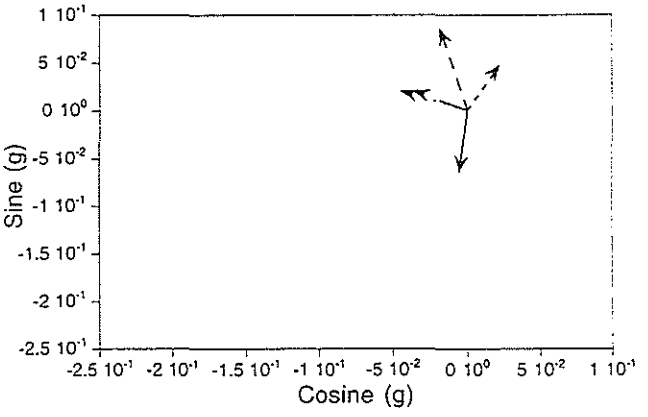

(c) 142 knots

Fig. 23 Effect of second order nonlinearity on 4/rev vertical vibration

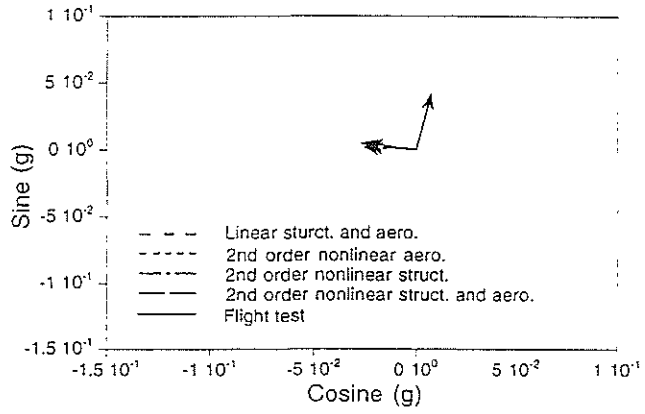

(a) 67 knots

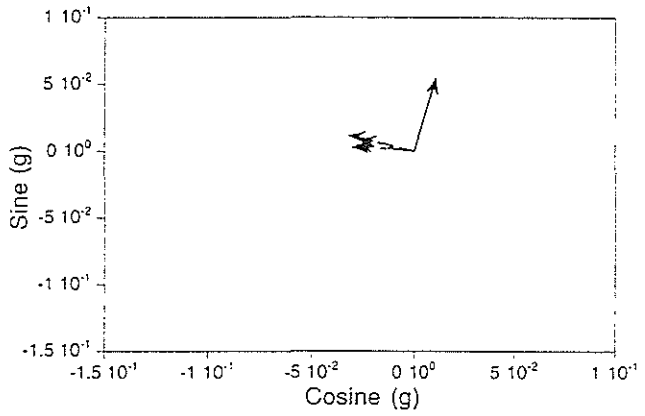

(b) 101 knots

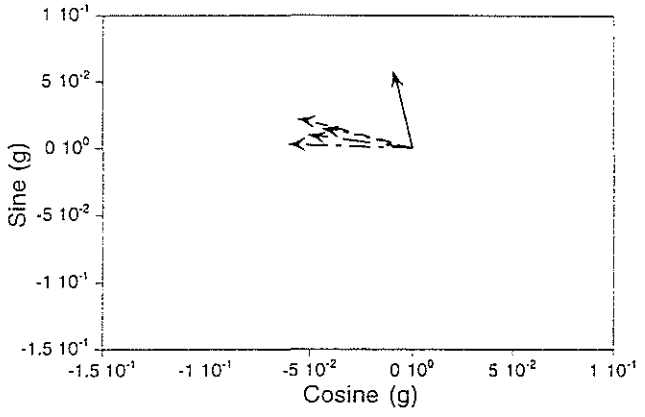

(c) 142 knots

Fig. 24 Effect of second order nonlinearity on 2/rev lateral vibration

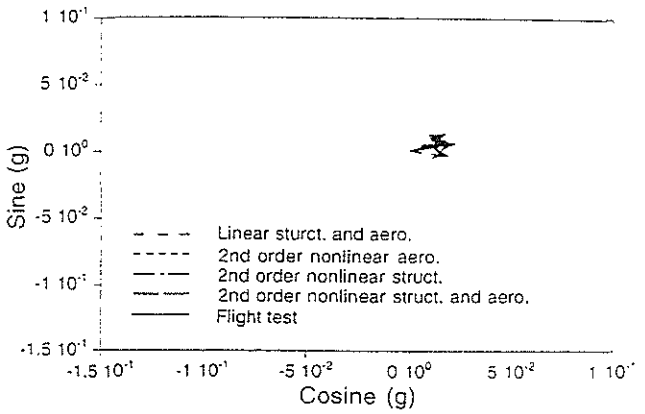

(a) 67 knots

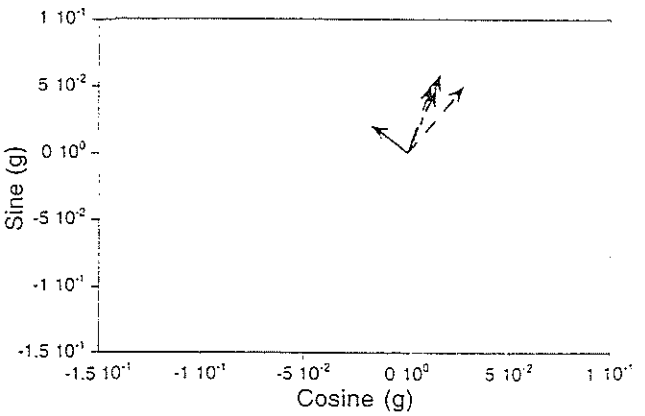

(b) 101 knots

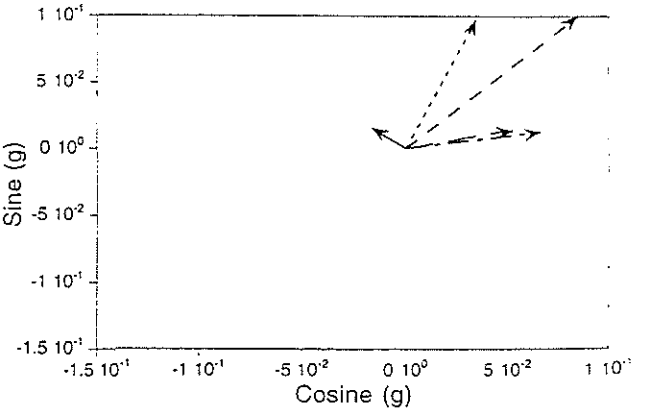

(c) 142 knots

Fig. 25 Effect of second order nonlinearity on 4/rev lateral vibration

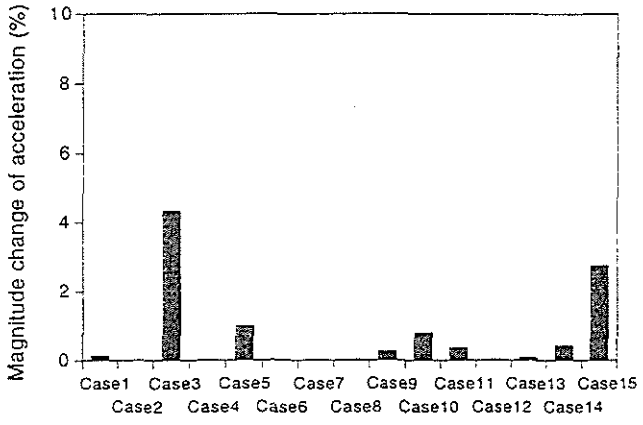

(a) 4/rev vertical vibration

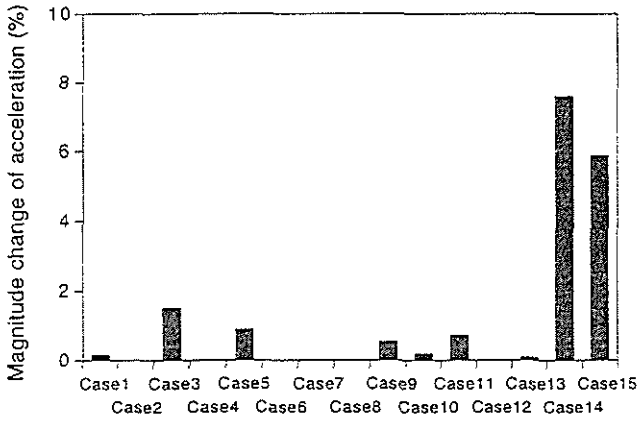

(b) 4/rev lateral vibration

Fig. 26 Effect of third order kinetic energy terms on the magnitude of 4/rev vibration

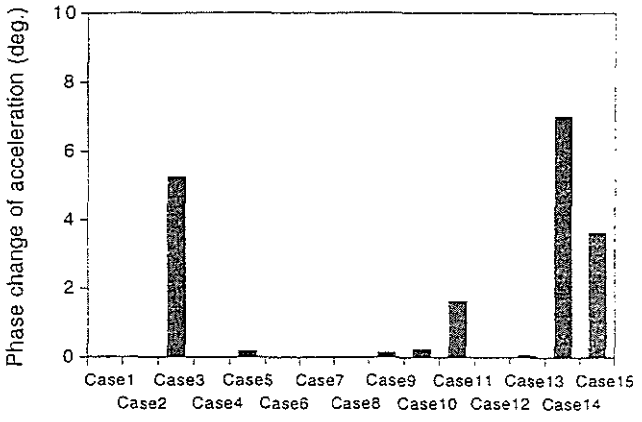

(a) 4/rev vertical vibration

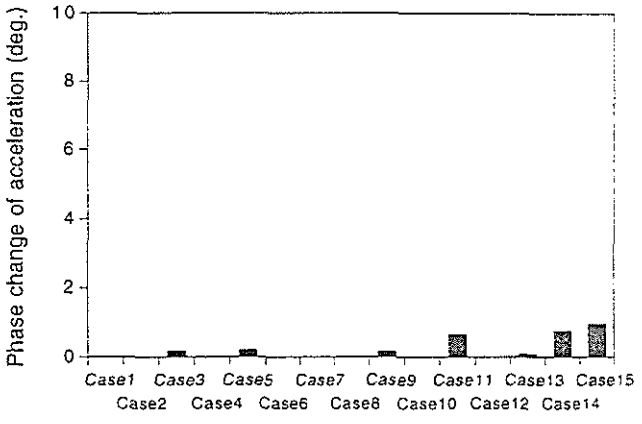

(b) 4/rev lateral vibration

Fig. 27 Effect of third order kinetic energy terms on the phase of 4/rev vibration

5. The contribution of airframe modes to vibration between 3-D fuselage and refined 3-D fuselage models shows a significant difference on the prediction of 4/rev lateral vibration. The modeling of difficult components appears to produce the coupling between modes. Accurate prediction of airframe natural frequencies up to about 38Hz(7/rev) appears essential to predict airframe vibration accurately.

6. Second order nonlinear terms have important effect on the prediction of vibration especially at high speed and high frequency. Second order nonlinear terms decrease the magnitude of 4/rev vertical vibration by about 60% and the magnitude of 4/rev lateral vibration by 65%.

7. Third order kinetic energy terms generally have a small influence on the prediction of vibration. Third order kinetic energy terms decrease the magnitude of 4/rev vertical vibration by about 7% and change the phase by 10 degrees.

Acknowledgments

This work was supported by the National Rotorcraft Technology Center under Grant No. NCC 2944; Technical monitor Dr. Yung Yu.

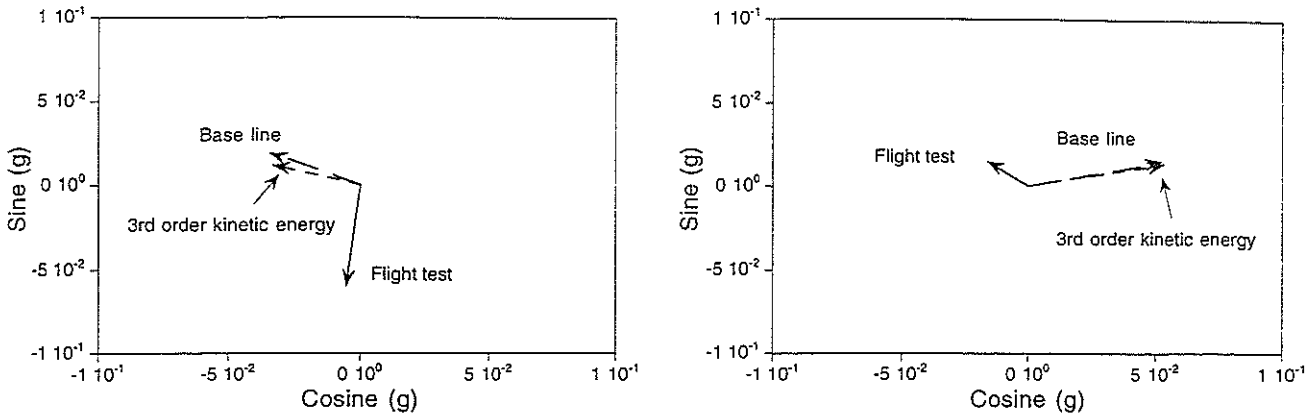

(a) 4/rev vertical vibration

(b) 4/rev lateral vibration

Fig. 28 Effect of third order kinetic energy terms on 4/rev vibration

Table 2 third order kinetic energy terms investigated

Case 1	axial-flap, linear	$T_u = -w \sin\beta_p \cos\beta_p$ $T_w = -u \sin\beta_p \cos\beta_p$
Case 2	flap-lag, nonlinear	$T_{w'} = e_g(\ddot{v} - v)v' \sin\theta_0$ $T_v = e_g(v'\ddot{w}' \sin\theta_0 - v'w' \sin\theta_0)$ $T_{v'} = e_g(\ddot{v} - v)w' \sin\theta_0$
Case 3	lag-torsion, linear	$T_{v'} = 2(k_{m_2}^2 - k_{m_1}^2)\hat{\phi} \cos\beta_p \sin\theta_0 \cos\theta_0$ $T_{\hat{\phi}} = -2(k_{m_2}^2 - k_{m_1}^2)\dot{v}' \cos\beta_p \sin\theta_0 \cos\theta_0$
Case 4	lag-torsion, nonlinear	$T_v = -2e_g v' \hat{\phi} \sin\theta_0 \cos\beta_p$ $T_{\hat{\phi}} = 2e_g \dot{v} v' \sin\theta_0 \cos\beta_p$
Case 5	lag-torsion, linear	$T_v = 2e_g \hat{\phi} \cos\theta_0 \sin\beta_p$ $T_{\hat{\phi}} = -2e_g \dot{v} \cos\theta_0 \sin\beta_p$
Case 6	lag, nonlinear	$T_v = -\frac{1}{2}e_g v'^2(\cos\theta_0 + \dot{\theta}_0^2 \cos\theta_0 + \ddot{\theta}_0 \sin\theta_0)$
Case 7	lag, linear	$T_v = -e_g(2v'\dot{v}'\dot{\theta}_0 \sin\theta_0 - \dot{v}'^2 \cos\theta_0 - v'\ddot{v}' \cos\theta_0)$
Case 8	flap, nonlinear	$T_w = -\frac{1}{2}e_g w'^2(\dot{\theta}_0^2 \sin\theta_0 - \ddot{\theta}_0 \cos\theta_0)$
Case 9	lag-torsion, nonlinear	$T_{v'} = \frac{1}{2}e_g x \hat{\phi}^2 \cos\theta_0 \cos^2\beta_p$ $T_{\hat{\phi}} = e_g x \hat{\phi} v' \cos\theta_0 \cos^2\beta_p$
Case 10	flap-torsion, nonlinear	$T_{w'} = -\frac{1}{2}e_g x \hat{\phi}^2 \sin\theta_0 \cos^2\beta_p$ $T_{\hat{\phi}} = e_g x \hat{\phi} w' \sin\theta_0 \cos^2\beta_p$
Case 11	flap-lag, linear	$T_{v'} = e_g w \sin\beta_p \cos\beta_p \cos\theta_0$ $T_w = e_g v' \sin\beta_p \cos\beta_p \cos\theta_0$
Case 12	lag, nonlinear	$T_{v'} = e_g(\ddot{v} - v)v' \cos\theta_0$
Case 13	flap, nonlinear	$T_w = e_g(\dot{w}'^2 \sin\theta_0 + w'\ddot{w}' \sin\theta_0 + 2w'\dot{w}'\dot{\theta}_0 \cos\theta_0)$
Case 14	flap-torsion, linear	$T_{w'} = 2(k_{m_1}^2 \cos^2\theta_0 + k_{m_2}^2 \sin^2\theta_0) \cos\beta_p \hat{\phi}$ $T_{\hat{\phi}} = -2(k_{m_1}^2 \cos^2\theta_0 + k_{m_2}^2 \sin^2\theta_0) \cos\beta_p \dot{w}'$
Case 15	flap-torsion, linear	$T_w = 2e_g \hat{\phi} \sin\beta_p \sin\theta_0$ $T_{\hat{\phi}} = -2e_g \dot{w} \sin\beta_p \sin\theta_0$

References

[1] Crews, S. T., Rotorcraft Vibration Criteria A New Perspective, Proceedings of the 43rd Annual Forum of the American Helicopter Society, St. Louis, MO, May 1987.

[2] Reichert, G., Helicopter Vibration Control–A Survey, *Vertica*, Vol. 5, No. 1, 1981.

[3] Hansford, R. E., and Vorwald, J., Dynamics Workshop On Rotor Vibratory Loads Prediction, *Journal of the American Helicopter Society*, Vol. 43, No. 1, January 1998.

[4] Yen, J. G., Yuce, M., Chao, C., and Schillings, J., Validation of Rotor Vibratory Airloads and Application to Helicopter Response, *Journal of the American Helicopter Society*, Vol. 35, No. 4, October 1990.

[5] Miao, W., Twomey, W. J., and Wang, J. M., Challenge of Predicting Helicopter Vibration, Proceedings of the AHS International Meeting on Advanced Rotorcraft Technology and Disaster Relief, Gifu, Japan, April 1998.

[6] Kvaternik, R. G., The NASA/Industry Design Analysis Proceedings of the 33rd AIAA Structures, Structural Dynamics and Materials Conference, Dallas, Texas, April 1992.

[7] Dompka, R. V., Investigation of Difficult Component Effects on FEM Vibration Prediction for the AH-1G helicopter, Proceedings of the 44th Annual Forum of the American Helicopter Society, Washington, D.C., June 1988.

[8] Loewy G. R, Helicopter Vibrations : A Technological Perspective, *Journal of the American Helicopter Society*, Vol. 29, No. 4, 1984, pp. 4–30.

[9] Kvaternik, R. G.,Bartlett, Jr. F. D., and Cline, J. H., A Summary of Recent NASA/Army Contributions to Rotorcraft Vibration and Structural Dynamics Technology, *NASA CP-2495*, February 1988.

[10] Hohenemser, K. H., and Yin, S. K., The Role of Rotor Impedance in the Vibration Analysis of Rotorcraft, *Vertica* , Vol 3, 1979, pp. 187–204.

[11] Hsu, T. K., and Peters, D. A., Coupled Rotor/Airframe Vibration Analysis by a Combined Harmonic-Balance Impedance Matching Method, 36th Annual Forum of the American Helicopter Society, Washington D.C., May 1980.

[12] Kunz, D. L., A Nonlinear Response Analysis for Coupled Rotor-Fuselage System, American Helicopter Society Specialists' Meeting on Helicopter Vibration Technology for the Jet Smooth Ride, Hatford, Nov. 1981.

[13] Rutkowski, J. M., The Vibration Characteristics of a Coupled Helicopter Rotor-Fuselage by a Finite Element Analysis, *NASA TP-2118*, January 1983.

[14] Chiu, T., and Friedmann, P. P., A Coupled Helicopter Rotor/Fuselage Aeroelastic Response Model for ACSR, Proceedings of the 36th Structures, Structural Dynamics and Materials Conference and Adaptive Structures Forum, New Orleans, April 1995.

[15] Yeo, H., and Chopra, I., Effects of Modeling Refinements on Coupled Rotor/Fuselage Vibration Analysis, Proceedings of the 54th Annual Forum of the American Helicopter Society, Washington, D.C., May 1998.

[16] Crespo da Silva, M. R. M, and Hodges, D. H., Nonlinear Flexure and Torsion of Rotating Beams with Application to Helicopter Rotor Blades-I. Formulation, *Vertica*, Vol. 10, No. 2, 1986.

[17] Crespo da Silva, M. R. M, and Hodges, D. H., Nonlinear Flexure and Torsion of Rotating Beams with Application to Helicopter Rotor Blades-II. Response and Stability Results, *Vertica*, Vol. 10, No. 2, 1986.

[18] Dompka, R. V., and Cronkhite, J. D., Summary of AH-1G Flight Vibration Data for Validation of Coupled Rotor-Fuselage Analysis, NASA CR-178160, November 1986.

[19] Bagai, A., and Leishman, J. G., Rotor Free-Wake Modeling using a Pseudo-Implicit Relaxation Algorithm, AIAA paper No. 94-1918, AIAA 12th Applied Aerodynamics Conference, Colorado Springs, Colorado, June 1994.

[20] Leishman, J. G., Validation of Approximate Indicial Aerodynamic Functions for Two Dimensional Subsonic Flow, *Journal of Aircraft*, Vol. 25, No. 10, October 1988.

TWENTYFIFTH EUROPEAN ROTORCRAFT FORUM

Paper n°G11

MATHEMATICAL MODELING OF LOADING OF BEARINGLESS MAIN ROTOR WITH ELASTIC ELEMENTS OF TORSIONAL TYPE

BY

V.B. KARTASHOV
KAZAN HELICOPTERS

S.A. MICHYLOV, E.I. NIKOLAEV, A.A. KHLEBNYKOV
KAZAN STATE TECHNICAL UNIVERSITY
RUSSIA

SEPTEMBER 14-16, 1999
R O M E
ITALY

ASSOCIAZIONE INDUSTRIE PER L'AEROSPAZIO, I SISTEMI E LA DIFESA
ASSOCIAZIONE ITALIANA DI AERONAUTICA ED ASTRONAUTICA

Summery

Some questions of creation the model of bearingless main rotor are under discussion in offered report. This model can be used in deciding serial tasks for specification of aircraft performance and calculation of load in rotorcraft flight structure of light helicopter ANSAT. In this modeling the laminated and multichannel elastic elements' behavior is described by parametric matrix of compliance (flexibility). The parametric matrix of compliance (flexibility) is defined by calculation and is revised by experimental researches. The developing model let us be more accurately in definition of load on elements of main rotor construction and to refine parameters of control actions on helicopter and supply (maintain) tuning of helicopter's wire guidance flight control.

Modern science and technical achievements ensure stability and a resource of units which are designed with use of composite. These achievements allow to create the main rotor with elastic holding of blades to the rotor bushing. In contemporary research papers this rotor is called as fillowsbearingless, rigid, semirigid, elastic, etc. A rotor with elastic attaching of blades is a special case of bearingless main rotors with absent axial, vertical and horizontal bearings (joints). Functions of all these bearings are executed thanks to the elastic element - an integral bearing. Using such elastic elements significantly simplifies the design, increases maneuverability and controllability of helicopter. In addition it ensures a service in the system "on the condition". The elastic elements are supposed to have definite softness in planes of flap, rotation and torsion. These are the conditions ensured the stiffness and air-elastic stability of main rotor constructive elements. The softness of such elements should be optimized in number of parameters. Constructive elastic elements can be composed of anisotropic composites with different elasticity modulus. In this case the modeling of their mode of deformation can be done thanking to account the relations between bending and torsion. The main gold of these work is to develop the strategy of numerical simulation of the main rotor elasticity when the rotor is composed of elastic elements of torsion types made of rubberfabric composites.

The modern tendency is to replace the metallic elastic elements of spring type (Bo-105, BK-117, Ka-62, Mi-34) by elastic elements made of composites (MD-900, EC-135) [1]. A modeling of rotor' aeroelasticity for helicopters having the take-off weight equal to 3000 kg has several characteristics which are analyzed in the given report. The object of the research is the torsion made of the rubber-fabric composites with the design cone angle and the displacement of axis in the plane of rotation. Constructive power scheme of such an element is a flat system of laminated space deformed beams of variable stiffness. This system is supposed to have the multichannel transfer of loads.

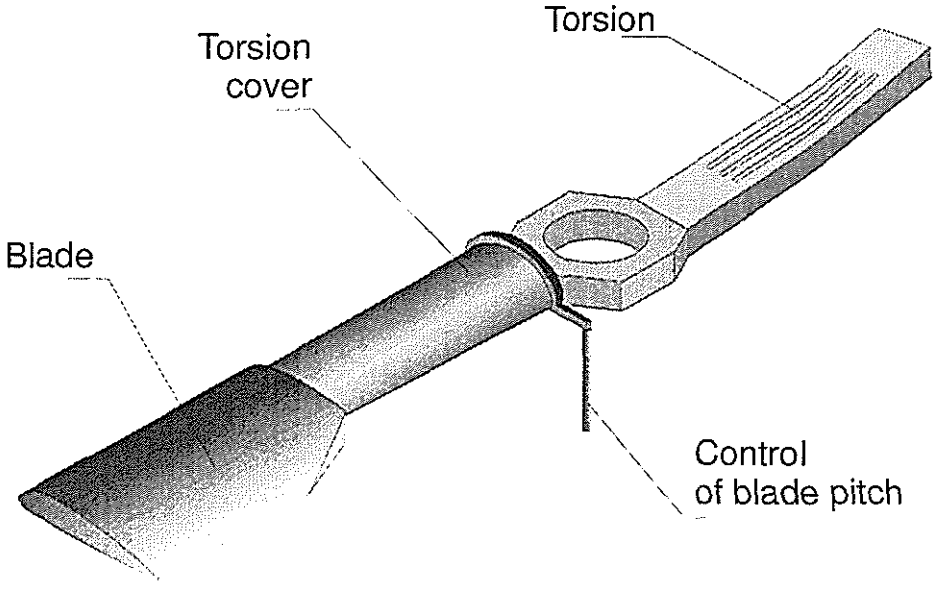

Fig. 1

The basic design power scheme of blades attaching to the bearing of rotor is shown in the Fig. 1. A blade is attached to the bushing by the spring torsion which allows the flapping motion and curving in the planes of the blade rotation. It is possible to transfer the controlling moment on the blade by means of the cover rotation. The torsion twisting is as effective as the rotation of the axial joint. The load transfer from blades onto the bushing can be done by several independent beams. That's why a rotor of this type sometimes is called a rotor with redundant, or multichannel ways of load transfer to the bearing [2]. It differs from a hinge and hingeless main rotor, which has only one way of load transfer onto the blade.

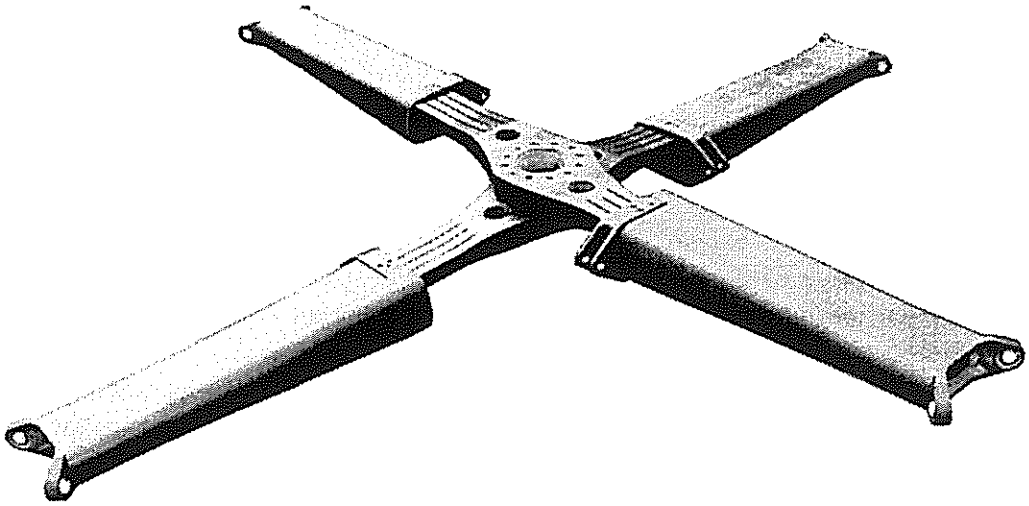

Fig. 2

When the load transfer to the bushing from the blade butt is done in the many-server way while the torsion is deformed the constructive nonlinear bending-torsion relations come to exist. This bending-torsion relations are caused by linear extention of the twisted elastic element. In this connection the analysis of bearingless rotor aeroelasticity is more complex then the analysis of the hingeless and hinge rotors. It is a very important task in developing of methods of aeroelastic analysis of the elastic main rotor to create the adequate concept of nonlinear behavior of elastic element under the controlling moment and environmental stress of blade. This analysis which includes the elastic element behavior can be divided into three main stages:

a) preliminary calculation of deforming of the elastic element in the prescribed limits of deformation and loading; determination of flexibility matrixes on the boundary of elastic blade element;

b) determination of blade dynamic behavior under the influence of aerodynamic and inertial loads taking into accounte the nonlinear behavior of elastic element;

c) validaty test of the level of flexibility matrixes elements for a set of operational conditions of the elastic element operating.

The process of separate beam deforming is described in the terms of shear models of Timoshenko type. The complete definition of kinematic variables and internal power factors for every beam of torsion can be given by using the expression of the internal power factors in kinematic parameters and corresponding rigidities. The analytical formulas for calculation of generalized displacement and forces in free section of beam number "k" can be written as [3]:

$$V_{k,x}(z^k) = V_{k,x}(0) + \omega_{k,y}(0)z^k + \frac{1}{EJ_y^k}[\frac{Q_x^k(0)}{k_x^3}(k_x z^k -$$

$$-sh(k_x z^k)) + \frac{M_y^k(0)}{k_x^2}(ch(k_x z^k) - 1)] + \frac{1}{GF_x^k}[\frac{Q_x^k(0)}{k_x} sh(k_x z^k) -- M_y^k(0)(ch(k_x z^k) - 1)],$$

$$V_{k,y}(z^k) = V_{k,y}(0) - \omega_{k,x}(0)z^k + \frac{1}{EJ_x^k}[\frac{Q_y^k(0)}{k_y^3}(k_y z^k -$$

$$- sh(k_y z^k)) - \frac{M_x^k(0)}{k_y^2}(ch(k_y z^k) - 1)] + \frac{1}{GF_y^k}[\frac{Q_y^k(0)}{k_y} sh(k_y z^k) + M_x^k(0)(ch(k_y z^k) - 1)],$$

$$\omega_{k,x}(z^k) = \omega_{k,x}(0) + \frac{1}{EJ_x^k}[-\frac{Q_y^k(0)}{k_y^2}(1 - ch(k_y z^k)) + \frac{M_x^k(0)}{k_y} sh(k_y z^k)], \qquad (1)$$

$$\omega_{k,y}(z^k) = \omega_{k,y}(0) + \frac{1}{EJ_y^k}[\frac{Q_x^k(0)}{k_x^2}(1 - ch(k_x z^k)) + \frac{M_y^k(0)}{k_x} sh(k_x z^k)],$$

$$V_{k,z}(z^k) = V_{k,z}(0) + \frac{N_z^k z^k}{EF_k} - \frac{1}{2}\int_0^{z^k}[(V_{x,z}^k)^2 + (V_{y,z}^k)^2]dz,$$

$$V_{x,z}^k = \omega_{k,y}(0) + \frac{Q_x^k(0)}{k_x^2 EJ_y^k} - \frac{Q_x^k(0)ch(k_x z^k)}{N_z^k} + \frac{M_y^k(0)sh(k_x z^k)}{N_z^k} k_x,$$

$$V_{y,z}^k = -\omega_{k,x}(0) + \frac{Q_y^k(0)}{k_y^2 EJ_x^k} - \frac{Q_y^k(0)ch(k_y z^k)}{N_z^k} - \frac{M_x^k(0)sh(k_y z^k)}{N_z^k} k_y,$$

$$M_x^k(z^k) = \frac{Q_y^k(0)}{k_y} sh(k_y z^k) + M_x^k(0)ch(k_y z^k),$$

$$M_y^k(z^k) = -\frac{Q_x^k(0)}{k_x} sh(k_x z^k) + M_y^k(0)ch(k_x z^k),$$

$$Q_x^k(z^k) = Q_x^k(0)\tilde{n}h(k_x z^k) - M_y^k(0)k_x sh(k_x z^k) \ ,$$

$$Q_y^k(z^k) = Q_y^k(0) - h(k_y z^k) + M_x^k(0)k_y sh(k_y z^k).$$

In the formulas (1) z^k is a local coordinate of beam number "k". The values (.)(0) correspond the coordinate $z^k = 0$, and k_x, k_y are defined by expressions

$$k_y = \frac{N_z^k}{EJ_x^k(1 + \frac{N_z^k}{GF_y^k})},$$

$$k_x = \frac{N_z^k}{EJ_y^k(1 + \frac{N_z^k}{GF_x^k})}. \qquad (2)$$

The correlations given above allow us to form a system of nonlinear algebraic equations which describe the process of torsion deformation. This equations system can be solved by methods, accepted in [4]. The mode of deformation and flexibility matrixes of elastic element with predetermined charac-

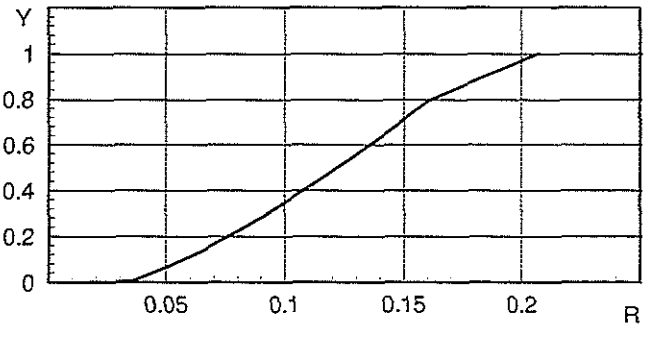

Fig. 3.

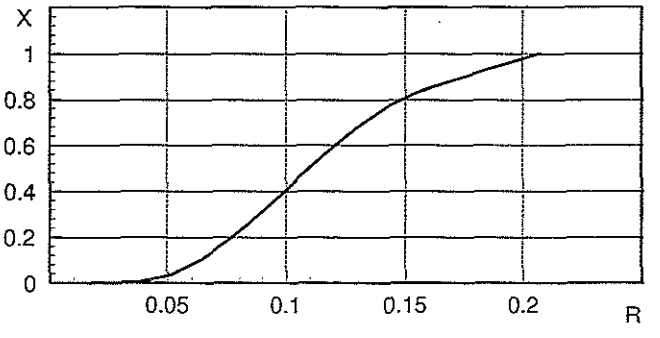

Fig. 4.

teristics of material and configuration are determined under the using of fine-element method.

The characteristic feature of torsion deforming is S-type form of the elastic line, which differs in quality from the beam line (Fig. 3, 4).

The parametric calculations allowing to find a relationship between the external load and deformation of torsion were conducted for various designs which are shown in Fig. 5. This relation can be presented using matrix mode of the following form:

$$\nu = \nu_0 + A\left(N_z, \varphi_{\text{отд}}\right) \cdot q = \begin{bmatrix} \nu_{x0} \\ \nu_{y0} \\ \omega_{x0} \\ \omega_{y0} \end{bmatrix} + \begin{bmatrix} A_{11} & A_{12} & A_{13} & A_{14} \\ A_{21} & A_{22} & A_{23} & A_{24} \\ A_{31} & A_{32} & A_{33} & A_{34} \\ A_{41} & A_{42} & A_{43} & A_{44} \end{bmatrix} \begin{bmatrix} Q_x \\ Q_y \\ M_x \\ M_y \end{bmatrix} \tag{3}$$

where ν - generalized displacement vector of torsion end section, ν_0 - initial displacement vector of torsion end section depended from the initial configuration; q - generalized loading vector, corrected the blade butt; A - flexibility matrix which elements depend of centrifugal load and twisting angle of torsion end section (angle of incidence). Elements of flexibility matrix are represented in the calculation as Lagrange polynomial of fifth degree. The approximation error cannot be over 2% (1).

The series of parametrical flexibility matrix for elastic elements of the main and tail rotor was obtained using the correlations given above.

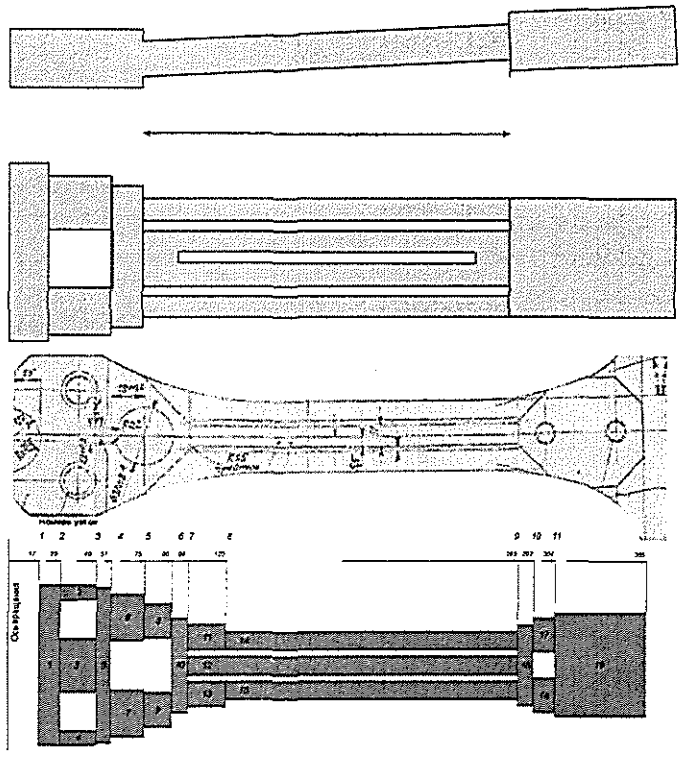

Fig 5

The blade loads are obtained by solving nonlinear equations of wing airfoil's beam motion. The system of these equations takes the following shape:

$$\begin{aligned} M\dot{u}_i &= Q_i' + q_i \\ \mathbf{J}\dot{\vartheta}_i &= M_i' + e_3 \times Q_i + m_i \\ \dot{u}_i' &= \tilde{u}_i' + \varepsilon_{kij}\chi_i\dot{u}_j = \varepsilon_{ij}\omega_j \\ M_{\vartheta_i} &= \mathbf{G}_i\left(\chi_i - \chi_{i0}^{(0)}\right) \\ \chi_i &= \mathbf{A}^*\tilde{\vartheta}_i' + \mathbf{A}\chi_{i0}^{(0)} \\ \vartheta_i' - \chi_i &= \varepsilon_{kij}\vartheta_i\chi_j . \end{aligned} \tag{4}$$

Q_i - internal force vector with components composed cutting and axial force; M_i - internal moment vector with components composed bending and rotational moment; q_i, m_i - distributed load and moment per-unite length in projection on coupled axes; u_i, ϑ_i - linear and angular replacement of

beam' element; $\dot{u}_i$, $\dot{\vartheta}_i$, $\ddot{u}_i$, $\ddot{\vartheta}_i$ - first and second time derivative for linear and angular replacement.

Environmental stress on the blade is non-conservative and is defined in each blade section as distribution of cutting force and moment per-unit length. Three components of each vector are determined in coordinate system connected with the blade section. Centrifugal force and force per-unit length are reduced to center of rigidity. The moments are defined in correlation with the main axes of blade section. Using a nonlinear system of integral-differential equations of motion it is possible to determine the elastic line position on each stage of calculation and in given moment of time.

The solution of the equation lets us to determine the loads on rotor system's elements in oder to define the stability and endurance (life time) of main rotor system and also to standardize external load for static and dynamic tests. The position of elastic axis of blade and torsion in one the given stage of calculation and load on the blade in flapping plane corresponding to this position is a good illustration of the concept

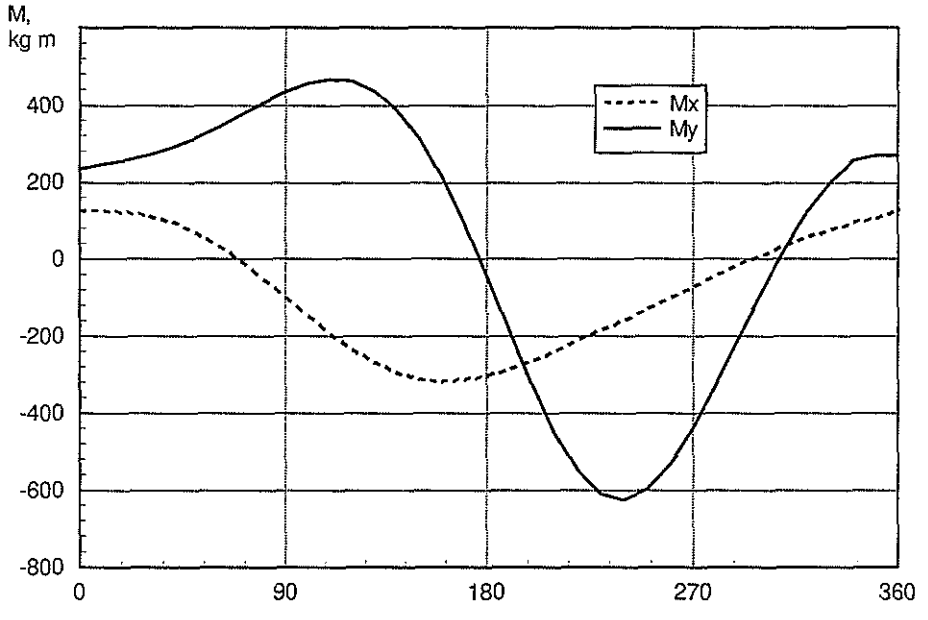

Fig. 6

Another way of studies of the bearingless main rotor with elastic torsional suspension of blades is to ensure helicopter balancing, stability and controllability for all modes of flight.

As a rule a number of parameters, which are found in the certain single aerodynamic calculation of main rotor are also used in the calculation of some features of helicopter balancing. They are corrected using the approximated formulas when the control parameters are changed. It is a traditional way to use a hinge main rotor model with the absolute rigid structure of blades and minor offset of axis of horizontal flight (<5%) in the calculation of aerodynamic features. Sometimes the spatial motion of helicopter is divided into two separate motions: longitudinal and transverse one.

This approach results in hard restrictions on control parameters and design features. The bearingless rotor with the elastic element of torsional type corresponds to these requirements only partly. Concerns to the studying rotor, it is necessary to choose the equivalent joint of such a rotor taking into consideration the coincidence of the first fluctuation of its own frequency in planes of flap, or the equality of controlling moments on the bushing. But these approach give different results.

In the given report there is a mathematical model of calculation of helicopter balancing features which is done using the spatial scheme. Rectilinear steady flight of single-rotor helicopter can be operated either without the slide but with roll angle, or without roll but with slide angle. This division of problem into two parts (longitudinal and transverse motion) is not quite correct.

Let's use the following equation of motion of a helicopter for solving a problem of helicopter balancing:

$$\begin{aligned}
&m\left(\dot{V}_x+\omega_y V_z-\omega_z V_y\right)=R_x-G_x;\\
&m\left(\dot{V}_y+\omega_z V_y-\omega_x V_z\right)=R_y-G_y;\\
&m\left(\dot{V}_z+\omega_x V_y-\omega_y V_x\right)=R_z+G_z;\\
&J_x\cdot\dot{\omega}_x+\left(J_z-J_y\right)\cdot\omega_z\omega_y=M_x;\\
&J_y\cdot\dot{\omega}_y+\left(J_z-J_x\right)\cdot\omega_x\omega_z=M_y;\\
&J_z\cdot\dot{\omega}_z+\left(J_y-J_x\right)\cdot\omega_x\omega_y=M_z.
\end{aligned}\qquad (5)$$

where $\bar{G}=\{G_x,G_y,G_z\}$ — gravity force (attached in center of mass of helicopter);; $\bar{V}=\{V_x,V_y,V_z\}$ —acceleration (speedup) of helicopter's center of mass in the coupled coordinate system; $\dot{\bar{\omega}}=\{\dot{\omega}_x,\dot{\omega}_y,\dot{\omega}_z\}$, —angular acceleration in relation of helicopter' center of masses, $\bar{\omega}=\{\omega_x,\omega_y,\omega_z\}$ — rate of helicopter' angular motion, $\bar{J}=\{J_x,J_y,J_z\}$ — tensor of helicopter' inertia, $\bar{R}=\{R_x,R_y,R_z\}$ $\bar{M}=\{M_x,M_y,M_z\}$ — main vector and main moment of aerodynamic force

The parameters of control (operation) which are necessary for helicopter balancing are obtained using an equations system of type (10). The main unknowns of the system are six controlling actions. A number of these actions are equal to the number of equations in the system: φ_0 - pitch blades main rotor; χ, η - deflection angles of wobble plate; φ_{tr} - pitch blades of tail rotor; γ - roll angle; ϑ - helicopter pitch angle.

In the calculation of spatial motion of the main rotor blades the elastic blade model is developed on the basis of theory of fine beam of wing airfoil when greate displacement takes place[5]. Besides the angular spatial turning of accounting sections in the local coordinate system is used.

Equilibrium equations of deformed blade in local coordinate system take the shape:

$$\begin{aligned}
\frac{\partial\varphi_1^*}{\partial s}&=\frac{1}{\cos\varphi_1^*}\left[\left(\frac{M_\xi}{EI_\xi}+\omega_{01}\right)\cdot\cos\varphi_3^*-\left(\omega_{02}+\frac{M_\eta}{EI_\eta}\right)\cdot\cos\varphi_3^*\right];\\
\frac{\partial\varphi_2^*}{\partial s}&=\left(\frac{M_\xi}{EI_\xi}+\omega_{01}\right)\cdot\sin\varphi_3^*+\left(\omega_{02}+\frac{M_\eta}{EI_\eta}\right)\cdot\cos\varphi_3^*;\\
\frac{\partial\varphi_3^*}{\partial s}&=\left(\omega_{03}+\frac{M_\zeta}{GI_\delta}\right)-tg\varphi_2^*\cdot\left[\left(\frac{M_\xi}{EI_\xi}+\omega_{01}\right)\cdot\cos\varphi_3^*-\left(\omega_{02}+\frac{M_\eta}{EI_\eta}\right)\cdot\sin\varphi_3^*\right],
\end{aligned}\qquad (6)$$

where $\varphi_1,\varphi_2,\varphi_3$ — an angle of rotation of section in the (flight) reference point, M_ξ,M_η,M_ς — moments of external (applied) forces, $\omega_{01},\omega_{02},\omega_{03}$ — initials of the curvature, EI_ξ,EI_η,GI_p — blade's rigidity in relation to the main axis of design section.

Numerical decision of equations of the blades motion in the frame of helicopter balancing equations system is fined by development of desired functions of a blade moving in harmonic series:

$$\Delta\beta_i=a_o^i+\sum_{j=1}^{\infty}\left(a_j^i\cdot\cos j\psi+b_j^i\cdot\sin j\psi\right),. \qquad (7)$$

were a_o^i,a_j^i,b_j^i — factor of (resolution) development; $\psi=\omega t$ - blade's azimuth; ω — angular velocity of rotation; t — time. When magnitudes a_o^i,a_j^i,b_j^i are known, it's possible to calculate the moving in every point of blade. A nodal point of blade's elastic axis can be described in following expression:

$$y_n = \sum_{i=1}^{n}\left[a_o^i + \sum_{j=1}^{\infty}\left(a_j^i \cdot \cos j\omega t + b_j^i \cdot \sin j\omega t\right)\right] \cdot \sum_{j=i}^{n} \Delta r_j \qquad (8)$$

Under the integrating matrixes [6] the obtained integral-differential equations can be reduced to the nonlinear algebraic equations using one of the methods of optimization search [7]. The flexibility matrix of torsion of type (3) is used as boundary conditions in the blade butt.

Thereby, when solving the balance equations it is possible to find not only parameters of helicopter control, but also dynamic loads and moving of the blades of main and tail rotor. The task of a helicopter balancing, calculation of loads on the blades of main and tail rotor of definition of required horsepower, which is necessary to calculate the aircraft performance characteristics can be correctly solved as a whole.

The strategy described above allows to receive the light helicopter balancing parameters. The influence of particularities of torsion elastic models on the light helicopter trim characteristics can be evaluate by means of comparative calculations for the follows three models of blade attaching to the rotor bushing:

- ·a classical rotor with hinge blades attaching; its shoulder of horizontal joint can be chosen according to the fundamental tone of fluctuations;
- ·a rotor which has rigidity in the horizontal joint. It linearly depends on rotation angle of blade;
- ·a rotor based on the elastic element of torsion type with parameters, defined by correlations of (3) shape.

Comparative analysis of the results which based on the models given above shows that a number of parameters have a different sensitivity degree connected with the chosen calculation models. Among the parameters which have low sensitivity there are hauling capacity, rotational moments and angle of incidence on main and tail rotors. The sensitivity of the operational parameters of longitudinal motion are less than sensitivity of transverse control parameters (Fig. 7 -19)

Thereby, characteristics of helicopter longitudinal moving with bearingless rotor can be correctly calculated using the rotor with the equivalent offset of horizontal joint. The reliable results connected with the parameters of transverse moving are obtained using the models with "real" elastic torsion. In other cases the divergence of results is over then 50%. It depends on the model chosen. The corner of transverse deflection of wobble plate changes even the sign depending on velocity of horizontal flight (Fig. 7).

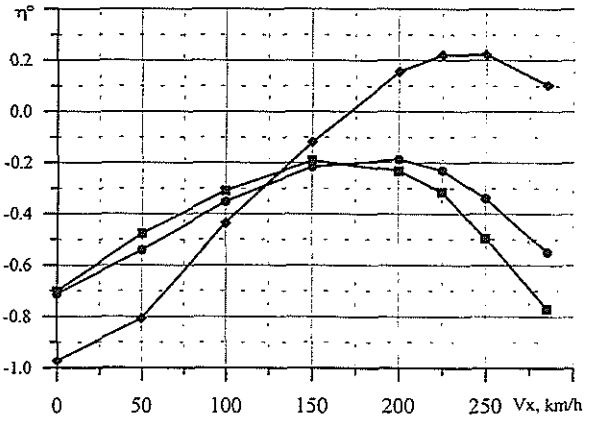

Fig. 7.

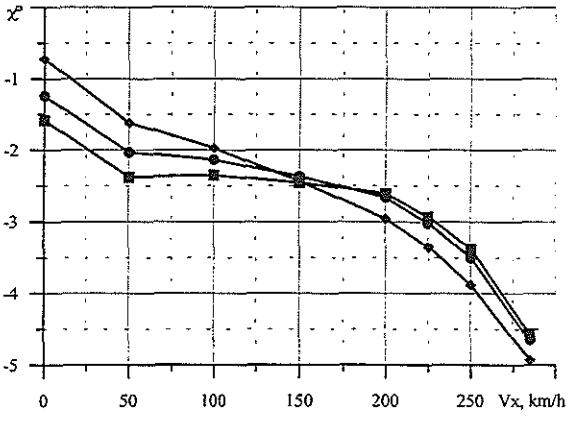

Fig. 8.

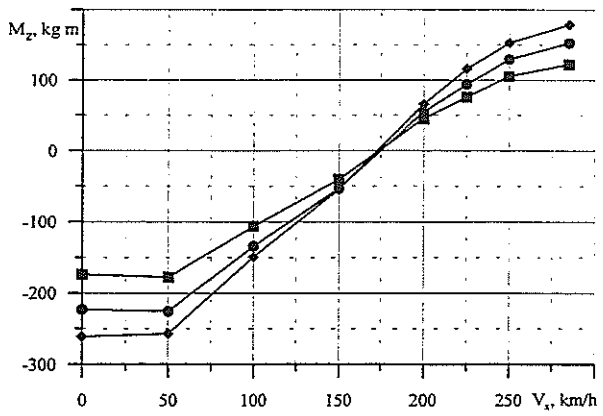

Fig. 9

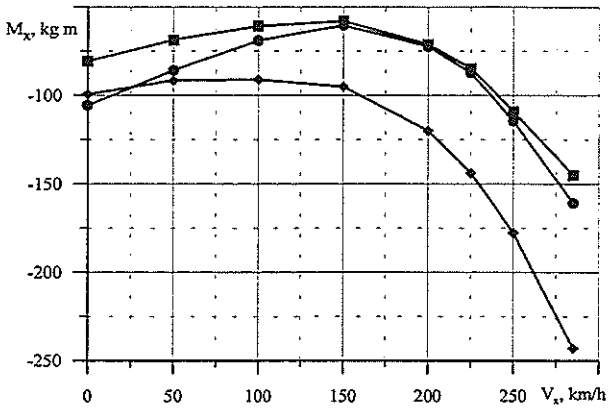

Fig. 10

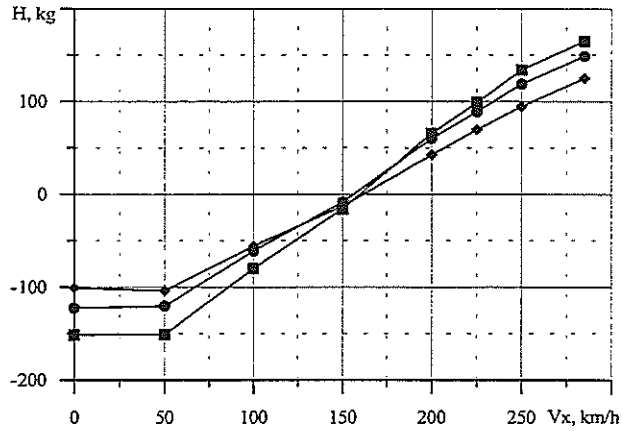

Fig. 11

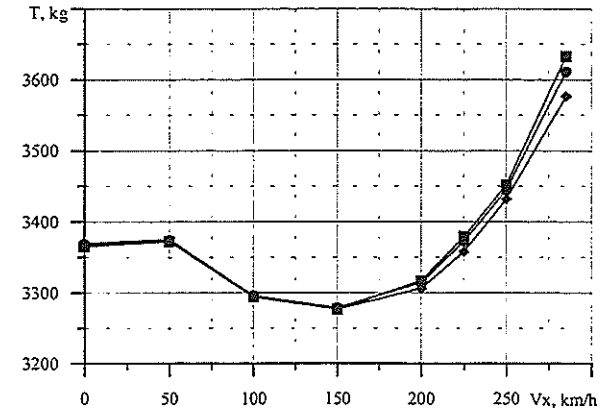

Fig. 12

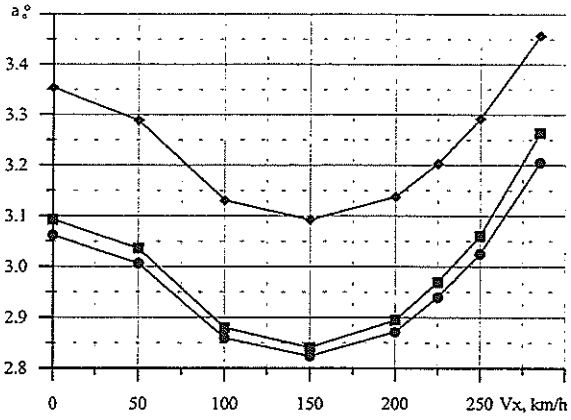

Fig. 13

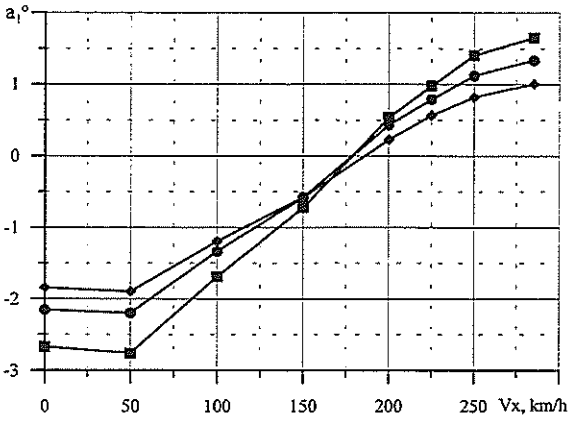

Fig. 14

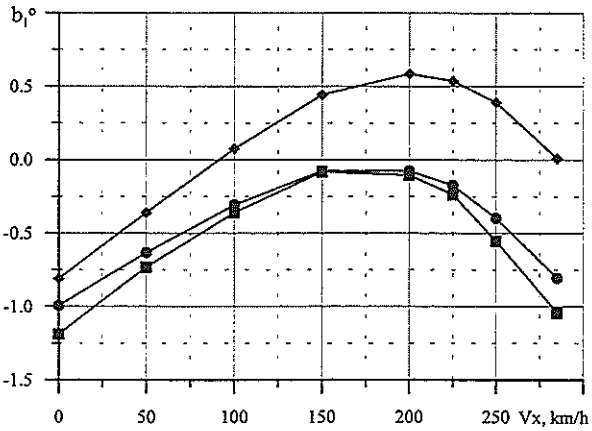

Fig. 15

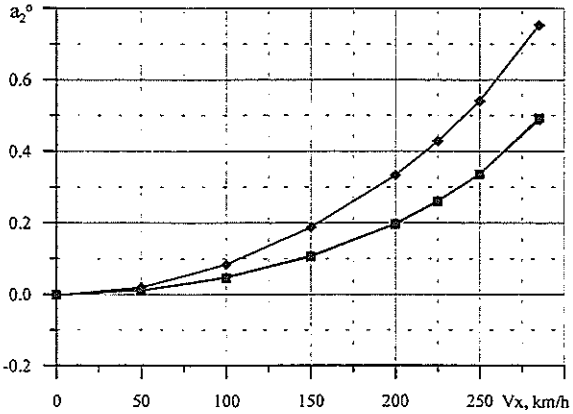

Fig. 16

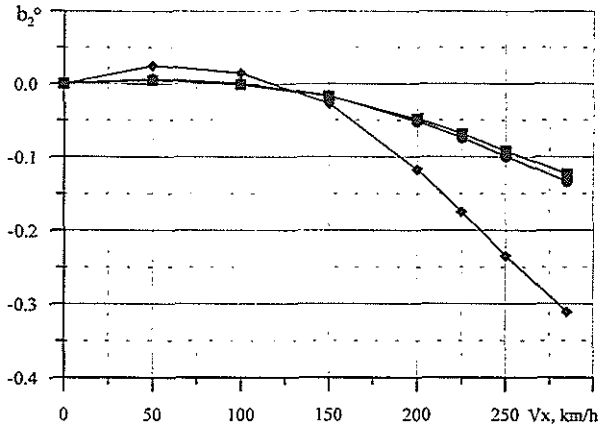

Fig. 17

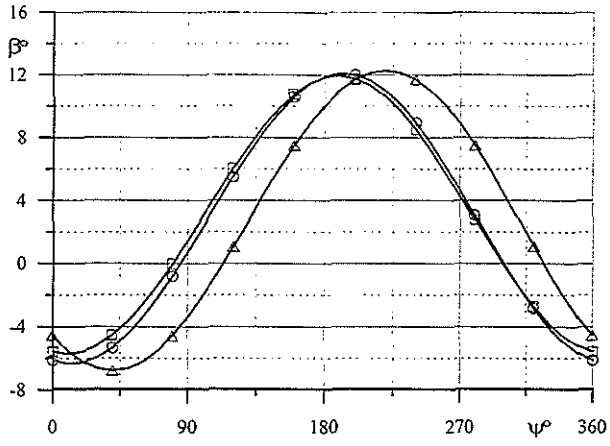

Fig. 19

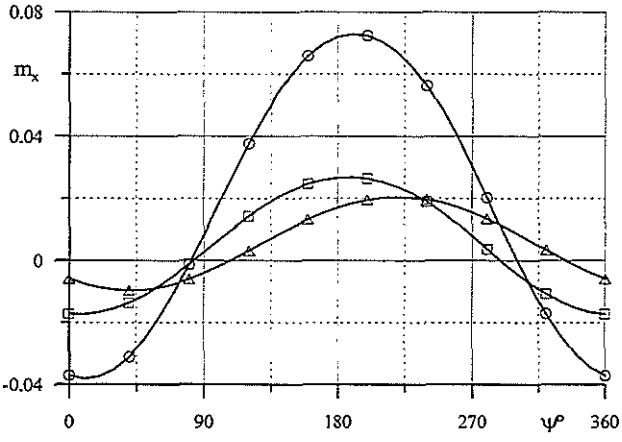

Fig. 18

Introduction of the elastic torsion models into numerical simulation has greatly influenced on the harmonic composition of the blades flapping motion. The latter determines the variable loads in sections, and enlarges bending moments on the rotor axis (Fig. 13-17).

The experimental studies of the choice and regulation of advanced angle of operation have shown the advantages of numerical evaluations of advanced angle on the stage of the overland regulation of helicopter rotor system (Fig. 8-10).

1. Ruzhitsky E.I. Helicopters. - M.: Victoria, ACT, 1997.
2. Finite Element Analyze for Bearingless Rotor Blade Aeroelasticity/ Sivaneri Nithiam Ti, Chopra Inderjit/ "J/Amer. Helicopt. Soc.", 1984, 29, •2, 42-51.
3. Savinov V.I., Sidorov I.N. The Development of Resolving Equations for Elastic Deformation of Composite Torsion of Helicopter Main Rotor. Dep. In A-RISRTI 25.07.97 •2493-V97, p.17.
4. Kornishin M.S. The Nonlinear Problems in Theory of Planes and Flat Shells and Methods of their Decision. - M.: Science, 1964. - 192 p.
5. Michilov S. The Analysis Problem of Airfoil Thin Beams in Conditions of Large Elastic Motions. The Stiffness Problems of Thin-Walled =Aircraft Units (Design).
6. Vakhiyov M.B., Safariev M.S., Snegirev V,F, The Stressing Calculation for Foil System. - Kazan: Tatknigoizdat, - 1975. - 212 p.
7. Moiseev n.i., Ivanilov U.P., Stolarova E.M. The Optimization Methods. - M.: Science, 1978. 351 p.

TWENTYFIFTH EUROPEAN ROTORCRAFT FORUM

Paper n° G12

MULTI-BODY SIMULATION OF A HELICOPTER LANDING WITH SKID LANDING GEAR IN VARIOUS ATTITUDE AND SOIL CONDITIONS

BY

C. CAPRILE, A. AIROLDI, A. BIAGGI, P. MANDELLI

SEPTEMBRE, 14-16, 1999
ROME
ITALY

ASSOCIAZIONE INDUSTRIE PER L'AEROSPAZIO, I SISTEMI E LA DIFESA
ASSOCIAZIONE ITALIANA DI AERONAUTICA ED ASTRONAUTICA

MULTI-BODY SIMULATION OF A HELICOPTER LANDING WITH SKID LANDING GEAR IN VARIOUS ATTITUDES AND SOIL CONDITIONS

C. Caprile*, A. Airoldi*, A. Biaggi **, P. Mandelli
*Aerospace Engineering Department – Politecnico di Milano, Italy
** AGUSTA, Un'Azienda Finmeccanica - Italy

Abstract

A skid landing gear multi-body model is presented. Plastic bending deformations of structural members, dampers behaviour and the characteristics of the attachments with fuselage are reproduced.

Simulations of landing in horizontal level attitude, landing with drag and landing with lateral loads conditions are carried on with VeDyaC, an explicit multi-body code developed at Aerospace Engineering Department of Politecnico di Milano, and compared with experimental results. A good correlation between numerical and experimental data is achieved with regard to the landing performance, the loads transmitted to the fuselage and the strain state in the elastic spring members.

Simulation in various attitudes and soil conditions were performed and the sensitivity to soil friction factors was investigated. After the validation of the model, the work indicates VeDyaC, and generally, multi-body modelling, capacities to predict landing performance not only in emergency landing conditions, but also in limit conditions with the required accuracy.

1 - Introduction

Skid landing gears are characterised by a structural energy absorbing mechanism, which relies upon the deflection of their cross members, usually circular light alloy tubes, connecting the skids to the fuselage. In hard landing, yielding of these members is in most cases needed and allowed by regulations to fulfil prescribed limits on the helicopter load factor by increasing the landing gear efficiency [1]. As a consequence, plastic bending of cross members largely influences the performance of the landing gear in limit conditions.

The typical design methodology is based on the separate modelling of both forward and rear cross member, taking in account plastic bending [1]. An iterative algorithm can be used to evaluate the cross member load-deflection curves, thus leading to the information needed to predict the overall landing performance.

As cross members are considered separately, this classic approach has an intrinsic limitation in predicting the performances in non-horizontal landing attitudes. Moreover, some not uncommon features of skid landing gears, such as inclination of cross members, the presence of viscous dampers and contact phenomena between cross members and fuselage, introduce difficulties in a non-linear static evaluation of load-deflection curves.

These limitations can only be overcome by developing a complete model of the landing gear. The model should attain a reliable prediction of landing performance and of structural loads in different attitudes and soil conditions. The time required for modelling and solving should be kept as limited as possible in order to develop a tool of valuable utility both in the design and in the analysis phases.

Following these considerations a skid landing gear was modelled with a multi-body approach. Solutions were carried out with VeDyaC, an explicit multi-body code developed at Department of Aerospace Engineering of Politecnico di Milano [3, 4]. VeDyaC has been yet successfully used to model full-scale helicopter crash landing [5, 6, 7]. In this case the multi-body approach was directed to simulate accurately the landing performance in limit conditions with the aim to validate its capabilities in predicting, with the required precision, all the data useful to improve the insight in gear behaviour and gear interactions with fuselage. Moreover, the validate landing gear model is now available for crashing landing condition simulation.

2 - The Skid Landing Gear and the Model

The cross members of the skid landing gear taken into consideration are 7075-T6 aluminium alloy hollow tubes, with variable outer diameters. The forward and rear members differ in respect of dimensions, constraints to fuselage and features. Cross members planes are slightly inclined with respect to the helicopter yaw axis (Fig. 1).

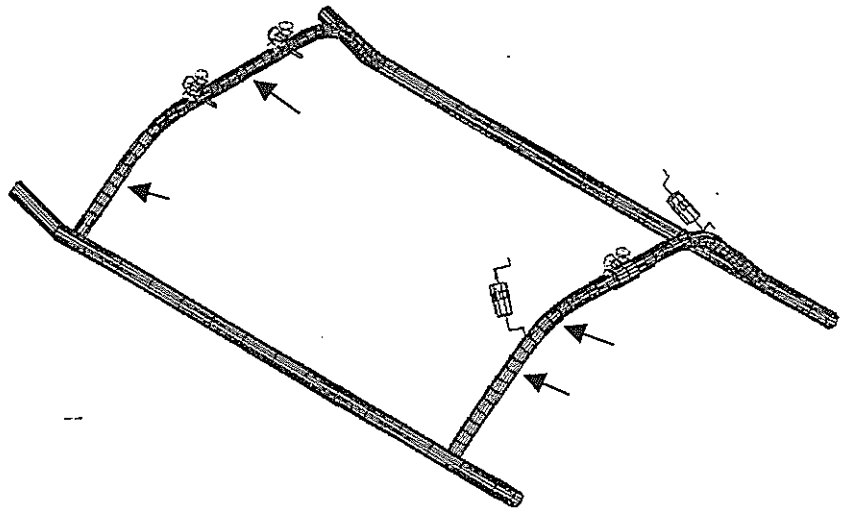

Fig. 1-The skid landing gear complete model

The forward cross member is constrained by clamps in two points, substantially allowing relative translation and rotation around and along the tube axis in its central straight part. Rings housed on the tube itself prevent sliding along the tube axis.

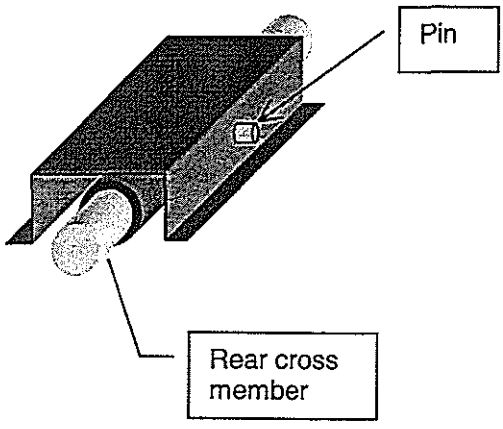

The more massive rear member is constrained in one point only, in the middle, where the tube is strengthened by a thickening reinforcement and connected by a pin to a hat shape case (Fig. 2).

Two axial viscous dampers are set between the rear cross members and the fuselage. Though dampers were introduced to prevent ground resonance, they play a significant role in landing performance. Modifications in their characteristics, location or alignment affect overall landing performances and loads introduced in the fuselage structure.

Fig. 2-Rear cross member constraint to fuselage

In the numerical multi-body model, the cross members and the skids are modelled with elasto-plastic *beam* elements (Fig. 3), while the fuselage body is retained as rigid, with its mass lumped in its centre of gravity. The simulations carried out, for validating the model, reproduce the drop tests where equivalent mass was used.

A total of 60 masses and 60 *beam* element are used to model skids and cross members. Cross members typical *beam* length is about 115 mm.

Nodes assigned to the fuselage rigid body are used to define the position of constraints and damper-fuselage attachments. Cross member constrains are modelled by single point elastic joints (*point* elements).

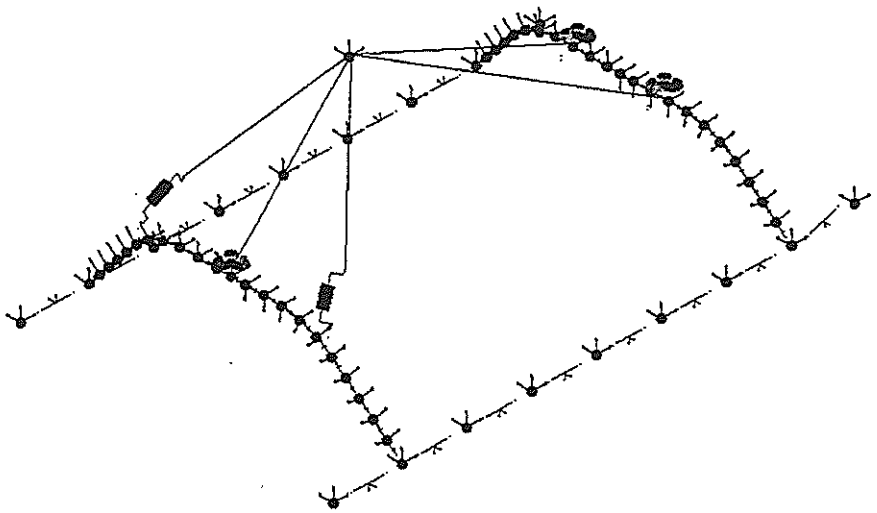

Fig. 3 - Multi-body mass and elements frame

Reactions are considered negligible in forward member constraints for a translation along tube axis in its straight part and a rotation around the same axis, as well as in rear member constraint for a rotation around the pin axis. The corresponding *point* elements leave these motions completely free.

Contacts are modelled in VeDyaC by using contact elements. They are characterised by geometrical characteristics and by two main contact properties: contact volume and contact pressure [4]. The contact behaviour depends upon the relative properties of interacting elements. Hysteresis and friction can also be introduced. Available shapes are cylinders, spheres, polyhedrons and plans. The gear frame is entirely coated by *cylinder* contact elements (Fig. 1). There are *polyhedron* elements to activate the contacts between the rear cross member and the case (Fig. 2) and the lateral contact between anti-slide rings and forward member clamps.

Multi-body models data can easily be ordered in separated assemblies. As each assembly defines a local reference frame, their relative positioning is straightforward. This feature has been widely used to easily reproduce different landing attitudes and conditions.

3 - Characterisation Procedures

To complete the definition of the model, elasto-plastic beams properties, dampers viscous behaviour and constraints stiffness had to be defined. The skid-soil contact was characterised by simple assumptions and tuned in a later phase.

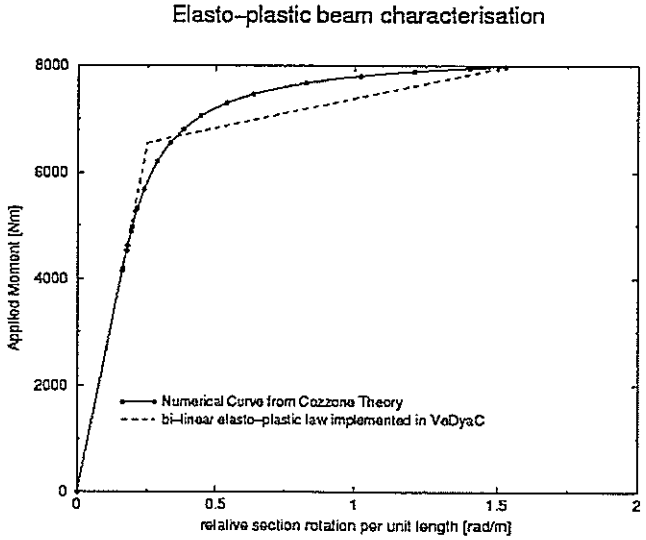

Fig. 4- bi-linear elasto-plastic beam section characterisation

Non-linear elasto-plastic bending behaviour was reproduced basing on the application of Cozzone's theory [8]. This procedure was available from the early design stage of the skid landing gear. It was used to characterise separately the cross member in order to define their diameters and optimal tapering laws along members axis.

As a fine description of the material stress-strain curve was used, numerical bending curves derived by Cozzone's theory implementation describe quite accurately plastic beam bending.

Elasto-plastic elements in VeDyaC are defined by bi-linear generalised force-displacement laws; hence the original curve had to be approximated with a bi-linear law by identifying a yielding point.

Taking in account the expected moment maximum values, available from early design phase predictions, the yielding point was set in correspondence of a stress value on the outer fibres about 3% higher than 0.2% yield strength. Fig. 4 shows an example referred to a section in the rear cross member.

A new type of elastic-plastic law, where plastic curve can be given more accurately, has been recently made available in VeDyaC. Considerations about the opportunity to utilise this new law will be presented later.

Dampers were characterised by their Force vs. velocity curve.

Skid gear attachments to fuselage modelled by *point* elements needs a stiffness characterisation. The analyses showed a negligible sensitivity of results to these parameters, provided that relative displacements between cross members and the rigid modelled fuselage are very small. For this reason, very stiff elastic properties were assigned to all restrained dof. Only the torque stiffness in rear cross member attachment was evaluated by a more accurate calibration, allowing for warping restraint [9].

Skids-soil contact was initially characterised by imposing conditions arising from following considerations:

- No deformation on skid surfaces was expected.
- A ground towing test was performed to evaluated friction on the same soil to be used in drop test (a tread plate laid over a concrete floor to reproduce a very rough ground). Low-velocity sliding friction was found to be about 0.40.
- After a rough estimation of vertical ground reaction distribution, a maximum penetration of 2 mm into soil was used to calibrate contact properties.

4 – Drop Tests and Simulation Results

Three main drop tests were carried out in level landing conditions at Augusta Laboratories, namely horizontal level landing, level landing with drag and level landing with lateral loads. Test were designed to reproduce the load conditions required by regulations [1]. Fig. 5 exemplifies drop test conditions.

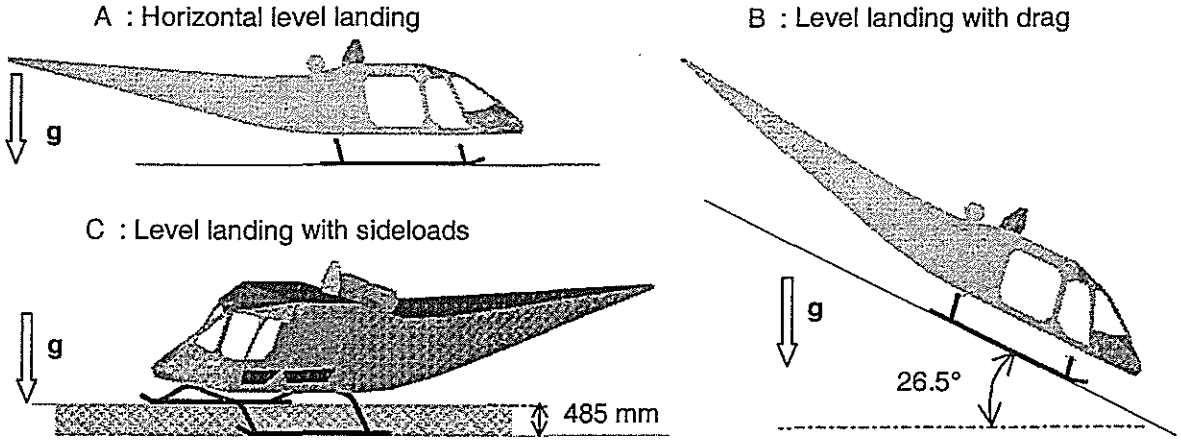

Fig. 5-Drop tests conditions

All drop tests were performed at 2 m/s sink speed, with an equivalent mass evaluated by assuming a rotor lift correspondent to the two-thirds of maximum design weight. The data acquisition system consisted of more than 20 measuring devices for each drop condition:

- Triaxial accelerometers, at centre of gravity and in two different locations with offsets along roll and pitch axis.
- LVDT potentiometers for measuring deflection of forward and rear member and the displacement of the equivalent mass centre of gravity.
- Two load cells housed in forward cross member clamps.
- Load cells and LVDT potentiometers to measure load and stroke of dampers.
- Strain gauges couples located on the forward and rear cross members and on the skids.

Acquisition was performed at 1000 Hz sampling frequency.

The previously described model attained an appreciable result (Fig. 6). Numerical vs. experimental data comparison is based on the load transmitted to fuselage by one the forward cross member, as it was acquired by the load cells housed in the forward member constraints. These signals are more suitable to be confronted with model solution

outputs, as the release mechanism introduced a disturbance into accelerometers experimental signals, imposing the use of a low-pass filter.

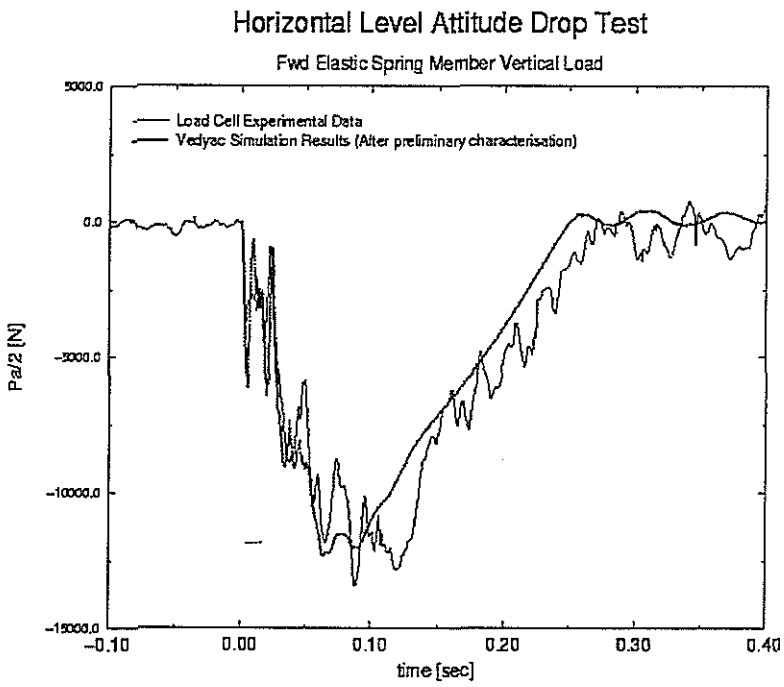

Fig. 6- Numerical vs. experimental loads in the forward cross member constraint with the original characterisation of soil properties in the model (cond. A)

The simulation result reproduces with good accuracy the loading ramp and the maximum value. Model solution configures a somewhat smoother curve and predicts an unloading ramp anticipated with respect to the experimental data. Furthermore load peaks are overestimated during the very first instants of the impact.

To improve the correlation between the two curves, a skid-soil contact tuning was performed. Histeresys phenomena was supposed to occur in the first instants, contact pressure was forced to grow more rapidly, and friction was decreased, allowing for a dynamic reduction effect with respect to the low-velocity towing test (from 0.40 to 0.30). The maximum penetration resulted substantially unchanged. The new curve is reported in Fig. 7.

The curve obtained after calibration follows very well the time history of load transmitted by forward cross member to fuselage. This is particularly true for the loading ramp, while the rebound phase is not perfectly reproduced, though overall impact duration is well predicted.

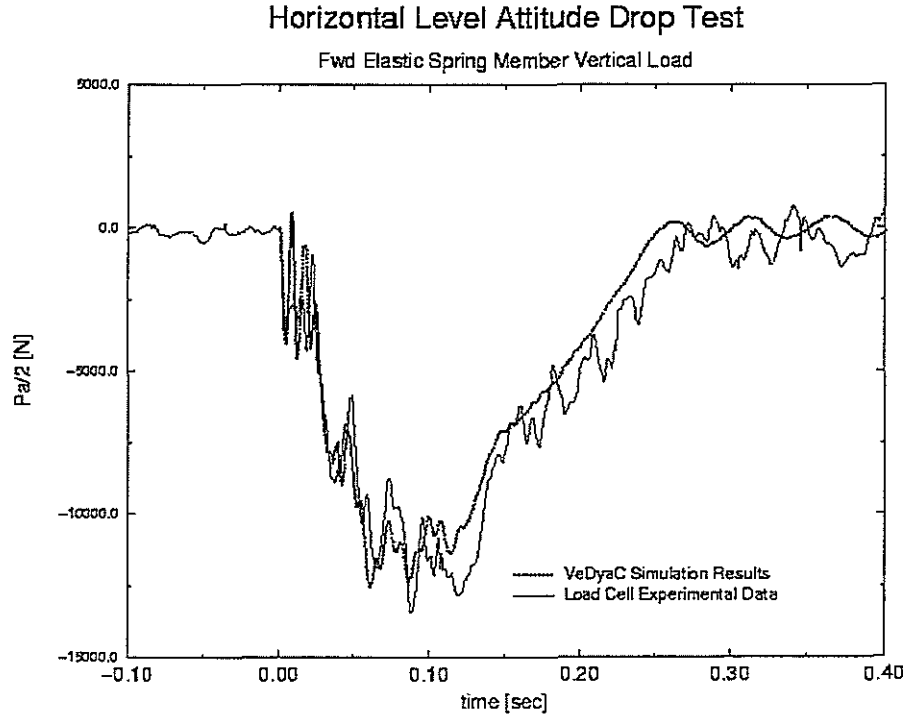

Fig. 7-Numerical vs. experimental loads in forward cross member constraint after skid-soil contact tuning (cond. A)

Fig. 8 reports numerical vs. experimental data for vertical acceleration in the horizontal drop simulation and test.

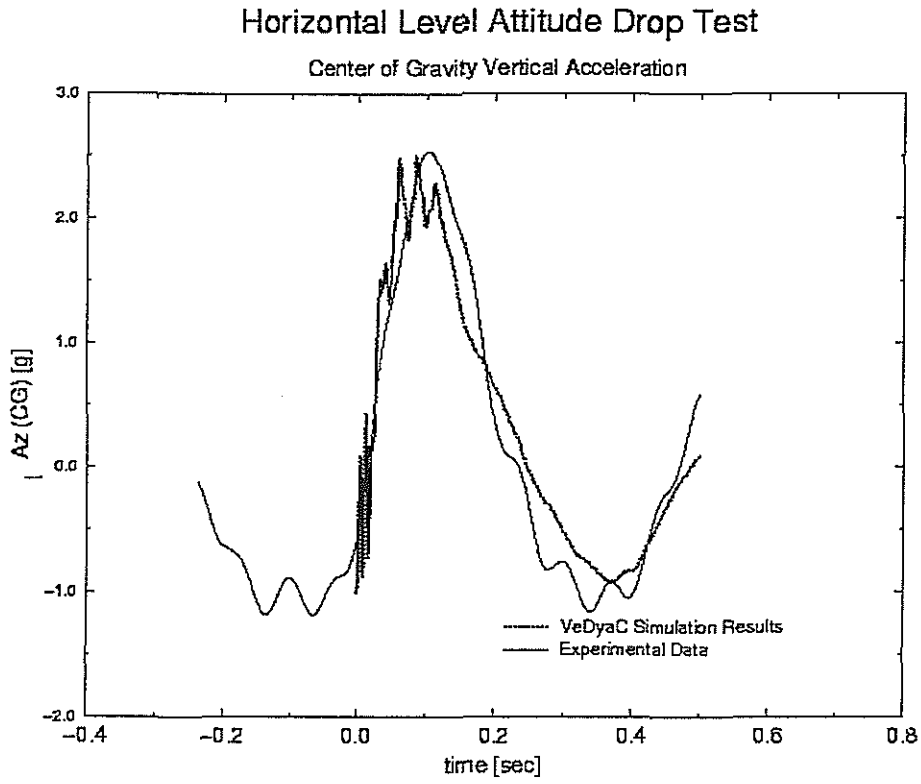

Fig. 8-Numerical and experimental CG vertical accelerations (cond. A)

Though the filtering of experimental curve does not allow detailed considerations, the error on maximum value of deceleration is limited to 2.4%. Table 1 indicates the percentages error between measured displacement and model solution.

Damper behaviour is also very well reproduced, particularly up to the onset of the rebound phase (Fig. 9).

Tab. 1: Numerical vs. Experimental percentage error for maximum CG displacement and cross members deflection (Horizontal level drop test)

Location	%Δ
CG displacement	+1.12%
FWD cross member	+0.5%
AFT cross member	-1.7%

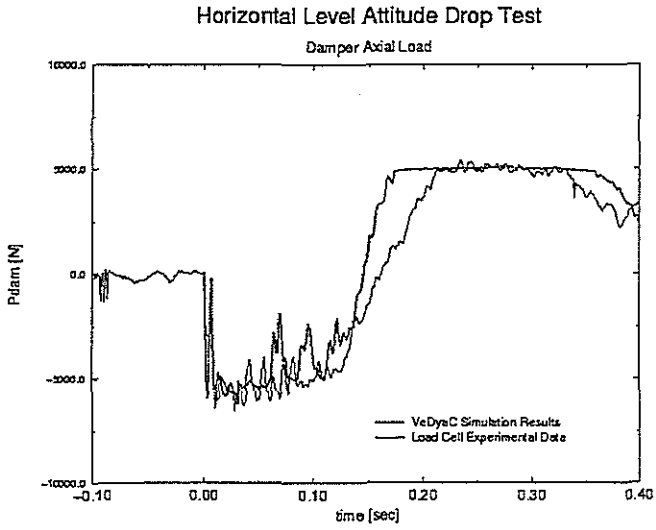

Fig. 9- Numerical and experimental damper loads

No further modification were introduced to simulate the other drop conditions. Fig. 10 to 12 report the results for the load in one of forward member constraints, as well as CG acceleration along Z and X helicopter body axis, for the simulation of landing with drag attitude (cond. B- Fig. 5). Fig. 14 is referred to CG displacement measured in a fixed reference frame and allows for the sliding along the inclined plane.

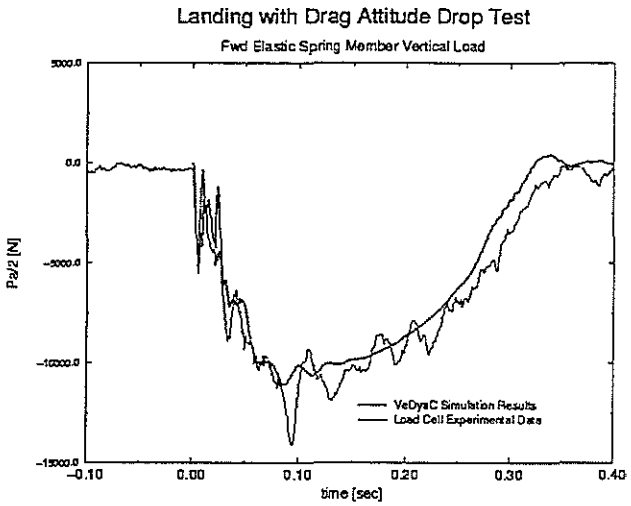

Fig. 10 - Load in forward member constraint (cond. B)

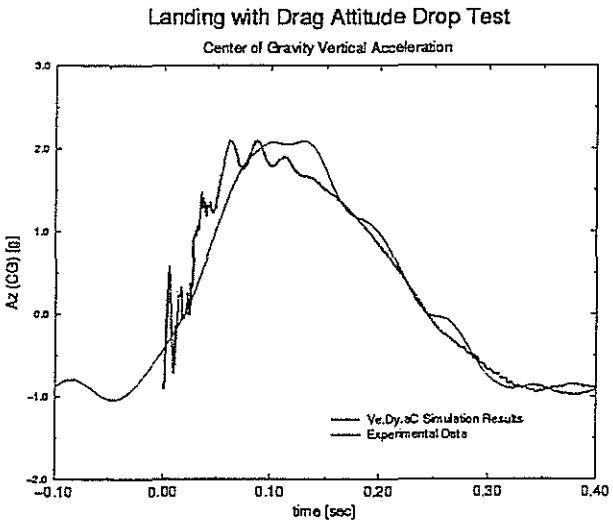

Fig. 11-Helicopter vertical axis acceleration (cond. B)

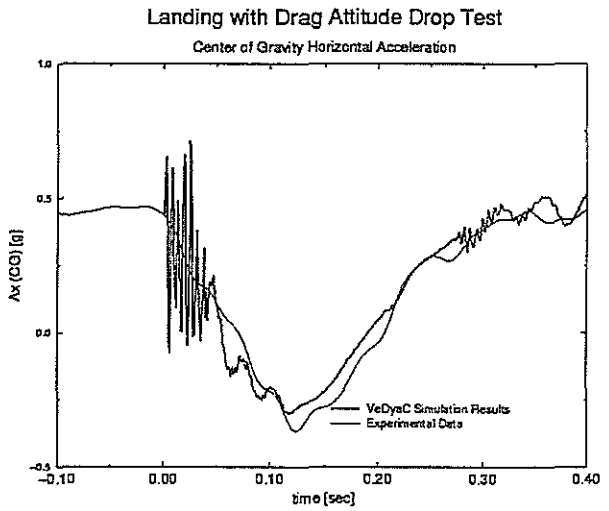

Fig. 12 -Helicopter roll axis acceleration (cond. B)

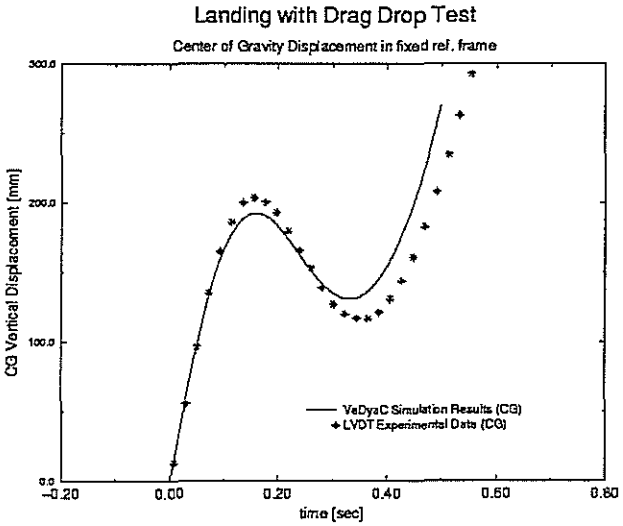

Fig. 13-Vertical displacement (cond. B)

Acceleration maximum values and pulse widths are well reproduced. The narrow load peak in the forward member load is not completely developed, but, as for the horizontal landing case, the loading ramp phase shape indicates that most of the details of the structural response are represented by the model with good numerical approximation. The picture in Fig. 14 shows the deformed shape of the skid landing gear in this condition.

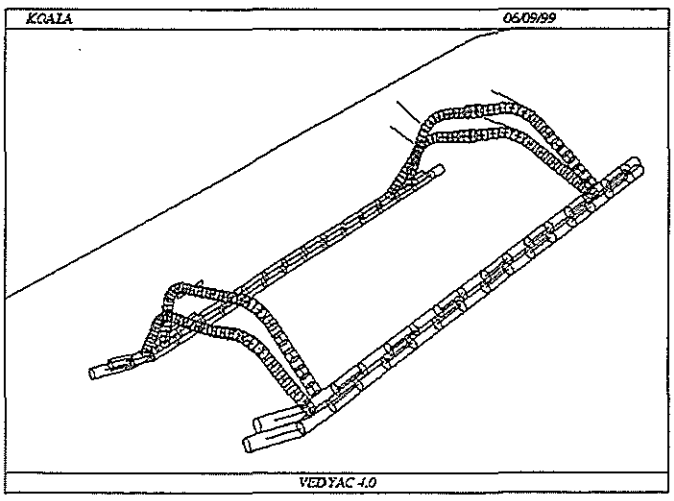

Fig. 14-Deformed shape in landing with drag attitude (cond. B)

Results for landing with lateral loads (cond. C - Fig. 5) are presented in Fig. 15 to 18. Fig. 15 and 16 are referred to acceleration along Z and Y helicopter body axis. Fig. 17 and 18 reports numerical vs. experimental data for the load cell housed in both forward cross member constraints to fuselage.

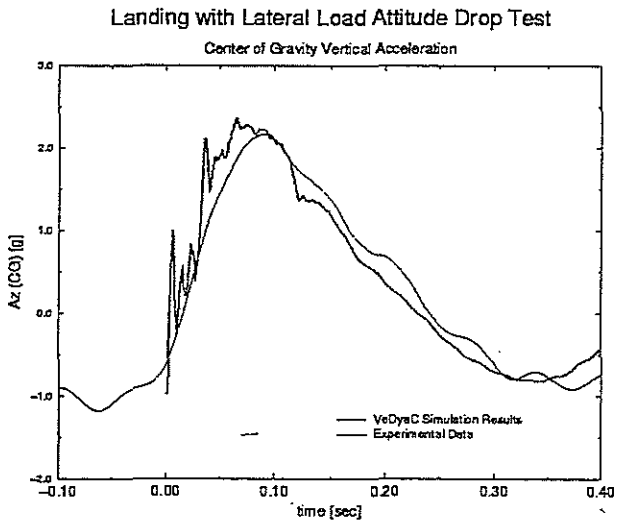

Fig. 15- Helicopter vertical axis acceleration (cond. C)

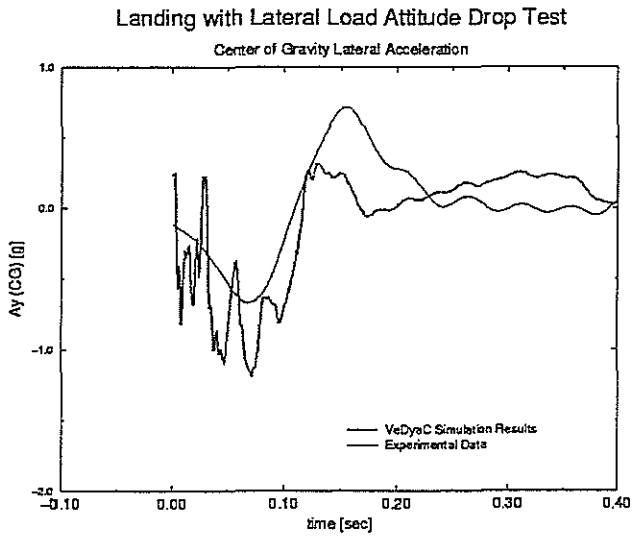

Fig. 16- Helicopter pitch axis acceleration (cond. C)

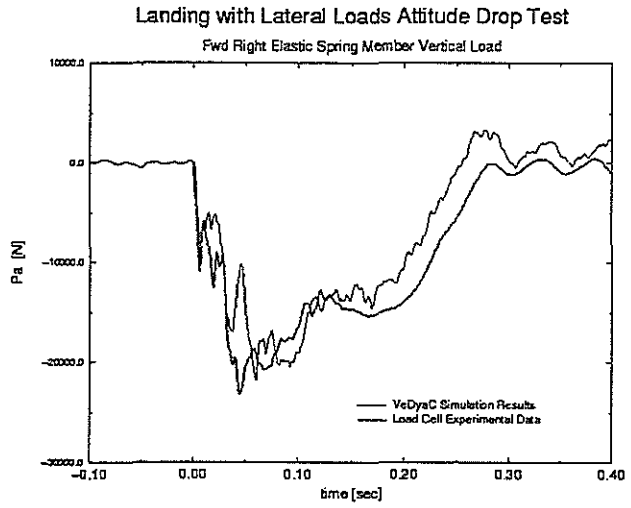

Fig. 17- Load in forward member left constraint (cond. C)

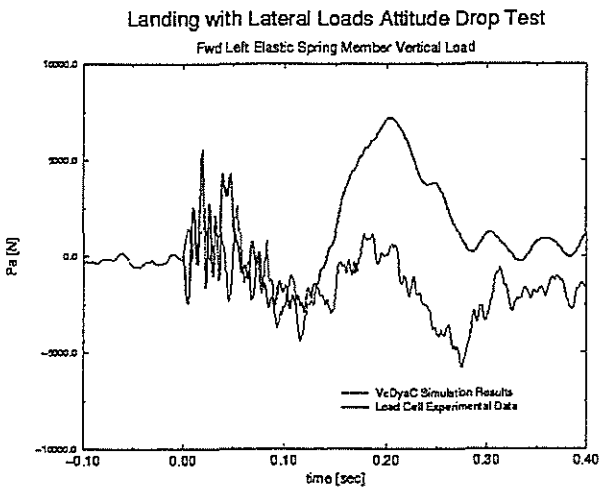

Fig. 18- Load in forward member right constraint (cond. C)

The load in the left constraint (Fig. 17) is up to 100% higher than in the horizontal level drop test (Fig. 7). The model reproduces its time history with good accuracy. The load in the other constraint is one order of magnitude lesser up to the rebound phase. This is as well reproduced by model solution (Fig. 18), though discrepancies between the model and the test are in this case evident during the rebound phase of the impact.

Fig 15 shows that the error on the maximum value of deceleration is limited to 5%.

The contact between the rear cross member and the upper hat case never became active in the simulations. This is in accordance with experimental evidence.

The evaluation of strain in the cross member is partially affected by the reduction of their bending behaviour to a bi-linear elasto-plastic law. Equivalent numerical strains were evaluated by the moment in the *beam* elements and then compared with the data acquired by the strain gauges couples in the correspondent locations (Fig. 1). Fig. 19 and 20 are referred to horizontal level landing conditions (cond. A).

Fig. 19 is referred to a location on the forward member inclined terminal part. The element has not experienced plastic strain during the simulation. The reproduction of strain gauges data is satisfactory. Fig. 20 is referred to the central and most loaded portion of forward cross member. Plastic strain occurs, thus showing a different behaviour from

the strain gauges experimental data. The inadequate characterisation of *beam* elements can give reason for most of the discrepancies between model and experimental data. A better result could surely be attained by a more accurate representation of the bending behaviour, now available in the solver code.

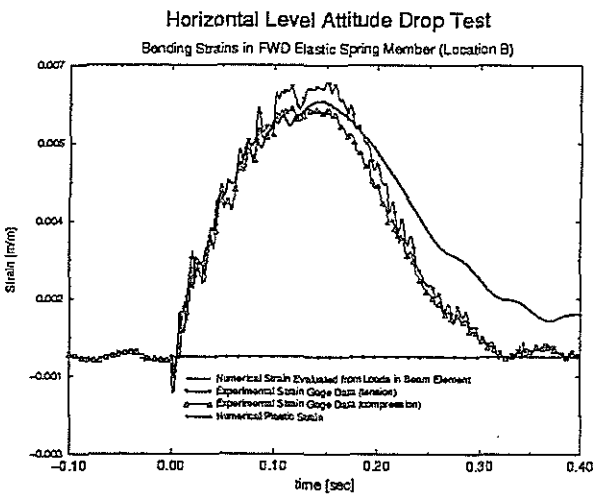

Fig. 19 – Numerical vs. experimental strain Location B (cond. A)

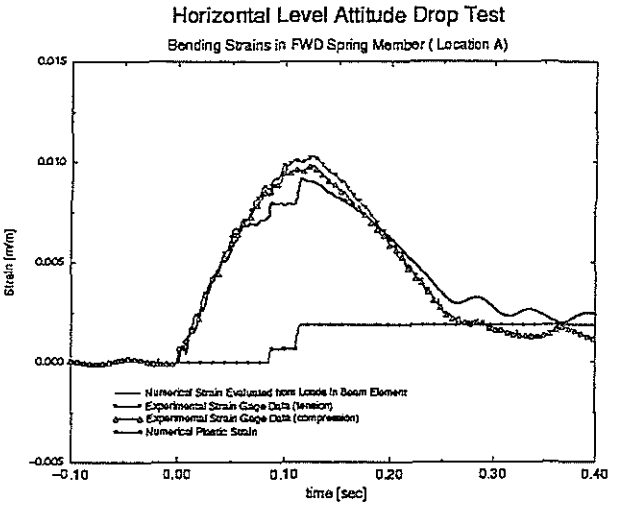

Fig. 20 – Numerical vs. experimental strain Location A (cond. A)

The simulations results, in drop test conditions, shows that both overall landing performance, as well as load transmitted to fuselage can be reproduced with a noticeable accuracy by the model which can be considered suitable to attain reliable prediction in conditions not reproduced by drop test.

The time required for model solution is extremely short, as a 0.5 seconds long simulation takes only 235 CPU seconds time on an Alphastation 600A 5/500.

5 – Model Predictions in Different Landing Conditions

Some results are here presented to allow an evaluation of landing gear behaviour as well as the capabilities of this kind of model.

Friction is a critical parameter in the performance of the skid landing gear. Drop test conditions were performed with a rough soil in order to attain a high friction coefficient and hence a high load factor, but low friction implies higher deflections of cross members and increases the arms of ground reactions.

Table 2: Percentage Variations of Maximum Displacements and loads acting in cross members for three friction coefficients

Friction Coeff.	0.40	0.25	0.10
CG displacement [mm]	171	186	202
Moment (loc. A)[N m]	6985	6997	6974
Moment (loc. C)[N m]	6939	7116	7312
Moment (loc. D)[N m]	8279	8456	8633

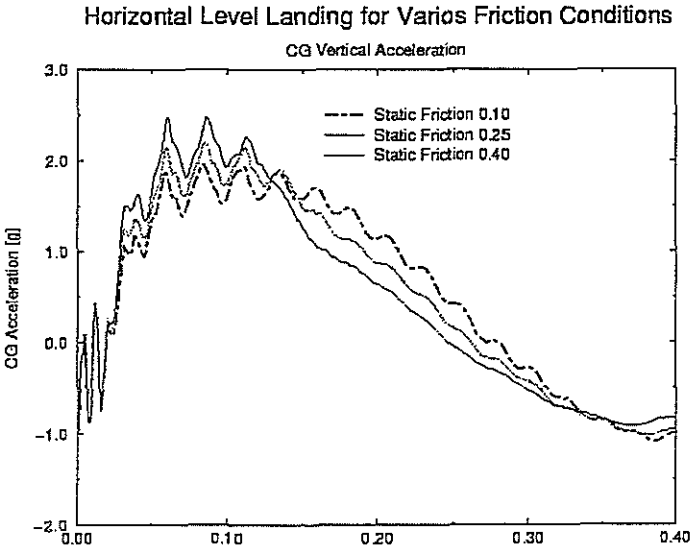

Fig. 21 – CG vertical accelerations at various soil friction conditions

Two simulations were carried out in horizontal level landing attitude, with frictions parameters equivalent to 0.10 and 0.25 static friction coefficients. Table 2 indicates the variations in the values of maximum CG vertical displacement and in moments in three locations of cross members (Fig. 1) with respect to drop test simulations. Fig. 21 compares the accelerations in the three conditions.

The simulation with the lowest friction coefficient (0.10) predicts a maximum CG deflection of about 20% more than the level horizontal drop test conditions (cond. A). This deflection does not imply any clearance problem.

The moments in the cross members are generally increasing as the friction factor decrease. This tendency is evident in rear cross member. As far as the forward cross member is concerned, the behaviour is different and the moment does not show a remarkable increase. This is due to the uniform bending load acting along its central straight part, which produces a diffused moderate plastic strain and increase the cross member efficiency.

Performance in limit conditions at different landing weights were evaluated by introducing in the model an averaged rotor lift equal to the two third of the landing weight.

Simulations at various landing weights measure the increasing in load factor at diminishing weights, as it is showed in Fig. 22. The landing gear stiffness remains unchanged while the weight and the energy to be absorbed decrease, thus leading to higher load factors. Ground reactions decrease but the forward cross member shows a tendency to reach a maximum typical load (Fig. 23).

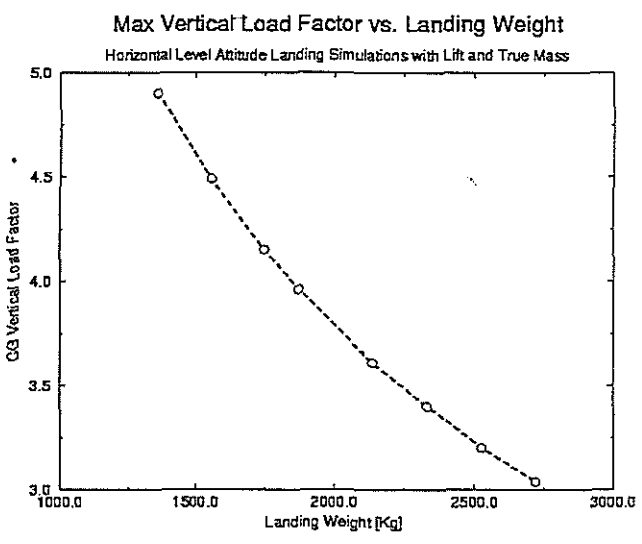

Fig. 23 – Maximum vertical load factor vs. landing weight (horizontal level attitude)

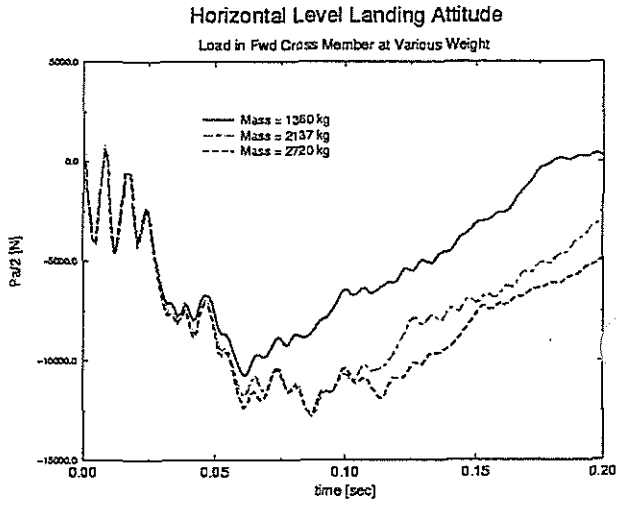

Fig. 24 – Load in forward member right constraint at various landing weight (horizontal level attitude)

Finally a simulation in a particular soil condition is presented. A landing was simulated in case of lateral obstruction. Friction coefficient and sink velocity were the same as in drop test conditions. The obstruction consisted of a very stiff contact element placed parallel at the skid, along one third of its length. Contact was set to occur immediately after the impact.

No remarkable increasing in vertical load factor was detected, but side acceleration was found to be higher than for the landing with lateral load condition (Fig. 22). Fig. 23 is referred to the instant of maximum deflection.

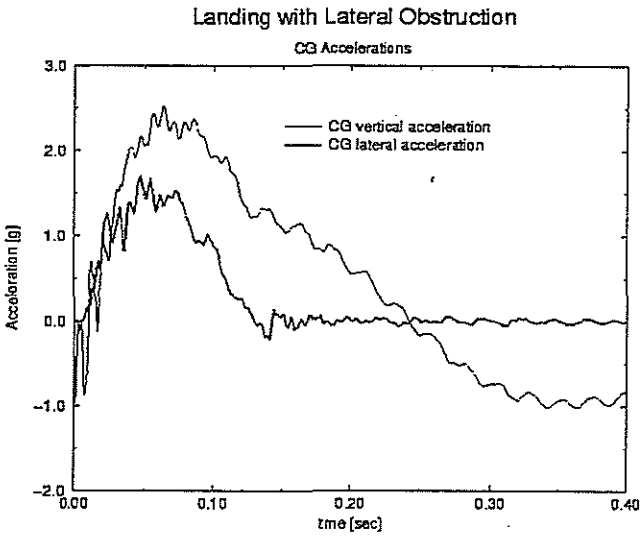

Fig. 22 – **CG accelerations for landing with lateral obstruction**

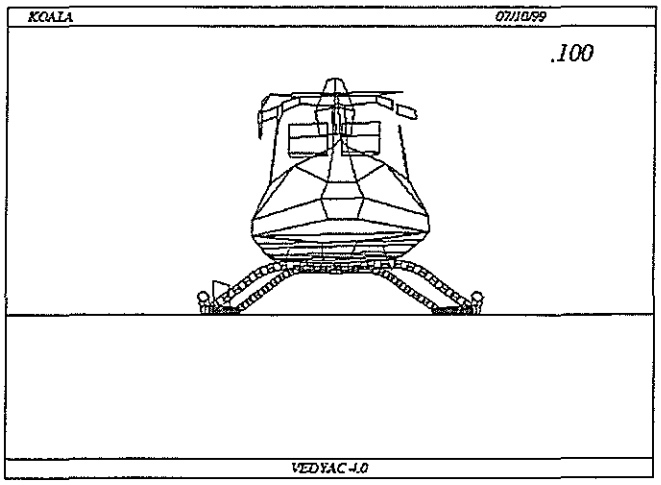

Fig. 23 – **Maximum deflection in landing with lateral obstruct**

6 - Concluding Remarks

Results attained by the multi-body approach in simulating limit landing condition can be considered very appreciable. Modelling required a correct evaluation of structural behaviour of the landing gear components and of constrains with fuselage. Most of the modelling effort was dedicated to the characterisation of elasto-plastic beam behaviour, but, as a matter of fact, even the apparently simpler classical approach, based on separated modelling of cross members, requires the same accuracy if reliable results have to be attained.

The landing performances for a skid landing gear are appreciably influenced by the soil properties, particularly by the skid-soil friction. In this case, a tuning of the soil contact properties was performed taking in account the experimental data. However, the curve in Figure 6 has shown that good results can be achieved by characterising soil with reasonable assumptions and performing, if needed, some tests to evaluated the friction in soil conditions to be used for design and testing.

The time required for a simulation, as well as the very little modifications needed to simulate different landing attitudes and soil conditions, indicates that this approach should be considered suitable to be used from the very earliest design phases. The simulation results should be even improved by characterising with a more accurate law the cross member elasto-plastic behaviour.

This case, as the model was developed after the design phase was concluded, can be considered a workbench at this regard.

Besides the overall landing performance, attention was focused on predictions regarding dampers behaviour and loads transmitted to the fuselage. Thanks to the exhaustive amount of data collected during the drop tests, these prediction have been compared with experimental data, showing good correlation for all the three attitudes taken into consideration.

The present results, together with the works by Astori [5,6 and 7], shows that a multi-body approach can be usefully applied to performance prediction and design of skid and wheels landing gear both in emergency and limit landing conditions.

References

1. FAA, FAR part 27, Airworthiness Standards: Normal Category Rotorcraft, 1998.
2. Max Chernoff (Republic Aviation Corporation -USA), Analysis and Design of Skid Gears for Level Landing, Journal of American Helicopter Society, 1962.
3. V. Giavotto, L. Puccinelli and M. Borri (Politecnico di Milano-Italy), Vehicle Dynamics and Crash Dynamics with Minicomputers, Computers & Structures, Vol. 16, No 1-4, pp. 381-393, 1983.
4. L. Puccinelli (Politecnico di Milano-Italy), Modelli di Contatto nei Programmi per la Simulazione di Crash (in Italian), Atti del X congresso Nazionale AIDAA, Pisa 16-20 Ottobre 1989.

5. P. Astori (Politecnico di Milano-Italy), Multi-Body Simulations for Helicopter Crasworthiness and Experimental Results, 22nd European Rotorcraft Forum, 17-19 Sept. 1996.
6. P.Astori (Politecnico di Milano-Italy), Full-Scale Helicopter Crash Landing Test and Multi-Body Analysis, International Crashworthiness Conference IJCRASH'98, Dearborn (MI, USA), 9-11 Sept. 1998.
7. P.Astori (Politecnico di Milano-Italy), M. Ignarra and S. Poggi (Agusta, a Finmeccanica Company-Italy), A129 Crash Test and Simulation, 24th European Rotorcraft Forum, Marseille (F), 15-17 Sept. 1998.
8. F.F. Bruhn, Analysis and Design of Flight Vehicles and Structures, S.R. Jacobs and Associates, Indianapolis (USA), 1973.
9. C. Young Warren, Roark's Formulas for Stress and Strain, 6th edition, Chap. 9, art. 9.3, Mc Graw Hill International Edition, 1989.
10. A. Barsony-Nagy and R. Rivlin (Mata Helicopters – Israel), Simulation of helicopter landing on a ship deck, Collection of Papers of the 30th Israel Annual Conference on Aviation and Astronautics, 1989.

TWENTY-FIFTH EUROPEAN ROTORCRAFT FORUM

Paper n° G14

VIBRATION SUPPRESSION IN HELICOPTERS WITH THE ACSR APPROACH USING AN IMPROVED CONTROL ALGORITHM

BY

R. CRIBBS, P. P. FRIEDMANN
UNIVERSITY OF MICHIGAN, USA

SEPTEMBER 14 - 16, 1999
ROME
ITALY

ASSOCIAZIONE INDUSTRIE PER L'AEROSPAZIO, I SISTEMI E LA DIFESA
ASSOCIAZIONE ITALIANA DI AERONAUTICA ED ASTRONAUTICA

VIBRATION SUPPRESSION IN HELICOPTERS WITH THE ACSR* APPROACH USING AN IMPROVED CONTROL ALGORITHM

R. Cribbs† and P.P. Friedmann‡
Department of Aerospace Engineering
University of Michigan
Ann Arbor, Michigan 48109-2140

ABSTRACT

This paper describes vibration modeling and control using a coupled rotor/fuselage aeroelastic response model with refined aerodynamics. The flexible fuselage, modeled by a three-dimensional structural dynamic finite element model, is combined with a flexible, four-bladed hingeless rotor. The unsteady aerodynamic loads are obtained from a free wake model combined with rotor/fuselage aerodynamic interaction effects. The effects of the various aerodynamic refinements on vibratory loads and fuselage accelerations are studied. Vibration reduction with active control of structural response (ACSR) is carried out with two control algorithms. The improved control scheme is capable of tailoring the vibration reduction process so as to produce low accelerations at locations of particular interest such as the pilot seat. Results indicate a large increase in vibratory loads and fuselage accelerations when using the refined aerodynamic model. Though both control methods reduce airframe vibrations, the improved control algorithm provides significantly lower accelerations when compared to the basic control algorithm with similar actuator requirements.

NOMENCLATURE

a	Blade lift curve slope
a_x, a_y, a_z	Fuselage longitudinal, lateral, and vertical accelerations at various locations
c_b	Blade chord
c_p	Coefficient of pressure
$\mathbf{C}_O, \mathbf{C}_I, \mathbf{C}_{NW}$	Matrices of induced velocity influence coefficients
C_T	Rotor coefficient of thrust
C_W	Helicopter coefficient of weight
$\mathbf{D}$	Wake distortion
EI_y, EI_z	Blade bending stiffnesses in flap and lead-lag
$\mathbf{F}_b^A, \mathbf{F}_b^G, \mathbf{F}_b^I$	Blade aerodynamic, gravitational, and inertial forces
$\mathbf{F}_{b_o}, \mathbf{F}_{b_{nc}}, \mathbf{F}_{b_{ns}}$	Fourier coefficients of blade equations of motion
fC_{df}	Fuselage equivalent flat plate drag area
$\mathbf{F}_{fus}$	Total fuselage forces
F_x, F_y, F_z	Vibratory hub shear components
GJ	Blade torsional stiffness
h	Rotor hub length
I_x, I_y, I_z	Fuselage moments of inertia about the center of mass
J	Quadratic control performance index
m_b	Blade mass distribution per unit length
$\mathbf{M}_b^A, \mathbf{M}_b^G, \mathbf{M}_b^I$	Blade aerodynamic, gravitational, and inertial moment

*Active Control of Structural Response
†Postdoctoral Scholar
‡François-Xavier Bagnoud Professor of Aerospace Engineering

$\mathbf{M}_{fus}$	Total fuselage moments
M_x, M_y, M_z	Vibratory hub moment components
N_b	Number of blades
p	pressure
$\mathbf{q}$	Response vector
$\mathbf{r}_w$	Position of wake element
R	Rotor radius
$\mathbf{T}$	Jacobian of the acceleration response with respect to the current control input
$\vec{u}$	Vector of control amplitudes
$\vec{u}^*$	Optimal control vector
$\|V\|$	Magnitude of air velocity
$\mathbf{W_u}, \mathbf{W_z}$	Weighting matrices on the control amplitudes and acceleration amplitudes, respectively
x	Blade spanwise coordinate
X_{FA}, Z_{FA}	X and z locations of the fuselage aerodynamic center relative to fuselage/hub intersection
X_{FC}, Z_{FC}	X and z locations of the fuselage center of mass relative to fuselage/hub intersection
$\vec{z}$	Vector of selected airframe acceleration amplitudes
α_R	Rotor trim pitch angle
β_p	Blade precone angle
γ	Lock number
Γ_I, Γ_O	Inboard and outboard circulation peaks defining the strength of the tip vortices
Γ_{ij}	Bound vorticity at azimuth j and spanwise location i
$\theta_o, \theta_{1c}, \theta_{1s}$	Blade collective pitch, cyclic cosine and sine pitch angles, respectively
θ_{tr}	Tail rotor collective pitch angle
λ	Non-dimensional induced velocity
μ	Advance ratio
ρ_A	Air density
σ	Rotor solidity ratio
ϕ_V	Velocity potential
ϕ_s	Rotor trim roll angle
ψ	Blade azimuth angle or non-dimensional time ($= \Omega$ t)
Ω	Angular speed of rotor

1 INTRODUCTION

One of the primary concerns in rotorcraft design is the issue of vibrations and its reduction. In recent years, requirements for vibrations in military helicopters have been established that limit vibration levels to 0.05g at certain fuselage locations. High levels of vibration lead to passenger discomfort, increased noise levels and fatigue of both pilot and aircraft which in turn decrease rotorcraft performance and increase cost. These issues are critical to the acceptance of rotorcraft, thus, the issues of vibration prediction and its reduction to acceptable levels are of primary importance to the rotorcraft designer.

The largest contributor to vibrations in a helicopter is the rotor. The rotor blades transfer vibratory loads from the hub to the fuselage at harmonics that are predominantly N_b/rev, where N_b is the number of blades. Blade vortex interactions (BVI) and rotor/fuselage interference effects add complexity to the vibratory loading environment. In order to determine the vibration levels at various fuselage locations, it is necessary to consider a coupled rotor/flexible fuselage model. Studies by Yeo and Chopra [1] have shown remarkable differences in vibration levels in a coupled rotor/flexible fuselage system when using linear inflow and comparing it to free wake models. At certain advance ratios, the loads obtained when using the free wake model resulted in vibration levels that were 100 times higher than those obtained using a linear inflow model. The fuselage model used in Ref. 1 consisted of a "stick" model of the AH-1G. Recent analyses [2–4] and wind tunnel investigations [5–7] have shown the influence of rotor/fuselage interaction on rotor loads. But these studies

were mainly concerned with the time averaged phenomena and not the rotor/fuselage interference effects on vibrations. It is thus clear that more accurate aerodynamic models are required in order to predict vibrations, and conduct aeroelastic response simulations for vibration control. Furthermore, the improved aerodynamics should be combined with equally refined structural dynamic models.

Recently, active control strategies have been developed that can reduce vibration levels well below those achieved through traditional passive methods such as dampers and mass tuning [8]. Among the active control approaches, two fundamentally different strategies have emerged. Three approaches: higher harmonic control (HHC), individual blade control (IBC) and the actively controlled flap (ACF) all attempt to control the vibrations, at their source on the rotor blades, by manipulating the unsteady aerodynamic loading in the rotating system. A second promising alternative approach is the active control of structural response (ACSR) where vibrations are reduced by actuators located in the fuselage. In this case, vibration reduction is carried out in the non-rotating system.

A schematic of the ACSR system is shown in Figure 1. Inputs to the actuators excite the fuselage so as to counteract the excitation due to the rotor system. Thus the combined input of the rotor disturbance and the actuator forces is minimized. Since the implementation of this method of vibration control occurs in the non-rotating system, the complexity and airworthiness issues associated with the alternative approaches are eliminated. Also, older aircraft may be retrofitted with the actuators to improve their vibration levels. This approach was initially developed by Staple at Westland [9,10] and was successfully flight tested by both Westland and Sikorsky [11,12]. This approach is currently implemented on a production helicopter, the Westland/Augusta EH101. A mathematical model capable of simulating this vibration reduction approach has been developed by Chiu and Friedmann [13,14] at UCLA. This mathematical model employs simplified aerodynamics for both the rotor and the fuselage. The model used was based on uniform inflow, quasisteady aerodynamics for the blades and a simple flat plate equivalent area model was used for the fuselage aerodynamics. This model neglects rotor/fuselage aerodynamic interference effects.

The present study is aimed at developing an improved understanding into the mechanisms of helicopter vibrations and their control using ACSR. The specific objectives of the paper are: (1) investigate the influence of a new aerodynamic model, that combines a free wake model of the rotor with a model capable of representing rotor/fuselage interactional aerodynamics, on the vibratory loading and resulting fuselage accelerations; (2) development of an improved control algorithm that permits vibration reduction to be preferentially applied to specific fuselage locations; (3) investigate the vibration reduction capabilities of the improved control algorithm; and (4) compare the improved control method accelerations to the results of the basic control algorithm previously studied at UCLA.

2 MATHEMATICAL MODEL

The coupled rotor/flexible fuselage model is capable of representing a helicopter rotor consisting of a number of flexible, hingeless blades combined with a three-dimensional flexible fuselage. The description of the model, given below, is separated into its components; namely, rotor, wake model, fuselage structural model, and fuselage aerodynamic model.

2.1 ROTOR MODEL

The hingeless rotor blade is modeled as a slender, inextensible beam cantilevered at the root. This isotropic blade model, taken from Ref. 15, includes coupled flap-lag-torsional dynamics in the presence of moderate deflections. The distributed aerodynamic, gravitational, and inertial loads per unit length, including the effects of fuselage motion, are combined to obtain the total distributed force and moment acting on the blade. The inertial and aerodynamic loads are derived implicitly.

The aerodynamic loads on the rotor are calculated using quasisteady, Greenberg type aerodynamics combined with a free wake model. The reverse flow region on the blade is accounted for by switching the direction of the drag acting on the cross-section of the blade and setting the lift and moment terms equal to zero inside the reverse flow region. Stall and compressibility effects are neglected.

2.2 WAKE MODEL

The rotor wake model has been extracted from the comprehensive rotorcraft analysis tool, CAMRAD/JA [16, 17], and modified to be compatible with the aeroelastic response analysis employed in our

simulation. It is comprised of a wake geometry model which determines the location of the wake in space and a wake calculation model which, given the wake geometry, calculates the induced velocity distribution.

The free wake geometry scheme was initially developed by Scully [18]. Each wake element is created at the blade and is convected with the air's local velocity which is composed of the free stream velocity and the wake induced velocity. The wake geometry is calculated as follows: first, the positions of the blade generating the wake elements are calculated; second, the undistorted wake is found by adding the contribution of the free stream velocity to the wake element creation points; third, the free wake geometry is found by adding the distortion due to the wake and fuselage induced velocities to the undistorted geometry. A wake element is thus described by the position of blade when the wake element was created and the time elapsed from the time of element creation to the current time, or:

$$\mathbf{r}_w(\psi,\phi) = \mathbf{r}_b(\psi-\phi) + \phi\mathbf{v}_w + \mathbf{D}(\psi,\phi) \tag{1}$$

The wake distortion, $\mathbf{D}(\psi,\phi)$, is calculated by integrating in time the wake and fuselage induced velocities acting on the wake element.

The wake calculation routine was developed by Johnson [19]. The model is based on a vortex lattice approximation of the wake consisting of two main elements: the tip vortex and an inboard vortex sheet. The tip vortex is a concentrated vorticity filament generated at the tip of the blade while the inboard vortex sheet is due to trailed and shed vorticity and is much weaker and more diffuse than the tip vortex. The tip vortices are modeled as vortex lines with small viscous core radii while the inboard sheet can be represented by either vortex sheet elements or vortex line segments with large core radii. Given the wake geometry and the bound circulation distribution, matrices of influence coefficients are calculated. These influence coefficients describe the wake induced velocities as a function of blade bound circulations. A simple matrix multiplication of influence coefficients times the circulation distribution provide the induced velocities as shown:

$$\lambda_i = \sum_{j=1}^{J}\Gamma_{Oj}\mathbf{C}_{Oj} + \sum_{j=1}^{J}\Gamma_{Ij}\mathbf{C}_{Ij} + \sum_{j=0}^{K_{NW}}\sum_{i=1}^{M}\Gamma_{ij}\mathbf{C}_{NW_{ij}} \tag{2}$$

where J and M are the numbers of azimuth and spanwise stations, respectively, at which the induced velocities are calculated and K_{NW} is the number of azimuth stations that describe the extent of the near wake.

2.3 FUSELAGE STRUCTURAL MODEL

The fuselage equations of motion are determined using a Lagrangian formulation. The elastic fuselage is modeled as a three dimensional assemblage of finite elements which allows the elastic displacements to be defined by a finite number of generalized coordinates. The fuselage equations of motion are decoupled into rigid body equations of motion and elastic fuselage equations of motion using a truncated set of fuselage natural modes and mean axes.

The finite element model used to obtain the natural modes and frequencies consists of Euler-Bernoulli beams and non-structural masses to model items such as fuel tanks, payload, transmission, engine, etc... The solution to the complete eigenvalue problem for the model with 966 degrees of freedom is carried out using the IMSL subroutine DGEGV [20].

2.4 FUSELAGE AERODYNAMIC MODEL

An equivalent flat plate area is used to calculate the drag of the fuselage due to viscous and profile effects. To model the influence of the fuselage on the rotor aerodynamic loads, the fuselage is represented by a set of sources/sinks that describe a body of revolution. As described in Ref. 21, a body of revolution resembling a helicopter fuselage in axial flow can be represented by as few as three three-dimensional sources/sinks. The shape of the body of revolution used in this study is shown superimposed on the fuselage structural model in Figure 3. This body of revolution is described by one three-dimensional source and two three-dimensional sinks. Using such a limited number of sources/sinks combination creates a computationally efficient model that is well suited to the complex coupled rotor/fuselage problem.

To satisfy the requirement that air should not penetrate the surface of the fuselage, two-dimensional line sources are distributed about the surface of the body of revolution to enforce that normal velocities at the fuselage surface be zero. These off axis velocities are due to rotor/wake induced velocities and pitch and

roll angles of the fuselage. The body of revolution is discretized into fifteen sections longitudinally. Within each longitudinal section, four line sources/sinks are used to satisfy the zero normal velocity criterion at four control points located on the body of revolution as shown in Figure 4. The figure shows a cross section of a longitudinal section. The four line sources/sinks extend into the page and are denoted A, B, C and D. The four normal velocities at the control points are denoted V_1 through V_4. By changing the strengths of the sources/sinks, V_1 through V_4 are set identically to zero.

The combination of the two and three-dimensional sources/sinks influences the air velocity at the rotor blade producing an upwash on the forward part of the rotor and a downwash on the aft region. Additionally, the rotor wake geometry is distorted due to the presence of the fuselage. In this study, only the distortion of the concentrated tip vortices is considered and the inboard vortex sheet is not distorted due to the fuselage. This fuselage induced distortion required two major changes to the wake model: a wake displacement procedure and a modification to the wake distortion integration.

For both the prescribed wake and free wake cases, vortex lines that penetrate the fuselage surface are moved to place them outside of the fuselage. Similar to the procedure used in Ref. 22, if the endpoint of a vortex line segment is within the fuselage body, that endpoint is displaced vertically upward until it is at 110% of the fuselage radius. The additional 10% is what was chosen as the nominal value in Ref. 22. Whereas the vortex lines that penetrated the fuselage in Ref. 22 were subdivided into 10 smaller vortex lines, the vortex lines in the current study were not subdivided. To perform this procedure of resolution improvement would have required an entire redevelopment of the free wake code since the free wake code adapted from CAMRAD/JA [16] is not adaptable in this manner.

To model the influence of the rotor and wake on the fuselage aerodynamics, the pressure is integrated over the surface of the body of revolution and these forces are added to the drag forces calculated using the equivalent flat plate area. Since inviscid, incompressible flow is assumed and all streamlines originate in the steady, uniform free stream, fuselage pressures are related to velocities through Bernoulli's equation:

$$\frac{\partial \phi_V}{\partial t} + \frac{|V|^2}{2} + \frac{p}{\rho} = constant \tag{3}$$

The unsteady term, $\frac{\partial \phi_V}{\partial t}$, is neglected in this study and instead a correction to the total pressure is added to account for the energy added to the fluid by the rotor. As described in Ref. 2, a steady increment of $\Delta c_p = 2C_T/\mu^2$ is added to the pressure at fuselage locations within the rotor wake. The body of revolution is discretized into 60 panels. The pressure is determined at the center of each of these panels and is assumed constant over the area of the panel to determine the force acting on the panel. These contributions are added up so as to provide aerodynamic forces on the fuselage due to the rotor/wake.

3 METHOD OF SOLUTION

The calculation of the wake induced velocity influence coefficients is done in a wake loop outside of the coupled trim/aeroelastic response solution. This wake loop consists of three distinct wake approximations: (1) uniform inflow; (2) prescribed wake; and (3) free wake. Within each wake iteration, the coupled rotor/fuselage trim and aeroelastic response solutions are determined. The aeroelastic response of this system is obtained using the harmonic balance technique. In this study, the trim and response solutions are obtained simultaneously by satisfying the trim equilibrium and the vibratory response of the helicopter for all the rotor and fuselage degrees of freedom together. The equations of motion for the coupled rotor/fuselage system are concisely represented by:

$$\mathbf{F}_b(\mathbf{q}, \dot{\mathbf{q}}, \ddot{\mathbf{q}}, \mathbf{q}_t; \psi) = \mathbf{0} \tag{4}$$

$$\mathbf{F}_r(\mathbf{q}, \dot{\mathbf{q}}, \ddot{\mathbf{q}}, \mathbf{q}_t; \psi) = \mathbf{0} \tag{5}$$

$$\mathbf{F}_e(\mathbf{q}, \dot{\mathbf{q}}, \ddot{\mathbf{q}}, \mathbf{q}_t; \psi) = \mathbf{0} \tag{6}$$

$$\mathbf{F}_t(\mathbf{q}, \dot{\mathbf{q}}, \ddot{\mathbf{q}}, \mathbf{q}_t; \psi) = \mathbf{0} \tag{7}$$

Equation (4) represents the blade flap-lag-torsional equations of motion. The vectors $\mathbf{F}_r$, $\mathbf{F}_e$, and $\mathbf{F}_t$ correspond to the fuselage rigid body, the fuselage elastic motion expressed in modal domain, and the trim equations, respectively. The vector $\mathbf{q}_t$ represents the propulsive trim solution which consists of the quantities $\theta_o, \theta_{1c}, \theta_{1s}, \theta_{tr}$, α_R and ϕ_s. The response vector $\mathbf{q}$ consists of the blade, fuselage rigid body, and elastic degrees of freedom. The spatial dependence in the blade equations of motion is eliminated using Galerkin's method

based upon two torsional, two lag and three flap uncoupled, rotating free vibration modes. These rotating modes are obtained from a combination of the first nine exact nonrotating modes of a uniform cantilevered beam.

In steady and level forward flight, a periodic solution in the form of Fourier series is assumed for the blade and fuselage degrees of freedom [23,24]. The equations of motion are expanded in a Fourier series as:

$$\mathbf{F}_b = \mathbf{F}_{b_o} + \sum_{n=1}^{N_H} \{\mathbf{F}_{b_{nc}} cos(n\psi) + \mathbf{F}_{b_{ns}} sin(n\psi)\} \tag{8}$$

where

$$\begin{aligned} \mathbf{F}_{b_o} &= \frac{1}{2\pi} \int_0^{2\pi} \mathbf{F}_b(\mathbf{q}, \dot{\mathbf{q}}, \ddot{\mathbf{q}}, \mathbf{q}_t; \psi)\, d\psi \\ \mathbf{F}_{b_{nc}} &= \frac{1}{\pi} \int_0^{2\pi} \mathbf{F}_b(\mathbf{q}, \dot{\mathbf{q}}, \ddot{\mathbf{q}}, \mathbf{q}_t; \psi) cos(n\psi)\, d\psi \\ \mathbf{F}_{b_{ns}} &= \frac{1}{\pi} \int_0^{2\pi} \mathbf{F}_b(\mathbf{q}, \dot{\mathbf{q}}, \ddot{\mathbf{q}}, \mathbf{q}_t; \psi) sin(n\psi)\, d\psi \end{aligned} \tag{9}$$

Similar equations apply to the fuselage rigid and elastic equations of motion. (The trim equations are the same as the constant part of the fuselage equations). These integrals over the azimuth describing the Fourier coefficients are determined using Gaussian quadrature. The set of trim, blade, fuselage rigid body, and elastic equations are combined and solved simultaneously for steady and level forward flight to yield the required solution vector. This system of equations is solved by the IMSL nonlinear algebraic equation solver, DNEQNF [20]. This routine uses the Levenberg-Marquardt algorithm to solve the trim/aerodynamic response simultaneously and calculates the Jacobian of the system using a finite difference scheme.

As described in the mathematical formulation of the wake model, the wake calculation routine returns influence matrices that relate the inflow distribution to the circulation distribution. However the circulation distribution is dependent on the required lift and the lift is dependent on the inflow distribution. Thus it is necessary to iterate on circulation convergence. Given the circulation distribution from the previous iteration, the inflow distribution is determined. From the inflow distribution, the distribution of lift is calculated. From the calculated lift, the required circulation is determined and the process repeats until the circulation converges within a prescribed limit.

4 CONTROL APPROACH

The coupled rotor/flexible fuselage model contains a provision for an ACSR system by mounting the rotor on a rigid plate. This rigid plate is connected to the fuselage with high force/small displacement actuators as shown in Figure 2. The corners of this plate are denoted P2, P4, P6 and P8. The actuators are connected to the fuselage at points P1, P3, P5 and P7. Control inputs are fed to these actuators at the rotor disturbance frequency (N_b/rev) in order to counteract the rotor forcing and minimize vibrations at selected fuselage locations such as the pilot seat and rear cabin.

The basic control strategy used in this study is described in detail in Ref. 14. Springs, used as a control parameter to distribute weighting between control power and control effectiveness, are introduced parallel to the actuators at the four corners of the rigid plate. The forces across the servo actuators, due to control inputs and spring forces caused by fuselage elastic deformation, are set to zero through the proper choice of control inputs. This in turn reduces overall airframe vibrations.

An improved control strategy based on the minimization of a performance index has been implemented. This is an adaptation of a control strategy used in previous HHC and IBC studies [8,25]. The performance index used in this study is a quadratic function of selected acceleration amplitudes $\vec{z}$ and control amplitudes $\vec{u}$.

$$J = \vec{z}^T \mathbf{W}_z \vec{z} + \vec{u}^T \mathbf{W}_u \vec{u} \tag{10}$$

The weighting matrices, $\mathbf{W_z}$ and $\mathbf{W_u}$, allow relative importance to be assigned to the components of acceleration at various locations and the control inputs. It is therefore possible to choose which degrees of freedom are most important and tailor the vibration reduction method to preferentially reduce those accelerations.

The optimal control is found by setting the gradient of the performance index J with respect to the control $\vec{u}$ to zero:

$$\frac{\partial J}{\partial \vec{u}} = 0 \tag{11}$$

To determine the gradient of the performance index with respect to the control, it is necessary to know the gradient of the accelerations with respect to the control. To this end, the accelerations are linearized about the current control input $\vec{u}_i$

$$\vec{z}(\vec{u}) = \vec{z}(\vec{u}_i) + \mathbf{T}_i(\vec{u} - \vec{u}_i) \tag{12}$$

where

$$\mathbf{T} = \frac{\partial \vec{z}}{\partial \vec{u}} \tag{13}$$

The transfer matrix $\mathbf{T}$ is the Jacobian of the acceleration response with respect to the current control input. This Jacobian is calculated numerically using the finite difference method.

Substituting this model of the acceleration response in the the performance index and minimizing with respect to the control produces

$$\vec{u}^*_{i+1} = -\mathbf{D}_i^{-1}\mathbf{T}_i^T\mathbf{W}_\mathbf{z}[\vec{z}_i - \mathbf{T}_i\vec{u}^*_i] \tag{14}$$

where

$$\mathbf{D}_i = \mathbf{T}_i^T\mathbf{W}_\mathbf{z}\mathbf{T}_i + \mathbf{W}_\mathbf{u} \tag{15}$$

This system is similar to the local controller described in References 25 and 15. This procedure can be started by setting the initial optimal control input to zero and repetitively applying Eq. 14 until the optimal control input converges. The resulting control vector is the optimal control vector for the given weighting matrices.

5 RESULTS AND DISCUSSION

In this study, a coupled rotor/flexible fuselage model resembling the MBB BO-105 helicopter is chosen. The non-dimensional properties are provided in in Table 1. The fuselage natural modes are coupled modes so the descriptions given in the table are qualitative and are not meant to denote classical yawing, pitching and torsional modes.

Figures 5 - 7 compare the vibratory hub shears obtained from the various aerodynamic models. Five distinct aerodynamic models are considered. The first two aerodynamic models are uniform inflow and the free wake model. The description 'fuselage aero 1' refers to the first refinement of the fuselage aerodynamic model. In this stage, sources/sinks are included to influence the velocities at the rotor blades which in turn influence the rotor loads. However, this version of the aerodynamic model lacks the integration of the pressures over the fuselage surface to account for rotor aerodynamic influences on the fuselage. 'Fuselage aero 2' is the second refinement of the model and includes the aforementioned sources/sinks as well as the integration of pressure over the fuselage surface. 'Fuselage aero 3' is the third refinement of the model. It includes the distortion of the wake due to the fuselage in addition to all previously described effects. This produces fully coupled rotor/fuselage aerodynamic interactions. As seen in the figures, vibratory hub shears obtained with the free wake model are significantly higher than the uniform inflow results, especially at lower advance ratios where blade vortex interaction plays a larger role. The inclusion of fuselage interference effects on the rotor results in vibratory loads significantly higher than that obtained with the free wake model alone. The second and third refinements of the fuselage aerodynamic model have little to no affect on the hub shears in the longitudinal and lateral directions. In the vertical direction, the inclusion of wake distortion affects due to the fuselage significantly alters the vibratory hub loads. Above an advance ratio of $\mu = 0.25$, the vertical vibratory hub shear when using the third refinement of the fuselage aerodynamic model is up to 100% larger than the free wake model alone. The vibratory hub moments show similar trends as the lateral and longitudinal shears.

Figures 8 and 9 show the 4/rev accelerations at the pilot seat and at a rear cabin position as a function of advance ratio. In both figures, the accelerations are shown for two different aerodynamic models: the uniform inflow model and the free wake model. The accelerations obtained using the free wake model are much higher than the uniform inflow results. As in the studies by Yeo and Chopra, at low advance ratios the accelerations at the pilot seat are shown to be orders of magnitude greater when using the free wake model. In Ref. 1, the effect of the free wake model is shown to result in an approximately constant increase to the vibration levels at advance ratios of 0.2 and above. However in our study, this increase diminishes at these higher advance ratios.

The location where accelerations are measured plays a significant role in the magnitude of the accelerations as evident from comparing the two figures.

Figures 10 and 11 compare the acceleration levels obtained using uniform inflow to those obtained using the free wake model with the addition of rotor/fuselage interaction effects. In Fig. 10, the pilot seat accelerations are plotted and the rear cabin accelerations are shown in Fig. 11. Large increases are noted in all accelerations with the inclusion of refined aerodynamics but are most notable in the pilot seat vertical and lateral accelerations and the rear cabin vertical accelerations. The effect is apparent at all advance ratios. The accelerations obtained using the free wake model alone are similar to those obtained with the inclusion of rotor/fuselage aerodynamic interactions at low advance ratios. At higher advance ratios, the inclusion of rotor/fuselage aerodynamic interactions results in accelerations that are up to 100% greater than those of the free wake model alone. At higher advance ratios, the influence of the wake on the rotor aerodynamic loads diminishes while the relative influence of the fuselage on the rotor increases.

The ability of the weighted control algorithm to drastically reduce airframe vibrations are shown in Figs. 12 to 14. These results were obtained without penalizing either the actuator force or actuator power requirements. This provides a best case scenario for vibration reduction if there are no practical constraints on the actuator system. The longitudinal accelerations for the controller both engaged and disengaged are shown in Fig. 12. For both airframe locations, vibrations are reduced by 45% to 68%. In the lateral direction, Fig. 13 shows vibrations at both locations to be almost completely eliminated when the controller is active. Pilot seat accelerations are reduced to between 1.0% and 1.6% of the uncontrolled values. Similarly, rear cabin lateral accelerations are reduced to between 1.8% and 3.3% of the uncontrolled values. The vertical accelerations are shown in Fig. 14. Again the accelerations are nearly eliminated by the controller. Pilot seat accelerations with the controller active are 2.8%-4.1% of the uncontrolled values. Rear cabin accelerations are 0.2%-0.3% of the uncontrolled values. Using the weighted control algorithm, accelerations at selected locations can be reduced to levels that are two orders of magnitude less than the uncontrolled values. But this near complete vibration elimination is accompanied by prohibitive power and actuator force requirements. With no control penalty, the actuators require between 2% and 15% of total rotor power and need to exert up to 40000 lbs force.

The weighted control method with practical constraints on the actuator forces and power, to model a feasible control scheme, is compared to the basic control scheme in Figs. 15 to 18. The longitudinal acceleration levels for both the pilot seat and the rear cabin location are shown for each control method in Fig. 15. The accelerations of the two airframe locations are nearly the same in this direction. Though the basic controller provides better vibration reduction at $\mu = 0.15$, the vibration levels are low for both control methods at this point. For higher advance ratios, $\mu \geq 0.20$, the weighted control method reduces vibrations further than the basic controller. The accelerations obtained using the weighted control method are up to 74% less than the basic control method accelerations.

In the lateral direction, shown in Fig. 16, the basic control scheme is ineffective in reducing accelerations. The accelerations obtained using the weighted controller are lower than the basic control accelerations at all advance ratios. The weighted control method provides rear cabin accelerations that are 19% to 50% lower than the basic control accelerations. Pilot seat lateral accelerations with the weighted control method are a minimum of 56% below the basic control accelerations and are reduced up to 81% at certain advance ratios. This reduction is especially noticeable at high advance ratios where the weighted control accelerations are 26% of the basic control accelerations at an advance ratio of $\mu = 0.40$.

The vertical pilot seat and rear cabin acceleration levels are shown in Fig. 17. The weighted control accelerations are lower than the basic control accelerations at all advance ratios for both airframe locations. The weighted control vertical acceleration levels at the pilot seat are from 34% lower than the basic control acceleration levels at low advance ratios, $\mu = 0.15$, to 49% lower at high advance ratios, $\mu = 0.40$. The greatest reduction is at $\mu = 0.30$ where the weighted control accelerations are 66% less than the basic control accelerations. At the rear cabin position, the weighted control method reduces accelerations to levels that are a minimum of 69% below and up to 82% below the basic control accelerations. At $\mu = 0.40$, the basic control method is only able to reduce vibrations at the rear cabin to 0.16g where the weighted control method reduces vibrations to 0.035g. This is a significant additional reduction that helps to meet the goal of a "jet smooth ride".

The power requirements of the two control schemes are compared in Fig. 18. The actuator power requirements are shown as a percentage of main rotor power. The two control methods have similar power requirements. Whereas the basic control method needs a greater percentage of rotor power as advance ratio increases, the weighted control method requires a relatively constant percentage of 1.5% of rotor power. Both

control schemes require actuators able to produce forces on the order of 6000 lbs at high advance ratios.

6 CONCLUDING REMARKS

A free wake model and a fuselage aerodynamic model capable of simulating rotor/fuselage aerodynamic interactions has been combined with a coupled rotor/flexible fuselage model to study vibrations and their reduction using ACSR. A control approach has been developed that preferentially reduces accelerations at prescribed airframe locations. This control method has been compared to an earlier control approach studied at UCLA. The results represent an important contribution towards vibration predictions and cost effective vibration reduction using the ACSR approach. Several conclusions are summarized below:
(1) Refined aerodynamics significantly affect the vibratory loads transfered from the rotor to the fuselage and the accelerations experienced at various fuselage locations.
(2) A free wake model and the inclusion of fuselage aerodynamic effects on the rotor and wake are necessary for vibration prediction at all forward speeds. The inclusion of rotor aerodynamic effects on the fuselage plays a minor roll in the production of vibrations.
(3) Accelerations obtained using the free wake model and including rotor/fuselage aerodynamic interactions are orders of magnitude greater than those obtained using uniform inflow at lower advance ratios and are significantly greater at higher advance ratios.
(4) The weighted control algorithm with no control penalty was able to nearly eliminate all acceleration components at the pilot seat and rear cabin position for all advance ratios. This exceptional vibration reduction capability required a prohibitive amount of control power and actuator force amplitude.
(5) Both the basic controller and the weighted controller with control penalty were unable to reduce lateral accelerations at the rear cabin position. A better alignment of actuators could allow for the reduction of these accelerations with realistic actuator requirements.
(6) The weighted control algorithm with control penalty was able to reduce accelerations at the desired locations significantly below the accelerations of the basic control scheme using similar actuator forces and power. The accelerations obtained using the weighted controller were up to 82% below the basic controller accelerations.

ACKNOWLEDGMENTS

This research is supported by the U.S. Army Research Office under grant No. DAAH04-95-1-0320 with Dr. Gary Anderson as grant monitor.

References

[1] Yeo, H. and Chopra, I. , "Modeling Issues Related to Vibration Prediction of a Coupled Rotor/Fuselage System," AIAA Paper No. 97-1212, Proceedings of the 38th AIAA/ASME/ASCE/AHS/ASC Structures, Structural Dynamics and Materials Conference, Kissimmee, FL, April 1997, pp. 2739–2751.

[2] Lorber, P. F. and Egolf, T. A. , "An Unsteady Helicopter Rotor/Fuselage Interaction Analysis," NASA CR-4178, September 1988.

[3] Mavris, D. N. , Komerath, N. M. , and McMahon, H. M. , "Prediction of Aerodynamic Rotor-Airframe Interactions in Forward Flight," *Journal of the American Helicopter Society*, October 1989, pp. 37–46.

[4] Berry, J. and Bettshart, N. , "Rotor-Fuselage Interaction: Analysis and Validation with Experiment," Proceedings of the 53rd Annual Forum of the American Helicopter Society, Virginia Beach, VA, 1997, pp. 343–367.

[5] Smith, C. A. and Betzina, M. D. , "Aerodynamic Loads Induced by a Rotor on a Body of Revolution," *Journal of the American Helicopter Society*, January 1986, pp. 29–36.

[6] Leishman, J. G. and Bi, N. , "Aerodynamic Interactions Between a Rotor and a Fuselage in Forward Flight," *Journal of the American Helicopter Society*, July 1990, pp. 22–31.

[7] Bi, N. and Leishman, J. G. , "Experimental Study of Rotor/Body Aerodynamic Interactions," *Journal of Aircraft*, Vol. 27, No. 9, September 1990, pp. 779–788.

[8] Friedmann, P. P. and Millott, T. A. , "Vibration Reduction in Rotorcraft Using Active Control: A Comparison of Various Approaches," *Journal of Guidance, Control, and Dynamics*, Vol. 18, No. 4, 1995, pp. 664–673.

[9] King, S. P. and Staple, A. E. , "Minimization of Helicopter Vibration Through Active Control of Structural Response," Rotorcraft Design Operations, AGARD-CP-423, October 1986, pp. I4–1 – I4–13.

[10] Staple, A. E. , "An Evaluation of Active Control of Structural Response as a Means of Reducing Helicopter Vibration," Proceedings of the 15th European Rotorcraft Forum, Amsterdam, Netherlands, September 1989, pp. 3–17.

[11] Welsh, W. A. , von Hardenberg, P. C. , von Hardenberg, P. W. , and Staple, A. E. , "Test and Evaluation of Fuselage Vibration Utilizing Active Control of Structural Response (ACSR) Optimized to ADS-27," Proceedings of the 46th Annual Forum of the American Helicopter Society, Washington, DC, may 1990, pp. 21–37.

[12] Welsh, W. A. *et al.*, "Flight Test on an Active Vibration Control System on the UH60 Black Hawk Helicopter," Proceedings of the 51st Annual Forum of the American Helicopter Society, Fort Worth, TX, may 1995, pp. 393–402.

[13] Chiu, T. and Friedmann, P. P. , "A Coupled Helicopter Rotor-Fuselage Aeroelastic Response Model for ACSR," AIAA Paper No. 95-1226, Proceedings of the 36th AIAA/ASME/ASCE/AHS/ASC Structures, Structural Dynamics and Materials Conference, New Orleans, LA, April 1995, pp. 574–600.

[14] Chiu, T. and Friedmann, P. P. , "ACSR System for Vibration Suppression in Coupled Rotor-Flexible Fuselage Model," AIAA Paper No. 96-1547, Proceedings of the 37th AIAA/ASME/ASCE/AHS/ASC Structures, Structural Dynamics and Materials Conference, Salt Lake City, UT, April 1996, pp. 1972–1991.

[15] Millott, T. A. and Friedmann, P. P. , "Vibration Reduction in Helicopter Rotors Using an Actively Controlled Partial Span Trailing Edge Flap Located on the Blade," NASA CR-4611, 1994.

[16] Johnson, W. , A Comprehensive Analytical Model of Rotorcraft Aerodynamics and Dynamics, Vol. I: Theory Manual. Johnson Aeronautics, Palo Alto, CA, 1988.

[17] Johnson, W. , A Comprehensive Analytical Model of Rotorcraft Aerodynamics and Dynamics, Vol. II: User's Manual. Johnson Aeronautics, Palo Alto, CA, 1988.

[18] Scully, M. P. , "Computation of Helicopter Rotor Wake Geometry and its Influence on Rotor Harmonic Airloads," Ph.D. Dissertation, Aeroelastic Research Laboratory, Massachusetts Institute of Technology, 1975.

[19] Johnson, W. , "Wake Model for Helicopter Rotors in High Speed Flight," NASA CR-177507, 1988.

[20] _, IMSL Library: Reference Manual. IMSL Inc., Houston, TX, 1980.

[21] Rand, O. and Gessow, A. , "Model for Investigation of Helicopter Fuselage Influence on Rotor Flowfields," *Journal of Aircraft*, Vol. 26, No. 5, May 1989, pp. 401–402.

[22] Lorber, P. F. and Egolf, T. A. , "An Unsteady Helicopter Rotor-Fuselage Aerodynamic Interaction Analysis," *Journal of the American Helicopter Society*, July 1990, pp. 32–42.

[23] Millott, T. A. and Friedmann, P. P. , "Vibration Reduction in Helicopter Rotors Using an Active Control Surface Located on the Blade," AIAA Paper No. 92-2451, Proceedings of the 33rd AIAA/ASME/ASCE/AHS/ASC Structures, Structural Dynamics, and Materials Conference, Dallas, TX, April 1992, pp. 1975–1988.

[24] Papavassiliou, I. , Friedmann, P. P. , and Venkatesan, C. , "Coupled Rotor/Fuselage Vibration Reduction Using Open-Loop Blade Pitch Control," *Mathematical Computer Modeling*, Vol. 18, No. 3, 1993, pp. 131–156.

[25] Johnson, W. , "Self-Tuning Regulators for Multicyclic Control of Helicopter Vibrations," NASA TP-1996, 1982.

Rotor Data	
$EI_y/m_b\Omega^2R^4 = 0.0106$	
$EI_z/m_b\Omega^2R^4 = 0.0301$	
$GJ/m_b\Omega^2R^4 = 0.001473$	
$N_b = 4$	$a = 2\pi$
$\gamma = 5.5$	$\beta_p = 0.0$
$\sigma = 0.07$	$c_b/R = 0.055$
Helicopter Data	
$C_W = 0.0050$	$fC_{d_f}/\pi R^2 = 0.01$
$Z_{FC}/R = 0.2851$	$Z_{FA}/R = 0.2851$
$X_{FC}/R = 0.0$	$X_{FA}/R = 0.0$
$h/R = 0.0931$	$I_x/m_bR^2 = 4.2216$
$I_y/m_bR^2 = 10.7781$	$I_z/m_bR^2 = 7.9366$

Fuselage Mode Shape Description and Frequency(Hz)	
Fuselage yawing	5.28
Fuselage pitching	5.36
Fuselage torsion	11.07
Fuselage compression	18.81
Tail boom bending	23.23
Fuselage torsion	25.11
Landing gear vertical	26.73
Landing gear lateral	29.02

Table 1: Helicopter Data

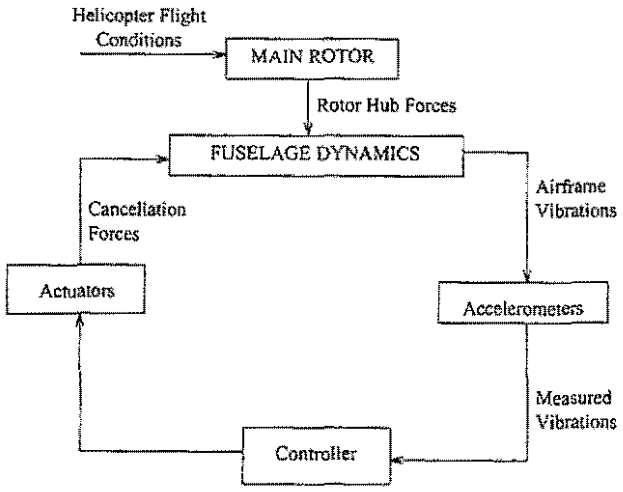

Figure 1: Helicopter System Schematic for ACSR

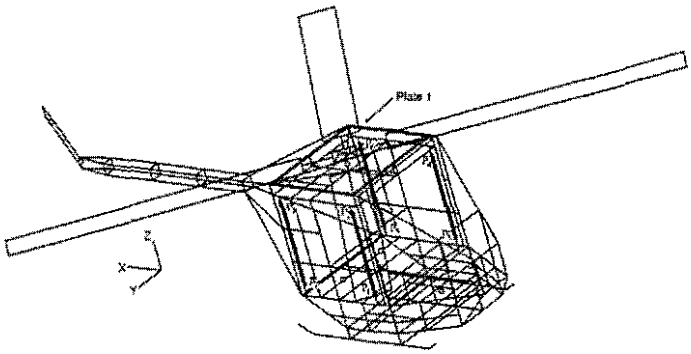

Figure 2: Coupled Rotor/Active Control/Fuselage Dynamic System

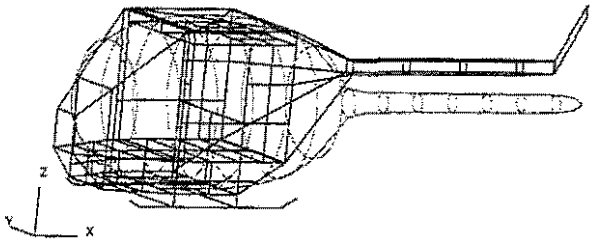

Figure 3: Body of Revolution/Fuselage Comparison

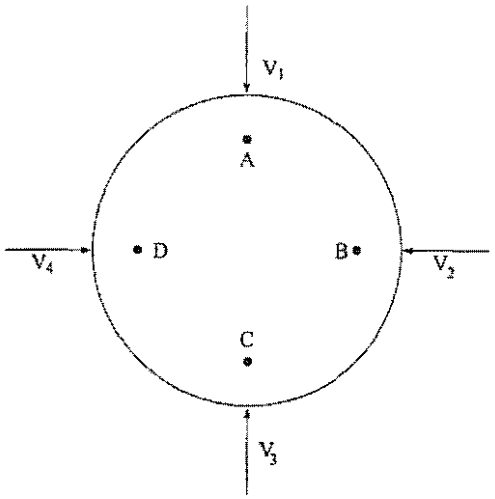

Figure 4: Cross Section of Body of Revolution

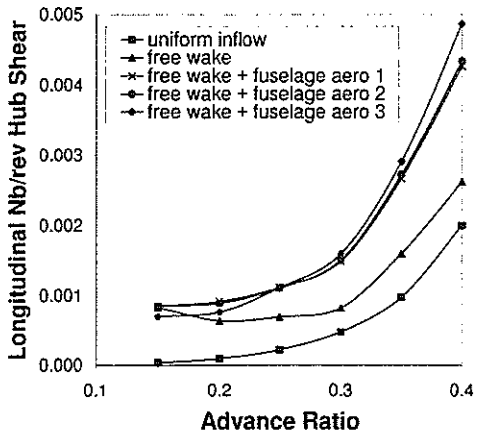

Figure 5: Longitudinal N_b/rev Hub Shears

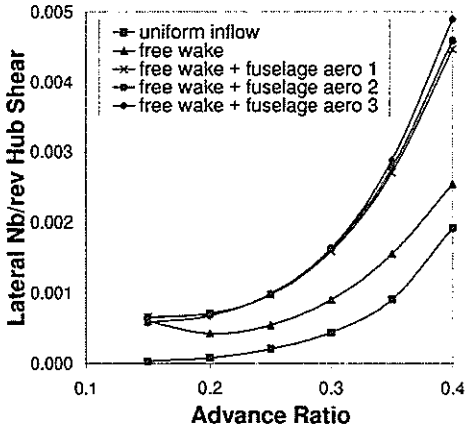

Figure 6: Lateral N_b/rev Hub Shears

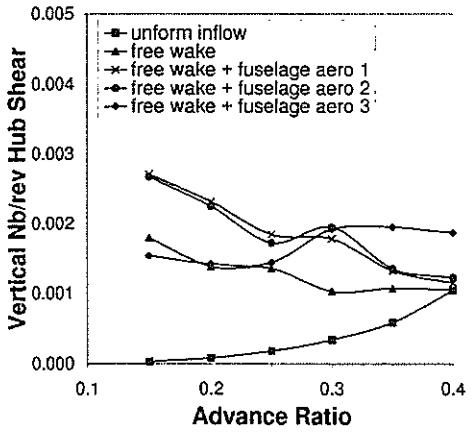

Figure 7: Vertical N_b/rev Hub Shears

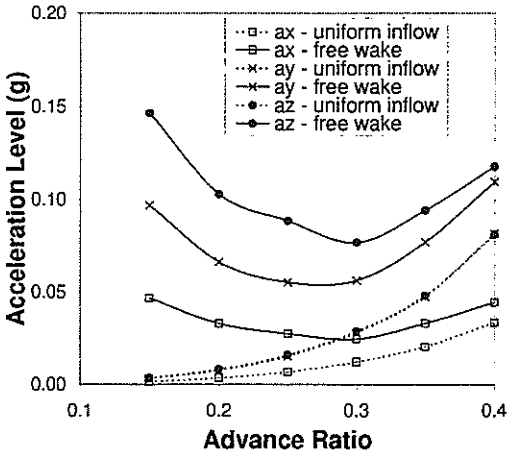

Figure 8: 4/Rev Accelerations at the Pilot Seat

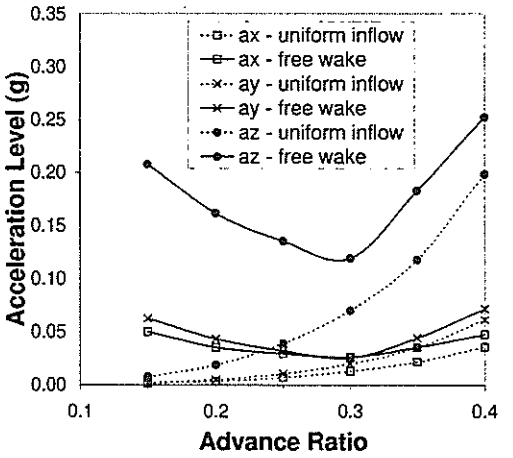

Figure 9: 4/Rev Accelerations at a Rear Cabin Position

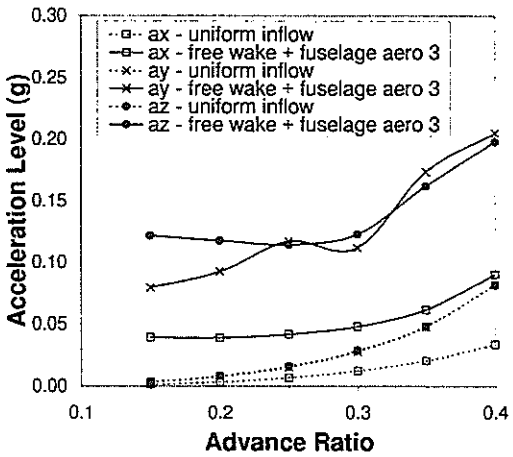

Figure 10: 4/Rev Accelerations at the Pilot Seat

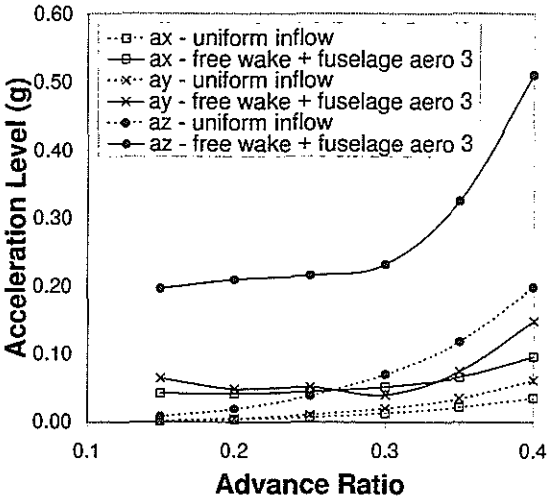

Figure 11: 4/Rev Accelerations at a Rear Cabin Position

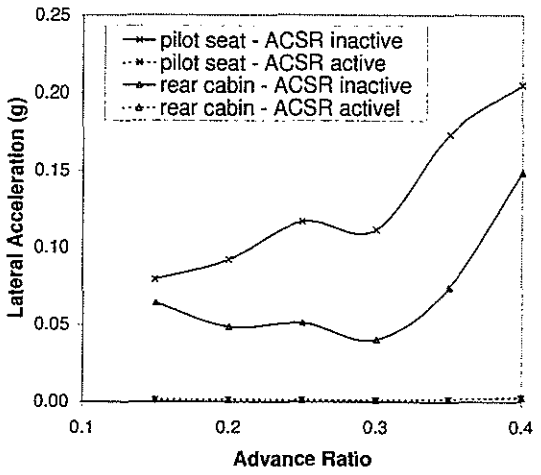

Figure 13: Lateral Accelerations, Weighted Controller with No Control Penalty

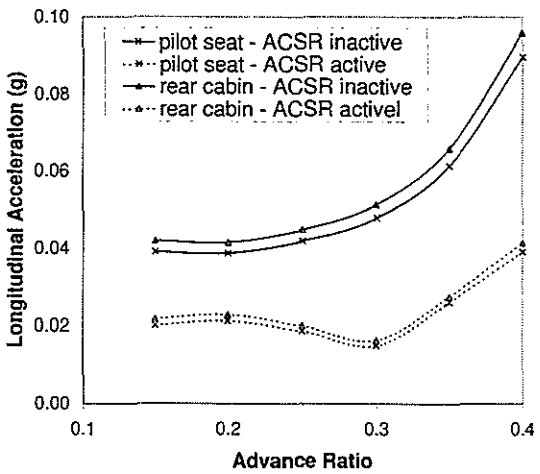

Figure 12: Longitudinal Accelerations, Weighted Controller with No Control Penalty

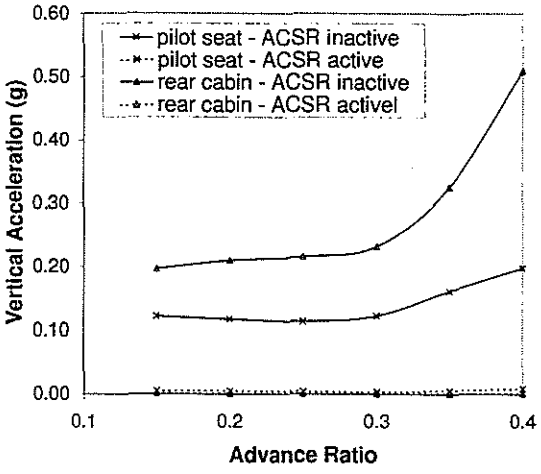

Figure 14: Vertical Accelerations, Weighted Controller with No Control Penalty

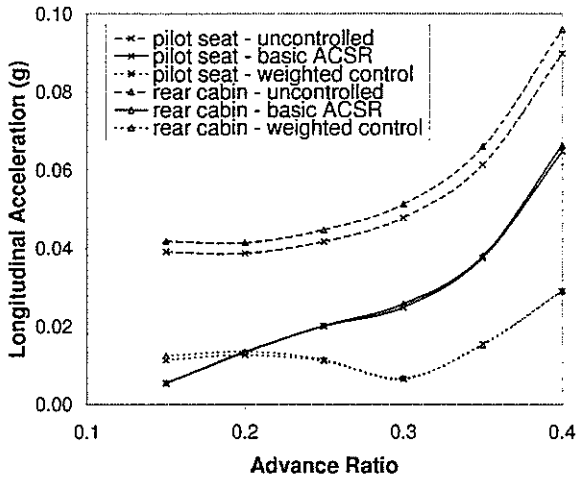

Figure 15: Longitudinal accelerations, comparison of control schemes

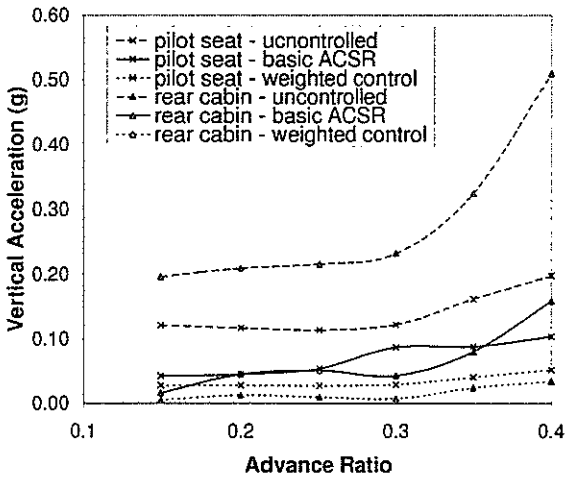

Figure 17: Vertical accelerations, comparison of control schemes

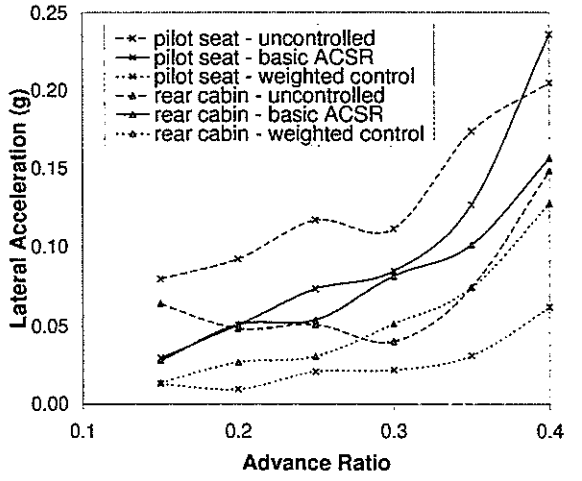

Figure 16: Lateral accelerations, comparison of control schemes

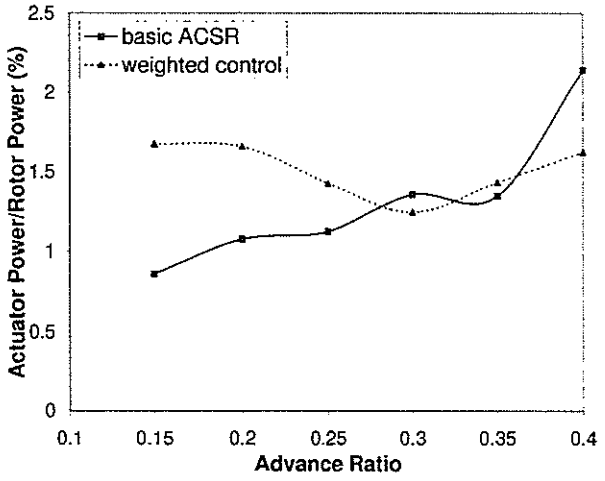

Figure 18: Power requirements, comparison of control schemes

TWENTYFIFTH EUROPEAN ROTORCRAFT FORUM

Paper n° G15

Derivation of High Order Control Laws for Active Rejection of Rotor Noise and Vibrations

by

R. Kube
DLR, Braunschweig, Germany

September 14 - 16, 1999
Rome
Italy

ASSOCIAZIONE INDUSTRIE PER L'AEROSPAZIO, I SISTEMI E LA DIFESA ASSOCIAZIONE ITALIANA DI AERONAUTICA ED ASTRONAUTICA

Derivation of High Order Control Laws for Active Rejection of Rotor Noise and Vibrations

R. Kube

Deutsches Zentrum für Luft- und Raumfahrt
Lilienthalplatz 7
38108 Braunschweig
Germany

Abstract

Based on the results of wind tunnel tests with active rotor control inputs applied to a hingeless model rotor the performance of an adaptive closed loop control algorithm for automatic BVI noise and vibration reduction is shown and the necessity of a high order control law which works with constant feedback gain is demonstrated. A suited feedback gain setting is determined using data from active rotor control step inputs which show that the disturbances react like a system of second order. For the identified system damping, amplification and time constant output vector feedback control algorithms are designed and compared to each other within the scope of simulations. The results demonstrate the achievable reduction of the minimum response time which is very important for a minimisation of the rotor noise emissions by active control techniques.

Introduction

Despite of a general positive trend on the aeronautical market, the helicopter industry is faced with nearly constant sales. Partially this can be attributed to the strong noise emissions which occur very pronounced in landing approach and in manoeuvring flight. They represent a strong annoyance for the population on ground which consequently accepts helicopter operations without evident reasons only exceptionally.

Especially in manoeuvring flight and in landing approach but also at normal cruise conditions, the noise emissions are accompanied by strong vibrations. They represent a considerable stress for the material thus leading to an abridgement of the maintenance intervals associated with higher maintenance costs. In addition, the high vibration level reduces the flight comfort not only for the passengers but also for the crew onboard the aircraft and therefore also affects the flight safety.

Both disturbances, the noise emissions and the vibrations, can be diminished by means of **A**ctive **R**otor **C**ontrol (ARC) techniques like **H**igher **H**armonic **C**ontrol (HHC), **I**ndividual **B**lade **C**ontrol (IBC) or **L**ocal **B**lade **C**ontrol (LBC). While HHC works with additional actuators below the swashplate, IBC in its classical form requires a substitution of the rotating pitch links by active devices. The main characteristic of LBC is an implementation of smart materials on the blade either in concentrated form of a piezoelectric stack for trailing edge flap actuation, for example, or distributed over the blade like in case of active fibers.

As turned out from wind tunnel and flight tests with HHC and IBC and from numerical investigations with LBC, the optimum commands for the HHC/IBC actuators and piezoelectric stacks or fibers respectively change with flight condition and, in addition, are affected by atmospheric disturbances. Therefore a closed loop control algorithm is necessary determining the control inputs which are required for a reduction of the rotor disturbances like noise emissions and vibrations.

Disturbance and Plant Characteristics

Considering a steady-state flight condition in a first step, the vibrations and noise emissions representing the disturbances to be suppressed are of periodic nature and mainly consist of so called rotor harmonics (fig. 1,2). While the blade-vortex interaction noise has a frequency content of 24/rev to 160/rev, the vibrations are of the 1st, 2nd, 4th and 8th

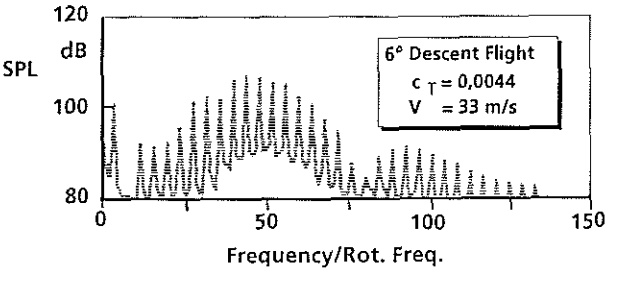

Fig. 1 Frequency Content of Rotor Noise

rotor harmonic. Due to their periodic nature the described disturbances can be represented by means of Fourier series which are characterised by their Fourier coefficients. The vibrations are dominated by integral multiples of the blade passage

Presented at the 25th European Rotorcraft Forum, Rome, Italy, September 14-16, 1999

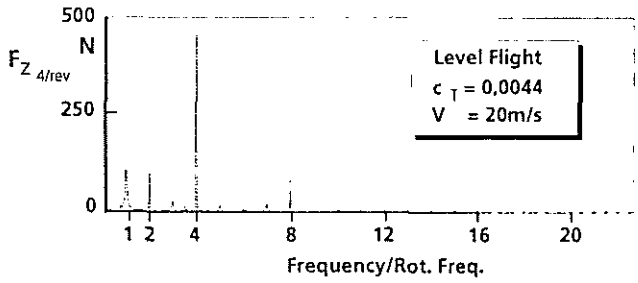

Fig. 2 Frequency Content of Vibrations

frequency for what reason the corresponding Fourier series becomes of the form

$$F_{FL} = \sum_{n=1}^{\infty} a_{nb} \sin(nb\psi) + b_{nb} \cos(nb\psi)$$

with

F_{FL} vibratory force acting on fuselage,

ψ rotor azimuth,

b number of rotor blades,

a_{nb}, b_{nb} Fourier coefficients

and

n integral number.

For simplicity, the vibratory forces and moments acting on the rotor hub are usually combined to the vibration intrusion index

$$J_{Vib} = \sqrt{\frac{F_{x_4}^2}{N} + \frac{F_{y_4}^2}{N} + \frac{F_{z_4}^2}{N} + \frac{M_{x_4}^2}{Nm} + \frac{M_{y_4}^2}{Nm}}$$

with

F_{x_4}, F_{y_4} 4/rev inplane rotor forces,

F_{z_4} 4/rev out of plane rotor forces

and

M_{x_4}, M_{y_4} 4/rev pitching and rolling moment

As is shown exemplarily in fig. 3 this intrusion index keeps fairly constant from one rotor revolution to another and only varies slowly with flight condition.

For the noise emissions the Fourier series becomes of the form

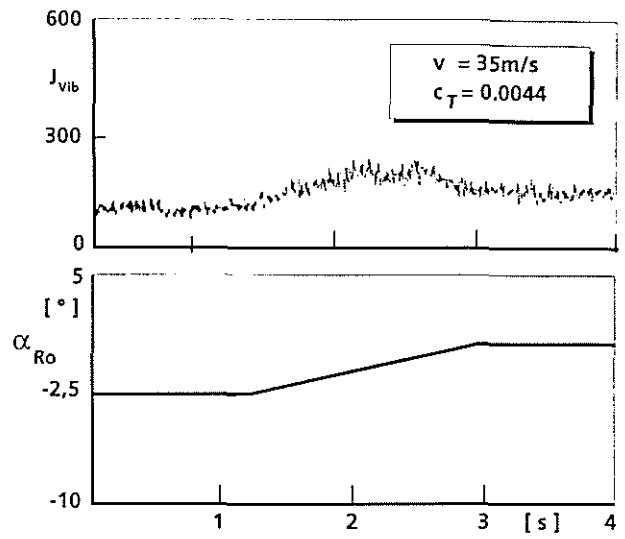

Fig. 3 Variation of Vibration Intrusion Index

$$J_{BVI} = \sum_{n=n_{min}}^{n_{max}} a_n \sin(n\psi) + b_n \cos(n\psi)$$

with

J_{BVI} BVI noise intrusion index

and

n_{min}, n_{max} integral numbers.

Although the noise intrusion index varies with flight condition, too, it also fluctuates strongly from one rotor revolution to another (fig. 4). These fluctuations can be assumed to be due to small changes of the local profile aerodynamics and the downwash geometry respectively which have a strong effect on the noise emissions when occurring at noise relevant rotor azimuth positions [1]. Nevertheless the averaged values of the BVI noise Fourier coeffi-

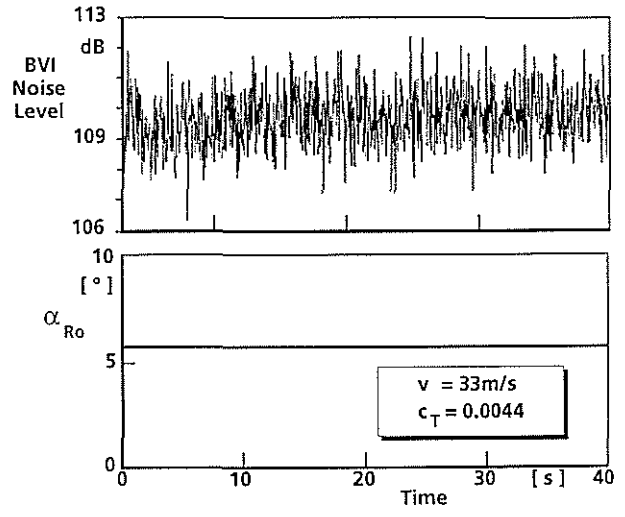

Fig. 4 Variation of BVI Noise Level

cients over a number of rotor revolutions can be reduced dramatically by means of active rotor control (fig. 5). This is true for the vibrations, too, in

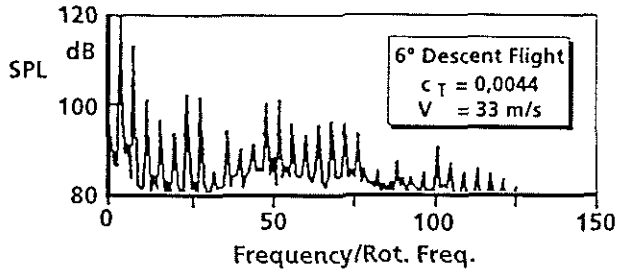

Fig. 5 ARC Effect on Rotor Noise Emissions

which case all 4/rev rotor forces and moments are simultaneously reduced in all degrees of freedom (fig. 6). A prerequisite, however, is a proper adjustment of the active rotor control inputs by means of a suited closed loop control algorithm. It is faced with a non-constant control efficiency which changes not only with flight condition but also with point of operation.
Therefore a proper closed loop control concept needs to be selected being able to deal with the special disturbance and plant characteristics existing in case of active rotor control.

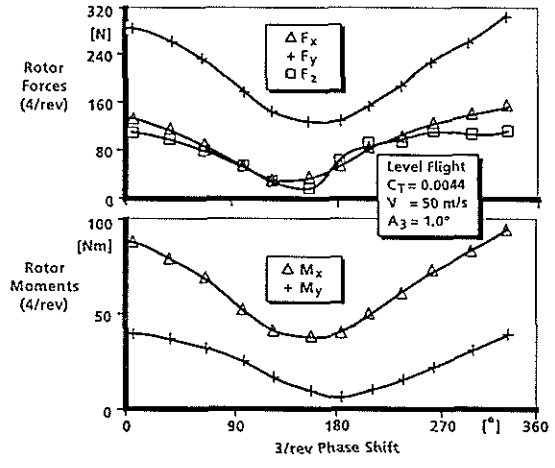

Fig. 6 ARC Effect on 4/rev Vibrations

Possible Closed Loop Control Concepts

In opposition to closed loop control applications for in-flight simulation or autopilot realisation where the flight path of an aircraft is tried to be kept as close as possible to a time-varying trajectory, the main objectives of an algorithm for automatic noise and vibration reduction through active rotor control is to achieve the steady state minimum of both disturbances within very short time. This can be achieved by means of robust control in time domain, for example, (fig. 7) where the disturbances are directly fed back onto the closed loop controller. The feedback gains are of constant type and originate from

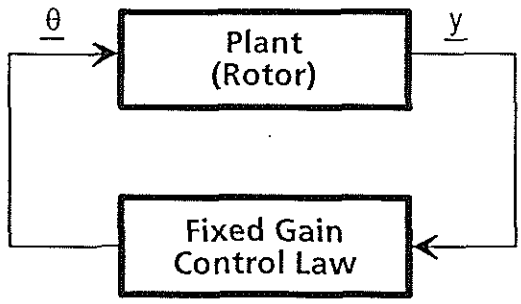

Fig. 7 Fixed Gain Control in Time Domain

an offline design procedure aiming on the realisaion of a minimum step response time and/or a maximum stability distance.

In case of adaptive closed loop control the feedback gains are not determined offline within a controller design procedure but are adjusted online during the control process in order to account for possible changes of the plant's transfer function. The block diagram of that type of controller is shown in fig. 8 which can be subdivided into the control loop itself and the adaptation loop. While the control loop consists of the controller and the process to be controlled, the adaptation loop is closed

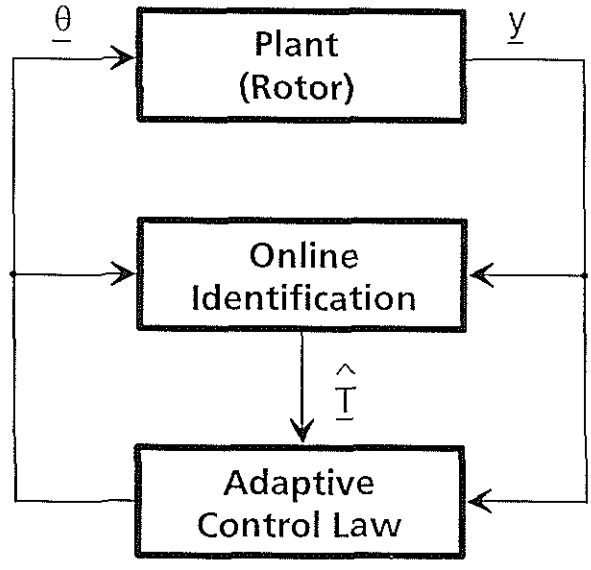

Fig. 8 Adaptive Control in Time Domain

via the online identifier. Based on the latter ones results, the control law is adjusted for the actual process transfer function in a first step before the optimum control commands are determined.

The same steps are performed by an adaptive controller working in frequency domain, however, in this case not the plant outputs themselves are fed back but the combined Fourier coefficients of their harmonics (fig. 9). On their basis the Fourier coefficients of the optimum command signals are deter-

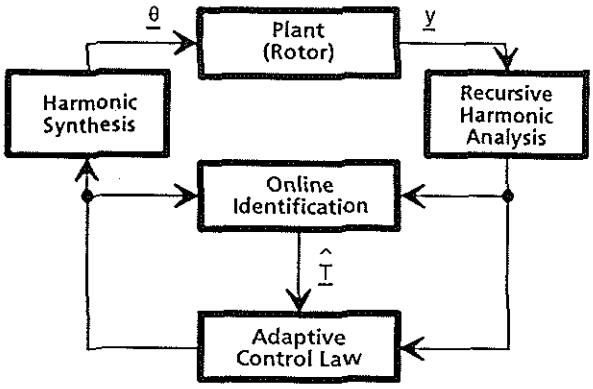

Fig. 9 Adaptive Control in Frequency Domain

mined in order to be used for harmonic synthetization of the plant outputs.

By suppressing the online feedback gain adjustment, a fourth possible closed loop control concept, can be realised (fig 10). Like the adaptive frequency domain controller it works with the Fourier coefficients of the plant output harmonics and determines the Fourier coefficients of the optimum command signal harmonics. This is done with feedback gains which are not adjusted online but kept constant during the control process. Independent of whether operating in time or frequency domain with adaptive or fixed gain respectively, the closed oop controller can be realised as low or high order type. An implementation in discrete time provided, the low order controller only works with the actual value of the

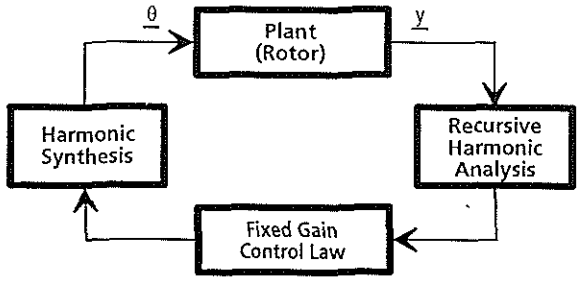

Fig. 10 Robust Control in Frequency Domain

feedback signals while in high order case their history is taken into account, too. Applied to a realisatio in continuous time, this corresponds to a controller making either use of the feedback signals only or of their derivatives in addition.

Control Concept Assessment

From the described closed loop control concepts, the robust time domain controller requires not only the smallest realisation effort but, furthermore, makes it possible to ensure stability at least for the nominal rotor transfer function. Disadvantageous, however, is the lack of controller self-adaptability and the resulting reduction in controller performance or even a controller instability in case of transfer function changes due to variations of the control efficiency, for example.

Both disadvantages can be eliminated by using an adaptive control algorithm which due to its feature of self-adaptability doesn't require a time-consuming offline feedback gain optimisation. In addition, the online adaption of the control law can be expected to lead to a very satisfying controller performance even in case of strong transfr function variations. Disadvantageous, however, is the high amount of mathematical operations to be performed online in addition to the control process itself. Since these operations have to be performed within a time interval which is inverse proportional to the feedback signal dynamics, an adaptive control algorithm working in time domain can hardly be realised for disturbances with high frequency content like rotor noise and vibrations, for example.

Realised, however, can be an adaptive closed loop controller for noise and vibration reduction which works in the frequency domain. It needs to take into account only a few of the feedback signal harmonics, for what reason the computational effort for the transformation from time to frequency domain by means of a recursive harmonic analysis (RHA, fig. 9) and from frequency to time domain by means of a harmonic synthesis (HS, fig. 9) can be kept small. The resulting Fourier coefficients of the feedback signal harmonics vary comparatively slowly with the ones of the vibrations being mainly affected by changes of the flight condition. The Fourier coefficients of the rotor noise harmonics, however, are in addition very sensitive to atmospheric disturbances, for what reason they fluctuate strongly from one rotor revolution to another [2].

Since the dynamics of these fluctuations are much lower than the ones of the noise emissions themselves, a frequency domain controller represents a very promissing solution for an active reduction of these disturbances. It can be operated at a low rate without running the risk to decrease the controller performance at least in steady state. In order to achieve, in addition, a satisfying transient behaviour of the closed loop system, the control law has to be of high order with the feedback gains not being adjusted during the control process according to an online identification of the rotor transfer function. Since the result of this process only represents an estimate of the real value, it is affected at least by small errors which may mislead or even destabilise the controller temporarily. Therefore a minimum step response time can only be achieved by a frequency domain controller which is of high order and, in addition, works with constant gain settings.

Control Law Design Procedure

Classical Approach

Due to the periodic characteristic of the rotor noise emissions and vibrations and the quasi-steady behaviour of their harmonics, the design of a frequency domain controller can in principle be based on the so called T-matrix model [3,4]. It establishes a linear relationship between the vector of active rotor control inputs and the disturbance vector and can be formulated either in global form

$$\underline{y}(k) = \underline{y}_0(k) + \underline{T}(k) \cdot \underline{\theta}_{ARC}(k)$$

with

$\underline{y}_0(k)$ disturbance vector in baseline case

and

$\underline{y}(k)$ disturbance vector in ARC case

or in local form

$$\Delta\underline{y}(k) = \underline{T}(k) \cdot \Delta\underline{\theta}_{ARC}(k)$$

with

$\Delta\underline{y}(k)$ vector of disturbance change

and

$\Delta\underline{\theta}_{ARC}(k)$ vector of ARC input change.

While the global model assumes linearity within the complete range of active rotor control inputs, the local model represents a linearization around the actual point of controller operation (fig. 11) and therefore also allows an approximation of non-linear

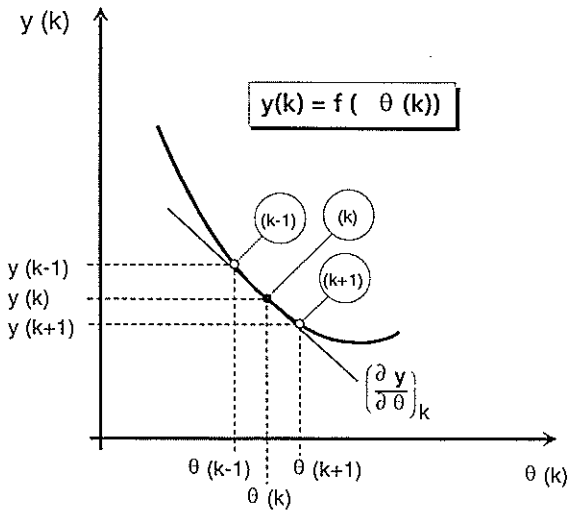

Fig. 11 Linearisation Around Actual Point of Operation

effects. The transients of the noise and vibrations due to a change of active rotor control inputs, however, are not taken into account because both models describe the rotor transfer function in a quasi-steady way via the T-matrix. Therefore a closed loop controller which is based on the T-matrix approach can not operate with a high frequency but needs to let the disturbance transients decay after a change of the active rotor control inputs before the next control input is determined using the control law

$$\Delta\underline{\theta}_{ARC}(k+1) = \underline{K} \cdot \underline{y}(k)$$

with

$\underline{K}$ feedback gain

for example [5]. With that control law the closed loop system becomes of the form shown in fig. 12 and can be described by means of the equation

$$\underline{y}(k+1) = (\underline{I} - \underline{T} \cdot \underline{K}) \cdot \underline{y}(k) + \underline{T} \cdot \underline{w}(k)$$

with

$\underline{w} = \underline{0}$ the command vector.

From this closed loop system equation it can be derived that the disturbance vector vanishes within one step if the feedback gain is set identical to the inverse of the T-matrix. Thus the theoretical possible controller response time is one step, a value which seems to be very small. The real response

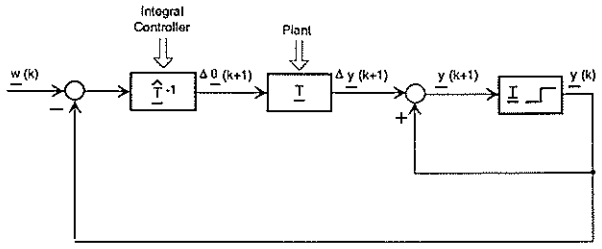

Fig. 12 Quasi-Steady Operating Closed Loop System

time required for minimisation of the rotor noise and vibrations, however, can become fairly large because on the one hand the T-matrix varies with flight condition and actual point of operation. Therefore the feedback gain can not be set identical to the inverse of the T-matrix in all cases and the number of steps required for vibration and noise minimisation becomes higher than one.

On the other hand, one control step corresponds to approximately two rotor revolutions in case of vibration and 10-15 rotor revolutions in case of noise reduction. The reason for the high numbers of rotor revolutions per control step occurring in noise case are the strong fluctuations of the Fourier coeffi-

cients from one rotor revolution to another. They need to be averaged 10-15 times before being fed back on the closed loop controller in form of the quasi-steady mean value. Thus, the time required for minimisation of the noise and vibration level becomes comparatively long, a characteristic which up to now was considered to be mandatory for a frequency domain controller.

The response time is extended further in case of an online feedback gain adjustement as it was considered to be mandatory up to now at least for closed loop control of the rotor noise emissions. This is due to the fact that strong nonlinearities obviously exist in case of BVI noise and vibration reduction through active rotor control with the gradients of the intrusion indices switching sign when passing either through the global or a local extremum (fig. 13, 14).

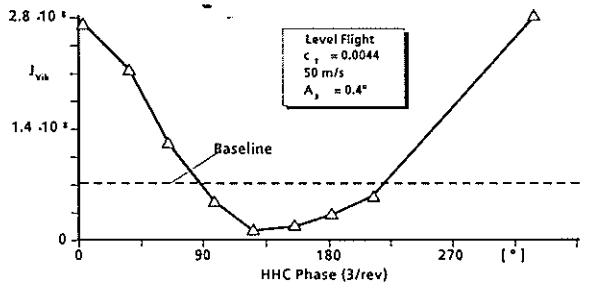

Fig. 13 Variation of Vibration Intrusion Index with 3/rev Phase Shift

Therefore a closed loop control algorithm which works with direct feedback of the intrusion indices is faced with a conversion of the control efficiency

$$T_{Vib} = \frac{\Delta J_{Vib}}{\Delta \theta_{ARC}}$$

and

$$T_{BVI} = \frac{\Delta J_{BVI}}{\Delta \theta_{ARC}}$$

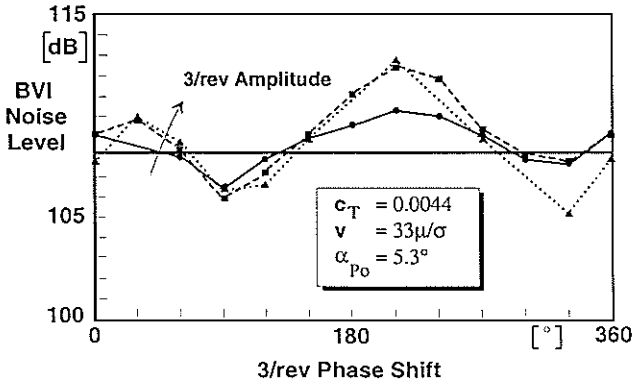

Fig. 14 Variation of BVI Noise Level with 3/rev Phase Shift

respectively and thus needs to adjust at least the gain setting sign accordingly online. The necessity for this online adjustement of the gain settings when feeding back the vibration and/or BVI noise intrusion indices directly can be demonstrated easily for the single input/single output case where the chracteristic system equation follows from the closed loop sysstem equation as

$$z - 1 + T \cdot K = 0 .$$

Thus

$$z = 1 - T \cdot K$$

demonstrating that z becomes located outside the unit circle as soon as the sign of T and K differ from each other (fig. 15). Therefore the gain setting needs to be adapted online according to the actual value of T in order to avoid a controller instability.

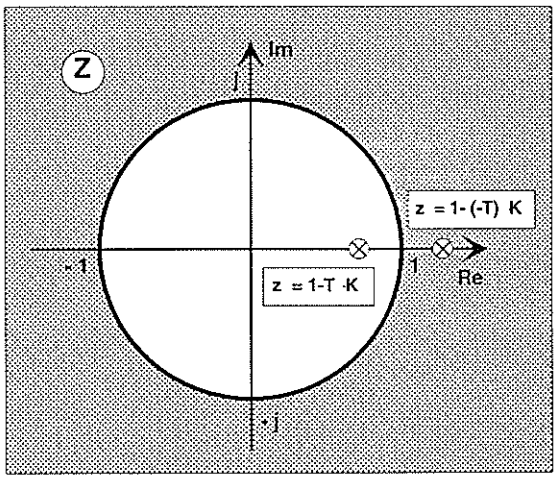

Fig. 15 Pole Placement for Conversion of Control Efficiency

The online adjustement of the gain settings, however, can be omitted when vibrations and noise are not fed back as scalar values but in form of a Fourier coefficient subset. If the real and imaginary parts of these Fourier coefficients are arranged within the vibration and BVI noise feedback vector according to

$$\underline{y}_{Vib}^{T} = \left(F_{x_{4R}}, F_{x_{4I}}, \cdots, M_{y_{4R}}, M_{y_{4I}}\right)$$

and

$$\underline{y}^{T} = \left(BVI_{38_R}, BVI_{38_I}, \cdots, BVI_{46_R}, BVI_{46_I}\right)$$

respectively, the effect of active rotor control inputs to noise and vibrations can be formulated in a linear way. In order to find out to what degree this linear formulation corresponds to reality again the HHC wind tunnel data were used. This time the real and imaginary part of the 38/rev noise emissions were

plotted against each other. The resulting vector diagramms are shown in fig. 16 which demonstrates that the 38/rev BVI noise vector describes a closed line around a point corrresponding to the

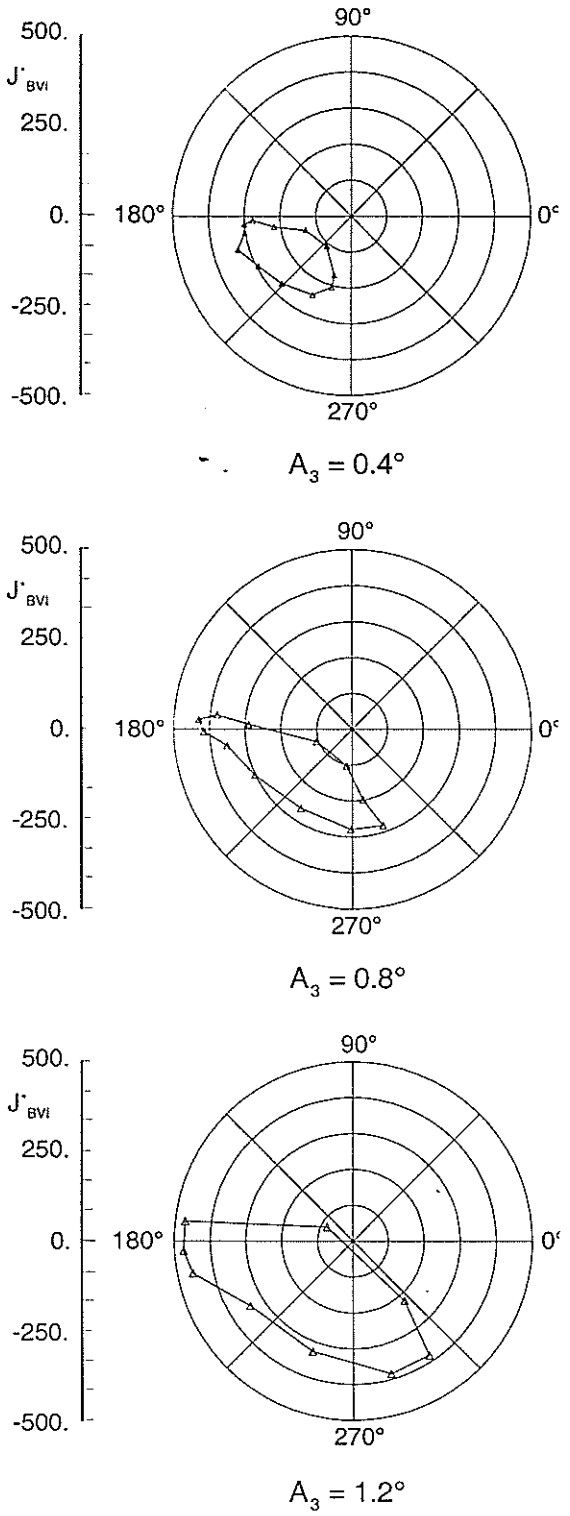

Fig. 16 ARC Effect onf 38/rev Noise Emissions

baseline case. Since the surrounded area increases clearly with ARC amplitude and the vector surrounds the area exactly one time when the ARC phase shift is varied from 0° to 360°, the linear formulation of the ARC effects on the rotor noise can be assumed to be valid. Due to this fact, no sign conversion of the control efficiency needs to be feared for what reason a robust closed loop control system can be designed.

The advantage of that type of control system compared to an adaptive one could be determined by

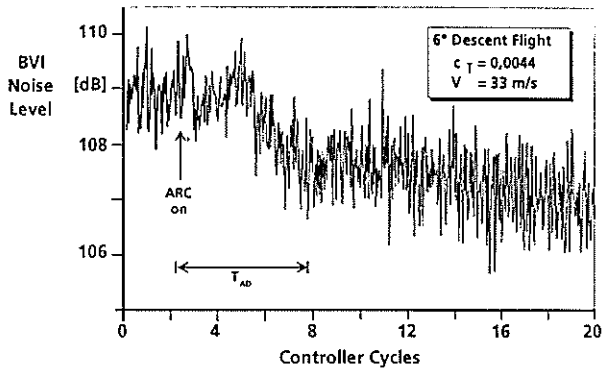

Fig. 17 Performance of Quasi-Steady Operating Controller with Online Gain Adaption

testing both type of controllers in combination with the DLR rotor test rig in the DNW. The results are shown in fig. 17 and 18 which demonstrate that the number of steps required to reach the disturbance minimum is much lower in case of a robust controller. However, since one control step still corre-

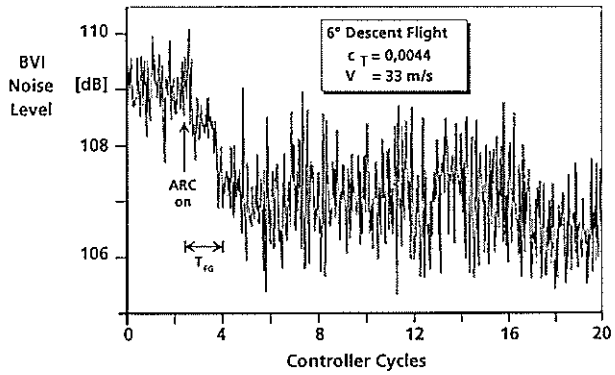

Fig. 18 Performance of Quasi-Steady Operating Controller with Fixed Gain

sponds to 15 rotor revolutions, the controller response time is still too high and needs to be reduced further.

Derivation of High Order Control Laws

This required reduction of the system response time can be achieved when the design of the frequency domain controller is not based on the quasi-steady T-matrix approach but on a model which is able to describe the steady-state as well as the transients of noise and vibrations. A model of that type can be achieved by investigating the reaction of the noise and/or vibration Fourier coefficients to ARC step inputs being represented by a stepwise change of the ARC control amplitude. Fig. 19

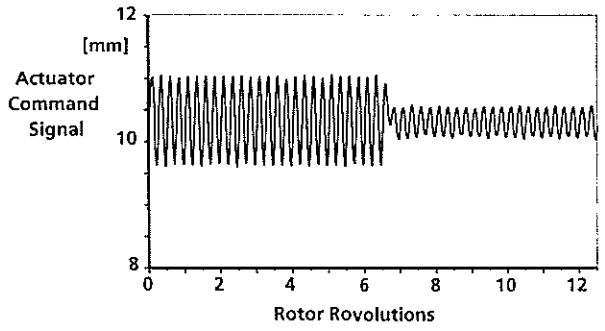

Fig. 19 ARC Step Input

shows for example the ARC signal of an actuator working with 4/rev and changing ist amplitude of operation between revolution 6 and 7. The reaction of the 4/rev vibrations to that ARC step input is shown in fig. 20 which demonstrates that the rotor disturbances behave approximately like a system of 2nd order which is well damped and which reaches the steady state within 2 rotor revolutions. With this knowledge it is possible to design a closed loop control algorithm which allow a reduction of the rotor disturbances within very short time. In opposition to an algorithm which is based on the T-

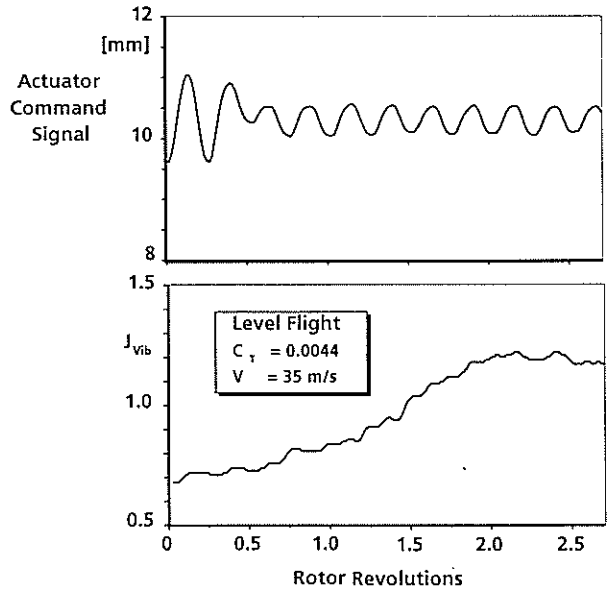

Fig. 20 Reaction of Rotor Disturbances to ARC Step Inputs

matrix model this control algorithm does not wait until the transients decay before the next cycle is initiated but which works with 64 steps per revolution. In fig. 21 and 22 the results of a controller are shown on which the system output vector is fed back. The results originate from numerical simulations of a 2nd order system consisting of a mass, damper and spring (fig. 23) and being excited with a force that leads to oscillations y_0 with 4/rev. The control objective is to eliminate the oscillations by determination of a suited control input amplitude

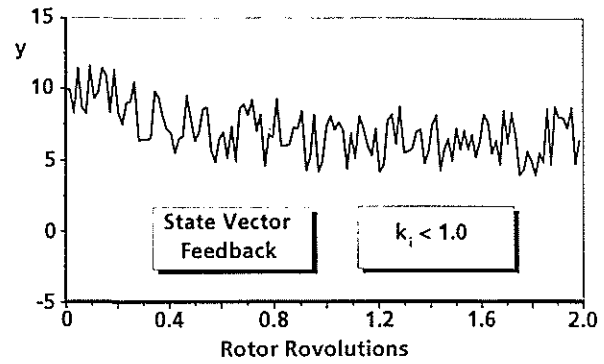

Fig. 21 Perfomance of High Order Low Gain Controller

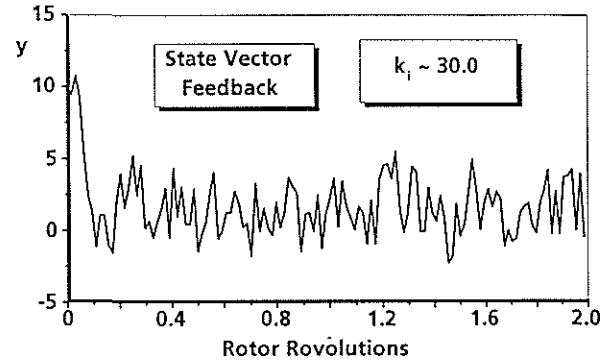

Fig. 22 Performance of High Order High Gain Controller

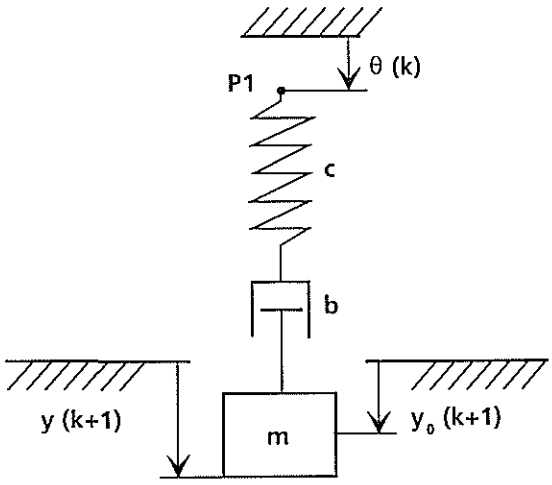

Fig. 23 System of 2nd Order for Numerical Simulations

θ at the spring. From fig. 21 it can be seen that the objective is already achieved when the feedback is selected to be comparatively low, i.e. smaller than 1. In this case the controller reaches steady state after approximately 0.8 rotor revolutions although the system output was heavily disturbed in order to account for the strong fluctuations of the noise intrusion indes measured in wind tunnel. This result can be improved further when the feedback gains are increase (fig. 22) In this case steady state is

already reached after 0.2 rotor revolutions and maintained although the heavily disturbed feedback signals are fed back via gain settings of approximately 30.

Conclusions

Wind Tunnel Results with activ rotor control demonstrated the necessity to work with high order control laws in order to reduce the rotor noise and vibrations within acceptable time. On the basis of results from step input tests a dynamic model for description of the disturbance reaction to ARC inputs was identified and two controll algorithms working with output vector feedback were developed. Numerical simulations of the control algorithms in combination with the identified model showed that a stable behaviour can be achieved despite of strong disturbances on the feedback signals. The controller response time is less than one rotor revolution even in case of low gain feedback.

References

1. Kube, R. et al "HHC Aeroacoustic Rotor Tests in the German Dutch Wind Tunnel: Improving Physical Understanding and Prediction Codes" 52nd Annual Forum of the American Helicopter Society, Washington, DC, 1996.

2. Kube, R.; Achache, M.; Niesl, G.; Splettstoesser, W.; "A Closed Loop Controller for BVI Impulsive Noise Reduction by Higher Harmonic Control" Annual Forum of the American Helicopter Society, Washington , DC, 1992.

3. Shaw, J. "Active Control of the Helicopter Rotor for Vibration Reduction" 36th Annual Forum of the American Helicopter Society, Washington, DC, 1980.

4. Shaw, J. "Higher Harmonic Control: Wind Tunnel Demonstration of Fully Effective Vibratory Hub Force Suppression" 41st Annual Forum of the American Helicopter Society, Fort Worth, Texas, 1985.

5. Kube, R. "Evaluation of a Constant Feedback Gain for Closed Loop Higher Harmonic Control" 16th European Rotorcraft Forum, Glasgow, Scottland, 1990.

TWENTYFIFTH EUROPEAN ROTORCRAFT FORUM

Paper n° G17

Aeroelastic Analysis and Design for On-blade Active Flap

BY

Noboru Kobiki , Eiichi Yamakawa , Yasumichi Hasegawa
ATIC , Japan

Hirohisa Okawa
ISC , Japan

SEPTEMBER 14 - 16 , 1999
ROME
ITALY

ASSOCIAZIONE INDUSTRIE PER L'AEROSPAZIO, I SISTEMI E LA DIFESA
ASSOCIAZIONE ITALIANA DI AERONAUTICA ED ASTRONAUTICA

Aeroelastic Analysis and Design for On-blade Active Flap

Noboru Kobiki , Eiichi Yamakawa , Yasumichi Hasegawa

ATIC (Advanced Technology Institute of Commuter Helicopter, Ltd.)
Kakamigahara City, Gifu Pref., Japan

Hirohisa Okawa

I S C
Kakamigahara City, Gifu Pref., Japan

Abstract

This paper presents the analytical results of the aeroelastic characteristics of the rotor blade with the active flap on a hypothetical rotor.

At first, the geometric parameters of the active flap is decided based on the hub load analysis; the active flap chord length, span length, outboard location are 10%c, 10%R and 80%R, respectively.

The effect on the rotor vibration reduction by the designed active flap is evaluated in the next step. The active flap analytically demonstrates its capability for vibration reduction at 30kt and 120kt level flight conditions.

The stability analysis is performed at last. It is analytically confirmed that the rotor blade with the active flap designed here has no significant flutter problem.

Notation

AF : Active flap
BAF : Flutter coupled between blade bending and AF
BTF : Bending torsion flutter
c : Blade chord length
cg : Center of gravity
Fh : In-plane force = $(Fx^2+Fy^2)^{1/2}$
HM : Hinge moment of AF
Mh : In-plane moment = $(Mx^2+My^2)^{1/2}$
R : Rotor radius

Introduction

There are several active techniques to reduce BVI noise and vibration of helicopters. Among them, active flap becomes very realistic because of not only its effectiveness, but also the recent progress in development of on-blade actuator made of smart materials. Some ambitious organizations have been working very hard in this area to be the first to make it true. (Refs. 1 to 9)

ATIC decided AF as one of the engineering challenges to be studied and activated two primary works; 1) the actuation system for AF by the smart material actuator with the stroke multiplier mechanism (Ref. 10), 2) the aeroelastic analysis for AF to establish the design policy and to evaluate its capability.

This paper describes the latter one summarizing the research work about the analysis for the aeroelastic characteristics of the rotor blade with the active flap configuration.

1. Objectives

The objectives of this paper are to analyze the items below for the hypothetical rotor.

(1) Describe AF design procedure.
(2) Demonstrate the vibration reduction capability of the designed AF.
(3) Stability analysis for the rotor blade with AF on generally assumed structural and operational conditions.

2. Conditions for Analyses

The geometrical property of the hypothetical rotor and the extent of the parametric study are shown here.

Rotor blade geometry

number of blades :	4
radius :	5.8m
chord length :	0.39m
planform :	rectangular

airfoil : AK100D

Rotor operating condition

hover, thrust : 4000 kgf

100% rotor speed : tip speed 210 m/sec

The unsteady aerodynamics is applied all the analyses with the compressibility correction based on the 2D wind tunnel test of the blade airfoil with trailing edge flap supplemented by the CFD code, UG2. The detail is described in Appendix.

3. AF Design

The aims to utilize AF on the helicopter rotor are vibration/BVI noise reduction and rotor performance enhancement. The design policy for AF here is set up to the vibration reduction by generating the sufficient hub load to compensate the vibratory load from each blade of the rotor. This comes from the two reasons;

1) If an AF has the vibration reduction capability, it is predicted that the AF has BVI noise reduction capability. Because the vibration reduction and BVI noise reduction have the same level of the actuation force. (Ref. 2) This is also valid between the vibration reduction and the rotor performance enhancement.(Ref. 1)
2) The direct evaluation can be performed by assuming that the generated hub load by AF on the hover condition represents the effect of AF on the rotor vibration reduction.

During this AF design process, the extent for the parametric study is as follows.

Active flap excitation condition

frequency : 3, 4, 5/rev

amplitude : 1 deg

Active flap geometry

chord length : 10, 15, 20, 25%c

span length : 10, 15, 20%R

3.1 AF chord length

One of the key features for AF sizing is to achieve lower hinge moment of AF because of powerlessness of on-blade AF actuators.(Ref. 10)

One typical analysis result is shown in Fig.1. The 4/rev hub load generated by AF increases in accordance with AF chord length increase, however, the hinge moment also grows as shown in the upper picture of Fig. 1. In order to make it clear the relationship between the 4/rev hub load generated by AF and the hinge moment, the hub loads are rearranged in the form of the load generated by unit hinge moment as shown in the lower picture of Fig. 1.

This indicates that the smaller chord length, the more effective is AF on a point view of the hinge moment. But the smaller chord length makes the more difficulty in the structural design of AF, which also has a large influence on the design of the actuation hardware.

Consequently, AF chord length is selected 10%c by the engineering compromise with the structural design of AF.

3.2 AF spanwise location

The spanwise location of AF should be selected by the consideration for the blade mode shape in order to efficiently generate the excitation force which engages the vibratory load.

Because 1F mode has a large damping and is difficult to be excited, 2F and 3F modes are regarded as the objects to be excited. 2F has its node at 81%R and 3F has its loop at 78% as shown in Fig.2. To avoid node and to make use of loop to efficiently generate the excitation force on the rotor hub by obtaining the sufficient modal deflection, the outboard location of AF is selected 80%R

3.3 AF span length

The AF span length effect on the generated hub load magnitude is almost linearly proportional as shown in Fig. 3. But a long AF span length sometimes has the unpredictable aeroelastic behavior as shown in Fig. 4, where it can be seen that the loads generated by unit hinge moment have their peaks at 20%c unlike those shown in Fig. 1. This may be caused by the coupling between AF and the over-all blade flapping motion whose node is on AF. AF has the opposite sign movement in the flapping direction across this node, which results in the opposite sign hinge moment distribution across the node, then the large part of the hinge moment is canceled out.

Although the shorter AF span length reduces the capability to generate the hub load, this can be compensated by larger AF amplitude.

Based on this discussion, 10%R AF span length is selected.

4. AF Effect on Vibration Reduction

The effect on the rotor vibration reduction by the designed active flap is evaluated here.

The level flight 30kt and 120kt are selected as the evaluation conditions, because, generally, there is the local maximum of the vibration level at about 30kt in the lower speed range. 120kt is selected as a representative of the cruise speed condition.

In order to study the effect of many AF input, a

multicyclic control algorithm (Ref. 6) is utilized here. AF amplitude which is restricted to 1deg in the parametric study of the previous paragraph is set free by the nature of the multicyclic control algorithm.

The vibration reduction effect on 4/rev hub load which is dominant among all the harmonics is shown in Fig. 5. Each component of the 4/rev hub load on AF-on case is normalized by that on the baseline case (AF-off). Although there can be seen an adverse AF effect in Fy on 120kt case, Fz component which is dominant in 4/rev harmonic is reduced in much larger degree on this case. This results in the 4/rev load reduction as a whole.

The designed AF analytically demonstrates its capability for vibration reduction on both the lower and the cruise speed cases. But we would like to notice that although the required AF amplitude calculated here is 4.5deg for 120kt case, it is required 17deg for 30kt, which can not be available by any smart material actuators at present. (Refs. 7 and 10)

5. Flutter Analysis

The stability analyses are performed to evaluate the possibility for several types of flutters for the rotor blade with AF configuration. The schematics of the structural model for analyses is shown in Fig. 6.
The main features of the structural boundary condition are that;

at 70%R : torsion stiffness Kh
rigid in flapwise and chordwise directions
at 75%R : rigid in flapwise and chordwise directions
at 80%R : torsion stiffness Kh
rigid in flapwise and chordwise directions

If there is no notice about the parameters, the all the flutter analyses are performed on the nominal values as below. These values are estimated from AF size selected in the previous paragraph.

AF natural frequency about hinge : 37.7Hz
Chordwise cg position of AF :
18.8mm aft from AF hinge at mid span of AF
Tip weight location : 31.3%c at 97.9%R
Chordwise cg position of AF actuator :
23.3%c at 76.7%R
Rotor control system stiffness : 57,800kgf/m
Rotor speed : 100%

5.1 AF natural frequency about hinge

The most important concern about the flutter for the rotor blade with AF is the control surface flutter caused by the coupling between the blade flapwise bending motion and AF. One of the two primary factors to this flutter is the torsion natural frequency of AF about the hinge, which comprises the inertia and control system stiffness of AF.

The influence of AF natural frequency about the hinge on the flutter characteristics are evaluated as shown in Fig. 7. 7^{th} mode becomes unstable at less than 29Hz where BAF takes place. But all the modes are stable at the nominal frequency 37.7Hz.

Smaller chord length of AF which enables higher natural frequency about the hinge by reducing the inertia is better for stability point of view as well as the AF efficiency stand point as mentioned before.

5.2 Chordwise cg position of AF

The other primary factor to the control surface flutter is the chordwise cg position of AF. This influence is evaluated as shown in Fig. 8. The analysis here is performed at the AF natural frequency 20Hz to impose the most critical condition to the stability among those shown in Fig. 7.

7^{th} mode is on the unstable side at more than 17mm of the cg position aft from the hinge where BAF takes place. But it is confirmed that there is no instability at the nominal AF natural frequency 37.7Hz (not shown here).

5.3 Chordwise cg position of blade

Nowadays aeroacoustically advanced rotor blades are apt to have the tip shape which makes the blade chordwise cg position aft of the quarter chord such as the swept tip. In order to take this tendency into account, the influence of the chordwise cg position of the blade on the flutter is evaluated as shown in Fig. 9. In this analysis, the blade cg travel is represented by the chordwise tip weight cg position at 97.9%R. The tip weight cg position 31.3%c is equivalent to the blade cg position 25%c.

Although 4^{th} mode decreases its stability as the tip weight cg position goes afterward, this mode is still on the stable side up to the maximum calculated value of the tip weight cg position 47.8%c.

5.4 Chordwise cg position of AF actuator

Another factor to reduce stability by pushing the blade cg further backward is the chordwise cg position of AF actuator. The influence of AF actuator position is investigated with the most aft tip weight cg position (47.8%c) to impose the critical condition.

Fig. 10 shows that although 4^{th} mode has the least stability at about 35%c of AF actuator cg, this mode is still on the stable side.

5.5 Rotor control system stiffness

The rotor control system stiffness is one of the difficulties to be predicted with sufficient accuracy, but this has the predominant influence on the blade dynamic property in torsion. Therefore, the stability analysis is needed over the wide range of the rotor control system stiffness. In order to impose the adverse condition, the analysis here is also performed with the most aft tip weight cg position (47.8%c).

As shown in Fig. 11, although 4th mode has its minimum stability at the nominal rotor control system stiffness (57,800kgf/m), this mode is still on the stable side.

5.6 Rotor speed

The rotor speed is also a factor to cause the flutter. The margin of the rotor speed for the flutter is evaluated as shown in Fig. 12. In order to impose the adverse condition, the analysis here is also performed with the most aft tip weight cg position (47.8%c).

4th mode enters the unstable side at more than 106% rotor speed where BTF takes place. But it is confirmed that there is no instability up to 120% rotor speed at the nominal tip weight cg position 31.3%c (not shown here).

6. Conclusions

1. The geometric parameters of AF are decided analytically based on the hinge moment, blade mode shape and the coupled blade-AF aeroelastic property.

2. The above designed AF has the sufficient capability to reduce the rotor vibration, which is analytically demonstrated on 30kt and 120kt level flight conditions.

3. The stability evaluation for the flutter is carried out for the rotor blade with AF configuration. It is concluded that the rotor with AF designed here has no serious flutter problem on various structural and operational conditions.

Acknowledgments

The authors gratefully acknowledge Mr. Katayama for the contribution to construct the structural input for the hypothetical rotor which is the base for all the analyses presented in this paper.

References

1. Dawson, S., Booth, E., Straub, F., Hassan, A., Tadghighi, H., Kelly, H., "Wind Tunnel Test of an Active Flap Rotor BVI Noise and Vibration Reduction", Proceeding of 51st American Helicopter Society, Fort Worth, TX, U.S.A., May, 1995.
2. Charles, B., Tadghighi, H., Hassan, A., "Higher Harmonic Actuation of Trailing-Edge Flaps for Rotor BVI Noise Control", Proceeding of 52nd American Helicopter Society, Washington D.C., U.S.A., June, 1996.
3. Straub, F., Hassan. A., "Aeromechanic Considerations in the Design of a Rotor with Smart Material Actuated Trailing Edge Flaps", Proceeding of 52nd American Helicopter Society, Washington D.C., U.S.A., June, 1996.
4. Milgram, J., Chopra, I., Straub, F., "A Comprehensive Rotorcraft Aeroelastic Analysis with Trailing Edge Flap Model: Validation with Experimentation Data", Proceeding of 52nd American Helicopter Society, Washington D.C., U.S.A., June, 1996.
5. Fulton, M., Ormiston, R., "Hover Testing of a Small-Scale Rotor with On-blade Elevons", Proceeding of 53rd American Helicopter Society, Virginia Beach, VA, U.S.A., April, 1997.
6. Milgram, J., Chopra, I., "Dynamic of an Actively Controlled Plain Trailing Edge Flap System for a Modern bearingless Rotor", Proceeding of 23rd European Rotorcraft Forum, Dresden, Germany, September, 1997.
7. Schimke, D., Jaenker, P., Wendt, V., Junker, B., "Wind Tunnel Evaluation of a Full Scale Piezoelectric Flap Control Unit", Proceeding of 24th European Rotorcraft Forum paper No. TE02, Marseille, France, September, 1998.
8. Straub, F., Charles, B., "Comprehensive Modeling of Rotors with Trailing Edge Flaps", Proceeding of 55th American Helicopter Society, Montreal, Canada, May, 1999.
9. Friedmann, P., "Rotary-Wing Aeroelastic Scaling and Its Application to Adaptive Materials Based Actuation", Proceeding of 24th European Rotorcraft Forum paper No. DY08, Marseille, France, September, 1998.
10. Hongu,T., Sato, M., Yamakawa, E., "Elementary Studies of Active Flap Control with Smart Material Actuators", Proceeding of 25th European Rotorcraft Forum, Rome, Italy, September, 1999.
11. Hariharan, N., and Leishman, J.G., "Unsteady Aerodynamics of a Flapped Airfoil in Subsonic Flow by Indicial Concepts," Proceedings of the 36th AIAA/ASME/ASCE/AHS/ASC Structures, Structural Dynamics, and Materials Conference, New Orleans, LA, Apr 1995.

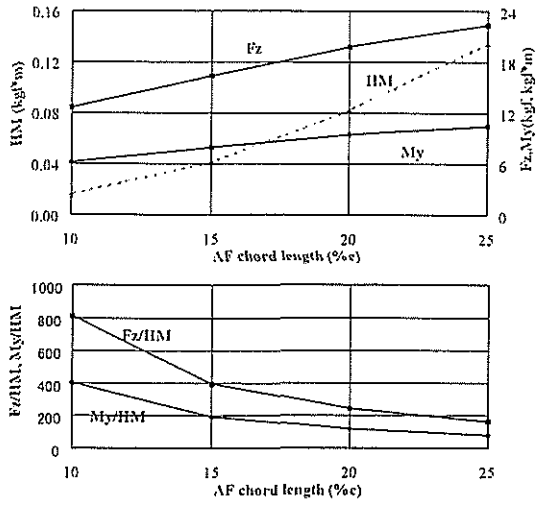

Fig. 1 AF chord length effect on 4/rev hub load
4/rev AF frequency with 1deg amplitude
AF span length 10%R, 70 - 80%R

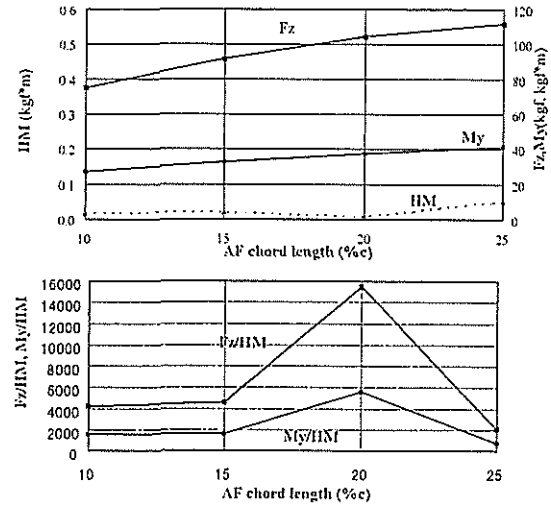

Fig. 4 AF chord length effect on 4/rev hub load
4/rev AF frequency with 1deg amplitude
AF span length 20%R, 60 - 80%R

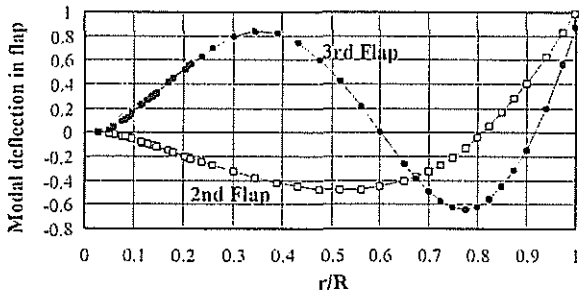

Fig. 2 Mode shape of rotor blade

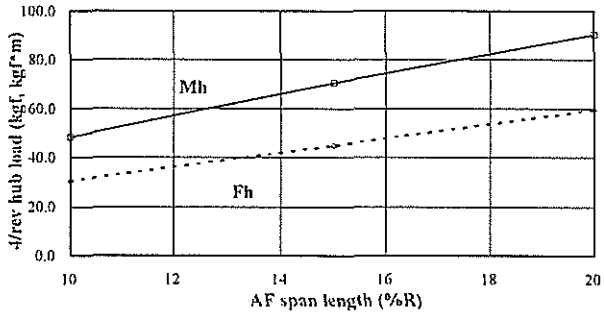

Fig. 3 AF span length effect on 4/rev hub load
4/rev AF frequency with 1deg amplitude
AF span length 10%R, 70 - 80%R

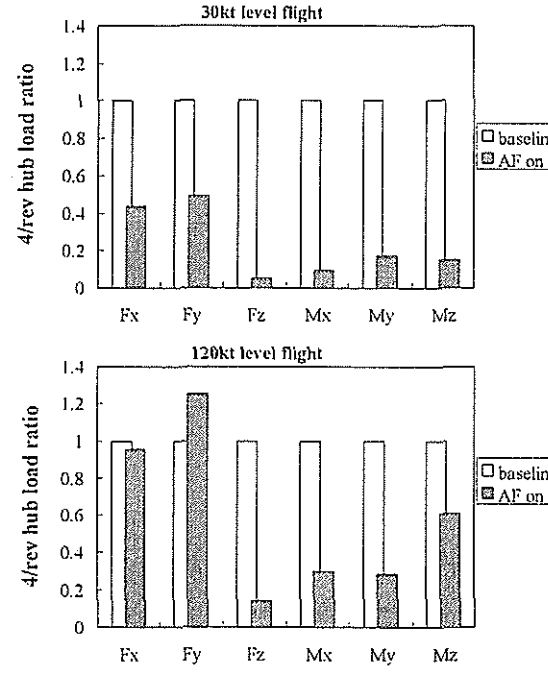

Fig. 5 Designed AF effect on rotor vibration reduction

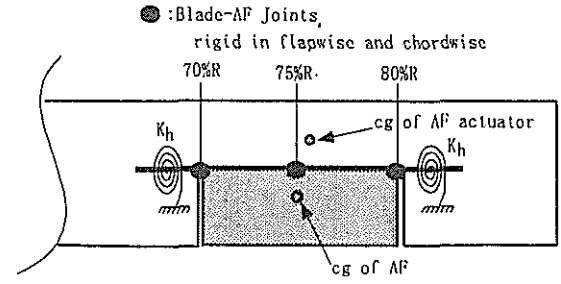

Fig. 6 Structural model for flutter analysis

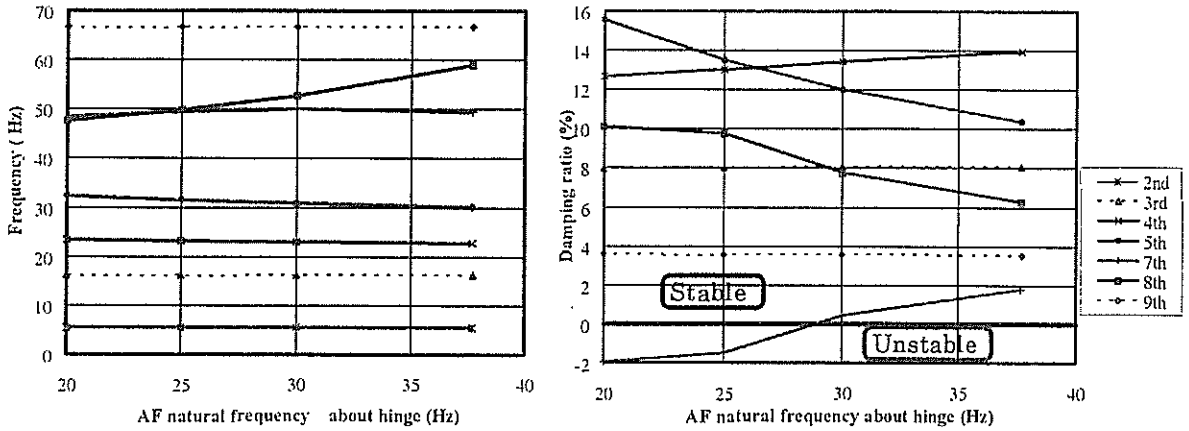

Fig.7 Influence of AF natural frequency about hinge on stability

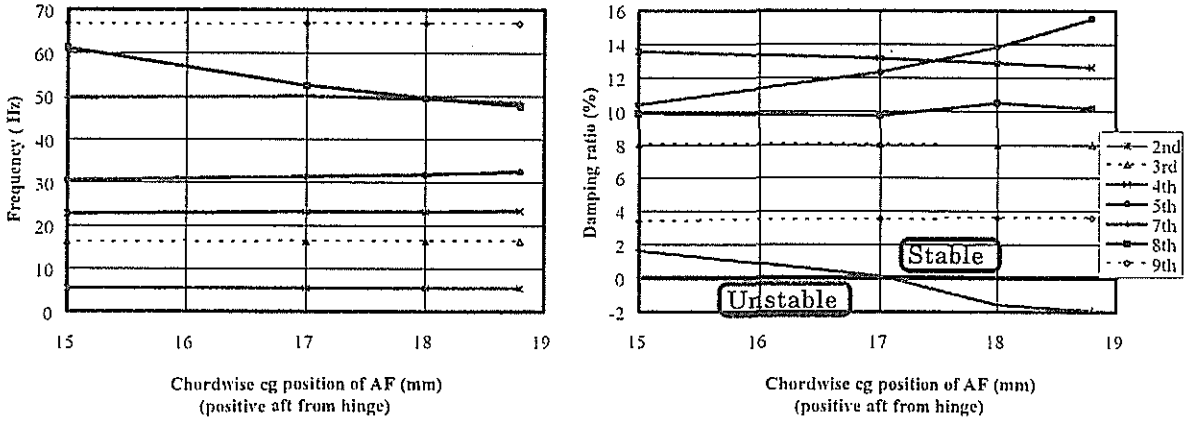

Fig. 8 Influence of chordwise cg position of AF on stability
AF natural frequency about hinge : 20Hz

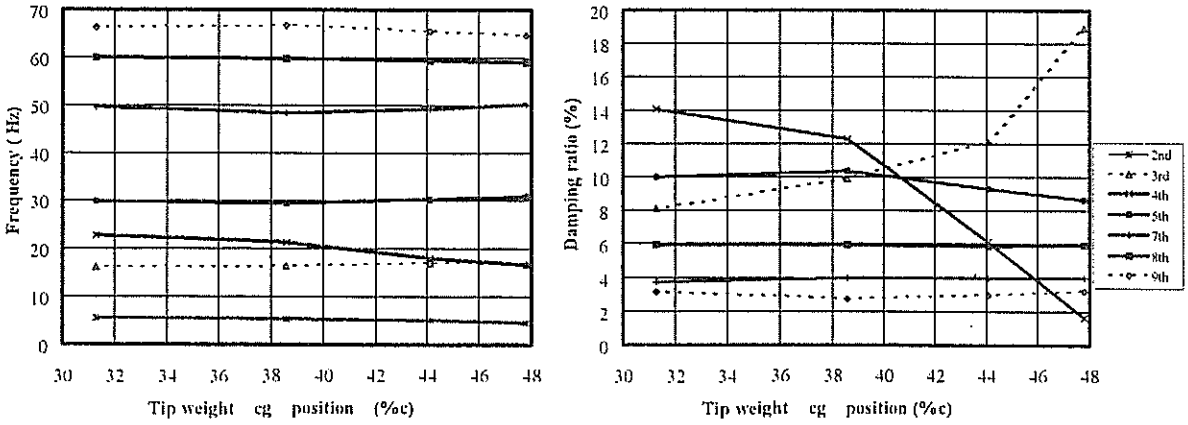

Fig. 9 Influence of chordwise cg position of blade on stability

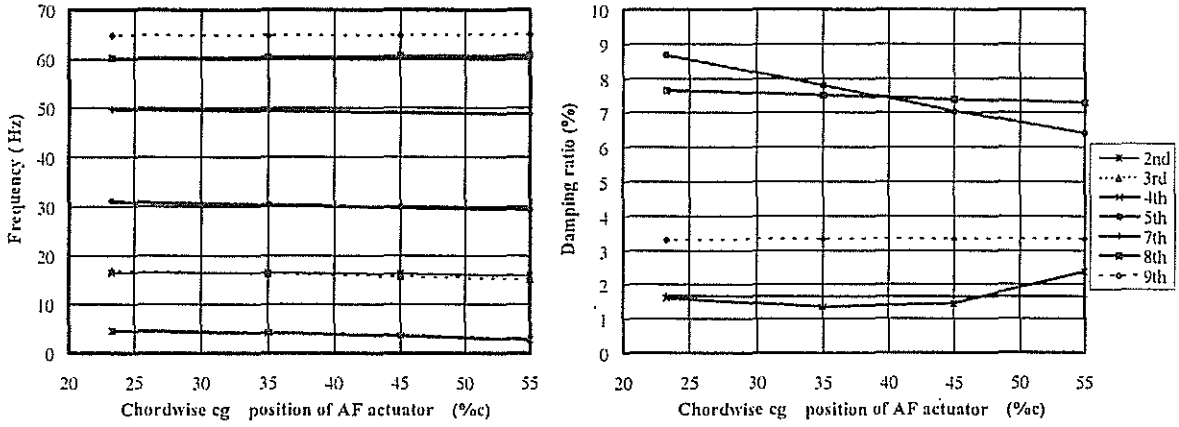

Fig. 10 Influence of chordwise cg position of AF actuator on stability
Tip weight cg position : 47.8%c

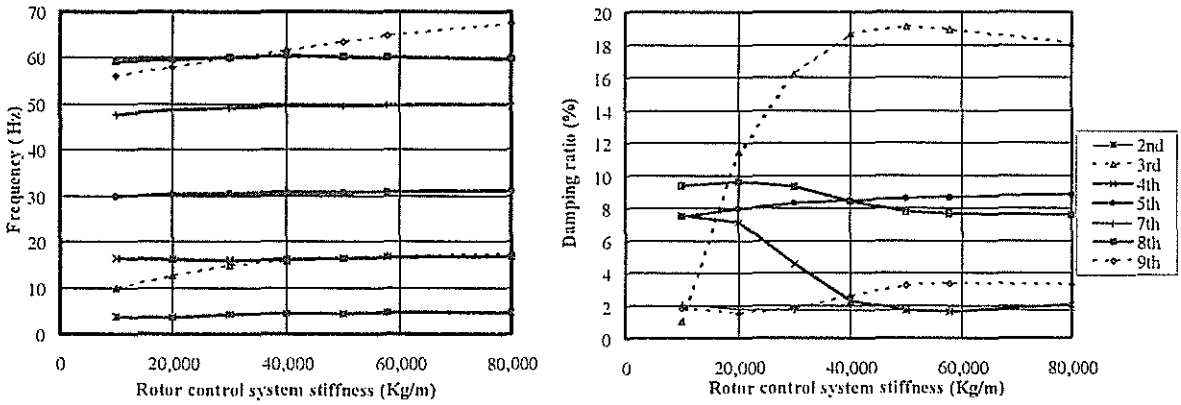

Fig. 11 Influence of rotor control system stiffness on stability
Tip weight cg position : 47.8%c

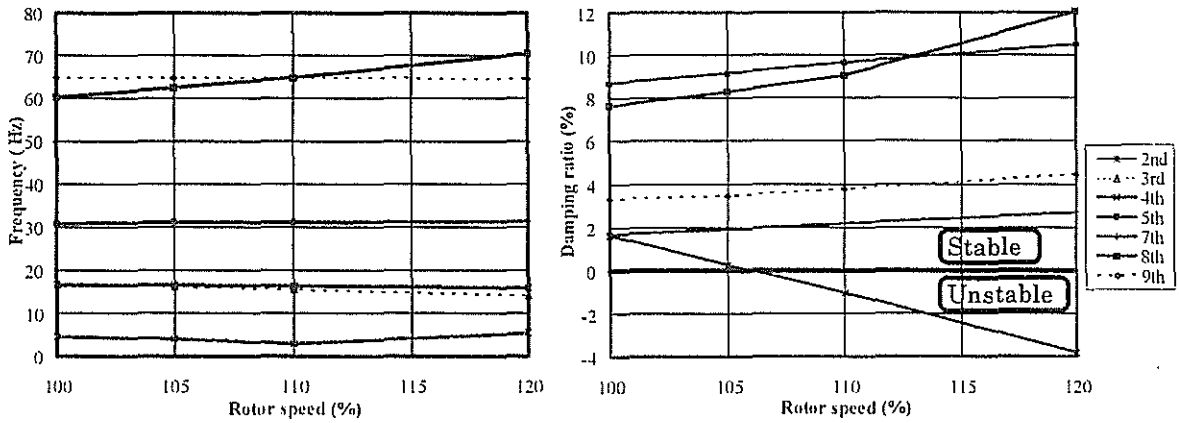

Fig. 12 Influence of rotor speed on stability
Tip weight cg position : 47.8%c

Appendix

Unsteady Aerodynamics for AF Analysis

This section describes the unsteady aerodynamics applied to the analysis in this paper. The incompressible unsteady aerodynamics with the trailing edge flap is formulated at first based on the thin airfoil theory, which contains some revised formulations for those described in Ref. 11. Then, the real airfoil effects such as compressibility and viscosity are taken into account based on the 2D wind tunnel test data of the airfoil with the trailing edge flap. In the last step, the chord length effect of the trailing edge flap is corrected by 2D N-S CFD code, UG2 which is developed in KHI, because the airfoil tested in the wind tunnel has only 25%c trailing edge flap and other chord lengths 20, 15, 10%c are necessary in the parametric study phase for AF design.

1. Incompressible unsteady aerodynamics for airfoil with trailing edge flap

$$C_L = 2\pi C(k)\left[\frac{\dot{h}}{V} + \alpha + b(\frac{1}{2}-a)\frac{\dot{\alpha}}{V}\right] + \frac{1}{V^2}\pi\cdot b\cdot\left[\ddot{h} + V\cdot\dot{\alpha} - a\cdot b\cdot\ddot{\alpha}\right]$$

$$C^f{}_L = \frac{b}{V^2}\left[-V\cdot F_4\cdot\dot{\delta} - b\cdot F_1\cdot\ddot{\delta}\right] + 2\pi C(k)\left[\frac{F_{10}\cdot\delta}{\pi} + \frac{b\cdot F_{11}\cdot\dot{\delta}}{2\pi\cdot V}\right]$$

$$C_G = 2F_{20}\cdot C(k)\left[\frac{\dot{h}}{V} + \alpha + b(\frac{1}{2}-a)\frac{\dot{\alpha}}{V}\right] + \frac{1}{V^2}\left[F_{20} + P_{24} - F_4\right]\cdot V\cdot b\cdot\dot{\alpha} + \frac{1}{V^2}\left[2\cdot F_9\cdot b\cdot\ddot{\alpha} - F_4\cdot\ddot{h}\right]$$

$$C^f{}_G = 2F_{20}\cdot C(k)\left[\frac{F_{10}\cdot\delta}{\pi} + \frac{b\cdot F_{11}\cdot\dot{\delta}}{2\pi\cdot V}\right] + \frac{2}{\pi}P_{21}\cdot\delta + \frac{1}{2V^2}\cdot\frac{2}{\pi}\cdot\left\{P_{21}\cdot(1-e) + P_{25} - \frac{F_5}{2}\right\}\cdot V\cdot b\cdot\dot{\delta} - \frac{1}{2V^2}\cdot\frac{1}{\pi}\cdot F_2\cdot b^2\cdot\ddot{\delta}$$

$$C_M = \frac{1}{2V^2}\pi\cdot\left[a\cdot b\cdot\ddot{h} - (\frac{1}{8}+a^2)\cdot b^2\cdot\ddot{\alpha}\right] + \pi(a+\frac{1}{2})\cdot C(k)\left[\frac{\dot{h}}{V} + \alpha + b(\frac{1}{2}-a)\frac{\dot{\alpha}}{V}\right] - \frac{\pi}{2V^2}(\frac{1}{2}-a)\cdot b\cdot V\cdot\dot{\alpha}$$

$$C^f{}_M = \frac{1}{2V^2}\left[\{F_7 + (e-a)\cdot F_1\}b^2\cdot\ddot{\delta}\right] + \pi(a+\frac{1}{2})\cdot C(k)\left[\frac{F_{10}\cdot\delta}{\pi} + \frac{b\cdot F_{11}\cdot\dot{\delta}}{2\pi\cdot V}\right] - \frac{1}{2V^2}\left[F_{15}\cdot V^2\cdot\delta + F_{16}\cdot V\cdot b\cdot\dot{\delta}\right]$$

$$C_H = -\frac{1}{2}\cdot F_{12}\cdot C(k)\left[\frac{\dot{h}}{V} + \alpha + b(\frac{1}{2}-a)\frac{\dot{\alpha}}{V}\right] - \frac{1}{2V^2}F_{17}\cdot V\cdot b\cdot\dot{\alpha} + \frac{1}{2V^2}\left[-2\cdot F_{13}\cdot b^2\cdot\ddot{\alpha} + F_1\cdot b\cdot\ddot{h}\right]$$

$$C^f{}_H = -\frac{1}{2}\cdot F_{12}\cdot C(k)\left[\frac{F_{10}\cdot\delta}{\pi} + \frac{b\cdot F_{11}\cdot\dot{\delta}}{2\pi\cdot V}\right] - \frac{1}{2\pi}F_{18}\cdot\delta + \frac{1}{2V^2}\left[\frac{1}{2\pi}\cdot F_{19}\cdot V\cdot b\cdot\dot{\delta} + \frac{1}{\pi}\cdot F_3\cdot b^2\cdot\ddot{\delta}\right]$$

The notation is identical to that in Ref. 11 except the followings;

$C_L, C^f{}_L$: identical to C_N and $C^f{}_N$ in Ref.11, respectively

C_G: Flap lift coefficient by airfoil motion, identical to C_F in Ref. 11.

$C^f{}_G$: Flap lift coefficient by flap motion

$$F_3 = -\frac{1}{2} - \frac{1}{8}e^2 + \frac{5}{8}e^4 - (\frac{1}{8}+e^2)\theta_e{}^2 + e\theta_e\sin(\theta_e)\frac{1}{4}(7+2e^2)$$

$$P_{21} = \sin^2(\theta_e) = 1-e^2$$

$$P_{24} = (2-e)\cdot\sin(\theta_e) - \theta_e$$

$$P_{25} = \frac{1}{2}(1-e)\cdot\sin(\theta_e)\cdot(\theta_e - \sin(\theta_e))$$

$$\theta_e = \cos^{-1}e$$

2. Compressibility and viscosity correction

The incompressible unsteady formulation described above is expanded to compressible and viscous form by utilizing 2D wind tunnel test data. Although only C_L and $C^f{}_L$ are presented here in order to save space, the other coefficients can be expanded in the same way.

The equation for C_L is modified to

$$C_L = C(k)\cdot C_{L\alpha}\left[\frac{\dot{h}}{V}+\alpha+b(\frac{C_{L\alpha}}{2\pi}+ac-a)\frac{\dot{\alpha}}{V}\right] + \frac{1}{V^2}\pi\cdot b\cdot\left[\ddot{h}+V\cdot\dot{\alpha}-a\cdot b\cdot\ddot{\alpha}\right]$$

The lift coefficient offset may not be zero in case of asymmetric airfoils. Furthermore, the lift curve slope depends on Mach number and angle of attack. These influences are incorporated as follows;

$$C_L = C(k)\cdot C_l(\beta)+\frac{1}{V^2}\pi\cdot b\cdot\left[\ddot{h}+V\cdot\dot{\alpha}-a\cdot b\cdot\ddot{\alpha}\right]$$

where

$$C_{l\alpha}=\frac{2\pi}{\sqrt{1-M^2}}$$

$$\beta=\frac{\dot{h}}{V}+\alpha+(\frac{C_{l\alpha}}{2\pi}+ac-a)b\frac{\dot{\alpha}}{V}$$

ac: Chordwise position of aerodynamic center

$C_l(\beta)$: 2D lift coefficient based on the wind tunnel data as a function of Mach number and angle of attack

The equation for $C^f{}_L$ is modified in the next. Assuming steady condition, the equation for $C^f{}_L$ becomes;

$$\frac{\partial C^f{}_L}{\partial\delta}=C_{L\alpha}\cdot\frac{F_{10}}{\pi}$$

This equation can be evaluated quantitatively, because $C_{L\alpha}$ and $\frac{\partial C^f{}_L}{\partial\delta}$ are obtained from the wind tunnel test data. But this relationship is not satisfied exactly. To cope with this, the correction factor L_{cor} is introduced as follows;

$$\left.\frac{\partial C^f{}_L}{\partial\delta}\right|_{wind\ tunnel}=L_{cor}\cdot C_{L\alpha}|_{wind\ tunnel}\cdot\frac{F_{10}}{\pi}$$

This correction factor is incorporated as follows;

$$C^f{}_L=\frac{b}{V^2}\left[-V\cdot F_4\cdot\dot{\delta}-b\cdot F_1\cdot\ddot{\delta}\right] + C_{L\alpha}\cdot C(k)\cdot L_{cor}\left[\frac{F_{10}\cdot\delta}{\pi}+\frac{b\cdot F_{11}\cdot\dot{\delta}}{2\pi\cdot V}\right]$$

Summing up C_L and $C^f{}_L$, the total lift is obtained;

$$C_{L\,Total}=C(k)\cdot C_l(\gamma)+\frac{1}{V^2}\pi\cdot b\cdot\left[\ddot{h}+V\cdot\dot{\alpha}-a\cdot b\cdot\ddot{\alpha}\right] + \frac{b}{V^2}\left[-V\cdot F_4\cdot\dot{\delta}-b\cdot F_1\cdot\ddot{\delta}\right]$$

where

$$\gamma=\frac{\dot{h}}{V}+\alpha+(\frac{C_{l\alpha}}{2\pi}+ac-a)b\frac{\dot{\alpha}}{V}+L_{cor}\left[\frac{F_{10}\cdot\delta}{\pi}+\frac{b\cdot F_{11}\cdot\dot{\delta}}{2\pi\cdot V}\right]$$

3. AF chord length correction

The correction factor L_{cor} is calculated here for several AF chord lengths used for the parametric study. As a preparation, $\frac{\partial C^f{}_L}{\partial\delta}$ is calculated with 25%c trailing edge flap configuration to get the correlation between the wind tunnel test data and UG2. Then, the calculation is performed at other flap chord lengths at several Mach numbers as shown in the table below.

$\frac{\partial C^f{}_L}{\partial\delta}$		M		
		0.4	0.55	0.7
c_f/c	25	3.74	3.88	4.32
	20	3.36	3.53	4.24
	15	2.83	2.98	3.53
	10	2.23	2.35	2.80

c_f/c : Flap chord length (%c)

Finally, L_{cor} is obtained from $\frac{\partial C^f{}_L}{\partial\delta}$ as shown in the table below.

L_{cor}		M		
		0.4	0.55	0.7
c_f/c	25	0.94	0.90	0.83
	20	0.94	0.91	0.91
	15	0.90	0.88	0.86
	10	0.86	·0.84	0.83

c_f/c : Flap chord length (%c)

TWENTYFIFTH EUROPEAN ROTORCRAFT FORUM

Paper n° G18

STABILIZATION OF A BLADE WITH A SEVERED PITCH LINK USING A TRAILING EDGE FLAP

BY

ROBERTO CELI
UNIVERSITY OF MARYLAND, COLLEGE PARK, USA

SEPTEMBER 14-16, 1999
ROME
ITALY

ASSOCIAZIONE INDUSTRIE PER L'AEROSPAZIO, I SISTEMI E LA DIFESA
ASSOCIAZIONE ITALIANA DI AERONAUTICA E ASTRONAUTICA

STABILIZATION OF A BLADE WITH A SEVERED PITCH LINK USING A TRAILING EDGE FLAP

Roberto Celi[1]
Department of Aerospace Engineering
Glenn L. Martin Institute of Technology
University of Maryland, College Park, USA

Abstract

This paper addresses the feasibility of using trailing edge flaps to reconfigure a helicopter rotor blade following a failure of the pitch link, which makes the blade free-floating in pitch and otherwise uncontrollable. A coupled rotor-fuselage model is developed which allowed for rotor anisotropy. A new, optimization-based, trim procedure is developed to determine the dynamics of the failed blade, and the flap inputs required for reconfiguration The trailing edge flap appears capable of correcting the otherwise catastrophic consequences of a pitch link failure. The residual 1/ and 2/rev components of the hub loads appear to be reasonably small. The flap acts by generating a rigid-body pitching motion of the free-floating blade that matches the angles that otherwise would have been generated by the swashplate. The steady-state flapping motion of the reconfigured blade is very nearly identical to those of the undamaged blades. Therefore, if a helicopter rotor is equipped with trailing edge flaps for other purposes such as vibration or noise reduction, these flaps could be used as emergency control surfaces.

Notation

S	Descent direction in optimization procedure for trim
X	Vector of design variables in trim procedure
β	Blade flapping angle
δ_F	Flap deflection
μ	Advance ratio
ψ	Azimuth angle of the reference blade (blade number 1)
ϕ	Rigid body pitch of the failed blade
Ω	Rotor speed

Subscripts and superscripts

$(\ )_{nc}$	cosine component of n-th harmonic
$(\ )_{ns}$	sine component of n-th harmonic
$(\ )_4$	Quantity for blade number 4 (failed blade)
$(\ )^4$	Quantity for blade number 4 (failed blade)

Introduction

In recent years there has been a renewed interest in the use of trailing edge flaps on the main rotor blades for noise and vibration reduction. Extensive theoretical research has been carried out, and model scale tests have been performed. Full-scale experimentation is now under way.

Trailing edge flaps provide additional control effectors, besides the conventional swashplate controls. Therefore, they offer some degree of control redundancy, and could potentially be used to reconfigure the rotor control chain in case of failures. Control reconfiguration has been successfully explored and tested in fixed-wing applications. On the other hand, the potential for helicopter applications has been severely limited by the lack of control redundancy, as shown by the few studies on this topic.

Aponso *et al.* [1] have studied a case in which the roll swashplate actuator of a Sikorsky UH-60 is jammed or floating. No additional control surfaces were assumed, and reconfiguration was carried out through changes in the flight control laws. A simple linearized aircraft model was used. Huang *et al.* [2] have considered a CH-47 tandem rotor configuration with combinations of jammed front and rear swashplate actuators. Reconfiguration was achieved through changes in the flight control laws. In one of the cases studied some control redundancy was obtained by assuming that the rotational speeds of the rotors could be varied by up to $\pm 10\%$. A simple linearized 6-DOF analysis model was used. In the only other published study on this topic, Heiges [3] has considered a configuration representative of the AH-64 with all the pitch links severed. Control was restored through the use of servo-flaps installed on all the blades. The study was based on a simple linearized rotor analysis.

The main objective of this paper is to study the dynamics and the reconfiguration of a single main rotor helicopter in which the pitch link of one of the blades has been severed, so that the blade is free-floating in pitch. The reconfiguration is achieved through the use of a trailing edge flap. The blade is schematically shown in Figure 1. The specific problem that will be addressed is whether one can determine a flap control history that: (i) allows the trimming of the failed rotor, and (ii) reduces the hub loads to acceptable levels. Because the focus of the study is simply to establish the theoretical feasibility of this type of reconfiguration, the control considered in this study is open-loop only, and no feedback is considered.

The mathematical model is much more detailed than in the studies mentioned above. It includes a full nonlinear, coupled rotor-fuselage dynamic model, from which

[1]Associate Professor, Alfred Gessow Rotorcraft Center; e-mail: celi@eng.umd.edu.

a linearized, time-varying model can also be extracted. The anisotropy of the rotor, which has one blade with a dynamics different from that of the other three, is fully taken into account. A new trim procedure is presented; the new procedure is required to deal with the rotor anisotropy and the flap control history.

Baseline simulation model

The mathematical model of the helicopter used in this study is a nonlinear blade element type model that includes fuselage, rotor, and main rotor inflow dynamics. The 6 degree of freedom rigid body motion of the aircraft is modeled using nonlinear Euler equations. Linear aerodynamics is assumed for fuselage and empennage. The blades are assumed to be rigid, with offset hinges and root springs. Flap and lag dynamics of each blade are modeled. The main rotor has four blades.

The coupled system of rotor, fuselage, and inflow equations of motion is written in first-order form. The state vector has a total of 28 elements: flap and lag displacements and rates for each of the 4 blades (16 states); 9 rigid body velocities, rates, and attitudes; and 3 inflow states.

In the absence of a failure, the trim procedure is the same as in Ref. [4]. Thus, the rotor equations of motion are transformed into a system of nonlinear algebraic equations using a Galerkin method. The algebraic equations enforcing force and moment equilibrium are added to the rotor equations, and the combined system is solved simultaneously. The solution yields the harmonics of a Fourier series expansion of the rotor degrees of freedom, the pitch control settings, the trim attitudes and rates of the entire helicopter, and the main and tail rotor inflow.

Modeling of the failed blade

The blade with the severed pitch link is assumed to be free-floating in pitch as a rigid body. The flap and lag dynamic model remains otherwise unchanged. The inertia moments due to the motion of the flap are neglected. Therefore, the pitch equation of motion is simply:

$$\ddot{\phi} + \Omega^2 \phi = M_\phi \qquad (1)$$

where Ω is the rotor speed and M_ϕ is the nondimensional aerodynamic pitching moment. The only aerodynamic pitching moment is that generated by the deflection of the trailing edge of the flap. The flap deflection $\delta_F(\psi)$, is assumed to have a harmonic variation, that is:

$$\delta_F(\psi) = \delta_0 + \sum_{n=1}^{N} (\delta_{nc} \cos\psi + \delta_{ns} \sin\psi) \qquad (2)$$

with $\delta_F > 0$ for a downward deflection of the flap. The cases $N = 1$ and $N = 2$ will be considered in the present paper. The pitching moment coefficient c_{mF} is assumed to be linearly proportional to the flap deflection, and is given by $c_{mF} = -0.64\delta_F$.

When the pitch link is severed, the swashplate pitch inputs are no longer applied to the blade. Therefore, the geometric angle of attack of the free floating blade is given by the sum of the rigid body pitch rotation ϕ and the twist angle θ_B. This angle is used to calculate all the aerodynamic forces acting on the blade (including the flap and lag dynamics).

While the pitching model of the blade is probably adequate for a feasibility study, its limitations should be kept in mind. The most serious is the lack of unsteady aerodynamic modeling. Even in the absence of a trailing edge flap, the motion of the airfoil introduces changes in both the magnitude and the phase of the lift, drag, and pitching moment coefficients; in particular, aerodynamic pitch damping is generated. The addition of the flap introduces further changes of the aerodynamic coefficients. A model such as that of Ref. [5] should be used for a more accurate representation of the unsteady aerodynamics of the flapped airfoil.

On the other hand, neglecting the elastic torsion of the free-floating blade is not likely to be a serious assumption. The changes in lead-lag dynamics can also be neglected, at least at the level of approximation used in the present study. It has been shown by Wang [6] that small dissimilarities in rotor blade dynamics tend to increase the aeroelastic stability of the rotor. Therefore, if the dynamics of the reconfigured blade is close or identical to that of the other blades, the rotor should at least maintain the level of stability that it had before the failure.

In summary, the coupled rotor-fuselage mathematical model consists of 30 nonlinear ODE, namely: 9 Euler equations for rigid body motion, 3 dynamic inflow equations, 2 equations for the flap and 2 for the lag dynamics of each of the 4 blades, and 2 pitch equations for the failed blade.

Trim procedure for the rotor with a failed blade

The trim procedure of Ref. [4] needs to be modified to take into account the damage to the blade. This is necessary for two primary reasons, namely: (i) the rotor anisotropy, and (ii) the need to determine the required flap trim control.

Treatment of rotor anisotropy

The free-floating blade has a dynamics different from that of the other three blades, and therefore it needs its own separate equations in the system of algebraic trim equations. Rigid-body flap and pitch dynamics of the free-floating blade are explicitly included in the trim procedure, whereas the lag dynamics is assumed to remain unchanged in trim. The flap and the pitch angles are represented in the form of a truncated Fourier series expansion, that is:

$$\beta^4(\psi) = \beta_0^4 + \sum_{n=1}^{2} (\beta_{nc}^4 \cos n\psi_4 + \beta_{ns}^4 \sin n\psi_4) \qquad (3)$$

$$\phi^4(\psi) = \phi_0^4 + \sum_{n=1}^{2} (\phi_{nc}^4 \cos n\psi_4 + \phi_{ns}^4 \sin n\psi_4) \quad (4)$$

where the subscripts and superscripts "4" indicate that the failed blade is the fourth, with $\psi_4 = \psi + 270°$. Compared with the trim procedure of Ref. [4] there are new trim unknowns, namely the coefficients of the Fourier series above. Therefore, anisotropy adds 10 unknowns to the trim problem. The corresponding 10 additional trim equations come from the application of Galerkin method [4]. For flap they are:

$$\int_0^{2\pi} \varepsilon_{F4}(\psi)\, d\psi = \int_0^{2\pi} \varepsilon_{F4}(\psi) \cos\psi\, d\psi =$$

$$= \int_0^{2\pi} \varepsilon_{F4}(\psi) \sin\psi\, d\psi = \int_0^{2\pi} \varepsilon_{F4}(\psi) \cos 2\psi\, d\psi =$$

$$= \int_0^{2\pi} \varepsilon_{F4}(\psi) \sin 2\psi\, d\psi = 0 \quad (5)$$

where $\varepsilon_{F4}(\psi)$ is the residual obtained when the tentative trim solution is substitutes into the flap equation of motion for the failed blade. Five similar equations are then written for the residual $\varepsilon_{P4}(\psi)$ of the blade pitch equation.

The total number of trim equations and unknowns for the case of the rotor with a failed blade case is 36. Besides the 10 unknowns just mentioned, the trim procedure yields values of the pitch settings of main rotor and tail rotor; fuselage angle of attack and sideslip angle; roll and pitch attitudes; roll, pitch, and yaw rates; and the harmonics of the steady-state flap and lag motions for the undamaged blades.

Determination of flap input

The coefficients δ_0, δ_{nc}, and δ_{ns} that describe the motion of the flap (see Eq. (2)) cannot be directly added to the set of trim unknowns, because there are no corresponding algebraic equations. Therefore, the trim formulation would consist of more unknowns than equations, and an infinite number of trim states would then exist.

The solution devised for this study is to insert the baseline trim procedure in an unconstrained optimization loop. The vector $\mathbf{X}$ of design variables of the optimization consists of the coefficients of the flap motion:

$$\mathbf{X}^T = [\delta_0\ \delta_{1c} \ldots\ \delta_{nc}\ \delta_{1s} \ldots\ \delta_{ns}] \quad (6)$$

Because the rotor is now anisotropic, multiblade load cancellations will not occur, and all harmonics of the hub loads will generally be present. If the generic hub force or moment component f is written in the form

$$f(\mathbf{X}) = f_0 + \sum_{n=1}^{2} (f_{nc} \cos n\psi + f_{ns} \sin n\psi) \quad (7)$$

the objective function to be minimized is

$$F(\mathbf{X}) = \left\{ \sum_{m=1}^{6} \sum_{n=1}^{2} \left[(f_{nc}^2)_m + (f_{ns}^2)_m \right] \right\}^{1/2} \quad (8)$$

where the subscript m denotes each of the three hub force and three hub moment components. In other words, the optimization loop attempts to minimize the coefficients of the 1/rev and 2/rev harmonics of all six hub components.

The resulting problem can be solved using any unconstrained minimization algorithm. In the present study the Fletcher-Reeves conjugate gradient algorithm [7] is used. Therefore, the improved value of the flap motion vector $\mathbf{X}_{k+1}$ is given by:

$$\mathbf{X}_{k+1} = \mathbf{X}_k + \alpha^* \mathbf{S}_k \quad (9)$$

where α^* denotes the minimum of $F(\mathbf{X})$ along the direction $\mathbf{S}_k$, which is obtained from

$$\mathbf{S}_k = -\nabla F(\mathbf{X}_k) + \beta \mathbf{S}_{k-1}$$

$$\text{with} \quad \beta = \frac{\nabla F^T(\mathbf{X}_k) \nabla F(\mathbf{X}_k)}{\nabla F^T(\mathbf{X}_{k-1}) \nabla F(\mathbf{X}_{k-1})} \quad (10)$$

where k denotes the iteration number and $\beta = 0$ for $k = 1$. Note that, for every value of $F(\mathbf{X})$ required during the optimization, a complete trim calculation is performed. The final solution consists of the vector $\mathbf{X}$ that minimizes the sum of the absolute values of all the components of the 1/rev and 2/rev hub loads plus the corresponding values of all the trim variables.

Results

The results presented in this section refer to a soft-in-plane, hingeless rotor helicopter configuration roughly similar to a BO-105. The chordwise extension of the flap is 20% of the blade chord. The flap extends over the outermost 20% of the blade.

Figure 2 shows the iteration history of the objective function of the new trim procedure, i.e., the RMS value of the 1/rev and 2/rev components of the hub loads at an advance ratio $\mu = 0.15$. One iteration is defined as the calculation of one direction of descent $\mathbf{S}_k$, Eq. (10), and a one-dimensional minimization along $\mathbf{S}_k$ to obtain the new vector of flap coefficients $\mathbf{X}_{k+1}$, Eq. (9). The direction finding problem requires the calculation of the gradient of the objective function, and therefore 4 function evaluations for the 1-harmonic flap input. The one-dimensional minimization requires another two function evaluations besides the baseline to calculate an initial quadratic approximation. The minimum of the approximation is the candidate 1-D minimum, and replaces the point with the highest value of the objective in the updated approximation. In all the results of the present study no more than three function evaluations were needed to achieve convergence on the 1-D minimum. Therefore, each iteration of the optimization-based trim procedure required a total of between 8 and 10 evaluations of the objective function $F(\mathbf{X})$, Eq. (8). The initial guess for $\mathbf{X}$ in Fig. 2 is a zero vector, corresponding to an inactive flap. The trim procedure clearly

converges quickly, and reduce the hub loads by almost two orders of magnitude within the first iteration.

The top part of Figure 3 shows the absolute values of the components of the 1/rev and 2/rev hub loads with the flap inactive; the bottom part shows the components with the flap activated, for the final iteration of the trim procedure. The advance ratio is again $\mu = 0.15$. All components should be equal to zero for a four-bladed rotor with identical blades and intact pitch links. Both sets of data refer to trimmed configurations. However, it is clear that for the rotor with the failed blade "trim" is just a mathematical statement, because the very large vibratory loads would quickly destroy the aircraft. The improvement brought about by the trailing edge flap is dramatic: the peak values are reduced by almost three orders of magnitude.

The objective function is plotted in Fig. 4 as a function of advance ratio. Recall that the objective function is the square root of the sum of the squares of the first and second harmonics of the six hub load components, Eq. (8). Although the residual loads increase almost quadratically with advance ratio, the flap clearly manages to contain them within reasonable limits.

The harmonics of the required flap motion are shown in Fig. 5 as a function of advance ratio. There is a constant, upward deflection of the flap of magnitude between 18.5 and 22 degrees, depending on speed. Smaller first harmonic motions are superimposed to it; their magnitudes are almost exactly zero at hover (a small amount of cyclic is needed in hover to counteract the effects of the tail rotor) and slowly increase with speed.

The mechanism of action of the trailing edge flap is evident from the results shown in Fig. 6. The figure shows the value of collective and cyclic pitch settings as a function of advance ratio, plus the first two harmonics of the rigid body pitching motion of the free-floating blade with the flap active. The constant harmonic of the pitch motion matches almost perfectly the collective pitch at every advance ratio. The same is true for lateral cyclic pitch and first harmonic cosine, and for longitudinal cyclic pitch and first harmonic sine respectively. The second harmonics of the rigid body pitch are almost negligible. Therefore, the trailing edge flap acts in such a way that the dynamic pitch response of the blade matches the pitch angles that the swashplate controls would have generated, if the pitch link had not been severed. In retrospect, this conclusion may appear obvious. It should be noted, however, that the optimization procedure used for trim does not include directly either the pitch dynamics of the failed blade or the rotor pitch settings. The match between the two types of quantity is a by-product of the attempt to minimize the 1/rev and 2/rev loads in the nonrotating system.

Because the action of the flap mimics almost perfectly the effect of the swashplate controls, the flap dynamics of the reconfigured blade is essentially identical to those of the undamaged blades. This is clearly shown in Fig. 5, which compares the first two harmonics of the flapping motion for both types of blades. Changes in lead-lag dynamics are neglected in this study, because the drag coefficient is assumed to be constant, and not affected by the flap motion. A more realistic flap model would have to take this effect into account: drag changes will likely introduce 1/rev (and higher) lead-lag oscillations.

Figures 8 through 10 show the hub load components with the largest nondimensional values of unbalanced harmonics. Figure 8 shows the first and second harmonics of the roll moment as a function of advance ratio. The roll moment is nondimensionalized by dividing it by the roll moment of inertia of the helicopter. These harmonics are all equal to zero for the undamaged rotor. The figure shows that the 1/rev and 2/rev harmonics are almost cancelled by the flap, with the exception of the 1/rev sine component, which turns out to be the largest unbalanced component among all hub loads. The 1/rev and 2/rev harmonics of the pitching moment are shown in Fig. 9, which is drawn in the same scale as Fig. 8. The pitching moment of inertia of the helicopter is used for the nondimensionalization. The 1/rev sine and cosine harmonics have about the same size, whereas the 2/rev components are negligible. The pitch 1/rev components are the next largest hub load components. Figure 10 shows the harmonics of the Z-force, nondimensionalized using the weight of the helicopter. For this hub load component it is the 1/rev portion to be negligible, whereas the 2/rev portion has the larger harmonics, which progressively increase with advance ratio.

Including a second harmonic in the trailing edge flap input has a negligible effect. This can be seen in Fig. 4, where the objective function is plotted as a function of advance ratio for the case of 1- and 2-harmonic flap input. As expected, adding a second harmonic reduces the value of the objective function at all advance ratios, but the improvement is negligible. The magnitude of the second harmonic input is never larger than 0.011 degrees. However, it should be kept in mind that a more sophisticated aerodynamic model will probably introduce a stronger higher harmonic forcing. As a consequence, higher harmonic flap inputs may also be required.

Figure 12 shows the coupled rotor-fuselage poles for the baseline and the failed configurations, and the latter with the trailing edge flap active and inactive. The top plot contains all the poles, the bottom plot only those closest to the origin. Perhaps unexpectedly, the poles are not dramatically changed by the blade failure. In particular, the pitch link failure does not trigger any new substantial instabilities. Rather, it produces very high forced responses. The distinction is probably only of academic interest, as the aircraft would be lost without reconfiguration anyway, but it may have some repercussions on the design of the reconfiguration control laws.

Summary and Conclusions

This paper addressed the feasibility of using trailing edge flaps to reconfigure a helicopter rotor blade following a failure of the pitch link, which makes the blade free-floating in pitch and otherwise uncontrollable. The problem was studied using a coupled rotor-fuselage model which allowed for rotor anisotropy in the form of three identical blades with a fourth dissimilar one. A new, optimization-based, trim procedure was developed to determine both the dynamics of the failed (and reconfigured) blade, and the flap inputs required to achieve the best possible reconfiguration. A very simple aerodynamic model was used for the flap. While this model is adequate for a feasibility study, its limitations should be kept in mind when evaluating the conclusions of the study.

The main conclusions of the present study are:

1. The new trim procedure is effective in calculating the trim state of the helicopter with the anisotropic rotor, and in providing the stabilizing flap input.

2. The trailing edge flap is capable of correcting the otherwise catastrophic consequences of a pitch link failure. The residual 1/ and 2/rev components of the hub loads appear to be reasonably small. This is accomplished primarily through 1/rev flap inputs. The required flap deflections are high, but not unreasonably so. Adding higher harmonics to the flap input does not bring significant benefits.

3. The flap acts by generating a rigid-body pitching motion of the free-floating blade that matches at every azimuth the angles that would have been generated by the swashplate input if the pitch link had not been severed. The steady-state flapping motion of the reconfigured blade is very nearly identical to those of the undamaged blades.

The previous conclusions suggest that, if a helicopter rotor is equipped with trailing edge flaps for other purposes such as vibration or noise reduction, these flaps could be used as emergency control surfaces to help reconfigure the flight control system following a failure or battle damage.

Acknowledgments

This research was supported by the National Rotorcraft Technology Center, under the Rotorcraft Center of Excellence Program, Technical Monitor Dr. Yung Yu.

References

[1] Aponso, B. L., Klyde, D. H., and Mitchell, D. G., "Development of Reconfigurable Flight Controls for Helicopters," Systems Technology Inc. Report STI TR-1295-1.

[2] Huang, C. Y., Celi, R., and Shih, I.-C., "Reconfigurable Flight Control Systems for a Tandem Rotor Helicopter," *Proceedings of the 52nd Annual Forum of the American Helicopter Society*, Washington, DC, June 1996, pp. 1569-1588; to appear in the *Journal of the American Helicopter Society.*

[3] Heiges, M., "Reconfigurable Controls for Rotorcraft — A Feasibility Study," *Journal of the American Helicopter Society*, Vol. 42, No. 3, July 1997, pp. 254-263.

[4] Celi, R., "Hingeless Rotor Dynamics in Coordinated Turns", *Journal of the American Helicopter Society*, Vol. 36, No. 4, Oct. 1991, pp. 39-47.

[5] Hariharan, N., and Leishman, J. G., "Unsteady Aerodynamics of a Flapped Airfoil in Subsonic Flow by Indicial Concepts," *Journal of Aircraft*, Vol. 33, No. 5, Sep.-Oct. 1996, pp. 855-868.

[6] Wang, J. M., and Chopra, I., "Dynamics of Helicopters with Dissimilar Blades," *Proceedings of the 47th Annual Forum of the American Helicopter Society*, Phoenix, AZ, May 1991, pp. 1399-1412.

[7] Vanderplaats, G. N., *Numerical Optimization Techniques for Engineering Design: With Applications*, McGraw-Hill, New York, 1984.

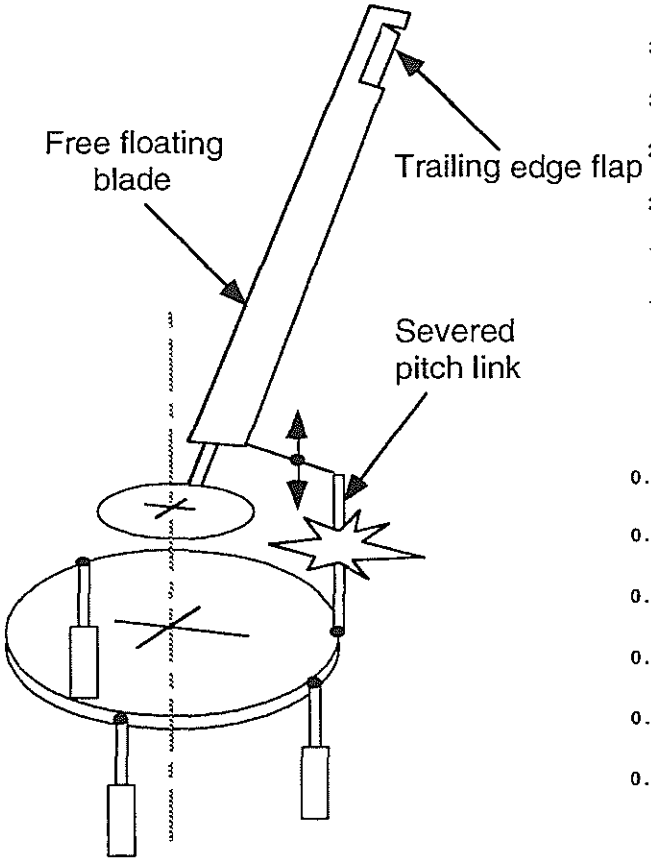

Figure 1: Blade with severed pitch link and trailing edge flap.

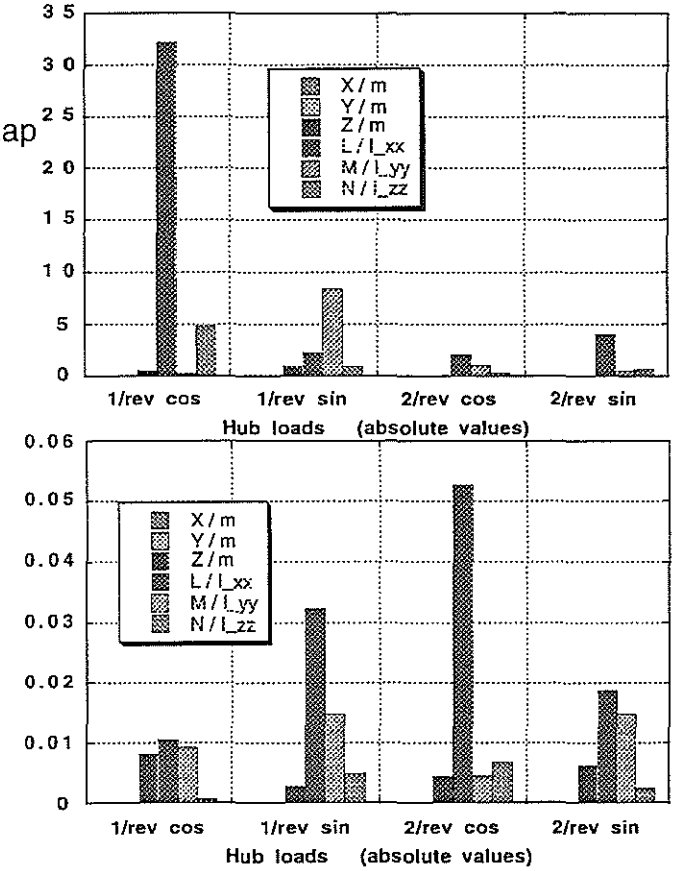

Figure 3: Components of the hub loads without flap (top) and with flap (bottom); one harmonic flap motion, $\mu = 0.15$.

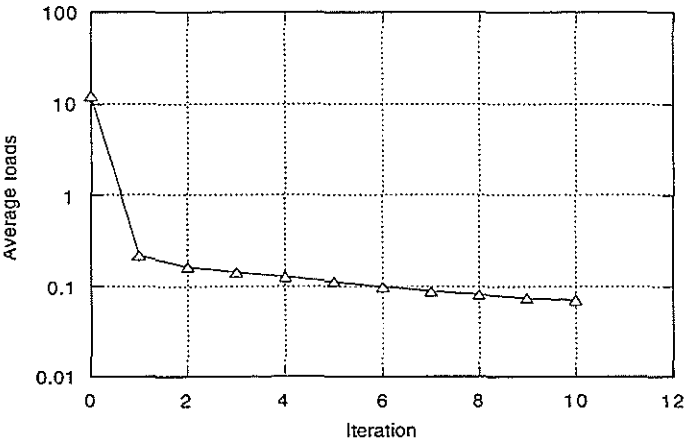

Figure 2: Iteration history of the objective function of the trim procedure; $\mu = 0.15$.

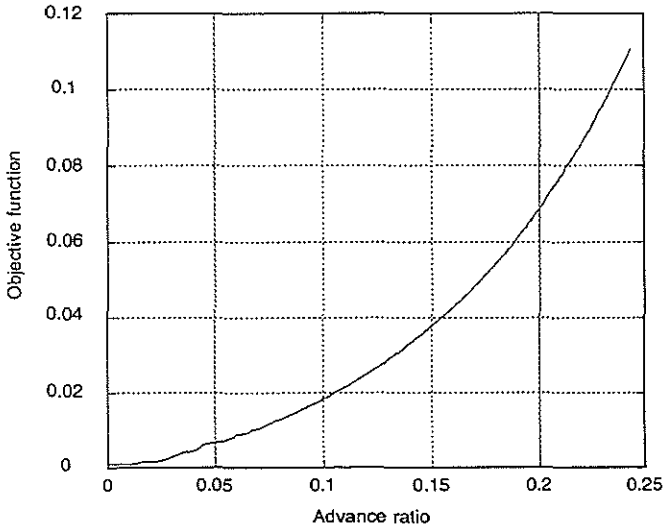

Figure 4: Objective function as a function of advance ratio.

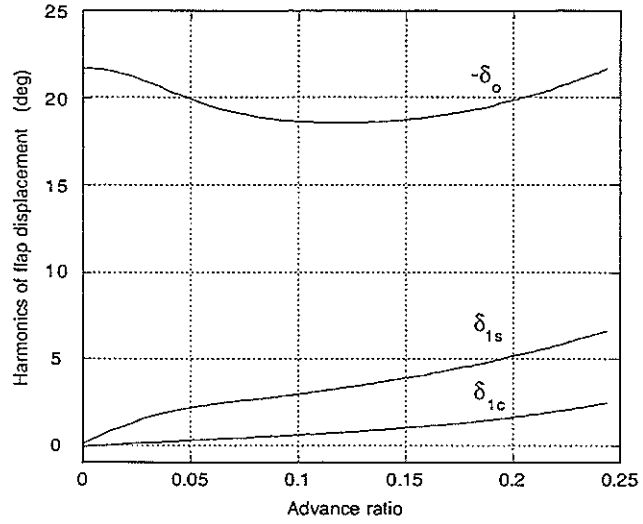

Figure 5: Harmonics of flap motion as a function of advance ratio.

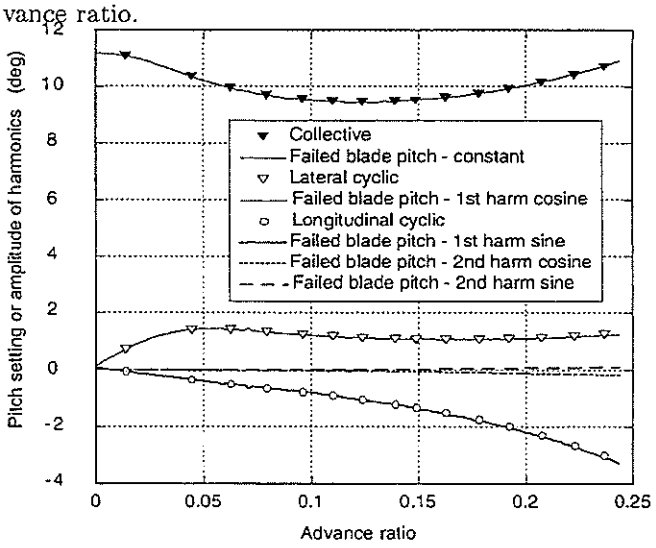

Figure 6: Pitch settings and harmonics of rigid body pitch motion of the failed blade as a function of advance ratio.

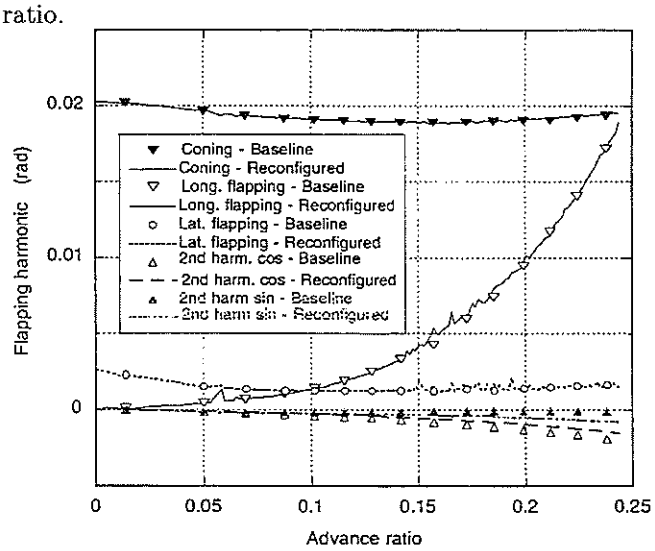

Figure 7: Flapping harmonics for baseline and reconfigured rotors as a function of advance ratio.

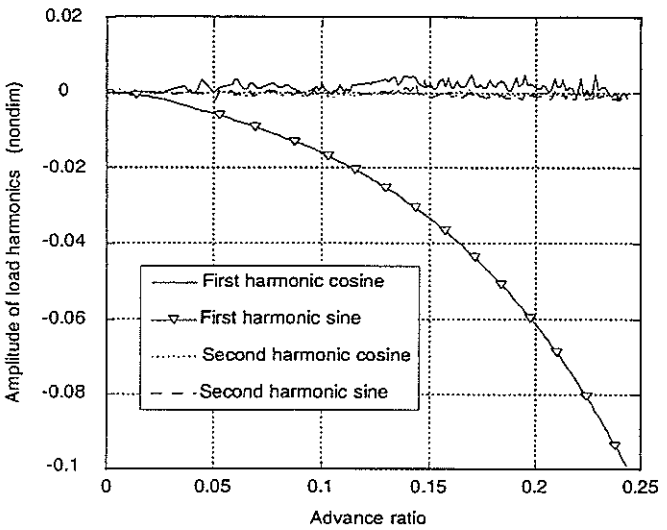

Figure 8: Harmonics of roll moment as a function of advance ratio.

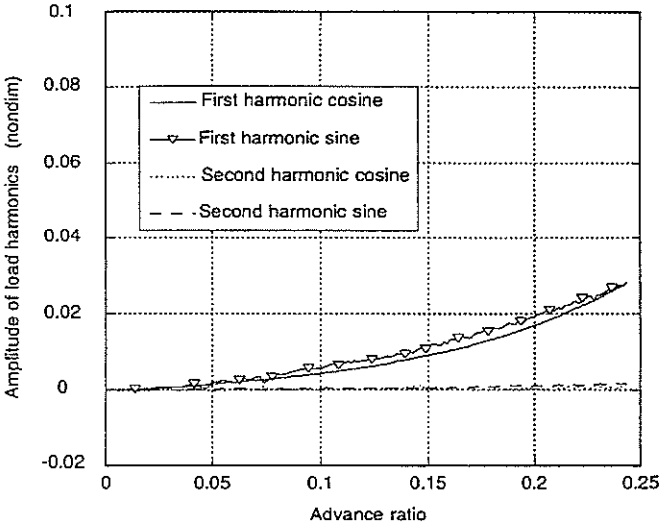

Figure 9: Harmonics of pitch moment as a function of advance ratio.

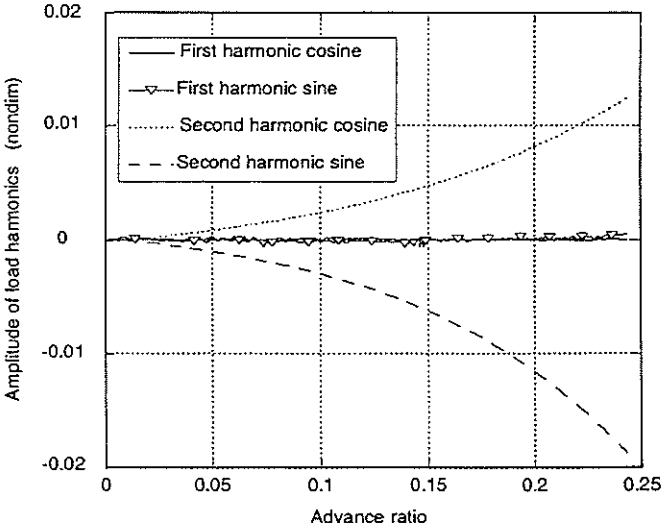

Figure 10: Harmonics of pitch moment as a function of advance ratio.

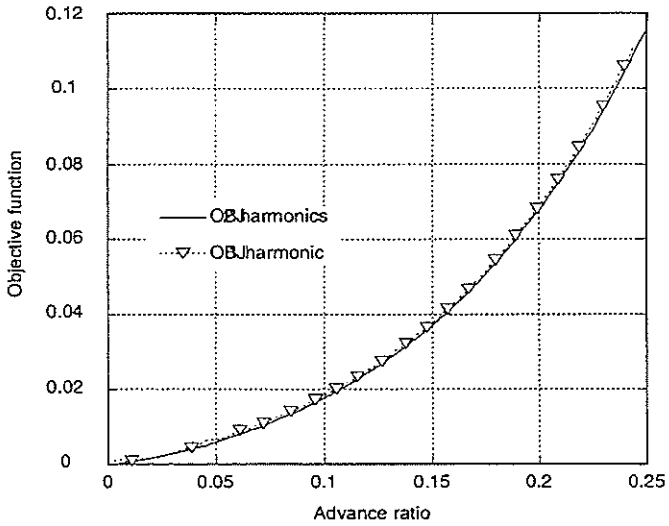

Figure 11: Objective function as a function of advance ratio for 1- and 2-harmonic flap input.

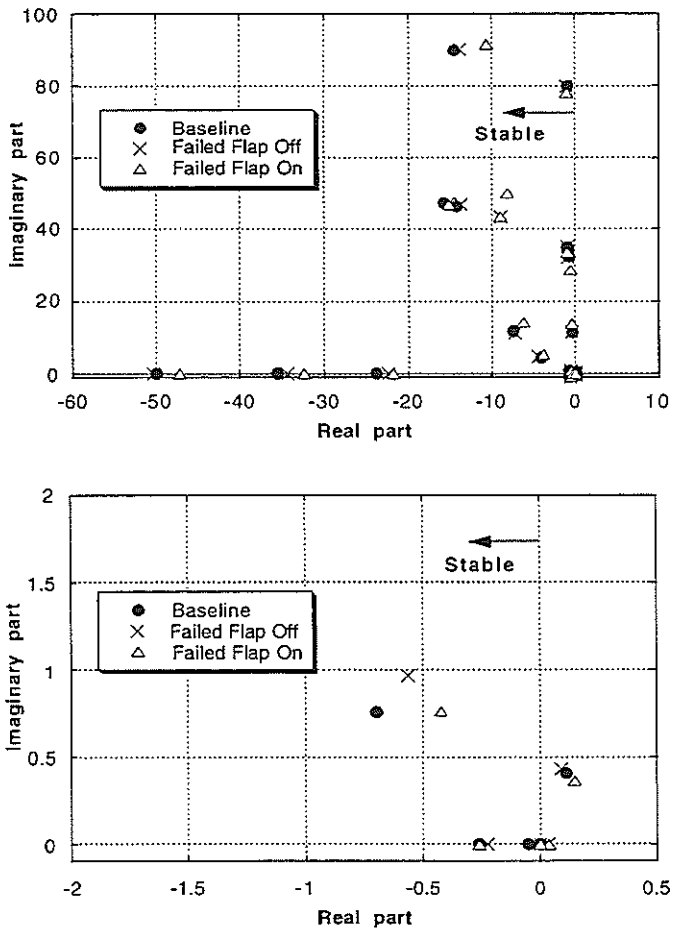

Figure 12: Coupled rotor-fuselage poles for baseline, damaged, and reconfigured rotors; advance ratio $\mu = 0.15$.

TWENTYFIFTH EUROPEAN ROTORCRAFT FORUM

Paper n° G19

Elementary Studies of Active Flap Control with Smart Material Actuators

BY

T.HONGU, M.SATO, E.YAMAKAWA

ADVANCED TECHNOLOGY INSTITUTE OF COMMUTER HELICOPTER

SEPTEMBER 14-16, 1999
R O M E
ITALY

ASSOCIAZIONE INDUSTRIE PER L'AEROSPAZIO, I SISTEMI E LA DIFESA
ASSOCIAZIONE ITALIANA DI AERONAUTICA ED ASTRONAUTICA

Elementary Studies of Active Flap Control with Smart Material Actuators

Tatsuro Hongu, Mitsumasa Sato, and Eiichi Yamakawa

Advanced Technology Institute of Commuter Helicopter, LTD.

Abstract

This paper describes the results of fundamental examination and wind tunnel test of smart material actuators for helicopter rotor system. At the first step, three types of experimental models were made and evaluated. Then, we developed the full scale wind tunnel model with trailing edge active flap which is driven by piezoelectric stack actuation system.

1. Introduction

For rotorcraft, it is very important to suppress the vibration and the noise. Because these vibrations not only affects the ride quality but also causes fatigue damage of the various structural components. And the Blade Vortex Interaction (BVI) noise will be limitation of helicopter operation because it is generated during descent conditions for landing.

In recent years, increasing attention has been devoted to Higher Harmonic Control (HHC) systems which uses swash plate to control the whole blade simultaneously, and Individual Blade Control (IBC) systems which uses individually located actuators to control the each blade. (Refs. 1 to 11)

Since the blade control could be implemented to each individual blade, IBC system can more efficiently suppress the vibration and the noise than HHC concept can. Furthermore IBC can also improve the rotor performance by 2/rev input which HHC can not generate.

ATIC is continuing analytical research about active flap to implement the IBC system(Refs. 12, 13) and smart material actuators to control the active flap on blade. (Ref. 14)

This paper describes the result of a fundamental study and wind tunnel test of such smart material actuators.

2. Fundamental examination

The overview of fundamental examination models are summarized in Table 1. The different two types of Smart Material Actuators are employed for three examination models. One of the actuator is the piezoceramic thin sheets which shaped into parallelogram form and another one is the magnetostrictive actuator.

The first model shown in figure 1 is the aluminum plate twist model which generates the twist deflections of the thin aluminum flat plate by piezoceramic sheets. One end of the plate is fixed to model base and another end is connected to output rod. The piezoceramic sheets are oriented to 45 degrees and directionally bonded to both surface of the aluminum flat plate.

The second model shown in figure 2 is the

X-sectioned composite twist model which generates the twist deflections of graphite-epoxy composite by same way as the aluminum plate twist model. The X-sectioned composite is used to avoid bending deflection loss of the plate and to get large area for piezoceramic sheets.

The third model shown in figure 3 is the hydraulic / mechanical stroke amplifier model which amplifies the stroke output of magnetostrictive actuator. The amplified stroke output of this model is linked to small active flap and the pitch angle of this flap is measured.

The hydraulic amplifier system is consist with a large input piston which is driven by the actuator and a small output bellows. The bellows is used instead of the small piston to minimize the friction and the leakage of oil. Another mechanical amplifier system is consist with long lever and its rotating rod which forms the L-shaped lever. This rod also has the small offset of own axis and the ratio of this offset and lever length is the stroke amplification ratio of this system.

As for the fundamental examinations, static and dynamic tests are conducted. In static condition, the twist deflection of the actuator output rod is measured by rotary encoder. And the moment of output axis is also measured. In dynamic condition, time history of the step response and the frequency response is measured.

3. Results of examination

The results of fundamental examinations are listed in Table 2. In static condition, twist deflection of more than 7 degrees was achieved by the aluminum plate twist model with piezoceramic actuator voltage at 200V. Figure 4 shows the relationship between twist deflection of output rod and actuator input voltage. We can see the hysteresis curve which commonly appears as the characteristics of smart materials. In table 2, the X-sectioned composite twist model shows almost the same twist deflection but doubled output moment against aluminum twist model with the same input voltage. This improvement of output moment is gained by the area increase of the piezoceramic sheets. The relationship between the moment and actuator input voltage for X-sectioned composite twist model is shown in Figure 5. The hysteresis of this figure is smaller than the aluminum twist model.

The result of hydraulic/mechanical stroke amplifier model in table 2 shows the disadvantage in comparison with mechanical

Table 1 Examination Models

Experimental Model	Smart Material Actuator	Stroke amplifier mechanism
Aluminum plate twist	Piezoceramic sheet	Twist the plate by strain of piezo ceramic sheets on both side of plate.
X-sectioned composite twist	Piezoceramic sheet	Use the X-sectioned composite instead of aluminum flat plate to increase piezoceramic sheets.
Hydraulic/mechanical stroke multiplier	Magnetostrictive	Simply multiplies the stroke of actuator by hydraulic piston or mechanical link.

Table 2 Examination results

Examination model	Deflection (degree)	Moment (kgf-mm)
Aluminum plate twist	±7.6	±2.3
X-sectioned composite twist	±7.1	±5.9
Hydraulic stroke multiplier	±3.4	±17.1
Mechanical stroke multiplier	±4.6	±25.8

stroke amplifier system in both deflection and moment output. This result was caused by the friction losses of hydraulic piston. Figure 6 and 7 shows the relationship between the flap deflection and actuator input electric current of hydraulic and mechanical stroke amplifier systems respectively. By the effect of the friction, the hydraulic system has larger hysteresis than mechanical stroke amplifier system.

As the example of result of dynamic response test, Figure 8 shows the time history of the step input response of mechanical stroke amplifier system. We can observe that the response of output twist deflection is very quick, but because of actuator's hysteresis and the friction, output twist deflection does not recover to zero when input current for actuator becomes to zero. As the example of frequency response, bode-plot of X-sectioned composite twist model is shown in Figure 9. Because of resonance with model base, actuator rod or flap model, there is a peak in gain plot at very low frequency (20Hz～30Hz) while the smart material actuator has very high frequency response characteristic.

4. Wind tunnel test

As the next step, we developed the full scale 2-D wind tunnel model to see the feasibility of flap actuation in the realistic environment.

Figure 10 and table 3 shows the overview of the wind tunnel model. The model blade is 1 m span and 0.39m chord with 10%c thick airfoil. And the model has active flap on its trailing edge which is 0.5m span length and 20% chord length.

We selected the piezoceramic stack actuator and mechanical stroke amplifier system which is shown in figure 11 to drive the active flap. And the stroke amplify rate was set to deflect the flap to ±5 degrees.

The actuator was located at 25% chord of the blade and the whole system was equipped inside the blade except the link to flap hinge.

The model has 4 types of sensors which are 3 HALL sensors at flap hinge to measure the flap deflection, LVDT stroke sensor at flap actuation rod to measure the stroke deflection of the rod, strain gauge on flap link to measure the flap hinge moment and stroke sensor of actuator.

The test was conducted with transonic wind tunnel at Kawasaki Heavy Industries,

Table 3 Wind tunnel model

Span	1 m
Chord	0.39 m
Flap span	0.5 m
Flap chord	20 %c
Airfoil section	AK-100D

Ltd. in June 1998. The mach number of this test was 0.3, 0.4, 0.62, and 0.7. And the angle of attack of the blade was varied to 0 and ±4 degrees.

5. Wind tunnel test result

Figure 12 to 15 shows the relationship between the flap hinge moment and the flap deflection of static response test at M=0.3, 0.4, 0.62, and 0.7.

From these figures, we can see that the flap hinge moment became larger as the air speed became higher. At M=0.7, the hinge moment of 90 kgf-mm to -55 kgf-mm was achieved. And the flap deflection which was 2.3 degrees at M=0.3 decreased until 1.1 degrees at M=0.7. And figure 16 shows the difference of the flap deflection by blade angle of attack. There are only small difference between angle of attack 0 and ±4 degrees.

Figure 17 shows the time history of the step input response at M=0.62. From the figure we can see that the LVDT stroke response is very quick.

As the results of frequency response test, figure 18 shows the bode-plot of flap deflection response at M=0.62. It is different from fundamental examination result that the gain plot has no peak because the resonant frequency became higher and the peak has weakened by the damping effect of the air.

From the result of wind tunnel test, we developed the twin actuator system and made the optimization of stroke amplifier ratio.

Figure 19 and 20 shows the schematics of twin actuator systems and concept of there movement. With the figure 19, type 1, both actuators moves in the same direction, and combine there force outputs. Another type, shown in figure 20, actuators moves opposite direction, and there stroke is doubled.

Figure 21 shows the test scene of type 1 model to measure the stiffness of several parts.

With this modification work, we could reach to flap deflection of ±3.2 degrees with 3, 4, 5/rev conditions.

6. Conclusions

In this paper, we described the results of fundamental examination and full scale wind tunnel test of smart material actuators.

By the results of these tests, we could find that the enlargement of actuator power and stiffness of stroke amplifier system is the key term to apply the smart material actuators to the helicopter rotors.

7. References

1 D. Schimke, et al., Individual Blade Control by Servo-Flap and Blade Root Control A Collaborative Research and Development Programme, 23rd ERF, 1997.

2 R. L. Spangler, S. R. Hall, Piezoelectric Actuators for Helicopter Rotor Control, Proc. 31st AIAA Structures, Structual Dynamics, and Materials Conference, 1990.

3 O. Ben-Zeev, I. Chopra, Development of an Improved Helicopter Rotor Model Employing Smart Trailing-Edge Flaps for Vibration Suppression, Proc. SPIE vol. 2443, 1995.

4 M. V. Fulton, R. A. Ormiston, Hover Testing of a Small-Scale Rotor with On-Blade Elevons, 53rd Annual AHS Forum, 1997.

5 F. K. Straub, et al., Application of Smart Materials to Helicopter Rotor Active Control, Proc. SPIE vol. 3044, 1997.

6 R. C. Derham, N. W. Hagood, Rotor Design Using Smart Materials to Actively Twist Blades, 52nd Annual AHS Forum, 1996.

7 F. K. Straub, Active Flap Control for Vibration Reduction and Performance Improvement, 51st Annual AHS Forum, 1995.

8 A. P. F. Bernhard, I. Chopra, Development of

a Smart Moving-Blade-Tip and an Active-Twist Rotor Blade Driven by a Piezo-Induced Bending-Torsion Coupled Beam, 53rd Annual AHS Forum, 1997.

9 S.R.Ghorayeb, et al., Application of Magnetostrictive Smart Materials in Rotor Servoflap Control, Proc. SPIE vol. 2443, 1995.

10 R.Chandra, I.Chopra, Actuation of Trailing Edge Flap in a Wing Model using Piezostack Device, 38th AIAA Structures, Structural Dynamics, and Materials Conference, 1997.

11 T.A.Millott, P.P.Friedmann, The Practical Implementation of an Actively Controlled Flap to Reduce Vibrations in Helicopter Rotors, 49th Annual AHS Forum, 1993.

12 N.Kobiki, et al., Elementary Study for the Effect of HHC and Active Flap on Blade Vortex Interaction, Proc. 23rd ERF Forum, 1997.

13 N.Kobiki, et al., Aeroelastic Analysis and Design for On-blade Active Flap, Proc. 25th ERF Forum, 1999.

14 T.Hongu, et al., Fundamental Study of Smart Material Actuators for Active Flap Control, Proc. AHS International Meeting Heli Japan 98, 1998.

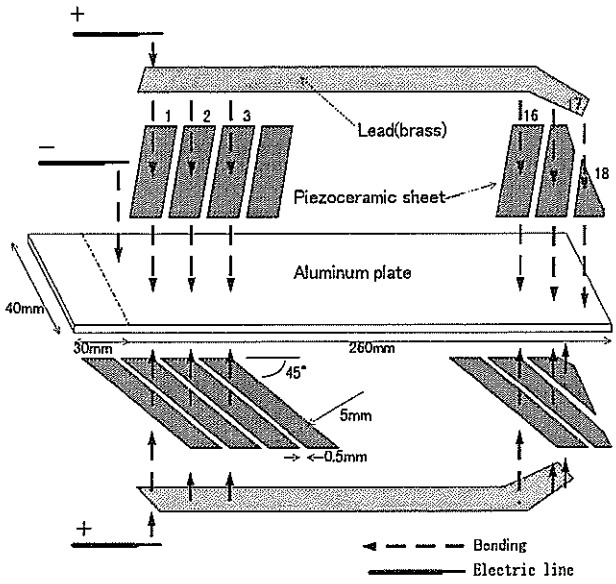

Figure 1 Aluminum plate twist model

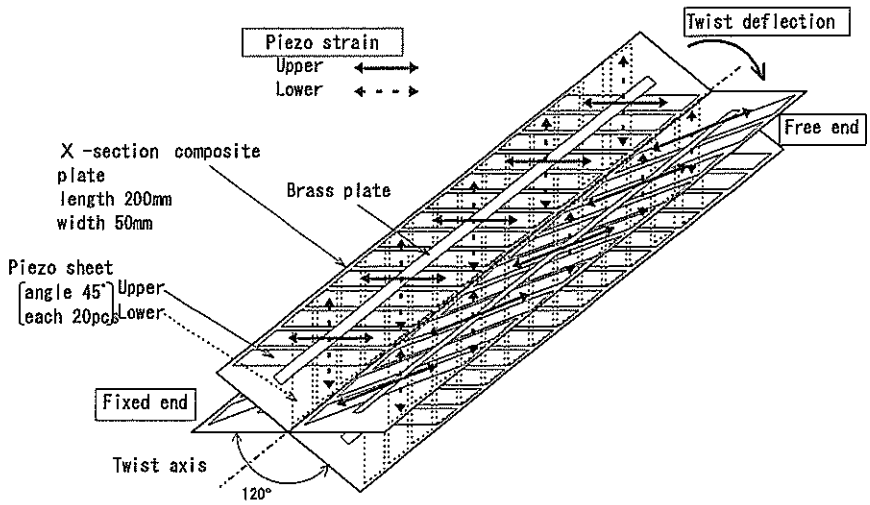

Figure 2 X-sectioned composite twist model

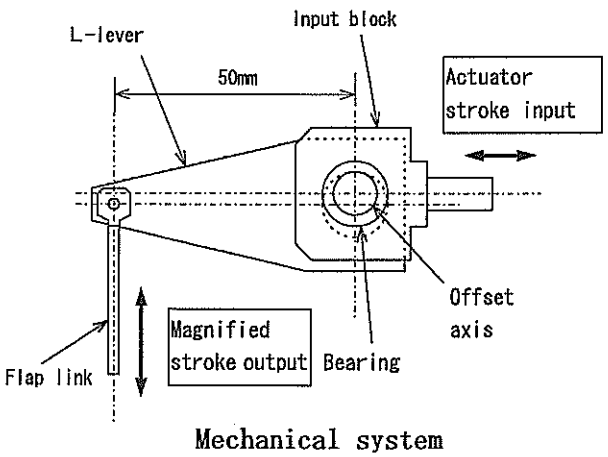

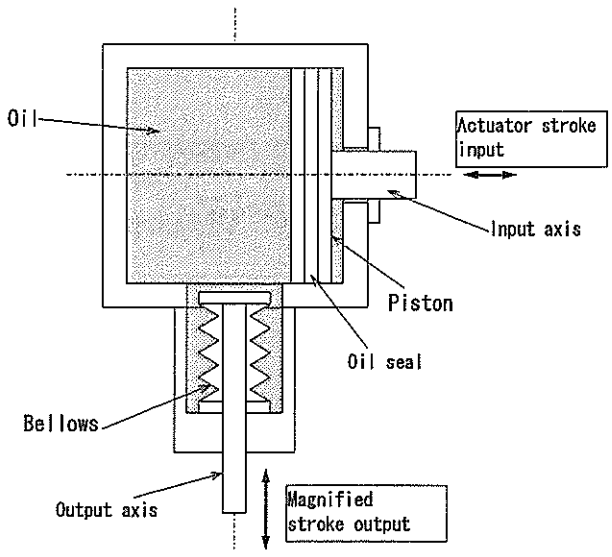

Figure 3 Hydraulic/mechanical stroke multiplier model

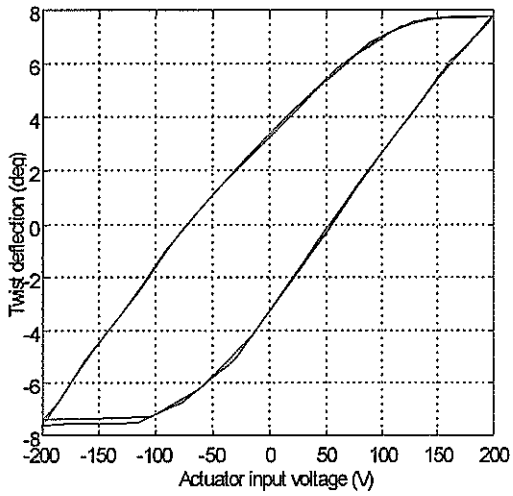

Figure 4 Twist deflection of aluminum twist model

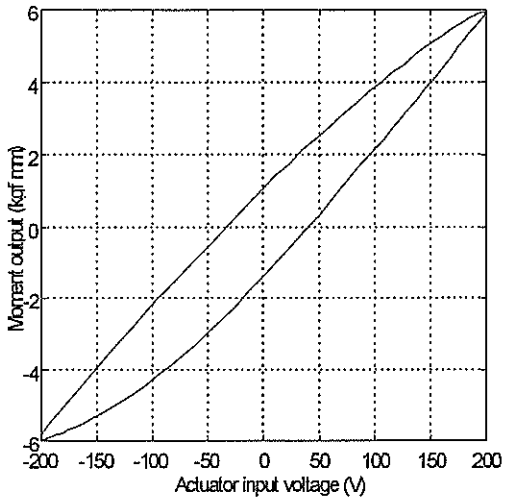

Figure 5 Moment output of composite twist model

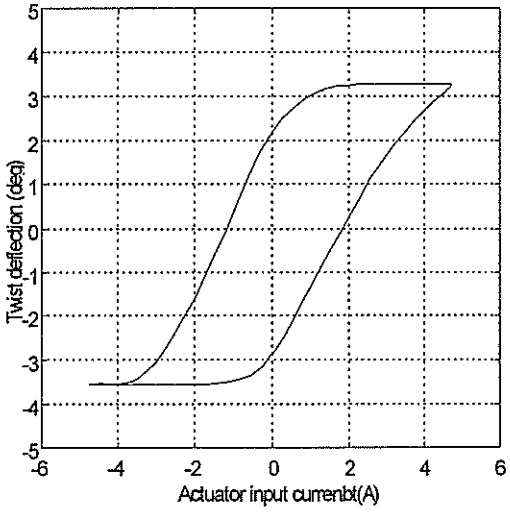

Figure 6 Twist deflection of hydraulic multiply system

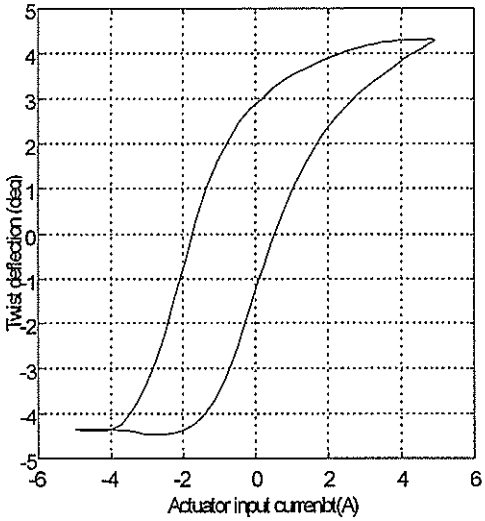

Figure 7 Twist deflection of mechanical multiply system

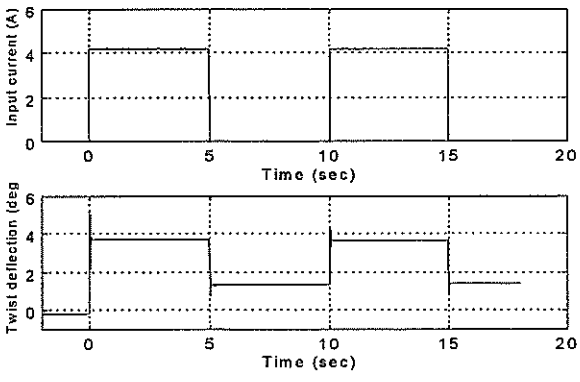

Figure 8 Step response of mechanical multiply system

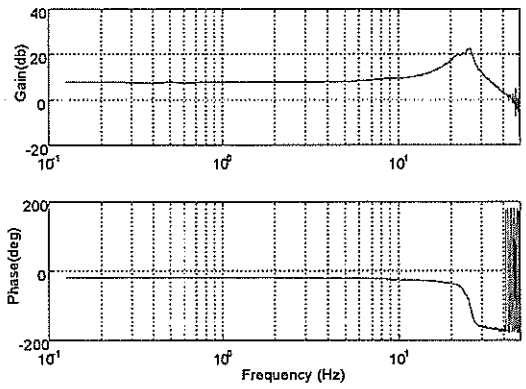

Figure 9 Frequency response of X-sectioned composite twist model

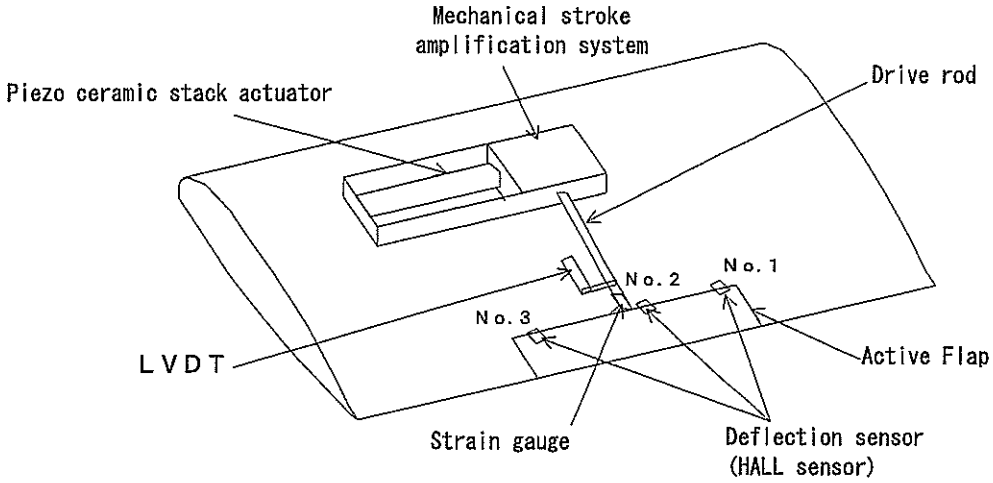

Figure 10 Wind tunnel model

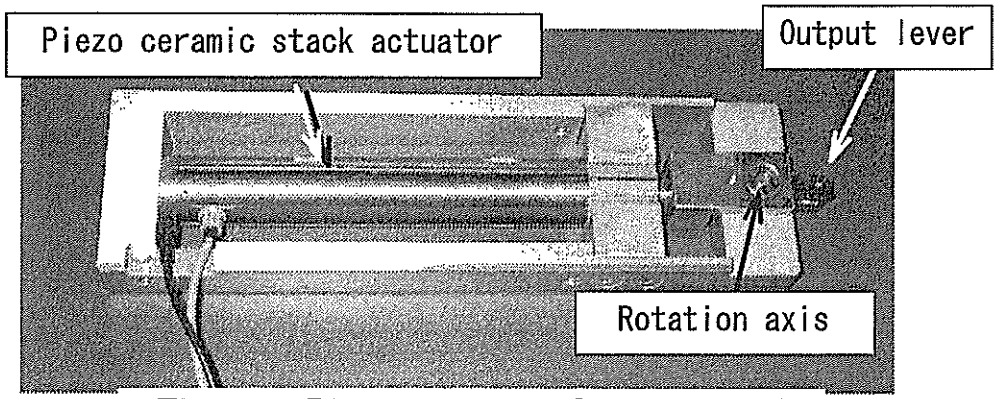

Figure 11 Piezo ceramic stack actuator and stroke amplification mechanism

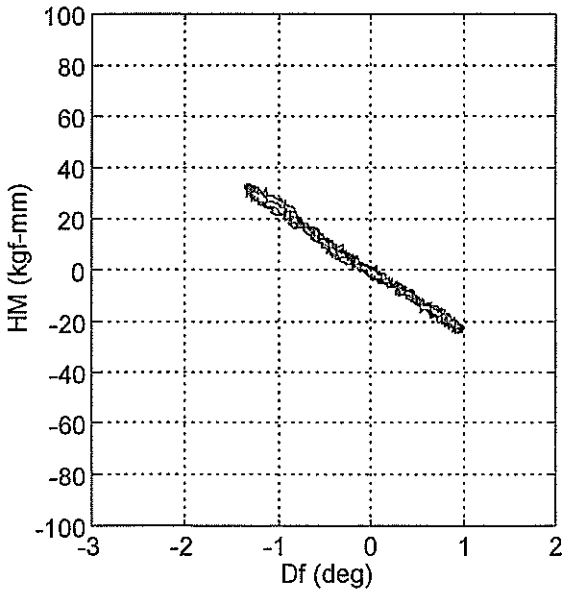

Figure 12 Static response (M=0.3)

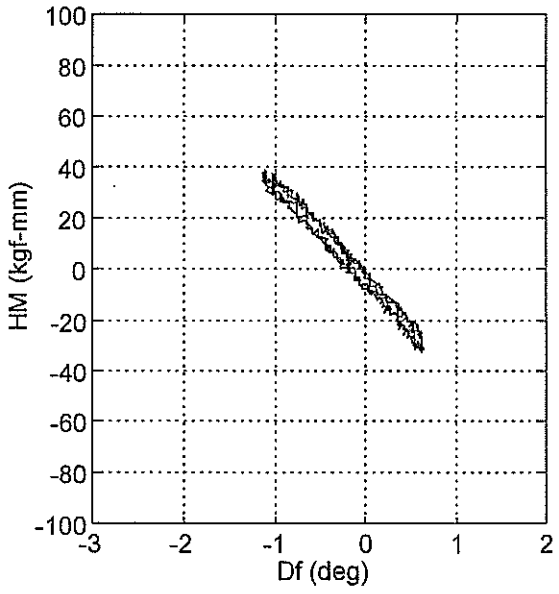

Figure 13 Static response (M=0.4)

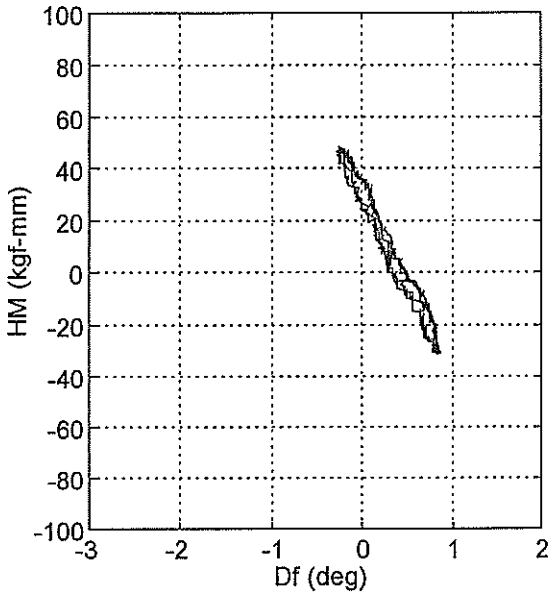

Figure 14 Static response (M=0.62)

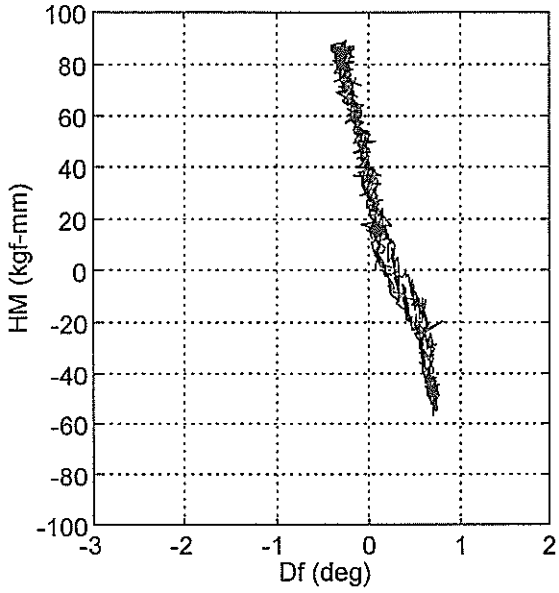

Figure 15 Static response (M=0.7)

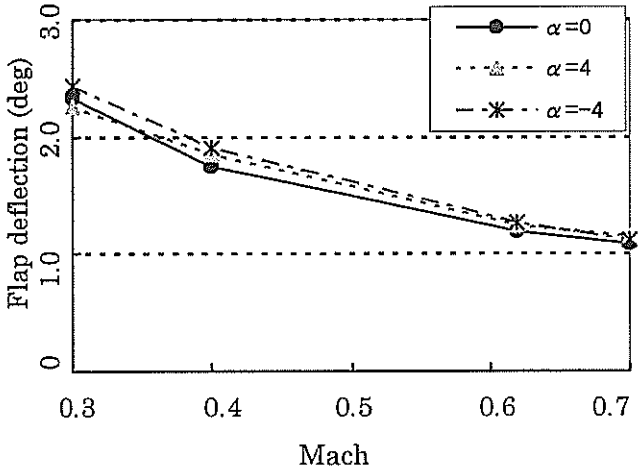

Figure 16 Flap deflection vs. Mach number

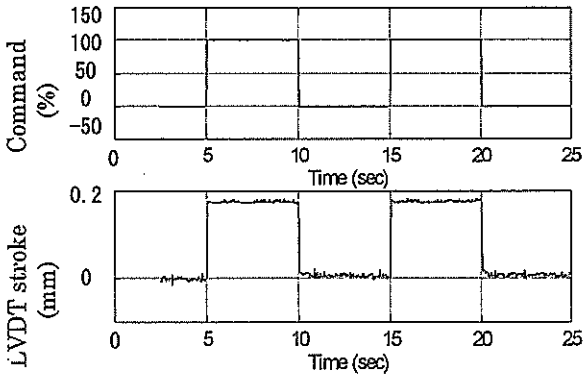

Figure 17 Step response of flap deflection(M=0.62)

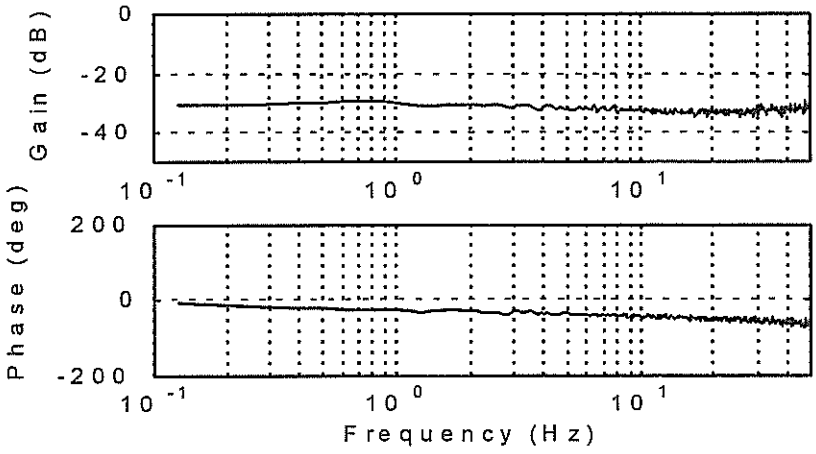

Figure 18 Frequency response of flap deflection(M=0.62)

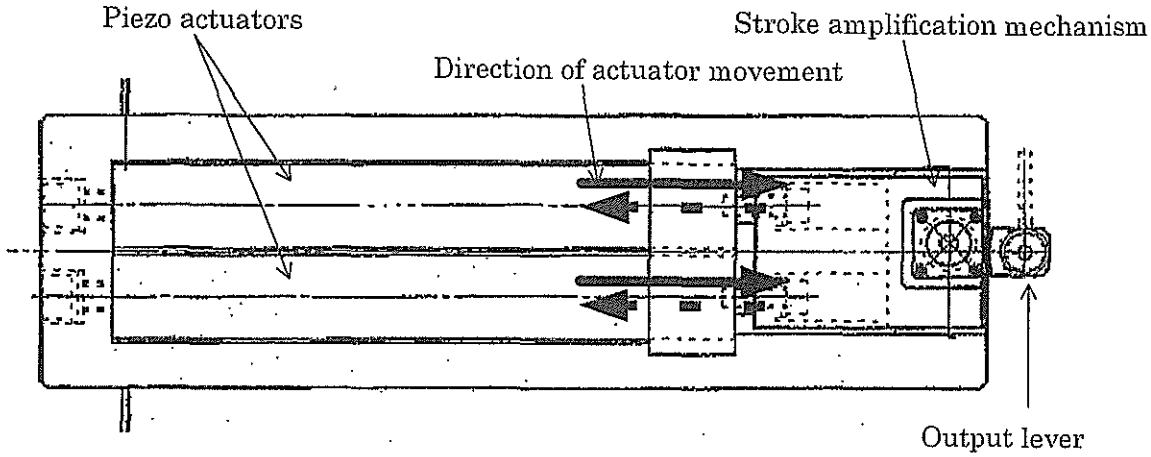

Figure 19 Twin actuation system Type 1

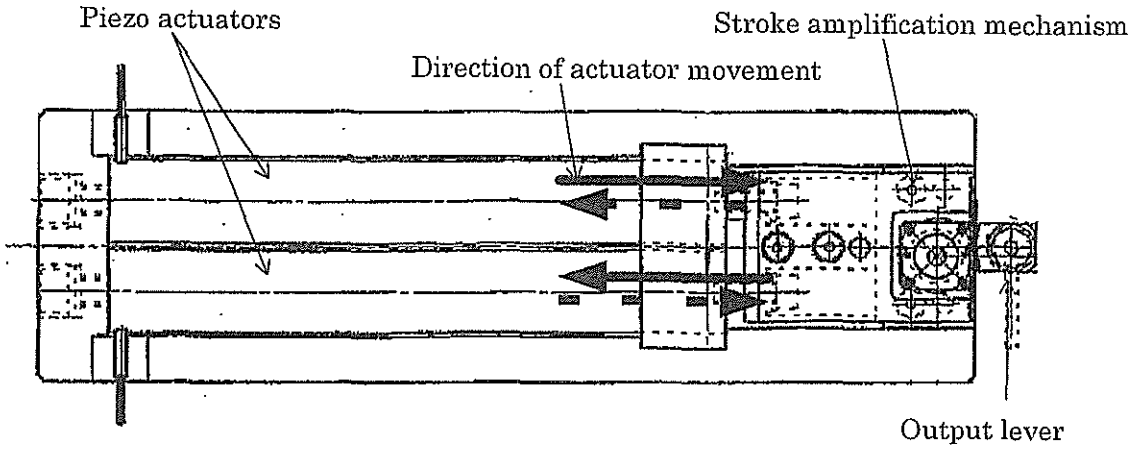

Figure 20 Twin actuation system Type 2

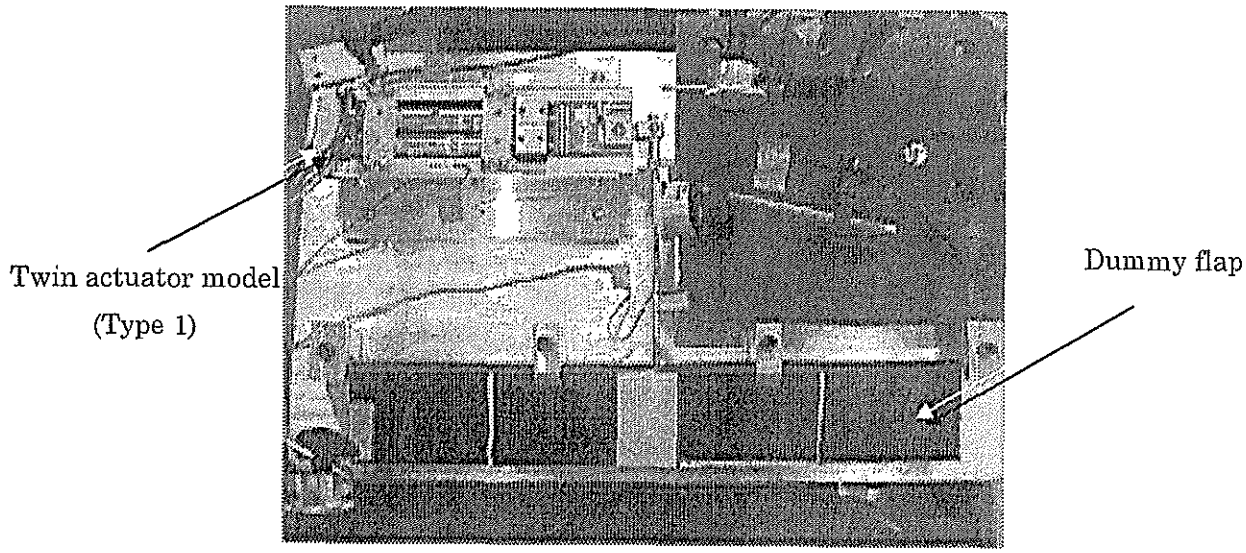

Figure 21 Test scene of type 1 model

TWENTYFIFTH EUROPEAN ROTORCRAFT FORUM

Paper G-20

Development of a Piezoelectrically Actuated Leading-Edge Flap for Dynamic Stall Delay

BY

T. Lorkowski, P. Jänker, F. Hermle S.Storm, M. Christmann, M. Wettemann
DaimlerChrysler AG
Research & Technology
P.O. Box 800 465
81663 Munich
Germany

SEPTEMBER 14-16, 1999
R O M E
ITALY

ASSOCIAZONE INDUSTRIE PER L'AEROSPAZIO; I SISTEMI E LA DIFESA
ASSOCIAZONE ITALIANA DI AERONAUTICA ED ASTRONAUTICA

DEVELOPMENT OF A PIEZOELECTRICALLY ACTUATED LEADING-EDGE FLAP FOR DYNAMIC STALL DELAY

T. Lorkowski, P. Jänker, F. Hermle, S. Storm, M. Christmann
DaimlerChrysler AG, Research and Technology
Research Section Structural Materials, P.O. Box 800 465, 81663 Munich, Germany

The design of a rotor blade requires a multitude of compromises due to the highly unsteady conditions during helicopter flight. Continuous adaptation to the constantly changing aerodynamic environment, e.g. by means of a variable airfoil geometry, should help to substantially improve the performance, safety and comfort of future helicopters and enhance their acceptability. One operational constraint is the phenomenon of dynamic stall on the retreating blade under certain flight conditions. In situ dynamic high-lift devices integrated in the blade to delay this undesirable phenomenon demand a compact and rapid-response drive mechanism. High-performance piezoceramic actuators developed by DaimlerChrysler provide a promising solution to this problem. Based on the analysis and benchmarking of various dynamic high-lift devices, an approach was derived that appears suitable for piezoelectric actuators: dynamic nose droop, whose aerodynamic benefit has already been demonstrated. A design proposal for the structural integration of a leading-edge flap is presented. Numerical two-dimensional simulation using a conventional rotor airfoil led to a trade-off between aerodynamic efficiency and mechanical performance. Implementation of the design gives special consideration to aerodynamic sealing and low-friction mounting without play at the actuator/flap coupling.

1. INTRODUCTION

With their ability to take off and land vertically, helicopters have become indispensable in many areas, rescue missions, off-shore supply, and surveillance being classical examples. Comparatively high operating costs and high noise and vibration levels have so far been tolerated for the most part. However, because of their predominantly low-altitude operations, helicopters with their specific characteristics are increasingly perceived as environmental disturbances. Noise and vibrations reduce in-flight comfort for pilot and passengers. Vibrations also cause premature fatigue to humans and material and lead to higher inspection and maintenance costs. Noise reduction, higher in-flight comfort and an expanded operational envelope with enhanced performance are therefore urgently needed in order to open up new potential applications for this attractive and unique aircraft and improve its acceptance.

To meet all these requirements, new, intelligent concepts must be devised, as conventional technologies are already approaching their limits. The partners within the Adaptive Rotor Systems project (AROSYS) — Eurocopter Deutschland (ECD), the German Aerospace Center (DLR), and the Research and Technology Department of DaimlerChrysler — are working intensively to impart competitive characteristics to future helicopter generations [1]. Measures such as an active strut or a trailing-edge flap (servoflap) for individual blade control are prime examples [2].

In contrast to a fixed-wing aircraft, where lift, thrust and control are provided by three separate systems, in a helicopter the main rotor essentially provides all these functions required for controlled flight. The design of a rotor therefore entails a number of trade-offs. Consequently, any rotor blade will exhibit aerodynamic deficits in certain areas. One problem is the possible occurrence of flow separation on the retreating blade of the rotor. Known as dynamic stall, this can cause strong vibrations as well as limiting the performance of the helicopter. A remedy is promised by active adaptation of the blade characteristics by means of dynamic high-lift devices.

2. DYNAMIC STALL

As a helicopter travels forward, vectorial superimposition of the forward and rotational speeds (V_∞, Ω) produces higher velocities of the oncoming flow for the rotor blade on the advancing side of the rotor than on the retreating side. To ensure symmetric lift distribution, the angle of attack of the blade is therefore varied cyclically. The faster the helicopter travels forward, the more the blade must be inclined on the retreating side. When a certain point is reached, this leads to flow separation called dynamic stall within a locally limited area (Fig. 1).

The phenomenon of dynamic stall has been extensively investigated both numerically and experimentally [3]-[6]. Most of the studies have been restricted to the two-dimensional case. This paper additionaly deals with what is known as "deep dynamic stall" only. Deep dynamic stall is characterized by distinct hysteresis loops in the aerodynamic force and moment coefficients (Fig. 2, left). If the amplitude of the angle-of-attack oscillation is sufficiently large, the maximum angle of attack of the blade is well above the static stall angle and the Mach number is relatively low, the phenomenon is largely independent of other parameters such as the blade geometry, type of motion, and Reynold's number.

Fig. 2 also shows the processes that occur during dynamic stall over one cycle. Once the static limits are exceeded during the oscillation, a reversed-flow area forms in the boundary layer starting at the trailing edge of the airfoil. The aerodynamic phenomenon that dominates in dynamic stall starts at the leading edge of the blade with the development of a vortex. This vortex moves

downstream across the blade in the direction of the air flow. In the process, far higher C_l, C_d and C_m values act than would be possible in the steady case. Before the vortex separates at the trailing edge, the lift reaches a maximum. As the vortex separates, however, very strong negative pitch moments occur. The separated airflow is now fully developed and, if the blade has again reached a low angle of attack in its oscillatory motion, it takes much longer for a "healthy" flow pattern to be restored. The strong pitch moments act via the control rods to produce vibration in the helicopter airframe.

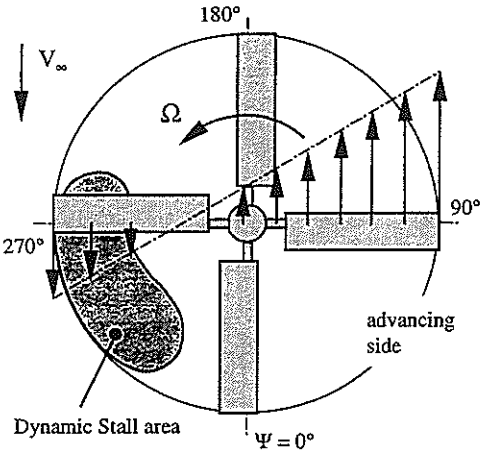

Fig. 1 Velocity vectors and dynamic stall area on the rotor disk in forward flight.

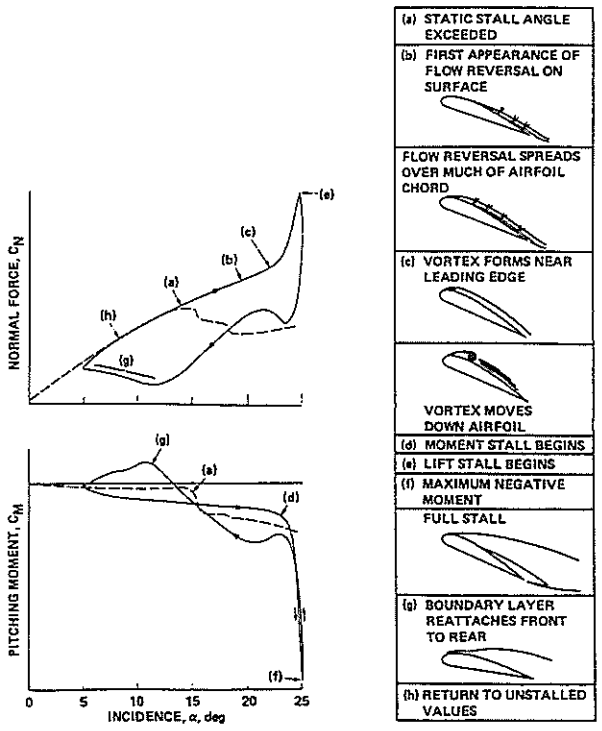

Fig. 2. Dynamic stall processes on the NACA 0012 airfoil (dashed lines represent static values) [4]

3. DYNAMIC HIGH-LIFT DEVICES

It is assumed that high-lift devices, as have been used successfully on fixed-wing aircraft, can, to a certain extent, be applied to helicopters as well [6]. The known measures can be divided into two groups: airfoil geometry variation and direct influence of the boundary layer. Measures that only ensure a delay of the flow separation by statically altering the airfoil properties are not considered here. These methods generally provide higher lift on the retreating side of the rotor but can cause disturbances at higher Mach numbers (higher drag, induction of shocks). To prevent negative effects, a dynamic process is required.

The work by McCloud et al. [7] was one of the first successful attempts to actively and dynamically influence blade characteristics in this way. In full-scale wind-tunnel tests, they succeeded in delaying flow separation on the retreating blade by blowing air tangentially into the boundary layer through small slits near the leading edge (x/c=0.085) on the upper side of the airfoil. First air was blown continuously on all the blades. By suitable control in the distributor for blowing on the retreating blade only, the mass flow, and thus the required power, was reduced by one half without any loss of the positive effect. Experiments in which blowing was carried out further downstream on the airfoil showed no effect. The above-described local limitation of the dynamic stall phenomenon to effects on the leading edge of the blade and in the retreating blade area is evident. In principle, tangential acceleration of the boundary layer fluid across the upper side of the airfoil also occurs with a slat, but in this case the air is taken from the bottom side of the airfoil and guided through a converging gap to the top. A moveable slat [8] or a gap, with a stationary leading-edge section, that is dynamically opened and closed [9] have been proposed.

A number of studies exist on dynamic geometry variations. The approaches range from a simple thickness variation of a symmetrical airfoil [10], to a dynamic increase of airfoil camber achieved by lowering the leading edge of the blade (nose droop) [11], [12], to a consideration of the influence of the airfoil nose radius [13], [14]. What they all have in common is a positive effect on delaying the dynamic stall onset. Continuous deformation of the blade contour has decisive aerodynamic advantages. Even very small changes produce an effect, especially in the sensitive leading-edge area.

From the multitude of the alternatives described above, the approach using a discrete leading-edge flap was selected. The positive aerodynamic effect of dynamically lowering the leading-edge of an airfoil (nose droop) had already been successfully demonstrated on various airfoil geometries. The high negative-pressure peaks at the leading edge are reduced, flow separation is delayed, and hysteresis loops are reduced. A discrete flap also permits the energy required for elastic deformation during continuous contour variation to be used to overcome the aerodynamic forces and moments or to provide greater movement authority. Based on existing flap technologies, integration in a rotor blade appears feasible.

4. ACTUATOR TECHNOLOGY

To operate a dynamic high-lift device, a actuation mechanism of some sort is needed. Systems that require extensive auxiliary components should be avoided from the outset. Local integration in the rotor blade itself places extreme demands on the system: very limited installation space, large centrifugal loads, highly dynamic control, high performance, and low weight. A promising approach is offered by actuators based on piezoceramic materials.

The characteristics of piezoceramic actuators are based on the inverse piezoelectrical effect. Piezoceramics are solid-state materials that change in shape when subject to an electric field. Their use as sensors is well known. In such applications, a mechanical deformation is converted into a voltage by internal charge shifts [15]. This combined ability makes piezoceramic elements ideal for integrated adaptive electromechanical systems. Thanks to their solid-state characteristics, very high forces, high precision, and high dynamics can be achieved. However, the small deflections must be amplified if these elements are to be used advantageously in macroscopic systems. The Research & Technology Department of DaimlerChrysler has successfully introduced several hybrid actuator systems that meet these requirements [16].

The double frame developed for flap actuation shown in Fig. 3 amplifies the displacement of the piezostack by a factor of about 10. The generated force is correspondingly reduced in accordance with the leverage law.

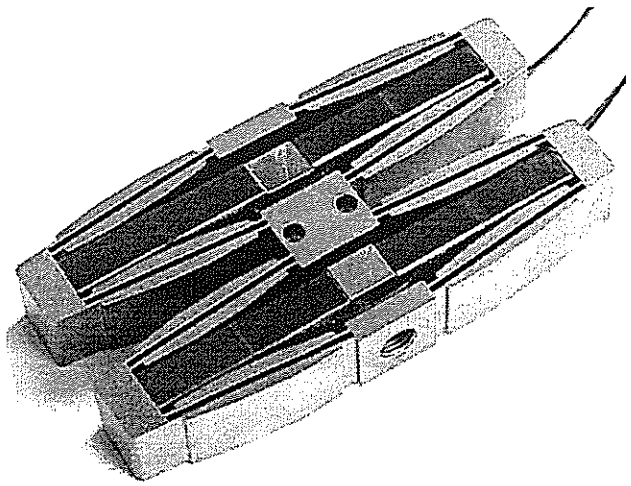

Fig. 3. Hybrid actuator with double transmission frame and integrated piezostacks.

This arrangement ensures absolutely playfree operation and only relatively small energy losses in the bending zones. Characteristic parameters of this actuator are a blocking force of 650 newtons with a free displacement of 1.10 mm. Easy scaling of these value allows custom-made design for different fields of application. Additionally piezoceramic actuators as relatively modern devices offer high potential for future improvements [16]. The high power density permits complete integration in the rotor blade contour. Only three lines through the blade are required for power supply, and the energy can be transmitted from the rotor to the nonrotating system via conventional slip rings.

5. NUMERICAL SIMULATIONS

The numerical simulations were performed with a conventional rotor-blade airfoil of medium relative thickness as used in modern helicopters. It represents an ideal compromise for use in current helicopters. To ensure a continuous data base this airfoil geometry is used throughout all subareas of AROSYS. However, it has certain deficiencies for investigating the dynamic stall effect, e.g. a relatively high camber in the leading-edge area. Nevertheless, these aspects are secondary to the demonstration of design feasibility. In principle, the system can be integrated in any airfoil providing the same installation volume.

The primary considerations for determining the flap dimensions are the aerodynamic efficiency together with the moments resulting from the necessary geometry variation and the forces acting on the actuators. In aerodynamic terms, a large flap with a large deflection is desirable. However, this desire places considerable demands on the actuators. Thus, here too the object is to find an optimum compromise. The numerical simulations consider only the two-dimensional case.

The first step is to generate suitable geometries. The pivot position x_0/y_0 is varied as well as the deflection angle ηf with intermediate steps at increments of 0.5°. From the pivot, a projection is made perpendicular to the upper side of the airfoil in order to define the end of the flap. A radius then begins at this point, which at the maximum deflection describes a gentle transition to the rest of the airfoil. The discontinuety in the contour of the bottom of the airfoil has no effect on the accuracy of the result. With the specified coordinates, the simulation tool used generates a new "interpolated" contour that exhibits a smooth transition (Fig. 4). The discussions in the further course relate to a pivot position in the y-direction that is always on the bottom side of the airfoil. This has three main advantages: a simplified method of geometry generation, maximum curvature radius at the transition area, and minimal influence on the aerodynamic effect.

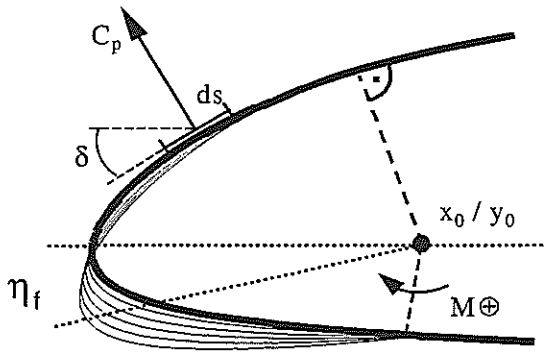

Fig. 4. Generation of the nose flap geometry.

For the aerodynamic simulations, three reference points were defined that are derived from one case of fast forward flight (TABLE 1). Here, case 1 is of main importance. Cases with higher Mach numbers were also investigated but are not discussed further. They are of interest with respect to "nonoperation" in the neutral position.

Case	Ma	Re	Ψ [°]	
1	0.33	2.29e6	270	Retreating blade
2	0.54	3.74e6	0 / 180	
3	0.74	5.13e6	90	Advancing blade

TABLE 1. Reference points for simulation (fast forward flight, $\mu = 0.37$)

For simulation, a program package was used which is based on the solution of Euler's equation with boundary-layer coupling [17]. The results obtained included the pressure distribution and the integral coefficients. From the pressure distribution, also the loads on the flap were calculated. Integration was then performed only over the flap surface with the pivot x_0, y_0 as a reference point (Fig. 4). Selective consideration of the friction coefficient c_f produced only fractions of the integral forces and moments of less than 3% and is not further pursued here. For faster convergence, a forced transition was set at x/c=0.06.

Fig. 5 shows the maximum lift coefficient of the airfoil as a function of the flap geometry. With increasing relative flap size x_f/c and increasing deflection angle η_f, an approximately linear growth of $C_{l\,max}$ can be observed. However, with small flap geometries, the curve flattens at larger angles. Increasing the flap angle then does not result in any further growth of $C_{l\,max}$. A limitation of the flap size and flap deflection due to the resulting loads acting directly on the actuators occurs relatively quickly.

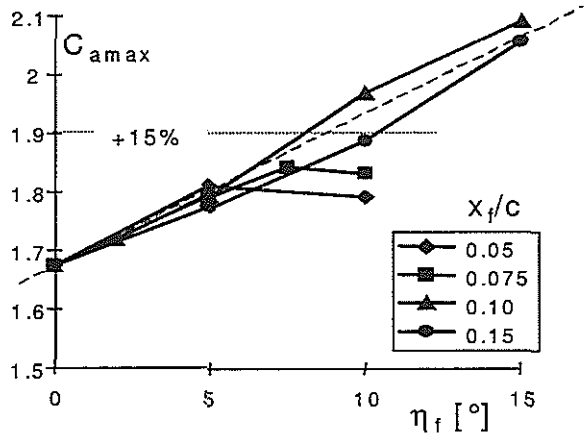

Fig. 5. Maximum lift coefficients for various flap configurations (case 1).

Fig. 6 presents the moment coefficient of the flap in relation to the flap pivot for various flap geometries on the original airfoil (flap in the neutral position). It can be seen that the moment coefficient is relatively independent of the pivot position in the y-direction in comparison to the flap size. A special feature is the possibility of moment-neutral mounting of the flap for a relative airfoil fraction of about 7.5%. However, such a small flap would not be very useful. Fig. 7 shows the dependence of the moment coefficient of the flap c_{mf} on the deflection angle η_f for a flap of 10% relative airfoil chord. The growth of the acting moment is smaller than that resulting by shifting the pivot position. The cluster of curves with open symbols shows the limits for an actuator with various levels of performance. The following applies to the hybrid actuator used here:

$$F_B \frac{s}{2} = 650N \cdot 0.55mm = 0.35Nm$$

Fig. 8 shows for the reference cases defined in TABLE 1 with the established flap size the expected moments that act on the actuators via the mechanism as forces to be overcome. It is noteworthy in this context that the coefficients for various Mach numbers are virtually identical over a large angle-of-attack range. For the maximum deflection, the moment increases further at high angles of attack. At lower angles of attack the moment acting on the flap becomes negative. This means that the actuators must hold the flap, for example on the advancing side, in the neutral position.

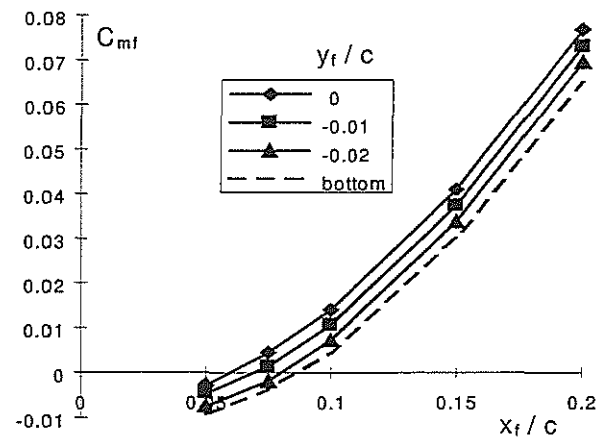

Fig. 6. Flap moment coefficient on the original airfoil as a function of pivot position and thus flap size (case 1, α=12.5°).

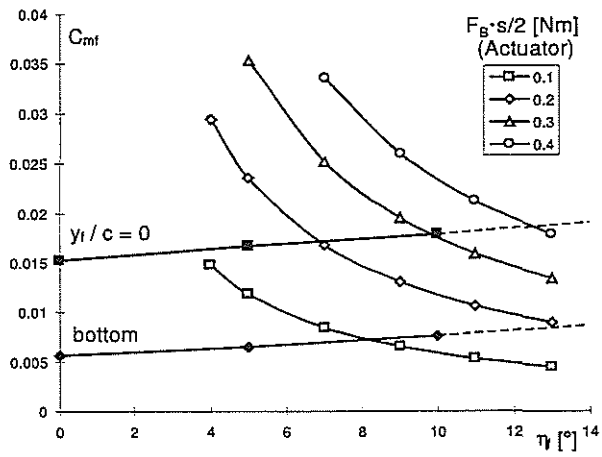

Fig. 7. Moment coefficient as a function of pivot position and flap angle in comparison to the performance of the actuator.

Thus, a flap size of 10% relative airfoil chord and 10° maximum deflection seems feasible. For this configuration the maximum lift coefficient increases by 17%. The angle of attack at which drag increases significantly and the stall angle are increased by about 2.5° (Fig. 9).

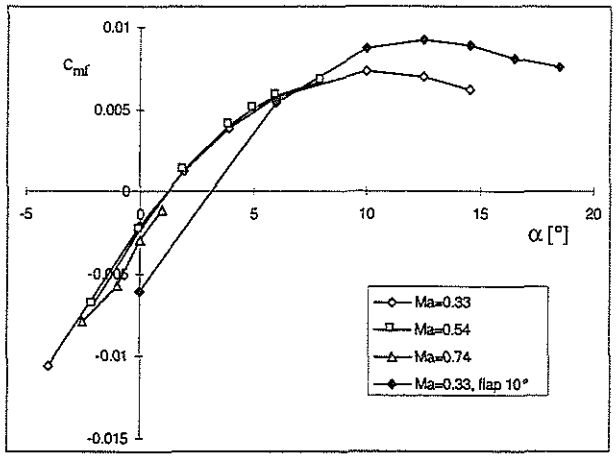

Fig. 8 Moment coefficient of the nose flap on the original airfoil for cases 1–3 and for the maximum deflection angle of the flap in case 1 versus angle of attack.

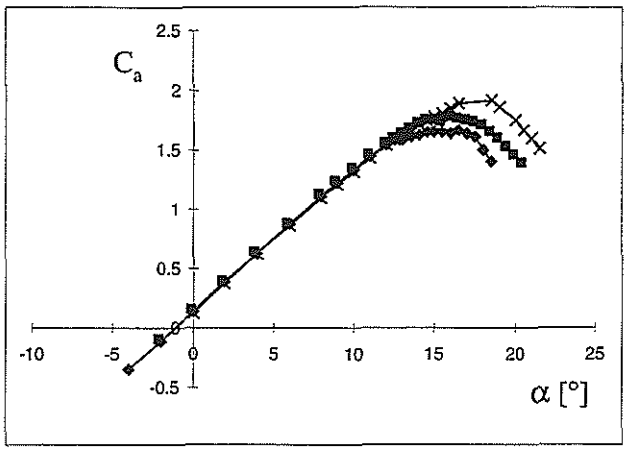

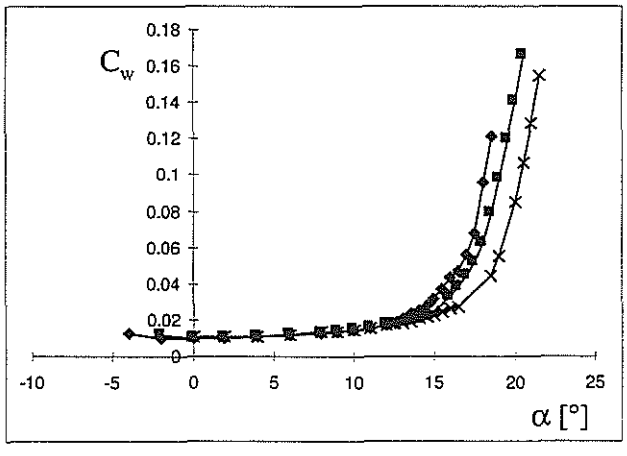

Fig. 9 Lift, resistance, and moment coefficients versus angle of attack for the original airfoil and with lowered nose flap (case 1).

6. STRUCTURAL DESIGN

General aspects for the structural implementation are shown in Fig. 10. To ensure a smooth airfoil contour at rest as well as in the deflected position, special attention must be given to the precise implementation of the interface from the flap to the trailing airfoil structure. The integratability and exchangeability of the erosion protection must also be considered. Here, a discrete flap has decisive advantages, as erosion protection can continue to be realized as before. All joints and connections must be free of play and as frictionless as possible.

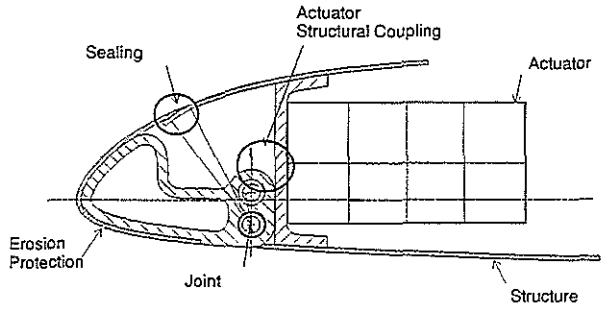

Fig. 10. General design aspects for implementation of the leading-edge flap for adaptive airfoil variation.

The assumptions made in the numerical simulations with regard to the pivot position cannot all be realized in the design of the flap. Fig. 11 schematically illustrates the functional principle. Asymmetric forces on the actuators should be avoided. Due to the installation height of the actuator, the line of action approximately coincides with the zero line of the airfoil (y/c=0). The paired actuators are arranged in series. The structural attachment is located in the center between the two frames. To monitor the force level and to characterize the system, two axial force transducers are initially integrated in the load path. However, these will not be integrated in the actual helicopter rotor blade, where the preload level will be set purely by means of geometric relationships.

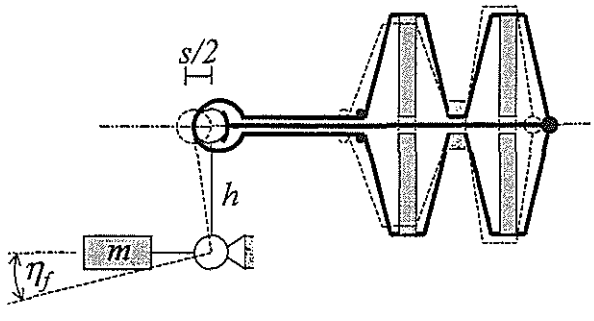

Fig. 11. Principle of the mechanism of action of the leading-edge flap.

By applying an offset voltage of half the maximum voltage to the piezostacks, the system is endowed with an additional preload. The actuators are wired in such a way that they always move in push-pull mode. For example, if the rear piezostack elongates, the transmission frame undergoes contraction in the direction of its width. This

movement is transmitted via the rear coupling point to the push rod. The rod extends through the entire arrangement to the front, where it causes a forward movement of the flap pivot. This leads to a downward deflection of the flap via the lever arrangement. The other piezostack contracts, producing a movement of the pull rod in the same direction via the frame. The adjusted force level remains constant in the process (ignoring losses). Deflection of the flap in the other direction, i.e. upward, is undesirable and is therefore prevented by a stop. Since no displacement is needed in this direction, a much higher force authority is available (blocking force) to keep the flap in the neutral position on the advancing side of the rotor (see Fig. 8).

The flap is hinged on high-precision ball-bearings. These only have to withstand the relatively small transverse aerodynamic forces. In order to maintain the required deflection angle of 10° in the context of the available displacement authority of the actuator of s/2=0.55 mm, a lever arm of 3.15 mm was selected. The small dimensions demand high-precision manufacturing of all the components. Particularly at the interface of the flap to the rest of the blade, care must be taken to ensure that no excessive gaps or steps occur. The curved surfaces will help to maintain a relatively high stiffness of the components. Fig. 12 shows the demonstrator built for test purposes. The voluminous force transducers will not be present when the mechanism is integrated in an actual rotor blade. The actuators can then be moved forward by about 40 mm. This will result in a weight reduction while at the same time helping to the keep the center of gravity line of the airfoil at 25%. In current airfoils, this is usually accomplished by integrating lead in the nose section. With a moving leading-edge flap, such a high weight within the flap would be disadvantageous. The leading-edge flap must be as lightweight as possible.

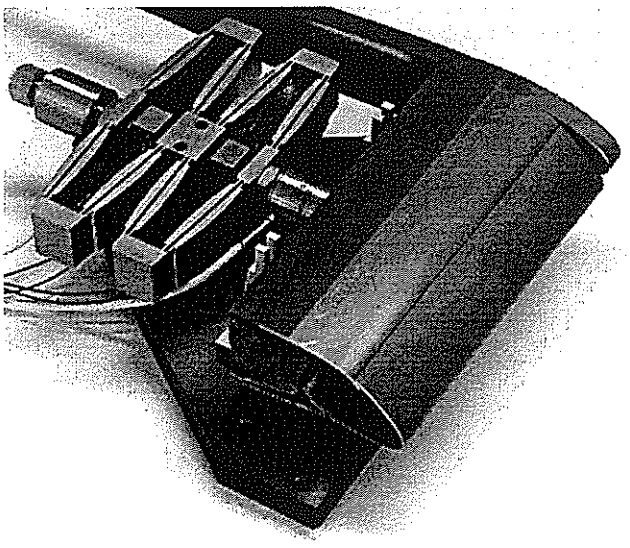

Fig. 12. Demonstration model for functional analysis of the leading-edge flap.

7. CONCLUSION AND OUTLOOK

The performance of current helicopters is limited by the occurrence of dynamic stall on the retreating side of the rotor. This situation may be remedied by the use of dynamic high-lift devices integrated in the rotor blades. From the large number of possibilities available, an approach was selected that appears suitable for implementation with reasonable effort: dynamic lowering of the leading edge of the blade by means of a discrete flap (nose droop). The discrete leading-edge flap has several advantages. Experience gained from the implementation of the discrete trailing-edge flap (servoflap) can be directly applied. The simple defined geometry variation, the already demonstrated efficiency, and the clear mechanical aerodynamic relationships further facilitate the design process. Numerical simulations led to a compromise between the aerodynamic efficiency resulting from the flap size and deflection and the resulting loads on the actuators. For a 10% flap with 10° maximum deflection angle, a 17% increase of the maximum lift and a 2.5° shift of the stationary stall angle were achieved at a low Mach number.

High-performance actuators based on piezoelectrical materials have been chosen as drives for the flap. Piezoactuators are distinguished by a high power density and, thanks to their specific properties, are superior to conventional approaches under the given conditions. An amplification frame makes their elongation at a high force level practicable for macroscopic applications. All interfaces are free of play and as frictionless as possible. Both the aerodynamic design and the structural implementation were limited to the two-dimensional case, which is sufficient for the planned wind-tunnel tests. The model discussed is intended to demonstrate the basic feasibility of structural integration.

For helicopter use, other important conditions must be taken into account. Here, we can draw upon the experience gained with the much further developed servoflap. Important points are a design suitable for rotational use, three-dimensional effects, and failsafe operation. A new, optimized design of the entire rotor system based on the assumption of the availability of integrated control surfaces has great potential. Thus, for example, the airfoil thickness in the outer blade area could be reduced. The resulting reduced lift could be compensated for by means of dynamic high-lift devices with a simultaneous power saving and possible reduction of high-impulsive noise. Combined use with a servoflap would also be conceivable. Considerable potential for improvement is thus available for future helicopter generations.

8. REFERENCES

[1] Martin, W., Jänker, P., Lorkowski, T., Neumann, H., Hübner, M., Leitkonzept Adaptive Rotorsysteme – Neue Technologien zur adaptiven Blatt-Geometrie und Sensorik, DGLR Jahrestagung, Bremen, 1998

[2] Schimke, D., Jänker, P., Wendt, V., Junker, B., Wind Tunnel Evaluation of a Full Scale Piezoelectric Flap Control Unit, TE02, 24th European Rotorcraft Forum, Marseilles, 1998

[3] McCroskey, W.J., The Phenomenon of Dynamic Stall, NASA TM-81264, 1981

[4] Carr, L.W., McAlister, K.W., McCroskey, W.J., Analysis of the Development of Dynamic Stall on

Oscillating Airfoil Experiments, NASA TN D-8382, January 1977

[5] Geissler, W. Vollmers, H., Unsteady Separated Flows on Rotor Airfoils, 18th European Rotorcraft Forum, Avignon, September 15-18, 1992

[6] Yu, Y.H., Lee, S., McAlister, K.W., Tung, C., High Lift Concepts for Rotorcraft Applications, 49th American Helicopter Society Annual Forum, St. Louis, May 19-21, 1993

[7] McCloud, J.L. Hall, L.P., Brady, J.A., Full-Scale Wind-Tunnel Tests of Blowing Boundary-Layer Control Applied to a Helicopter Rotor, NASA TN D-335, September 1960

[8] Tung, C., McAlister, K.W., Carr, L.W., The Quest for Stall-Free Dynamic Lift, Workshop on Physics of Forced Unsteady Separation, Moffet Field, April 17-19, 1990

[9] Ruffin, S.M., Mavris, D.N., Application of Dynamic Slot and Circulation Control Technologies to Rotors for Noise reduction and Dynamic Stall Elimination, Georgia Institute of Technologie Research Proposal, 1997

[10] Geissler, W., Raffel, M., Dynamic Stall Control by Airfoil Deformation, 19th European Rotorcraft Forum, Cernobbio, September 14-16, 1993

[11] Geissler, W. Sobieczky, H., Dynamic Stall Control by Variable Airfoil Camber, AGARD FDP Symposium on Aerodynamics and Aeroacoustics of Rotorcraft, Berlin, October 10-13, 1994

[12] Lee, S., McAlister, K.W., Tung, C., Characteristics of Deformable Leading Edge for High Performance Rotor, AIAA-93-3526, AIAA 11th Applied Aerodynamics Conference, Montgomery, August 9-11, 1993

[13] Geissler, W., Carr, L.W., Chandrasekhara, M.S., Wilder, M.C., Sobieczky, H., Compressible Dynamic Stall Calculations Incorporating Transition Modelling for Variable Geometry Airfoils, AIAA-98-0705, AIAA 36th Aerospace Sciences Meeting and Exhibit, Reno, January, 12-15, 1998

[14] Chandrasekhara, M.S., Wilder, M.C., Carr, L.W., Control of Flow Separation Using Adaptive Airfoils, AIAA-97-0655, AIAA 35th Aerospace Sciences Meeting and Exhibit, Reno, January 6-10, 1997

[15] Koch, J., Piezooxide – Eigenschaften und Anwendungen, ISBN 3-7785-1755-4, Valvo Unternehmensbereich Bauelemente der Philips GmbH, Hüthig Verlag, Heidelberg, 1. Auflage, 1988

[16] Jänker, P., Hermle, F., Lorkowski, T., Storm, S., Christmann, M, Wettemann, M., Development and Evaluation of Advanced Flap Control Technology Utilizing Piezoelectric Actuators, 25th European Rotorcraft Forum, Rome, September 1999

[17] Drela, M., Giles, M.B., ISES: A Two-Dimensional Viscous Aerodynamic Design and Analysis Code, AIAA-87-0424, AIAA 25th Aerospace Sciences Meeting, Reno, January 12-15, 1987

TWENTYFIFTH EUROPEAN ROTORCRAFT FORUM

Paper G-21

Development and Evaluation of Advanced Falp Control Technology Utilizing Piezoelectric Actuators

BY

P. Jänker, F. Hermle, T. Lorkowski, S.Storm, M. Christmann, M. Wettemann
DaimlerChrysler AG
Research & Technology
P.O. Box 800 465
81663 Munich
Germany

AND

V. Klöppel
Eurocopter Deutschland GmbH
81663 Munich
Germany

SEPTEMBER 14-16, 1999
R O M E
ITALY

ASSOCIAZONE INDUSTRIE PER L'AEROSPAZIO; I SISTEMI E LA DIFESA
ASSOCIAZONE ITALIANA DI AERONAUTICA ED ASTRONAUTICA

Development and Evaluation of a Hybrid Piezoelectric Actuator for Advanced Flap Control Technology

P. Jänker, V.Klöppel, F. Hermle, T. Lorkowski, S. Storm, M. Christmann, M. Wettemann

DaimlerChrysler AG, Eurocopter Deutschland
81663 Munich, Germany

Abstract:

One key element of a rotor with individual blade control (IBC) based on an advanced flap control technology is a powerful and reliable actuator system. The need for highly dynamic system response, compact and robust design makes actuators based on piezoelectric materials a promising approach.

Piezoelectric materials deliver a solid-state displacement when subjected to an electric field. For successful application in mechanical subsystems this displacement normally needs to be amplified. Research efforts at DaimlerChrysler's Research and Technology Labs for Advanced Material Systems led to a highly efficient amplification mechanism that follows a rhombic, multiple frame design with no play and wear.

During extensive bench tests and when implemented in a rotor-blade segment for a three-week wind-tunnel test series, the actuator system demonstrated excellent performance and durability [1].

A further important step now is to ensure the ability of the system to withstand high centrifugal loads. The actuator itself, its mounting and the structural flap coupling have been optimized using FEM analysis tools. Again, bench tests demonstrated the functionality of the system. Results of the behavior of the piezoelectric actuator under centrifugal loads and the performance compared to the nonrotating case are presented. In addition to the test results, the test facility itself will be described, including the basic whirl tower, the energy- and data transmission system and the experimental rotating system.

1. Introduction

Some of the most urgent development tasks in the area of helicopters are to reduce noise pollution and vibrations and to enhance flight performance. An example of a promising technology that has been promoted by ECD and DaimlerChrysler Research and Technology is Active Rotor Control, which represents the key element of a future helicopter. For control purposes, trailing-edge flaps are installed in the outer part of the rotor blades which are driven by piezoelectrical actuators [3]. Control of each rotating rotor blade is effected with high speed and precision. The electronically controlled deflection of the relatively small flap causes, especially for torsionally soft designs, blade twisting with the effect of a considerable aerodynamic change in lift. The high energetic efficiency of the rotor control is based on this servo effect. For specific rotor and control data, also direct lift effects are active.

The active rotor control has four main technical objectives:

- Reduction of impulsive main-rotor noise and cabin vibrations
- Stall delay
- Stabilization of the rotor dynamics.
- Automatic blade tracking

The impulsive main rotor noise occurring during descent and manoeuver flight is excited by blade vortex interaction. This interaction is strongly reduced by increasing the misdistance between blade tip vortices and blades through local increase of the rotor downwash, e.g. by a 2/rev control input. The blade vortex interaction is detected either by pressure transducers on the blades or by on-board microphones.

For vibration reduction of a four-bladed rotor, a 3/rev, 4/rev and 5/rev control input creates "artificial" dynamic blade loads which counteract the immanent blade loads responsible for the cabin vibrations. These are measured either by strain gauges at the blade roots or by accelerometers at the main gear or in the cabin.

The stall onset can be delayed by locally decreasing the blade pitch on the retreating side. The resulting loss of moment balance and lift is compensated by a correspondingly reduced blade pitch on the advancing side and an increased pitch in the fore and aft region of the rotor azimuth. Stall onset is detected either by pressure transducers on the blades or by strain gauges on the pitch links.

For the rotor stabilization in lead-lag a feed-back of lead-lag angle and velocity leads through coupling between blade torsion, flapping and lagging to increased lead-lag damping. The lead-lag motion is sensed by strain gauges at the blade roots.

The automatic blade tracking can be attained by measuring the 1/rev unbalance in the fixed system and by introducing an appropriate constant flap angle.

For all of these methods, fast closed loop algorithms have to be applied in order to cope with the non-steady behaviour of helicopter flight.

The flap system comprises a flap with hinged supports that is driven by linear actuators. In order not to unacceptably change the nominal position of the c.g. line at approx. 25% of the blade depth, the actuator is mounted near the blade leading edge. A control rod is used for force transmission.

Controlling a flap integrated in the outer area demands a great deal of the actuator system:

- Only little installation space is available in the rotor blade. In addition, the required c.g. position of the blade at approx. 25% of the blade chord requires mass concentration in the leading-edge area.
- The high centrifugal acceleration (typically 800 - 1,000 g) results in large mass forces. Consequently, the overall weight of the actuator-flap system must be minimized.
- The actuator must cope with high air loads. The actuator dynamics must allow a 5/rev control or even higher frequencies. In the EC135 helicopter this corresponds to 35 Hz.

- The actuator system must generate sufficient stroke to control a flap deflection of ±8°. In the concrete case of an EC135, the actuator system must achieve a stroke of approx. 1 mm and a force of 2,000 N.

2. Solid State Actuator Technology

The realization of Active Rotor Control depends primarily on the performance of the actuator. Careful analysis of actuator technologies was a main focus of work at the start of the project, particularly innovative actuator technologies based on active materials.

Actuators based on mechanically active materials (smart materials) represent a new approach. Research activities in this area are being vigorously pursued in the USA, Japan and Germany. A number of alternative actuators are being considered. These can be classified according to the type of control energy needed, namely thermal actuators, i.e. elongating bodies made of polymers, waxes and SMAs (Shape Memory Alloys); electrical and magnetic actuators, i.e. piezoactuators and magnetostrictors (terfenol-D) [1]; chemical actuators, i.e. electrochemical-pneumatic actuators, pyrotechnical actuators.

Of extraordinary technical importance are electrically controlled actuators that can be integrated into electronic control systems and represent the core modules of mechatronic systems. Within this major group, piezoelectric ceramics (PZT) offer a high potential compared to the more widely used electromagnetic actuators [2].

Piezoelectrical ceramic materials convert electrical energy directly into mechanical movement. The energy conversion takes places as soon as electrical energy is applied and is limited only by the dynamics of the mechanical system. An element of piezoelectrical material constitutes an actuator in itself. From these primitive prototypes, more complex actuator constructions can be derived. For example, a flexing actuator is formed by bonding a piezoceramic plate onto a passive substrate. Block-shaped piezoelectrical elements that generate only small deflections can be advantageously combined with gear elements to form hybrid actuators.

In conclusion, the outstanding advantages of piezoelectrical actuators are their high dynamics. high deflection resolution, high force generation, high specific working capacity and simple construction.

3. Actuator Design

The required actuator stroke in the mm range with actuator forces in the range of 1,000 N is about one order of magnitude greater than the stroke capacity of previously available piezoelectrical actuators.

After having analyzed the requirements, it is seen that, from today's point of view, only piezoelectric actuators are suitable for operating a flap in the outer area of a rotor blade. The decisive technical hurdle in developing the piezoelectrically controlled flap system was the low elongation capacity of PZT materials.

Many applications in mechanical engineering demand high-performance actuators with a stroke in the mm range. Because of the low elongation capacity of piezoelectrical materials, stack actuators are unsuitable. A suitable method of construction that was developed by Daimler-Benz Research in recent years is the hybrid actuator.

A hybrid construction method, comprising a piezostack with a hydraulic or mechanical step-up gear, is suitable for actuator forces of $F_b > 500$ N. The step-up gear must meet the following requirements:

- Stiff support of the piezostack
- No mechanical play, no/slight friction
- High gear stiffness
- High energy efficiency: low elastic energy losses
- Gear ratio n - 10
- Low weight relative to the piezostack
- Production-oriented construction

A number of different designs for the implementation of a step-up gear were put forward. The influence of the mounting frame alone on the overall performance of the hybrid actuator is discussed below with the aim of revealing the limitations of the hybrid construction method.

An important criterion of the quality of a design as regards working capacity is the mechanical efficiency η_{MECH}, which is defined as the ratio of the working capacity of the hybrid actuator (W_H) to the working capacity of the piezo (W_P):

$$\eta_{MECH} = W_H / W_P \qquad (1)$$

Assuming that the stroke at the mechanical output corresponds ideally to the theoretical transmission ratio n and is not reduced by restoring elastic forces, the mechanical efficiency is defined solely by the ratio of the real to the theoretical blocking force at the mechanical output (F_{HR} and F_{HT}):

$$\eta_{MECH} = F_{HR} / F_{HT} \qquad (2)$$

The reduction of the blocking force is calculated from the ratio of the overall stiffness of the mechanical series connection of the stack (S_P) and frame (S_R) to the stiffness of the piezostack alone:

$$\eta_{MECH} = F_{HR} / F_{HT} = (1 + S_P / S_R)^{-1} \qquad (3)$$

In order to increase the efficiency, greater stiffness of the frame (and gear) is required. However, massive and voluminous construction is not desirable, as a low overall weight is the objective. A high specific working capacity is aimed at. A further important criterion of the design quality is therefore applied, namely the mass efficiency η_{MASS}, the ratio of the specific working capacity of the hybrid actuator and piezostack:

$$\eta_{MASS} = \eta_{MECH}\, m_H / m_P \qquad (4)$$

To arrive at an estimate, the frame is assumed to be a prismatic rod as long as the piezostack. The frame data are scaled with respect to the piezostack:

$$a := A_R/A_P$$
$$y := Y_R/Y_P$$
$$r := \rho_R/\rho_P$$

where:

R,P	=	index frame, piezo
A	=	cross-sectional area
Y	=	Young's modulus
ρ	=	mass density

The base plates are neglected. Hence, the mechanical efficiency and the mass efficiency are calculated as follows:

$$\eta_{MECH} = (1+a^{-1} r^{-1})^{-1} \quad (5)$$

$$\eta_{MASS} = (1+a\, r)^{-1}(1+a^{-1} y^{-1})^{1} \quad (6)$$

The mass efficiency reaches a maximum for the relative cross section $a_{OPT} = (ry)^{-0.5}$. For steel, a_{OPT} is 43%, assuming a Young's modulus for the piezoceramic material of 38 Gpa. The maximum mass efficiency η_{MASS} is 48%.

Designing the frame cross section to be larger than the cross-sectional ratio a_{OPT}, which is optimal with regard to the mass efficiency, is in any case expedient. Above a_{OPT} there is a conflict of goals between mass efficiency and mechanical efficiency.

In view of this compromise, the working capacity is assessed higher, as the technical (electrical power supply) and the economic price of the piezo is always higher than the effort involved for the mechanics.

An integrated design is considered to be the optimum construction method for a weight- and volume-optimized hybrid actuator. The stiff mounting frame, which is required in any case, is designed by the integration of joints as a gear. In order to prevent play and wear, flexures are used as joints. Fig. 4 shows the diamond-shaped geometry of the gear.

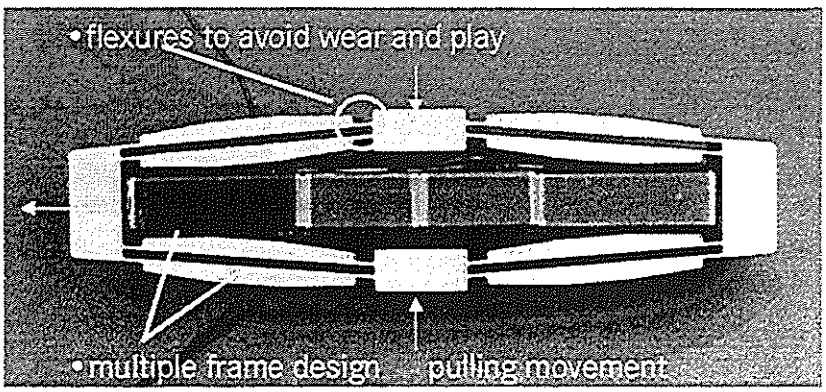

Figure 1: DWARF

Due to the geometric arrangement, an expansion movement of the piezostack is transformed into a pulling movement. Critical elements of the design are the flexures that are loaded in the movement and bending directions. The flexures act as a spring load on the piezostack to reduce the free stroke. At the same time, the flexures are a determining factor for the stiffness S_R of the frame. A compromise must be made between high axial stiffness and low bending stiffness. At the same time, the material load with respect to the joints (axial tension and bending) must be designed so as to achieve high fatigue strength.

The efficiency of the gear was optimized by designing it as a multiple frame. With high axial frame stiffness, the bending stiffness of the joints is reduced, the material load on the joints is decreased and the stroke is increased.

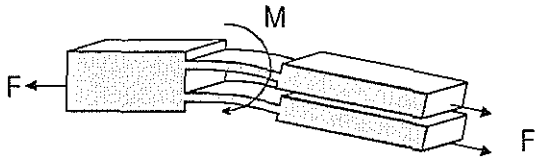

Figure 2: Multiple frame. Joint area.

With n-fold subdivision of the frame, the bending stiffness is reduced by a factor n^{-2} and the boundary fiber elongation by n^{-1}. The detailed computational optimization of the DWARF system was effected using analytical methods and FEM. The dynamics of the hybrid actuator are very good, with the first resonance frequency occurring at 220 Hz.

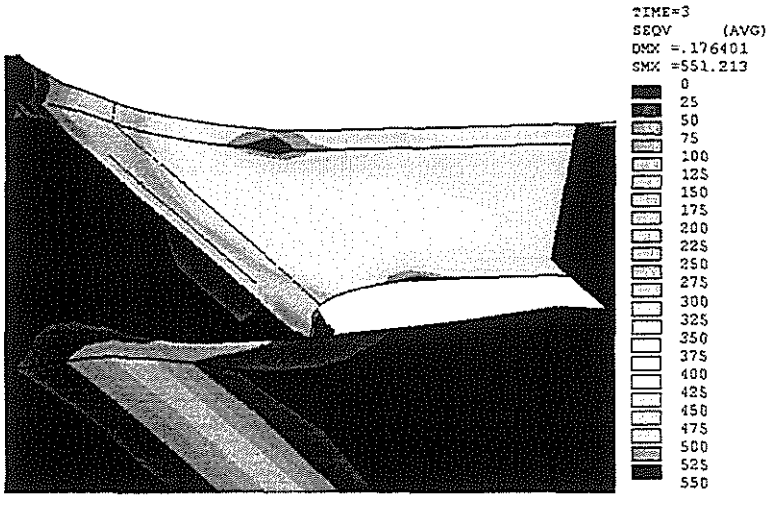

Figure 3: FEM calculation. Detailed study of the joint area.

The performance data of the DWARF actuator were decisively improved over several development phases. The main characteristic data at present, determined at 35 Hz, are given below:

- Blocking force 780 N
- Free stroke 1.26 mm
- Mechanical efficiency 83%
- Mass efficiency 33%
- Mass 400 g

The thermal expansion of the piezoactuator over an extended operating-temperature range must be taken into consideration. The thermal expansion coefficients of the frame and the piezo can be adjusted by selecting suitable materials or material combinations.

4. Flap Design

The pursued design comprises a hinged flap that is driven by a linear activator via a control rod. Fig. 4 shows the actuator integrated in a wind-tunnel model. Four actuators are mounted near the blade leading edge. Two flap halves are driven via control rods. This arrangement is consistent with the requirement that the c.g. line must be at about 25% of the blade depth.

The flap stroke is controlled via a dual-circuit electronic system. An outer control circuit analyzes the signals relating to the flight state and relays a correct path to the inner control circuit. In the inner circuit, a processor analyzes a flap-deflection signal from a sensor and generates a control signal that is transmitted to the piezoelectrical actuators via a power output. The inner circuit compensates for the effects of hysteresis and friction as well as for external loads and perturbations and ensures a linear relationship of the control signal and flap stroke. Key elements of this technology are the power generators. Installation space is restricted, and only low construction weight is allowed. Moreover, the power consumption must be kept low. For these reasons, only switching amplifiers come into consideration as power outputs for recovering the electrical energy stored in the piezoactuators and thus minimizing net consumption from the onboard power supply.

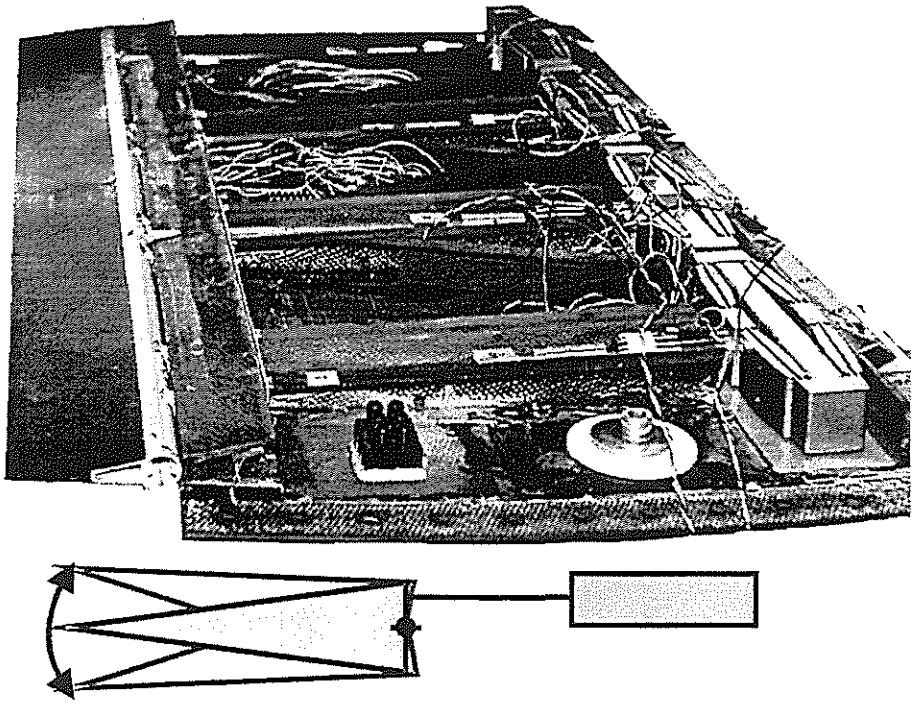

Figure 4: Wind-tunnel model. View of the actuator-flap module.

5. Test Procedure

The newly developed flap technology was subjected to an extensive test series. The procedure is divided into the following phases:

- Electromechanical characterization of the piezoelectrical actuators
- Characterization and fatigue testing of the DWARF actuators
- Performance test of the actuator-flap module
- Wind-tunnel tests
- Tests of the DWARF actuators on a rotational test bed

Important milestones of the project are the attainment of sufficient performance in the wind tunnel and the demonstration of mechanical strength in the centrifugal field.

5.1 Wind-tunnel tests

A rotor-blade segment fitted with a flap-actuator module was subjected to an exhaustive two-week test series in a wind tunnel. The aim of the tests was to demonstrate sufficient authority of the piezoelectrical actuators under realistic aerodynamic loads and to clarify the basic aerodynamic relationships [3]. The tests successfully demonstrated the suitability of the flap technology. The system operated flawlessly throughout the entire period.

5.2 Centrifugal Testing

In later use in a rotor blade, the actuators will be subjected to extraordinarily high mechanical loads as a result of centrifugal acceleration. After detailed mathematical analysis and design work, an actuator was tested on a rotational test bed (Fig. 5).

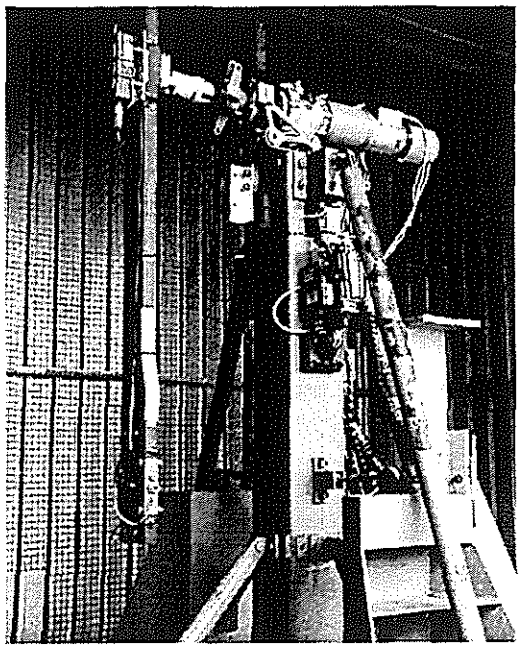

Figure 5 Test bed for the centrifugal test.

The DWARF actuator was mounted inside a rotating arm. During rotation, the actuator was controlled via an electrical slip ring. Measurement signals for the actuator force and path were transmitted to the stationary system and recorded. The illustration below presents a sample of measurements of the blocking force, showing constant behavior across operating frequency and rotational speed. The rotation tests demonstrated adequate strength of the DWARF actuator for use in a rotor blade. Successful conclusion of the rotational tests marked an important milestone in the project.

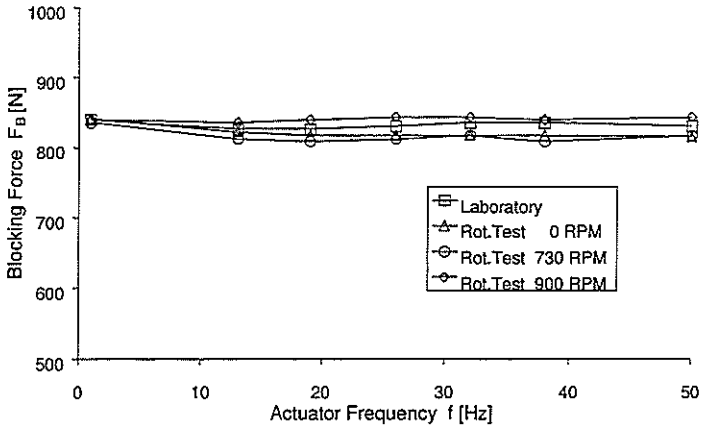

Figure 6: Measurement of the blocking force of the DWARF actuator during centrifugal testing. 900 rpm, corresponding to a centrifugal acceleration of 800 g

6. Conclusion

An innovative flap-control technology is being developed for future helicopters. At the heart of the technology is a piezoelectrical actuator. The high-performance DWARF actuator was designed to drive a flap integrated in a rotor blade and was optimized in terms of energy and mass efficiency as a figure of merit. Detailed tests, including rotational tests, demonstrated the basic suitability of the system. In the next step, full-scale rotor blades will be fitted with this new technology and tested on a whirl tower. Subsequently, it is planned to test the rotor equipped with high-frequency flap control in flight. Up to the stage of production maturity, special challenges will be to demonstrate the reliability and service life of the piezoelectrical actuators under realistic load conditions.

References:

[1] D. Schimke, P. Jänker, V. Wendt, B. Junker, *Wind Tunnel Evaluation of a Full Scale Piezoelectric Flap Control Unit*, 24th European Rotorcraft Forum, Marseille, France, 15-17 September 1998

[2] P. Jänker, W. Martin, "Performance and Characteristics of Actuator Materials", Fourth International Conference on Adaptive Structures, 2-4 November 1993, Cologne, Germany

[3] D. Schimke, P. Jänker, A. Blaas, R. Kube, and Ch. "Keßler, Individual Blade Control by Servo-Flap and Blade Root Control A Collaborative Research and Development Programme", 23rd European Rotorcraft Forum in Dresden, Germany, September 16-18, 1997

TWENTYFIFTH EUROPEAN ROTORCRAFT FORUM

Paper n° G22

COAXIAL HELICOPTER ROTOR DESIGN & AEROMECHANICS

BY

Boris N. Bourtsev, Sergey V. Selemenev, Victor P.Vagis
KAMOV Company, Moscow Region, Russia

SEPTEMBER 14 – 16 , 1999
ROME
ITALY

ASSOCIAZIONE INDUSTRIE PER L'AEROSPAZIO, I SISTEMI E LA DIFESA
ASSOCIAZIONE ITALIANA DI AERONAUTICA ED ASTRONAUTICA

Introduction

The advanced technology is based on mathematical simulation (software), on a model testing, on a flight tests and on an experience of helicopter development, on the new developed materials.

The Fig.1A & Fig.1B show basic parameters of coaxial KAMOV's helicopters.

1. Coaxial rotor mathematical simulation & physical experiments

The survey of the theoretical and experimental coaxial rotor aerodynamic research published by Coleman, C.P. [4] and by Bourtsev, B.N. [9,10].

The paper [9,10] presents the results of figure of merit analysis for single and coaxial main rotors at hover as well as for a helicopter with a tail rotor and a coaxial helicopter. The analysis has been performed using a simple physical model based on the results of numerical simulation, wind tunnel tests and full scale flight tests.

It is demonstrated [9,10] that a characteristic feature of coaxial main rotor is a high aerodynamic perfection at hover caused by an additional amount of air being sucked in by the lower main rotor (Fig.2). The coaxial rotor at hover demonstrates a 13% larger figure of merit value in comparison with a single rotor unbalanced by torque (Fig.2). Absence of tail rotor power losses provides a 20% larger figure of merit for a coaxial helicopter as a rotorcraft (Fig.2, Fig.4). Fig.3 presents the coaxial rotor figure of merit. These results were obtained by measuring in full scale flight test at hover.

Full-scale flight investigation of a Ka-32 coaxial helicopter tip vortex wake structure was successfully completed [5,6]. A smoke visualization method was applied using blades smoke generators installed. A tip vortex wake was visualized in hover, at low flight speeds and medium flight speeds (Fig.3, Fig.5). A specific dimensionless number has been adopted to determine inductive velocities and flight speeds related to an ideal inductive velocity in hover (Fig.5). The wake form was determined and the tip vortex velocities were measured in hover. The tip vortex vertical velocities turned out to be less then the inductive velocity of the ideal rotor in hover. The measured wake contractions were equal to 0.85R for the upper rotor and 0.91R for the lower rotor (Fig.3).

The tip vortex coaxial rotor wake was visualized in a forward flight. In the rotor front part the free tip vortices were positioned above the tip path planes. That flat part of a free wake could extend along the rotor up to 3/4 of its radius (Fig.5).

2. Basic design solutions and aeroelastic phenomena

It is very important to have a substantiation of aeromechanical phenomena. This is feasible given adequate simulation making possible to explain and forecast:

- natural frequencies of structures;
- loads & deformation;
- aeroelastic stability limits: stall flutter, transsonic flutter, ground resonance;
- helicopter performance & maneuverability.

KAMOV Company has developed software to simulate a coaxial rotor aeroelasticity [1,2,3,8,9,10]. Aeroelastic phenomena to be simulated are shown in the Fig.6 as (1-7) lines in the following way:

(1) - system of equations of coaxial rotor blades motion ;
(2) - elastic model of coaxial rotor control linkage (boundary data);
(3) - model of coaxial rotor vortex wake;
(4,5,6) - steady and unsteady aerodynamic airfoils data;
(7) - elastic / mass / geometry data of the upper / lower rotor blades and of the hubs.

The lines (1-8) in Fig.6 show functional capabilities of the software. Columns (1-5) conform to versions of the software . Both steady flight modes and manoeuvres of the helicopter are simulated .

Based on experience of KAMOV Company new key design approaches regarding the coaxial rotors of the Ka-50 helicopter were developed.

The blade aerofoiles were developed by TsAGI for the Ka-50, Ka-115, Ka-226 helicopter specially (Fig.7). Optimal combination of $C_L, C_D, C_M(\alpha, M)$ characteristics was a necessary condition to achieve:

- high G-load factor & stall limit ;
- acceptable margin of flutter speed ;
- low loads of rotor & linkage ;
- low vibration level ;
- high helicopter performance.

Blade sweep tips developed by KAMOV Company affords for the same purposes.

Usage of all key approaches regarding rotors becomes an sufficient condition to achieve high performance of the rotor system and therefore of the helicopter as whole.

3. KAMOV's Key Technologies

3.1 Fiberglass & fiber graphite rotor blades

In the end - 1950's KAMOV Company designed, built and tested fiberglass rotor blades. In 1965 first production fiberglass rotor blades were successfully flown on the KAMOV Ka-15 helicopter. In 1967 first production fiberglass rotor blades were successfully flown on the KAMOV Ka-26 helicopter. In the end 1970's the graphite & glass fiber rotor blades were successfully produced by KAMOV Company.

The graphite fibers had potential specific stiffness values which six times those of current aircraft materials. This proved to be highly significant in addressing elastic stability and aeroelastic design problems.

The combination of glass and graphite fibers resulted in excellent, benign failure modes and provided aerodynamics, structures and dynamic engineers.

Ka-50 helicopter advanced rotors geometry is:

- special airfoil;
- blade optimal twist;
- blade swept tip (Fig.7).

All KAMOV's blades fitted with electrothermal de-icing system.

3.2 Advanced rotor blade retention technology

All before Ka-50 KAMOV's helicopters had full articulated rotor hubs. Ka-32 helicopter has metal hubs, mechanical & elastomeric bearings & dampers (Fig.8).

Ka-50 helicopter has metal and composite hubs, elastomeric bearing & damper, flex element for pitch, flapping and lag (Fig.8).

3.3 Rotor control linkage

The rotor control linkage parameters determine a flap-lag-pitch motion and a motion stability of rotor blades (Fig.6, Fig.8, Fig.9).

The mathematical model of coaxial rotor control linkage was developed by KAMOV Company [1]. This math model is used for control linkage design and for frequency & stability analysis.

The control linkage elasticity matrix-functions was measured for full scale coaxial helicopters of four types.

The analysis of the experimental results determined to develop a control linkage mathematical model and a adequate formula for the "approximation-calculation" of the matrix-function elements. With the help of this formula the rigidity characteristics of the control linkage aggregates were determined without their physical measuring for coaxial helicopters of four types. It is demonstrated that the eigenvectors of the elasticity matrix are actually torsional modes of the six blades on the control linkage and the eigenvalues are actually linkage "dynamic elasticities" of the corresponding mode which are usually measured in a different way - that is by the linkage frequency testing. The study results are illustrated on Fig.9 [1].

4. The basic design aeromechanic & aeroelastic problems of coaxial rotor helicopter have been developed and key technologies have been achieved

4.1 KAMOV Company experience concentrated in the Ka-50 attack helicopter

Acceptable margin of flutter speed and stall flutter speed of the Ka-50 helicopter were substantiated by mathematical simulation and validated by flight test results (Fig.10). Flight tests results are shown by (V_{TAS} - ωR) relation in Fig.10. A part of flight test points is given in the frame, namely the following range: from $\mathbf{V_{TAS} \sim 300\ km/h}$ to $\mathbf{V_{NE} = 350\ km/h}$, till $\mathbf{V_{TAS} = 390\ km/h}$. Flutter is non-existent in restricted range of calculated curve what is verified by flight test results. Calculated curve presents that there is a flutter speed margin of about **50 km/h** (Fig.10).

Vibration level of the coaxial helicopter have been discussed in paper [2]. The alternating forces apply to hubs of the upper/lower rotors and excite airframe vibration. Configuration of the Ka-50 helicopter rotors affords applying of minimal alternating forces to the airframe. In this case vibration level of the airframe is minimal too.

Vibration level is not in excess of 0.01g in main flight modes. Rotor pendulum and anti-resonant isolation system are not used. The example shown on Fig.11 [2].

Special task for the coaxial helicopter is making a provision for the acceptable lower-to-upper rotor blade tips clearances. As a task of aeromechanics it is analogous with a task to provide the blade tips-to-tail boom clearance of the helicopters with the tail rotor.

KAMOV Company applies at analysis both calculation methods and flight tests [3, 8]. The clearances are measured with the help of optic devices at each of 6 crossing points when the upper blades are arranged above lower blades during their relative rotation with doubled angular speed.

The mechanics can be outlined as following (Fig.12). The planes of the upper / lower rotor blade tips are in parallel at hover. Their clearance is even more than a clearance between rotor hubs.

At forward flight variable azimuthal airloads occur in the rotor disk, that results in flapping motion. Because of this , planes of the upper / lower rotor blade tips are inclined to equal angles in flight direction (forward / backward) .

In lateral direction (viewed along flight direction) the planes of blade tips are inclined to each other because of counter-rotation of the rotors (Fig.12).

The upper-to-lower tips clearances on one disk side decreases and increases on the opposite one. In lateral direction an inclination angle of blade tip planes is approximately equal to blade tip flapping angle (to the left / to the right) and depends on flight mode (Fig.12). As known from aeromechanics, there are relations between blade flapping angle and the rotor parameters, especially to Lock number, blade geometrical twist angle and blade/control linkage torsional stiffness.

Calculation and flight test results show the values of coaxial rotor parameters mentioned above which ensure acceptable safety clearance.

Fig.12 demonstrates measured blade tip flapping angles made during flight tests of Ka-50 helicopter and comparison with calculation data .

Ka-50 helicopter generalised measurement results for the forward flight and manoeuvres are presented in the Fig.12, Fig.13.

The acceptable upper-to-lower rotor blade tips clearances were substantiated by mathematical simulation and validated by flight tests results for all approved envelope of manoeuvres.

The acceptable lower rotor blades to tail boom clearances were validated .

4.2 Ka-50 helicopter maneuverability features

Load factor / speed envelope was substantiated and validated by Ka-50 flight test results:

- within operational limitations (pitch, roll, rotor speed, rotor loads,...);
- within special aerobatic limitations.

A part of flight test points is illustrated by the Fig.13 :

at **3.5 > g-factor > 2** & at **g-factor ≈ 0.**

Each point corresponds to one of the performed manoeuvres . The most part of them are shown at the Fig.13 No established limitations have been exceeded .

Fig.13 also shows the test flight results of Tiger's helicopter [13].

The table on the Fig.14 presents parameters of manoeuvres within special limitations for aerobatic flights. It is notable in this case parameters of "flat turn" and pull-out from the skewed loop at **g–factor = 3.5.**

4.3 The means of aerobatic flight monitoring and analysis

The NSTAR software was created to provide processing and analysis of Ka-50 helicopter test flight data. Using records made by aircraft test instrumentation the NSTAR software makes possible to restore the flying path and to calculate flight parameter additional values [14].

NSTAR software is comparable both with test flight record system and with standard record system. NSTAR results are used for the following purposes:

- analysis of actions , assistance in pilot training;
- examination for critical parameter limits;
- as input data for simulation.

Fig.14 presents an example for skewed loop path recovery.

5. Conclusions

5.1 The basic aeromechanic & aeroelastic problems of a coaxial rotor helicopter have been developed and Key Technology have been achieved.

5.2 Key Technology determine the coaxial helicopter performance and manoeuvrability.

7. References

1. Bourtsev, B.N., "Aeroelasticity of Coaxial Helicopter Rotor", *Proceedings of 17th European Rotorcraft Forum*, Germany, Berlin, Sept. 1991.

2. Bourtsev, B.N., "The Coaxial Helicopter Vibration Reduction", *Proceedings of 18th European Rotorcraft Forum*, France, Avignon, Sept. 1992.

3. Bourtsev, B.N., Selemenev, S.V., "The Flap Motion and the Upper Rotor Blades to Lower Rotor Blades Clearance for the Coaxial Helicopters", *Proceedings of 19th European Rotorcraft Forum*, Italy, Como, 14 – 16 Sept. 1993.

4. Coleman, C.P., "A Survey of Theoretical and Experimental Coaxial Rotor Aerodynamic Research", *Proceedings of 19th European Rotorcraft Forum*, Italy, Como, 14 – 16 Sept. 1993.

5. Akimov,A.I., Butov, V.P., Bourtsev, B.N., Selemenev, S.V., "Flight Investigation of Coaxial Rotor Tip Vortex Structure", *ASH 50th Annual Forum Proceedings*, USA, Washington, DC, May 1994.

6. Акимов,А.И., Бутов, В.П., Бурцев, Б.Н., Селеменев, С.В., "Летные исследования и анализ вихревой структуры винтов соосного вертолета", *Российское Вертолетное Общество, Труды 1го Форума*, Россия, Москва, 20 – 21 Сентября 1994.

7. Bourtsev, B.N., Gubarev, B.A., "A Ka-115 Helicopter a New Development of KAMOV Company", *Proceedings of 22nd European Rotorcraft Forum*, Russia, Saint-Petersburg, 30 August – 1 Sept., 1995.

8. Bourtsev, B.N., Selemenev, S.V., "The Flap Motion and the Upper Rotor Blades to Lower Rotor Blades Clearance for the Coaxial Helicopters", *Journal of AHS*, No1, 1996.

9. Bourtsev, B.N., Kvokov, V.N., Vainstein, I.M., Petrosian, E.A., "Phenomenon of a Coaxial Helicopter High Figure of Merit at Hover", *Proceedings of 23rd European Rotorcraft Forum*, Germany, Dresden, 16 – 18 Sept. 1997.

10. Бурцев, Б.Н., Вайнштейн, И.М., Квоков, В.Н.,Петросян,Э.А.,"Феномен высокого коээфициента полезного действия соосных несущих винтов на режиме висения", *Российское Вертолетное Общество, Труды 3го Форума*, Россия, Москва, 24 – 25 Марта 1998.

11. Bourtsev, B.N., Koptseva, L.A., Animitsa, V.A., Nikolsky, A.A., "Ka-226 Helicopter Main Rotor – as a New Joint Development by KAMOV & TsAGI ", *Aviation Prospects 2000, International Symposium*, Russia, Zhukovsky Moscow Region, 19 – 24 August 1997.

12. Бурцев, Б.Н., Копцева, Л.А., Анимица, В.А., Никольский, А.А., "Несущий винт вертолета Ка-226 – новая совместная разработка фирмы КАМОВ и ЦАГИ", *Российское Вертолетное Общество, Труды 3го Форума*, Россия, Москва, 24 – 25 Марта 1998.

13. Kurt Gotzfried, "Survey of Tiger Main Rotor Loads from Design to Flight Test", *Proceedings of 23rd European Rotorcraft Forum*, Germany, Dresden, 16 – 18 Sept. 1997.

14. Bourtsev,B.N.,Guendline,L.J., Selemenev, S.V.,"Method and Examples for Calculation of Flight Path and Parameters While Performing Aerobatics Maneuvers by the Ka-50 Helicopter based on Flight Data Recorded Information", *Proceedings of 24th European Rotorcraft Forum*, France, Marseilles, 15 – 17 Sept. 1998.

15. Mikheyev,S.V.,Bourtsev,B.N.,Selemenev, S.V., "Ka-50 Attack Helicopter Aerobatic Flight", *Proceedings of 24th European Rotorcraft Forum*, France, Marseilles, 15 – 17 Sept. 1998.

16. Mikheyev,S.V.,Bourtsev,B.N.,Selemenev, S.V., "Ka-50 Attack Helicopter Aerobatic Flight", *ASH 55th Annual Forum Proceedings*, Canada, Montreal, 25 – 27 May 1999.

17. Самохин, В.Ф., Ермилов, А.М., Котляр, А.Д., Бурцев, Б.Н., Селеменев, С.В., "Импульсное акустическое излучение вертолета соосной схемы при крейсерских скоростях полета", *Тезисы докладов на семинаре "Авиационная акустика"*, Россия, Дубна Московской области, 24 – 27 Мая 1999.

Basic Parameters of Coaxial KAMOV'S Helicopters

POWER LOADING

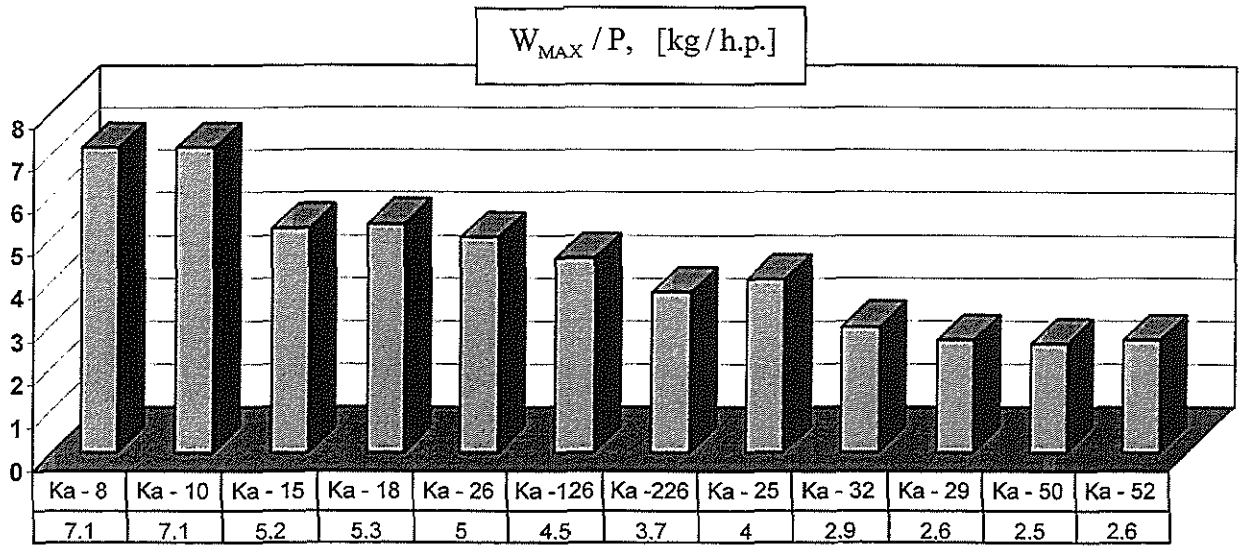

MAX SPEED

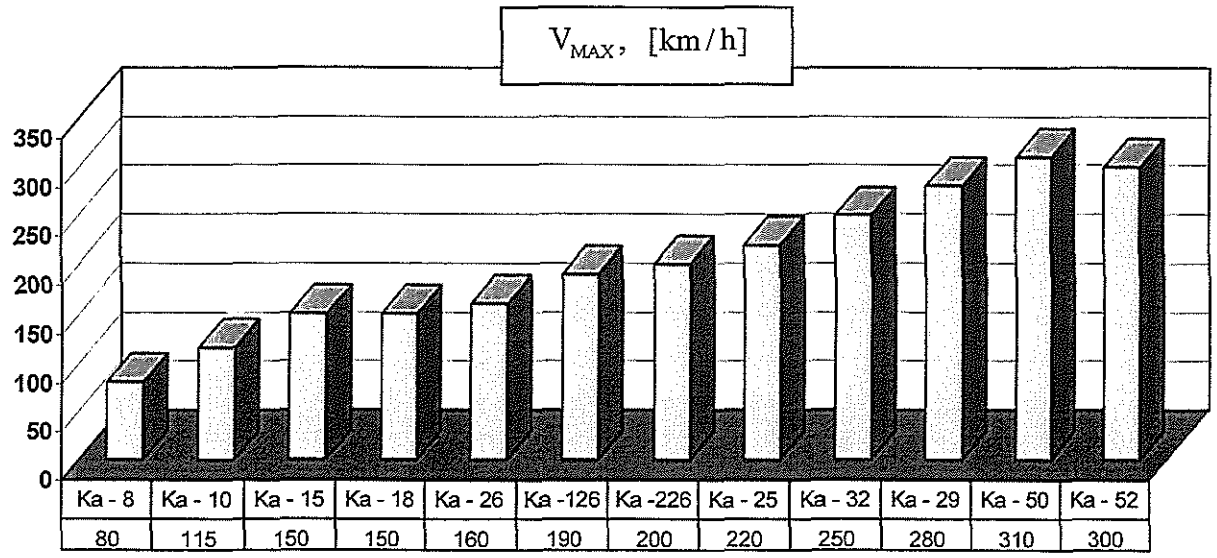

Fig.1A

Basic Parameters of Coaxial KAMOV'S Helicopters

RELATIVE HUB CLEARANCES

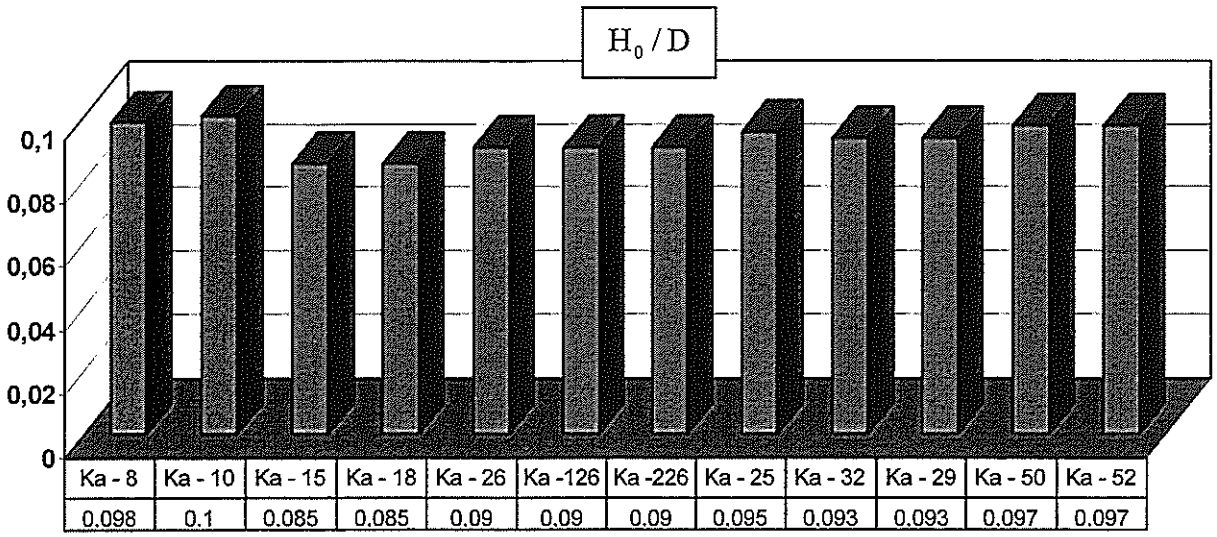

Ka - 8	Ka - 10	Ka - 15	Ka - 18	Ka - 26	Ka -126	Ka -226	Ka - 25	Ka - 32	Ka - 29	Ka - 50	Ka - 52
0.098	0.1	0.085	0.085	0.09	0.09	0.09	0.095	0.093	0.093	0.097	0.097

DISK LOADING

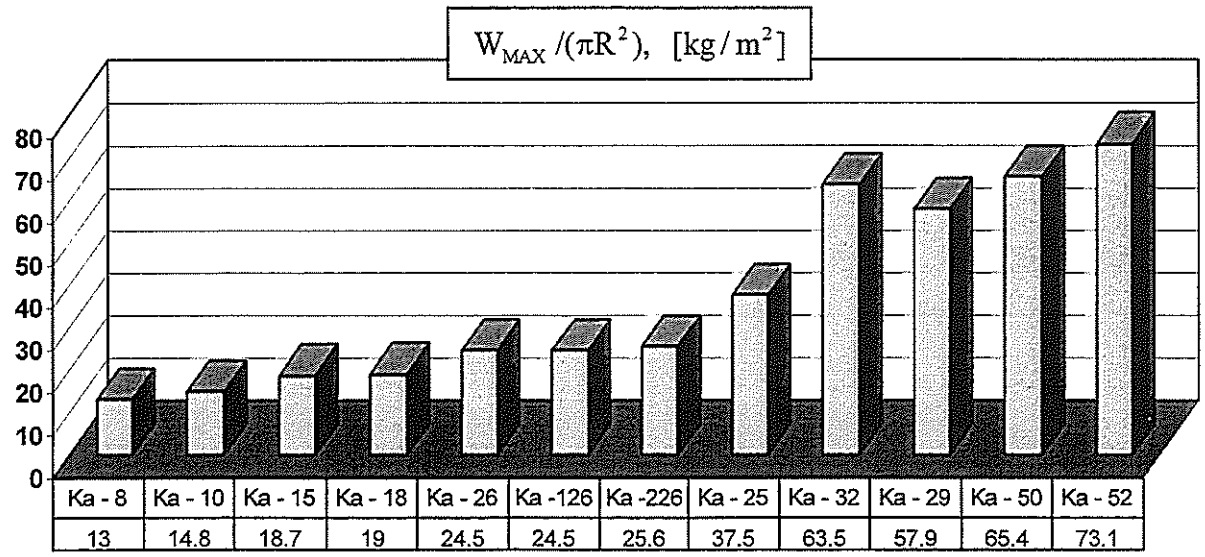

Ka - 8	Ka - 10	Ka - 15	Ka - 18	Ka - 26	Ka -126	Ka -226	Ka - 25	Ka - 32	Ka - 29	Ka - 50	Ka - 52
13	14.8	18.7	19	24.5	24.5	25.6	37.5	63.5	57.9	65.4	73.1

Fig.1B

Single & Coaxial Rotors

active disk areas , effective diameters , power & thrusts at hover

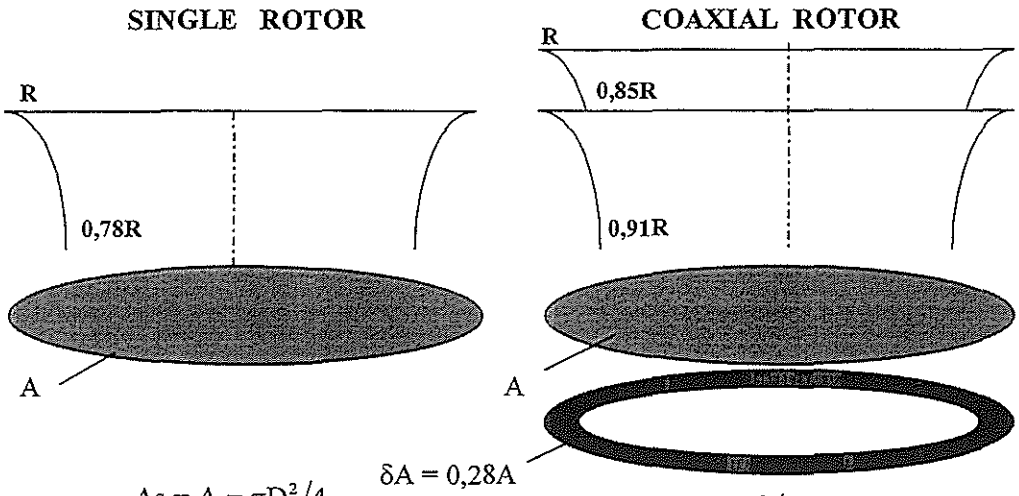

$As = A = \pi D^2/4$

$Ac = \pi D^2/4 + \delta A = 1{,}28\,As$

$D_{EFF} = \sqrt{4\,As/\pi} = 1{,}13\,D$

$Ts = (33{,}25 \cdot \eta_S \cdot D \cdot P\sqrt{\Delta})^{2/3}$

$Tc = (33{,}25 \cdot \eta_C \cdot D \cdot P\sqrt{\Delta})^{2/3}$

$$\eta_C = \frac{D_{EFF}}{D} \cdot \eta_S = 1{,}13\eta_S$$

Single & Coaxial Rotor Helicopters

main rotor diameter , power & thrust at hover

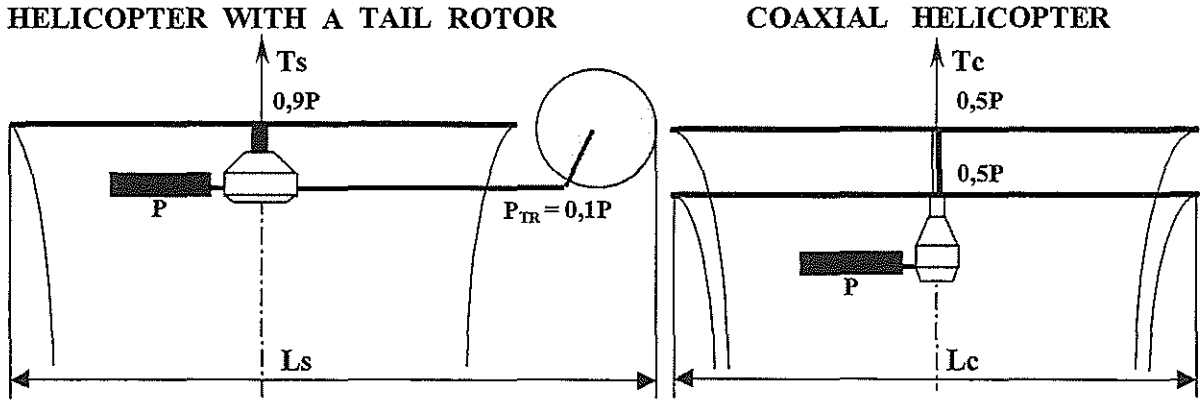

$Ts = \left(33{,}25 \cdot \eta_S \cdot Ds \cdot 0{,}9P\sqrt{\Delta}\right)^{2/3}$

$Tc = \left(33{,}25 \cdot \eta_C \cdot Dc \cdot P\sqrt{\Delta}\right)^{3/3}$

From $\eta_c / \eta_s = 1{,}13$ and $Pc = Ps = P$ and $P_{TR} = 0{,}1P$:

1. At $Dc = Ds$ the thrust ratio is $Tc / Ts = (1{,}13 / 0{,}9)^{2/3} = 1{,}16$;
2. At $Ts = Tc$ the diameter ratio is $Ds / Dc = 1{,}13 / 0{,}9 = 1{,}26$.

Fig.2

Figure of merit of coaxial rotors
(Flight test measured data)

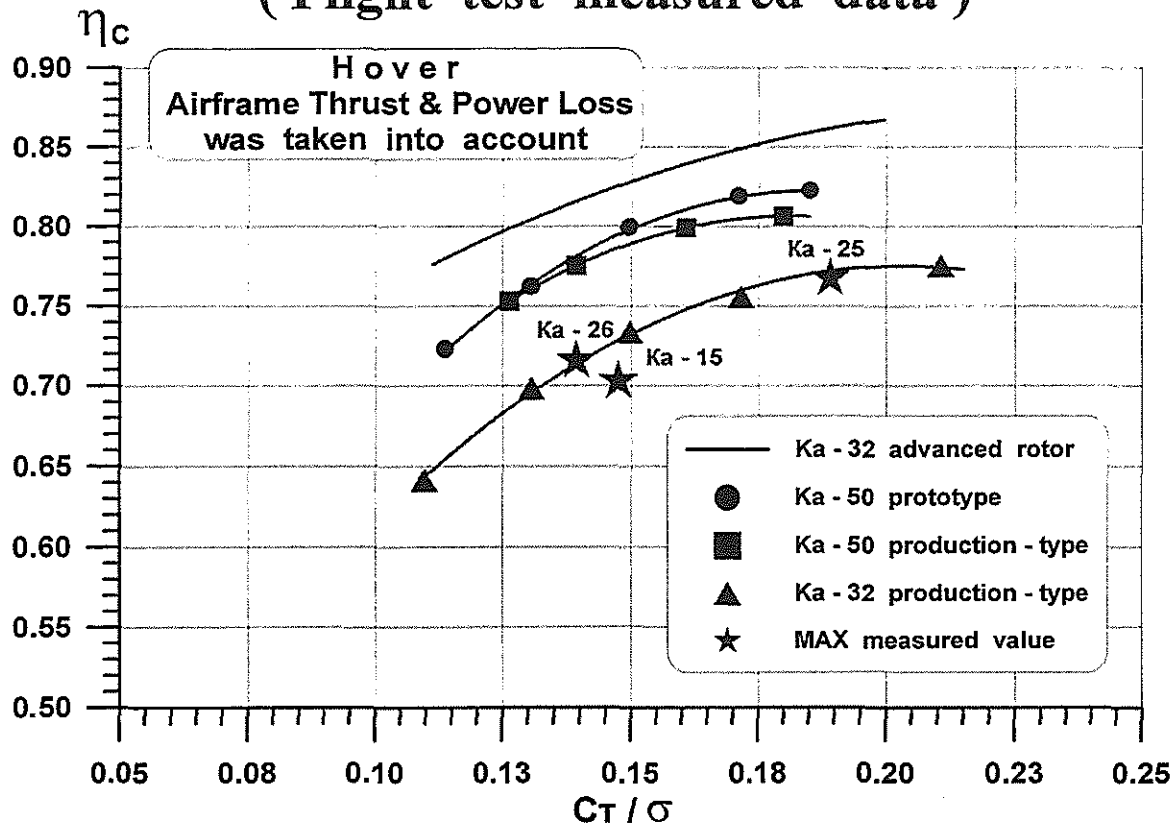

Wake form in hover & its approximation

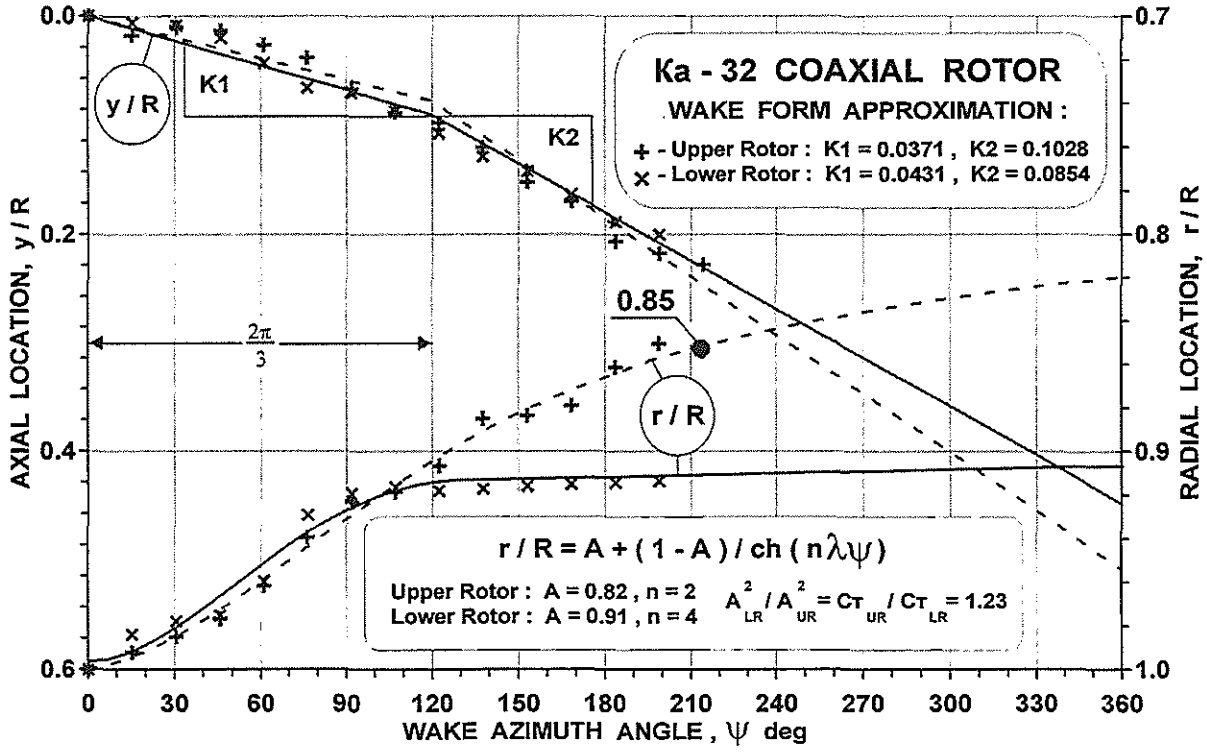

Fig.3

THE STATISTICAL CHART

Power Loadind - Disk Loading - Design Figure of Merit of Coaxial Helicopters & Helicopters with a Tail Rotor

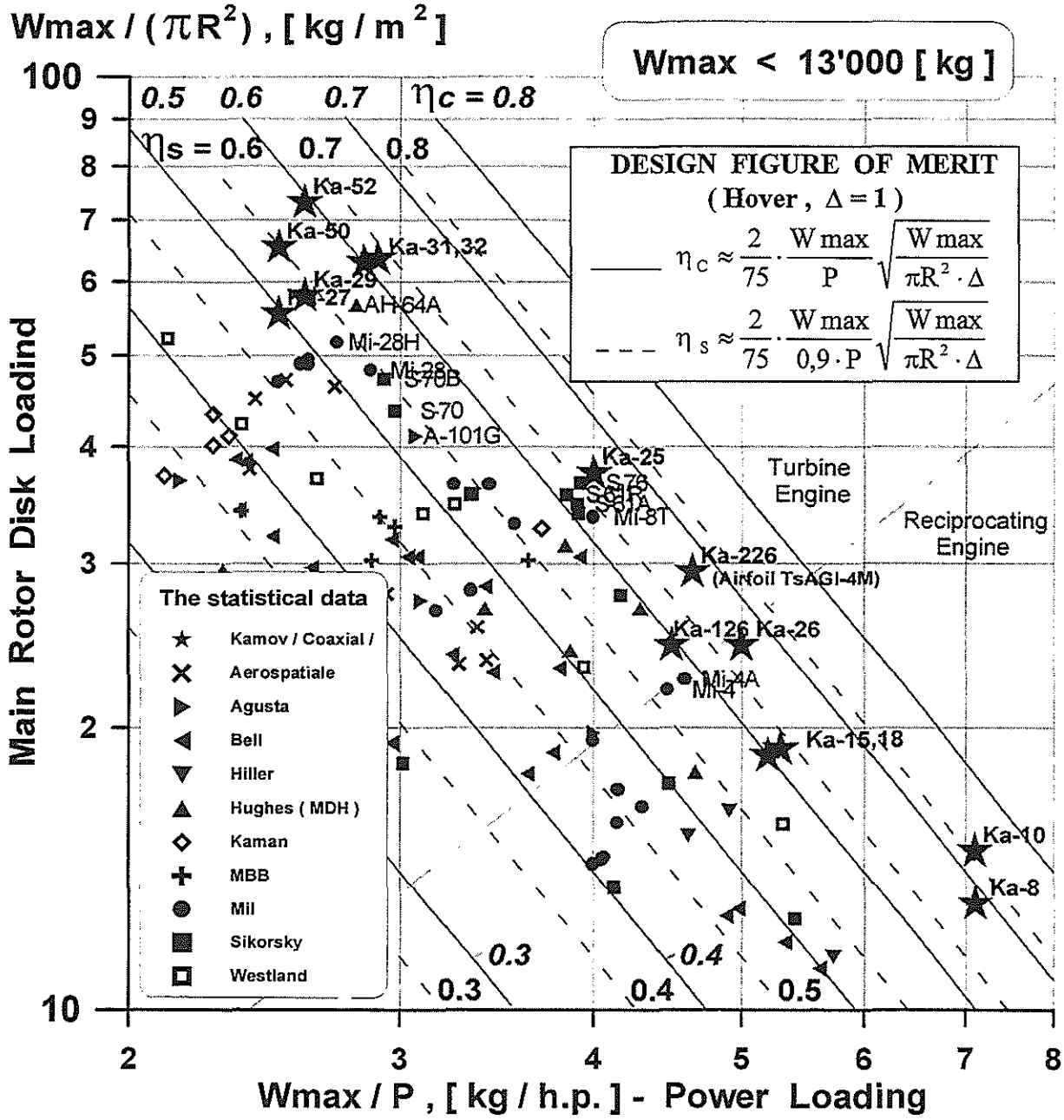

Fig.4

Coaxial Rotor Wake Side Views for Several Flight Speeds

V_{TAS} = 5 [km/h]

V_{TAS} = 73 [km/h]

V_{TAS} = 138 [km/h]

V_{TAS} = 227 [km/h]

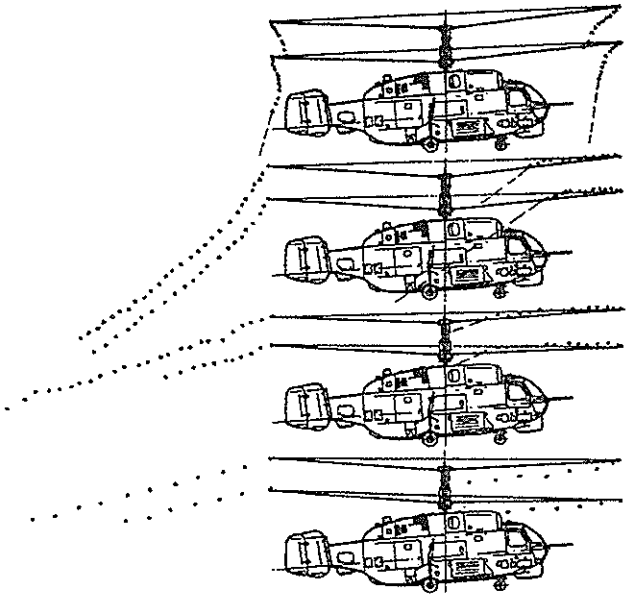

Wake Front Boundary Longitudinal Position Versus Flight Speed

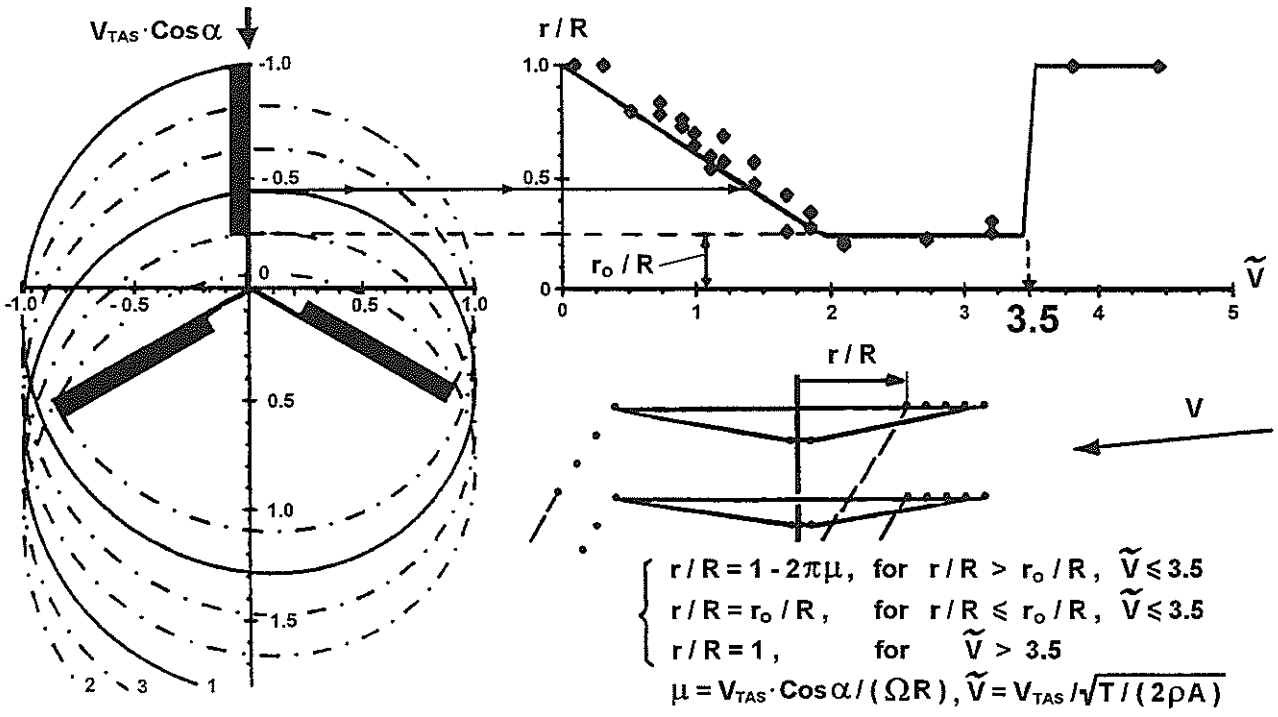

Fig.5

Simulated Aeroelastic Phenomena of Coaxial Rotor

	Simulated Phenomena	SIMULATION VERSION				
		ULISS-6	ULISS-1	ULMFE	FLUT	MFE
1	$EI_x(r/R,\omega t)$ $EI_y(r/R,\omega t)$ $GI_p(r/R,\omega t)$	✓	✓			
2	$\bar{\varphi}_o=\|\|U_{ij}\|\|\times\bar{M}$	✓			✓	✓
3	$V_i(r/R,\psi)$	✓				
4	C_L, C_D, C_M $(\alpha, \dot{\alpha}, M, \dot{M})$	✓	✓	✓		
5	C_{L_MAX} $(\alpha, \dot{\alpha}, M)$	✓	✓	✓		
6	Airfoil Aeroelastic Deformation	✓	✓	✓	✓	
7	Upper/Lower Rotor Data	✓	✓	✓	✓	✓

Analysis Results of Coaxial Rotor Aeroelastic Simulation

	Analysis Results	SIMULATION VERSION				
		ULISS-6	ULISS-1	ULMFE	FLUT	MFE
1	Stall flutter boundary	Coaxial Rotors	Blade	Blade		
2	Bending moments, Pitch link loads, Actuator loads	Coaxial Rotors	Blade	Blade		
3	Elactic Deformations	Coaxial Rotors	Blade	Blade		
4	Alternate loads on Hubs	Coaxial Rotors				
5	Blade tips Clearances	Coaxial Rotors				
6	Flight test flutter	Coaxial Rotors	Blade	Blade		
7	Ground test flutter	Coaxial Rotors			Blade	
8	Natural frequencies			Blade		Blade

Fig.6

Blade Aerofoil Data

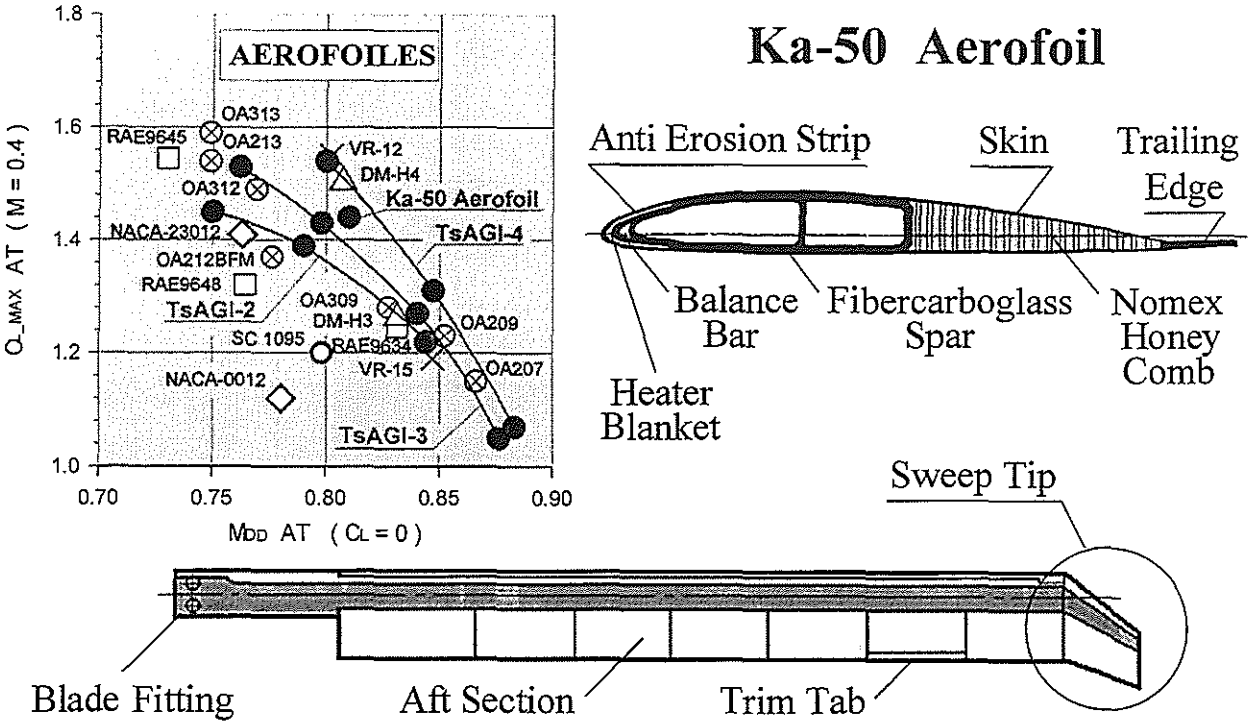

Ka-50 Aerofoil

Aerodynamic moments of existing TsAGI-2, TsAGI-4 airfoils & advanced TsAGI-4M airfoil

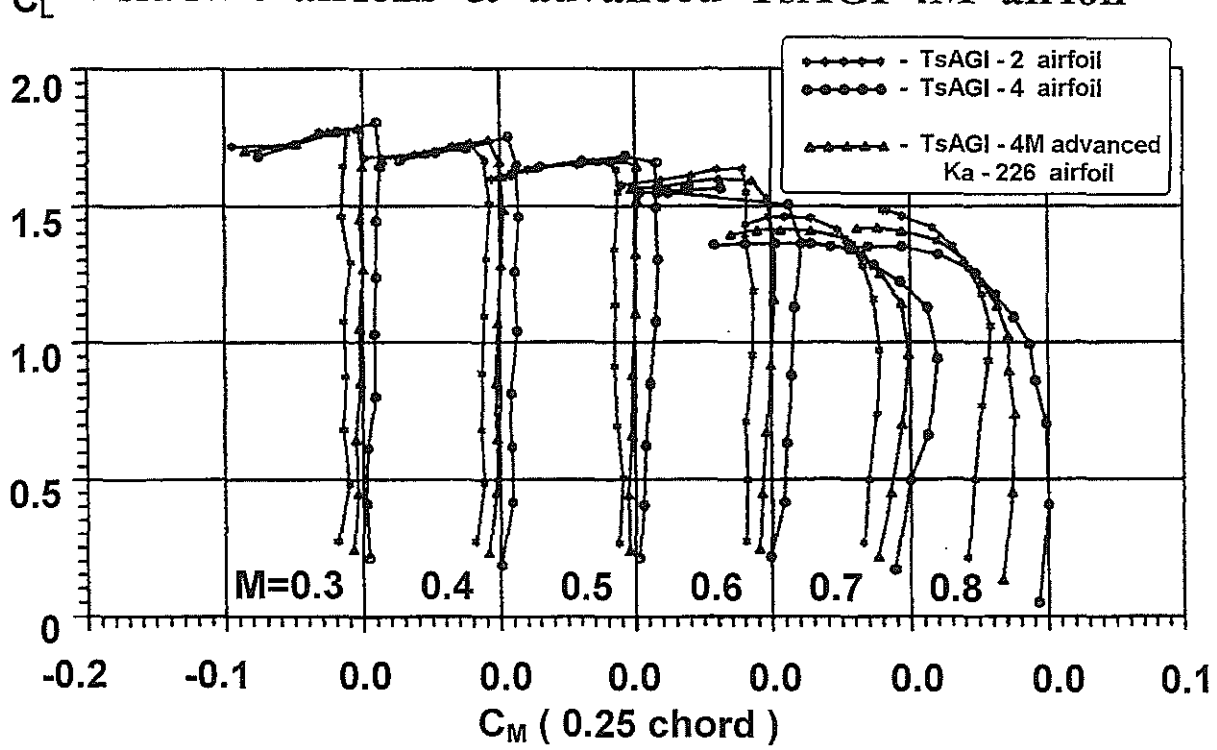

Fig.7

Ka-32 rotors control linkage model

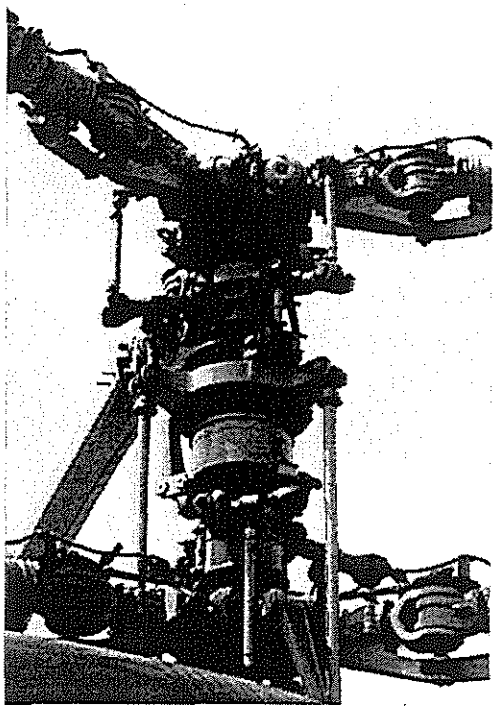

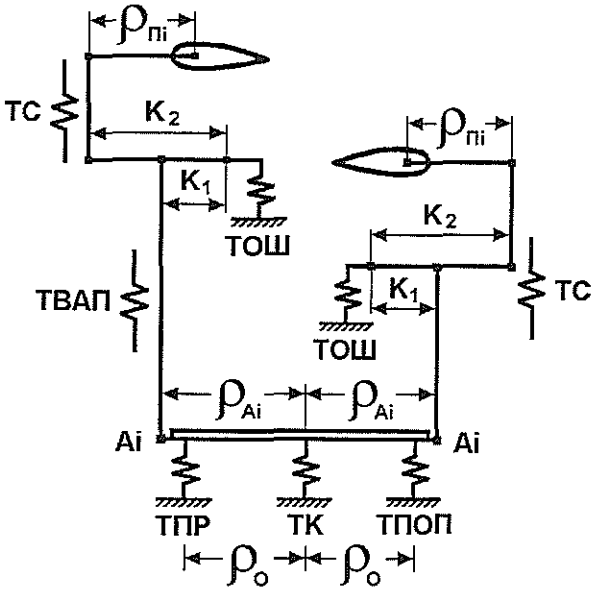

Ka-50 rotors control linkage model

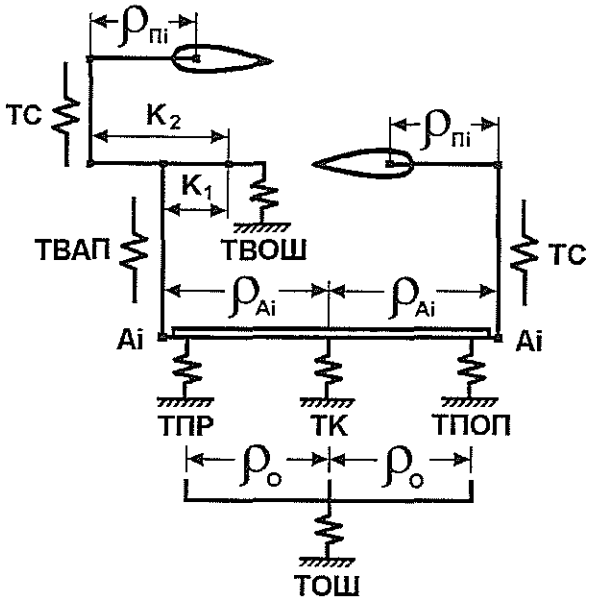

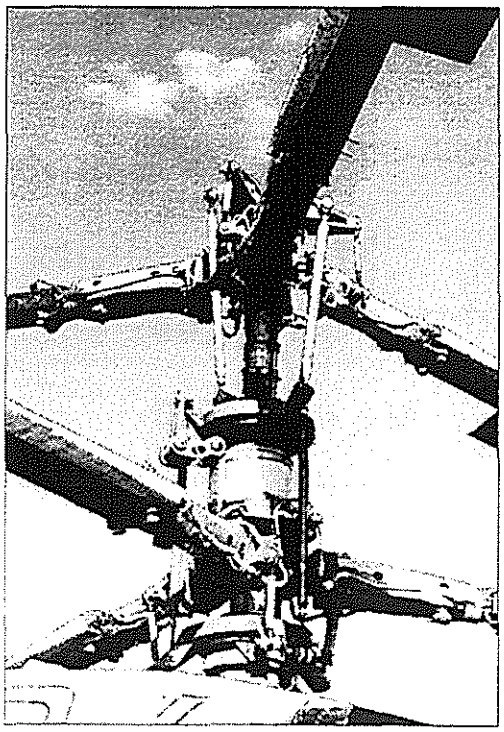

Fig.8

The scheme of experiment on determination of the control linkage elasticity matrix

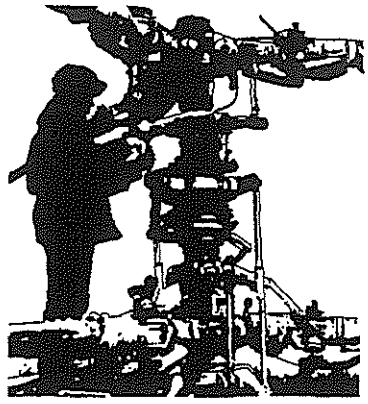

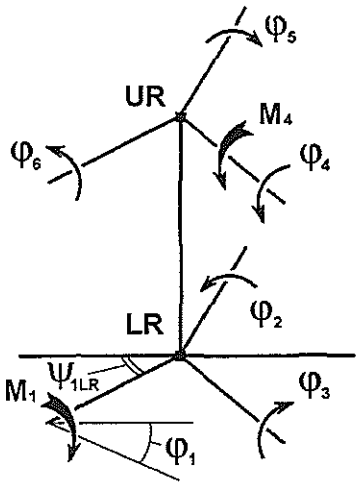

$$\bar{\varphi} = \| \vartheta_{I,J} \| \times \bar{M}$$

$$\begin{vmatrix} \bar{\varphi}_1 \\ \bar{\varphi}_2 \\ \bar{\varphi}_3 \\ \bar{\varphi}_4 \\ \bar{\varphi}_5 \\ \bar{\varphi}_6 \end{vmatrix} = \left\| \begin{array}{ccc|ccc} \vartheta_{11} & \vartheta_{12} & \vartheta_{13} & \vartheta_{14} & \vartheta_{15} & \vartheta_{16} \\ \vartheta_{21} & \vartheta_{22} & \vartheta_{23} & \vartheta_{24} & \vartheta_{25} & \vartheta_{26} \\ \vartheta_{31} & \vartheta_{32} & \vartheta_{33} & \vartheta_{34} & \vartheta_{35} & \vartheta_{36} \\ \hline \vartheta_{41} & \vartheta_{42} & \vartheta_{43} & \vartheta_{44} & \vartheta_{45} & \vartheta_{46} \\ \vartheta_{51} & \vartheta_{52} & \vartheta_{53} & \vartheta_{54} & \vartheta_{55} & \vartheta_{56} \\ \vartheta_{61} & \vartheta_{62} & \vartheta_{63} & \vartheta_{64} & \vartheta_{65} & \vartheta_{66} \end{array} \right\| \times \begin{vmatrix} M_1 \\ M_2 \\ M_3 \\ M_4 \\ M_5 \\ M_6 \end{vmatrix}$$

Elasticity matrix

APPROXIMATION : $\vartheta_{I,J}(\psi_{1LR}) = f(TC, TK, TПОП, TПР, TВАП, TОШ, TВОШ, \psi_{1LR})$

CALCULATION :

$$\vartheta_{I,J}(\psi_{1LR}) = \frac{КАЧ_J}{\rho_{ПЦ}} \cdot \frac{КАЧ_I}{\rho_{ПЦ}} \cdot \{TK \cdot [KA_I \cdot (\mathrm{Sin}\varphi_I + \mathrm{Cos}\varphi_I) - 1] \cdot [KA_J \cdot (\mathrm{Sin}\varphi_J + \mathrm{Cos}\varphi_J) - 1] +$$
$$+ KA_I \cdot KA_J \cdot (TПОП \cdot \mathrm{Cos}\varphi_I \cdot \mathrm{Cos}\varphi_J + TПР \cdot \mathrm{Sin}\varphi_I \cdot \mathrm{Sin}\varphi_J)\} + TC + TВАП + \vartheta_{0\,I,J};$$

$$\vartheta_0 = \begin{Vmatrix} TОШ & 2TОШ \\ 2TОШ & 4TОШ + TВОШ \end{Vmatrix}; \quad \varphi_I = \begin{cases} \psi_{1LR} + ОП - \frac{\pi}{2} - \frac{2\pi}{K}(I-1); & I = 1, 2, \ldots, K \\ 2\pi - (\psi_{1LR} + ОП + DFI) - \frac{\pi}{2} - \frac{2\pi}{K}(I-K-1); & I = K+1, \ldots, 2K \end{cases}$$

Main rigidities of the elasticity matrix & dynamic rigidities obtained from frequency testing

$$\begin{cases} M\ddot{\varphi} + \vartheta^{-1}\varphi = 0 \\ \varphi = u \cdot e^{ipt} \\ (\vartheta M - E/P_K^2) \cdot u = 0 \\ P_K^2 = 1/(\lambda_K I) \end{cases}$$

MEASURED Ka – 32 ROTOR LINKAGE RIGIDITY ⇒

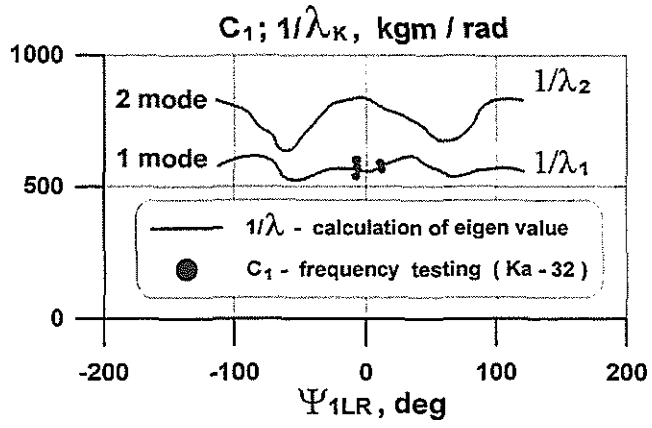

Fig.9

Demonstrated Rotor Speed Range

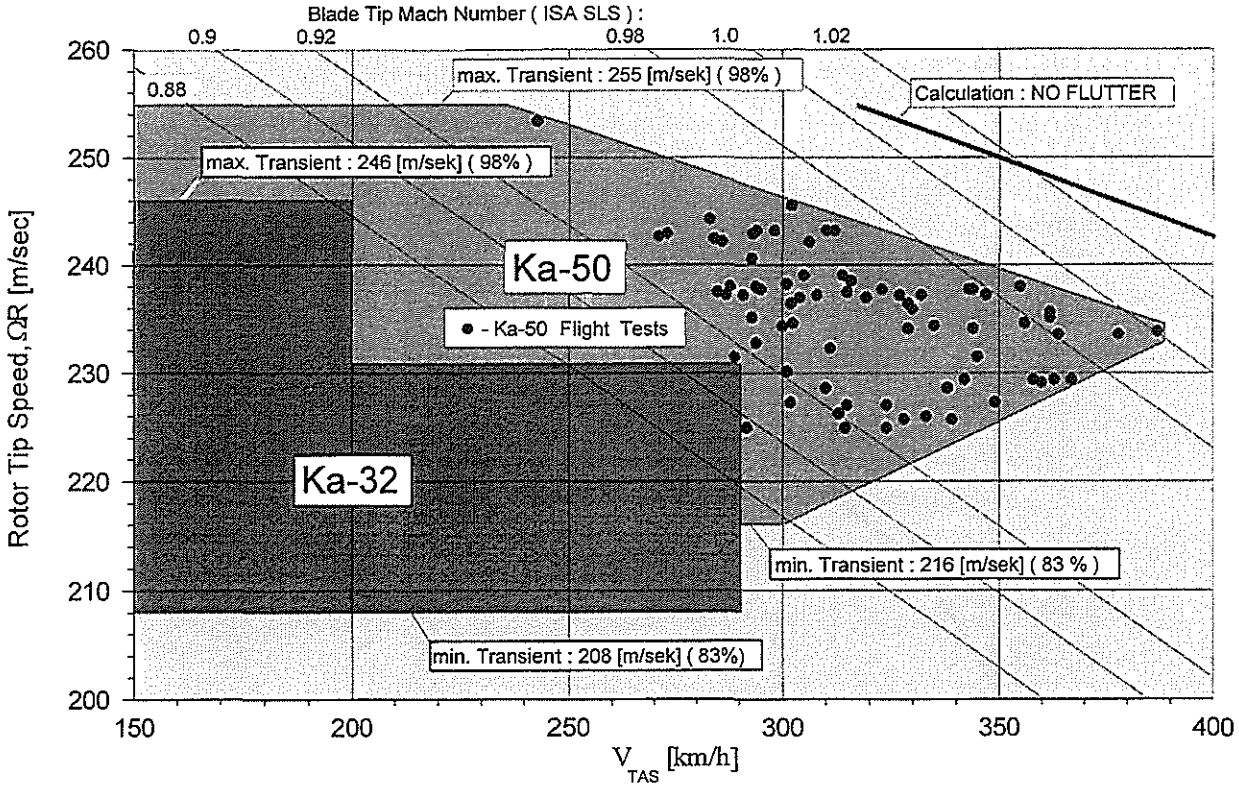

Stall Flutter Boundary

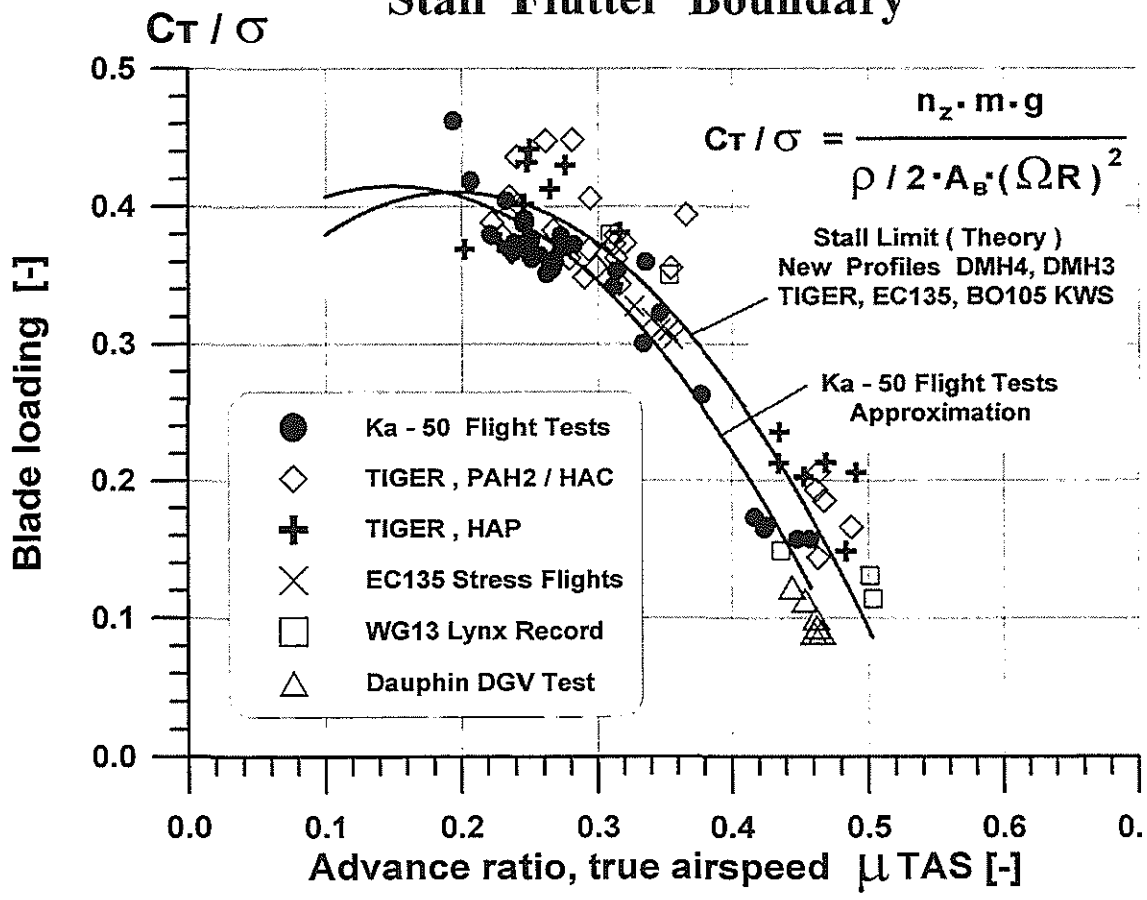

Fig.10

Ka - 25 Helicopter 3ω Vertical Vibrations

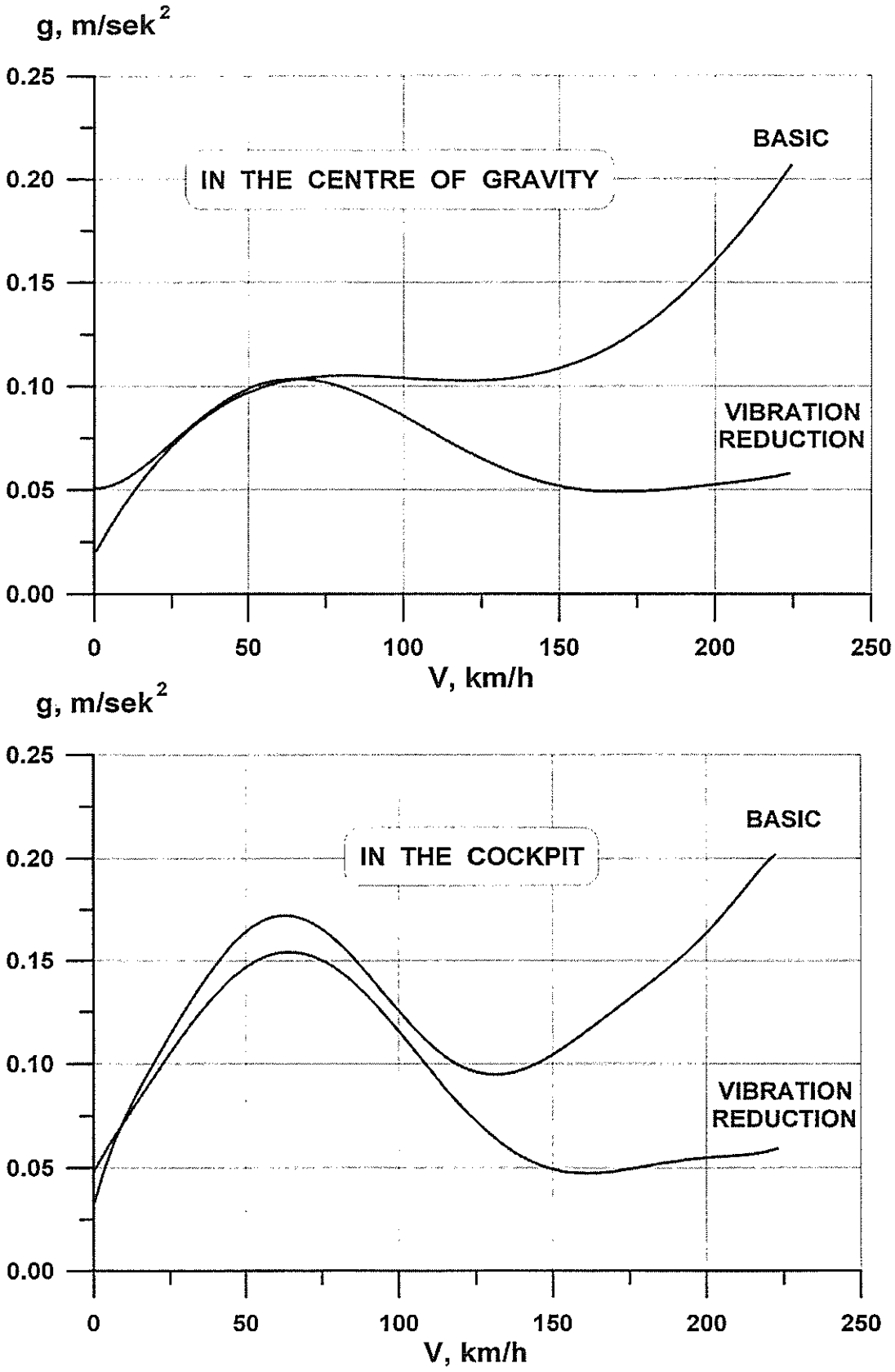

Fig.11

Blade Tip Coefficients

Comparision of Calculations and Flight Test Results

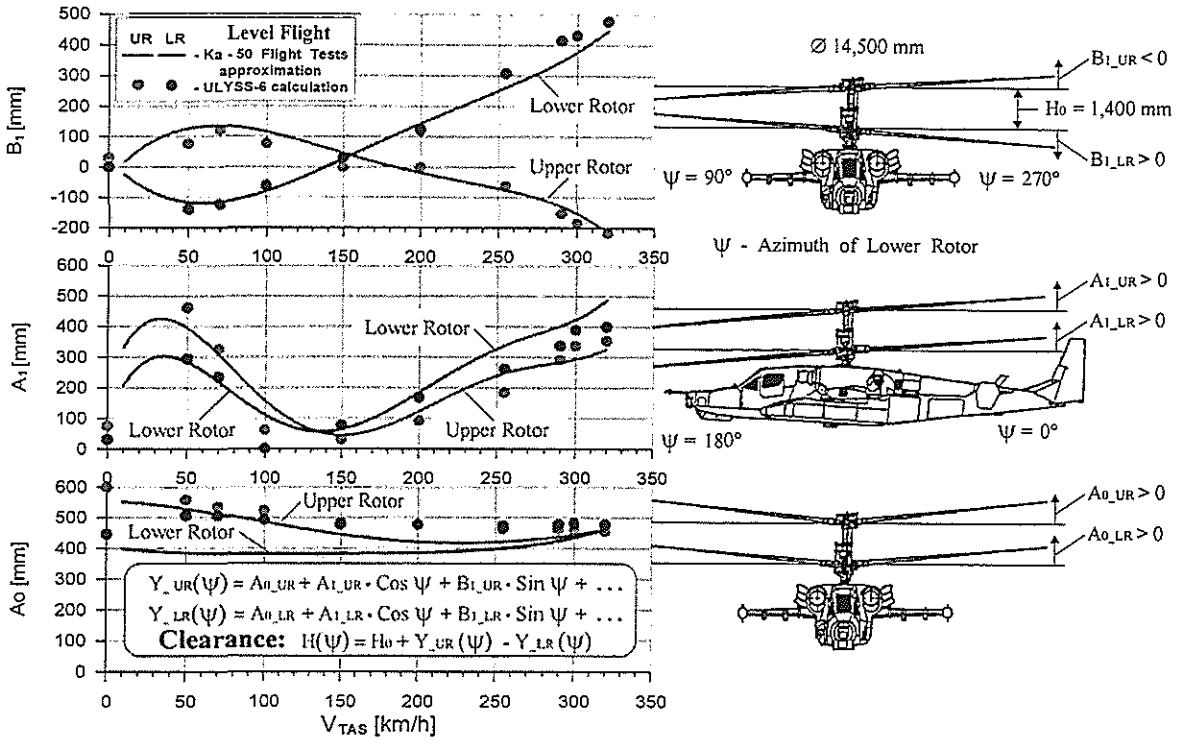

The Upper-to-Lower Rotor Blade Tips Clearancies

Versus Level Forvard Speed & Blade Azimuth

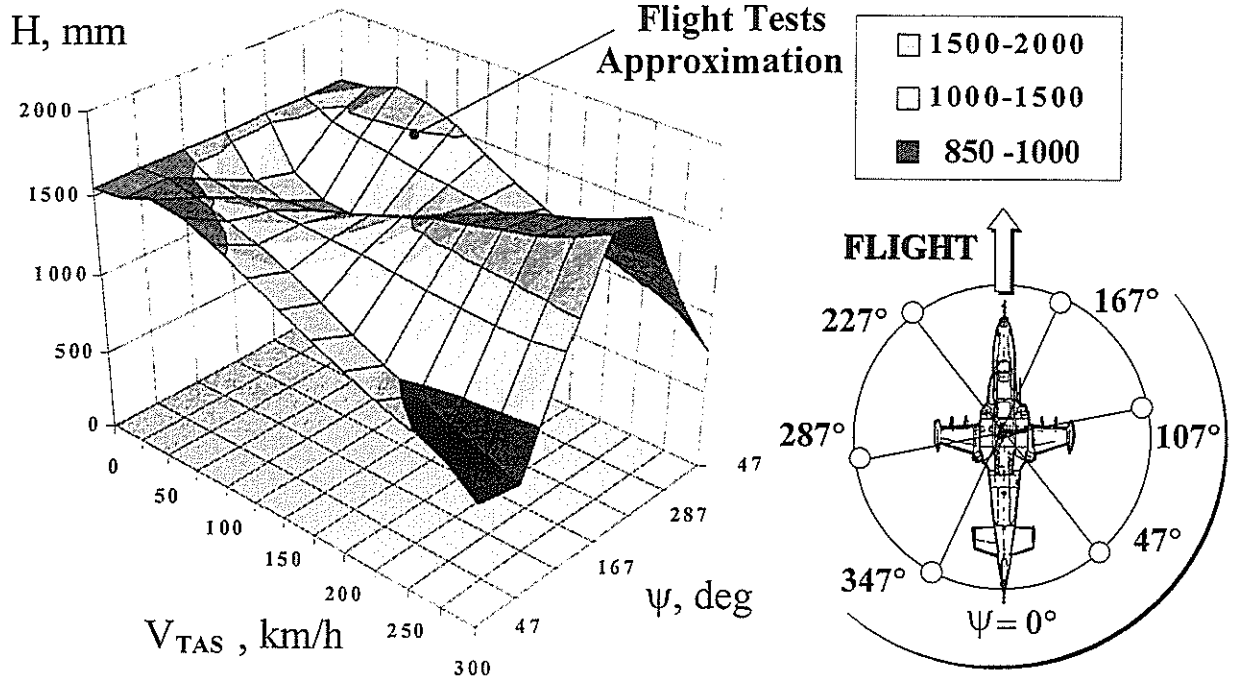

Fig.12

Measured Upper-to-Lower Rotor Blade Tips Clearancies

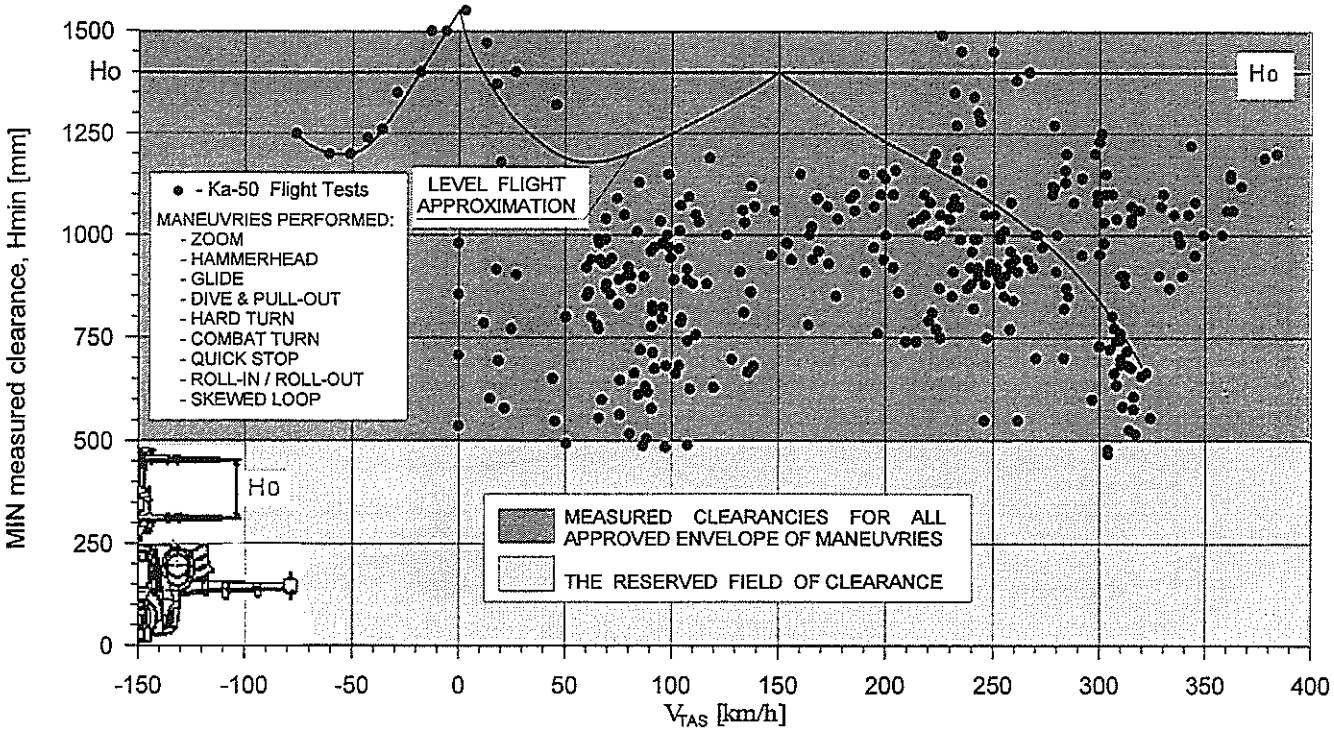

Load Factor / Speed Envelope

(Structural Qualification)

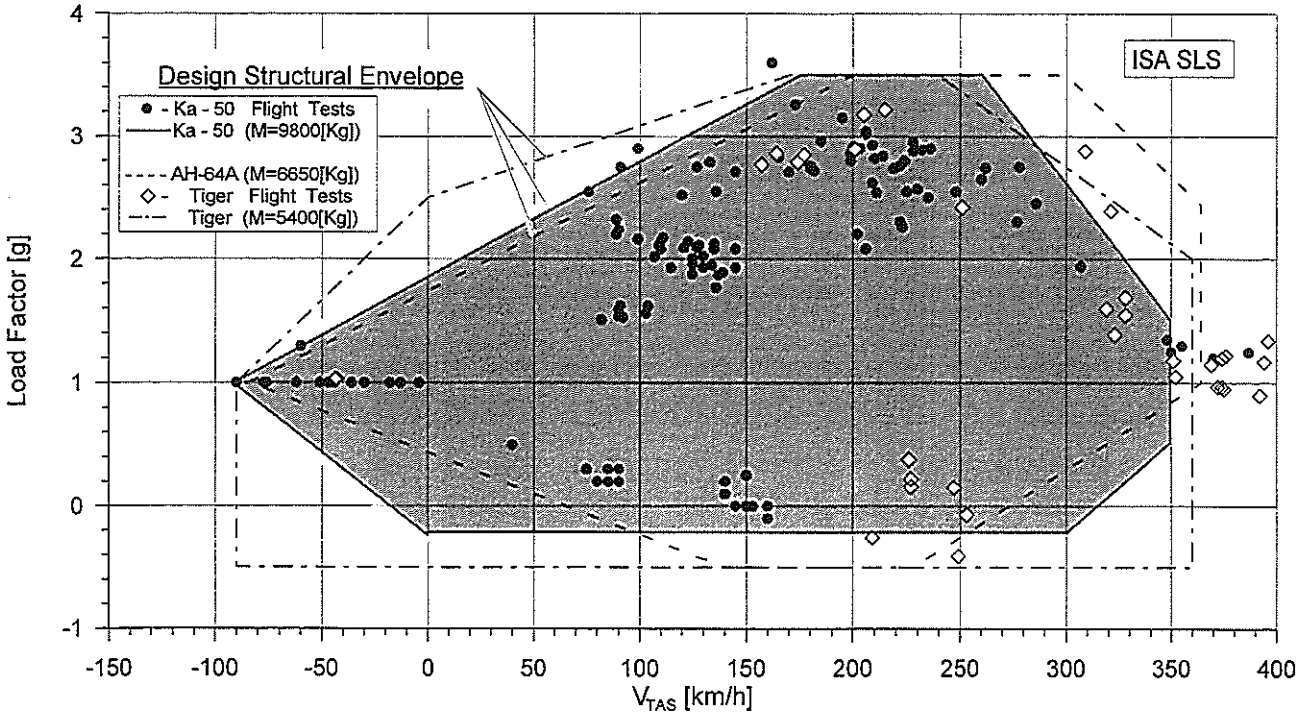

Fig.13

Ka-50 Aerobatic Maneuvries

MANEUVER	The Measured Parameter Values (min/max)				DESCRIPTION
	Airspeed V_{TAS} [km/h]	Load Factor [g]	Pitch attitude [deg]	Roll attitude [deg]	
Hard Turn (Right/Left)	280 ÷ 60	1.0 → 2.9 → 1.0	20 ÷ 50	0 ÷ -70	Unsteady Turn with Pitch & Roll
Flat Turn (Right/Left)	220 ÷ 0	1.0 → 1.5 → 1.0	±5	±20	Jaw Attitude ±80 ÷ ±90 [deg]
Hammerhead (Right/Left)	280 ÷ 0	1.0→ 2.9 → 1.0 → 2.9 → 1.0	0 ÷ ±90	±90	
Dive	0 ÷ 390	1.0 → 0.25 → 2.9 → 1.0	0 ÷ -90	±30	Push-Down, Dive & Pull-Out
Skewed Loop (Right/Left)	280 ÷ 70	1.0 → 2.9 → 1.2 → 3.5 → 1.0	0 ÷ 360	±150	
Quick Stop (Right/Left)	150 ÷ 40	1.0 → 2.0 → 1.2 → 1.0	0 ÷ 40	±55	Pitch / Roll Decceleration
Pull-Up with the Tail Forward	-90 ÷ 0	1.0 → 1.5 → 1.0	0 ÷ -70	±10	Backward Acceleration & Pull-Up with the Tail Forward/Up

Flight Path While Performing Skewed Loop

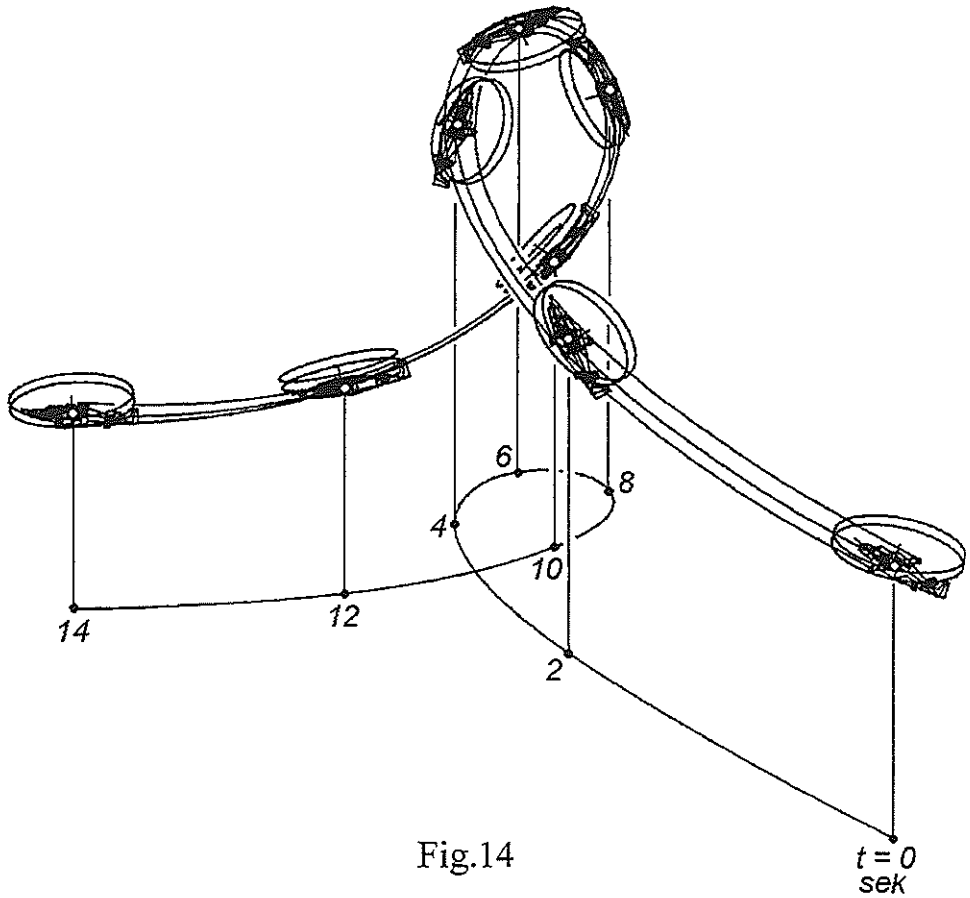

Fig.14

TWENTYFIFTH EUROPEAN ROTORCRAFT FORUM

Paper n° G23

HELICOPTER ACTIVE NOISE AND VIBRATION REDUCTION

BY

T. MILLOTT, W. WELSH
SIKORSKY AIRCRAFT, CT, USA

SEPTEMBER 14-16, 1999
ROME
ITALY

ASSOCIAZIONE INDUSTRIE PER L'AEROSPAZIO, I SISTEMI E LA DIFESA
ASSOCIAZIONE ITALIANA DI AERONAUTICA ED ASTRONAUTICA

HELICOPTER ACTIVE NOISE AND VIBRATION REDUCTION

Thomas A. Millott
Sr. Acoustics Engineer

William A. Welsh
Sr. Technical Engineer

Sikorsky Aircraft Corporation
Stratford, CT

1 ABSTRACT

High levels of noise and vibration continue to hamper the utility of helicopters. Lower cabin noise and vibration levels will reduce crew and passenger fatigue, resulting in fewer crew task errors, and thereby improving the mission effectiveness of helicopters. Reduced airframe vibration levels will lead to longer life spans for critical components, lower maintenance costs, and higher reliability. Although passive approaches for these problems have been implemented, they carry significant cost and weight penalties. In addition, passive technology has reached its limit in attaining further reductions within helicopter cost and weight constraints. The innovative use of active control technology provides the potential to reduce noise and vibration levels below those currently achievable with purely passive approaches, or alternatively, to achieve reductions comparable to passive approaches but with a lower weight penalty. Sikorsky has developed and flight tested active noise and vibration control systems. A prototype active vibration control (AVC) system has been flight tested on an UH-60 aircraft and achieved significant reductions in the main rotor 4P vibrations felt inside the helicopter cabin and cockpit. A productionized version of the AVC system is currently undergoing development flight testing on the Sikorsky S-92 Helibus™. Also, an active noise control (ANC) system has been successfully flight tested on an S-76 aircraft and achieved tonal noise reductions of up to 20dB in the helicopter cabin.

2 INTRODUCTION

Active Noise Control

Interior noise is an increasingly important discriminator in the commercial helicopter market, with "acceptable" noise levels traditionally being achieved passively, albeit with substantial weight penalties. Increasing performance demands (i.e., longer range, higher payloads) have driven the pursuit of lighter-weight solutions. Furthermore, continuing reductions in the noise levels commonly experienced by passengers in various other modes of transportation, including ground vehicles and commercial fixed-wing aircraft, have heightened the awareness and sensitivity of passengers to helicopter internal noise. In the last decade the continuing trend towards cheaper, faster, and more powerful computers has lead to the evolution of active noise control (ANC) from a laboratory experiment to a practical approach for reducing aircraft cabin noise levels (Ref. 1-2). ANC, properly integrated with traditional passive techniques, offers substantial promise of reducing helicopter cabin noise levels with lower weight penalties than purely passive treatments. This will benefit the helicopter industry by improving commercial acceptance and expanding the helicopter market.

There are three primary components of helicopter interior noise: (1) large amplitude, low frequency rotor harmonics; (2) broadband noise; and (3) higher frequency structure-borne tones generated within the gearbox, power train, and hydraulic system. A typical spectrum is shown in Fig. 1. The low frequency tones (<200Hz) are less important to passenger comfort than this figure would imply due to the natural attenuation of the ear at low frequencies. The high frequency gear-mesh tones (>700Hz) fall into the speech interference range and, since these tones generally rise far above the broadband noise floor (Fig. 1), are generally considered the most intrusive and irritating component of noise in a typical helicopter. The primary gear-mesh tone generally falls in the frequency range of 700-1000Hz, and is typically much louder than its higher harmonics. It is this tone which is typically the most irritating to passengers and crew, and unfortunately falls into a frequency range in which traditional passive treatments are not very weight efficient.

Recently, a multi-year program was initiated at Sikorsky Aircraft Corporation to develop a flight-worthy ANC system to actively cancel gear-mesh noise inside the cabin interior. Initial concepts explored for the helicopter gear-mesh ANC problem included both structural acoustic control of accelerometers/microphones using force generating actuators and acoustic control of microphones using speakers. However, the speaker/microphone control approach that has proven successful in lower frequency tonal applications such as turbo-prop aircraft (Ref 1) and for the low frequency rotor harmonics in helicopters (Ref 2) is not practical for this problem due to the high frequencies and resulting number of participating acoustic modes. In this approach, the speakers must set up a sound field inside the cabin that matches and cancels that created by the disturbance. For global noise reductions this requires that the number of speakers be at least equal to the number of relevant acoustic modes (Ref 3). There are several hundred acoustic modes present in the gear-mesh frequency range (>700Hz) for a cabin the size of the S-76 (Ref. 4), thus requiring at least as many speakers to achieve global noise reductions.

A more promising approach for the gear-mesh ANC problem is to use a choke-point methodology to prevent the structure-borne gear-mesh vibrational energy from entering the cabin by placing actuation where the gearbox is mounted to the structure. The approach described in this paper, and flight tested on the S-76 helicopter (Ref. 5), involves the use of point force (proof-mass) actuators surrounding the gearbox mounts to actively cancel the gear-mesh vibrations before they enter the airframe. This approach avoids interrupting the primary load path of the helicopter, thus avoiding flight safety concerns, and is generally more effective with a wider frequency range of operation than tuned passive absorbers. A schematic of the gear-mesh ANC approach is shown in Fig. 2. The approach taken in Refs. 6-7 to address helicopter gear-mesh noise used structural actuators mounted parallel with struts supporting the gearbox to introduce the canceling forces directly into the load path. However, in the case of the S-76, the mechanical interface between the gearbox and the airframe is significantly different, in that the gearbox is bolted directly to a pair of transmission beams integral to the airframe structure. Thus the actuators were mounted on the transmission beams near the gearbox mounting points as in Ref. 8. The gear-mesh ANC system utilizes microphones distributed throughout the cabin as feedback control sensors, as shown in Fig. 2.

Active Vibration Control

Helicopter vibration is largely a result of vibratory aerodynamic loads generated by the rotor as it moves edgewise through the air in forward flight. Traditional passive approaches to reducing vibrations involve the use of tuned-mass absorbers. These absorbers tend to be very heavy, are only effective in a very narrow band about the tuned frequency, and generally only

reduce vibrations in close proximity to their mounting location. Furthermore, passive systems appear to be approaching an asymptotic limit in terms of weight efficiency. A major leap forward in terms of passive vibration reduction in helicopters was the introduction of the hub absorber. The hub absorber, which reduces the inplane NP (blade passage frequency) vibratory loads at the hub, results in significant reductions in the NP vibrations in the cockpit and the cabin. An example of the magnitude of vibration reduction provided by the hub absorber is shown in Fig. 3 for the Sikorsky S-61. As described in Ref. 9 and also shown in Fig. 3, significant reductions in the failure rates of critical components were observed in connection with the lower vibration levels, which ultimately translated into reduced maintenance costs.

Since the introduction of the hub absorber, however, the vibration levels of modern helicopters appear to be hovering about an asymptotic limit of 0.10-0.15 g. This is due to the fact that the hub absorber does not affect the vertical vibratory hub load component that propagates unattenuated into the airframe. This component is generally attacked in Sikorsky helicopters using tuned passive absorbers located in the cabin. These devices are generally very heavy and incur significant weight penalties. Lower vibration levels can be achieved by increasing the number of passive absorbers, but this tends to result in diminishing returns. Thus modern helicopters appear to be approaching a vibration limit driven by weight efficiency. What is required is a paradigm shift in vibration reduction technology.

Active vibration control (AVC) systems have the potential for significantly reducing helicopter vibration while decreasing weight dedicated to vibration reduction. Many studies and tests have shown that active systems are effective. Early AVC studies summarized in Refs 10-12 focused on higher harmonic control (HHC) and showed that significant vibration reduction could be achieved using this approach. HHC systems introduce additional higher harmonic control inputs into the conventional swashplate to attempt to minimize NP vibrations as measured by accelerometers located in the helicopter cockpit and cabin. Although receiving considerable attention over a period of 25 years, HHC has yet to be incorporated into production aircraft. Some of the major impediments are the excessive hydraulic power requirements of HHC (Ref 10) and concerns that high frequency operation of the main rotor servos may potentially cause excessive wear to this flight critical system. A similar approach commonly referred to as individual blade control (IBC) utilizes active pitch links instead of the conventional swashplate to oscillate the blade (Ref 13). This approach has some advantages over HHC such as enabling greater control over the blade motions, but suffers from the same drawbacks of high power consumption and, in this case, being in series with the primary flight control system of the helicopter. A third approach, commonly known as active blade control (ABC), utilizes control surfaces such as trailing edge flaps on the blade to affect the blade motion (Ref 13). Moving a flap requires an order of magnitude less power than oscillating the entire blade, and does not use components of the primary flight control system. This approach offers significant promise of providing significant vibration reduction, in addition to possibly reducing the helicopter radiated noise signature and enhancing performance. However, there are many technological barriers that must be overcome before this approach can be implemented on a production helicopter.

For implementation on production aircraft, several criteria should be met by an AVC system. It must: 1) reduce aircraft vibration more effectively and over a greater range of flight conditions than passive systems; 2) result in a lower weight penalty that passive systems; 3) have low energy consumption; 4) be based on proven, reliable technology; and 5) have reasonable life-cycle costs.

One AVC approach that seems to fulfill these criteria is derived from the active control of structural response (ASCR™) method. ACSR, developed by Westland Helicopters Ltd.

(Refs. 14-15), places its actuation between two hardpoints in the fuselage to produce equal and opposite forces between these two hardpoints. The ACSR approach utilizes these dual-point actuators to minimize the response of the fuselage to the NP vibratory loads. In the case of the production ASCR system for the Westland/Agusta EH101 helicopter (Ref. 15), dual-point actuators are integrated into four of the struts supporting the main gearbox.

Unlike the EH101, Sikorsky Aircraft helicopters such as the UH-60 bolt the main gearbox directly to the airframe instead of using struts. As a consequence, ACSR dual-point type actuators are not applicable. The AVC actuator configuration discussed in this paper, and flight-tested on the UH-60 (Ref. 16), utilized single-point inertial actuators mounted at various locations in the helicopter fuselage. Unlike dual-point actuators that produce a force on the fuselage by actuating between two fixed points, single-point inertial actuators produce a force by oscillating a reaction mass that is free to vibrate. In general, to develop large forces either a large reaction mass or a large stroke of the mass is required. These two approaches, however, are neither weight efficient or power efficient. In the former case the system mass is excessive, and in the latter case the power consumption is excessive.

The single-point actuators used in the flight test, termed servo-inertial force generators (SIFGs), solved this problem by utilizing a mechanical resonance and a novel inner-loop electronic control system. Tuning the SIFGs to be near the NP frequency minimizes the required mass and power to achieve a given vibratory force output. The SIFG actuation system was designed and developed by Moog Inc. The SIFGs are devices that integrate a Sikorsky UH-60 passive vibration absorber with a hydraulic servo-actuator. The moving mass of the absorber is usually connected to the helicopter structure via three leaf springs. However, by inserting a hydraulic actuator between the structure and the middle spring, the passive vibration absorber is transformed into an active device. A schematic of the SIFG is shown in Fig. 4. Since the SIFGs were based on a modification of the passive absorber, they were capable of operating in two different modes – a passive mode (i.e., hydraulics off) in which they operated like a traditional tuned passive absorber, and an active mode in which the hydraulic actuator drives the SIFG to a desired force output. Each SIFG was capable of generating +/- 1500 lbs at NP.

A schematic of the AVC system flight tested on the UH-60 is shown in Fig. 5. The AVC system utilizes accelerometers distributed throughout the cockpit/cabin as feedback control sensors, as shown in Fig 5. The tuned passive absorber typically installed in the cabin overhead just forward of the main gearbox and in the helicopter nose were removed and two SIFGs were installed in the cabin overhead. The SIFGs could be operated in passive mode to operate just like the passive absorbers, or alternatively, operated in active mode as part of an AVC system. When in active mode, a closed-loop controller utilizes feedback from the accelerometers to determine the optimal SIFG commands to minimize the NP vibrations.

3 CONTROL ALGORITHM

The algorithm used in the ANC and AVC systems is based upon that developed by Sikorsky Aircraft and United Technologies Research Center for helicopter higher harmonic control (HHC) of rotor vibrations (Ref 17-18). In this approach the disturbance frequency is obtained from a tachometer sensor, a harmonic analyzer is used to identify the desired tonal information (i.e., magnitude and phase of frequency components of interest), and a minimum variance control algorithm is used to generate control signals based on an estimate of the plant transfer function. In Ref. 19, numerous approaches for tonal control are described, and

the connection between the underlying approach used for HHC, and other tonal control approaches, is illustrated.

In the narrow bandwidth required for control about each tone, the actuator/sensor transfer function is roughly constant, and thus the system can be modeled in the frequency domain as linear time-invariant using a single quasi-steady transfer function matrix, denoted by T. The derivation of the control algorithm given below follows from Refs. 17-18 and is described more fully in Ref. 4. Assuming linearity, the change in the sensor response vector z due to a change in the actuator command vector u can be written as a local model:

$$\Delta z = T\,\Delta u + w$$

The control law is derived to minimize the quadratic performance index:

$$J = z^T z + u^T W_u u + (\Delta u)^T W_{\delta u} (\Delta u)$$

that is a weighted sum involving the squared magnitudes of the sensor measurements, control commands, and rates-of-change of control. Substituting the local system model into the above expression and solving for the control u which minimizes J yields:

$$u_{k+1} = u_k - Y_k(W_u u_k + T_k^T z_k); \quad Y_k = (T_k^T T_k + W_u + W_{\delta u})^{-1}$$

The subscript k has been added to indicate the recursive nature of the feedback control algorithm resulting from the introduction of control rate weighting. The matrix Y_k determines the rate of convergence, but does not affect the steady state solution (Ref. 4). Greater control over the stability of the above control law is obtained with a step-size multiplier $\beta<1$:

$$u_{k+1} = u_k - \beta Y_k(W_u u_k + T_k^T z_k)$$

The behavior of the above control law is described in detail in Ref. 4.

4 FLIGHT TEST SETUP AND PROCEDURE

Active Noise Control

Two ANC flight tests were conducted on a Sikorsky S-76B commercial helicopter with a nominal gross weight of 10,000 lbs. The first flight test, conducted in 1995, is the first known successful flight test of a high frequency gear-mesh ANC system on a helicopter. The primary focus of this developmental flight test was proof-of-concept and architecture validation. The second flight test, conducted in 1996-97, focused on validating the pre-production ANC algorithms and architecture, and determining system requirements and performance tradeoffs for production.

The aircraft was equipped with a partial utility interior consisting of only the cabin ceiling and sidewall trim panels. A total of 64 microphones were distributed throughout the cabin interior, with the majority mounted on the cabin ceiling. Several microphone configurations were evaluated during the flight tests. A schematic of a typical microphone configuration tested is shown in Fig. 6.

Proof-mass actuators were bolted to each side of the transmission beams. The actuators were located on the beams as close to the gearbox mounting points as possible, since this is where the gear-mesh vibrational energy enters the airframe. Extensive ground testing validated that this approach was capable of achieving greater than 20dB tonal noise reductions. This method of mounting the actuators on the transmission beams is considered a viable approach for retrofitting an ANC system on current helicopter production lines and aircraft already in service.

The ANC flight tests included conditions such as: (1) ground runs at flat pitch (Q ~ 15%) and light-on-wheels (Q ~ 45%); (2) out-of-ground effect (OGE) hover; (3) steady flight ranging from 40 knots to V_{CR} at 145 knots, up to V_H at ~155 knots; and (4) transient maneuvers such as takeoffs, accelerations, turns, autorotations, decelerations, approaches and flares to landing.

Active Vibration Control

The AVC testing was performed on a UH-60 BlackHawk that was ballasted to 16,800lbs. The UH-60 is a four-bladed helicopter with a nominal rotor speed of 258 rpm, yielding a NP frequency of 17.2 Hz. The two baseline UH-60 tuned passive absorbers were removed and the resulting NP vibrations were measured in flight to establish a baseline. Two SIFGs were then installed in the cabin overhead just forward of the main gearbox (see Fig. 7). Accelerometers were installed at ten locations on the cockpit-cabin floor, as shown in Fig. 7, in both the vertical and lateral directions. Ten of these accelerometers, 8 in the vertical direction and 2 in the lateral direction, were selected as AVC feedback sensors.

Several flights were performed with the SIFGs operating in both passive and active mode to evaluate the benefits of AVC over conventional passive vibration reduction. The performance of the AVC system was evaluated in steady level flight at various airspeeds and rotor speeds, and during maneuvering flight.

5 FLIGHT TEST RESULTS

Active Noise Control – First Flight Test

All results presented for the ANC flight tests are for the reductions achieved in the primary bull gear tone (778Hz) of the S-76. A typical time history of gear-mesh tonal noise when the ANC system is activated, and then deactivated, is shown in Fig. 8 for an OGE hover condition. The quantity plotted in the figure represents the average reduction achieved on 24 controlled microphones. As shown in the figure, an average reduction of 9dB was achieved in the primary gear tone within 10 seconds of the ANC system being activated.

Similar reductions to those shown in Fig. 8 were achieved over a wide range of steady flight conditions, as shown in Fig. 9, with tonal reductions of 7-9dB over this speed range, including 8dB at V_{CR}. The two curves plotted in Fig. 9 represent the average gear tone level at the 24 controlled microphone locations with ANC "off" (upper curve) and with the ANC system "on" (lower curve), for various steady airspeeds.

Though the performance of the ANC system during this first flight test was sufficient to validate the system architecture for proof-of-concept, the noise reductions were much poorer than the 20dB expected based on extensive ground testing of the ANC system. Post-flight simulations based on T-matrix and ambient measurement data collected during the flight test indicated that much greater reductions should have been achieved with the architecture

implemented. Analysis of flight test data revealed excessively poor signal-to-noise ratios during the system identification procedure used to construct the T-matrix. Thus, in preparation for the second flight test, a more sophisticated system identification procedure was developed which better accounted for the high background noise levels encountered during the flight test.

Active Noise Control – Second Flight Test

The new system identification method developed for the second flight test greatly improved the estimate of the T-matrix, which resulted in dramatic improvements in ANC performance compared to the first flight test in all conditions tested, including ground runs, hover, steady forward flight, and transient maneuvers such as speed sweeps. It should be noted that all the results presented in this section were obtained using a PC-based ANC system. This system was utilized more extensively than the prototype ANC computer since the PC-based system was capable of controlling a greater number of microphones, which is more representative of the planned production version of the ANC system.

Typical noise reductions at the various microphone locations in an OGE hover condition are shown in Fig. 10. This figure shows an average reduction of 18dB on the 36 controlled microphones, compared to only 9dB on 24 microphones achieved during the first flight test (Fig. 8). It is interesting to note from Fig. 10 that the maximum tonal noise level measured in the cabin was 23dB lower with the ANC system "on" than with the ANC system "off". This is a very substantial improvement. The gear-mesh tonal reductions achieved in all steady flight conditions are very similar to those shown in Fig. 10; the OGE hover case was selected for presentation as a critical ANC condition due to the relatively high gearbox torque and resulting high gear-mesh noise levels in this condition.

Further examination of Fig. 10 reveals some interesting qualities of the noise reductions which are very noticeable to a passenger in the helicopter cabin, but may not be evident from a casual examination of the figures. The high degree of spatial variation in the ambient noise levels (i.e., with ANC "off") with microphone position should be noted in Fig. 10. For example, there is about a 20dB difference in the ambient tonal noise level between microphones 9 and 10, even though they are only about one foot apart. This spatial variation is quite evident to passengers whenever they move their heads, even for small motions, e.g. when just leaning forward. With the ANC system activated ("on") however, this spatial variation is significantly reduced, as shown in the figure. Due to the reduced overall noise levels, this reduced spatial variation is almost imperceptible to passengers, even when moving about the cabin.

ANC performance was substantially improved over the entire flight envelope, including speed sweeps from hover to V_H, compared to results obtained during the first flight test. As shown in Fig. 11, average gear-mesh tonal noise reductions of 14-16dB were achieved during a quasi-steady speed sweep, compared to typical reductions of only 7-9dB obtained during the first flight test (Fig. 9).

Also included in Fig. 11 is the ANC performance during a transient maneuver consisting of a typical acceleration from OGE hover to V_H, followed by a deceleration back to hover. It should be mentioned that the acceleration commenced immediately after take-off to hover without waiting for the ANC system to fully converge to a steady state solution. This was done to simulate actual flight procedures. As shown in Fig. 11, the ANC system not only remained stable, but maintained 8-14dB reductions relative to steady state ambient levels during the acceleration phase, and 12-14dB reductions during the deceleration phase. During accelerations, the actual ambient gear tone levels (not shown on the figure) are typically ~3dB

higher than steady flight levels due to the higher torque loads required from the gearbox. Conversely, ambient gear-mesh tonal levels are generally ~3dB lower during decelerations due to reduced gearbox torque requirements.

A typical time history of ANC performance is shown in Fig. 12 for steady flight at 120 knots. The quantity plotted in the figure represents the average reduction achieved on the 36 controlled microphones. As is evident from the figure, the controller achieved a 10dB noise reduction after three seconds, a 12dB reduction after five seconds, and then slowly converged to a steady 16dB noise reduction after 30-40 seconds. Faster convergence rates (i.e., higher controller bandwidths) were also tested without driving the controller unstable. However, these faster rates had no impact on ANC performance during steady flight conditions, and produced only minimal improvements in performance during transient maneuvers such as that shown in Fig. 11.

Active Vibration Control

The NP vibration results for 145 knots and 100% Nr are shown in Fig. 13. The three bars in the figure for each of the ten accelerometer locations represent a comparison of the ambient vibration, passive vibration control, and active vibration control cases. Also shown in the figure is a comparison of the average value of the ten accelerometers for the three cases. As expected, the AVC levels shown in Fig. 13 are lower than for the ambient case, but more significantly, these levels are substantially better than the passive case. This is a crude indication that AVC is more efficient than passive vibration control, i.e. that lower vibrations can be achieved for the same or lower weight. Especially interesting is that the vibration reductions are global in nature, i.e. reductions are realized at the forward cabin accelerometer locations which are not part of the AVC feedback sensor suite.

A global measure of the aircraft vibration is the average vibration level defined as the root-mean-square of the NP vibration magnitudes measured by the cockpit-cabin accelerometers. The average vibration measured at 12 accelerometer locations (10 AVC and 2 midcabin accelerometers) are plotted in Fig. 14 for a forward speed sweep at 100% Nr. Notice that the average NP vibrations are dramatically reduced over the entire range of flight speeds, and that the AVC reductions are significantly better than the passive case.

As discussed previously, one major advantage of AVC over passive systems is their ability to adapt to changing rotor speeds. The passive system on the UH-60 aircraft is a fixed tuned vibration absorber system optimized to a rotor speed of 100% Nr. A comparison between the passive and AVC system performance versus rotor speed is shown in Fig. 15. The classical "bucket" is shown for the passive system, i.e. the vibration is a minimum at 100% Nr. In contrast, the AVC system can readily follow the rotor speed variation, producing a virtually flat response. Of special interest is that the AVC case yields lower vibration levels than passive at 100% Nr. This is further confirmation that AVC can be more efficient than passive methods. Of course the SIFG hydraulic actuators must work harder as the Nr departs from 100%, but sufficient hydraulic power is available over the typical range of rotor speeds.

Sikorsky S-92 AVC

Encouraged by the SIFG flight test on the UH-60, a trade-off study of AVC versus tuned passive vibration absorbers was performed during the preliminary design phase of the S-92, and the decision was made to include the AVC system as baseline on all S-92 aircraft. The results of the trade study indicated that an AVC system would provide a lighter-weight

solution than a comparable tuned passive absorber system. Furthermore, an AVC system of comparable weight to a passive system would provide greater vibration reduction.

The S-92 began development flight testing in December 1998 and included an AVC system from first flight. Typical AVC performance is plotted in Fig. 16 for a steady Vcruise condition. The plot compares the NP vibration levels with AVC off and AVC on at 10 accelerometer locations in the cockpit-cabin. The AVC system is similar to the SIFG system, except that the SIFGs have been replaced with purely mechanical actuators referred to as force generators (FGs). The results shown in Fig. 16 were obtained with 3 FGs. It should be noted that the FG locations flight tested so far are trial locations only and are most likely not optimal. But as shown in the figure, AVC achieves substantial vibration reduction in cruise. Developmental flight testing of the AVC system on the S-92 will continue through 1999 and 2000 and will focus on optimizing the FG locations with the goal of maximizing vibration reduction for systems with one, two or three FGs.

6 CONCLUDING REMARKS

Active Noise Control

An approach for actively controlling high frequency structure-borne tonal noise in helicopters has been validated in a flight test program on the S-76 aircraft. Structural actuation near the gearbox mounts has been used to cancel the disturbance before it enters the airframe. This approach has been successfully demonstrated to produce substantial reductions in the primary gear-mesh tone of the helicopter, over a wide range of flight conditions. These reductions have bee maintained during maneuvers such as typical accelerations and decelerations with good system stability. Application of this ANC technology will provide noise suppression and create a quieter passenger environment.

Active Vibration Control

AVC systems using single point actuators is a viable vibration reduction technology. The system uses minimal power due to the resonant behavior of the SIFGs and can revert to a passive absorber in the event of a controller failure. A global vibration metric shows that AVC is more efficient than passive systems for a wider range of forward speeds and rotor speeds. AVC systems have the capability to adapt to changes in helicopter loading and rotor speed whereas traditional passive tuned absorbers cannot. AVC technology, properly integrated with traditional passive vibration reduction systems, offers promise of yielding a significant improvement in helicopter vibration levels.

7 REFERENCES

1. Elliott, S.J., Nelson, P.A., Stothers, I.M., and Boucher, C.C., In-flight experiments on the active control of propeller-induced cabin noise, Journal of Sound and Vibration, (1990) 140(2), pp. 219-238.
2. Boucher, C.C., Elliott, S.J., and Baek, K.H., Active control of helicopter rotor tones, Inter-noise '96, pp. 1179-1182.
3. Nelson, P.A., and Elliott, S.J., Active Control of Sound, Academic Press Limited, 1992.

4. MacMartin, D.G., Davis, M.W., Yoerkie Jr, C.A., and Welsh, W.A., Helicopter Gear-Mesh ANC Concept Demonstration, Active '97, Budapest - Hungary, August 1997, pp. 529-542.
5. Millott, T.A., Welsh, W.A., Yoerkie, C.A., MacMartin, D.G., Davis, M.W., Flight Test of Active Gear-Mesh Noise Control on the S-76 Aircraft, Proceedings of the 54th American Helicopter Society Annual Forum, Washington, D.C., May 1998.
6. Elliott, S.J., "Active Control of Structure-Borne Noise", Journal of Sound and Vibration (1994) 177(5), 651-673.
7. Sutton, T.J., Elliott, S.J., Brennan, M.J., and Heron, K.H., Active isolation of noise transmission through a helicopter gearbox support strut using multiple magnetostrictive actuators, 1996 International Conference on Noise and Vibration Engineering, Leuven, Belgium, pp.315-328, 1996.
8. Yoerkie Jr., C.A., Welsh, W.A., and Sheehy, T.W., Helicopter Active Noise Control System, US Patent Number 5,310,137, May 1994.
9. Veca, A.C., Vibration Effects On Helicopter Reliability and Maintainability, USAAMRDL Technical Report 73-11, April 1973.
10. Miao, W., Kottapali, S.B.R., Frye, H.M., Flight Demonstration of Higher Harmonic Control (HHC) on S-76, Proceedings of the 42nd Annual Forum of the American Helicopter Society, Washington, D.C., June 1986.
11. Achache, M., Polychroniadis, M., Higher Harmonic Control – Flight Tests of an Experimental System on the SA349 Research Gazelle, 42nd Annual Forum of the American Helicopter Society, June 1986.
12. Welsh, W.A., Higher Harmonic and Trim Control of the X-Wing Circulation Control Wind Tunnel Model Rotor, Proceedings of the 45th Annual Forum of the American Helicopter Society, Boston, MA, May 1989.
13. Friedmann, P.P., Millott, T.A., Vibration Reduction in Rotorcraft Using Active Control: A Comparison of Various Approaches, Journal of Guidance, Control, and Dynamics, Vol. 18, No. 4, July-August 1995.
14. Staple, A.E., An Evaluation of Active Control of Structural Response as a Means of Reducing Helicopter Vibration, 15th European Rotorcraft Forum, September 1989.
15. Staple, A.E., Wells, D.M., Development and Testing of an Active Control of Structural Response System for the EH101 Helicopter, Proceedings of the 16th European Rotorcraft Forum, September 1990.
16. Welsh, W., Frederickson, C., Rauch, C., Lyndon, I., Flight Test of an Active Vibration Control System on the UH-60 BlackHawk Helicopter, Proceedings of the 51st Annual Forum of the American Helicopter Society, Fort Worth, TX, May 1995.
17. Taylor, R.B., Farrar, F.A., and Miao W., "An Active Control System for Helicopter Vibration Reduction by Higher Harmonic Pitch," AIAA paper No. 80-0672, American Helicopter Society 36th Annual Forum, Washington D.C., May 1980.
18. Davis, M.W., "Refinement and Evaluation of Helicopter Real-Time Self-Adaptive Active Vibration Controller Algorithms", NASA Contractor Report, UTRC Report R83-956149-16.
19. Sievers, L.A., and von Flotow, A.H., Comparison and Extensions of Control Methods for Narrow-Band Disturbance Rejection, IEEE: Transactions on Signal Processing, Vol. 40 No. 10, October 1992.

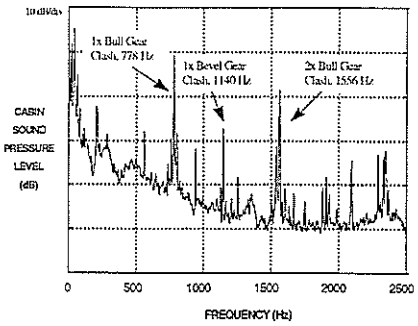

Fig. 1 Interior noise spectrum (unweighted) of a S-76 helicopter

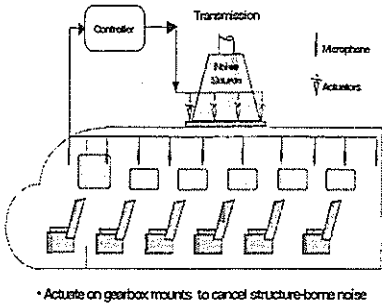

Fig. 2 Control architecture for helicopter gear-mesh ANC

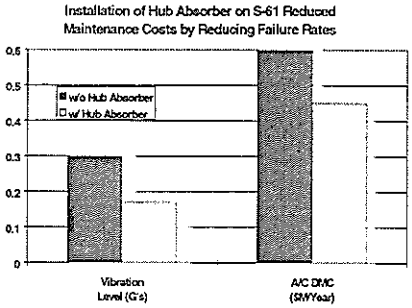

Fig. 3 Impact of hub absorber on vibrations and maintenance costs

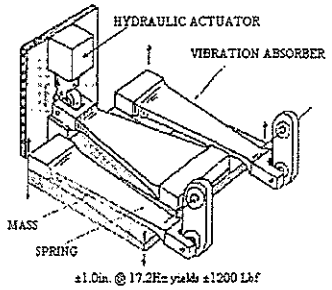

Fig. 4 Servo Initial Force Generator (SIFG)

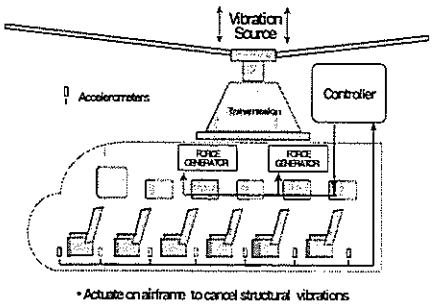

Fig. 5 Control architecture for AVC

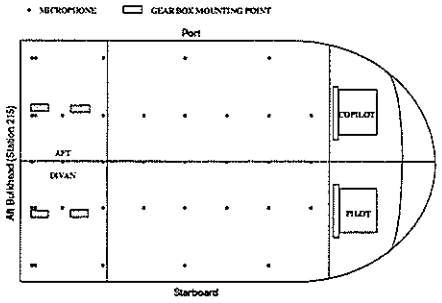

Fig. 6 Typical arrangement of feedback control mics used in S-76 ANC

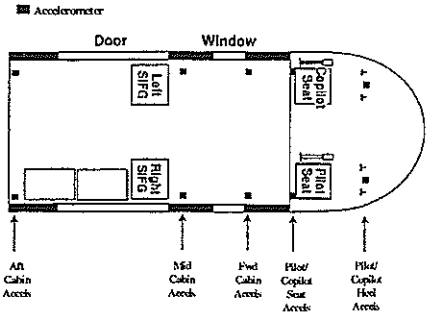

Fig. 7 AVC aircraft installation in a Sikorksy UH-60

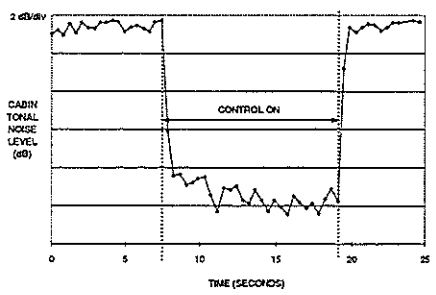

Fig. 8 Typical gear-mesh ANC performance time history in OGE hover.

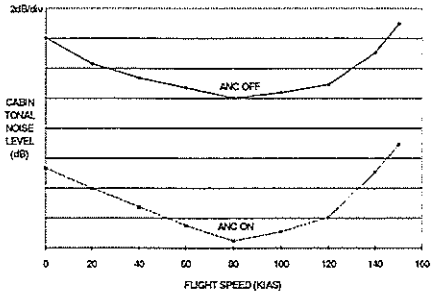

Fig. 9 ANC performance achieved during quasi-steady speed sweep.

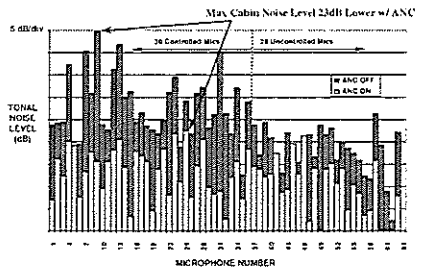

Fig. 10 ANC achieves 18 dB average reductions in OGE hover.

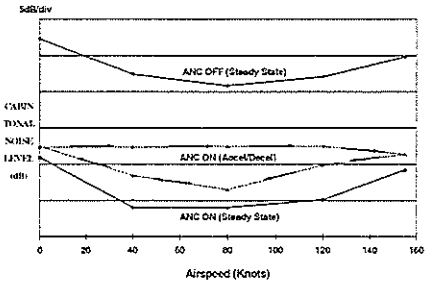

Fig. 11 ANC performance during quasi-steady & transient speed sweep.

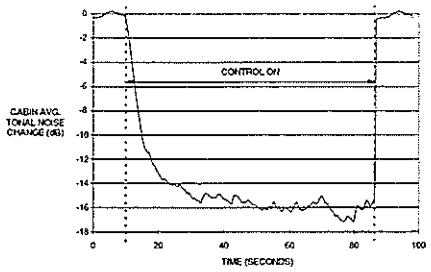

Fig. 12 Typical time history of gear-mesh ANC performance at 120 knots.

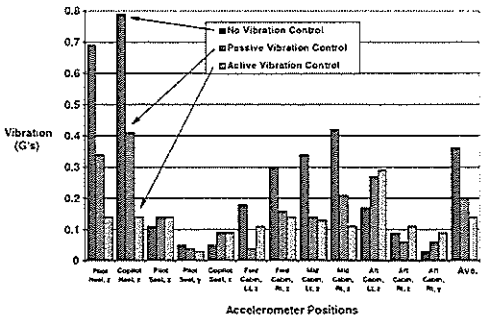

Fig. 13 SIFG vibration reduction during steady flight at Veruise

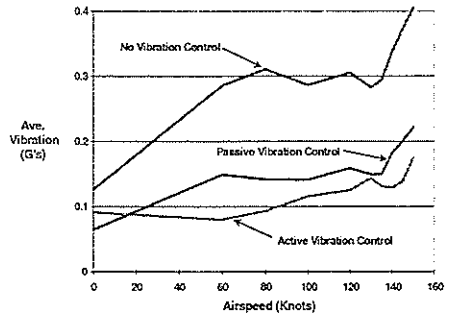

Fig. 14 SIFG vibration reduction during a speed sweep at 100% Nr

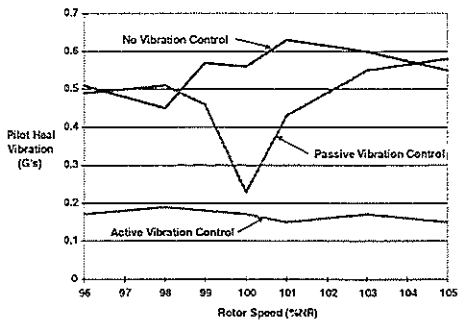

Fig. 15 SIFG performance versus rotor speed

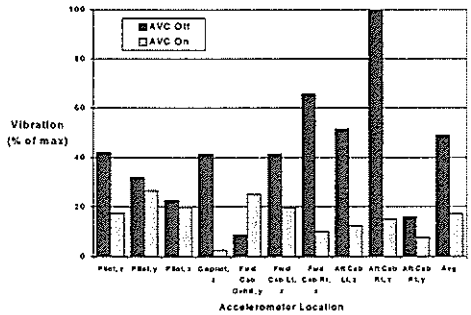

Fig. 16 S-92 AVC performance at Veruise

TWENTY-FIFTH EUROPEAN ROTORCRAFT FORUM

Paper no. G24

THE USE OF DISCRETE OBSERVER THEORY TO TRIM AND STABILIZE PERIODIC COEFFICIENT DYNAMIC SYSTEMS

BY

MICHAEL H. PETERS
Graduate Research Assistant

PHILIP V. BAYLY
Associate Professor

DAVID A. PETERS
McDonnell Douglas Professor
and Chairman

DEPARTMENT OF MECHANICAL ENGINEERING
WASHINGTON UNIVERSITY
ST. LOUIS, MO 63130 USA

SEPTEMBER 14-16, 1999
ROME
ITALY

ASSOCIAZIONE INDUSTRIE PER L'AEROSPAZIO, I SISTEMI E LA DIFESA
ASSOCIAZIONE ITALIANA DI AERONAUTICA ED ASTRONAUTICA

The Use of Discrete Observer Theory to Trim and Stabilize Periodic Coefficient Systems

by

Michael H. Peters
Graduate Research Assistant

Philip V. Bayly
Associate Professor

and

David A. Peters
McDonnell Douglas Professor and Chairman
Department of Mechanical Engineering
Washington University – Campus Box 1185
St. Louis, MO 63130

Abstract

The nonlinear differential equations for rotorcraft simulation (in this case, flap-lag-pitch and ground resonance equations) are sampled once a period (or once a blade passage) and the resultant sampled errors in periodicity and trim are considered a discrete system. The algebraic Riccati Equation is then used to design a controller to trim this discrete system. The resultant controller is applied to the original nonlinear simulation in that the errors at each blade passage are fed back to give discrete control changes. When all states cannot be measured, a discrete observer is used to estimate them. The resultant algorithm is shown to be a robust tool both for trimming and for stabilizing a nonlinear set of rotorcraft equations.

Notation

a	lift curve slope, /radian
[A]	matrix multiplying states in discrete system
$[A]_t$	modified matrix = $A - BG$
b	blade semi-chord, m
[B]	matrix multiplying controls in discrete system
c_d	blade profile drag coefficient
C_T	thrust coefficient, $T/\rho(\Omega R)^2 \pi R^2$
$[C_z]$	observer matrix
$[C(\psi)]$	damping matrix, period T
$d_k, \hat{d}$	desired constraint values
dpl	lag damper setting, percent critical damping
f_j	state-derivative functions
$f_\beta, f_\theta, f_\zeta$	generalized loads
$J_\beta, J_\theta, J_\zeta$	blade principal moment of inertia in flap, torsion, lag, $kg-m^2$
g_k	constraints
G_k	constraint integrand
$[J]$	Jacobian matrix
K_β	flap stiffness, N-m/rad
K_ζ	lag stiffness, N-m/rad
K_θ	pitch stiffness, N-m/rad
$[K(\psi)]$	stiffness matrix, period T
$[M]$	mass matrix
P	stiffness parameter for blade

	flap $1+K_\beta/\Omega J_\beta$
Q	number of blades
R	radius of rotor, m
T	period of system
V_i	induced flow, normal to disk
V_x	inplane flow of disk
V_z	normal flow to disk
x_j	state variables
Z_n	discrete states
β	flap angle positive flap and angle positive up, rad
β_0	coning angle, rad
β_s	lateral cyclic flap angle, rad
γ	Lock number $\rho acR^4/J_\beta$
$\Delta(\,)$	difference of ( )
θ_b	pilot pitch control $\theta_b=\theta_0+\theta_s\sin\psi+\theta\cos\psi$
θ_0	collective pitch angle
θ_s	longitudinal cyclic pitch angle
θ_c	lateral cyclic pitch angle
Θ_m	vector of controls
λ	inflow ratio, $(V_i+V_z)/\Omega R$
$[\Lambda]$	square matrix with eigenvalues on the diagonal
μ	advance ratio, $V_x/\Omega R$
ρ	density of air, kg/m^3
σ	rotor solidity, $Qc/\pi R$
ψ	rotor azimuth angle = Ωt, rad
Ω	rotor angular velocity, rad/sec
ω_ζ	dimensionless nonrotating lead-lag frequencies at $\theta=0,\sqrt{K_\zeta/\Omega^2 J_\beta}$
ω_θ	dimensionless nonrotating elastic pitch frequencies at $\theta=0,\sqrt{K_\theta/\Omega^2 J_\beta}$
$(\,)_n$	n-th iteration of vector

Introduction

The analysis of a rotary-wing system consists of three steps. First, one must assemble a set of ordinary differential equations that describes the physics of the system. Unlike modeling in many other technical disciplines, the equations so assembled are generally nonlinear, have periodic coefficients, and contain certain unknown parameters called "trim settings". It is the job of the analyst to solve these equations subject to a number of side constraints on the solution equal in number to the number of unknown parameters. Thus, the second step in a rotary-wing analysis is to find simultaneously the unknown parameters and the corresponding solution that satisfies these constraints. (This is called the "trim" solution.) The third step in the analysis is to analyze the stability of the solution about this periodic orbit. Many times, the solution strategy used to find the trim solution holds the key to the stability analysis.

There are several reasons that the trim solution is difficult. First, although there may be only a few trim variables (usually 3-7), there may be thousands of dynamic states. Thus, an iterative solution of the state-space equations for a periodic solution may be prohibitive. Second, there are often hidden states that occur due to the various mathematical algorithms that are used to evolve the system equations through time. Thus, the states may not be in the form to be interrogated numerically. Third, the periodic trim solution is often unstable (due to aeroelastic effects or due to flight mechanics modes) so that it is impossible simply to time-march until transients decay.

Recent work has found that, when all states are known and limited to a hundred or so, a very effective trim strategy is the discrete auto-pilot, Ref. [1]. Such an auto-pilot makes adjustments to the trim settings every blade passage based on an optimized gain and controller. Such a controller can fly even an unstable system to equilibrium and satisfy the trim constraints. Since a discrete auto-pilot does not change the poles of the system, it is perfect for a subsequent stability analysis, Ref. [2].

Despite the successes of such a system, it is still subject to the limitation that all

states must be known and that they must be limited to about one hundred. In this paper, we offer an alternative strategy designed for the case in which states are hidden. In particular, a discrete-time observer is created that gives an estimate of the hidden states that can be used in the discrete auto-pilot. This paper will describe how such an observer can be created and will give some simple examples for helicopter flap-lag-torsion stability.

The use of observers is not new to rotorcraft analyses, Refs. [3] and [4]; but this paper uses them in the sense of discrete systems and for mathematical trim and stabilization rather than real-time vibration control.

Mathematical Background

The nonlinear differential equations for a rotorcraft following general form:

$$\dot{x}_j = f_j\left(x_k, t, \Theta_m\right) \qquad (1)$$

where the x_j are the state variables, Θ_m are the trim parameters, and t is time. For every unknown trim parameter, there is a trim constraint of the form:

$$g_k \equiv \int_0^T G_k\left(x_i, t, \Theta_m\right)dt = d_k \qquad (2)$$

In general, states can be comprised of positions (displacement or rotations), rates, pressures, inflows, engine temperatures or pressures, damper states, etc. Trim variable can be collective and cyclic pitch position, throttle position, prescribed fuselage attitudes, RPM, or any unknown parameter in the equations. The trim constraints can be force or moment equilibrium, time averages or space averages of vehicle positions or velocities, etc. In trimming, one usually considers the equations to be linearized about some periodic equilibrium, $\bar{x}$ during each part of the design process. Thus, for simplicity, we consider the linearization of Eq. (1) about $\bar{x}_j$,

$$\left\{\dot{x}_j\right\} = \left[A(t)\right]\left\{x_j\right\} + \left[b(t)\right]\left\{\Theta_m\right\} \qquad (3)$$

where x_j are the new states which are perturbation states; and it is understood that $A(t)$ and $b(t)$ depend on $\bar{x}_j$. Equation (3) is never actually used in our trim algorithm, but it is an important conceptual tool.

The trim problem is to find the initial conditions $x_j(0)$ and trim parameters, Θ_m, that will result in a periodic solution to either Eq. (1) or Eq. (3) that satisfies the trim constraints. One way which has been tried in the past, Ref. [1], is to design an auto-pilot for the linear system in Eq. (3) that produces a Θ_m proportional to the current errors in the trim constraints. Three disadvantages of this approach are: 1) it produces unsteady $\Theta_m(t)$ when they should be constants, 2) it is hard to find a suitable auto-pilot since this requires solution of a periodic-coefficient Riccati Equation, and 3) the method cannot work if the system is unstable. References [1] and [2] have shown that this can be overcome with a discrete auto-pilot. In particular, if the system is sampled once a period, the errors in periodicity, $x(T) - x(0)$, and the errors in the trim constraints in Eq. (2), $e_k = g_k - d_k$, can be considered as a discrete system vector, Z_n

$$Z_{n+1} = A_n Z_n + B_n \Theta_n \qquad (4)$$

where n is an iteration index, not a vector subscript. Again, Eq. (4) is not actually used in the discrete auto-pilot, but it is a conceptual step that is used to understand how to design such an auto-pilot.

Naturally, it is important to know how the discrete matrices, A_n and B_n, relate to the continuous matrices, $A(t)$ and $B(t)$, or to perturbations of the original nonlinear system in Eq. (1). In particular, we consider how A_n and B_n would be related to the Jacobian matrix that would be formed by

making perturbations to an initial guess for the $x(0)$ and Θ_m.

The Z_n vector is defined as follows:

$$Z_n = \begin{Bmatrix} x_n - x_{n-1} \\ g_n - \hat{d} \end{Bmatrix} \equiv \begin{Bmatrix} \Delta x_n \\ e_n \end{Bmatrix} \qquad (5)$$

where g_n is the nth iteration on constraints, and $\hat{d}$ is the vector of desired constraint values. Next, one defines the following Jacobian matrix (J) for the linear system in Eq. (3). This Jacobian can be computed by time-marching with perturbations to x_j and Θ_m.

$$\begin{Bmatrix} x_{n+1} - x_n \\ g_{n+1} - \hat{d} \end{Bmatrix} = [J] \begin{Bmatrix} x_n \\ \Theta_n \end{Bmatrix} \qquad (6)$$

Here is exactly how A and B are computed from a given J. In general:

1) partition J according to x and Θ.

$$[J] = \begin{bmatrix} J_{xx} & J_{x\Theta} \\ J_{\Theta x} & J_{\Theta\Theta} \end{bmatrix} \qquad (7)$$

2) Rearrange the top partition of equation (6) to be in standard form

$$\begin{aligned} \{x_{n+1}\} &= [J_{xx} + I]\{x_n\} + [J_{x\Theta}]\{\Theta_n\} \\ \{x_n\} &= [J_{xx} + I]\{x_{n-1}\} + [J_{x\Theta}]\{\Theta_{n-1}\} \end{aligned} \qquad (8)$$

3) Subtract to obtain equations for errors in periodicity

$$\{\Delta x_{n+1}\} = [J_{xx} + I]\{\Delta x_n\} + [J_{x\Theta}]\{\Delta\Theta_n\} \qquad (9)$$

4) Similarly, consider that the constraint errors from equation (6) are

$$\begin{aligned} \{e_{n+1}\} \equiv \{g_{n+1} - \hat{d}\} &= [J_{\Theta x}]\{x_n\} + [J_{\Theta\Theta}]\{\Theta_n\} \\ \{\Delta e_{n+1}\} &= [J_{\Theta x}]\{\Delta x_n\} + [J_{\Theta\Theta}]\{\Delta\Theta_n\} \end{aligned} \qquad (10)$$

5) Recombine Eq. (9) into the form of Eqs. (4) and (5)

$$\begin{Bmatrix} \Delta x_{n+1} \\ e_{n+1} \end{Bmatrix} = \begin{bmatrix} J_{xx} & 0 \\ J_{\Theta x} & I \end{bmatrix} \begin{Bmatrix} \Delta x_n \\ e_n \end{Bmatrix} + \begin{bmatrix} J_{x\Theta} \\ J_{\Theta\Theta} \end{bmatrix} \Delta\Theta_n \qquad (11)$$

It is now clear that the partitioned matrices in Eq. (11) are the A_n and B_n of the discrete time model. Thus, one can find A_n and B_n from a numerical Jacobian of the original, non-linear time domain system.

Discrete Controller

What we would now like to do is to design a controller that produces changes to the controls at the end of every period (or blade passage) based on the errors in periodicity and trim constraints (i.e., the Z_n). In general, we would like a feedback law that would give

$$\Delta\Theta_n = -GZ_n \qquad (12)$$

If one can find an appropriate *gain* matrix G, then Eq. (4) would become:

$$Z_{n+1} = (A - BG)Z_n \qquad (13)$$

where $(A - BG)$ is designated A_r.

Although we plan to use $\Delta\Theta_n$ on the original continuous nonlinear equations to perturb the controls after every simulation of blade passage, we will design the controller G based on the *discrete* form in Eq. (4). We desire a G that places all of the eigenvalues of A_r less than unity and as close to zero as possible. Such eigenvalues will drive a difference equation to equilibrium. For linear systems, such a G can be found from an algebraic Riccati equation, Ref. [6]. Once A, B, and G are found, Eq. (13) is a feedback system the states of which converge to an equilibrium; thus, the thought experiment using the linear discrete system is over.

As the simulation runs, we sample the continuous system to obtain e_n and x_n and compare the sample with the previous sample to form a Δx_n. These form Z_n by Eq. (5). Equation (12) is then used to adjust the controls. It is important to keep in mind that x_n must be completely measurable in order for Eq. (12) to be used.

We now come to the consideration of what happens if some states cannot be measured or the case in which we can measure only certain combinations of the states. This can happen for either of two reasons. Either there are too many states to measure, or some states are truly hidden due to the nature of time-marching algorithm. For example, a pure time delay in a dynamic stall model or in a drive-train model has an infinite number of states, and they are all hidden. Another example would be when a structures code is linked to a CFD or free-wake code in which states are hidden in the "black box" that is the aerodynamic algorithm for generating induced flows. The idea here is to use an observer to estimate states that cannot be measured.

If we only know some of Z_k, say,

$$Y_k = C_z Z_k \tag{14}$$

we will make a new system in $\hat{Z}_k$ which will be an estimate of Z_k. The $\hat{Z}_k$ dynamic system should be a discrete, dynamic feedback system having a forcing function dependent on Y_k and that we can control such that $\hat{Z}_k = Z_k$ a time increases. In other words, we want to build a dynamic observer that will estimate $\hat{Z}_k$ given the measurements that are known, Y_k

$$\hat{Z}_k = A_c \hat{Z}_{k-1} + L Y_k \tag{15}$$

for some A_c and L. Thus, we have $\hat{Z}_k$ dependent on $\hat{Z}_{k-1}$ and Y_k.

Now replace Z_k in Eq. (14) above with $\hat{Z}_k$ such that all terms in Eq. (15) are $k-1$. This yields

$$\hat{Z}_k = A_c \hat{Z}_{k-1} + L C_z A_t Z_{k-1} \tag{16}$$

Now define $E_k = Z_k - \hat{Z}_k$ by Eqs. (4) and (16). After collecting Z_{k-1} terms, and setting:

$$A_c = A_t - L C_z A_t \tag{17}$$

we have

$$E_k = (A - L C_z A) E_{k-1} \tag{18}$$

All that is needed is to find an L which will minimize the eigenvalues of $A - LC_zA$. This can be done by eigenvalue placing or by a Riccati solution.

Now, the $\hat{Z}$ term can be used entirely in place of the Z term which could not be measured. Specifically, we use instead of Eq. (12)

$$\Delta\Theta_k = -G\hat{Z}_k \tag{19}$$

where $\hat{Z}_k$ is computed from Eq. (15).

For the case in which we want to stabilize the system (rather than trim it), the mathematics is identical. There are no trim constraints, and the θ_k become the controls used to stabilize. As the controller drives the solution toward a periodic solution, it will automatically stabilize it.

Mathematical Model

We are now ready to apply this theory to an actual case. In this study, we will use the rigid-blade, flap-lag-torsion equations for a rotor in forward light which implies 6 states. We assume quasi-steady aerodynamics and neglect reversed flow. For trim variables, we include collective pitch and the two cyclic pitch values. The corresponding trim constraints are the time-

averaged coning minus the desired value, and the time-averaged tip-path-plane tilts. Equations of motion for this system are based on Ref. [7], but with some corrections, and appear in the Appendix of Ref. [8].

To proceed with our methodology, an initial guess on controls and initial conditions is used to time march through one period for a baseline. Next, a Jacobian of perturbations is computed during which all states are measurable. Later, we will assume that, even if all states are not measurable for use in the feedback law, that the Jacobian is still available by some other method. $[A]$ and $[B]$ are computed from the partitioned $[J]$ as in Eq. (11). To find G , we tried two kinds of software. First, we tried using software which simply placed the eigenvalues of A_t. This resulted in an ill-conditioned G because such software works by first asking the user to input the exact desired placement of the eigenvalues of A_t, $[\Lambda]$, and then iteratively (by brute force) finding a G which satisfies the characteristic equation for the given $[\Lambda]$. This iterative algorithm in MATLAB, called "PLACE", created a matrix of very large numbers (order 1,000 or higher). Such an ill-conditioned G, when used in Eq. (12) tends to give huge $\Delta\Theta_n$.

An alternative approach is to do an optimal control in which the squares of controls and states are minimized over the iterations. The weighting functions of the errors and controls are set equal to unity for our work. The fact that states are in the objective function keeps the system stable. The fact that controls are in the objective function keeps the gains from becoming too large, as they do in eigenvalue placement. The result is a Riccati equation for G. The G computed by this Riccati solver is used as the feedback law in the discrete controller. The results work well in this application.

Next, we turn to creation of the observers. L must be computed by the same type Riccati method used to compute G for Eq. (12). The MATLAB command used here is called "DLQR."

Note that a Riccati solver may require that a matrix be in the form $A-BG$. Equation (18) is not in this form, however. Instead, we have the form $A-GB$. The equivalent system is $A^T-B^TG^T$ which can be "plugged into" the Riccati solver to yield a gain matrix which is the transpose of the G needed for $A-GB$. Also note that the MATLAB command "DLQR" does not work very well in this case because it does not accept non-square A's and B's. We therefore made a copy of the source code for DLQR in a new file, named it ndlqr (for New-DLQR), and changed it to work with non-square matrices. The math is the same as long as the dimensions agree, because the Riccati equation does not care if its arguments are square. The alternative is to put the non-square matrices from Eq. (20) into large square matrices the rest of which are just zeros.

Next, the simulation is started; and, after the n^{th} simulated blade revolution, a $\Delta\Theta_n$ is computed by Eq. (12) or Eq. (19). Then $\Delta\Theta_n$ is applied to the controls. This process is repeated until the error in the trim constraint is within certain parameters at which point the current controls are said to be approximately the "trim" control setting for the given system.

The above is similar to the development in Ref. [8] except that we have improved some of the derivations to give a better observer theory.

Results and Discussions

The equations of motion for all numerical experiments are given in Refs. [8] and [9]. The system of equations used for the numerical experiments were first run with the following constant parameters.

b/R	=	0.10
c_d/a	=	0.0016
dlp	=	0.10

P	=	$(1.05)^2$
σ	=	0.1
γ	=	5.0
μ	=	0.3
ω_ζ	=	0.49
ω_θ	=	14.1
C_T	=	0.003
J_ζ/J_β	=	1.01
J_Θ/J_β	=	.01

The above parameters yield an inherently stable system which simulates a helicopter in forward flight. In other words, even if there is not a closed-loop feedback control, the states will converge to a periodic flight path, although this equilibrium will probably not fulfill the trim constraints.

We begin with a discrete controller when all states can be measured. Figure 1 gives the error in trim constraints and the control settings as a function of iteration number. The first guess is identically zero. One can see that, after about 20 iterations, the system is trimmed; and the controls have reached their final values. Although not shown, the periodicity errors have also gone to zero. (Since these errors are in terms of radians of flapping angle, the final error of .001 is only .05 degrees.) This is typical of the trim convergence of a discrete auto-pilot with unity weighting matrices. In general terms, the control system is over-damped and could be improved by other weighting factors.

Next, we consider the same system but assume that we can measure only the trim-constraint errors. No states are assumed to be measurable. Thus, the C_z matrix is assumed to be a 9x3 matrix of all zeroes except for an identity at the far right. This makes the computation of the L for the observer very straightforward. The result is indistinguishable from that of Fig. 1. In other words, the direct measurement of states is not that important to the trim auto-pilot.

In the next case, we consider a system that is unstable. We switch to a stiff-inplane rotor $\left(\omega_\zeta = 0.70\right)$ at a higher advance ratio $\left(\mu = 0.4\right)$. We remove the lag damper (dpl = 0.10) and replace it with 1% negative damping (dpl = -.01). This gives a powerful flap-lag instability. We assume that only the three trim constraints can be measured. Thus, this is a case with an observer. Figure 2 shows the errors in trim constraints and the developing control settings. Also shown on the lower half of Fig. 2 are the evolving controls when all states are measured. Although the lack of state measurements causes some initial oscillations, the ultimate convergence is the same as when all states are measured. The convergence is also about the same as it was for the stable system, Fig. 1.

These results are much better than those previously published in Ref. [8] due to an improvement in the observer equations. The observer equations here are slightly different than those in Ref. [8].

In the next set of results, we apply the control to a 4-bladed ground resonance model. Thus, these are no trim side constraints; and the control to a periodic equilibrium is actually a stabilizing control to eliminate the ground resonance instability. Equations for the system can be found in Ref. [9]. The control is assumed to be an applied roll moment accomplished by force actuators at the base. It is assumed that only 2 of the twelve states can be measured, roll angle and pitch angle. Thus, an observer is used.

Figure 3 shows the resulting roll and pitch angles as well as the necessary control torque to achieve stabilization. Note that torque is discretely changed once per revolution. Figure 4 shows the motion (with the same step input in roll) when the controller is not used One can see the powerful ground resonance instability.

Summary and Conclusions

The method of discrete control with observer theory is applied to the problem of

numerical trim of a rotorcraft simulation. First, the general problem of rotorcraft trim is reformulated in a discrete-time framework. Second, we show how to do numerical perturbations of simulation code in order to find a Jacobian. Third, we show how to use the partitioned Jacobian to form the discrete-time system matrices. These can then be sent to standard Riccati tools to find the controller and the observer.

The methodology is applied to nonlinear, flap-lag-torsion equations for a rotor blade in forward flight and to ground resonance. The results shown that the above scheme can successfully trim both stable and unstable cases in the absence of all measurements. For stable cases, only the trim constraints need to be measured. For unstable cases, the method stabilizes the system.

Acknowledgment

This work was sponsored by the United States Army Research Office AASERT Grant No. DAAH04-96-1-011, Dr. Gary Anderson, Technical Monitor.

References

1. Li, Si-Hao and Peters, David A., "A Combined Periodic-Shooting, Auto-Pilot Technique for Rotorcraft Analysis," International Conference on Computational Engineering Science, Mauna Lani, Hawaii, July 30-August 5, 1995.
2. Schmitt, John M., Bayly, Philip V., and Peters, David A., "Stabilization of Periodic Flap-Lag Dynamics in Rotor Blades," AHS 2nd International Aeromechanics Specialists' Conference, Bridgeport, October 11-13, 1995.
3. Davis, Mark, "Development and Evaluation of a Generic Active Helicopter Vibration Controller," Proceedings of the 40th Annual Forum of the AHS, May 16-18, 1994.
4. Sopher, Robert and Hallock, Daniel, "Time-History Analysis for Rotorcraft Dynamics Based on a Component Approach," 2nd Decennial Specialists' Meeting on Rotorcraft Dynamics NASA Ames Research Center, Moffett Field, CA, November 1984.
5. Peters, David A., and Barwey, Dinesh, "A General Theory of Rotorcraft Trim," *Mathematical Problems in Engineering,* Vol. 2, 1996, pp. 1-34.
6. Ramirez, W. Fred, *Process Control and Identification,* Academic Press, Boston, 1994, Chapter 4.
7. Li, Si-Hao, *A Hybrid Periodic-Shooting, Auto-Pilot Method for Rotorcraft Trim Analysis,* Doctoral Dissertation, Washington university in St. Louis, May 1997.
8. Peters, Michael H. and Peters, David A., "Discrete Control Theory and Dynamic Observers Applied to Rotorcraft Stability and Trim," Proceedings of the 54th Annual Forum of the American Helicopter Society, Washington, D.C., May 20-22, 1998.
9. Powell, et. al, *A Modern Course in Aeroelasticity,* Kluwer Academic Publishers, Dordecht, The Netherlands, Third Revised Edition, 1995, pp. 400-411.

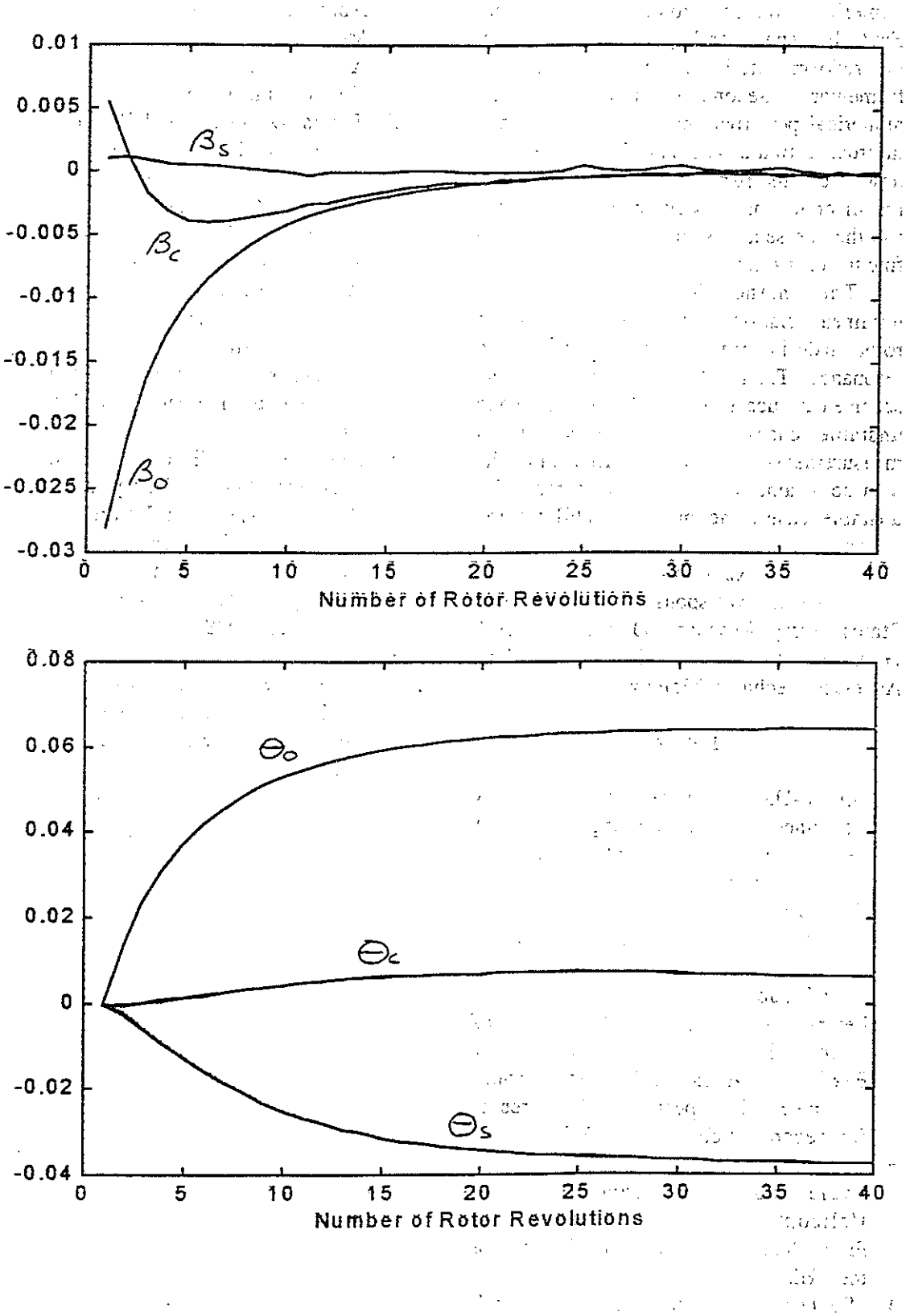

Figure 1. Trim Errors (top) and Controls (bottom) for Flap-Lag-Torsion.

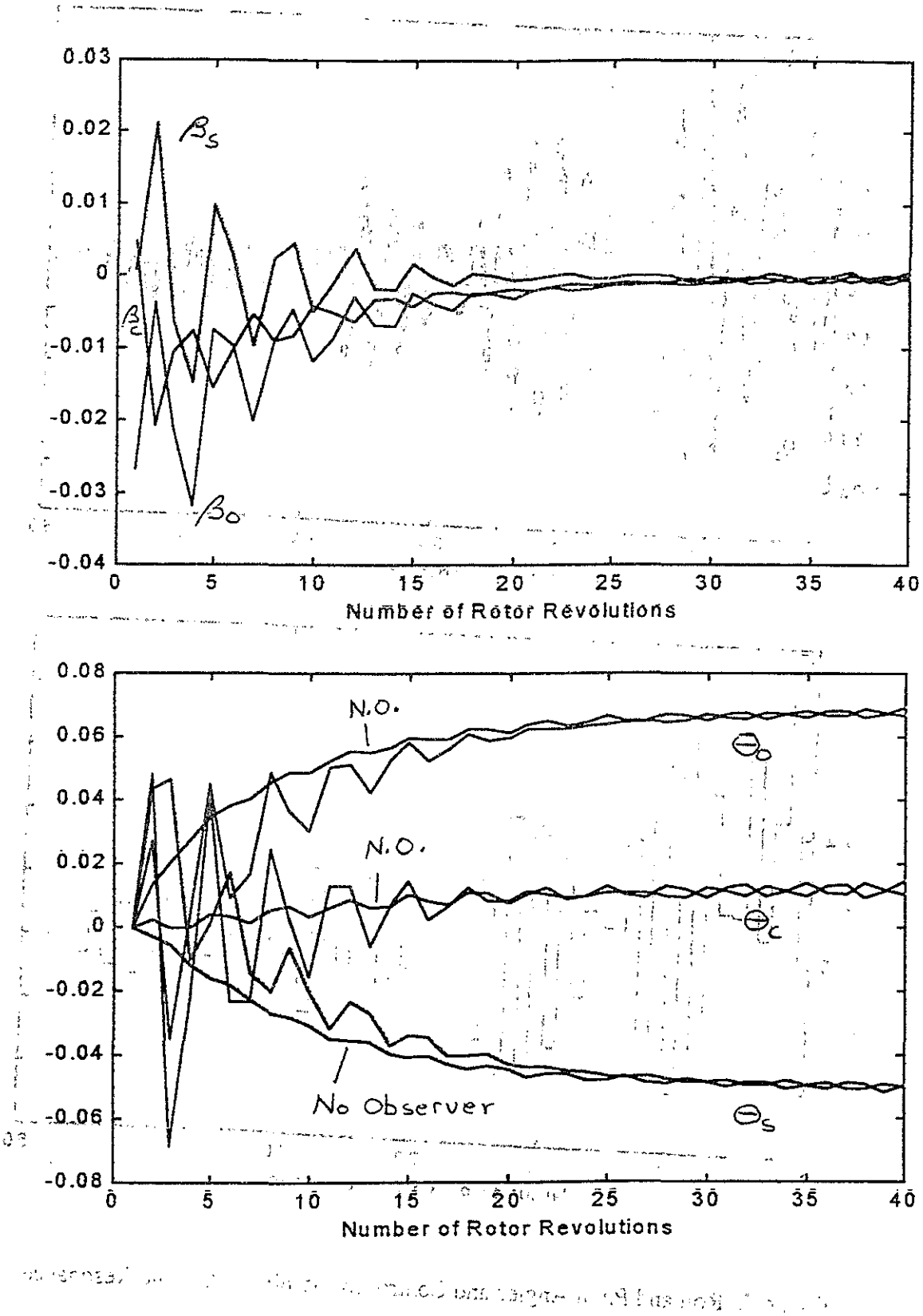

Figure 2. Trim Errors and Controls for Unstable F-L-T with Observer.
[Smoother curves on bottom are with all states measured.]

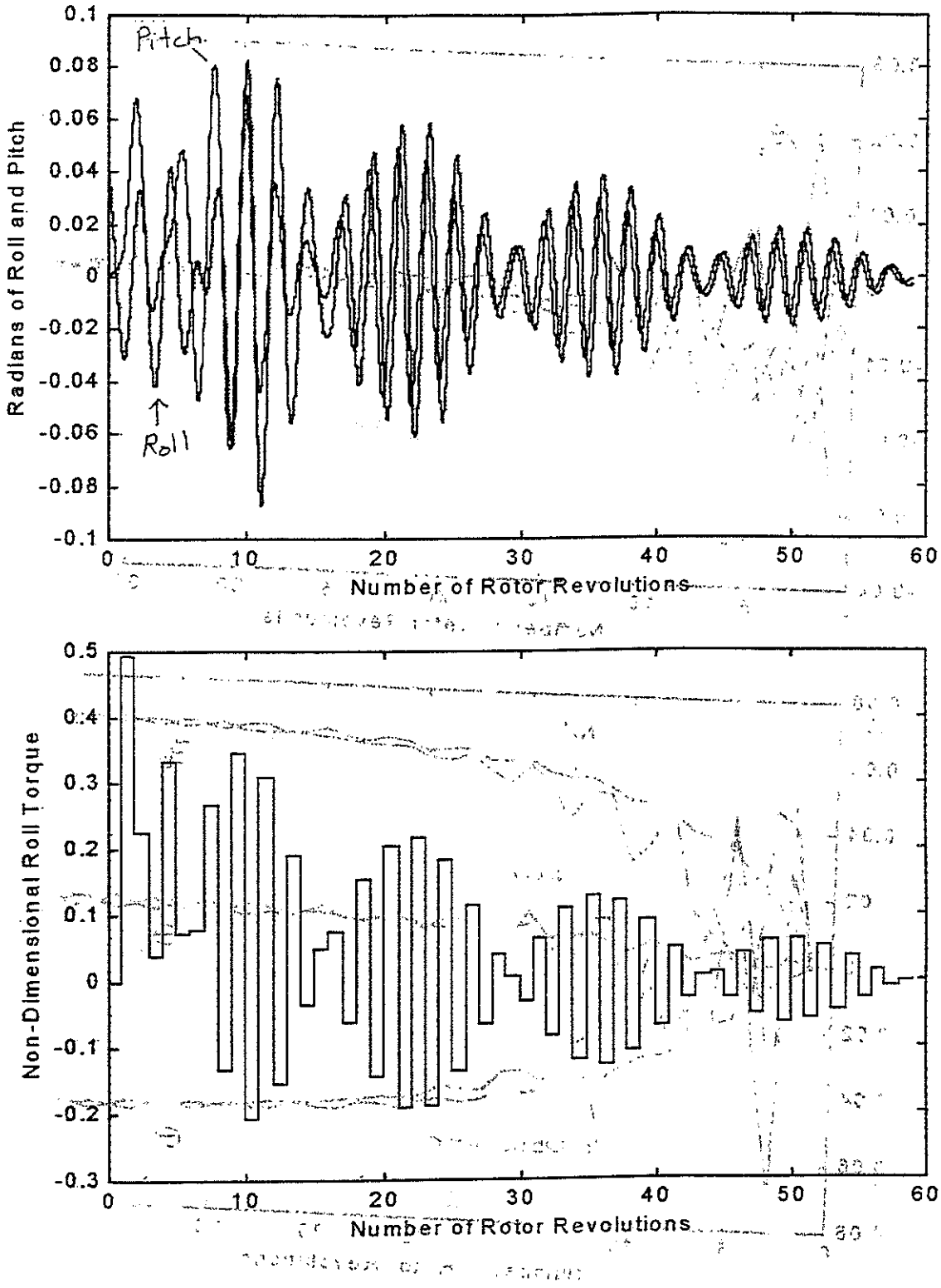

Figure 3. Roll and Pitch Angles and Control for Stabilized Ground Resonance.

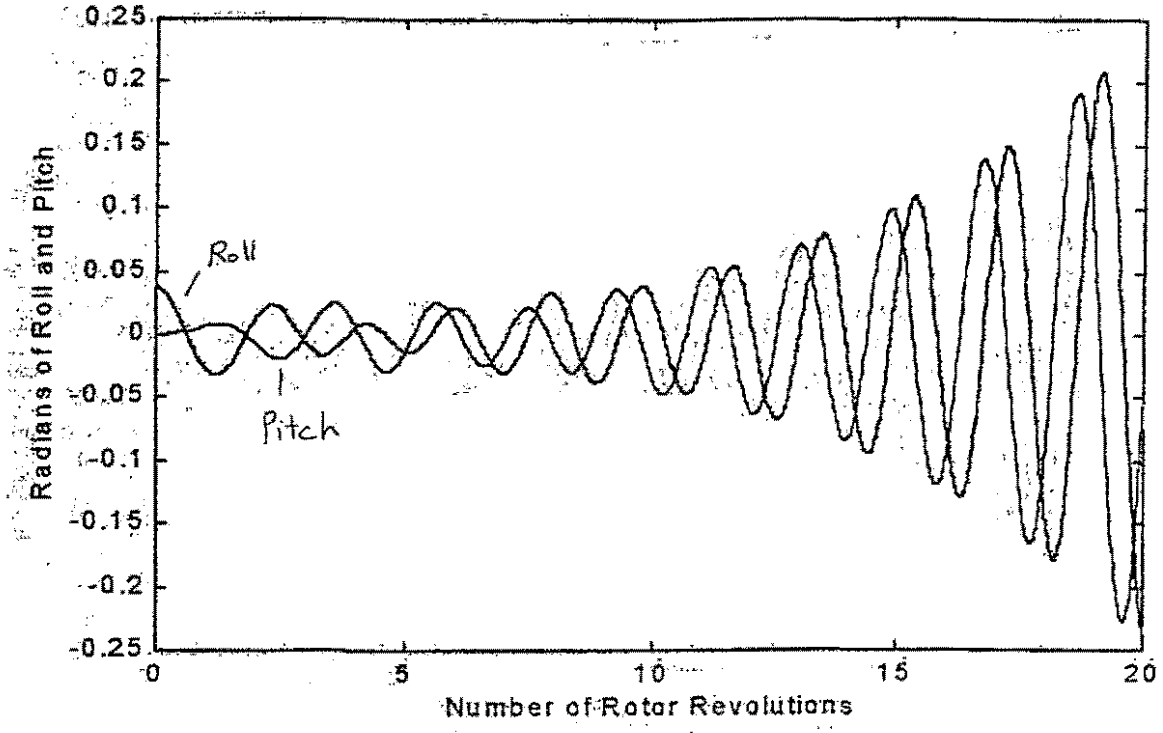

Figure 4. Roll and Pitch Angles for Ground Resonance Case with No Control.